Main group borohydrides as building blocks
Developing new synthetic methodologies to introduce phosphorus to p- and s-block compounds

Dissertation
zur Erlangung des Grades
des Doktors der Naturwissenschaften
der Naturwissenschaftlich-Technischen Fakultät der
Universität des Saarlandes

von
M. Sc. Sergi Danés Pibernat

Saarbrücken
2024

Tag des Kolloquiums: 30.09.2024
Dekan: Prof. Dr. -Ing. Michael Vielhaber
Berichterstatter: Dr. Diego M. Andrada
Prof. Dr. Dominik Munz
Prof. Dr. Pedro Salvador Sedano
Vorsitz: Priv. -Doz. Dr. André Schäfer
Akademischer Mitarbeiter: Prof. Dr. Gregor Jung

I

II

*"**És la creença en la figura del lluitador,***
*…**en la metàfora de la batalla**"*
Laura Moré

v

The present dissertation was prepared in the time between November 2019 and October 2023 at the Institute of General and Inorganic Chemistry of the Faculty of Natural Science and Engineering at Saarland University and the Institute of Computational Chemistry and Catalysis (IQCC) at Girona University in the groups of Dr. Diego M. Andrada and Dr. Pedro Salvador.

Die vorliegende Arbeit entstand in der Zeit von November 2019 bis Oktober 2023 and der Universitäat des Saarlandes am Institut für Allgemeine und Anorganische Chemie der Naturwissenschaftlich-Technischen Fakultäat und Universität des Girona der Institut für Computerchemie und Katalyse (IQCC) im Arbeitkreis von Dr. Diego M. Andrada und Dr. Pedro Salvador.

Aquesta dissertació ha sigut preparada a l'interval entre Novembre del 2019 i Octubre del 2023 a l'Institut de Química General i Inorgànica de la Facultat de Ciències Naturals i Enginyeria de la Universitat de Saarland i a l'Institut de Química Computacional i Catàlisis (IQCC) de la Universitat de Girona als grups de recerca de Dr. Diego M. Andrada i Dr. Pedro Salvador.

Acknowledgements

Abstract

The quest for multiple bonds between group 13 and group 15 elements has been pursued for decades due to their applications for materials with optoelectronic and semiconducting properties. This Thesis aims at finding new synthetic routes for the stabilization of Al=P bond. Our synthetic approach relies on an aluminium (III) precursor stabilised with a monoanionic *NacNac* ligand and different phosphorus(III) building blocks. We demonstrate that aluminium borohydrides are suitable synthons for nucleophilic substitutions, allowing the preparation of a new library of phosphanylalumanes. The isolated compounds are tested for β-elimination reaction aiming at the formation of the Al=P bond. We rationalize the role of the leaving group on aluminium to direct the synthesis towards the phosphaalumene.

Finally, we demonstrate that magnesium borohydrides are reagents for salt metathesis reactions to prepare phospha-Grignard reagents. We investigate the reactivity towards benzophenone, exploring the reaction mechanism by experimental and computational techniques.

Overall, in this Thesis, we introduce a new category of building blocks for main-group chemistry. We showcase that aluminium and magnesium borohydrides are suitable synthons for nucleophilic substitutions, particularly for the preparation of synthetically challenging bonds such as Al-P and Mg-P. The synergy between experimental and computational chemistry allowed us to direct the synthetic strategies to targeted motifs.

Zusammenfassung

Die Suche nach Mehrfachbindungen zwischen Elementen der Gruppen 13 und 15 hat die Aufmerksamkeit der anorganischen Chemie auf sich gezogen. Ihre isoelektronischen Verhältnisse zu Kohlenstoffverbindungen hat zur Herstellung von Materialien mit optoelektronischen und halbleitenden Eigenschaften geführt. Das Ziel dieser Arbeit ist es, Herstellung der neuen synthetischen Methoden, um die Al=P Doppelbindungen zu stabilisieren. Der synthetischer Ansatz beruht auf einer Aluminium(III)-Vorstufe, die durch einen monoanionischen NacNac-Liganden stabilisert ist und mit verschiedenen Phosphor(III)-Bausteinen substituiert ist. Zu Beginn wurde der Fokus auf die Synthese von Phosphanylalumanen gelegt, die durch ß-Eliminierung zur Bildung einer Al=P Doppelbindung führt.

Schließlich zeigen wir die Herstellung von Phospha-Grignard-Reagenzien von Magnesiumborhydride Reagenzien. Wir untersuchen die Reaktivität und erforschen den Reaktionsmechanismus mit experimentellen und theoretischen Methoden.

In dieser Arbeit, zeigen wir dass Aluminium- und Magnesiumborhydride geeignete Synthone für nukleophile Substitutionen sind, insbesondere für die Herstellung der Bindungen wie Al-P und Mg-P. Die Entwicklung dieser Synthesewege erfolgt auf synergetischer Weise, indem sowohl experimentelle als auch theoretische Bereiche der Chemie miteinander verknüpft werden.

Resum

La recerca dels enllaços múltiples entre els elements de grup 13 i grup 15 és d'interès per a les aplicacions per materials amb propietats optoelectròniques i semiconductores. L'objectiu d'aquesta Tesis és trobar noves rutes sintètiques per estabilitzar l'enllaç Al=P. L'estratègia sintètica es basa en sintons d'alumini(III) i diverses fosfines. Primerament, demostrem que els borhidrurs d'alumini són bons sintons per a addicions nucleòfiles, permetent preparar una nova llibreria de fosfanilalumans. Els compostos aïllats són sotmesos a β-eliminacions per generar l'enllaç Al=P, racionalitzant el rol del grup sortint. Finalment demostrem que els borhidurs de magnesi també poden ser reactius per a reaccions de metàtesis salina per preparar reactius de fosfa-Grignard. També investiguem la reactivitat amb la benzofenona explorant el mecanisme de reacció tant experimental com computacionalment.

En conjunt, aquesta Tesi introdueix un nou grup de sintons per a la química de grups principals. Demostrem que els borhidrurs d'alumini i magnesi es poden funcionalitzar amb nucleòfils neutres i aniònics, especialment per formar enllaços Al-P i Mg-P. La sinèrgia entre la química experimental i computacional ens ha permès dirigir i entendre les rutes sintètiques per aconseguir els estructures moleculars desitjades.

List of Publications

This thesis has been published in parts in:

- The Oxidation State in Low-Valent Beryllium and Magnesium Compounds. Martí Gimferrer‡, Sergi Danés‡, Eva Vos, Cem B. Yildiz, Inés Corral, Anukul Jana, Pedro Salvador, Diego M. Andrada. *Chem. Sci.* **2022**, *13*, 6583-6591. †These authors contributed equally to this work.
- Reply to the 'Comment on "The Oxidation State in Low-Valent Beryllium and Magnesium Compounds"'. Martí Gimferrer‡, Sergi Danés‡, Eva Vos, Cem B. Yildiz, Inés Corral, Anukul Jana, Pedro Salvador, Diego M. Andrada. *Chem. Sci.* **2023**, *14*, 384-392. †These authors contributed equally to this work.

Other publications:

- On the Bonding Situation in Stannocene and Plumbocene N-Heterocyclic Carbene Complexes. Sergi Danés, Carsten Müller, Lisa Wirtz, Volker Huch, Theresa Block, Rainer Pöttgen, André Schäfer, Diego M Andrada. *Organometallics* **2020**, *39*, 4, 516-527.
- A theoretical study of the hydrolysis mechanism of A-234; the suspected Novichok agent in the Skripal attack. Yadhav A Imrit, Hanusha Bhakhoa, Tetiana Sergeieva, Sergi Danés, Nandini Savoo, Mohamed I Elzagheid, Lydia Rhyman, Diego M Andrada, Ponnadurai Ramasami. *RSC Adv.* **2020**, *10*, 27884-27893.
- Metalloradical Cations and Dications Based on Divinyldiphosphene and Divinyldiarsene Ligands. Mahendra K Sharma, Dennis Rottschäfer, Beate Neumann, Hans-Georg Stammler, Sergi Danés, Diego M Andrada, Maurice van Gastel, Alexander Hinz, Rajendra S Ghadwal. *Chem. Eur. J.* **2021**, *27*, 5803-5809.
- Unveiling the Electronic Structure of the Bi(+1)/Bi(+3) Redox Couple on NCN and NNN Pincer Complexes. Martí Gimferrer, Sergi Danés, Diego M Andrada, Pedro Salvador. *Inorg. Chem.* **2021**, *60*, 23, 17657-17668.
- Merging the Energy Decomposition Analysis with the Interacting Quantum Atoms Approach. Martí Gimferrer, Sergi Danés, Diego M Andrada, Pedro Salvador. *J. Chem. Theory Comput.* **2023**, *19*, 12, 3469-3485.

Contents

List of Figures

Chapter 1 - Introduction

Chapter 2 - Objectives

Chapter 3 – A new criterion to settle fragment reference states for EDA schemes

Chapter 4 – Aluminium borohydrides as versatile synthons

Chapter 5 – Tailoring phosphanylalumanes towards the synthesis of phosphaalumene

Chapter 6 – Synthesis and reactivity of phospha-Grignards

List of Schemes

List of Tables

Chapter 3 – A new criterion to settle fragment reference states for EDA schemes

Chapter 4 – Aluminium borohydrides as versatile synthons

Chapter 5 – Tailoring phosphanylalumanes towards the synthesis of phosphaalumene

List of Abbreviations

AIM	Atom in Molecule
ALMO	Absolutely Localized Molecular Orbitals
AO	Atomic Orbitals
Ar	Aryl
BArF$_4$	tetrakis-(perfluorophenyl)borate
^{t}Bu	tert-butyl
BSSE	Basis Set Superposition Error
C	Celsius
cAAC	cyclo(alkyl)(amino)carbene
CASSCF	Complete Active Space Self Consistent Field
CC	Coupled Cluster
Cp	Cyclopentadienyl
Cp*	Pentamethylcyclopentadienyl
CSS	Closed-Shell Singlet
CVD	Chemical Vapor Deposition
Cy	Cyclohexyl
DFT	Density Functional Theory
DMAP	4-dimethylaminopyridine
DME	Dimethoxyethane
Dmp	2,6-dimethylphenyl
EDA	Energy Decomposition Analysis
EFO	Effective Fragment Orbital
EPR	Electron paramagnetic resonance
eq	Equivalents
ESI	Electron Sharing Index
FCI	Full Configuration Interaction
FT-IR	Fourier-Transform Infrared Spectroscopy
HF	Hartree-Fock
HOMO	Highest Occupied Molecular Orbital
HMDS	bis(trimethylsilyl)amide
Hz	Hertz
IBO	Intrinsic Bond Orbital
LDA	Lithium diisopropylamide
IQA	Interacting Quantum Atoms
ISC	Inter-System Crossing
LED	Light-Emitting Diodes
LUMO	Lowest Unoccupied Molecular Orbital
LSA	Local Spin Analysis
M	Molar
Me	Methyl
MeOTf	Methyl triflate
Mes	2,4,6-trimethylphenyl
MO	Molecular Orbital
MO-LCAO	Molecular Orbitals as Lineal Combination of Atomic Orbitals
MOCVD	Metal-Organic Chemical Vapor Deposition
NacNac	β-diketiminate
NAO	Natural Atomic Orbitals
NBO	Natural Bond Orbitals
NHC	N-heterocyclic carbene

NHC^{iPrMe}	1, 3-diisopropyl-4,5-dimethyl-imidazol-2-ylidene
NMR	Nuclear Magnetic Resonance
NOCV	Natural Orbitals for Chemical Valence
NONDip	[O(SiMe2NDip)]$^{-2}$
OTf	trifluoromethanesulfonate
OS	Oxidation State
OSS	Open-Shell Singlet
PES	Potential Energy Surface
Ph	Phenyl
PI	Photoiniciator
ppm	Parts per million
RT	Room temperature
SC-XRD	Single Crystal X-ray Diffraction
THF	Tetrahydrofuran
Tip	2, 4, 6-tri-iso-propylphenyl
Tip*	2, 4, 6-tri-tert-butylphenyl
TMS	Trimethylsilyl
UV	Ultraviolet
Vis	Visible
VT	Variable Temperature

CHAPTER 1 - Introduction

The constant development of electronic devices requires materials featuring properties such as electronic conduction and/or photophysical activity. The semiconductors fulfil these demands being, for instance, the key component on transistors or light-emitting diodes (LEDs). The group 14 elements, such as silicon or germanium, have shown effective semiconducting properties, and given their natural abundance, they are the first choice for production. As a drawback, however, the effective conduction sharply depends on the temperature. The preparation of semiconductors follows the Czochralski or Bridgman methodology, which is time-consuming and expensive mainly due to the crystal size used (bigger than 30cm).[1] The synthesis of these materials is currently performed by the Chemical Vapor Deposition (CVD) method. This technique consists of growing a thin layer of crystal from the vapor deposition of the semiconducting material onto a substrate, resulting more economical and faster method than the Czochralski or Bridgman methods. The Metal-Organic Chemical Vapor Deposition (MOCVD) is a variant of CVD that uses organometallic sources for the synthesis of the crystal. [2-4] The CVD technique allows the synthesis of semiconductors composed of two elements (binary semiconductors). The main advantage of binary material over non-binary materials, such as GaAs, is the nature of the band gap. The Si or Ge-based semiconductors present an indirect band gap, while GaAs possess a direct band gap with proven efficient optoelectronic properties. Moreover, binary semiconductors display better thermal stability than Si or Ge semiconductors.
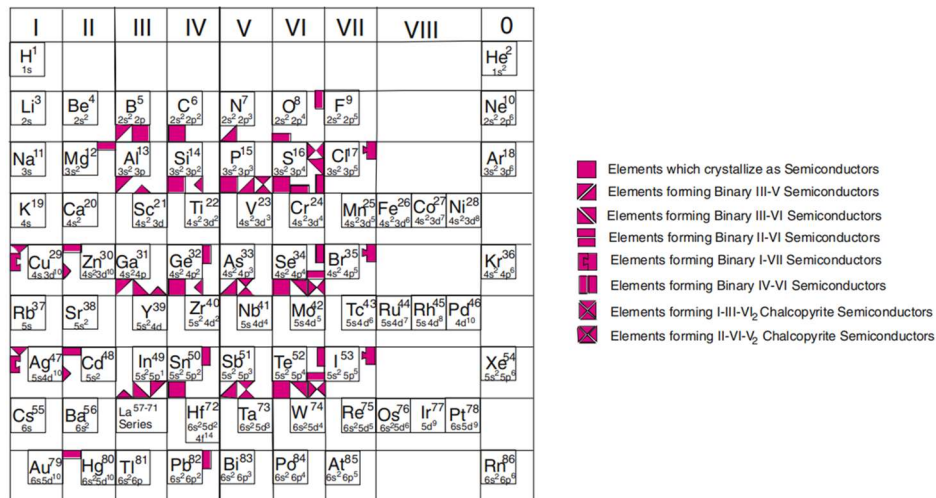
Figure 1. 1. The periodic table "Semiconducting-Forming" Elements. Figure from ref.[1]

Figure 1.1 depicts all the possible combinations of elements that produce a semiconducting material. Most of the group 13 (G_{13}) and group 15 (G_{15}) element combinations, except thallium and bismuth, can take part in binary semiconductors. The GaAs has enhanced properties over silicon semiconductors such as electron mobility. However, gallium is an expensive material due to its low abundance and arsenic is highly toxic, being not the most convenient combination. Although the semiconducting properties of other G_{13}-G_{15} combinations are worse than GaAs, they might satisfy the actual needs. Aluminium is the most abundant group 13 element in the earth's crust and the third in the *p*-block elements. Due to its high abundance, it represents an eco-friendly option for semiconducting materials. The AlN have already shown applications for opto-

electronics or transistors.[5] However, the synthesis of these materials requires harsh conditions.

The preparation of binary semiconductors with CVD brings difficulties in controlling the reaction stoichiometry of the two reactant sources. The single source precursors, which are molecules containing a pre-established combination of both elements, can overcome this problem. However, the substituents must be selected thoroughly to avoid carbon contamination. Species with a lower number of substituents inherently lead to multiple bonded species (Figure 1.2).[6] However, the multiple bonded units featuring heavier elements are highly reactive, bringing about challenges in the preparation. In particular, the synthetic strategies to prepare aluminium-group 15 *genuine* multiple bonds are very limited. Up to today, there is only one synthetic pathway to prepare the heavier congeners (Al=P and Al=As). Thus, there is still the need to find new strategies to prepare them.
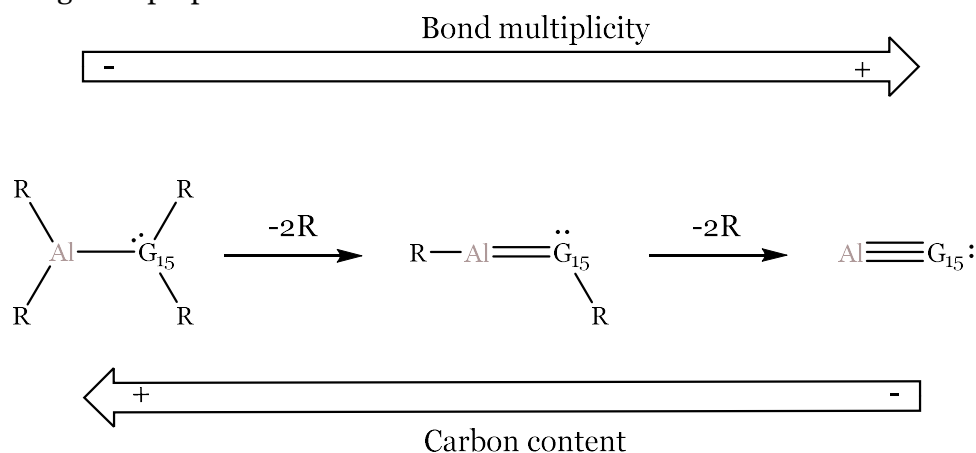
Figure 1. 2. Schematic representation along the bond multiplicity with the carbon content.

The following sections describe the state of the art of aluminium hydrides and halides chemistry, which are the archetypical synthons in aluminium chemistry. Stress on the stabilization approaches and their reactivity, especially focusing on the chemistry with phosphorus, will be addressed. Then, a summary of the more relevant multiple bonds will be briefly introduced, particularly describing the synthesis of group 13 and group 15 multiple bounded compounds. Finally, the main electronic structure methods and chemical bonding tools used in this thesis will be described.

1.1 Synthesis and reactivity of molecular alumanes

In the last decades, the chemistry of molecular main group elements has experienced exponential growth, enclosing a wide variety of applications in catalysis and material science.[7, 8] The constant seek to improve their properties or activity needs the rationalization of physicochemical properties origin. Different approaches can be number as gas phase studies, low temperature matrix trapping experiments and chemical control.[9] The gas phase experiments allow the study of species generated by thermal or discharge reactions which are too reactive to be studied in condensed phase. The analysis of their spectroscopic fingerprint enables the assessment of their physical properties. The trapping experiments consist of generating the reactive target molecule in cold matrixes, being *trapped* in a low-temperature inert solid. Finally, the chemical control approach uses ligands to provide kinetic and thermodynamic stability to unstable motifs. The resulting compounds are *stable,* facilitating the study of their chemistry. The

use of Schlenk techniques for sensitive chemistry has led to countless main group compounds with unexpected chemical properties and applications. The following sections will describe the different approaches to stabilize aluminium hydrides and halides. They are an important family of aluminium compounds because they are common building blocks to introduce molecular complexity to any aluminium complex.

1.1.1 Aluminium hydrides

Metal hydrides are compounds with applications in the field of material science and catalysis. The capacity to release H_2 under certain conditions has triggered the interest in developing materials based on metal hydrides for solid-state hydrogen storage.[10] The s- and p-block hydrides possess good volumetric and gravimetric hydrogen storage capacities, making them promising candidates for developing efficient hydrogen storage materials. The chemistry of main group hydrides has expanded not only given the discoveries on unusual bonding situations but also the effective catalysis for the reduction of organic substrates. In this vein, molecular aluminium hydrides can take part in non-redox catalytic cycles for hydroboration of ketones and aldehydes or dehydrocoupling of boranes with amines, thiols or phenols.[11, 12]

The aluminium hydride was early described by Wiberg and co-workers in 1942.[13] The solid-state structure is polymeric forming up to 6 different polymorphic phases obtained from different crystallization conditions.[14] The *naked* monomeric AlH_3 has been only characterized in matrix isolation experiments.[15, 16] The diborane analogue Al_2H_6 could also be detected in hydrogen matrixes. Its instability became evident polymerizing above 6.8K.[17] The polymeric nature of the aluminium hydride faces synthetic difficulties such as uncontrollable reaction stoichiometry. The stabilization of the monomeric AlH_3 can be achieved by forming adducts with neutral Lewis bases, bringing better control of the reactivity. Depending on the steric and electronic properties of the Lewis base, the alanes can form different types of adducts (Figure 1.3). Strong σ-donors or sterically demanding Lewis bases, such as NHC, cAAC or bulky phosphines, tend to form monomeric alanes (Type C). However, weak σ-donors and low steric hindered Lewis bases promote the formation of penta-coordinated alane (Type A) or dimeric structures (Type B) bearing Al-H-Al bridges.

Type A   **Type B**   **Type C**
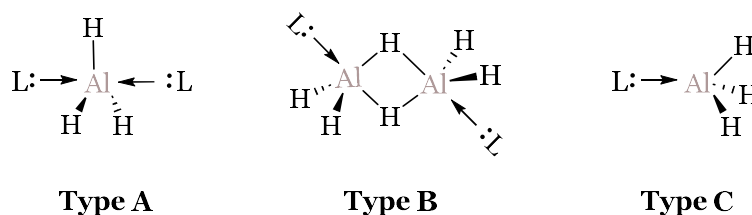
Figure 1. 3. Selected type of alane adducts with mono-dentate Lewis bases (L:).

The chemistry of Type C adducts has been mostly explored with NHC or cAAC Lewis bases. The NHC·AlH_3 have shown ring opening and ring expansion reactions towards NHCs meanwhile the cAAC is inserted into the Al-H bond.[18] [19] The reduction of NHC alanes yields unprecedented products. For instance, Bonyhady *et al.* considered the β-diketiminate magnesium(I) dimer as a plausible reducing candidate. The equimolar reaction of NHC AlH_3 adduct with β-diketiminate magnesium(I) yields Al-Al bond formation (**1**) and the β-diketiminate magnesium hydride dimer.[20] The NHC alane adducts also react with hydride abstractors yielding monomeric and dimeric aluminium hydride dications (**2** and **3**). Mellerup *et al.* isolated the monomeric aluminium (I) hydride (**4**), which is isostructural to **3**. The enhanced σ-donor and π-acceptor properties of cAAC allowed the stabilization of the Al(I)-H motif. Compound **4** is obtained from the

reduction of the cAAC stabilised haloalane with KC_8.[21] Unlike most aluminium compounds, compound **4** exhibits nucleophilic reactivity, which agrees with the aluminium (I) description. However, quantum chemical calculations suggest a non-negligible bi-radical aluminium (III) character.
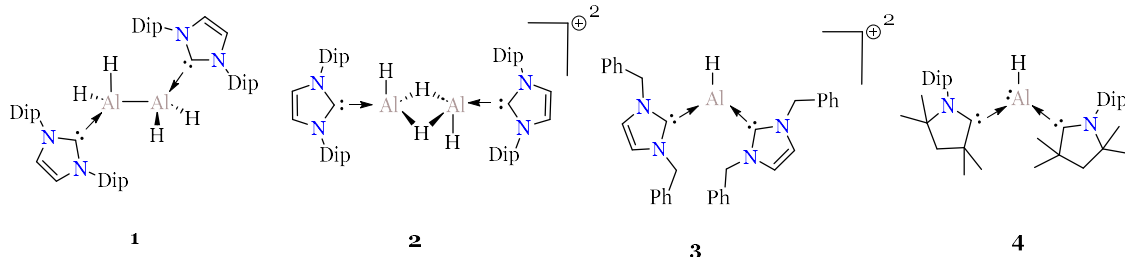
Figure 1. 4. Selected examples of aluminium hydride compounds supported by NHC and cAAC ligands. (Ph= phenyl, Dip= 2,6-*iso*-propylphenyl).

Another common approach to stabilize aluminium hydrides is by introducing anionic substituents to aluminium. The DIBAL-H (di-*iso*-butylaluminium hydride) is one of the most well-known compounds of this family, being a classic reductive reagent in organic synthesis. The arylalanes are typically dimeric in solid state, even with very bulky substituents. For instance, Power and co-workers prepared the hydro arylalane **5**. Even though the huge steric hindrance of the Ar^{Pri8} ligand, compound **5** was determined to be dimeric in the solid state. However, there are some examples that can be in equilibrium with the monomer species in solution.[22, 23] The reactivity of **5** was explored towards alkenes and alkynes (Figure 1.5). The Al-H inserts towards terminal alkynes and alkenes under mild conditions, resulting in the hydroalumination product **6**.[24]
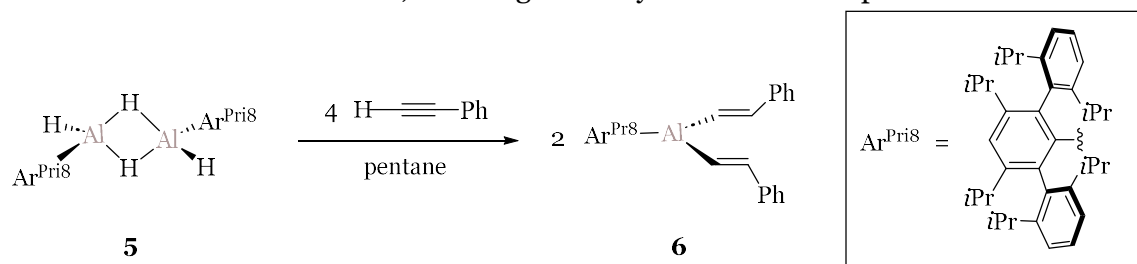
Figure 1. 5. Hydroalumination of phenylacetylene with **5** (*i*Pr=*iso*-propyl).

The aryl substituents cannot effectively prevent the formation of Al-H-Al bridges. A common approach to avoid the dimerization is the anchoring of a Lewis base to the ligand. The Lewis base stabilizes the empty *p*-orbital of aluminium, preventing the formation of the Al-H-Al bridge (see examples in Figure 1.6). Alan Cowley and co-workers stabilised a monomeric aluminium hydride through the intramolecular stabilization of a Lewis base, forcing the aluminium into a trigonal bipyramidal geometry (**7**).[25] Nowadays, this approach is repeatedly found in monomeric aluminium hydrides.[26] There is a plethora of different ligand systems developed to stabilize the monomeric aluminium hydrides, such as aminidate, troponiminate (**8**)[27] and *β*-diketiminate (**9**), among others.
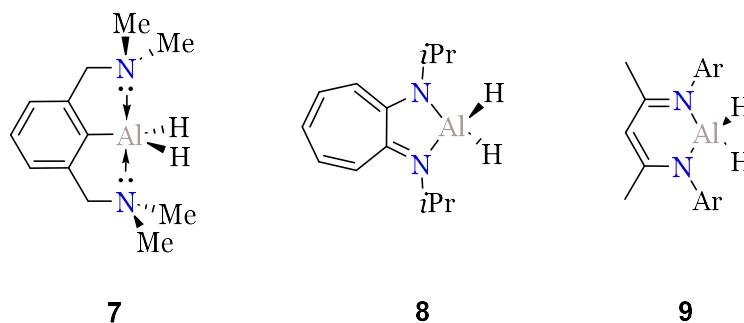
Figure 1. 6. Selected examples of monomeric aluminium hydride compounds stabilised by anchored Lewis base (Me= Methyl, *i*Pr=*iso*-propyl).

1.1.2 The *NacNac* aluminium hydrides

The β-diketiminate, commonly known as *NacNac,* is one of the most well-known ligands within the anchoring Lewis base stabilization approach. It was introduced by Holm in 1968 for the synthesis of nickel complexes.[28] The *NacNac* gained interest given the easy preparation and versatile electronic and steric properties changes. A myriad of *NacNac* compounds from along the periodic table have been reported, finding applications in metal-mediated catalysis for different types of chemical transformations.[29-31]

The *NacNac* ligand is a common choice in aluminium chemistry. It stabilizes aluminium with a broad scope of functionalities and different oxidation states. The most common synthetic route to prepare the *NacNac* aluminium hydride is through the dehydrogenation reaction of *NacNac-H* with AlH_3 NH_3 or $LiAlH_4$ (Figure 1.7).[32, 33] Although not for preparative proposes, the *NacNac*AlH$_2$ can be synthesised by reacting the *NacNac* aluminium carbenoid with molecular dihydrogen.[34] [35]
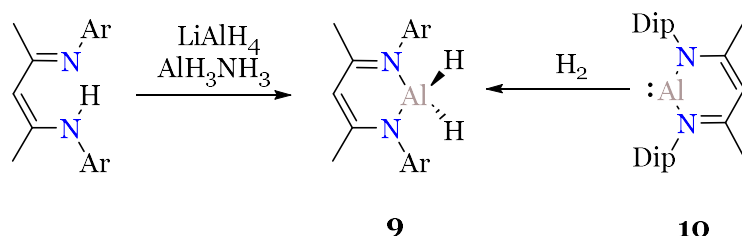
Figure 1. 7. Synthesis of NacNacAlH$_2$ (Dip=2,6-*iso*-propylphenyl).

The synthesis of mono-substituted *NacNac* aluminium hydrides can be achieved via the dehydrogenation of protic substrates with **9**. The electronegativity difference between aluminium and hydrogen (χ(Al)=1.613 and χ(H)=2.300) makes the Al-H bond highly polarized towards hydrogen. This feature renders a highly hydric character to hydrogen and readily reacts with protic substrates. There are many examples of stoichiometric dehydrogenation reactions of *NacNac*AlH$_2$ with protic substrates (Figure 1.8). It reacts with half equivalent of water releasing two equivalents of dihydrogen, forming the μ-oxo hydroalumoxane (**11**).[36] The reactivity towards N-H and S-H bonds is exemplified with the dehydrogenation of 2-aminobenzenethiol, forming the 5-member ring **12**.[37]
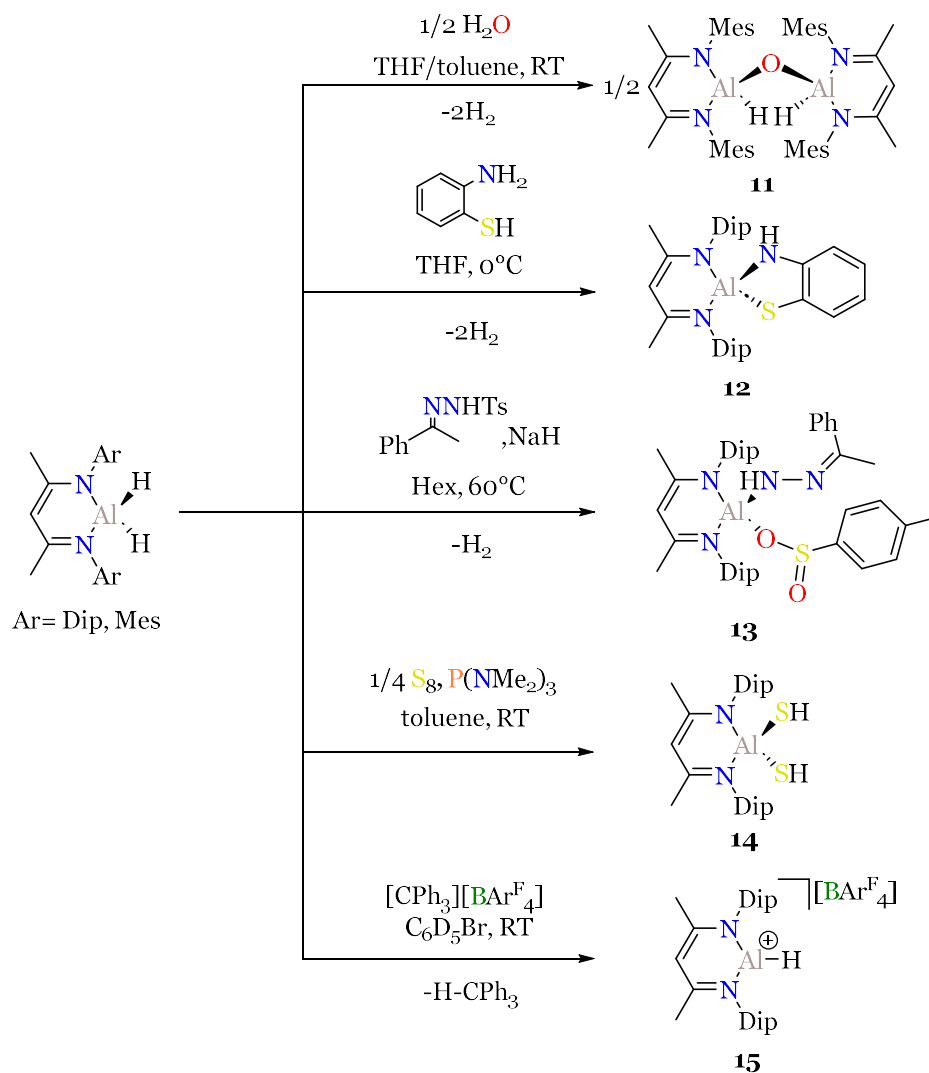
Figure 1. 8. Selected examples of stoichiometric reactions of *NacNac*AlH₂ (Dip=2,6-di-iso-propylphenyl, Mes= 2,4,6-tri-methylphenyl, Ph=phenyl, BArF4=tetrakis-(perfluorophenyl)borate).

The dehydrogenation reactions are limited to protic substrates. Roesky and co-workers investigated the Al-H insertion chemistry of *NacNac*AlH₂ to different substrates, an alternative pathway to increase molecular complexity. They explored the insertion of Al-H bonds into diazo derivatives, which display different reactivity patterns depending on the nature of the substrates. For instance, the diazobenzylethane reacts with *NacNac*AlH₂ through the insertion of the diazo group into the Al-H bond. It further reacts with the sodium tosylate activation of the S=O forming the compound **13**.[38] The *NacNac*AlH₂ can also activate elemental chalcogens under mild conditions. It reacts with elemental selenium in toluene at room temperature, yielding the terminal selenol, which was elusive in main group chemistry.[32] Similarly, the terminal thiol (**14**) is synthesised by reacting *NacNac*AlH₂ with elemental sulphur in the presence of the catalytic amount of tri(di-methylamino) phosphine, which is proposed to react as sulfur transfer reagent.[39] Roesky and co-workers found that *NacNac*AlH₂ can undergo hydrogen abstraction with MeOTf forming the *NacNac*AlH(OTf) complex, which is an active catalyst for hydroboration reactions.[40] Similarly, Nikonov and co-workers reacted the *NacNac*AlH₂ with trityl cation [CPh₃][BArF4.], forming the cationic hydroalumane **15**. It has shown catalytic activity towards hidrosilylation of olefins.[41]

The synthesis of mono-functionalized *NacNac* aluminium hydrides can also be achieved via the oxidative addition of the *NacNac*Al(I) carbenoid to different substrates

(Figure 1.9). This approach might not be the most synthetic appealing because of the low isolation yields of the *NacNac*Al(I). However, its high reactivity allows the incorporation of unusual substituents into the aluminium atom. Chu *et al.* explored the oxidative addition of different types of σ-bonds, assessing novel *NacNac* aluminium hydride derivatives (**16**) such as (hydrido)phosphanylalumanes, (hydrido)borylalumane or (hydrido)silylalumane.[35] Moreover, they observed the equilibrium between *NacNac*Al(I) and *NacNac*AlH$_2$ with the hydridodialumane **17**. This is a very rare case of an equilibrium between oxidative addition and reductive elimination in aluminium chemistry.[42] Similarly, Harder and co-workers explored the insertion of *NacNac*Al(I) towards other metallic hydrides, namely Zn-H and Mg-H, yielding the bimetallic compounds **18** and **19**.[43]
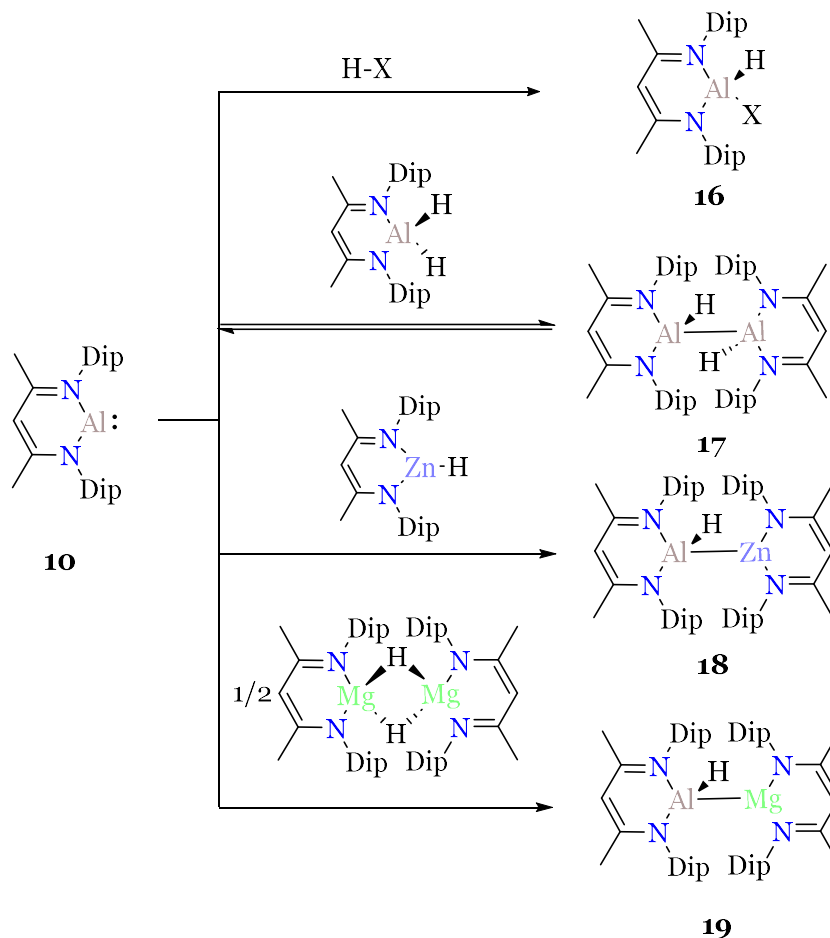
Figure 1. 9. Selected examples of oxidative additions of aluminium (I) towards different type of substrates (Dip=2,6-di-iso-propylphenyl, X=SiHPhMe, BPin, Cp*, NHMe, PPh$_2$, O*i*Pr).

The coordination chemistry of *NacNac*AlH$_2$ has been explored during the last decades. The resulting compounds bear interesting bonding situations and have found applications for bond activation (see examples in Figure 1.10).[44] Aldridge and co-workers introduced the first examples of σ-alanes complexes between *NacNac*AlH$_2$ with transition metals. The photolysis of transition metal carbonyl complexes in the presence of *NacNac*AlH$_2$ yields the formation of compounds such as **20**.[45] Alternative to photolytic decarbonylation, the bimetallic aluminium-TM complexes can also be accessed through [M(CO)$_4$COD] starting materials.[46] Crimmin and co-workers have described several examples of bimetallic systems featuring bond activation chemistry.[47] They explored the cooperativity between *NacNac*AlH$_2$ with Pd(PCy$_3$)$_3$ to activate C-H and C-F bonds.[48, 49] In 2012 they reported the thermolysis of [Cp*Rh(H)$_2$(SiEt$_3$)$_2$] in the

presence of *NacNac*AlH$_2$, obtaining the bimetallic complex **22**.[50] The Al-Rh bond length is in the range of single bond (Al-Rh= 2.4527(8) Å) with weak interactions with the Al-H bond. The partial dehydrogenation of *NacNac*AlH$_2$ was achieved by coordinating palladium complexes.[51] Recently, the same group isolated the hexacoordinated compound **23** by reacting the *NacNac*AlH$_2$ and FeBr$_2$ in the presence of PMe$_3$. The reduction of **23** with Mg yields the formation of **24**, which is characterized by an Al-Fe single bond. Compound **24** has shown bimetallic cooperativity for *ortho* C-H bond activation of pyridine or dehydrogenation of acetonitrile.[52, 53]

20	**21**	**22**	**23**
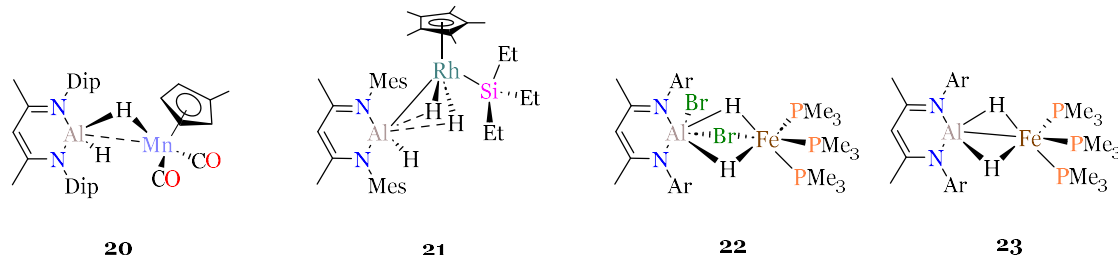
Figure 1. 10. Selected examples of bimetallic complexes of *NacNac*AlH$_2$ (Ar=Aryl, Dip=2,6-di-iso-propylphenyl, Mes= 2,4,6-tri-methylphenyl, Et=Ethyl).

1.1.3 Aluminium Borohydrides

Most of the *d*- and *f*- block borohydrides are known with a diverse types of ancillary ligands.[54, 55] The coordination chemistry of these complexes is very rich due to the polyhapto nature of [BH$_4$]$^-$ and the accessibility to the *d*- and *f*- orbitals. The [BH$_4$]$^-$ can coordinate by one (κ^1), two (κ^2) or three (κ^3) hydrogens in monomeric complexes (Figure 1.11). In dimeric or trimeric complexes, the [BH$_4$]$^-$ can bridge the metals increasing its coordination number. Since the hydrogen atoms have difficulties to be located in X-ray diffraction, the metal-boron distance serves as an indicator of the coordination number of the borohydride ligand. The shorter is the metal-boron distance, the higher is the coordination number. The third-row transition metal complexes have the tendency to display lower denticity than first-row metals.[56] The nature of the ancillary ligands, the steric properties and the ligand field splitting can tune the denticity of borohydride ligand. This family of complexes have found applications in catalysis [57-59] and they have served as a model to study C-H activation of methane.[60] Interestingly, the *f*-block borohydrides are important synthons to prepare more complex entities where the [BH$_4$]$^-$ ligand behaves as a *pseudo*-halide.[61]

κ^1-coordination κ^2-coordination κ^3-coordination
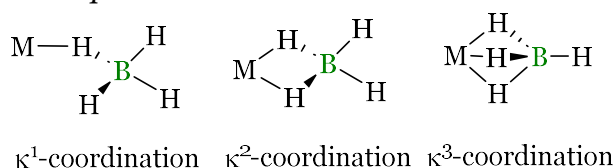
Figure 1. 11. Schematic representation of the coordination modes of [BH$_4$]$^-$.

The molecular aluminium borohydrides have been well-established for many years. Figure 11 depicts some relevant examples reported in the literature. The first description of an aluminium borohydride was described by Burg and co-workers in 1939.[62, 63] The reaction of trimethylaluminium with diborane furnished the formation of compound **24**. Unlike *f*- and *d*-block analogues, such as Y(BH$_4$)$_3$, Ce(BH$_4$)$_3$ or La(BH$_4$)$_3$ to name a few, compound **24** is described as a highly reactive pyrophoric liquid. In fact, the solid state structure could not be determined after 50 years later.[64] The crystal structure refinement shows two different polymorphic phases (α- and β- phase), obtained from different crystallization temperatures. Compound **24** readily

dehydrogenates with water and hydrogen chloride and slowly polymerizes at room temperature. It has been tentatively suggested the metathesis reaction of compound **24** towards ethyl-lithium, forming of LiBH$_4$ and unidentified products. Moreover, compound **24** has found applications as a reducing and dehydrogenative reagent.[65, 66]

Similar to AlH$_3$, compound **24** possesses a Lewis acid character. Wallbridge and co-workers prepared a palette of Lewis base stabilised Al(BH$_4$)$_3$ in order to prevent the oligomerization process.[67, 68] The solid-state structure resulted to be monomeric and the aluminium adopts a tetrahedral geometry where each [BH$_4$]$^-$ is coordinated in a κ^2 fashion. The coordination of a [BH$_4$]$^-$ to form a tetrakis-borohydridealumane (**26**) was a sought-after at that time. Titov and Nöth groups described the formation of **26** but its full characterization was not possible due to the equilibria with LiBH$_4$ and Al(BH$_4$)$_3$.[69, 70] Two decades later, Dou *et al.* achieved the solid-state structure of **26** by using the trimethylphosphonium counterion.[71] The X-Ray structure reveals that aluminium adopts a tetrahedral geometry where all the [BH$_4$]$^-$ are in a κ^2 coordination. Years later, Filinchuk achieved the synthesis of **26** with potassium counterion.[72] Compound **26** represents a rare example of aluminium in dodecahedral coordination, which has found applications for energy production.[73]

The introduction of anionic organic ligands generally increases the stability of aluminium borohydrides. For example, Bissinger *et al.* reported the first substituted aluminium borohydride by introducing trimethysiloxyl groups (**27**), which was determined to form a four-membered ring in the solid state.[74] It was prepared via salt metathesis between the aluminium dihalide analogue and LiBH$_4$. Similarly, Franz *et al.* reported the imidazoline-2-imidato analogue of **27** by reacting the dihydride analogue with DMS·BH$_3$.[75] The dimerization process can be blocked by anchoring of a Lewis base to the ligand. Harder and co-workers prepared the monomeric aluminium borohydride **29** by reacting *NacNac*AlH$_2$ with a bulky primary boramine via S$_N$2 reaction.[76] They observed that low sterically hindered ammonia-boranes (i.e. NH$_3$BH$_3$, MeNH$_2$BH$_3$ and *i*PrNH$_3$BH$_3$) undergo a dehydrogenation pathway, however, the bulky ammonia-borane DipNH$_2$BH$_3$ transfers the BH$_3$ to the Al-H bond, forming the aluminium borohydride. Following the same synthetic strategy, Less *et al.* reacted a low sterically hindered *NacNac* with *tert*-butyl ammonia- borane isolating the *NacNac^{DMP}*Al(H)BH$_4$ (**30**).[77] This compound has been postulated to be catalytically active towards the dehydrocoupling of ammonia-boranes. Aldridge and Goicoechea groups obtained **31** as a minor product from the reduction of *NacNac*Al(Et)(OC(H)O) with DMS·BH$_3$.[78]
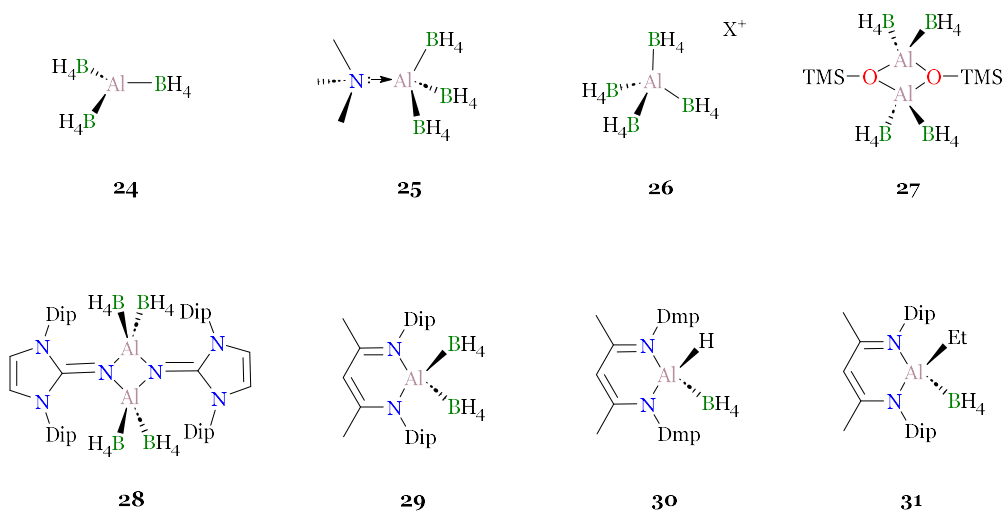
Figure 1. 12. Selected examples of aluminium borohydride compounds (Dip=2,6-di-iso-propylphenyl; Dmp=2,6-di-methyphenyl, Et=Ethyl, X=Li,K, PMe$_3$Ph, NBu$_4$).

1.2 The *NacNac* aluminium halides

The synthetic pathways to prepare the *NacNac* aluminium halides depends on the nature of the halide atom (Figure 1.13). In the case of chlorine and bromine, the synthesis is undertaken via salt elimination from the lithiated *NacNac* with the corresponding aluminium halide.[79] In the case of iodide, the synthesis is obtained by reacting the *NacNac*AlMe$_2$ with elemental iodine.[34]
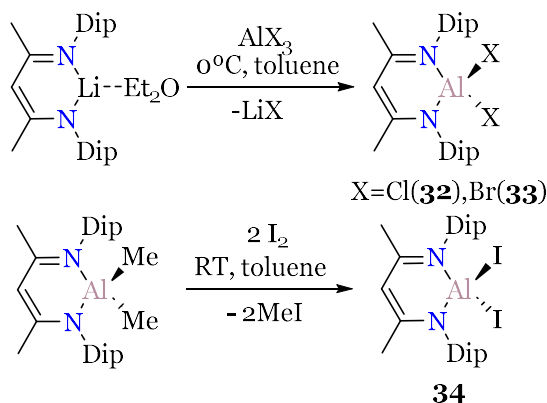
Figure 1. 13. Synthesis of *NacNac* aluminium halides (Dip=2,6-di-iso-propylphenyl).

The functionalization of aluminium halides is typically performed via salt metathesis or reduction reactions. Compounds **32**, **33** and **34** undergo salt elimination with anionic nucleophiles such as LiNMe$_2$ (**35**),[80] LiNEt$_2$(**36**),[81] AgOTf,[82] lithiated phenylacetylene (**37**) or *tert*-butylacetylene (**38**).[83] Aldridge group explored the reactivity of *NacNac* aluminium halides with strong bases. The equimolar reaction of *NacNac*AlCl$_2$ with *tert*-butyl lithium yields the backbone deprotonation, obtaining the anionic compound **39**.[84] Roesky and co-workers showed that the reduction of *NacNac*AlI$_2$ with potassium yields the aluminium (I) carbenoid **40**.
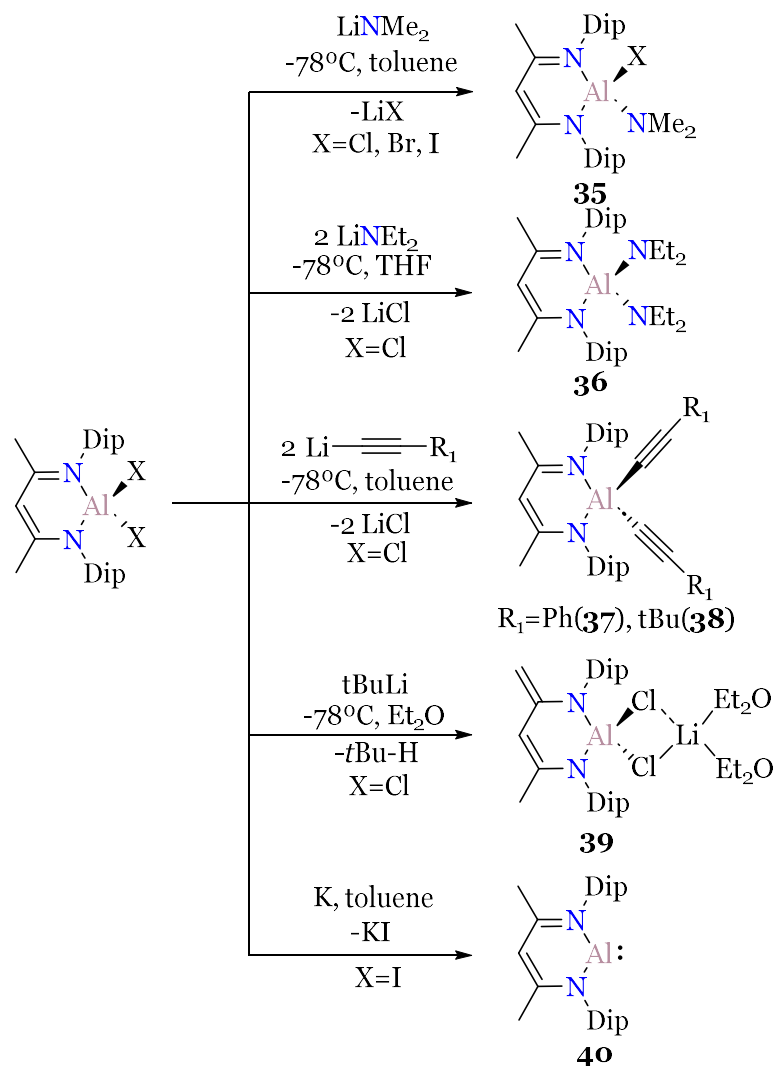
Figure 1. 14. Reactivity of *NacNac* aluminium halides (Me=methyl, Et=ethyl, Dip=2,6-di-iso-propylphenyl, Ph= phenyl, tBu=*tert*-butyl).

1.3 Synthesis of phosphanylalumanes

The synthesis of monomeric compounds bearing aluminium and phosphorus bonds can be synthetically challenging. The weak nature of the Al-P and its tendency to oligomerize complicates the stabilization of the Al-P motif.[85] Over the years, different synthetic strategies have been reported in the literature. The most common routes are the dehydrogenation or the salt metathesis reactions.

In 1942, Davidson and Brown studied the polymerization of trimetlhylaluminium with dimethylamine and dimethylphosphine, among other substrates.[86] In the case of dimethylphosphine, they observed the methane release at high temperatures (215°C) yielding the trimeric compound **41**. The methane exclusion with dimethylamine undergoes at 90°C isolating the aminoalumane in dimeric form. After two decades, Fritz and co-workers reported the synthesis of phosphanylalumanes in milder conditions.[87] By heating an equimolar mixture of lithium-diethylphosphide with aluminium trichloride in diethylether led to the trimeric phosphanylalumane **42** and the LiCl elimination. Similarly, the reaction of H_2AlCl with lithium triethylphosphide yielded the formation of **43**.[88] The tuning of the steric properties of the aluminium and phosphorus building blocks permits the control of the oligomerization process. Paine and co-workers reported dimeric phosphanylalumanes by reacting the ethereal *tris*-trimethlysilylalumane

(TMS$_3$Al·Et$_2$O) with different primary and secondary phosphines.[89] In the case of secondary phosphines, the dimeric phosphanylalumanes **44** and **45** were isolated while primary phosphine forms the trimeric phosphanylalumane. Power and co-workers envisioned that extremely bulky substituents in both aluminium and phosphorus synthons could yield a monomeric phosphanylalumane.[90] The equimolar mixture of Tip$_2$AlBr with LiPAdSiPh$_3$ or LiPMesSiPh$_3$ undergoes salt metathesis reaction yielding the monomeric **46** and **47** phosphanylalumanes and LiBr. The X-ray diffraction determined an Al-P distance of 2.342(2) Å, which is shorter than the dimeric and trimeric analogues, e.g. Al-P=2.446 Å and Al-P=2.458 Å in **44**.

41 (R$_1$=R$_2$=Me)
42 (R$_1$=Et ; R$_2$=Cl)
43 (R$_1$=Et ; R$_2$=H)

44 (R$_1$=TMS ; R$_2$=Ph)
45 (R$_1$=TMS ; R$_2$=Ph,TMS)

46 (R$_1$=Ad)
47 (R$_1$=Mes)
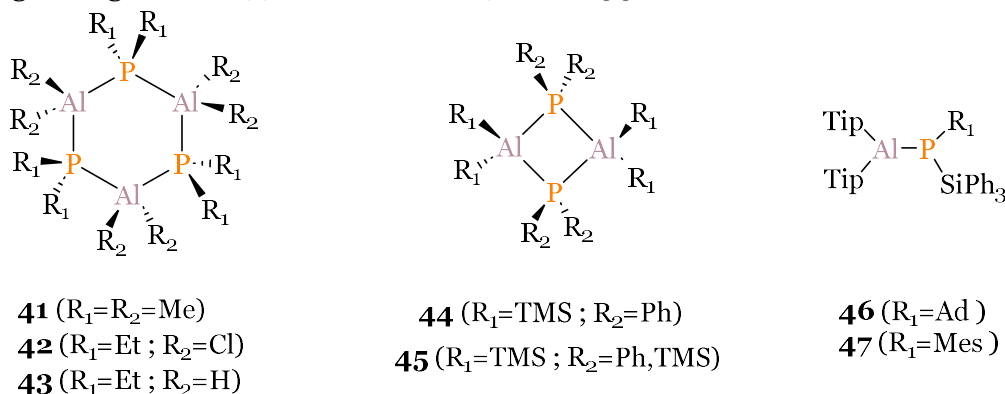
Figure 1. 15. Selected examples of trimeric, dimeric and monomeric phosphanylalumanes (Me=Methyl, Et=Etyl, TMS=tri-methylsilyl, Ph= phenyl, Ad= adamantly, Mes=mesityl).

The incorporation of a Lewis acid or/and Lewis base to the Al-P motif is an alternative strategy to prevent the oligomerization reaction. Initial studies considered the use of only a Lewis base with unprotected aluminium synthons, yielding different aggregates. For example, Driess and co-workers explored the dehydrogenation reaction of NMe$_3$·AlH$_3$ with the primary phosphine iPr$_3$SiPH$_2$, obtaining the hexameric cluster **48**.[91] Following a similar synthetic approach, von Hänisch and co-workers reacted a bulky primary phosphine (tBuPh$_2$SiPH$_2$) with NMe$_3$·AlH$_3$ obtaining the dimers **49**. [92] The substitution of the NMe$_3$ by an NHC was not sufficient to monomerize **49**, isolating the four-membered rings **50** and **51**. The same group isolated the dimer **52** by reacting a ladder-shaped polycyclic aluminium phosphorus compound with pyridine.

48

49

50 and 51

52
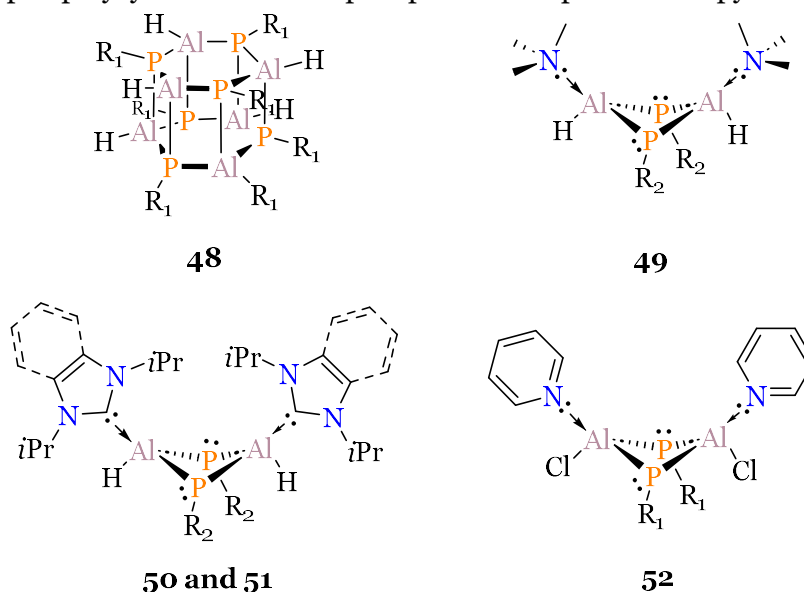
Figure 1. 16 Lewis base stabilised cyclic phosphanylalumanes (R$_1$=iPr$_3$Si, R$_2$=tBuPh$_2$Si).

The first indications of monomeric Lewis-base stabilised phosphalumanes were reported by Fritz and co-workers.[87, 88] They explored the ring-opening reaction of compound **43** with three equivalents of trichlorophosphate ($P(O)Cl_3$). The lone pair of the oxygen displaces the phosphorus coordination, yielding a red-orange viscous oil identified as **53**. Unfortunately, no structural data of **53** has been reported to date. Twenty years later, Beachley and Rowen groups isolated and fully characterized the Lewis acid/base stabilised phosphanylalumane **54**.[93] This compound is prepared by reacting the phosphanylalumane $Me_3SiCH_2AlPPh_2$ with $Cr(CO)_5NMe_3$ in benzene. The lone pair of the phosphorus displaces the trimethylamine from the chromium complex, which rebounds to the aluminium. The solid-state structure of **54** features an Al-P bond length of 2.485(1) Å, in the range of dimeric and trimeric phosphanylalumanes. Interestingly, the Al-P distance is longer (*c.a.* 0.14 Å) than monomeric phosphanylalumanes (**46** and **47**). In 2001, Scheer and co-workers demonstrated that the Lewis acid/base approach can stabilize low steric hindered phosphanylalumanes. The dehydrogenation of $NMe_3 \cdot AlH_3$ adduct with $[W(CO)_5PH_3]$ complex yielded the formation of **55**.[94] The solid-state structure shows a dimer with long hydride bridges, similarly found in Lewis base stabilised aluminium hydrides type B (*vide supra*). The same group reported the synthesis of phosphanylalumanes only stabilised by an NHC (**56**).[95] The synthesis can be undertaken via salt metathesis between $NHC \cdot AlH_2X$ (X= Cl, I) adduct and $DME \cdot LiPH_2$ or through dehydrogenation of $NHC \cdot AlH_3$ and phosphine gas (PH_3). The Al-P distance of **56** (2.3131(10) Å) is shorter than other Lewis acid/base stabilised compounds. Recently, Haider *et al.* reported a palette of Lewis-base stabilised phosphanylalumanes (**57**).[96] They reacted different types of σ-donor ligands, including DMAP, NHCs or cAAC, to a trimeric phosphanylalumane yielding the monomeric Lewis base stabilised phosphanylalumanes. The isolated compounds presented reactivity towards CO_2 activation. Tokitoh and co-workers isolated the Lewis base stabilised phosphanylalumane (**58**) which bears an *α*-proton on the phosphine and a halide on the aluminium atom.[97] This compound was prepared with the aim to prepare the Al=P bond but it was unsuccessful.
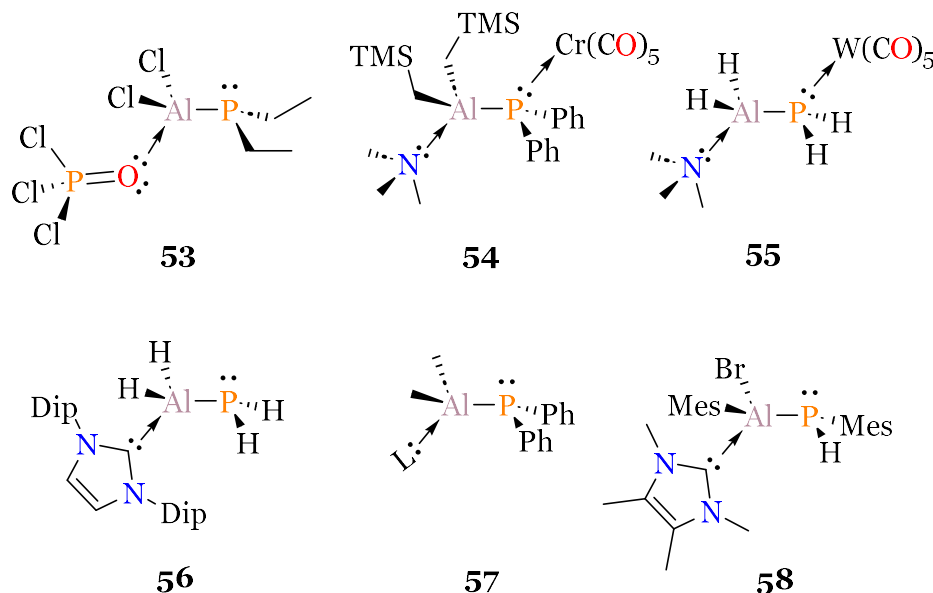
Figure 1. 17. Phosphanylalumanes stabilised by donor-acceptor interactions (L:= DMAP, NHCs or cAAC, Dip=2,6-di-iso-propylphenyl, Ph=Phenyl, Mes=Mesityl).

The use of ligands featuring an anchoring Lewis base can also stabilize monomeric phosphanylalumanes. As mentioned above, one of the most popular ligands for this type of stabilization is the *NacNac*. However, only few examples are described in the literature (Figure 1.18). The first one was reported by Nikonov and co-workers. The

oxidative addition of *NacNac*Al(I) carbenoid to diphenylphosphine (PHPh$_2$) yields the formation of the (hydrido)phosphanylalumane **59**.[35] The Al-P bond length is in the range of aforementioned phosphanylalumanes (2.3971(6) Å). The same group reported the oxidative addition of *NacNac*Al(I) to diphosphide Ph$_2$P-PPh$_2$, isolating the compound **60**. The Al-P bond lengths in the equatorial position (2.3775(5) Å) is slightly shorter than the axial position (2.3979(5) Å). Alternative to oxidative addition, the *NacNac* phosphanylalumanes can also be prepared via salt metathesis. Scheer group reported the synthesis of **61** via reacting *NacNac*AlI$_2$ with DME·LiPH$_2$.[98] Analogously to **60**, the equatorial and axial positions of aluminium display different Al-P distances (2.3474(5) Å and 2.3718(5) Å, respectively).
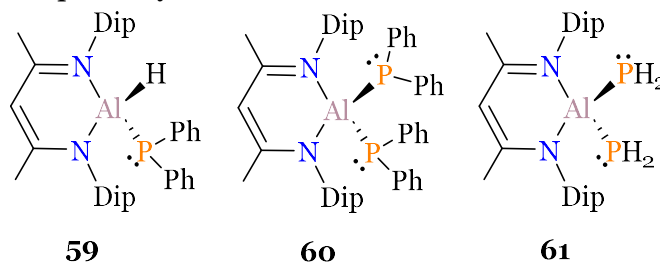
Figure 1. 18. *NacNac* stabilised phosphanylalumanes (Ph=Phenyl, Dip=2,6-di-iso-propylphenyl).

1.4 Multiple bonds in *p*-block chemistry

The interest in *p*-block multiple bonds has exponentially grown during the last decades. The stabilization approaches and synthetic pathways are quite diverse. In this section, we aim to summarize the different types of homo- and hetero-atomic multiple bonds in *p*-block elements together with their synthetic methods and bonding models.

1.4.1 Homo-atomic multiple bonds

Molecular oxygen and nitrogen are textbook examples of homo-diatomic *p*-block multiple bonds found in nature. However, their heavier analogues are remarkably more reactive. It was long believed that heavier multiple bonds are synthetically inaccessible. Mulliken[99] and Pitzer[100] formalized the so-called *double bond rule*, which asserted the impossibility of main group elements with a principal quantum number higher than 2 to form stable multiple bonds. Those studies only considered electronic effects, ignoring the role of steric protection as a stabilizing source. Jutzi conceived the idea to kinetically stabilize heavier multiple main group compounds with bulky substituents.[101] The Sn=Sn isolated by Lappert and co-workers,[102] or the isolation of disilene (**62**) and diphosphane (**63**) by West[103] and Higuchi,[104] respectively, break down the double bond rule, proving the relevance of the steric hindrance in the stabilization of heavier multiple bonds. With the same idea, Power and Sekiguchi groups completed the series of the heavier group 14 alkynes.[105-108] Their geometry is distinct from acetylene. Instead, heavier alkynes adopt a *trans*-bent conformation which increases along the group. Those differences can be rationalized by the increase of the *s*-character along the group (inner pair effect) and the weakening of the π-stabilization.[109]

A complementary way to assess multiple bonds is through the stabilization with Lewis bases. This approach has been particularly useful in isolating *p*-block multiple bonded species in low oxidation states. This idea was based on low-temperature matrix experiments. Knight and co-workers detected the HBBH molecule in argon and neon matrixes in 1995. This molecule was determined to be in triplet state and predicted to be highly reactive.[110] Robinson and co-workers envisioned that the exceptional σ-donor

properties of NHC might be appropriate to stabilize the HBBH. The reduction of the NHC-BBr$_3$ adduct with KC$_8$ yields the neutral diborene (**64**).[111, 112] Following the similar synthetic approaches, heavier bis-tetrylenes and bis-pnictenes analogues have also been reported.[113-116] It is noteworthy to mention that the NHCs permit the stabilisation of multiple bonds which are unstable even with huge steric protection. That is the case for the isolation of neutral dialumene. Initial attempts were made by Power and co-workers to stabilize the neutral Al=Al moiety with bulky aryl substituents. However, it was unsuccessful, undergoing to [4+2] cycloaddition with benzene, which was used as a solvent.[117] Instead, Inoue and co-workers achieved the stabilization of neutral Al=Al by reducing an NHC stabilised dibormoalane with KC$_8$.[118]

The same logic and development occurred to the isolation of the first boron-boron triple bond. In 2002, Zhou and co-workers detected the OC-BB-CO molecule in argon matrix.[119] Braunschweig group foresee that by exchanging the CO ligands by NHC, the diboryne could be isolable. Upon reduction of the bis-NHC tetrabromodiborane furnished the diboryne (**65**), which is stable at ambient temperature.[120] The geometry was found to be linear, being isolobal to acetylene.

62   **63**   **64**   **65**
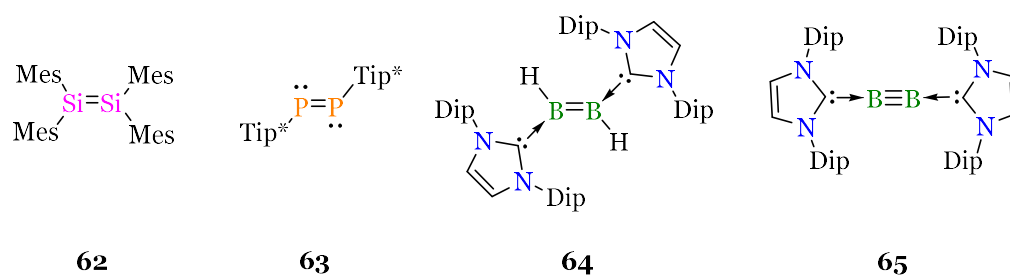
Figure 1. 19. Selected examples of homo-atomic *p*-block multiple bounded compounds (Mes=mesityl, Tip*=2,4,6-tri-tert-butylpenyl, Dip=2,6-di-iso-propylphenyl).

A bonding model for **65** was proposed by Frenking and co-workers, analysing the electronic structure of the isolated B$_2$ moiety. The B$_2$ molecule has a triplet ground state ($^3\Sigma_g^-$), which the $1\pi_u$ orbitals are partially occupied leading to a low triple bond character (Figure 1.20, left). The promotion of the $1\sigma_u^+$ electrons to the $1\pi_u$ orbital yields the genuine triple bond in the excited state $^1\Sigma_g^+$ (Figure 1.20, right). The NHCs stabilize the empty $1\sigma_u^+$ orbitals, stabilizing the B$_2$ motif in the $^1\Sigma_g^+$ state.[121]
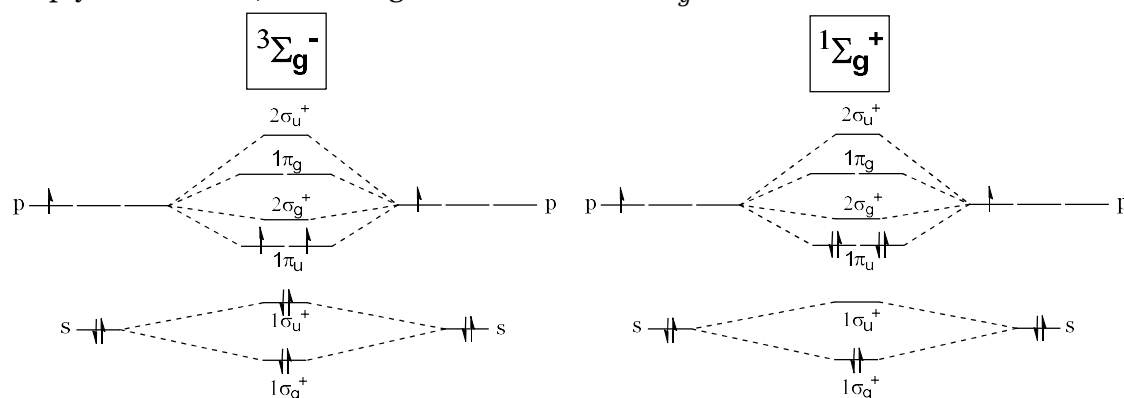
Figure 1. 20. On the left, molecular orbital diagram of $^3\Sigma_g^-$ triplet ground state of B$_2$. On the right, molecular orbital diagram of $^1\Sigma_g^+$ singlet excited state of B$_2$.

1.4.2 Heteroatomic multiple bonds

Heteroatomic multiple bonds of *p*-block elements are ubiquitous in nature. Most of the functional groups in organic chemistry possess a hetero atomic multiple bonds such as acids, esters, imines, enamines or ketenes, to name a few. The development of heavier heteronuclear multiple bonds grew in parallel with their homoatomic analogues. In 1983, Alan Cowley and co-workers reported the synthesis of phosphorus-arsenic double bond (**66**).[122] It represents the first example of a *p*-block heteroatomic double bond between elements with a principal quantum number higher than two. Since then, most of the combinations within *p*-block elements have been reported in the literature.[123]

As mentioned above, there is a special interest on multiple bonds between group 13 and group 15 elements due to their isolobal analogy with alkenes and their potential application in MOCVD process. Albeit multiple bonds between group 13 and group 15 elements are well-established in Zintl anions, their insolubility in common organic solvents makes them inconvenient synthons for practical proposes. There are two types of bonding scenarios which can be found in doubly bounded G_{13} and G_{15} elements (Figure 1.21). A partial double bond, which bears a σ covalent interaction and a π-donation interaction from the lone pair on the G_{15} element to the G_{13} atom. In the case of boron, this π-interaction is strong for nitrogen, phosphorus and arsenic. In aluminium, gallium, indium and thallium, the π-stabilization is rather weak (around 10 kcal/mol), questioning the multiplicity of the bond.[109] The genuine double bond is characterized to have covalent σ- and π-interactions, isolobal to phosphalkenes.[124] Since G_{13} elements have three valence electrons, a Lewis base is needed to stabilize the G_{13} element. Note that the G_{15} element has a lone pair which is non-bonding.
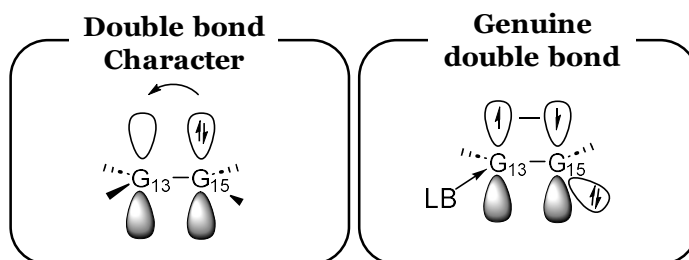
Figure 1. 21.. Plausible bonding interactions between group 13 - group 15 elements.

The synthesis of these multiple bonds in the condensed phase is challenging due to weak π-stabilization. Additionally, the presence of an adjacent Lewis acid and Lewis base entities prone these compounds to oligomerization reactions. Starting from boron chemistry, Alan Cowley and co-workers detected the phosphaborene formation by pyrolyzing a cyclo-diphosphaboretane, but could not be isolated.[125] In 1983, Power and co-workers obtained the first structural characterized anionic phosphaborene (**67**) by a deprotonation reaction of a phoshaborane.[126] Years later, the anionic ansaborene analogue was isolated from the salt metathesis of Mes_2BF and Li_2AsPh.[127] The stabilization of neutral phosphaborenes was achieved by Nöth co-workers by making use of Lewis acids.[128] They trapped the phosphaborene by reacting a cyclo-diphosphaborane with chromiumhexacarbonyl (**68**). Alternatively, Power and co-workers isolated neutral phosphaborenes and arsaborenes employing a Lewis base such as DMAP (**69**)[129, 130] or NHC.[131] Recently, Liu group has reported the synthesis of a *free* phosphaborene, which displays a π push-pull stabilization.[132] There are other examples of phosphaborenes reported in the literature. A detailed description of them is out of the scope of this Thesis, but they are reviewed elsewhere.[6]
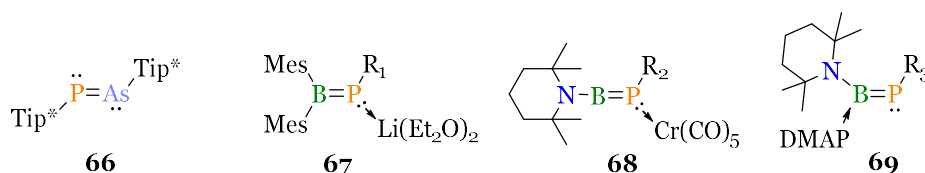
Figure 1. 22. Selected examples of hetero-atomic *p*-block multiple bounded compounds (Mes=mesityl, Tip=2,4,6-tri phenyl, R$_1$=mesityl, cylcohexyl, R$_2$=tri-ethylmethyl, R$_3$=C$_6$H$_3$-2,6-(C$_6$H$_2$-2,4,6-iPr$_3$).

Recently, the chemistry of heavier pnictagallenes has notably expanded. Albeit the beginning of this chemistry is not clear,[6] the first structural characterization of a gallium−pnictogen multiple bond was reported by von Hänishch and co-workers.[133] The salt metathesis of GaCl$_3$ with 2 equivalents of *in-situ* prepared Li$_2$AsSi*i*Pr$_3$ resulted in the formation of compound **70**. The employment of *NacNac* ligand has boosted the chemistry of neutral pnicatgallenes. Schulz and co-workers reacted 2 equivalents of *NacNac*Ga carbenoid with Cp*AsCl$_2$ obtaining the monomeric gallaarsene (**71**), using one equivalent as sacrificial oxidant.[134] The Ga-As distance is 2.267(1) Å, which is shorter than the anionic **70** (Ga-As=2.318(2) Å). Shortly after, the stibagallene was isolated by reducing the [*NacNac*^{Dip}Ga]Sb radical with KC$_8$.[135] Two years later, Wilson *et al.* reported the first example of a phosphagallene. The reaction of a phosphaketene with *NacNac*^{Dip}Ga (I) promotes the exclusion of carbon monoxide forming **72**.[136] The reactivity of compound **72** has been explored for bond activation of different types of substrates, such as H$_2$, CO$_2$, NH$_3$, among others. [137] Since then, Schulz and Goicoechea groups achieved different phosphagallenes with different phosphorus synthons, having in common the use on *NacNac*^{Dip}Ga(I) as gallium synthon.[6] Recently, Hering-Junghans reported the reversible formation of phosphagallene.[138] The combination of GaCp* (Cp*=tetramethylcycopentadienyl) with phospha-Witting reagent (Ar*PPMe$_3$) in the presence of light undergoes PMe$_3$ exclusion, forming the phosphagallene **73**. In the absence of light, the nucleophilic addition of PMe$_3$ to the Ga=P moiety occurs, reverting the equilibrium towards starting materials. In solid-state, compound **78** displays a Ga-P distance of 2.2104(5) Å and 2.2176(5) Å, which is remarkably longer than **73** (Ga-P =2.1650(7) Å and 2.1766(3) Å). Those differences suggest a weaker bonds, which explains the reversibility of **78** with starting materials in solution.
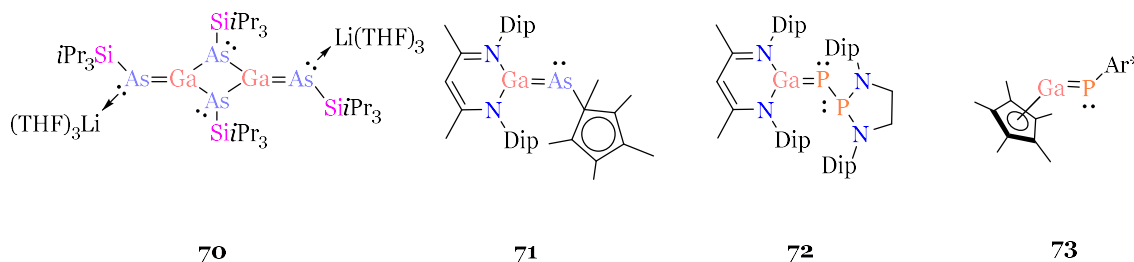
Figure 1. 23.. Selected examples of pnictagallenes. (Dip=2,6-di-isopropylphenyl, iPr=iso-propyl, Ar*=2,6-(di-2,6-iso-propylphenyl)phenyl or 2,6-(tri-2,4,6-iso-propylphenyl)phenyl).

The examples of heavier pnictalenes are scarcer than boron and gallium analogues. Hering-Junghans and Braunschweig groups published together the isolation of the first phospha- and arsaalumenes (**74**).[139, 140] The synthesis consists on reacting (AlCp*)$_4$ (Cp*=pentamethylcycopentadienyl) equimolarly with high steric protected Ar*PnPMe$_3$ phospha- or arsa-Witting reagents (Pn=P,As; Ar*=2,6-Dip$_2$penyl (P,As) or 2,6-Tip$_2$penyl (P)). Upon heating at 80°C, the release of PMe$_3$ is promoted forming the pnictaalene. The distance between of Al-P is 2.2113(6) Å (Ar*=^{Dip}Ter) and 2.2022(6) Å (Ar*=^{Tip}Ter), remarkably shorter than the phosphanylalumanes (*c.a.* 0.1 Å). Note that the Al=P distance is shorter with bulkier substituents which can be regarded to the stronger steric interactions. The reactivity changes with the steric hindrance on the

aluminium cyclopentadienyl compound. The equimolar AlCp^{3t} with the phospha-Witting reagent yielded the cyclic structure **75**. The authors proposed the formation of **75** by, firstly, forming the transient Cp^{3t}Al=P^{Mes}Ter. Secondly, a [2+1] cycloaddition of Cp^{3t}Al=P^{Mes}Ter with an additional equivalent of Cp^{3t}Al. Similarly, half equivalent of the (Cp*Al)$_4$ with ^{Mes}TerPPMe$_3$ yielded compound **75**. Interestingly, DFT calculations supported that compound **75** is 2π-Hückel aromatic.
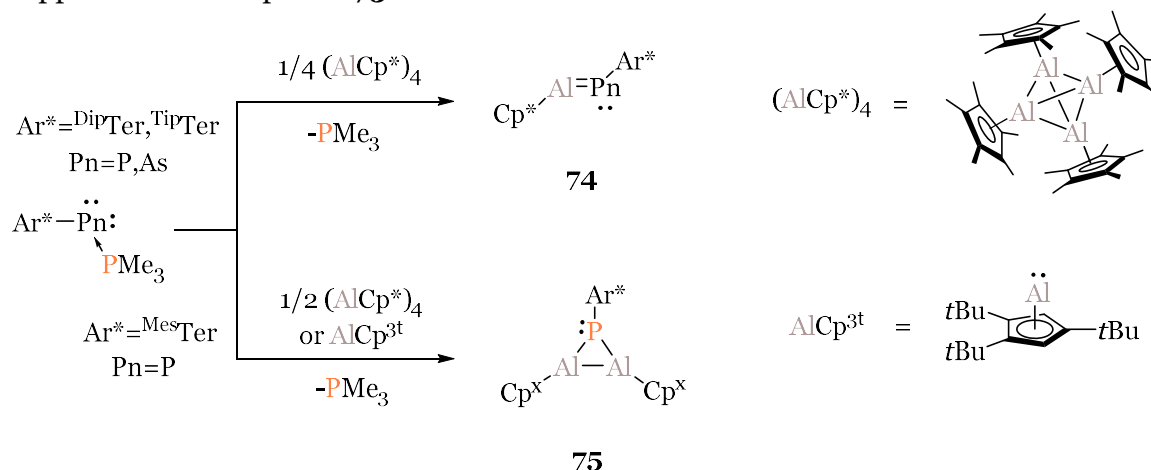
Figure 1. 24. Synthesis of phosha- and arsa-alumenes (Cp^X=Cp* or Cp^{3t}).

Hering-Junghans and Braunschweig groups explored further the chemistry of phospha-Witting reagents with aluminium(I) cyclopentadienyl compounds, isolating a palette of cyclo-diphosphalanes (Figure 1.25).[141] The alternating rings **76** are isolated by using small substituents on the phosphorus and aluminium synthons. Interestingly, the head-to-head isomers (**77**) are favoured with sterically demanding substituents on the aluminium and phosphorus building blocks. Attempts to obtain the monomeric Al=P with NHC failed. Upon the coordination of NHC to aluminium, the cyclopentadienyl ligand changes the hapticity from η^5 to η^1, isolating the butterfly-shaped dimeric structure **78**.
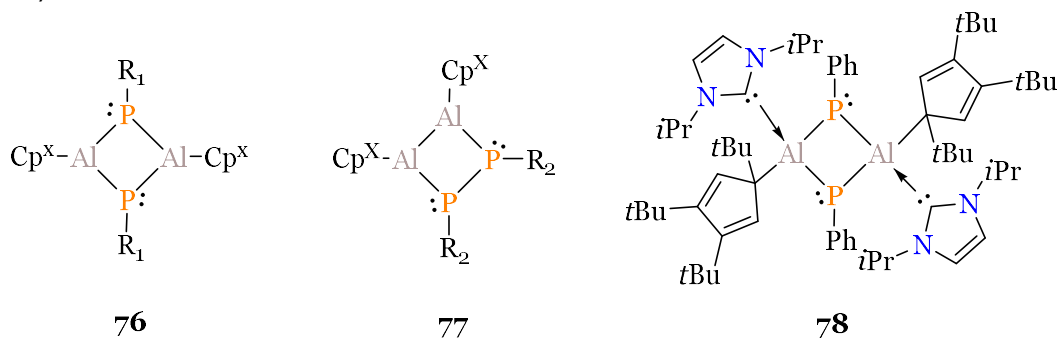
Figure 1. 25. Selected examples of cyclo-diphosphalenes.(Cp^X=Cp* or Cp^{3t})

The same groups attempted to stabilize the phosphaalumene by making use of the *NacNac* ligand. The equimolar reaction of *NacNac*Al(I) carbenoid with the phospha-Witting reagent Tip*PPMe$_3$ (Tip*=2,4,6-tris-*tert*-butylphenyl) undergoes PMe$_3$ release and a subsequent C-H activation of a methyl from the *ortho-tert*-butyl group (**79**).[142] The authors propose the transient formation of *NacNac*Al=PTip* (**80**), but the C-H activation occurs due to the huge thermodynamic stability of **79** with respect to **80**.
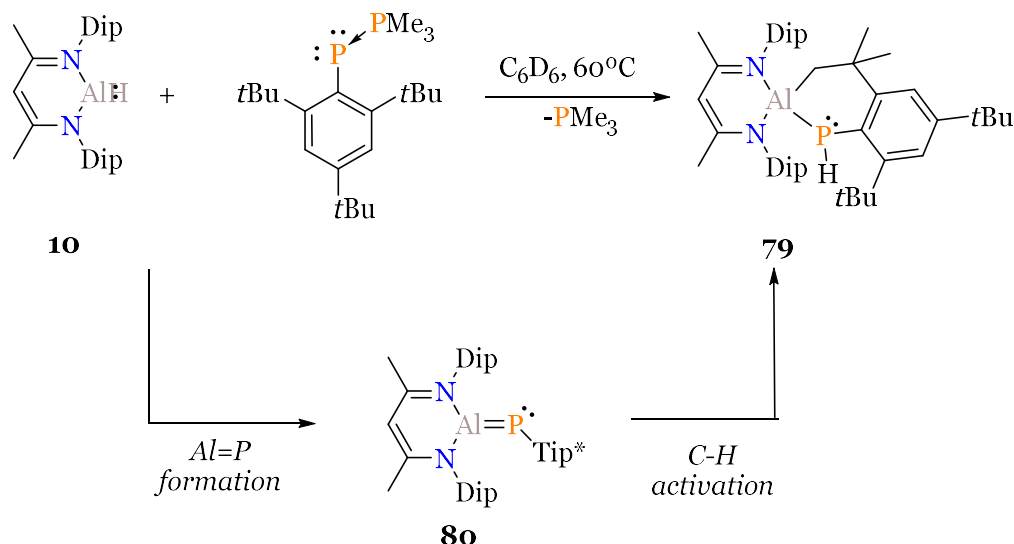
Figure 1. 26. Attempted synthesis of phosphaalumene stabilised by *NacNac* ligand.

In 2022, Hering-Jughans and Braunschweig groups explored the reactivity of phosphaalumene towards alkynes and alkanes. Disubstituted alkynes undergo [2+2] cycloaddition forming the 1,2-phosphaalumetes (**81**) while terminal alkynes or acetylene undergo threefold insertion to form barrelene-like structure **82**. Similar reactivity is observed with alkenes. The treatment of phosphaalumene with an excess amount of styrene forms the 1,2-phosphaalumate (**83**). Longer reaction times promote the twofold insertion forming the 6-membered ring 1,4-aluminophosphorinane (**84**).
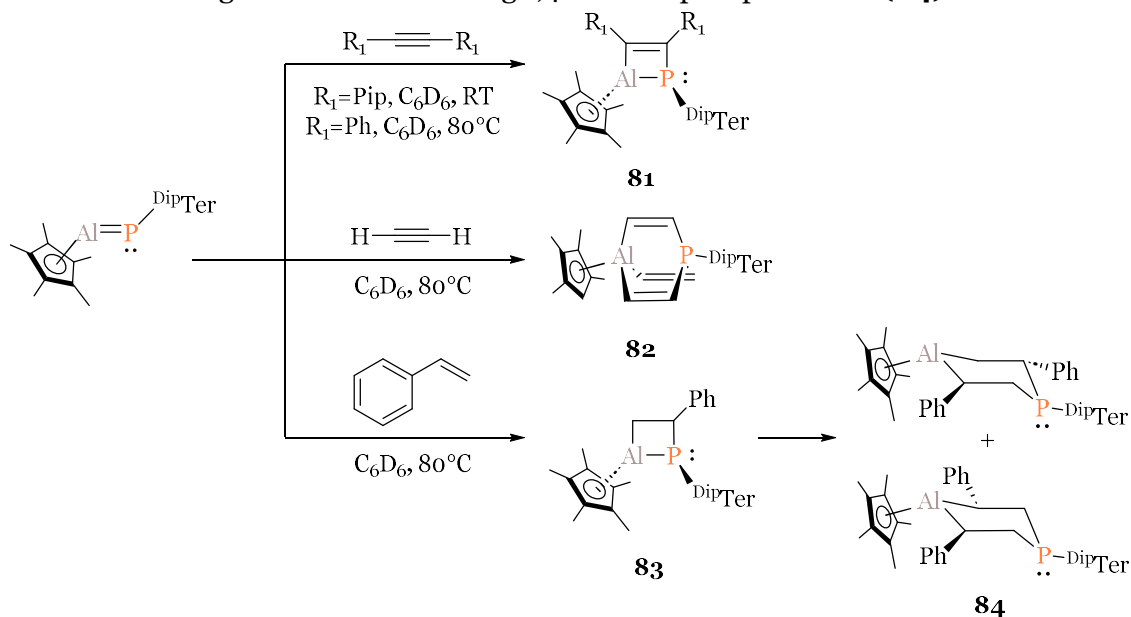
Figure 1. 27. Selected examples of [2+2] cycloaddition reaction of phosphaalumene.

1.5 Electronic Structure and Quantum Chemical Bonding Tools

Electronic structure methods help to understand or predict unusual molecular structures, spectroscopic features or reaction mechanisms of molecular systems. These methods represent the application of quantum mechanics to chemical systems (Quantum Chemistry) and are theoretically sound. On the other hand, over the years

(and way before the advent of Quantum Mechanics), chemists have built empirical models and come up with concepts that have been proven to be extremely useful to systematize and rationalize all types of chemical phenomena. Chemical concepts like oxidation state, aromaticity, steric repulsion, covalence or even the chemical bond, are not observables in the Quantum Mechanical sense, which opens the door to multiple approaches to quantify them, leading to controversy in some cases.

This section aims at exposing the different electronic structure methods, namely Hartree-Fock, post-Hartree-Fock and Density Functional Theory, with their strengths and drawbacks. Then, the different state-of-the-art chemical bonding tools employed in this Thesis will be described.

1.5.1 Electronic structure methods

In the stationary state, the energy of a quantum state i (ε_i) is given by the time-independent Schrödinger equation

$$\hat{H}\Psi_i(\boldsymbol{q}, \boldsymbol{R}) = \varepsilon_i \Psi_i(\boldsymbol{q}, \boldsymbol{R}), \tag{1}$$

where $\Psi_i(\boldsymbol{q}, R)$ is the wavefunction which describes the quantum state i and $\hat{H}$ is the Hamiltonian operator which account for the kinetic and Coulomb interactions between the electrons and the nuclei. The $\boldsymbol{r}$ represents the set of all spatial (r_i) and spin coordinates (σ_i) of the electrons ($\boldsymbol{q} \equiv \{r_i, \sigma_i\}, \forall i$) and $\boldsymbol{R}$ represents the nuclear coordinates. Unfortunately, the Schrödinger can only be analytically solved for one-electron systems, i.e. for hydrogen or hydrogenoid molecules. Approximations are needed to assess bigger systems, in particular molecules. The most common is the Born-Oppenheimer approximation, which decouples the movement of the electrons with the movement of the nuclei. Since the mass of the electron is much smaller than the mass of the nucleus, the movement of the electron can be considered independent of the nuclear motion. In practice, this means one can try to solve the Schrödinger Eq. 1 for the electronic motion by fixing the nuclear coordinates at a given position. Then, the nuclear motion can be captured by solving the Schrödinger equation for the nuclei in the presence of the potential created by the electrons. Thus, by fixing the nuclear coordinates $\boldsymbol{R}$ one obtains the following equation-from

$$\hat{H}^{elect}\Psi_i^{elect}(\boldsymbol{q}; \boldsymbol{R}) = \varepsilon_i^{elect}(\boldsymbol{R})\Psi_i^{elect}(\boldsymbol{q}; \boldsymbol{R}), \tag{2}$$

where $\Psi_i^{elect}(\boldsymbol{q}; \boldsymbol{R})$ is the electronic wavefunction, $\hat{H}^{elect}$ is the electronic Hamiltonian, and $\varepsilon_i^{elect}(\boldsymbol{R})$ is the electronic energy on the state i. The $\hat{H}^{elect}$ gathers all contributions except for the kinetic energy of the nuclei. This energy depends, of course, on the position of the nuclei, and it is often referred to as the potential energy surface for state i. From now on, $\Psi_i^{elect} \equiv \Psi_i$ and $\hat{H}^{elect} \equiv \hat{H}$ to simplify the notation.
. Thus, the electronic Hamiltonian is written as

$$\hat{H} = \hat{T}_e + \hat{U}_{en} + \hat{U}_{ee} + \hat{U}_{nn} \tag{3}$$

where $\hat{T}_e$ is the kinetic energy of the electrons, $\hat{U}_{en}$ is the electron-nuclei attraction, $\hat{U}_{ee}$ is the electron-electron repulsion and $\hat{U}_{nn}$ is the nuclei-nuclei repulsion.

The electronic wavefunction must ensure the Pauli's antisymmetry principle. It guarantees that the wavefunction is antisymmetric

$$\Psi_i(\boldsymbol{q_1}, \boldsymbol{q_2}, \boldsymbol{q_3}, \dots, \boldsymbol{q_N}) = -\Psi_i(\boldsymbol{q_2}, \boldsymbol{q_1}, \boldsymbol{q_3}, \dots, \boldsymbol{q_N}) \tag{4}$$

The simplest way is to rely on the orbital approximation which treats each electron $\boldsymbol{q}_i$ individually. In a molecular system, these orbitals are known as spin molecular orbitals ($\varphi_n(\boldsymbol{q}_i)$). The typical way to construct $\varphi_n(\boldsymbol{q}_i)$ is by making use of Lineal Combination of Atomic Orbitals (MO-LCAO) approximation,

$$\varphi_i = \sum_{\mu}^{N_{AO}} c_{i\mu}\, \chi_\mu \tag{5}$$

here $\{\chi_\mu\}$ is a set of functions centred on the atoms that play the role of the Atomic Orbitals (AO) of the isolated atoms. Then, the molecular orbital coefficients $\{c_{i\mu}\}$ are usually variationally determined to minimise the total energy of the system. In order to build an antisymmetric wavefunction, the molecular orbitals used to construct the so-called Slater determinant,

$$\Psi_i(\boldsymbol{q_n}) = \frac{1}{\sqrt{N!}} \begin{vmatrix} \varphi_1(\boldsymbol{q_1}) & \cdots & \varphi_n(\boldsymbol{q_1}) \\ \vdots & \ddots & \vdots \\ \varphi_1(\boldsymbol{q_n}) & \cdots & \varphi_n(\boldsymbol{q_n}) \end{vmatrix}, \tag{6}$$

where $\frac{1}{\sqrt{N!}}$ is the normalization factor.

1.5.1.1 Hartree-Fock and post-Hartree-Fock methods

Solving the electronic Schrödinger equation (Eq. 2) has been one of the most important tasks for quantum chemistry. Let's consider the electronic Hamiltonian written as

$$\hat{H} = \sum_{A}^{M} \sum_{B>A}^{M} \frac{Z_A Z_B}{r_{AB}} + \sum_{i}^{N} -\frac{1}{2}\nabla_i^2 - \sum_{i}^{N} \sum_{A}^{M} \frac{Z_A}{r_{iA}} + \sum_{i}^{N} \sum_{j>i}^{N} \frac{1}{r_{ij}} \tag{7}$$

Within the Born-Oppenheimer approximation, the nuclear repulsion is a constant (first term of Eq.7), so it can be simply added to the electronic energy at each nuclear configuration. The kinetic energy and electron-nuclear attraction are one electron operators (second and third terms of Eq.7), which means that only depend on one electron coordinate r_i. The electron-electron repulsion (last term of Eq. 7) is a two-electron operator which depends on two electron coordinates (r_i and r_j). The latter term makes the problem not solvable (many-body problem), hence we need to introduce approximations. The Hartree-Fock (HF) method constitutes the first attempt approximate the Schrödinger equation. The variational principle states that the best wave function, Slater determinant in orbital approximation, is the one which yields the lowest energy

$$E_0 = \langle \Psi_0 | \hat{H} | \Psi_0 \rangle . \tag{8}$$

Constraining the molecular orbitals $\{\varphi_i\}$ to be orthogonal, one obtains the following one-electron equation

$$\hat{F}(\boldsymbol{r_1})\, \varphi_i(\boldsymbol{r_1}) = \varepsilon_i \varphi_i(\boldsymbol{r_1}), \tag{9}$$

where $\hat{F}(\boldsymbol{r})$ is the Fock operator and ε_i is the orbital energy of φ_i The Fock operator accounts the energy of one electron written as

$$\hat{F}(\boldsymbol{r}_1) = \hat{h}(\boldsymbol{r}_1) + \hat{v}^{HF}(\boldsymbol{r}_1), \tag{10}$$

where $\hat{h}(\boldsymbol{r}_1)$ accounts for all the one-electron operators,

$$\hat{h}(\boldsymbol{r}_1) = -\frac{1}{2}\nabla_1^2 - \sum_A \frac{Z_A}{r_{1A}}, \tag{11}$$

and $\hat{v}^{HF}(\boldsymbol{r}_1)$ is the Fock potential, which approximates the electron-electron repulsion as an average potential produced by the *N-1* electrons. The $\hat{v}^{HF}(\boldsymbol{r}_1)$ is constructed from Coulomb ($\hat{v}^C(\boldsymbol{r}_1)$) and the Exchange ($\hat{v}^{Ex}(\boldsymbol{r}_1)$) potentials,

$$\hat{v}^{HF}(\boldsymbol{r}_1) = \hat{v}^C(\boldsymbol{r}_1) - \hat{v}^{Ex}(\boldsymbol{r}_1). \tag{12}$$

The Coulomb potential accounts the average classical electron-electron repulsion and the exchange potential is a quantum effect arising from the antisymmetry principle, that leads to a decrease in the electron-electron repulsion for same spin electrons. These operators are built from contributions from the remaining occupied spin orbitals that enter in the Slater Determinant

$$\hat{v}^C(\boldsymbol{r}_1) = \sum_{j \neq i} \hat{J}_j(\boldsymbol{r}_1) \tag{13}$$

$$\hat{v}^{Ex}(\boldsymbol{r}_1) = \sum_{j \neq i} \widehat{K}_j(\boldsymbol{r}_1), \tag{14}$$

defined as

$$\hat{J}_j(\boldsymbol{r}_1)\,\varphi_i(\boldsymbol{r}_1) = \left(\int \frac{1}{r_{12}}\varphi_j^*(\boldsymbol{r}_2)\varphi_j(\boldsymbol{r}_2)\,d\boldsymbol{r}_2\right)\varphi_i(\boldsymbol{r}_1) \tag{15}$$

$$\widehat{K}_j(\boldsymbol{r}_1)\varphi_i(\boldsymbol{r}_1) = \left(\int \varphi_j^*(\boldsymbol{r}_2)\frac{1}{r_{12}}\varphi_i(\boldsymbol{r}_2)\,d\boldsymbol{r}_2\right)\varphi_j(\boldsymbol{r}_1) \tag{16}$$

The HF method is nowadays mostly used as reference of the so-called post-Hartree-Fock methods (*vide infra*) but it is not employed for quantitative purposes. The main disadvantage of HF method is the underestimation of the interaction between electrons with opposite spin. In 1959, Löwdin defined the so-called *electron correlation* energy (E_{corr}) as

$$E_{corr} = E_{exact} - E_{HF}, \tag{17}$$

were E_{exact} is the exact energy and E_{HF} is the energy obtained from the HF method.[143] Most, but not all, of the correlation energy comes from the description of repulsion between odd spins. This energy contribution has often named as *chemical glue*, having a vital influence for chemical modelling.[144]

The electron correlation has different flavours. Among them, the dynamic and static correlation are the most popularly known. The dynamic correlation is due to the influence of the motion of one electron with the rest of the electrons. This type of correlation is important to properly model, for instance, dispersion interactions. The static correlation is related with long range electron interactions, which becomes important when a system presents MOs degeneracies in the HOMO orbital. The introduction of static correlation is not plausible by making use of one Slater

determinant. A combination of them is needed to properly describe this type of correlation.

The *ab-initio* or post-Hartree-Fock (post-HF) approaches are a family of methods which improve the HF wavefunction by introducing electron correlation. The most natural method is the Configuration Interaction (CI), which consists of constructing the wavefunction by a lineal combination of Slater determinants

$$\psi_{CI} = c_0\psi_{HF} + \sum_{ar} c_a^r\psi_a^r + \sum_{\substack{a<b \\ r<l}} c_{ab}^{rl}\psi_{ab}^{rl} + \sum_{\substack{a<b<c \\ r<l<t}} c_{abc}^{rlt}\psi_{abc}^{rlt} + \cdots, \qquad (18)$$

and obtaining variationally the expansion coefficients. The HF wavefunction (ψ_{HF}) is generally used as *reference* and the rest of Slater determinants are constructed by exchanging (excitations) occupied (*a,b,c*) and virtual (*r,l,t*) MOs from the HF calculation. The mono excitations (ψ_a^r) involve the excitation of the *a*-th occupied orbital to the *r*-th orbital, the biexcitations (ψ_{ab}^{rl}) correspond to the simultaneous excitations of a→r and b→l, and so on. The Full Configuration Interaction (FCI) includes all the possible excitations, achieving the *exact* solution within the non-relativistic Born-Oppenheimer approximation, and the chosen one-electron AO basis. However, the computational cost of FCI is enormous, only being accessible for small systems and minima basis with the actual computational power. An option is to restrict the number of excitations in eq. 9, leading to the truncated-CI methods. The inclusion of excitation decreases the energy, mostly through the biexcitations which recover the dynamic correlation.

For molecules where the HOMO present orbital degeneracies, the inclusion of CI excitations does not improve the energy. In these cases, one Slater determinant is not enough to model the system. One needs to assess a linear combination of Slater determinants (Multireference methods). The most popular one is the Complete Active Space Self Consistent Field (CASSCF) which has broadly used to model systems with high amount of static correlation. Within this method, one needs to select *a priori* the electrons and MO which belong to the internal, active and external spaces. External MOs are not used at all, and internal MOs are always present on the Slater determinants. Then, one generates all possible configurations of the active electrons among the active orbitals (according to the specified spin state). Then, the CASSCF wavefunction is constructed as a linear combination of all Slater determinants associated to the configurations. In the CASSCF procedure, both the occupied orbitals and the expansion coefficients are simultaneously optimized (often to the ground state, but also to any desired excited state). In Figure 1.28 is represented the of CASSCF subspaces calculation of simple example which 2 electrons and 2 MO are selected in the active space (CASSCF(2,2)).
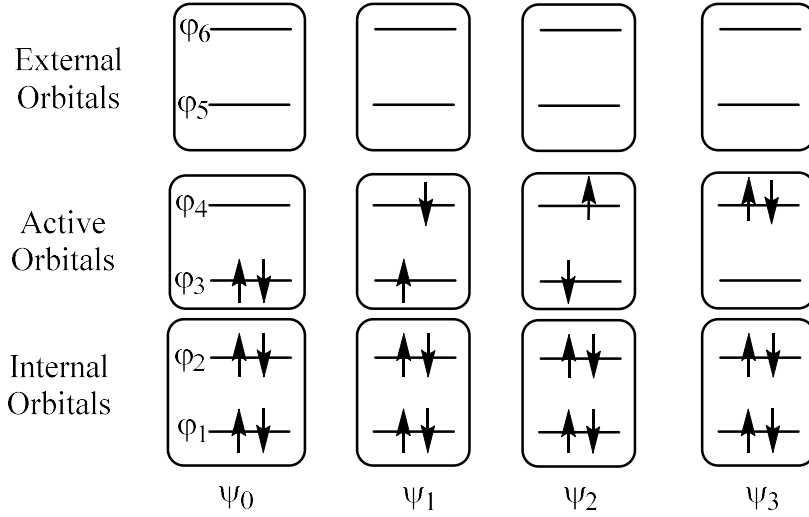
Figure 1. 28. Schematic representation of the Slater determinants in a CASSCF (2,2) calculation.

In 1966, Cizek and co-workers introduced the Coupled Cluster (CC) theory, a very accurate method which includes dynamic correlation. The CC wavefunction is expressed as

$$\psi_{CC} = e^{\hat{T}}\psi_{HF} , \tag{19}$$

where $\hat{T}$ is the Cluster operator. It is written as

$$\hat{T} \equiv \hat{T}_1 + \hat{T}_2 + \hat{T}_3 + \cdots + \hat{T}_N, \tag{20}$$

which generates all the Slater determinants form the reference wavefunction. The $\hat{T}_1$ is the single excitation operator. When it acts on ψ_{HF} generates all the single excitation determinants from the HF wavefunction with their expansion coefficients (t_a^r), known as amplitudes. The $\hat{T}_2$ is the is the double excitation operator which generates all the double excitation determinants and so on to the *N*-th excitation operator. In practice, the CC operator is typically truncated to a single (CCS) or double (CCSD) excitation degree.

$$\hat{T}_1|\psi_{HF} >= \sum_a \sum_r |\psi_a^r > t_a^r \tag{21}$$

$$\hat{T}_2|\psi_{HF} >= \sum_{a<b} \sum_{s<r} |\psi_{ab}^{rs} > t_{ab}^{rs} \tag{22}$$

The CC operator can be expressed in Taylor series,

$$e^{\hat{T}} = 1 + \hat{T} + \frac{1}{2}\hat{T}^2 + \frac{1}{3!}\hat{T}^3 + \cdots, \tag{23}$$

Inserting equation 20 to 23, we obtain the following expression,

$$e^{\hat{T}} = 1 + \left(\hat{T}_1 + \hat{T}_2 + \hat{T}_3 + \cdots\right) + \frac{1}{2}\left(\hat{T}_1 + \hat{T}_2 + \hat{T}_3 + \cdots\right)^2 + \frac{1}{6}\left(\hat{T}_1 + \hat{T}_2 + \hat{T}_3 + \cdots\right)^3, \tag{24}$$

which can be sorted by type of excitations as

$$e^{\hat{T}} = 1 + \hat{T}_1 + \left(\hat{T}_2 + \frac{1}{2}\hat{T}_1^2\right) + \left(\hat{T}_3 + \frac{1}{6}\hat{T}_1^3 + \hat{T}_1\hat{T}_2\right) + \cdots. \tag{25}$$

Because of the exponential nature of the operator, one always gets all the excited determinants in the wavefunction. For instance, if the CC operator is truncated to the single excitations, one obtains the CC operator expression

$$e^{\hat{T}} = 1 + \hat{T}_1 + \frac{1}{2}\hat{T}_1{}^2 + \frac{1}{6}\hat{T}_1{}^3 + \cdots. \tag{26}$$

The CCSD(T) is the most popular method, truncating the CC operator up to double excitations. The single and double excitations are computed iteratively meanwhile the triply excitations are perturbationally introduced, which reduces the computational cost without significantly losing accuracy. The CCSD(T) is generally considered as the *golden standard* in computational chemistry, being used as *true* reference. However, it is important to mention that CCSD(T) poorly introduces the static correlation.

1.5.1.2 Density Functional Theory

Albeit wavefunction methods can provide a high accurate estimation of energy, the computational cost can be prohibitively high. Nowadays, the Density Functional Theory (DFT) has become a very appealing method for computational chemists, being able to model reaction mechanisms or spectroscopic data, of relatively big systems. These methods provide good compromise between computational cost and accuracy.

The most important ingredient of DFT methods is the one-electron density $\rho(\boldsymbol{r_1})$. It is described as

$$\rho(\boldsymbol{r_1}) = N \int d\boldsymbol{\sigma_1} \int d\boldsymbol{q_2} \int d\boldsymbol{q_3} \dots \int d\boldsymbol{r_N}\, \Psi|\boldsymbol{q_1},\boldsymbol{q_2},\boldsymbol{q_3},\dots,\boldsymbol{q_N}|^2 . \tag{27}$$

For restricted single determinant wavefunctions, the $\rho(\boldsymbol{r_1})$ can be constructed from the doubly occupied molecular orbitals as

$$\rho(\boldsymbol{r_1}) = 2 \sum_i^{N/2} \varphi_i^*(\boldsymbol{r_1})\varphi_i(\boldsymbol{r_1}). \tag{28}$$

Hohenberg and Kohn elaborated two theorems which are crucial for DFT. The first one stands that the energy can be determined by an energy functional

$$E_{exact} = E[\rho_{exact}(\boldsymbol{r})]. \tag{29}$$

The second theorem says that the minimum energy is reached when the exact energy is considered. Therefore, the variational principle can be applied within DFT framework.[145]

The total energy functional is composed by kinetic ($T[\rho(\boldsymbol{r})]$), electron-nuclei attraction ($V_{en}[\rho(\boldsymbol{r})]$) and electron-electron ($V_{ee}[\rho(\boldsymbol{r})]$) energy functionals

$$E_{exact}[\rho(\boldsymbol{r})] = T[\rho(\boldsymbol{r})] + V_{en}[\rho(\boldsymbol{r})] + V_{ee}[\rho(\boldsymbol{r})]. \tag{30}$$

Unfortunately, the exact expression of the universal energy functional is not known, which implies the use of approximations. The Kohn and Sham DFT (KS-DFT) is a popular (if not the most) DFT methodology. It considers a fictitious model system of non-interacting electrons ($\rho_s(\boldsymbol{r})$) which have the same density for the system of

interacting electrons.[146] Since the fictitious system has no electron-electron interaction, the exact solution can be expressed with an Slater determinant. Then, a potential $V_{ee}[\rho(r)]$ must be introduced to obtain the *real* density. The $V_{e-}[\rho(r)]$ is composed by the electron-electron repulsion functional ($J[\rho(r)]$) and the Exchange-Correlation functional ($E_{xc}[\rho(r)]$), which encompass all the energy differences between the Kohn-Sham energy and the exact energy and the electron correlation. The Kohn-Sham energy functional ($E_{KS}[\rho(r)]$) is written as

$$E_{KS}[\rho(r)] = T_s[\rho_s(r)] + V_{en}[\rho(r)] + V_{ee}[\rho(r)]. \tag{31}$$

Note that the $E_{KS}[\rho(r)]$ expression has similarities with the Hartree-Fock equations (*vide supra*), which the exchange contribution is substituted by the Exchange-correlation functional. The expression of the $E_{xc}[\rho(r)]$ remains unknown to the date. Nowadays, a plethora of approximations of the $E_{xc}[\rho(r)]$ expression has been developed, such as Local Density Approximation (LDA), Generalized Gradient Approximation (GGA), Meta-generalized Gradient Approximation (meta-GGA) or Hybrid Functional Approximation. Those methodologies are based on an exact solution of a system in certain conditions or based on experimental/computational observations. One of the bottlenecks of DFT is the underestimation of the dispersion energy. Grimme and co-workers introduced an effective semi-empirical method (DFT-D) to correct the energies with a very low computational cost.[147, 148]

1.5.2 The atomic definition – Hilbert and Real space approaches

The Greek philosopher and scientist Democritus conceptualized a theory which described the matter as an ensemble of individual entities, baptized as atoms. This name remained along the centuries, being adopted by the modern atomic theories, going from Dalton to Schrödinger. From a chemical perspective, the atoms interact by electron pairs forming chemical bond. The classification of the chemical bonds helps chemists to understand the structure and reactivity of molecules. The nature of the interactions is rationalized with the so-called chemical bonding tools, which extract information of the physical origin of the chemical interaction. Accordingly, the chemical bonds are classified building chemical bonding models such as ionic, donor-acceptor or covalent bonds. Nowadays, most of (if not all) the chemical bonding tools need to use a definition of the atom in the molecule (AIM). Since the atom is not an observable, several AIM definitions have been developed along the years, aiming to provide a consistent interpretation with the experimental observables or chemical intuition. The AIM definition is attached to an atomic partition. They can be divided in two families, namely Hilbert and Real space. In the following section will be described the different AIM used in this Thesis, providing insights of their pros and cons.

1.5.2.1 The Hilbert-space analysis

Hilbert-space analyses consider that the atom is formed by its nucleus and the set of atomic orbitals attached to it, $\left\{\chi_\mu(r_1)\right\}_{\mu \in A}$. Then, for a restricted single determinant wavefunction, the one-electron density can be written as

$$\rho(\boldsymbol{r_1}) = \sum_i^N \sum_{\mu\nu}^{N_{AO}} c_{\nu i}^* c_{\mu i}\, \chi_\nu^*(\boldsymbol{r_1})\chi_\mu(\boldsymbol{r_1}) = \sum_{\mu\nu}^{N_{AO}} D_{\mu\nu}\, \chi_\nu^*(\boldsymbol{r_1})\chi_\mu(\boldsymbol{r_1})\,, \tag{32}$$

where $D_{\mu\nu}$ is the so-called density matrix in the AO basis. The total number of electrons is recovered upon integration of equation 32 as

$$N = \int \rho(\boldsymbol{r_1})\, d\boldsymbol{r_1} = \sum_{\mu\nu}^{N_{AO}} D_{\mu\nu} \int \chi_\nu^*(\boldsymbol{r_1})\chi_\mu(\boldsymbol{r_1})d\boldsymbol{r_1} = \sum_{\mu\nu}^{N_{AO}} D_{\mu\nu}\, S_{\mu\nu}\,, \tag{33}$$

where $S_{\mu\nu}$ is the overlap integral of the AOs, written as

$$S_{\mu\nu} = \int \chi_\nu^*(\boldsymbol{r_1})\chi_\mu(\boldsymbol{r_1})\, d\boldsymbol{r_1}\,. \tag{34}$$

The summation of equation 33 can be systematized accordingly to the Hilbert-subspaces obtaining the Mulliken net atomic populations (N_{AA}^{net}) and the overlap populations (N_{AB}^{olvp}).[149]

$$N = \sum_{AB}^{N_{At}} \sum_{\mu\in A}^{N_{AO}} \sum_{\mu\in B}^{N_{AO}} D_{\mu\nu} S_{\mu\nu} = \sum_{A}^{N_{At}} N_A^{net} + \sum_{A,B\neq A}^{N_{At}} N_{AB}^{olvp}\,. \tag{35}$$

If on instead decomposes N into only atomic contributions, the gross atomic populations are obtained

$$N = \sum_{A}^{N_{AO}} \sum_{\mu\in A}^{N_{AO}} (DS)_{\mu\mu} = \sum_{A}^{N_{At}} N_A^{gross}\,. \tag{36}$$

The Mulliken analysis has two main drawbacks. On the one hand, it is basis set dependent. It means that atomic populations varies with the type of underlying AO basis used in the calculation.[150] The employment of large basis set yields unphysical results. On the other hand, the atomic populations do not converge to a value at the basis set limit. By increasing the basis set size, the atomic population does not converge to a discrete value.[151]

Several schemes have been developed to overcome the Mulliken weaknesses. A convenient approach is to apply an orthogonalization of the AO basis by introducing a matrix transformation. Löwdin suggested $U = S^{-1/2}$ as a plausible option.[152] This transformation allows to construct a set of orthogonalized orbitals (Löwdin basis) from the original AOs,

$$|\chi^{Lowd} > = |\chi > S^{-\frac{1}{2}}\,. \tag{37}$$

Since there is no overlap in the orthogonal basis, there is no overlap population. Then, the gross and net atomic populations are equivalent. The molecular quantities (*e.g.* the electron density) expressed in terms of the Löwdin basis have been shown to be more robust with respect to the original AO basis used. Moreover, the generalized Löwdin schemes are an extension of the Löwdin orthogonalization, where an additional unitary matrix is introduced

$$|\chi^{Lowd} > = |\chi > S^{-1/2}\, U\,. \tag{38}$$

Alternatively, in the so-called weighted-Löwdin schemes, $S^{-\frac{1}{2}}$ is replaced by the following matrix

$$S^{-\frac{1}{2}} \rightarrow W(W^T S W)^{-1/2} \, , \tag{39}$$

where use a weighting matrix W is introduced.

During the last years, different ways to construct matrix W have been developed. One of the most popular ones are the Natural Atomic Orbitals (NAO),[153] which is broadly use for analysing charge distribution of a molecule (Natural Population Analysis) or to build Natural Bond Orbitals (NBO).

1.5.2.2 The Real-space partition

In the real space analysis, the atom is formed by its nucleus and a region of the space assigned to it. This region is known as the atomic domain. Within this formalism, any molecular quantity described by a one-electron density function $f(\boldsymbol{r_1})$ can be decomposed into atomic contributions (F_A) by restricting the integration over the atomic domains (Ω_A) or by weight function (w_A) as

$$F_A = \int_{\Omega_A} f(\boldsymbol{r_1}) \, d\boldsymbol{r_1} = \int w_A(\boldsymbol{r_1}) f(\boldsymbol{r_1}) \, d\boldsymbol{r_1} \, . \tag{40}$$

A molecular quantity described by a two-electron function ($f(\boldsymbol{r_1}, \boldsymbol{r_2})$) can be decomposed into mono and diatomic terms, F_{AA} and F_{AB}, respectively.

$$F_{AA} = \int_{\Omega_A} \int_{\Omega_A} f(\boldsymbol{r_1}, \boldsymbol{r_2}) \, d\boldsymbol{r_1} d\boldsymbol{r_2} = \int \int w_A(\boldsymbol{r_1}) w_A(\boldsymbol{r_2}) f(\boldsymbol{r_1}, \boldsymbol{r_2}) d\boldsymbol{r_1} d\boldsymbol{r_2} \tag{41}$$

$$F_{AB} = \int_{\Omega_A} \int_{\Omega_B} f(\boldsymbol{r_1}, \boldsymbol{r_2}) \, d\boldsymbol{r_1} d\boldsymbol{r_2} = \int \int w_A(\boldsymbol{r_1}) w_B(\boldsymbol{r_2}) f(\boldsymbol{r_1}, \boldsymbol{r_2}) d\boldsymbol{r_1} d\boldsymbol{r_2} \tag{42}$$

The atomic domains can be disjoint or can be allowed to overlap. In the case of disjoint domains, the most popular model is given by Quantum Theory of Atoms in Molecules (QTAIM). In QTAIM the atom domains (Bader basin) are constructed accordingly to the zero-flux surface or separatrix ($S(\boldsymbol{r})$) condition

$$\nabla \rho(\boldsymbol{r}) \cdot \vec{n}(\boldsymbol{r}) = \vec{\boldsymbol{0}} \; ; \; \forall \boldsymbol{r} \in S(\boldsymbol{r}), \tag{43}$$

where $\vec{n}(\boldsymbol{r})$ is the unit vector perpendicular to t he $S(\boldsymbol{r})$. Each point of the density belongs to only one atom. Thus, the weight function is either $w_A = 1$, for the regions which belong to atom A, or $w_A = 0$, for regions which do not belong A. The gradient of the electron density, $\nabla \rho(\boldsymbol{r})$, gives a set of critical points (CP), which are categorized accordingly to their second derivative, the so-called Hessian matrix $\boldsymbol{H}[\rho(\boldsymbol{r})]$,

$$H[\rho(\mathbf{r})] = \begin{pmatrix} \dfrac{\partial^2 \rho(\mathbf{r})}{\partial x^2} & \dfrac{\partial^2 \rho(\mathbf{r})}{\partial x \partial y} & \dfrac{\partial^2 \rho(\mathbf{r})}{\partial x \partial z} \\[2mm] \dfrac{\partial^2 \rho(\mathbf{r})}{\partial y \partial x} & \dfrac{\partial^2 \rho(\mathbf{r})}{\partial y^2} & \dfrac{\partial^2 \rho(\mathbf{r})}{\partial x \partial z} \\[2mm] \dfrac{\partial^2 \rho(\mathbf{r})}{\partial z \partial x} & \dfrac{\partial^2 \rho(\mathbf{r})}{\partial y \partial z} & \dfrac{\partial^2 \rho(\mathbf{r})}{\partial z^2} \end{pmatrix}. \tag{44}$$

Upon diagonalization of $H[\rho(\mathbf{r})]$, the sign of the eigenvalues λ_1, λ_2 and λ_3 describes the curvature of the electron density. Accordingly, the CPs are categorized as:

- *Attractor*: all the eigenvalues are negatives, indicating a maximum of the electron density. The position of the attractor coincides with the position of the nuclei. In some cases, this is not fulfilled known as Non-Nuclear attractors (NNA).
- *Bond critical point (BCP)*: two eigenvalues are negative and one is positive. The BCP is found between two nuclear attractors.
- *Ring critical point (RCP):* One negative and two positive eigenvalues.
- *Cage critical point (CCP):* Three positive eigenvalues indicating a minimum of the electron density. This CCPs are typically found in cage-like structures.

The gradient line which connects two attractors is called bond path (BP). According to the QTAIM theory, if two atoms are connected though a BP indicates that there is a chemical bond. This condition is fulfilled for most of the chemical but does not always an signifies the existence of an *strict* chemical bond.[154, 155] Pendás and co-workers referred to the BP as "*Privileged Exchange-Correlation channels*".[156] They demonstrated that the existence of a BP indicates an stabilizing interaction, lowering the energy of the system.
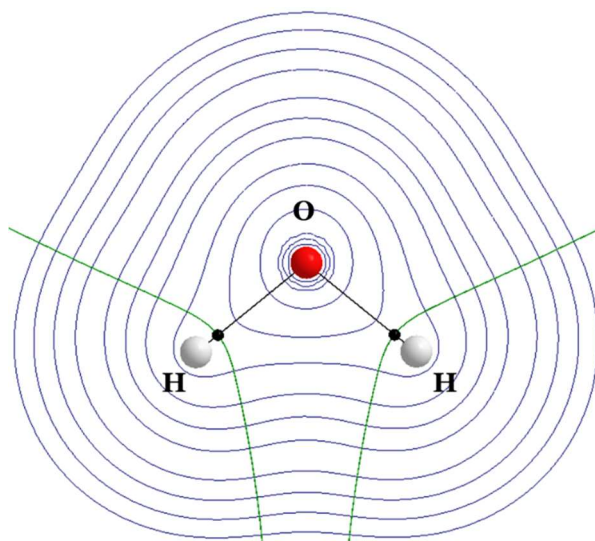
Figure 1. 29. Representation of the electron density (blue line), separatrix (green line), bond path (black line) and the bond critical point (black dot).

The Laplacian of the electron density ($\nabla^2 \rho(\mathbf{r})$),

$$\nabla^2 \rho(\mathbf{r}) = \frac{\partial^2 \rho(\mathbf{r})}{\partial x^2} + \frac{\partial^2 \rho(\mathbf{r})}{\partial y^2} + \frac{\partial^2 \rho(\mathbf{r})}{\partial z^2}, \tag{45}$$

is a function used for chemical bond analysis. If the $\nabla^2 \rho(\mathbf{r}) < 0$ indicates electron accumulation, and if $\nabla^2 \rho(\mathbf{r}) > 0$ there is charge depletion. It is very useful to understand the polarization of a bond or to identify lone pairs in the electron density chart. From

QTAIM analysis, there are other descriptors such as ellipticity o non-covalent index (NCI) which can be useful for chemical bond analysis, but they are out of scope of this Thesis.

The AIM definitions which $w_A = [0,1]$ are called fuzzy or overlapping schemes. In these cases, the atomic domains are overlapped with each other. Consequently, a point of the space can be *shared* within different atoms. There are several ways to construct the $w_A(\boldsymbol{r})$ in the fuzzy schemes. For example, the Hirshfeld partition, sometimes named stockholder partition, constructs the weight function w_A as the ratio between the isolated atom A density ($\rho_A^0(\boldsymbol{r})$) respect to the promolecular density ($\rho_X^0(\boldsymbol{r})$) as

$$w_A(\boldsymbol{r}) = \frac{\rho_A^0(\boldsymbol{r})}{\sum_X \rho_X^0(\boldsymbol{r})} \; . \tag{46}$$

Thus, the atomic population of A in the molecule is introduced as

$$N_A = \int \frac{\rho_A^0(\boldsymbol{r})}{\sum_X \rho_X^0(\boldsymbol{r})} \rho(\boldsymbol{r}) \; . \tag{47}$$

The Hirshfeld partition has been successfully applied to extract many chemical properties, such as partial charges or dipole moment, showing good coherence with the chemical knowledge. The main weak point of the Hirshfeld partition is rooted on the arbitrary definition of the promolecular density. To overcome this problem, different atomic partitions have been developed, such as iterative-Hirshfeld or Topological Fuzzy Voronoi Cells (TFVC).

1.5.3 Modern Chemical Bonding Tools

The chemical bonding tools help chemists to analyse and understand the nature of a chemical bond in a molecule. The chemical bond is a fundamental chemical concept used to rationalize any chemical phenomena. For instance, the Lewis structures are molecular models based on the chemical bonds, or a reaction mechanism is rationalized by chemical bond breaking/formation processes. Since there is not a *direct* experimental way or operator to measure a chemical bond, there are different approaches to reveal the physical/chemical origin of a chemical bond from different perspectives. In this section is aimed to describe the different chemical bonding tools used in this Thesis.

1.5.3.1 Partial charges and bond orders

The atomic or partial charge (Q_A) quantifies the average number of electrons associated to an atom A. They are defined as

$$Q_A = Z_A - N_A \; , \tag{48}$$

where N_A is the electron population and Z_A is the atomic number of A. Obviously, the N_A can be extracted from any type of AIM definition. The most sophisticated AIM definitions, such as NAOs or QTAIM, yield consisted partial charges with the basis set and the method used. The partial charges are generally used to understand charge distribution of a molecule or bond.

The strength or the distance of a bond can be rationalized by the bond multiplicity. The single bond is expected to be weaker than double or triple bonds, albeit there are some exceptions. In computational chemistry, the bond multiplicity is extracted with the so-called bond order (BO), which approximates the bond multiplicity.

For instance, a single and triple bond should give a BO=1 and BO=3, respectively. Initially, Pauling proposed an empirical method which stated that the bond order should depend exponentially with the bond length.[157, 158] Coulson proposed a more elaborated method based on coefficients of the MO from Hückel molecular orbital theory.[159] Wiberg defined a BO for orthogonal AO basis in the context of semiempirical methods. Later on, Mayer generalized the BO for any atomic basis.[160, 161] Nowadays, Mayer Bond Order (MBO) is the most common in the literature, applicable to any type of wavefunction. The exchange density ($\rho^x(r_1, r_2)$) is the element for the MBO. For a single determinant wavefunction, the integration of $\rho^x(r_1, r_2)$ yields, in AO basis,

$$\int\int \rho^x(\boldsymbol{r_1}, \boldsymbol{r_2})\, dr_1\, dr_2 = \frac{1}{2}\sum_{\mu\nu}^{N_{AO}}[(DS)_{\mu\nu}(DS)_{\nu\mu} + (D^s S)_{\mu\nu}(D^s S)_{\nu\mu}] \tag{49}$$

Then, by grouping the basis orbitals to the atoms which are centred, the MBO between atom A and B is written as

$$MBO_{AB} = \sum_{\mu\in A}^{N_{AO}}\sum_{\nu\in B}^{N_{AO}}[(DS)_{\mu\nu}(DS)_{\nu\mu} + (D^s S)_{\mu\nu}(D^s S)_{\nu\mu}]. \tag{50}$$

where D is the density matrix and D^s is the spin-density matrix, which are defined as

$$D = D^\alpha + D^\beta \tag{51}$$
$$D^s = D^\alpha - D^\beta \tag{52}$$

Obviously, for a restricted molecule, D^s vanishes yielding the left-hand side of equation 50. In real space analysis, Bader and Stephans introduced the electron pair concept within the QTAIM theory, distinguishing the electron pairs localized in the atom A or shared between atom A and B.[162] The main ingredient is the exchange-correlation density ($\rho^{xc}(\boldsymbol{r_1}, \boldsymbol{r_2})$), which is written in general as

$$\rho^{xc}(\boldsymbol{r_1}, \boldsymbol{r_2}) = \rho(\boldsymbol{r_1})\rho(\boldsymbol{r_2}) - \rho_2(\boldsymbol{r_1}, \boldsymbol{r_2}) \tag{53}$$

where $\rho(\boldsymbol{r_1}, \boldsymbol{r_2})$ is the pair density. The integration of the two-electron function $\rho^{xc}(\boldsymbol{r_1}, \boldsymbol{r_2})$ naturally decomposes into atomic and diatomic terms (Eq 41 and Eq. 42). The one-center term is known as Localization index,

$$LI_A = \int_{\Omega_A}\int_{\Omega_A} \rho^{xc}(\boldsymbol{r_1}, \boldsymbol{r_2})d\boldsymbol{r_1}d\boldsymbol{r_2}, \tag{54}$$

and the two-center term is named as Delocalization Index,

$$DI_{AB} = \int_{\Omega_A}\int_{\Omega_B} \rho^{xc}(\boldsymbol{r_1}, \boldsymbol{r_2})d\boldsymbol{r_1}d\boldsymbol{r_2} + \int_{\Omega_B}\int_{\Omega_A} \rho^{xc}(\boldsymbol{r_1}, \boldsymbol{r_2})d\boldsymbol{r_1}d\boldsymbol{r_2}. \tag{55}$$

For single determinant wavefunctions, the exchange-correlation density and the exchange density coincide. The delocalization index in this case is fully analogous to the MBO of Eq 50 but in the framework of real space analysis.[163] In AO basis one obtains

$$DI_{AB} = \sum_{\mu\nu}^{N_{AO}} [(DS^A)_{\mu\nu}(DS^B)_{\nu\mu} + (D^sS^A)_{\mu\nu}(D^sS^B)_{\nu\mu}. \tag{56}$$

where the atomic orbital overlap matrix elements ($S_{\mu\nu}^A$) in real space are obtained by restricting the integration on the domain Ω_A,

$$S_{\mu\nu}^A = \int_{\Omega_A} \chi_\mu(r_1)\chi_\nu(r_1) \, dr_1. \tag{57}$$

1.5.3.2 Energy Decomposition Analysis

The Energy Decomposition Analysis (EDA) schemes are a family of chemical bonding tools which split the interaction energy of two (or more) fragments/molecules into chemically meaningful contributions. Since the chemical bond is not an observable, there are several approaches to assess them. They can be divided in two classes. On the one hand, the energy partitioning or Interactive Quantum Atoms (IQA),[164] which decompose the molecular electronic energy into atomic (ε_A) and diatomic (ε_{AB}) contributions,

$$E = \sum_A \varepsilon_A + \sum_{A,B>A} \varepsilon_{AB} . \tag{58}$$

On the other hand, there are plenty of approaches which consider the formation of the molecule from different fragments, which can be atoms, molecular entities or molecules. Considering an AB molecule which is formed by A and B fragments, the stabilization energy (ΔE_{stab}) is calculated as the energy difference between the energy of the AB molecule (E_{AB}) and the energy of the A and B fragments,

$$\Delta E_{stab} = E_{AB} - E_A - E_B, \tag{59}$$

neglecting the Basis Set Superposition Error (BSSE). The ΔE_{stab} is split into preparation energy (ΔE_{prep}) and interaction energy (ΔE_{int}),

$$\Delta E_{stab} = \Delta E_{prep} + \Delta E_{int}. \tag{60}$$

The ΔE_{prep} is obtained as the energy difference between the fragments in the geometry and electronic state in the bonding situation (E_A^{AB} and E_B^{AB}) and the fragments in the ground state,

$$\Delta E_{prep} = E_A^{AB} - E_A + E_B^{AB} - E_B \equiv \Delta E_{prep,A} + \Delta E_{prep,B}. \tag{61}$$

The ΔE_{prep} accounts for the geometric and electronic effects. By definition, it is always positive magnitude (destabilizing). The stabilizing energy upon the interaction of the fragments or molecules is included in the ΔE_{int}. It can divide into different contributions by making use of intermediate (*pseudo*)-states, capturing different flavours of the chemical bond. Since there is not a unique way to decompose ΔE_{int}, there are many ways to split the ΔE_{int},[165] leading to different decomposition schemes. The Morokuma-Kitaura[166] and Ziegler-Rauk[167] scheme is one of the most popular EDA approach, which is available for molecular and periodic systems.[168] It decomposes the ΔE_{int} into electrostatic (ΔE_{elect}), Pauli repulsion (ΔE_{Pauli}), orbital (ΔE_{orb}) and dispersion (ΔE_{disp}) energy contributions,

$$\Delta E_{int} = \Delta E_{elect} + \Delta E_{Pauli} + \Delta E_{orb} + \left(\Delta E_{disp}\right). \tag{62}$$

A series of intermediate (*pseudo*)-states are constructed in order to get the different energy terms. Firstly, one constructs the *pseudo*-state ($E(A \cup B)$) by superposing the frozen of fragments A and B (ρ_A^0 and ρ_B^0, respectively). The $E(A \cup B)$ is referred as *pseudo*-state because it does not fulfil the antisymmetry principle (*vide supra*). The energy difference between $E(A \cup B)$ and E_A and E_B is written as

$$\Delta \tilde{E}(A \cup B) = E(A \cup B) - E_A - E_B = \Delta E_{elect} + \Delta \tilde{E}_{XC}. \tag{63}$$

The ΔE_{elect} accounts for the Coulomb interaction between the frozen densities of A with nucleus (or nuclei) of B and vice versa, the repulsion between nucleus (or nuclei) of A and B and the electrostatic repulsion between the frozen densities.

$$\Delta E_{elect} = -\sum_{i \in B} \int \frac{\rho_A^0(r) Z_i}{|r - R_i|} dr - \sum_{i \in A} \int \frac{\rho_B^0(r) Z_i}{|r - R_i|} dr + \int \int \frac{\rho_A^0(r_1)\rho_B^0(r_2)}{r_1 - r_2} dr_1 dr_2 + \sum_{\substack{i \in A \\ j \in B}} \frac{Z_i Z_j}{|Z_i - Z_j|} \tag{64}$$

The second step consist of antisymmetrizing the $E(A \cup B)$. By applying Löwdin orthogonalization of the occupied MO to $E(A \cup B)$ is constructed the $E(AB')$ state, which fulfils the antisymmetry principle. The energy difference between $E(AB')$ and $E(A \cup B)$, one obtains the ΔE_{Pauli} energy contribution as

$$\Delta \tilde{E}_{Pauli}(AB') = E(AB') - E(A \cup B) = \Delta E_{Pauli} + \Delta \tilde{E}_{XC} \tag{65}$$

The ΔE_{Pauli} repulsion is generally positive and has been shown to be an important component in the course of catalytic reactions, such as Lewis acid catalyzed Diels-Alder reactions, dihalogen catalysed aza-Michael addition reactions or hydrogen bonded assisted catalysis.[169] It can also be found in the literature the steric interaction (ΔE_{steric}) which is the sum of the electrostatic and Pauli repulsion contributions,

$$\Delta E_{steric} = \Delta E_{elect} + \Delta E_{Pauli}. \tag{66}$$

The last step consists of relaxing the densities to the ground state. It is simply obtained from the difference between $E(AB')$ and E_{AB},

$$\Delta E_{orb} = E_{AB} - E(AB'). \tag{67}$$

The ΔE_{orb} is generally negative and it has been a very relevant term to understand the nature of a chemical bond. It is important to note that the ΔE_{orb} has different flavours. It accounts for polarization, electron-pairing and charge transfer effects, which are not dividable within this scheme.[170] Other EDA approaches such as ALMO-EDA split the orbital stabilization into polarization and charge transfer contributions.[171, 172]
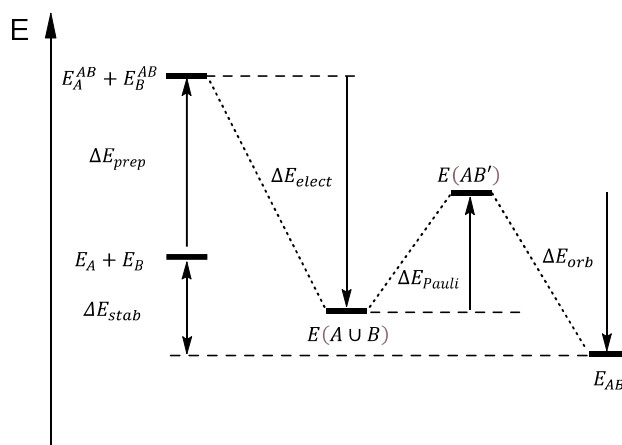
Figure 1. 30. Schematic representation of the different intermediate (pseudo) – states and its energy components in the Morokuma-Kitaura and Ziegler-Rauk scheme.

Finally, the dispersion stabilization energy is obtained independently of the intermediates process. It can only be obtained by using energy correction schemes, such as DFT-D3, which are out of the functional formula. It is obtained as

$$\Delta E_{disp} = E_{disp,AB} - E_{disp,A} - E_{disp,B}. \tag{68}$$

The EDA is a very powerful chemical bonding tool to understand the nature of a chemical bond, however, it has its own limitations. Firstly, the different energy components are path dependent.[173-175] This means that the energy components will depend on the nature of the fragments employed. This is a consequence of using non-interacting intermediate states. Secondly, the charge and electronic state of the interacting fragments is arbitrarily selected. The energy components of EDA in an ionic fragmentation (A^+ and B^-) of the AB molecule will yield different results than the neutral fragmentation (A^0 and B^0). Frenking and co-workers proposed a criterion which helps to select which is the most adequate fragmentation to study a bond. It stands that the best fragment representation in a molecule is the one which lowers the ΔE_{orb} in absolute value. It has been broadly applied to understand the chemical bond of main group compounds in an exotic bonding situation.[176]

1.5.3.3 Combining Energy and Charge Decomposition Analysis

The EDA provides a comprehension on the different energy components involved during the bond formation. However, the description on how the fragment electron densities rearrange is lost. For instance, the charge transfer and polarization of a given fragment or molecule have a thermodynamic *cost,* but they are also related with inter- and inter-fragment density rearrangement, respectively. The quantification from both perspectives is desirable to deeply understand the nature of the chemical bond.

There are some methods which compact both perspectives in one analysis, providing a very detailed information during the bond formation. For instance, Head-Gordon and co-workers combined the ALMO-EDA together with a complementary occupied-virtual orbital pairs (COVP-ALMO-EDA),[177] which provides the charge transfer description with few localized orbitals. In the Morokuma-Kitaura and Ziegler-Rauk scheme, Mitoraj *et al.* proposed a combined energy and charge decomposition by making use of the Natural Orbitals for Chemical Valence (EDA-NOCV).[178] This scheme is based on the deformation density ($\Delta\rho(r)$), which is the density difference between the final

molecule AB ($\rho_{AB}(r)$) and the sum of fragment densities in the optimized geometry ($\rho_A(r)$ and $\rho_B(r)$). It is written as

$$\Delta\rho(r) = \rho_{AB}(r) - \rho_A(r) - \rho_B(r). \tag{69}$$

The NOCVs (θ_k) are the orbitals which diagonalize the deformation density matrix. Therefore, the deformation density can be expressed in terms of NOCVs. The n non-zero eigenvalues (v_k) have the "pairing property", which means that they appear by pairs with opposite sign ($+v_k, -v_k$). The chemical interpretation is that each pair of v_k conform a bonding channel k which a donor-NOCV (θ_{-k}) *loses* $-v_k$ electrons and an acceptor-NOCV (θ_{+k}) *receives* $+v_k$ electrons. It allows to rewrite the equation into k bonding channels $\Delta\rho_k(r)$, written as

$$\Delta\rho(r) = \sum_k^{n/2} |v_k|(-\theta(r)^*_{-k}\theta(r)_{-k} + \theta(r)^*_k\theta(r)_k) = \sum_k^{n/2} \Delta\rho_k(r). \tag{70}$$

The $|v_k|$ is the total electron flow associated to the k-th bonding channel. The θ_k can be expanded into orthonormalized symmetry adapted fragment orbitals (SFO). Upon integration of the deformation density of a bonding channel, one obtains

$$\int \Delta\rho_k(r)\, dr = \sum_\mu |v_k||c_\mu^k|^2 - |v_{-k}||c_\mu^{-k}|^2, \tag{71}$$

where c_μ^k are the coefficients of the NOCV in the SFO basis. The energy associated to each deformation density can be obtained, fulfilling that the sum over the n/2 bonding channels is the ΔE_{orb}.

$$\Delta E_{orb} = \sum_k^{n/2} \Delta E_{orb,k} \tag{72}$$

1.5.4 Assessing the oxidation and valence state

The Oxidation State (OS) is a chemical concept which has been broadly used to rationalize chemical properties or reactivity. It measures the degree of oxidation of an atom or fragment respect to the elemental state. Originally, the OS was termed as "oxydationsstufe", introduced to understand the products formed in the reactions with oxygen. Nowadays, this concept has a broader scope, having a vital importance in red-ox process. For instance, the cross-coupling reactions catalysed by transition metal complexes occur in three elemental reactions: oxidative addition, transmetallation and reductive elimination. Two of these steps are rationalized by the change of the oxidation state of the metal. The OS is not only narrowed in transition metal chemistry. During the last decades, the research on the synthesis and reactivity of compounds bearing *s*- and *p*- block elements with low OS has exponentially increased. The unusual electronic structure and reactivity have attracted the interest of the inorganic community, finding similarities with transition metal chemistry and discovering new chemical spaces.

Albeit OS is popularly employed in different types of chemistries, its definition has remained unclear for many years. The most recent definition provided by IUPAC's Golden Book says that the OS is the "atom's charge after ionic approximation of its heteronuclear bonds".[179] In the case of homonuclear bonds, the electrons are assigned

equally. Apart from the OS definition, they provided an algorism to assign OS in molecular compounds. It consists of firstly drawing the Lewis structure of the studied system and assign the electron pairs to the most electronegative atom/fragment. The resulting atom/fragment charge corresponds to the OS. The electronegativity has multiple definitions which Allen's atomic electronegativities is recommended.

The IUPAC definition and algorithm has successfully worked for many types of systems but it has several exceptions. One of the main drawbacks is that Allen's electronegativity is an atomic property of the uncombined atom. Thus, it does not take into account the chemical environment of the atom or fragment. Additionally, the ionic approximation does not distinguish the σ and π electrons which do not necessarily need to be assigned in equal footing. Those discrepancies can be pictured by considering the different type of transition metal-carbene complexes (Figure 1.31). They can be classified as Fischer carbenes, where the σ-electrons are assigned to the CR_2 fragment and the π-electrons to the metal, Schrock carbenes, which assign both σ- and π- electrons are assigned to CR_2 fragment, and Radical carbenes, where the σ-electrons are assigned to the CR_2 and π- electrons are equally assign to the metal and CR_2 fragment. According to the ionic approximation, the distinction of the different type of carbenes is blurred. The four bonding electrons of the $M=CR_2$ bond are always assigned to the CR_2 fragment because carbon is more electronegative ($\chi_C = 2.544$) than any transition metal. Thus, according to the ionic approximation, all the carbenes should be characterized as Schrock carbenes.
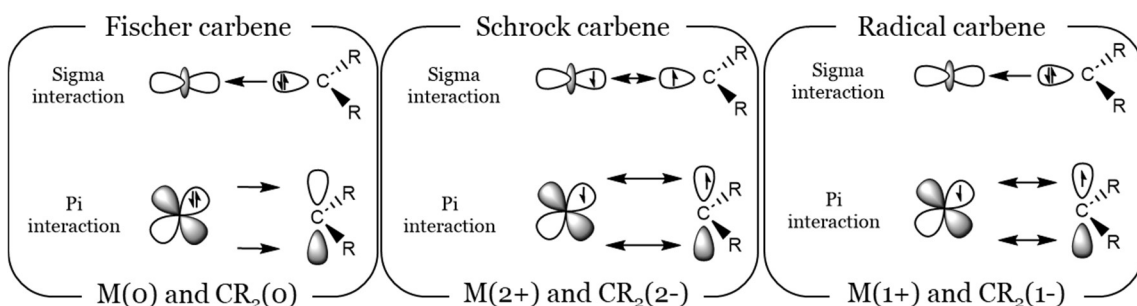
Figure 1. 31. Schematic representation of the orbital interactions of TM carbene complexes together with their OS.

During the las decades, several computational tools have been designed or adapted to elucidate oxidation states. They can be divided by density-based methods, which analyse the molecular wavefunction, and energy-based approaches, which extract the OS from an energy component. The density-based methods have a common ingredient: the localized molecular orbitals (LMO). These orbitals are obtained by applying a unitary transformation to the canonical molecular orbitals. The LMOs are restricted in a region of the space, which helps for the chemical interpretation. Some authors have proposed to analyse the position of the centroid of a LMO to assign OS. Even though it works for some systems, it fails on the assignation of trivial molecules such as H_2O.[180] Alternatively, the LMOs can be coupled with a population analysis to assign OS. That is the case of Localized Orbitals Bonding Analysis (LOBA) or Oxidation State Localized Orbitals (OSLO).[181, 182] These methodologies are restricted to single determinant wavefunctions, thus, not applicable to multideterminant wavefunctions. Salvador and co-workers introduced the Effective Oxidation State (EOS) analysis which is, to the date, the only methodology which can be applied to any type of wavefunction.[183] It has been successfully applied to a broad type of transition metal complexes, including transition metal carbenes.[184]

The EOS is based on the effective atomic orbitals (eff-AO) obtained from the diagonalization of the net atomic density.[185, 186] Following similar procedure, one can obtain the Effective Fragment Orbitals (EFOs), constructed from *a priori* fragmentation pattern. Moreover, the EFOs can be constructed with any type of AIM definition (Hilbert and Real space). The general procedure to extract OS from EOS analysis is depicted in Figure 1.32.
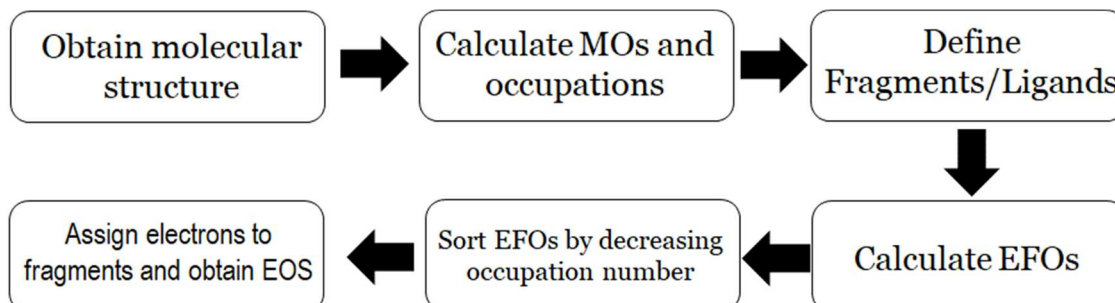
Figure 1. 32. Workflow chart of EOS procedure.

Firstly, one needs to obtain the molecular orbitals and its occupations. Then, the fragments are defined from which the EFOs will be constructed. The EFOs are calculated within an AIM definition together with their occupancies. Afterwards, the EFOs are sorted by decreasing number of occupations which integer electrons are assigned to the atom/fragment obtaining the OS. The assignation comes with a Reliability index (R(%)). It is constructed from the occupancies (λ^{σ}) of last occupied EFO (LO), which an electron is assigned, and the first unoccupied (FU) EFO as

$$R(\%) = \ 100 \min \left(1, \max(0, (\lambda^{\sigma}_{LO} - \lambda^{\sigma}_{FU}) + \ 1/2)\right). \tag{73}$$

The most clear assignation (ionic compounds, highly polarized bonds) exhibit R(%) values close to 100, while the most unclear scenarios (strong covalency, apolar bonds) corresponds to a R=50% value.

From the energy-based methods, the EDA-NOCV analysis is the most common chemical bonding tool to assign OS and valence states. Albeit EDA-NOCV was not designed to assign OS, the interpretation of the energy components has been *adapted* to assign OS. Based on the maxima *the fragmentation which minimizes the ΔE_{orb} interaction is the one which better represents molecular system* (*vide supra*), the OS of the fragments are extracted. Within this approach, one needs to consider a set of fragmentations with different OS and valence state combinations of isolated fragments. The fragmentation which minimizes the *ΔE_{orb}* corresponds to the OS and valence state in the *molecular system*. Probably, the carbones are the most paradigmatic systems which the OS has been characterized through EDA-NOCV analysis. These compounds are characterized by a divalent carbon atom in the OS of 0. Tonner *et al.* thoroughly analysed the electronic structure of series of carbodiphosphoranes by means of different chemical bonding tools.[187, 188] In the EDA, they tested several fragmentation patterns considering the carbon atom in different electronic states, being the carbon in ^{1}D state the best representation for the carbon atom. From that, they suggested that the carbon has an OS of 0 stabilised by donor-acceptor interaction from the phosphine ligands. However, this bonding model is still under debate. [189, 190]

CHAPTER 2 - Objectives

The synthesis and isolation of compounds exhibiting hitherto unknown chemical bonds are leading quests in chemistry. The discovery of new bonding motifs opens the door to unexplored chemistry, which might flourish in materials with interesting properties. The modern chemistry is evolving in great harmony with computational chemistry. Therefore, the combination of experiments with molecular modelling has led to a detailed understanding structure-activity relationship.

In this context, we undertake a synergistic approach involving both computational and synthetic chemistry to develop new synthetic strategies and to isolate new molecules. **Our main goal is the synthesis of phosphaalumene**. The high reactivity of the Al=P bond precludes its isolation. The synthetic protocols for the preparation of phosphaalumenes are scarce and only known via unstable low-valent reagents. **We target the synthesis with the premise of using more stable Al(III) and P(III) derivatives as starting materials**.

       The first **specific target of this Thesis is to develop a synthetic route towards compounds with the Al=P motif**. Our hypothesis is that the Al=P motif could be achieved via the *β*-elimination reaction of the corresponding phosphanylalumane. Such a reaction can be induced from a H,halide-functionalized phosphanylalumane building block. Thus, the first specific goal was set as the **preparation of phoshanylalumanes bearing H, halide- functionalities** as it is outlined in Figure 2.1.
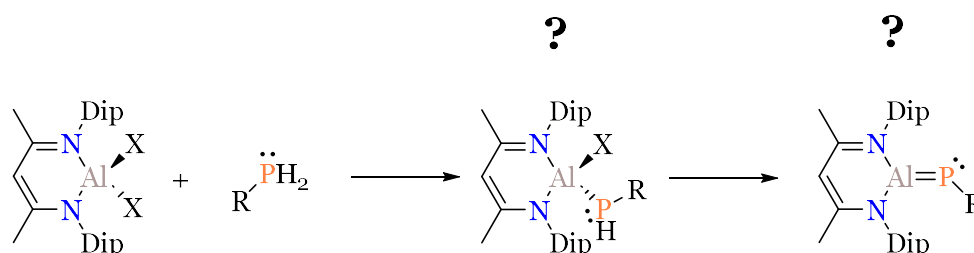
Figure 2. 1. Proposed synthetic strategy to prepare a phosphaalumene (X=Leaving group).

       To the intended extension towards other main group elements whose protocols are limited has been set as the second goal. Thus, **we target to prepare a compound with the Mg-P motif** based on the methodology developed in aluminium chemistry. The reactivity of the new compounds is explored towards ketone substrates, characterizing the reaction mechanism through a combined approach of experimental and computational chemistry.

The Energy Decomposition Analysis is a recurrent chemical bonding tool in main-group chemistry. Within this method, the understanding of the chemical bond nature is based on considering the interaction between fragments. It is somewhat well-established that the fragmentation pattern which minimizes the ΔE_{orb} in absolute value better represents the bonding situation. Following this criterion, OS assignations have been proposed pointing to unprecedented low-valent species. Conversely, no systematic study has ever been performed to validate such energetic criterion. In this context, another aim of this Thesis is to **put the lowest ΔE_{orb} criterion to the stringent test**. Our hypothesis is that the reference states for charged fragmentations, because of the gas-phase ionization energies, are far too high in energy, making ΔE_{orb} too large as compared to neutral fragmentations. Also, the usual procedure in EDA typically involves two interacting fragments. Grouping different sets of non-interacting atoms/ligands into a unique fragment may lead to intra-fragment reorganization energy that can have a significant

effect in the ΔE_{orb} term. We will seek more appropriate and robust criteria in the context of EDA-NOCV, focusing on the charge displacement among different fragments, rather than on energetics.

CHAPTER 3 – A new criterion to settle fragment reference states for EDA schemes

Let the record shows I took all the blows and did it my way

Frank Sinatra

The EDA-NOCV is a well-established and powerful analysis tool to shed light on the nature of chemical bonds or intermolecular interactions. It is a method that falls in the generic category of energy decomposition schemes. In EDA, the dissociation/formation energy of a molecular system builds up from two or more fragments is dissected into chemically sound contributions. The relative magnitude and sign of these contributions has been extensively used to rationalize and categorize a wide number of molecular systems and interactions.[191-193]

Molecular fragments (e.g. functional groups, ligands, etc) are often defined to group atomic (and diatomic) contributions obtained by analysis tools such as atomic populations, IQA or even for methods to assign oxidation states like EOS. In EDA, however, one must specify not just the atoms that form a given molecular fragment but also the electronic state. Then, the energy components obtained in EDA are dependent on the nature of the defined fragments. For the study of inter-molecular or non-covalent interactions, such as hydrogen bonds or π-π stacking,[194] the selection of the fragments is straightforward because each fragment belongs to a molecule in its ground state. In the case of intra-molecular interactions, such as electron-sharing or dative bonds, the definition of the charge and electronic state of the fragments is not an easy task and sometimes can be controversial. The interacting fragments do not need to be in their ground state, opening the door to a large number of plausible fragmentations. For example, let us suppose the study of the C=C bond in an *N*-heterocyclic olefin through EDA-NOCV (Figure 3.1). One has the *freedom* to place the four bonding electrons in different orbitals of the fragments. For instance, one can consider two closed-shell singlet fragments bearing a σ-lone pair on the carbenic carbon. (Fragmentation A, Figure 3.1). Alternatively, one can examine the fragments in their triplet state (Fragmentation B, Figure 3.1) or open-shell singlet (Fragmentation C, Figure 3.1). The fragmentation employed in the examination of the chemical bond is relevant for two reasons. On the one hand, the energetic components of the EDA-NOCV are dependent on the type of fragmentation. Therefore, a fragmentation which does not adequate to the actual bonding situation can yield misleading results. On the other hand, the fragmentations are typically tagged in a bonding model. For instance, Fragmentation A will consider C=C to be donor-acceptor while Fragmentation B and C will categorize the C=C bond as electron-sharing.

Bonding model
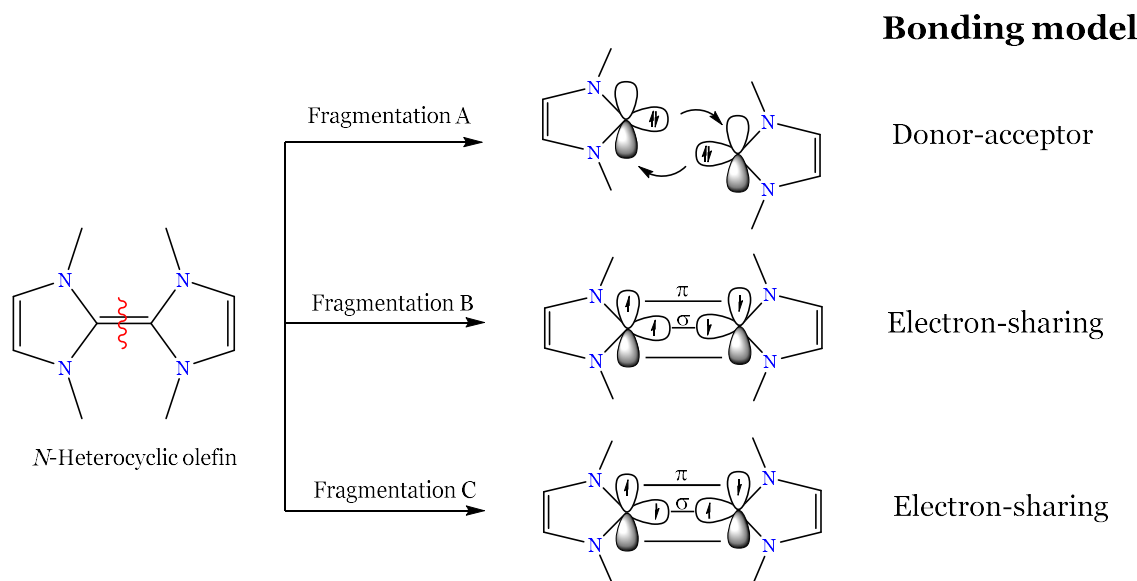
Figure 3. 1. Plausible fragmentations for an N-heterocyclic olefin.

In Table 3.1 we show the EDA-NOCV results of the C=C bond in NHO in different fragmentations. Except for the ΔE_{Disp}, all the energy components are substantially different within the tested fragmentations. In this context, there is the need to have a criterion to guide the user to faithfully select the fragmentation which captures the nature of the chemical bond. Frenking and co-workers introduced a criterion based on the ΔE_{orb} component (see Section 1.8.2). The fragmentation that has the lowest ΔE_{orb} absolute value is considered the best fragment representation of the bonding situation.[195, 196] This criterion is rooted on "*the least alteration of the electronic charge distribution is required to yield the electronic structure of the molecule*".[187] In the former example, the fragments in the triplet state give the lowest $|\Delta E_{orb}|$. Thus, this fragmentation will be the most adequate to analyse the nature of the chemical bond. The C=C bond would be covalent, in agreement with the chemical intuition.

Table 3. 1 The EDA-NOCV results of the N-heterocyclic olefin at the BP86-D3(BJ)/TZ2P// BP86-D3(BJ)/def2-TZVPP. The lowest ΔE_{orb} is highlighted in bold. The energies are given in kcal/mol.

	Fragmentation A	Fragmentation B	Fragmentation C
ΔE_{int}	-357.4	-194.6	-212.4
ΔE_{Pauli}	564.8	316.0	313.3
ΔE_{Elstat}	-312.6	-209.1	-209.1
ΔE_{Disp}	-10.1	-10.1	-10.1
ΔE_{Orb}	-599.6	**-291.4**	-306.5

In main group chemistry, the EDA-NOCV has been broadly used to discern between an electron-sharing to a donor-acceptor interaction. This distinction has been applied to different types of systems.[192, 197, 198] In a typical EDA-NOCV, the electron-sharing bond minimizes the $|\Delta E_{orb}|$ in the homolytic fragmentation. When the heterolytic fragmentation minimizes the $|\Delta E_{orb}|$, the interaction is categorized as dative-acceptor. In Figure 3.2 we show the ΔE_{orb} of in the homolytic and heterolytic fragmentation of ammonia-borane and ethane molecules, which are archetypical examples of dative and covalent bonds, respectively. In ethane the $|\Delta E_{orb}|$ is minimized for the homolytic fragmentation while ammonia-borane displays the lowest $|\Delta E_{orb}|$ in the heterolytic fragmentation.

Homolytic frag.   **Heterolytic frag.**

ΔE_{orb}= **-184.1** kcal/mol ΔE_{orb}= -286.4 kcal/mol

ΔE_{orb}= -252.5 kcal/mol ΔE_{orb}= **-76.4** kcal/mol
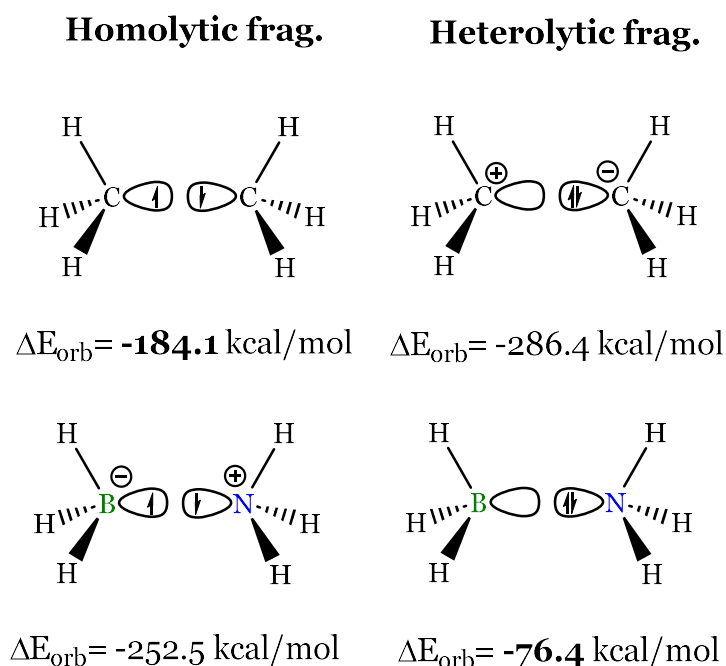
Figure 3. 2. ΔE_{orb} values of the homolytic and heterolytic fragmentations of ethane and ammonia-borane at the B3LYP-D3(BJ)/TZ2P//B3LYP-D3(BJ)/def2-TZVPP level of theory.

Interestingly, the obtained fragmentations have been coined as a plausible way to assign oxidation and valence states. It is considered that the oxidation/valence state of the isolated fragments corresponds to the same in the molecular system. Although this interpretation is somewhat extended in the community, some authors have pointed out the mismatch with chemical bonding tools which analyse the molecular wavefunction. For instance, Landis *et al.* analysed the chemical bond of TM(cAAC)$_2$ (TM=Cu, Ag, Au) complexes which the ΔE_{orb} criterion resulted to be not satisfactory.[199]

3.1 Shortcomings of the ΔE_{orb} criterion to assign oxidation/valence states

During the last decades, the chemistry of low-valent main group compounds has raised the interest of the inorganic community.[192, 198, 200, 201] Their reactivity showcases similarities to transition metal complexes and the exotic bonding situations triggered the research in this field. The EDA-NOCV has been a recurrent chemical bonding tool to rationalize the nature of the chemical bond and, furthermore, the OS of the main group elements. Many compounds have been characterized in low-oxidation states stabilised by donor-acceptor interactions based on the ΔE_{orb} criterion. That is the case of the landmark Be(cAAC^{Dip})$_2$ complex reported by Braunschweig and co-workers.[202] They tested a series of different fragmentations including Be(II), Be(I) and Be(0). The fragmentation corresponding to the Be in the excited state ^1D ($1s^2 2s^0 2p^2$) together with the cAAC^{Dip} in the ground state yielded the lowest $|\Delta E_{orb}|$ (See Supplementary Table S1 of ref [202]). Thus, the authors described Be(cAAC^{Dip})$_2$ as beryllium (0) stabilised by the σ-interaction from the lone pair of the cAAC^{Dip} together with a π-backdonation from the p-orbital of beryllium to the cAAC^{Dip} ligand (Figure 3.3, left), similarly to Dewar-Chatt-Ducanson bonding model applied to TM complexes.

Be(0)
Be(II)
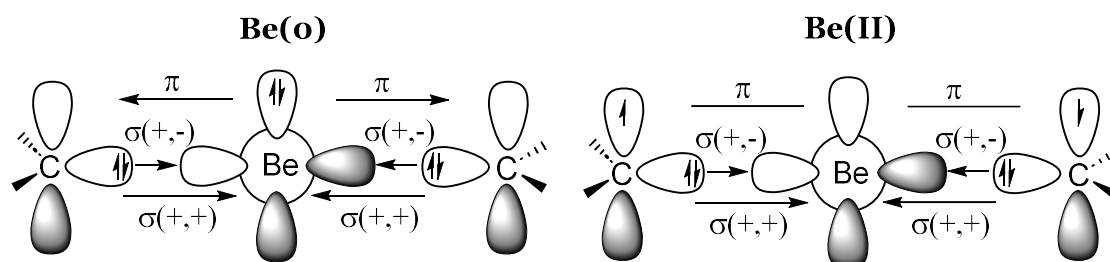
Figure 3. 3. Schematic representation of two plausible bonding situations in Be(cAAC^{Dip})$_2$.

Recently, Gimferrer *et al.* proposed an alternative oxidation state assignation in Be(cAAC^{Dip})$_2$ and related Be and Mg compounds.[203] The two π-electrons are assigned to the cAAC^{Dip} ligands (Figure 3.3, right), thus leading to a more conventional Be(2+) picture. Indeed, cAAC^{Dip} ligands are known to have strong π-acceptor properties. The non-innocence of cAAC^{Dip} has been proposed in analogous complexes such as Zn(cAAC^{Dip})$_2$, which is characterized as a Zn(II) singlet biradical compound.[204] The bonding model proposed by Gimferrer *et al.* goes in this direction, supported by state-of-the-art wavefunction analysis tools using both DFT and CASSCF wavefunctions.

A remarkable finding is the stability analysis of the DFT wavefunctions. The Closed Shell Singlet (CSS) solution of Be(cAAC^{Dip})$_2$, which is considered in the original work, was only found to be stable for BP86 functional. However, the Open-Shell Singlet (OSS) solution for more elaborated functionals, namely B3LYP, PBE0, M06-2X and ωB97XD, was found to be lower in energy than the CSS solution (from 5.2 kcal/mol to 11.5 kcal/mol). In the case of B3LYP, the CSS solution is not stable. Thus, the OSS wavefunction must be used to perform chemical bond analysis (see Table S1 in Supporting Information in ref [203]). The EOS analysis on the OSS wavefunction (B3LYP-D3(BJ)) yields the Be(II) assignation, in odds with the original assignment. Different AIM definitions, namely Löwdin, NAO, QTAIM and TFVC, converge on the Be(II). These results show the robustness of the EOS procedure to the AIM partition. On the contrary, the partial charges bear a huge dependency on the AIM employed. They range from -0.07 e (Löwdin) to +1.56 e (QTAIM). The Be(cAAC^{Dip})$_2$ system reflects that the partial charges can yield a misleading OS assignment.

The most desirable method to model diradicals is by using multireference approaches such as CASSCF (See section 1.5.2). This method avoids the spin contamination problem found in broken-symmetry DFT (BS-DFT). The EOS obtained from the CASSCF wavefunction assigns a Be(II) with an R(%)=78.9%. In Figure 3.4 we show the frontier EFOs with their occupations. The EFO corresponding to the *p*-orbital on the cAAC ligand is more occupied (0.435) than the EFO of the *s*-orbital on the beryllium (0.175), yielding a clear picture of Be(II). The diradicaloid character of the Be(cAAC^{Dip})$_2$ complex was supported with the Local Spin Analysis (LSA).[205] This is a chemical bonding tool which quantifies the local spins on atoms or fragments and their couplings. It can be applied to single determinant to multireference methods. The LSA of Be(cAAC^{Dip})$_2$ at the CASSCF level of theory points to an unpaired electron in the cAAC^{Dip} ligand ($<S^2>_{cAAC}$=+0.39).
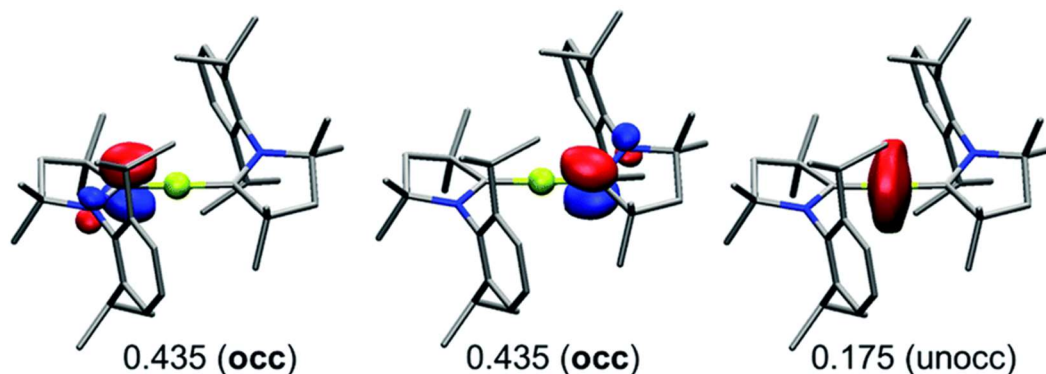
Figure 3. 4. Frontier EFOs with their corresponding gross occupancies for Be(cAAC^{Dip})$_2$ at the CASSCF/cc-pVDZ//B3LYP-D3(BJ)/def2-SVP level of theory. Image extracted from ref [203].

The elucidation of the beryllium OS extracted from the EOS analysis differs from the EDA-NOCV assignation (*vide supra*). In order to decipher the origin of these differences, one can analyse the charge decomposition of the EDA-NOCV. The OS is a property that depends on the electronic distribution of the molecule. Hence, the charge decomposition is *a prior* more appropriate to assign the OS than the energy decomposition itself. There are different approaches to assess charge decomposition. For instance, the Charge Displacement Function (CDF) introduced by Belpassi and co-workers allows to analyse the electron flow for the different bonding channels.[206] The CDF measures the charge fluctuation along an intermolecular axis (z'),

$$CDF(z) = \int_{-\infty}^{\infty} dx \int_{-\infty}^{\infty} dy \int_{-\infty}^{z} \Delta\rho(x, y, z')dz'. \tag{74}$$

Within this approach, two coordinates of the space are arbitrarily ignored, and the interpretation relies on the visual inspection of the CDF shape. Alternatively, one can analyse the contributions of the fragment orbitals to the NOCVs as

$$\int \Delta\rho_k(\boldsymbol{r}) \, d\boldsymbol{r} = \sum_{\mu} |v_k||c_\mu^k|^2 - |v_{-k}||c_\mu^{-k}|^2. \tag{75}$$

Gimferrer *et al.* thoroughly analysed the charge decomposition in the Be (0) and Be (+2) fragmentations using the OSS molecular wavefunction ($<S^2>=0.571$). The inspection of the contribution of the molecular fragments allowed us to rationalize the differences between the EOS and EDA-NOCV assignations. In Figure 3.5 we depict the deformation densities corresponding to the π-bonding channel in the ^{1}D Be(0) (Figure 3.5, A) and the ^{1}S Be(+2) (Figure 3.5, B) fragmentations together with associated energy associated ($\Delta E_{orb-\pi}$) and electron flow ($v_{\alpha\beta}$).

(A) Deformation density   *p*-orbital of Be   *p*-orbital of (cAAC^{Dip})$_2$

$\Delta E_{orb-\pi}$ = -150.7 kcal/mol
$|\upsilon_{\alpha\beta}|$=1.5

υ_α=-0.75; υ_β=-0.74

υ_α=+0.49; υ_β=-0.44

(B) Deformation density   *p*-orbital of Be   *p*-orbital of (cAAC^{Dip})$_2$

$\Delta E_{orb-\pi}$ = -221.6 kcal/mol
$|\upsilon_{\alpha\beta}|$=1.8

υ_α=+0.20; υ_β=+0.22

υ_α=-0.84; υ_β=-0.84
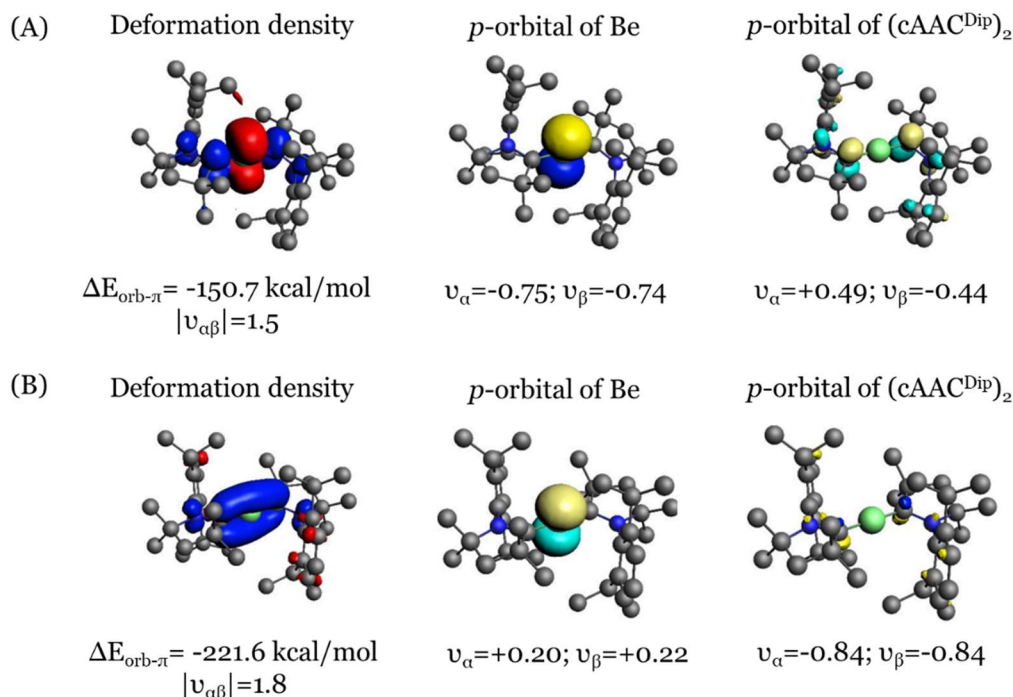
Figure 3. 5. (A) Plot of the deformation densities of between Be(0) (^1D, $1s^22s^02p^2$) and (cAAC^{Dip})$_2$ in singlet state at the B3LYP-D3(BJ)/TZ2P//B3LYP-D3(BJ)/def2-SVP level of theory. (B) Plot of the deformation densities of between Be(+2) (^1S, $1s^22s^02p^0$) and [(cAACDip)$_2$]$^{-2}$ in singlet state at the B3LYP-D3(BJ)/TZ2P//B3LYP-D3(BJ)/def2-SVP level of theory. The red color shows the charge outflow, whereas blue shows charge density accumulation. The occupied fragment molecular orbitals are shown in blue and yellow, while virtual orbitals are cyan and pale yellow. Hydrogens are omitted for clarity. Figure adapted from ref [203].

In the Be(0) fragmentation, the Be p_π orbital transfers the 0.75 α and 0.74 β electrons to the (cAAC^{Dip})$_2$ fragment. The energy associated with the π-bonding channel is -150.7 kcal/mol. In the Be(+2) fragmentation, the p_π orbital receives 0.20 α and 0.24 β electrons with an energy associated with -221.6 kcal/mol. It seems contradictory that the fragmentation with smaller charge transfer to the beryllium atom yields higher energy values. There are two reasons which explain it. On the one hand, the ΔE_{orb} considers the charge transfer, polarization and electron pairing energies.[170] Thus, the energy associated with the charge transfer is not possible to *neatly* obtain within the Morokuma-Kitaura scheme. Other EDA schemes, such as ALMO-EDA, can dissect the ΔE_{orb} to polarization and charge transfer energies which would be more faithful to OS. Nevertheless, IUPAC recommendations never suggest an energetic-based criterion.[207] On the other hand, the ionic molecules are less stable than the neutral in the gas phase. Thus, ionic fragments tend to give numerically higher energy components than neutral fragments.[208]

Another drawback of the EDA-NOCV is that the energy components are not sensible to the nature of the wavefunction. For example, the CaCO$_2$ compound is characterized by singlet diradical.[209] The energy components of the EDA-NOCV are almost identical yielding the interpretation (see Table 2 in ref[210]). In the same vein, Salvador *et al.* revealed that the ΔE_{orb} criterion cannot distinguish between an electron-sharing from a spin-polarized bond in the [NaBH$_3$]$^-$ system.[211] The energy differences between the CSS (ΔE_{orb}=-16.6 kcal/mol) and OSS (ΔE_{orb}=-19.2 kcal/mol) are very small. Note that the reference states, the ΔE_{elect} and ΔE_{Pauli} values are equal for CSS and OSS wavefunctions. The associated (pseudo)-states are identical because, by construction, they are independent of the nature of the final wavefunction. Only the orbital relaxation

ΔE_{orb} depends on the nature of the molecular wavefunction, but the energy differences are too small to recognize a bonding model.

The charge decomposition provides more evident differences within different wavefunctions. Considering the $CaCO_2$ example, we analysed the σ-interaction between the Ca and the CO_2 molecule with the CCS and OSS wavefunctions (Figure 3.6). The energy associated with the σ-bonding channel is almost the same in the CCS and OSS solutions. However, the electron flow differences ($|v_{\alpha\beta}|$) are up to 0.60 e. In the CSS wavefunction, the electron flow ($|v_{\alpha\beta}|=1.26$ e) is higher than the OSS ($|v_{\alpha\beta}|=0.60$ e). These results suggest that the charge decomposition might be a better indicator of the best fragmentation than the ΔE_{orb}.

Closed-shell singlet (CSS)

Deformation density — Orbitals of the fragments

$CO_2^-(D)$ — $Ca^+(4s^1)$

$\Delta E_{orb}= -25.4$; $|v_{\alpha\beta}|=1.26$

SOMO ($\varepsilon=2.81$ eV)
$v_\alpha = -0.46$; $v_\beta = +0.54$

SOMO ($\varepsilon=-8.96$ eV)
$v_\alpha = +0.46$; $v_\beta = -0.54$

Open-shell singlet (OSS)

Deformation density — Orbitals of the fragments

$CO_2^-(D)$ — $Ca^+(4s^1)$

$\Delta E_{orb}=-26.9$; $|v_{\alpha\beta}|=0.60$

SOMO ($\varepsilon=2.81$ eV)
$v_\alpha = -0.14$; $v_\beta = +0.17$

SOMO ($\varepsilon=-8.97$ eV)
$v_\alpha = +0.13$; $v_\beta = -0.24$
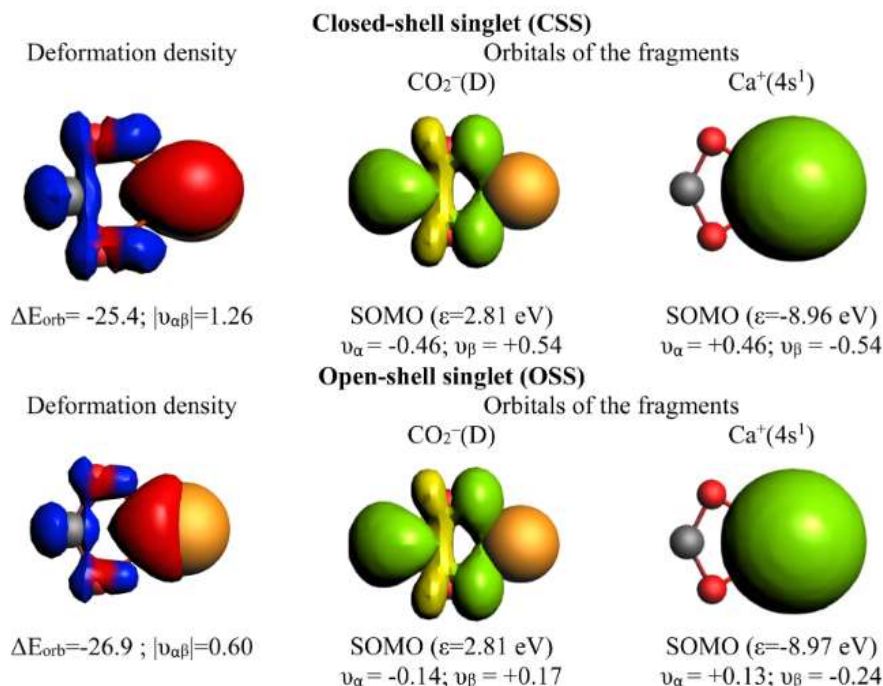
Figure 3. 6. The plot of the deformation densities of the $CaCO_2$ complex in the closed-shell singlet (CCS) and open-shell singlet (OSS) wavefunctions. The fragments are Ca^+ ($4s^1$) and CO_2 in a doublet spin state. Image from ref [210].

3.2. Design of a criterion based on electron flow for EDA schemes

In the former section, we have disclosed the weaknesses of the ΔE_{orb} to assign oxidation states. Given the coherence of the charge decomposition with the OS, we were prompted to design a new criterion based on the electron flow instead of relying on an energy component of the EDA. In this section, we design simple indexes to measure the net charge transfer within the fragments. Several examples will be presented comparing the new index with the established one.

The EDA-NOCV method can be disclosed into two independent decomposition schemes (Figure 3.7). On the one hand, the Energy Decomposition builds different intermediate (*pseudo*)-states whose energy differences result in ΔE_{prep}, ΔE_{Elect}, ΔE_{Pauli} and ΔE_{orb} energy components. On the other hand, the Charge Decomposition analyses the electron flow during the bond formation. The $\Delta \rho(\mathbf{r})$ is the main ingredient of the charge decomposition which, in EDA-NOCV, is analysed through the NOCVs. These orbitals are very appealing to understand the electron flow from a chemical perspective.

They are coupled by pairs which allows to describe an interaction by donor and acceptor NOCV orbitals building *bonding channels*. Ziegler and co-workers applied the Extended-Transition State (ETS) formalism to express the ΔE_{orb} as a sum of the contributions from different *bonding channels* obtained from NOCV pairs.[178] This approach unified both *worlds*, obtaining a very detailed picture of the bonding situation.

The ΔE_{orb} is the energy associated with the orbital relaxation of the fragments. In fact, it is the energy difference between the electronic energy of the intermediate state AB' and the electronic energy of the molecular system AB (Figure 3.7). The intermediate state AB' is constructed independently of the nature of the final wavefunction. Thus, the valence or the OS of the AB molecule is not *encoded* in the AB´ intermediate state. On the contrary, the $\Delta \rho(\boldsymbol{r})$ is directly constructed from the density difference between the molecular density ($\rho_{AB}(\boldsymbol{r})$) and the fragment's densities $\rho_A(\boldsymbol{r})$ and $\rho_B(\boldsymbol{r})$, which do depend to some extent on the chosen fragment valence state.
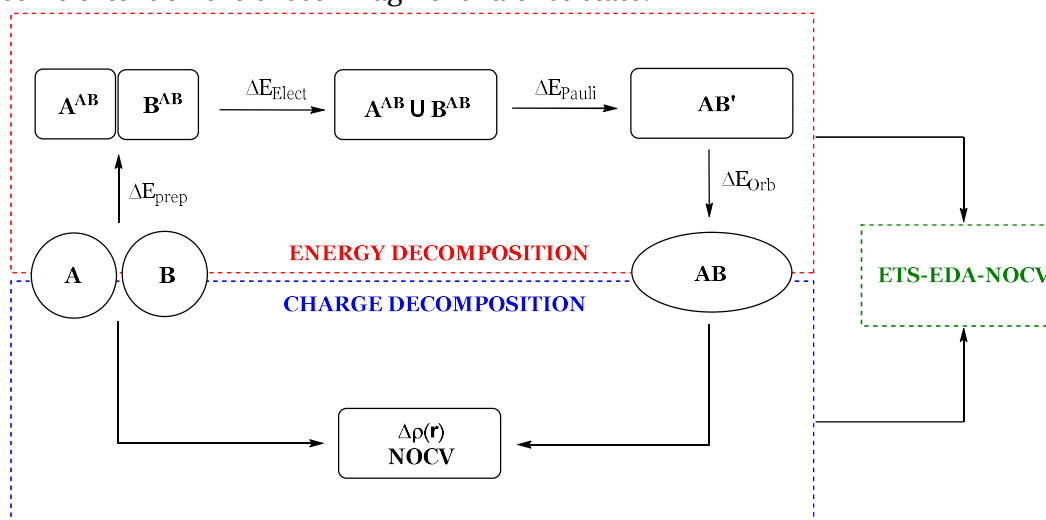
Figure 3. 7. Schematic representation of the (ETS)-EDA-NOCV method.

Previous work by Schwarz and Ayers have pointed out the need to minimize the $\rho(\boldsymbol{r})$ to maximally transfer information from $\rho_{AB}(\boldsymbol{r})$ to $\rho_A(\boldsymbol{r})$ and $\rho_B(\boldsymbol{r})$.[212, 213] Utilizing NOCVs, each *bonding channel* should minimize the electron flow. Ideally, the donor and acceptor NOCVs would be located in different fragments. However, the NOCVs are typically spread over the molecule. This is a consequence of the coexistence of two types of electron transfer: the intra-fragment charge transfer, associated with the electron reorganization in the fragment during the *bond formation*, and the inter-fragment charge transfer, which accounts for the electrons moving from fragment to fragment. From the OS point of view, only the latter is relevant. In the inter-fragment charge transfer, one fragment is *oxidized* while the other gets *reduced*. But, in the intra-fragment charge transfer occurs within the fragment, not affecting the OS. Thus, our index should only account for the inter-fragment charge transfer of the bonding channels. Technically, there are two plausible ways to proceed depending on the type of AIM employed, namely Hilbert and real-space. In Hilbert space, the coefficients of the SFO ($c_\mu^{\sigma,k}$) need to be grouped by fragments for each bonding channel k. Over the summation, the intra-fragment contributions will be cancelled obtaining the inter-fragment charge transfer for each fragment ($\delta_A^{\sigma,k}$) (Equation 76).

$$\int \Delta\rho_k^\sigma(\boldsymbol{r})\mathrm{d}\boldsymbol{r} = \sum_A^N \sum_{\mu \in A} |v_k^\sigma||c_\mu^{\sigma,k}|^2 - |v_{-k}^\sigma||c_\mu^{\sigma,-k}|^2 = \sum_A^N \delta_A^{\sigma,k} \qquad (76)$$

In real-space, one needs to restrict the integration of the $\Delta\rho_k^\sigma(\boldsymbol{r})$ over the atom/fragment domains. This can be accomplished in the most general way by introducing atomic/fragment weight functions ($w_A(\boldsymbol{r})$) and integrating over the whole space to obtain the corresponding atomic/fragment contribution $\delta_A^{\sigma,k}$ as

$$\delta_A^{\sigma,k} = \int w_A(\boldsymbol{r})\Delta\rho_k^\sigma(\boldsymbol{r})d\boldsymbol{r}. \tag{77}$$

To account for the overall inter-fragment charge transfer of fragment *A*, Fragment Electron Flow (FEF$_A$), one can sum the *k* –th $\delta_A^{\sigma,k}$ in each spin σ. The sum needs to be in absolute value because the $\delta_A^{\sigma,k}$ can be positive or negative. Otherwise, the different contributions will vanish.

$$FEF_A = \sum_{\sigma=\alpha,\beta} \sum_k^{n/2} |\delta_A^{\sigma,k}| \tag{78}$$

Then, the sum over the *N* fragments yields the total inter-Fragment Electron Flow (*iFEF*) (Equation 78). A factor of ½ is introduced to avoid the double counting of the electrons:

$$iFEF = \frac{1}{2}\sum_A FEF_A \tag{79}$$

It might be interesting to analyse the electron flow of different bonding channels separately. For instance, when multiple bonding channels have relevant contributions, one might want to detect the bonding channel where the electron flow is more prominent. We designed the inter-fragment charge transfer of a bonding channel (*iFEF^k*), which is obtained as Equation 80

$$iFEF^k = \sum_{\sigma=\alpha,\beta} \sum_A \delta_A^{\sigma,k}, \qquad \forall\, \delta_A^{\sigma,k} > 0 \tag{80}$$

The sum of the *k*-th iFEF^k values yields the total *iFEF* (Equation 81).

$$iFEF = \sum_k iFEF^k \tag{81}$$

3.2.1 Validation of the *iFEF* index and comparison with the ΔE_{orb} criterion

Firstly, we tested the *iFEF* with systems in which OS assignation is straightforward. We selected a set of small molecules (AH$_n$) bearing hydrides (KH, NaH, LiH, CaH$_2$, MgH$_2$, BH$_3$) and protons (H$_2$Se, H$_2$S, H$_2$O, HBr, HCl, HF and NH$_3$). We computed the EDA-NOCV and compared the obtained assignation from the *iFEF* and ΔE_{orb} minimization. It is important to note that the ΔE_{orb} criterion was established *ad-hoc* which, to the best of our knowledge, lacks a systematic evaluation. Both criteria were evaluated with different fragmentation patterns, namely atomic, H-AH$_{n-1}$ and A-H$_n$ fragmentations, to check how robust are towards the fragmentation pattern. The numerical values of ΔE_{orb} and *iFEF* index are gathered in Table A-I.7 of Appendix I. The *iFEF* distinguishes the hydride to

proton assignations, while the ΔE_{orb} criterion assigns hydrogens for some of the tested systems. Moreover, the *iFEF* assignation does not change with the fragmentation pattern while ΔE_{orb} shows dependency.

We evaluated the tendency of the criteria along the electronegativity differences. The ratio between the electronegativity of atom A (χ_A) with the hydrogen (χ_H) dictates the hydride ($\frac{\chi_A}{\chi_H} > 1$) and proton ($\frac{\chi_A}{\chi_H} < 1$) character. Since *iFEF* and ΔE_{orb} are extensive indexes, they will increase with the number of atoms of the AH_n. Thus, the comparison of *iFEF* and ΔE_{orb} among systems with different numbers of atoms is not *fair*. We converted them into intensive values by normalizing them with the number of hydrogens in the system.

In Figure 3.8 is depicted the normalized *iFEF* (*iFEF-norm*) and $|\Delta E_{orb}|$ ($|\Delta E_{orb}|$-*norm*) along the $\frac{\chi_A}{\chi_H}$ values in different reference states, namely hydride (H(1-)), proton (H(1+)) and hydrogen (H(0)). One can readily observe that the *iFEF-norm* lines crossover close to the point (1,1). When $\frac{\chi_A}{\chi_H} = 1$, the ionic approximation is not valid and yields an *iFEF-norm=1* for all the reference states. The line concerning the homolytic splitting (H(0)) is almost constant along the series but always higher than either H(1+) or H(1-) reference states, assigning the expected OS. The $|\Delta E_{orb}|$-*norm* has three crossing points. The H(0) reference state line stands lower than H(1+) or H(1-) reference states in, approximately, the range of $\frac{\chi_A}{\chi_H} = 0.5$ to $\frac{\chi_A}{\chi_H} = 1.3$. It evidences that the $|\Delta E_{orb}|$-*norm* tends to favour the neutral fragmentations unless the electronegativity differences are big (highly polarized bonds). In this regard, the *iFEF* criterion is more faithful and robust to OS than the ΔE_{orb} criterion. Moreover, the *iFEF* agrees with the IUPAC´s ionic approximation.
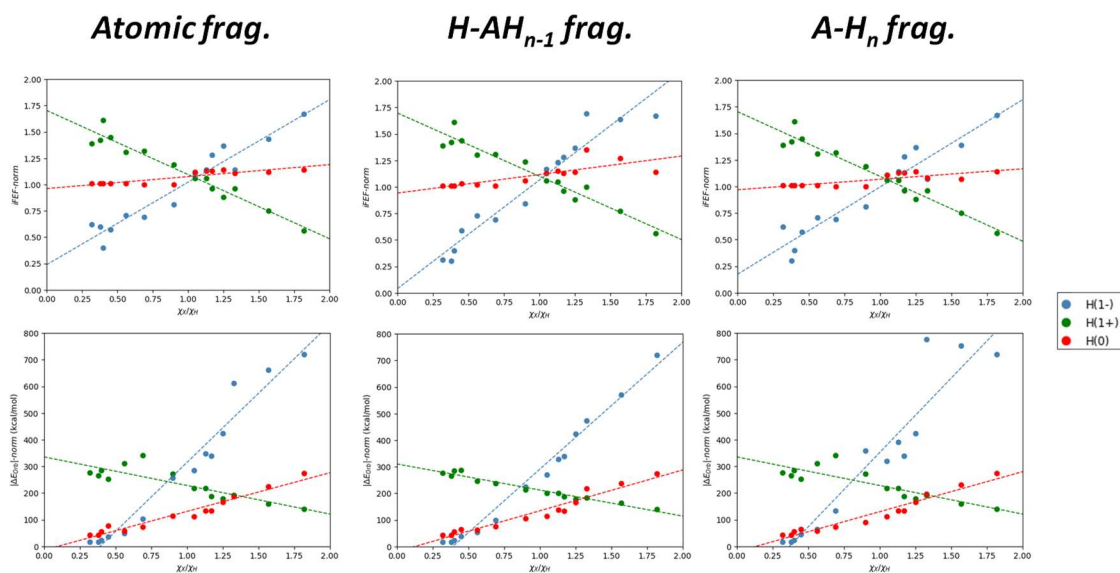
Figure 3. 8. Normalized *iFEF* (top) and ΔE_{orb} (bottom) of AH_n systems in different fragmentation patterns.

Most of the A-H bonds of the AH_n systems are highly ionic and OS is straightforward. We have considered the halomethane series CH_3X (X= F, Cl, Br, I) where the interaction C-X is electron-sharing. In those systems, there are three plausible fragmentations. Two heterolytic fragmentations, $X^- + CH_3^+$ and $X^+ + CH_3^-$, and one homolytic fragmentation $X\bullet + \bullet CH_3$. Table 3.2 gathers the ΔE_{orb} and *iFEF* values of the different fragmentation patterns. The ΔE_{orb} criterion favours the homolytic fragmentation with the exception of CH_3F, in which the $X^- + CH_3^+$ minimizes the $|\Delta E_{orb}|$.

On the contrary, the *iFEF* index exhibits lower values in the heterolytic fragmentation X^- + CH_3^+ whose values increase from 0.60 (CH_3F) to 0.92 (CH_3I) in the Löwdin partition. The *iFEF* in the Hirshfeld partition displays lower values than Löwdin, 0.43 (CH_3F) to 0.70 (CH_3I), but exhibits the same trend. The X^+ + CH_3^- fragmentation is discarded for both criteria.

Table 3. 2. ΔE_{orb} and *iFEF* in Löwdin (Löw) and Hishfeld (Hirsh) partition of CH_3X (X=F, Cl, Br, I) in BP86-D3(BJ)/TZ2P//BP86-D3(BJ)/def2-TZVPP level of theory. The lowest $|\Delta E_{orb}|$ and *iFEF* are highlighted in bold. Energy values are given in kcal/mol.

	Homolytic X(0)			Heterolytic X(1-)			Heterolytic X(1+)		
	ΔE_{orb}	iFEF		ΔE_{orb}	iFEF		ΔE_{orb}	iFEF	
		Löw	Hirsh		Löw	Hirsh		Löw	Hirsh
CH_3F	-289.0	1.11	0.82	**-205.4**	**0.60**	**0.43**	-703.3	1.57	1.22
CH_3Cl	**-171.9**	1.05	0.76	-208.3	**0.82**	**0.57**	-383.4	1.27	0.94
CH_3Br	**-139.5**	1.08	0.76	-204.2	**0.85**	**0.62**	-305.1	1.40	0.86
CH_3I	**-112.2**	1.03	0.76	-200.5	**0.94**	**0.70**	-233.9	1.22	0.78

It is interesting to analyse the differences in the chemical bond interpretation between the heterolytic splitting $CH_3(1+)$ and X(1-) and the homolytic splitting $CH_3(0)$ and X(0). We focused our analysis on the σ-bonding channel, which is the major contribution to the ΔE_{orb}. In the heterolytic fragmentation, the σ-interaction in CH_3X becomes more stabilizing (more negative) along the group, ranging from -162.6 kcal/mol (CH_3F) to -183.6 kcal/mol (CH_3I). Similarly, the C-X MBO ranges from 0.81 (CH_3F) to 1.24 (CH_3I). Therefore, the stronger σ-orbital interaction can be regarded as an increase in covalence. The $iFEF^\sigma$ also increases along the group (0.51 for CH_3F and 0.88 for CH_3I), indicating a decrease in the C-X bond for heavier elements. In the homolytic splitting, the energy associated with the σ-bonding channel decreases along the group, from -162.5 kcal/mol (CH_3F) to -103.0 kcal/mol (CH_3I) (Table 3.3). This trend is opposed to the ΔE_{orb} in the heterolytic splitting and the MBOs. Interestingly, the $iFEF^\sigma$ is almost constant along the series, bearing values close to 1, similarly found in AH_n systems (*vide supra*).

Table 3. 3. $\Delta E_{orb-\sigma}$ and $iFEF^\sigma$ of CH_3X (X=F, Cl, Br, I) in Löwdin partition at BP86-D3(BJ)/TZ2P//BP86-D3(BJ)/def2-TZVPP. Energies are given in kcal/mol.

	σ-bonding channel											
	Heterolytic ($CH_3(1+)$ and X(1-))						Homolytic ($CH_3(0)$ and X(0))					
	$\Delta E_{orb-\sigma}$	$\Delta E_{orb-\sigma(\alpha)}$	$\Delta E_{orb-\sigma(\beta)}$	$iFEF^\sigma$	$\delta_{CH_3}^{\alpha,\sigma}$	$\delta_{CH_3}^{\beta,\sigma}$	$\Delta E_{orb-\sigma}$	$\Delta E_{orb-\sigma(\alpha)}$	$\Delta E_{orb-\sigma(\beta)}$	$iFEF^\sigma$	$\delta_{CH_3}^{\alpha,\sigma}$	$\delta_{CH_3}^{\beta,\sigma}$
CH_3F	-162.5	-81.3	-81.3	0.51	0.26	0.26	-266.1	-219.4	-46.8	1.00	-0.74	0.27
CH_3Cl	-181.2	-90.6	-90.6	0.76	0.38	0.38	-156.6	-106.6	-49.9	0.99	-0.60	0.39
CH_3Br	-181.7	-90.8	-90.8	0.78	0.39	0.39	-127.4	-80.3	-47.1	1.00	-0.60	0.40
CH_3I	-183.6	-91.8	-91.8	0.88	0.44	0.44	-103.0	-57.2	-45.8	0.99	-0.54	0.45

We inspected the *α*- and *β*- charge transfer ($\delta_{CH_3}^{\alpha,\sigma}$ and $\delta_{CH_3}^{\beta,\sigma}$, respectively) to rationalize the differences. The *β*-electron is located in the CH_3 fragment and the *α*-electron in the halide atom. The $\delta_{CH_3}^{\beta,\sigma}$ increases along the series, displaying similar values to the heterolytic fragmentation (Table 3.3). On the contrary, the $\delta_{CH_3}^{\alpha,\sigma}$ in lighter halides undergo strong charge transfer, e.g. -0.74 (X = F), diminishing for heavier analogues, e.g.

-0.54 (X = I). The high charge transfer goes along with an energy *cost*, increasing (more negative) the $\Delta E_{orb-\sigma(\alpha)}$, blurring the analysis of the σ-bond interaction.

3.2.2 Dependency of *iFEF* index with the number of fragments

So far, we have only considered simple systems with one relevant bonding channel per interaction, namely one main σ-bonding channel. Let us analyse the CO_2 molecule, where both σ- and π-bonding channels are relevant for the bonding. CO_2 represents a simple textbook example, where straightforward application of the ionic approximation leads to the expected -2 OS for each oxygen atom and +4 for carbon. We performed EDA-NOCV calculations using atomic fragments and different valence electronic states, as shown in Figure 3.9. In particular, we considered the neutral carbon atom (C(o)) in the [5]F ($2s^12p_x^12p_y^12p_z^1$) electronic state, the C(2+)) in the [3]P electron configuration ($2s^12p_x^12p_y^02p_z^0$) and the C(4+)) in the [1]S ($2s^02p_x^02p_y^02p_z^0$) state.
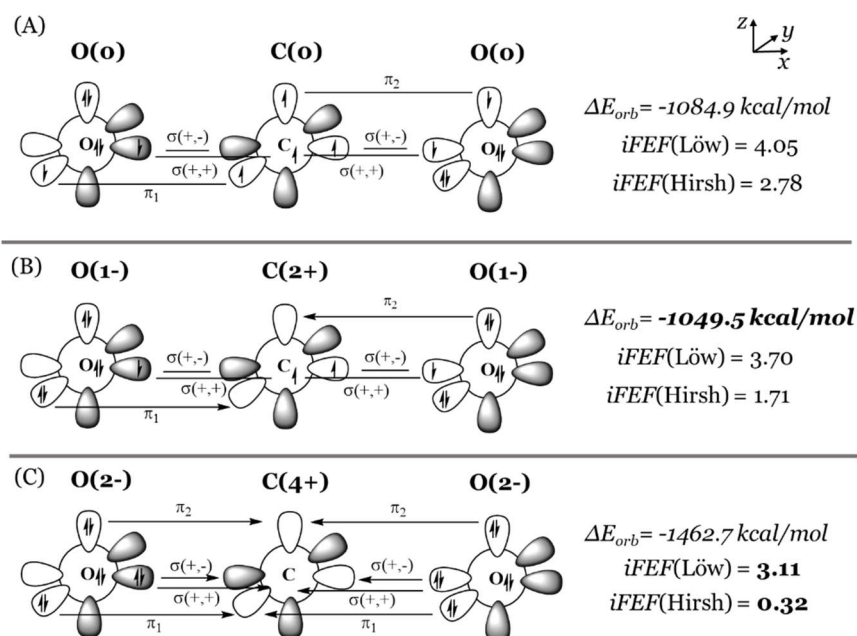
Figure 3. 9. ΔE_{orb} and *iFEF* values with different fragmentation of the CO_2 system at the BP86-D3(BJ)//BP86-D3(BJ)/def2-TZVPP level of theory. (A) Schematic representation of the [5]F C(o) fragmentation; (B) Schematic representation of the [3]P C(+2) fragmentation: (C) Schematic representation of the [1]S C(+4) fragmentation.

The [3]P fragmentation yields the lowest $|\Delta E_{orb}|$ (1049.5 kcal/mol), which is ca. 40 kcal/mol lower than the [5]F fragmentation (ΔE_{orb} = -1083.5 kcal/mol). The $|\Delta E_{orb}|$ in [1]S fragmentation is 400 kcal/mol above the [3]P and [5]S fragmentations (ΔE_{orb} = -1463.4 kcal/mol), being the worst fragment representation according to the energetic criterion. Hence, CO_2 is best characterized as a formally C(+2) and two oxyl O(1-) centres, at odds with the notion of OS. The *iFEF* values obtained using both Löwdin and Hirshfeld partitions follow the opposite trend, as shown in Figure 3.9. The [5]F fragmentation presents the highest *iFEF* values (4.05e and 2.78e for Löwdin and Hirshfeld, respectively) and it is minimal in the [1]S fragmentation (3.11e and 0.32e for Löwdin and Hirshfeld, respectively). Hence, the *iFEF* minimization recovers the expected C(4+) and O(2-) picture.

Taking into consideration the simple illustrative systems discussed thus far, it is apparent that the lowest ΔE_{orb} criterion is clearly biased towards neutral fragmentations,

and hence to low oxidation states. Except for rather clear donor-acceptor situations or extremely polarized covalent bonds, the energetic criterion does not follow IUPAC's ionic approximation, so it should not be used in general to determine oxidation states. The $|\Delta E_{orb}|$ values are also strongly affected by the number of fragments defined. Artificially grouping atoms into a given fragment (e.g. the two O atoms in CO_2) leads to lower (more negative) ΔE_{orb} contributions. For instance, the orbital relaxation energy in ^5F fragmentation differs by 67 kcal/mol between the two fragmentation patterns. The fact that $|\Delta E_{orb}|$ values significantly increase for highly charged fragments should not be surprising. High-order ionization potentials and electron affinities of atoms can be very large, which makes the intermediate reference states much higher in energy with respect to the final ground state of the molecule.

The *iFEF* values in the 2-fragments pattern are lower than the atomic fragmentation. Those differences can be rationalized by inspecting the shape of the NOCVs. Let us consider a π-bonding channel of the CO_2 molecule (Figure 4). In the atomic fragmentation (3-Fragments), the donor-NOCV is mainly located in one carbon and oxygen while the acceptor-NOCV basically lies in one oxygen (right). Thus, each fragment is either donating or receiving electrons suggesting a small intra-fragment charge transfer. In the 2-fragments pattern, the donor-NOCV is spread over the CO_2 molecule while the acceptor –NOCV is located on the oxygen atoms. It indicates that the oxygen atoms are both donating and receiving electrons, revealing intra-fragment charge transfer within O_2 fragment. The *iFEF* index cancels the intra-fragment electron flow, reducing the $iFEF^\pi$. The energy associated with the π-bonding channel ($\Delta E_{orb(\pi,\alpha)}$) in the atomic fragmentation is less stabilizing than the 2-fragments pattern. Those differences can be regarded as a higher intra-fragment charge transfer.
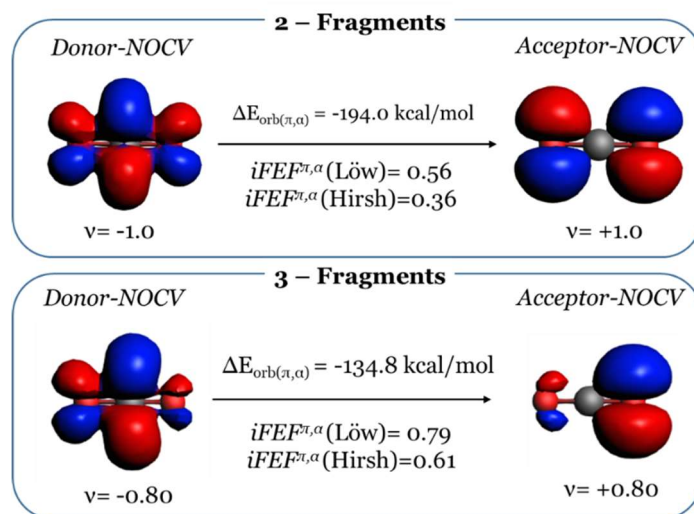
Figure 3. 10. π-NOCVs and the associated $\Delta E_{orb-\pi}$ and $iFEF^\pi$ values with the different fragmentation patterns of CO_2 at the BP86-D3(BJ)/TZ2P//BP86-D3(BJ)/def2-TZVPP level of theory. Isovalue=0.03 a.u.

3.2.3 Applied examples of the iFEF indexes

Most of the evaluated systems already revealed that the ΔE_{orb} tends to be higher for ionic fragmentations. Consequently, the ΔE_{orb} minimization biases the characterizations towards low OS fragmentations for very trivial systems. To increase the molecular complexity, we decided to analyse the OS of low-valent main group compounds. We selected the N-heterocyclic ylidenes (**1E,** Figure 3.11), typically described as a divalent tetrel atom (**E**) with an OS of +2 bearing a σ-lone pair. We characterized these compounds through EDA-NOCV calculations under the ΔE_{orb} and

iFEF criteria. Additionally, the EDA-NOCV assignations are compared with EOS and OSLO procedures.

We considered three reference states owning different valence and OS states (Figure 3.9). The E atom in the ^{3}P ($ns^2\,np_\sigma{}^1\,np_{||}{}^1\,np_\perp{}^0$) configuration, which has two σ-type electron sharing bonds and one formally empty p_z orbital stabilised by π-donation from the nitrogen atoms, the ^{1}D ($ns^2\,np_\sigma{}^0\,np_{||}{}^0\,np_\perp{}^2$) state represents the coordinative bonding situation where **E** has two lone pairs and the nitrogen atoms are stabilizing via donor-acceptor interaction, and in the charged ^{1}S ($ns^2\,np_\sigma{}^0\,np_{||}{}^0\,np_\perp{}^0$) state two σ-interactions and π-donation of donor-acceptor nature are present. The **E** presents a 2+ OS in the ^{1}S state while neutral fragmentations an E(0) for both ^{3}P and ^{1}D reference states.
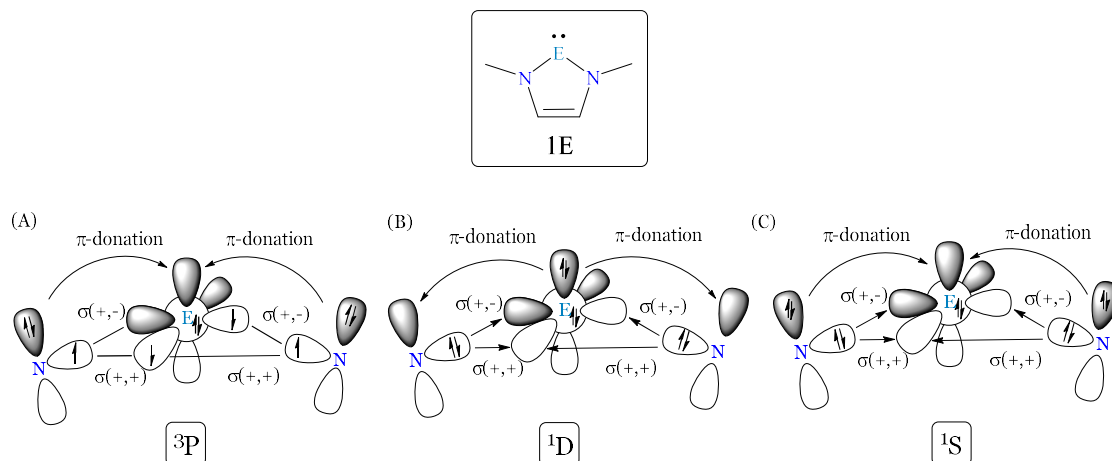
Figure 3. 11. Schematic representation of the major orbital interactions between groups 14 and E with the neighbor atoms. (A) The ^{3}P electronic state; (B) the ^{1}D electronic state; (C) the ^{1}S electronic state.

The EDA-NOCV results are collected in Table 3.4 together with the *iFEF* values and OS obtained with EOS and OSLO. According to EDA-NOCV, the ^{1}D fragmentation minimizes ΔE_{orb} along the **1E** series. Therefore, the tetrel atom is characterized with an OS of 0. On the contrary, the *iFEF* is minimal for the ^{1}S fragmentation, which leads to the E(+2) assignment independently of the AIM employed. The assignation obtained from the $|\Delta E_{orb}|$ minimization is at odds with the well-accepted E(+2) in the inorganic community.[214] Again, these results reflect that EDA-NOCV tends to provide lower $|\Delta E_{orb}|$ values for the neutral fragmentations, leading to the wrong OS assignments. The E(+2) is obtained by minimizing the *iFEF* in agreement with the EOS and OSLO methods, as both procedures undoubtedly assigned the +2 OS for all **1E** compounds independently of the AIM definition employed.

Table 3. 4. *iFEF* and *ΔE$_{orb}$* values of compounds **1E** evaluated ate the BP86-D3/TZ2P//BP86-D3(BJ)/def2-TZVPP level of theory. EOS and OSLO analysis are performed at BP86-D3(BJ)/def2-TZVPP level of theory. The values in brackets indicate the Reliability index (R(%) for EOS and Δ-FOLI for OSLO.

Frag	Criterion	C	Si	Ge	Sn	Pb
¹S (E(+2))	*ΔE$_{orb}$*	-1128.6	-500.3	-424.9	-336.9	-297.4
	*i*FEF (Löw)[a]	**2.19**	**1.74**	**1.83**	**1.55**	**2.06**
	*i*FEF(Hirsh)[b]	**1.23**	**1.02**	**1.08**	**1.10**	**1.12**
¹D (E(0))	*ΔE$_{orb}$*	**-672.6**	**-327.7**	**-259.1**	**-199.0**	**-165.8**
	*i*FEF (Löw)[a]	2.80	2.52	2.46	2.19	2.06
	*i*FEF(Hirsh)[b]	1.87	1.83	1.81	1.76	1.70
³P (E(0))	*ΔE$_{orb}$*	-686.1	-444.9	-377.1	-323.1	-290.2
	*i*FEF (Löw)[a]	2.88	2.85	2.91	2.83	2.84
	*i*FEF(Hirsh)[b]	1.73	1.81	1.94	2.06	2.15
EOS[c]		+2 (100)	+2 (100)	+2 (97.9)	+2 (91.9)	+2 (86.4)
EOS[d]		+2 (79.9)	+2 (97.3)	+2 (93.3)	+2 (86.8)	+2 (81.7)
OSLO[c]		+2 (0.15)	+2 (1.50)	+2 (1.09)	+2 (0.95)	+2 (0.84)

[a]Löw=Löwdin [b]Hirsh=Hirshfeld [c]TFVC AIM [d] NAO AIM

The *iFEF^k* provides the electron flow for each *k* bonding channel. Together with their associated energy (*ΔE$_{orb-k}$*), one obtains a deep understanding of the interaction arising from the fragments. Figure 3.12 depicts the *ΔE$_{orb-k}$* and *iFEF^k* values from the main bonding channels on **1E** in the ¹S reference state. One can readily observe that the σ(+,+) and σ(+,-) bonding channels display similar trends. The *ΔE$_{orb-σ(+,+)}$* and *ΔE$_{orb-σ(+,-)}$* of **1C** are significantly lower (more stabilizing) which increases for heavier analogues. Accordingly, *iFEF$^{σ(+,+)}$* and *iFEF$^{σ(+,-)}$* are maximal for **1C** and minimal for **1Pb**. The **1Si** displays lower *iFEF$^{σ(+,+)}$* and *iFEF$^{σ(+,-)}$* values than **1Ge**. It is regarded to the lower electronegativity of silicon (χ(Si)= 1.916) with respect to germanium (χ(Ge)= 1.994). The features of the π-bonding channel are different than the σ-bonding channels. While the *ΔE$_{orb-π}$* follows a similar trend as σ(+,+), σ(+,-) interactions, the *iFEF^π* is different. The **1Si** shows the lowest *iFEF^π* value (0.61) while **1Pb** has the highest (0.74). Thus, the charge transfer of the π-interaction reduces the stabilization of heavier yilidenes. In contrast, the σ-bonding charge transfer favours the interaction.
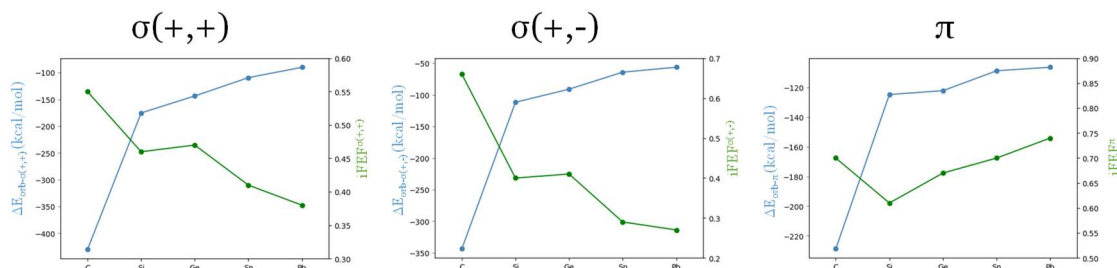
Figure 3. 12. *ΔE$_{orb-k}$* (blue line) and *iFEF^k* (green line) of the σ(+,+), σ(+,-) and π bonding channels of compounds **1E** (E=C, Si, Ge, Sn, Pb).

We decided to test the *iFEF* index with a more challenging system such as the well-discussed [NaBH$_3$]⁻.[215-222] The nature of the Na-B bond has been analysed through different chemical bonding tools, but, to date, none of them addresses it from the OS perspective.[219] Additionally, it represents an adequate example to test the ability of *iFEF* towards the nature of the wavefunction. In Table 3.5 are gathered the EDA-NOCV results together with the *iFEF* values considering the CSS and OSS wavefunctions. Two different

reference states are considered. The heterolytic splitting, in which Na and BH_3 have an OS of -1 and 0, respectively, and homolytic splitting is represented by a Na(0) and a BH_3(-1). According to the ΔE_{orb} criterion, the $[NaBH_3]^-$ features a Na(0) and a BH_3 (-1), independently of the nature of the wavefunction. Instead, the *iFEF* gives different assignations for OSS and CSS solutions. Considering the CSS wavefunction, the *iFEF* is minimized in the heterolytic splitting while the OSS solution yields lower *iFEF* values in the homolytic splitting. Thus, the *iFEF* index assigns a Na(-1) in the CCS solution and a Na(0) in the OSS wavefunction. It is important to note that the ΔE_{orb} values do not significantly change with the nature of the wavefunction. For instance, in the homolytic splitting, the ΔE_{orb} values differ for approximately 2 kcal/mol, while the *iFEF* differs for 0.6 *e*.

Table 3. 5. EDA-NOCV and *iFEF* values of the $[NaBH_3]^-$ at PBE0-D3BJ/TZ2P//CCSD(T)/aug-cc-pVTZ level of theory.

Wavefunction	CCS		OSS	
Splitting	Heterolytic	Homolytic	Heterolytic	Homolytic
OS Fragments	Na(1-)/BH_3(0)	Na(0)/BH_3(-1)	Na(1-)/BH_3(0)	Na(0)/BH_3(-1)
ΔE_{int}	-18.6	-31.3	-21.0	-33.7
ΔE_{Pauli}	32.9	24.8	32.9	24.8
ΔE_{elstat}	-17.0	-38.1	-17.0	-38.1
ΔE_{disp}	-0.7	-0.7	-0.7	-0.7
ΔE_{orb}	-33.7	**-17.3**	-36.1	**-19.7**
ΔE_{orb-HF}	0.0	0.0	0.0	0.0
$\Delta E_{orb-corr}$	-33.7	**-17.3**	-36.1	**-19.7**
$<S^2>$	0.00	0.00	0.54	0.54
iFEF (Löw)	**0.63**	1.08	0.70	**0.44**
iFEF (Hirsh)	**0.44**	0.66	0.56	**0.24**

The assignations obtained from the EDA-NOCV were contrasted with the EOS method. In Figure 3.11 is depicted the EOS assignations with CSS and OSS together with their frontier EFOs. For the CSS wavefunction, the EOS assigns a Na(-1) and a BH_3(0) with an R(%)=69.4. Inspecting the occupations of the EFOs (Figure 3.11, (B)), the occupation of the *s*-orbital (0.562) of sodium fragment is higher than the *p*-orbital on BH_3 (0.368), assigning the two σ-electrons to the sodium atom. In the case of the OSS wavefunction, the EOS assigns Na(0) and BH_3(-1) with an R(%)=93.5. Since the OSS wavefunction is unrestricted, the *α* and *β* EFOs need to be analysed separately. The last *α* electron is assigned to the *s*-orbital of the sodium atom and the last *β* electron is assigned to the *p*-orbital of the BH_3. Therefore, the two σ-electrons are homolytically assigned, in perfect agreement with the diradicaloid character of the $[NaBH_3]^-$ molecule. Again, the EOS assignations are in perfect agreement with the *iFEF* minimization criterion, proving its robustness towards biradical systems and the type of wavefunction.

(A) EOS assignation with CSS and OSS WF

	CSS	**OSS**
Na	-1	0
BH$_3$	0	-1
R(%)	69.4	93.5

(B) Frontier EFOs in CSS WF

Occ = 0.562

Occ = 0.368

(C) Frontier EFOs in OSS WF

Occ(α) = 0.843

Occ(β) = 0.248

Occ(α) = 0.105

Occ(β) = 0.684
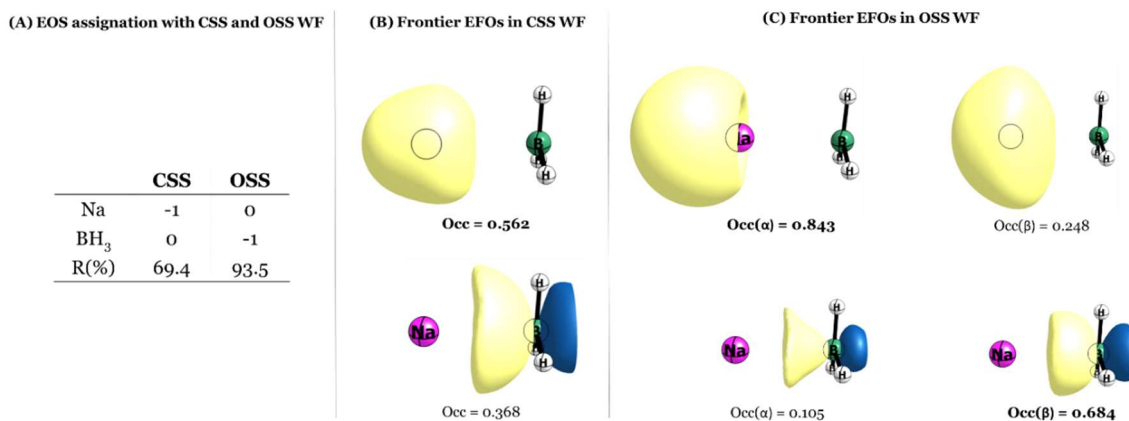
Figure 3. 13. (A) EOS analysis of the [NaBH$_3$]$^-$ at PBE0-D3(BJ)/def2-TZVPP//CCSD(T)/aug-cc-pVTZ level of theory using OSS and CSS wavefunctions. (B) Frontier EFOs using CSS wavefunction. (C) Frontier EFOs using OSS wavefunction. The occupied EFOs are highlighted in bold.

69

CHAPTER 4– Aluminium borohydrides as versatile building blocks

The synthesis of phosphaalumenes is one of the goals of this Thesis. To date, there is only one synthetic protocol to prepare the Al=P bond, reported in the course of this Thesis.[139] In Scheme 4.1 is represented the synthesis of phosphaalumene **74**, which consists of reacting the $(AlCp^*)_4$ with a phopha-Witting reagent at 70°C in benzene.[139] The release of trimethylphosphine (PMe₃) yields the formation of the Al=P bond.

$$1/4 \ (AlCp^*)_4 \quad + \quad Ar^*-\overset{\cdot\cdot}{P}: \quad \xrightarrow[-PMe_3]{70^\circ C, \ C_6D_6} \quad Cp^* \underset{\cdot\cdot}{\overset{Ar^*}{Al=P}}$$

$$\underset{PMe_3}{}$$
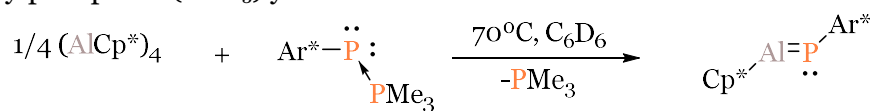
74

Scheme 4. 1. Reported synthesis of phosphaalumene **74**.

Our synthetic strategy is based on the use of Al(III) and P(III) reagents, given their easy accessibility and diversity of structures. In Figure 4.2 we show our initial retrosynthetic analysis. We hypothesized that the β-elimination of a H, halide-functionalized phosphanylalumane (**86**) could yield the Al=P bond (**85**). This type of phosphanylalumanes bear a proton in the α-position of the phosphine and a halide on the aluminium atom. Unfortunately, there are no synthetic procedures for synthesizing this type of phosphanylalumanes supported with *NacNac* ligand. However, they are known with other ligand systems.[97, 223] The synthesis involves a salt metathesis between an alkali phosphide and a haloalumane. In this context, we rationalized that a salt metathesis might be a good strategy to prepare **86** derivatives, using *NacNac*AlX₂ (X=Cl, Br, I) and a primary boraphosphine (R₂PH₂BH₃) as building blocks.

target molecule   **building blocks**
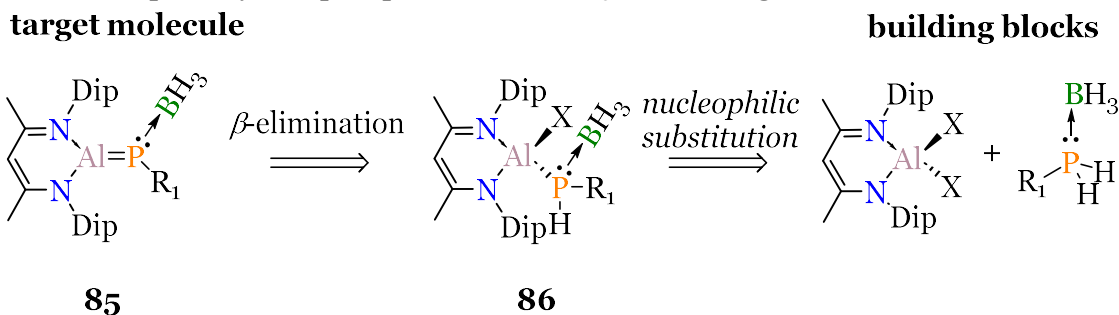
Scheme 4. 2. Retrosynthetic analysis of targeted **85** (R₁=Aryl, alkyl, amine; Dip=2,6-di-iso-propylphenyl).

The first step consists of achieving the mono-substitution reaction using a phosphorus nucleophile to isolate **86**. To the date, the reported salt metathesis reactions to prepare *NacNac* phosphanylalumanes undergo double substitution reaction (see section 1.3). This is not exclusively happening with phosphorus nucleophiles. In Section 1.2, we have shown that most of the salt metathesis reactions undergo double substitution (see Section 1.2). However, some of them can be controlled to mono-substitution product. For instance, the salt elimination reaction between LiNMe₂ and *NacNac*AlX₂ (X=Cl, Br, I) leads to the mono-substitution. Therefore, one might consider adjusting the steric properties of the nucleophile to achieve the mono-substitution. Alternatively, one may explore the tunning of the stereoelectronic properties of the aluminium building blocks. The *NacNac* ligand offers the flexibility to modify the α- and β-positions with diverse types of substituents. Moreover, this ligand stabilizes

aluminium with distinct types of functionalities, making it possible to evaluate different types of aluminium building blocks.

In a salt metathesis reaction, the halides are the most common choice for leaving group. However, one can consider other leaving groups such as pseudo-halides. In this Chapter, we propose aluminium borohydrides as suitable building blocks for aluminium chemistry. We demonstrate a good lability of the $[BH_4]^-$ towards different types of nucleophiles, including anionic and neutral. This synthetic route allows to control the mono-substitution for most nucleophiles, having a vital relevance for the synthesis of the H,X-functionalized phosphanylalumanes.

4.1 Synthesis and characterization of mono-substituted boralumanes

The pseudo-halides refer to organic or inorganic substituents that exhibit reactivity akin to halides. In a salt metathesis reaction, the pseudo-halides might function as a leaving group. In some cases, the use *pseudo*-halides might afford better control in a substitution reaction instead of halides.[224] The aluminium *pseudo*-halides have been known for many decades, however, they have been barely used for preparative proposes. We explore the possibility of using *pseudo*-halides as leaving groups in salt metathesis reactions in *NacNac*-supported alumanes. Our motivation was rooted in the serendipitous formation of *NacNac* aluminium borohydride which presented metathetic reactivity towards anionic phosphorus nucleophiles (see Chapter 5).

Firstly, we computationally scrutiny the leaving group quality of different halides and pseudo-halides, namely triflate (TfO$^-$), isocyanate (NCO$^-$), isothiocyanate (NCS$^-$) and borohydride ($[BH_4]^-$). The latter is not a common pseudo-halide in organic or *d*-block chemistry, but it is frequently used for salt metathesis reactions in *f*-bock elements.[61] Brook and co-workers described the metathetic reaction between $Al(BH_4)_3$ and ethyl-lithium (see section 1.1.3), supporting the potential pseudo-halide behaviour of $[BH_4]^-$ in alumanes. Ayers and co-workers computationally examined the leaving group quality of halogens in alkyl halides.[225] They identified that the enthalpy of the carbon-halide bond serves as an indicator to determine the leaving group quality. Considering that the salt elimination reaction undergoes through a dissociative mechanism, we examined the bond enthalpy (ΔH_r) of *NacNac*AlHX into the electrophile [*NacNac*AlH]$^+$ (or electrofugal) and the leaving group X$^-$ (or nucleofugal) (Scheme 4.3).

Electrofugal   *Nucleofugal*
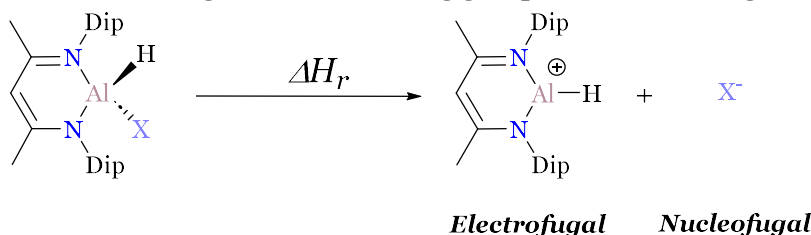
Scheme 4. 3. Model charge disproportion reaction of *NacNac*AlHX (X=H⁻, Cl⁻, Br⁻, I⁻, TfO⁻, NCO⁻, NCS⁻, [BH₄]⁻, Dip=2,6-di-iso-propylphenyl).

Table 4.1 gathers the ΔH_r considering different leaving groups. The pseudo-halides TfO$^-$, NCO$^-$ and NCS$^-$ display the highest ΔH_r values (93.8 kcal/mol (X$^-$=TfO$^-$), 124.1 kcal/mol (X$^-$=NCO$^-$) and 109.7 kcal/mol (X$^-$=NCS$^-$)). These values are remarkably higher than halides, which range from 68.7 kcal/mol (Cl$^-$) to 51.6 kcal/mol (I$^-$). The bond enthalpy of X=Cl$^-$ and X=Br$^-$ are smaller than the C-X bond reported by Ayers *et al.* but the X=I$^-$ is higher than C-I. Interestingly, the $[BH_4]^-$ has the lowest ΔH_r within the pseudo-halides series (56.2 kcal/mol), aligning between bromine and iodine ΔH_r. Thus,

according to the ΔH_r values, the $[BH_4]^-$ is a promising leaving group in a salt metathesis reaction. Remarkably, the dissociation enthalpy of $[BH_4]^-$ is notably smaller than X=H⁻ (88.3 kcal/mol), predicting the enhanced lability of a borohydride with respect to the hydride.

Table 4. 1. Reaction enthalpy (ΔH_r) and vertical electron affinity (EA) of the nucleofugal X⁻ at the B3LYP-D3(BJ)/def2-TZVPP//B3LYP-D3(BJ)/def2-SVP level of theory. The energies are given in kcal/mol.

X	ΔH_r
H⁻	88.3
Cl⁻	68.7
Br⁻	59.0
I⁻	51.6
TfO⁻	93.8
NCO⁻	124.1
NCS⁻	109.7
$[BH_4]^-$	56.2

We explored the salt metathesis reaction between *NacNac*Al(BH₄)₂ (**29**) and different type of anionic nucleophiles (Scheme 4.4). We started testing O-donor anionic nucleophiles such as sodium *tert*-butoxide (Na*t*BuO) and sodium 2-phosphaethynolate (NaPCO). These nucleophiles form stable compounds with aluminium given the intrinsic strength of the aluminium-oxygen bond. Therefore, they are a good starting point to prove the *pseudo*-halide behaviour of borohydride in alumanes. The equimolar reaction of **29** with Na*t*BuO and NaPCO in diethylether at room temperature resulted in the formation of a white precipitate identified as NaBH₄ (δ(^{11}B)=-41.56 ppm). Upon filtration and crystallization, the mono-substituted *NacNac* aluminium borohydride **87** and **88** are isolated in acceptable yields.
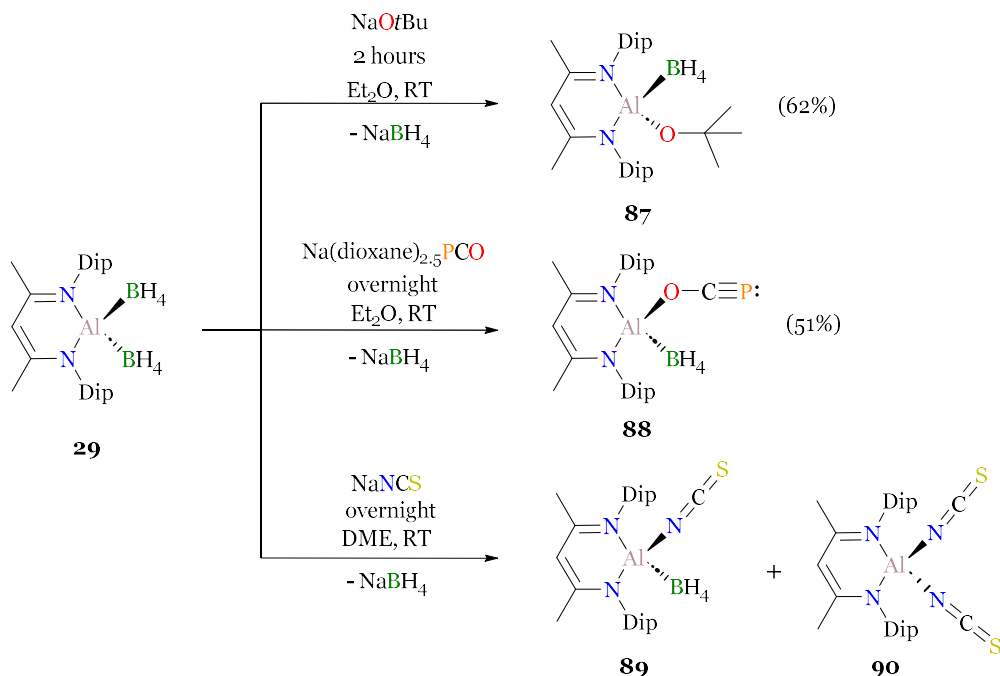
Scheme 4. 4. Salt metathesis reaction of **29** with NaOtBu, Na(dioxane)₂.₅PCO and NaNCS nucleophiles (Dip= 2,6-di-iso-propylphenyl, tBu = tert-butyl).

The compounds **87** and **88** were analysed by multinuclear NMR, FT-IR and SC-XRD techniques (see Appendix II). The ^{1}H-NMR spectrum of **87** exhibits two septets at 3.37 ppm ($^3J_{H-H}$=6.27 Hz) and 3.50 ppm ($^3J_{H-H}$=6.81 Hz) assigned to the methine protons from the *iso*-propyl substituents from the *Dip* group. It agrees with the inequivalent

substituents on axial and meridional positions of aluminium. We identify a singlet at δ=0.90 ppm corresponding to the magnetically equivalent methyl group from *tert*-butyl group. The ^{11}B–NMR shows a well-resolved quintuplet resonance at δ=-37.12 ppm ($^1J_{B-H}$=86.09 Hz), in agreement with a [BH$_4$]$^-$ group. The chemical shift is slightly shifted towards high field respect to **29** (δ=-36.6 ppm).[76]

Compound **88** displays similar ^{1}H-NMR features to **87**. The coordination of PCO was confirmed by ^{31}P-NMR featuring a singlet at δ=-319.4 ppm. It is in the range of previously reported O-coordinated PCO alumane.[226] Additionally, in ^{13}C{^{1}H}–NMR is identified a doublet signal at 148.9 ppm ($^1J_{C-P}$=3.16 Hz), assigned to the quaternary carbon of the PCO motif. The coupling constant $^1J_{C-P}$ is similar to the salen-supported Al-OCP ($^1J_{C-P}$ =4.7 Hz) but smaller than to other main group and transition metal O-bounded PCO compounds, which range from $^1J_{C-P}$=9.8 Hz to $^1J_{C-P}$=17.6 Hz.[227] In the FT-IR spectrum is identified an absorption band at 1693.0 cm^{-1}, assigned to the C-O stretching mode of the PCO motif. The ^{11}B–NMR spectrum displays a well-resolved quintuplet signal at δ=-44.37 ppm ($^1J_{B-H}$=86.06 Hz) in agreement with a [BH$_4$]$^-$ moiety. The chemical shift is remarkably up-fielded, similar to ionic borohydrides species such as [Na(15-crown-5)][BH$_4$] (δ=-43.7 ppm).[228] The ^{27}Al-NMR features a broad singlet at δ=+66.83 ppm (see Figure 4.1), which is more high fielded than **29** (δ=+110.7 ppm).[229]
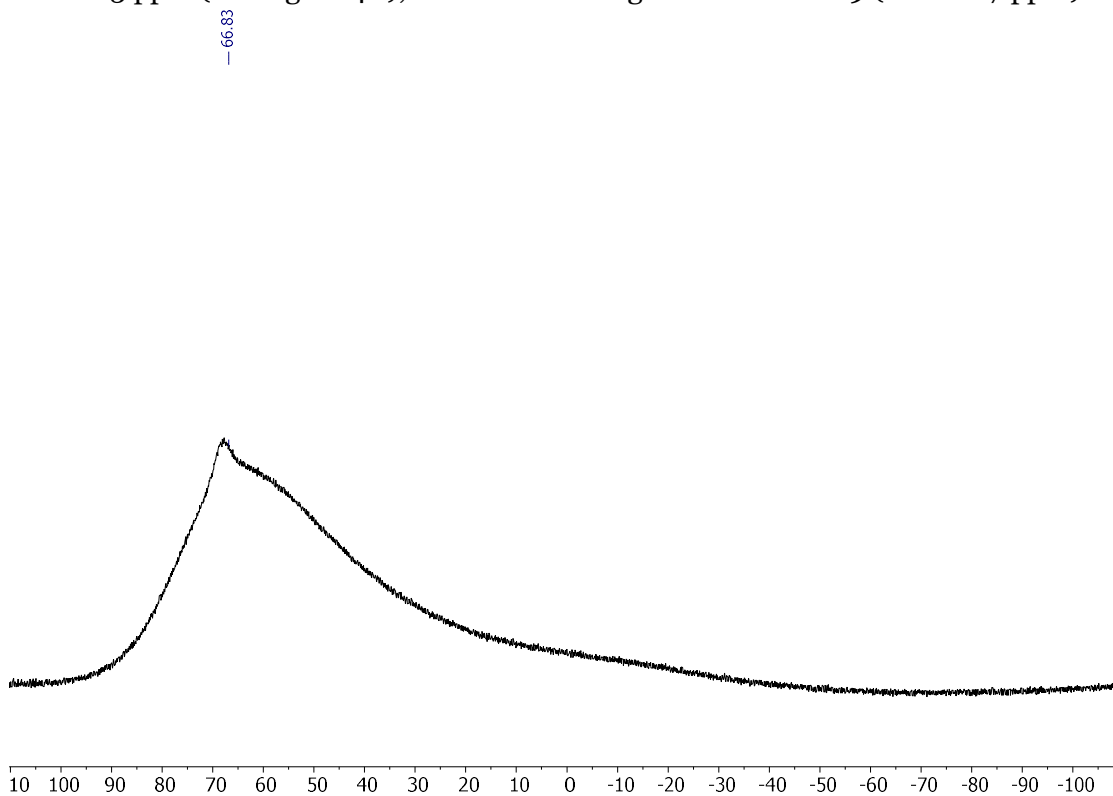
Figure 4. 1. ^{27}Al-NMR (104.3 MHz,293 K) of compound **88** in C$_6$D$_6$ in the range of 110 ppm to -110 ppm.

Single crystals suitable for XRD of compounds **87** and **88** were obtained from saturated solutions in diethylether. The structures showed a *t*BuO and PCO substituent on the aluminium atom (Figure 4.2). In both complexes, the aluminium adopts a distorted tetrahedral geometry (for **87**, N2-Al1-N1=96.1(6)° and O1-Al1-B1=115.4(7)°; for **91**, N2-Al1-N1=98.8(4)° and O1-Al1-B1=111.7(7)°). The *t*BuO group occupies the equatorial position while PCO is O-coordinated on the axial site. Those differences are presumably regarded to steric hindrance. The Al-O distance in compound **87** (Al1-O1=1.696(2) Å) is marginally shorter than reported Al-O distances in *β*-diketiminate alumanes.[230] Notably, the Al-O distance (Al-O=1.781(6) Å) of compound **88** is remarkable longer than **87**, exhibiting a difference of 0.14 Å. The distance between Al⋯B

ranges from 2.158 Å (**87**) to an extremely short 2.064 Å (**88**). The latter distance aligns in the range of single (Al-B = 2.11 Å) and double bond (Al=B =1.91 Å).[231, 232] Interestingly, it is close to the B=Al double bond length (Al-B=2.069(2) Å) of the compound [(CAAC^{Dip})PhB=AlCp^{3t}] reported by Braunschweig and co-workers.[233]

The [BH$_4$]$^-$ has a very rich coordination chemistry, displaying κ^1, κ^2 and κ^3 coordination modes. In TM borohydride chemistry, the TM···B distance is related with the coordination number of the BH$_4$.[234] In general, the short TM···B are related with higher coordination number. The good quality of the crystals allowed to allocate the hydrides of the BH$_4$ moiety on the electron density Fourier map, enabling the characterization of the hapticity type. Compound **87** revealed a κ^2 coordination towards aluminium bearing identical Al-H distances (Al1-H1D=1.732(6) Å and Al1-H1C=1.732(6) Å). The κ^2 coordination is typically found in other aluminoborates.[76, 77, 229] It calls our attention that the BH$_4$ coordination in **88** has a κ^3 mode. It bears two almost equivalent Al-H distances (Al1-H1=1.813(4) Å and Al-H2=1.850(1) Å) and a longer Al-H distance (Al-H3=1.969(8) Å). The κ^3 coordination is not common in aluminium chemistry. However, some examples are found in *s*-block, such as [Na(15-crown-5)][BH$_4$], (TMEDA)Mg(BH$_4$)$_2$ or [Ca(BH$_4$)(THF)$_5$]BPh$_4$,[228, 235, 236] and early transition metal complexes.[56]
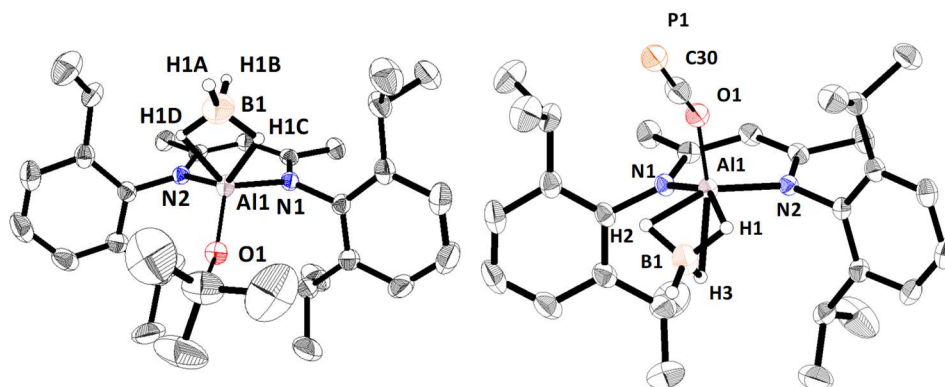
Figure 4. 2. Solid state structure of **87** (left) and **88** (right). Thermal ellipsoids set to 50% probability. Selected experimental bond lengths in Å and angles in degrees. Compound **87**: Al1-O1=1.6962(15), Al1-B1=2.158(3), Al1-H1D= 1.7327(537), Al1-H1C= 1.7327(537), B1-H1D=1.1110(592), B1-H1C=1.1110(592), Al1-N1=1.89926(11), Al1-N2=1.8276(11), B1-Al1 = 2.158(3), B1-Al1-O1=115.48(11), N1-Al1-O1=112.16, N2-Al1-O1=112.16, N1-Al1-B1=109.60(7), N2-Al1-B1=109.61(7); Compound **88**: P1-C30 1.549(1), C30-O1=1.256(6), O1-Al1= 1.781(6), Al1-B1 2.064(3), Al1-N2 1.876(9), Al1-H1 1.813(4), Al1 −H2 1.850(1), Al1-H3 1.969(8), B1-H3=1.028(4), B1-H2=1.157(2); B1-H1=1.166(4); B1-H4=1.018(6); C30-O1-Al1=141.3(6); Al1-N1 1.870(9) , O1 −Al1 – B1=111.7(6), O1-Al1-N2=103.6(4) , O1- Al1-N1=105.12.

The FT-IR spectroscopy is an important technique to characterize transition metal borohydrides. Due to the difficulties in locating the hydrogen atoms in X-ray diffraction, the FT-IR analysis has been useful to determine the coordination number of [BH$_4$]$^-$ in monomeric transition metal borohydrides.[56] The bridging hydrogens (H$_b$) weaken the B-H bond while the terminal (H$_t$) B-H bond is strengthened. Therefore, the B-H stretching bands help to determine the hapticity of the [BH$_4$]$^-$ group (Scheme 4.5). The κ^1-coordination displays two bands in the region of 2300-2450 cm^{-1} assigned to the stretching of B-H$_t$ while B-H$_b$ stretching absorbs at 2000 cm^{-1}. The κ^2-coordination mode can be identified as doublet from the B-H$_b$ stretching between 1650-2150 cm^{-1} and the B-H$_t$ at the region of 2400-2600 cm^{-1}. Finally, the κ^3-coordination is identified by an absorbance between 2450-2600 cm^{-1}, which is assigned to the B-H$_t$ stretching and a doublet between 2100-2200 cm^{-1}, assigned to B-H$_b$ stretching.

κ¹-coordination / κ²-coordination / κ³-coordination

κ¹-coordination $\qquad$ κ²-coordination $\qquad$ κ³-coordination

υ(B-H$_t$)=2300-2400 cm^{-1}
υ(B-H$_b$)=2000 cm^{-1}

υ(B-H$_t$)=2400-2600 cm^{-1}
υ(B-H$_b$)=1650-2150 cm^{-1}

υ(B-H$_t$)=2450-2600 cm^{-1}
υ(B-H$_b$)=1650-2150 cm^{-1}

Scheme 4. 5. Coordination modes of [BH$_4$]$^-$ and the B-H stretching modes (M=transition metal).
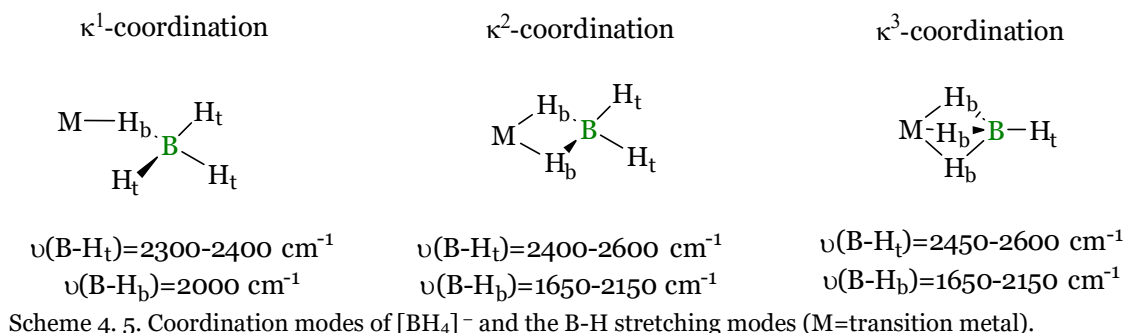
In Figure 4.3 are plotted the FT-IR spectra of **87** and **88** (black lines) together with the simulated IR spectra (red lines). The FT-IR of **87** reveals two signals at 2195.7 and 2277.9 cm^{-1}, assigned to the B-H$_t$ stretching, and another doublet at 2404.8 cm^{-1} and 2477.1 cm^{-1}, assigned to the B-H$_t$ stretching. In the case of **88**, we can identify three bands at 2498.8 cm^{-1}, 2318.6 cm^{-1} and 2169.5 cm^{-1}. We computed the IR spectrum at the B3LYP/def2-SVP level of theory. The obtained geometries reveal a κ²-coordination for **87** and κ³-coordination for **88**, in agreement with the SC-XRD analysis. The simulated spectra are in good agreement with the experimental ones. In the case of **87**, the bands at 2404.8 cm^{-1} and 2477.1 cm^{-1} are assigned to the symmetric and asymmetric stretchings of the B-H$_b$ while the signals at 2404.8 cm^{-1} and 2477.10 cm^{-1} correspond to the B-H$_t$ stretchings. In the case of **88**, the simulated spectrum assigns the band at 2498.8 cm^{-1} to the stretching of B-H$_t$ bond. One B-H$_b$ stretching is assigned to the signal at 2318.6 cm^{-1} and symmetric and antisymmetric stretchings of the B-H$_b$ bonds are assigned to the band at 2169.5 cm^{-1}. The B-H$_b$ stretching bands can be distinguished from those of B-H$_t$. However, the differences are not as pronounced as those found in TM borohydrides. In compound **87**, the band at 2404.8 cm^{-1} is assigned to the terminal B-H. In compound **88**, one of this bands is shifted to 2318.6 cm^{-1}, reflecting the bridging configuration of the B-H bond.

87 $\qquad$ **88**
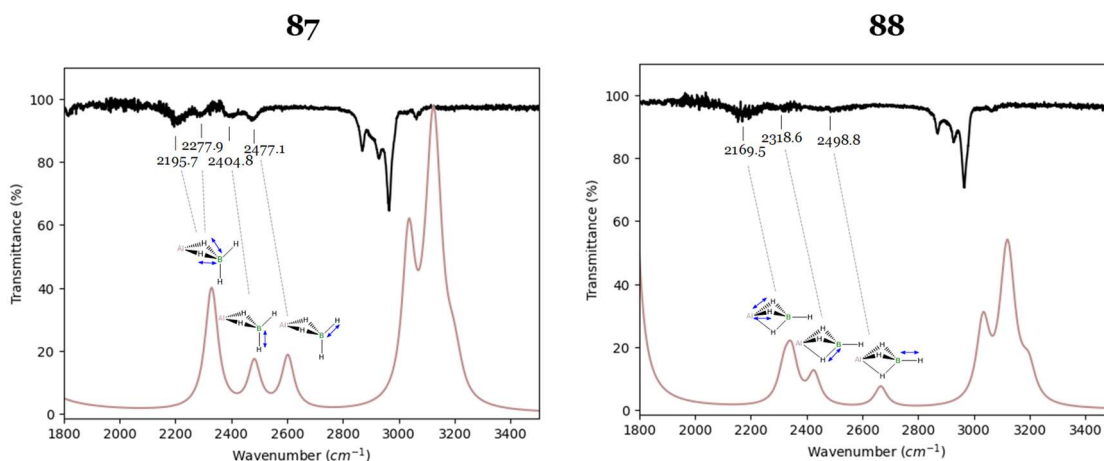
Figure 4. 3. Experimental and simulated FT-IR of compound **87** (left) and **88**(right). The computed spectra (red line) are at the B3LYP-D3(BJ)/def2-SVP level of theory. The blue lines indicate the vibrational mode.

We also explored the equimolar reaction between **29** and NaNCS nucleophile, obtaining a mixture of compounds. The ¹H-NMR revealed to singlets at δ=4.77 ppm and δ=4.67 ppm corresponding to the proton in γ-position of the *NacNac* backbone in a ratio of 8:2. The major product displayed two septets at δ=3.48 ppm and δ=3.02 ppm, consistent two different substituents on aluminium, and the minor product presented a one septet at δ=3.17 ppm, in agreement with two identical substituents on aluminium. Thus, the ¹H-NMR data suggests the formation of the mono- and di-substitution products (**89** and **90**). Additionally, the ¹¹B-NMR shows high field quintuplet resonance

at -42.26 ppm, similar to the chemical shift of **88** (δ=-44.37 ppm). The incorporation of NCS$^-$ of **89** and **90** is further supported by FT-IR. The two absorption bands at 2068.70 and 2050.83 cm^{-1} are assigned to the NCS$^-$ stretching vibrational modes, which are blue-shifted with respect to NaNCS (ν=2074 cm^{-1} and ν=2057 cm^{-1}).[237] Unfortunately, compound **89** could not be isolated presumably due to the similar solubility with **90**. In order to confirm the formation of the di-substituted product, we reacted **29** with an excess of NaNCS in DME (Scheme 4.6). The ^{1}H-NMR showed one singlet resonance at δ=4.67 ppm, assigned to the proton in γ-position of the *NacNac* backbone, and a septet resonance at δ=3.17 ppm (^{1}J$_{H-H}$ =6.72 Hz), assigned to the methine proton from *iso*-propyl substituents from *Dip* group. Additionally, the ^{11}B-NMR is silent supporting the double salt metathesis reaction. The chemical shifts are in agreement with the ones reported by Roesky and co-workers, who synthetized **90** by reacting NacNacAl(I) carbenoid with two equivalents of AgNCS.[238] Compound **90** was isolated in 53% yield, which is lower than the one reported by Roesky and co-workers.[238]
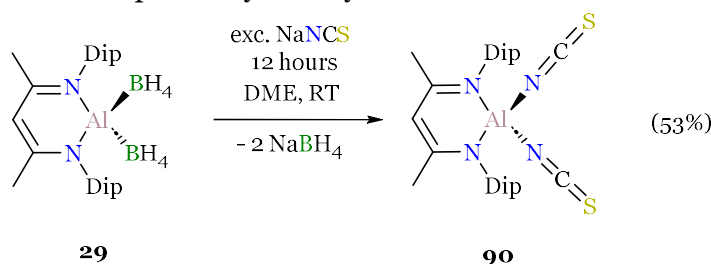
Scheme 4. 6. Synthesis of compound **90** (Dip= 2,6-di-iso-propylphenyl).

The reactivity of [BH$_4$]$^-$ as leaving group was also examined with neutral nucleophiles such as NHCs. Compound **29** was reacted with two equivalents of NHC^{MeiPr} in diethylether at 40°C in a pressure tube (Scheme 4.7). We observed the immediate formation of a white precipitate which we identified as a carbene-borane adduct **92** (δ(^{11}B)=-34.86 ppm, ^{1}J$_{B-H}$=87.8 Hz), featuring similar ^{11}B-NMR with analogous compounds.[239] After workout, the Lewis base stabilised aluminoborate **91** was obtained as white solid in 55% yields. The ^{1}H-NMR spectrum agrees with the inequivalent substituents on aluminium. We identified two doublets are at 3.99 ppm (^{1}J$_{H-H}$=1.03 Hz) and 3.23 ppm (^{1}J$_{H-H}$=1.02 Hz), suggesting the –CH$_2$ group in the *NacNac* backbone.[240, 241] The latter is supported by ^{13}C{^{1}H}-NMR and ^{13}C-DEPT135 (δ=83.64 ppm) (See Appenix II, Figure A-II.26 and Figure A-II.28). ^{11}B-NMR features a broad signal at -36.28 ppm with an insignificant shifting respect to the starting material **29** (δ=-36.6 ppm).[76] The coordination of the NHC^{MeiPr} was confirmed by ^{13}C{^{1}H}-NMR. The carbenic carbon is identified at +165 ppm, which is slightly low-field shifted compared to the free carbene (160.7 ppm).[242]
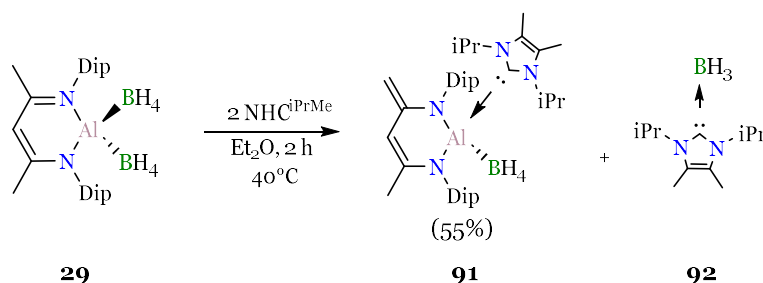
Scheme 4. 7. Synthesis of compound **91** (Dip=2,6-di-iso-propylphenyl, iPr=iso-propyl).

Single crystals of **91** were obtained in diethylether at -30 °C. In Figure 4. 4 is depicted the crystal structure of **91**. The aluminium adopts a distorted tetrahedral coordination (N1-Al1-N2=102.4(1)° and C30-Al1-B1=105.9(3)°) where NHC^{MeiPr} is placed on the axial position. The distance between aluminium and carbenic carbon (Al1-

C30=2.061(4) Å) in the expected range of NHC stabilised alumanes.[243] The [BH₄]⁻ is located at the equatorial position bearing a Al-B distance of 2.243(6) Å. Interestingly, it is drastically longer than the Al···B distance of **87** (2.158(3) Å),and **88** (2.064(3) Å). The asymmetric Al-H distances (Al1-H1=1.876(6); Al-H2 1.728(2)) and the long Al···B distance suggest a κ¹ coordination. The Al-N distances are almost equal (Al1 – N2 =1.842(8) Å and Al-N1 = 1.843(8) Å) similar to the hydride analogues.[241] The terminal C-C bonds of the *NacNac* backbone are inequivalent, 1.502(3) Å and 1.358(3) Å, which confirms a single and double bond, respectively.
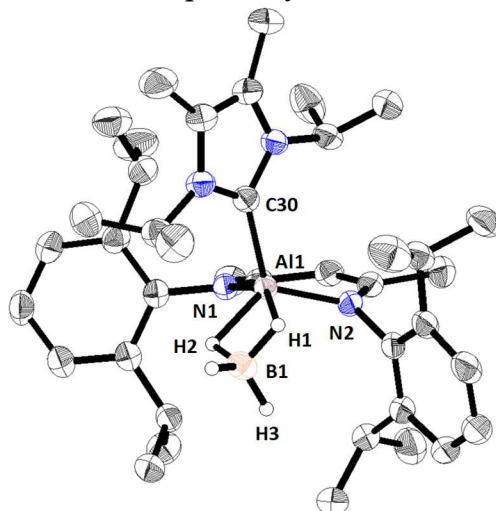
Figure 4. 4. Solid state structure of **91** Thermal ellipsoids set to 50% probability. Selected experimental and computational [B3LYP-D3(BJ)/def2-SVP] bond lengths [Å] and bond angles [°]:Al1-C30 2.061(4) [2.065], Al1-N2 1.842(8) [1.857], Al1-N2 1.843(8) [1.865], Al1 – B1 2.243(6) [2.216], Al1-H1 1.876(6) [1.884], Al1-H2 1.728(2) [1.823], Al1-H3 2.754(4) [2.278], C30-Al1-N2 116.9(9) [115.3], C30- Al1-N1 105.9(3) [103.7], C30-Al1-B1 108.8(2) [109.5].

4.2 Mechanistic insights on the formation of 91

The NHCs are known to be good nucleophiles but they can also react as a Brønsted-bases. For instance, Schulz and co-workers reacted 2 equivalents of NHC with *NacNac*GaCl₂ yielding *NacNac*Ga(NHC^iPrMe)Cl (Scheme 4.8). The NHC^iPrMe reacts both as a Brønsted and Lewis base.[244]
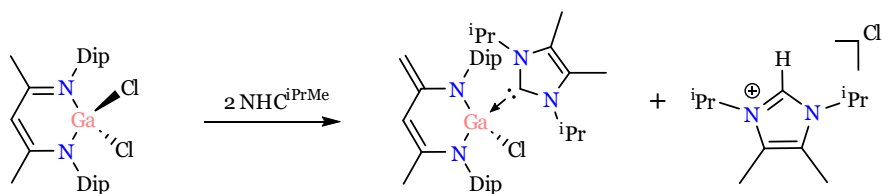
Scheme 4. 8. Synthesis of *NacNac*Ga(NHC^iPrMe)Cl (Dip=2,6-di-iso-propylphenyl, iPr=iso-propyl).

In this context, we decided to decipher whether the NHC^iPrMe reacts as a Brønsted-base or Lewis-base (or both) with **29**. We started monitoring the reaction in C₆D₆ at 40°C with NMR spectroscopy. In Figure 4.5, we show the ¹H-NMR along different reaction times. After 10 min of reaction, we can clearly identify the starting materials. For instance, at δ=3.95 ppm, one can identify the septet signal of the methine proton from the NHC^iPrMe, or the singlet signal from the Cᵧ-H of the *NacNac*Al(BH₄)₂ at δ=4.94 ppm. Those signals decrease the intensity along reaction time while the signals assigned to compound **91** increase, such as the singlet at δ=5.52 ppm assigned to the Cᵧ-H proton or the two doublets at δ=3.27 ppm and δ=3.99 ppm assigned to the methylene group. At the range of δ=2.7 ppm to δ= -1.7 ppm, we observed a broad quadruplet consistent with a compound bearing a BH₃ moiety. Additionally, we observed the formation of another

compound (marked with a yellow star in the Figure 4.5), which has a similar spin pattern as **91**.
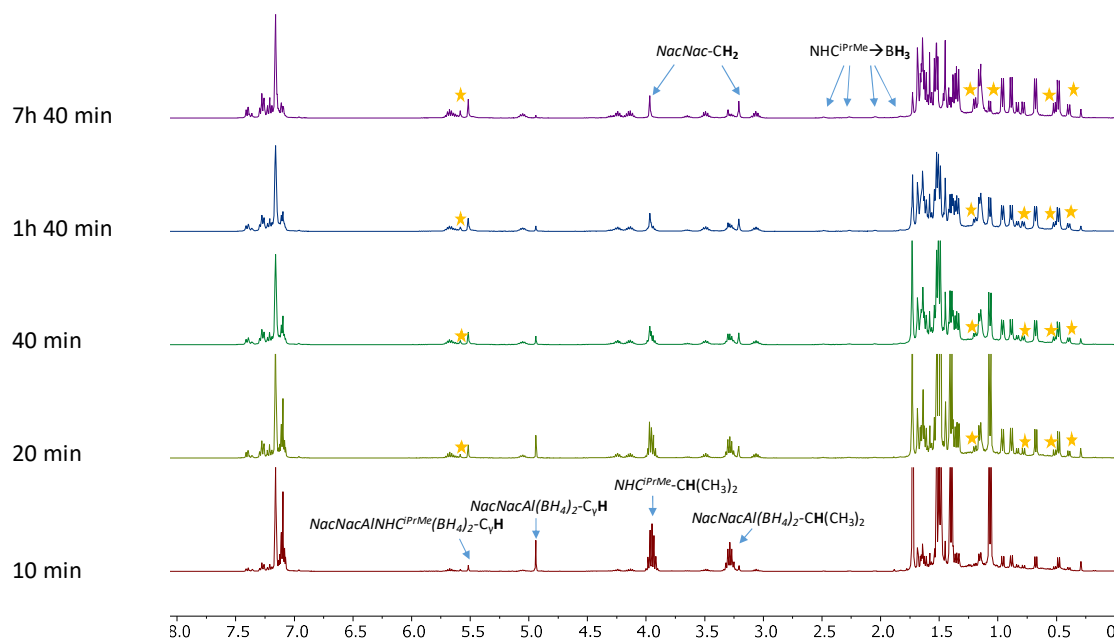
Figure 4. 5. ^{1}H-NMR (400.1 MHz) along different reaction times between *NacNac*Al(BH$_4$)$_2$ and two equivalents of NHC^{iPrMe} in C$_6$D$_6$.

We depict the ^{11}B{^{1}H}-NMR at different reaction times in Figure 4.6. At 10 min. of reaction time, we observed the singlet signal from **29** (δ=-36.6 ppm) which decreased along time. We observed the formation of two new boron species over the reaction time. A broad signal at approximately δ=-36.5 ppm is assigned to **91**, and the singlet at δ=-34.86 ppm is assigned to the carbene-borane **92**. Those observations are consistent with the ^{1}H-NMR. Additionally, there is the formation of one intermediate (marked with a yellow star in Figure 4.6) which we could not determine its nature.
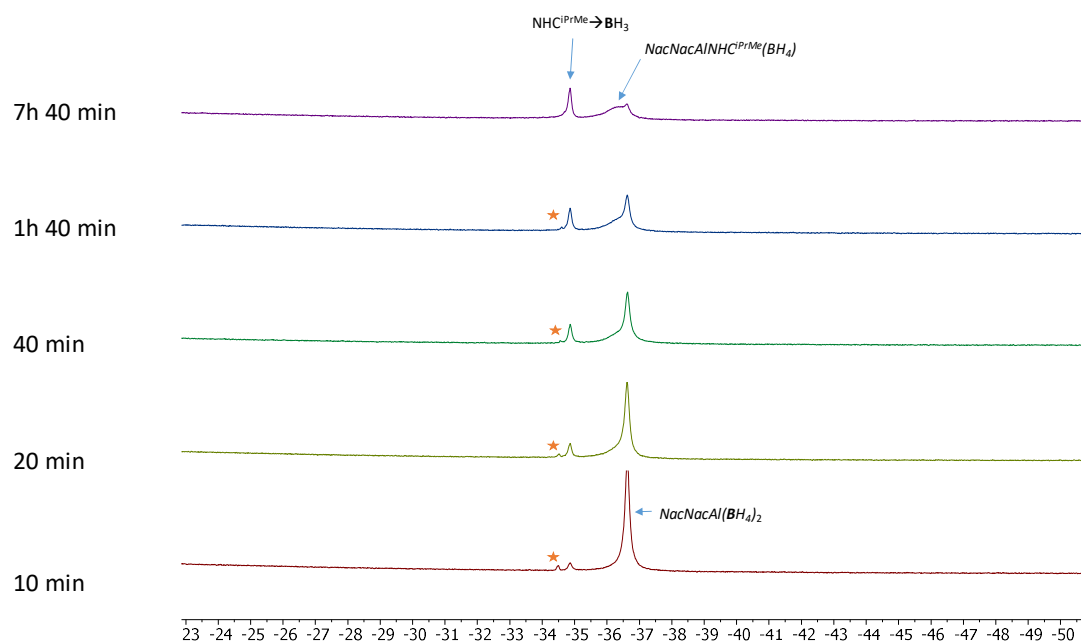
Figure 4. 6. ^{11}B{^{1}H}-NMR (128.4 MHz) along different reaction times between *NacNac*Al(BH$_4$)$_2$ and two equivalents of NHC^{iPrMe} in C$_6$D$_6$.

From the spectra presented in Figure 4.5 and Figure 4.6, we speculated the formation of one intermediate and two side products. However, due to the overlap with other species, we were not able to determine the nature of these compounds or gain an understanding of the reaction mechanism. Thus, we considered performing blank reactions to get a clearer picture on how the reaction proceeds. We started to evaluate if the NHC^{iPrMe} can deprotonate the methyl of the *NacNac* ligand. We thought of blocking the nucleophilic substitution by decreasing the leaving group quality of the substituents bonded to the aluminium atom. For example, the hydride is significantly worse leaving group than $[BH_4]^-$ (see Table 4.1). Thus, the nucleophilic substitution of NHC^{iPrMe} on *NacNac*AlH$_2$ (**9**) is expected to be less prominent than with *NacNac*Al(BH$_4$)$_2$.

On the course of the equimolar reaction of *NacNac*AlH$_2$ with NHC^{iPrMe} in diethylether at 40°C, we did not observe the formation of a white precipitate. In the ^{1}H-NMR of the crude, we did not evidence the deprotonation product (see Appendix II, Figure A-II.45). The same observations was reported by Hill and co-workers.[245] They reacted *NacNac*AlH$_2$ with NHC^{iPrMe} in toluene for 8 days at 80°C without noticing any reaction.
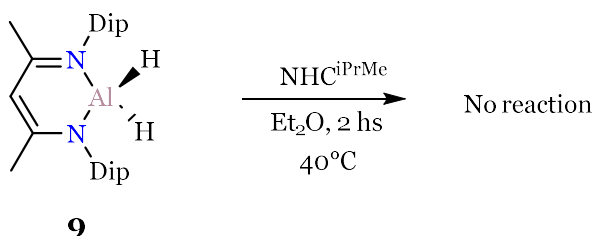
Scheme 4. 9. Equimolar reaction of **9** with NHC^{iPrMe} (Dip=2,6-di-iso-propylphenyl).

To comprehend the role of the $[BH_4]^-$ in the nucleophilic substitution, we considered reacting NHC^{iPrMe} with *NacNac*AlH(BH$_4$) (**92**). This reaction ensures the involvement of only one $[BH_4]^-$ unit in the reaction. Unfortunately, the synthesis of *NacNac*AlH(BH$_4$) is not reported to the date. Crimmin and co-workers prepared series of *NacNac*AlHX (X=halide) by exchange reaction between *NacNac*AlH$_2$ and *NacNac*AlX$_2$.[246] By following similar protocol, the *NacNac*AlH$_2$ and *NacNac*Al(BH$_4$)$_2$ were reacted in benzene at 70°C for 3 hours obtaining the *NacNac*AlH(BH$_4$) (**93**) in 87% yield (Scheme 4.10). The ^{1}H-NMR of **93** displays two overlapped septets at 3.34 ppm and 3.27 ppm which indicates the inequivalent substituents on aluminium. In the FT-IR, we observed two broad bands at 2453 cm^{-1} and 2178.6 cm^{-1}, assigned to the B-H stretching modes, and the band at 1890.3 cm^{-1} assigned to the Al-H stretching.
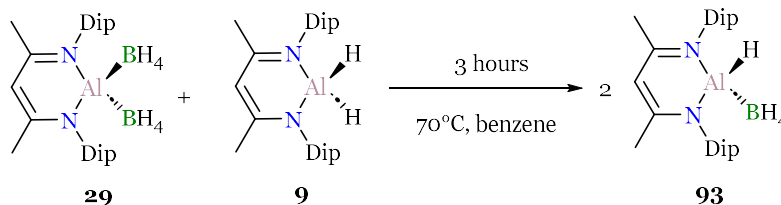
Scheme 4. 10. Synthesis of **93** compound (Dip=2,6-di-iso-propylphenyl).

Single crystals of **93** were grown at -30°C in diethylether. The crystal structure of **93** is depicted in Figure 4.8. The aluminium presents a distorted tetrahedral geometry (N1-Al1-N2=96.4(4)° and H1-Al1-B1=107.1(4)°). The $[BH_4]^-$ is bounded to the equatorial position of aluminium. The aluminium-boron distance is 2.200(7) Å in the range of κ²-coordination. The hydrides could be located on the electron density map. The Al-H1 distance (1.480(1) Å) is shorter than Al1-H4 and Al-H3 (1.760(2) Å and 1.756(8) Å, respectively). The bridging hydrides present longer B-H distances (B1-H4=1.599(8) Å and B1-H3=1.119(5) Å) than the terminal B-H (B1-H6=1.117(7) Å and B1-H5=0.995(2) Å).
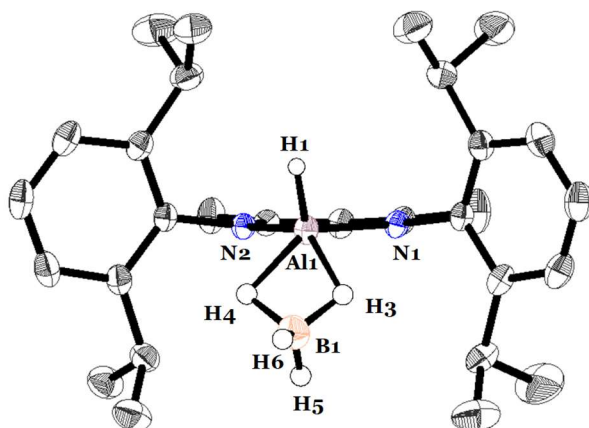
Figure 4. 7. Solid state structure of **93**. Thermal ellipsoids set at 50% probability. Selected experimental and computational [B3LYP-D3(BJ)/def2-SVP] bond lengths [Å] and bond angles [°]: Al1-N1=1.890(2), Al1-N2=1.891(8), Al-B=2.200(7), Al1-H1=1.480(1), Al1-H4=1.760(2), Al1-H3=1.756(8), B1-H4=1.599(8), B1-H3=1.119(5), B1-H6=1.117(7), B1-H5=0.995(2), N1-Al1-N2=96.4(4), H1-Al1-B1=107.1(4)).

We proceeded to equimolarly react NHC^{iPrMe} with **93** for two hours at 40°C in diethylether. We observed the formation of compound **94**, which was previously reported by Roesky and co-workers.[241]
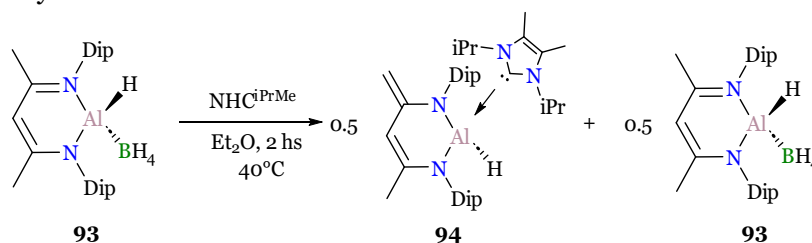
Scheme 4. 11. Blank reaction of compound **96** with one equivalent of NHC^{iPrMe} (iPr=iso-propyl, Dip=2,6-di-iso-propylphenyl).

In Figure 4.9, we show the ^{1}H-NMR of the reaction crude from Scheme 4.11 (red spectrum) together with ^{1}H-NMR of the starting material NHC^{iPrMe} (green spectrum) and **93** (blue spectrum). The septet at δ=3.95 ppm of the methine protons of the *iso*-propyl groups from NHC^{iPrMe} is not identified in the reaction crude after two hours of reaction. However, we identified the singlet at δ=4.88 ppm assigned to the proton on γ-position of the *NacNac* ligand, indicating the presence of unreacted **93**. At δ=3.98 ppm and δ=3.31 ppm, two doublets ($^1J_{H-H}$=1.16 Hz) are recognized, similar to **91** (δ=3.99 ppm ($^1J_{H-H}$=1.03 Hz) and δ=3.23 ppm ($^1J_{H-H}$=1.02 Hz)). Those signals are assigned to the methylene group of the backbone. Surprisingly, we did not observe the formation of carbene borane adduct (**92**) which is observed in the reaction from Scheme 5.7.
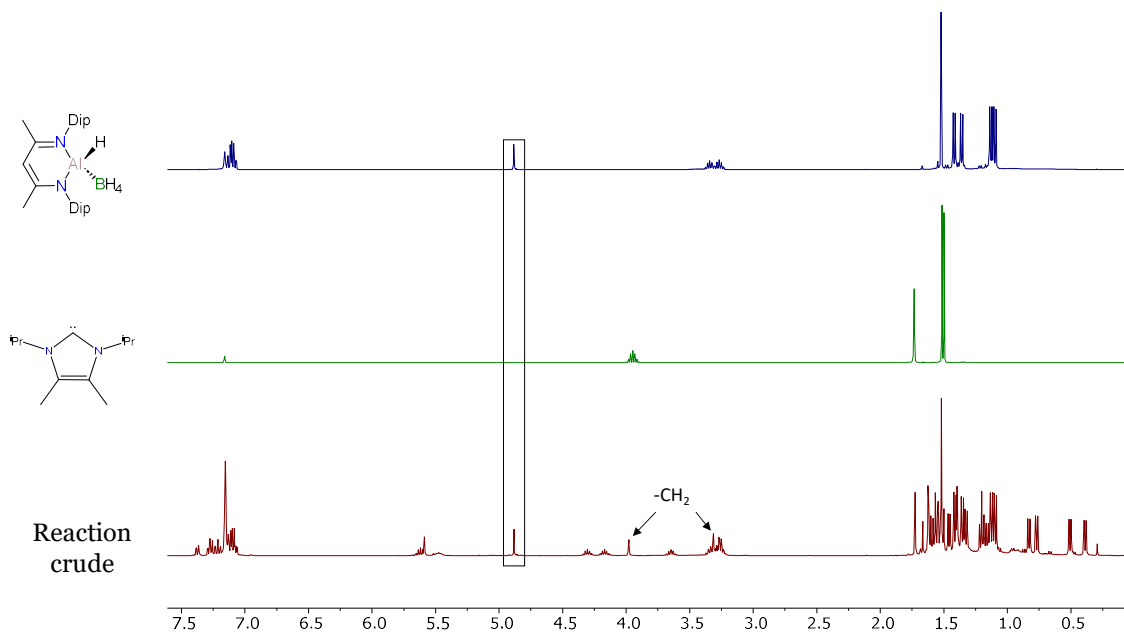
Figure 4. 8. Stacked ^{1}H-NMR (400 MHz,297 K) of the reaction crude, NHC^{iPrMe} and **93** in benzene-d$_6$.

To confirm that nucleophilic addition proceeds with two equivalents of NHC^{iPrMe}, we reacted **93** to two equivalents 2.1 equivalents of NHC^{iPrMe} (Scheme 4.12).
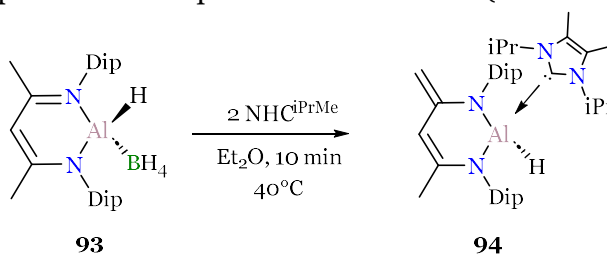
Scheme 4. 12. Blank reaction of compound **93** with one equivalent of NHC^{iPrMe} (iPr=iso-propyl, Dip=2,6-di-iso-propylphenyl).

In Figure 4.10, we depict the stacked ^{1}H-NMR spectra of the reaction crude of Scheme 4.11 (red spectrum), NHC^{iPrMe} (turquoise spectrum), *NacNac*AlH$_2$ (green spectrum) and **93** (purple spectrum). We could not identify the signals of **92**, indicating the full consumption of the reagent. The doublets at δ= 3.98 ppm and δ= 3.31 ppm suggest the presence of the methylene group, exactly found in Figure 4.9. The formation of carbene-borane adduct was not detected by ^{1}H-NMR or ^{11}B{^{1}H}-NMR. Therefore, it is exclusively formed when two units of BH$_4$ coordinated to aluminum.
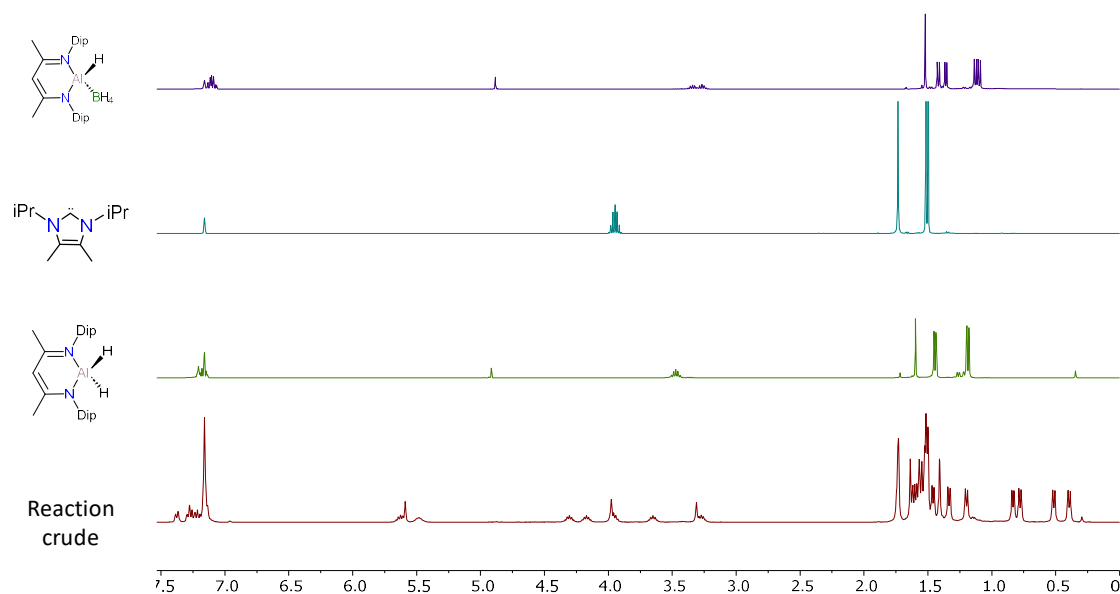
Figure 4. 9. Stacked ^{1}H-NMR (400 MHz, 297 K) of the reaction crude, NHC^{iPrMe} and **93** in benzene-d$_6$.

In Figure 4.10, we stacked the ^{1}H-NMR of the reaction crude from Scheme 4.7 (turquoise spectrum) and Scheme 4.11 (red spectrum). We realized that the signals from compound **94** can be identified in the crude of Scheme 4.8. For instance, the region between 6 ppm and 5.5 ppm can be identified the C$_\gamma$-H from compound **91** but also the C$_\gamma$-H from **93** compound. Similarly, in the region between 0 ppm and 1 ppm we can identify the doublets from **93** in the crude of Scheme 4.8. This implies that **93** is a by-product during the synthesis of **94**.
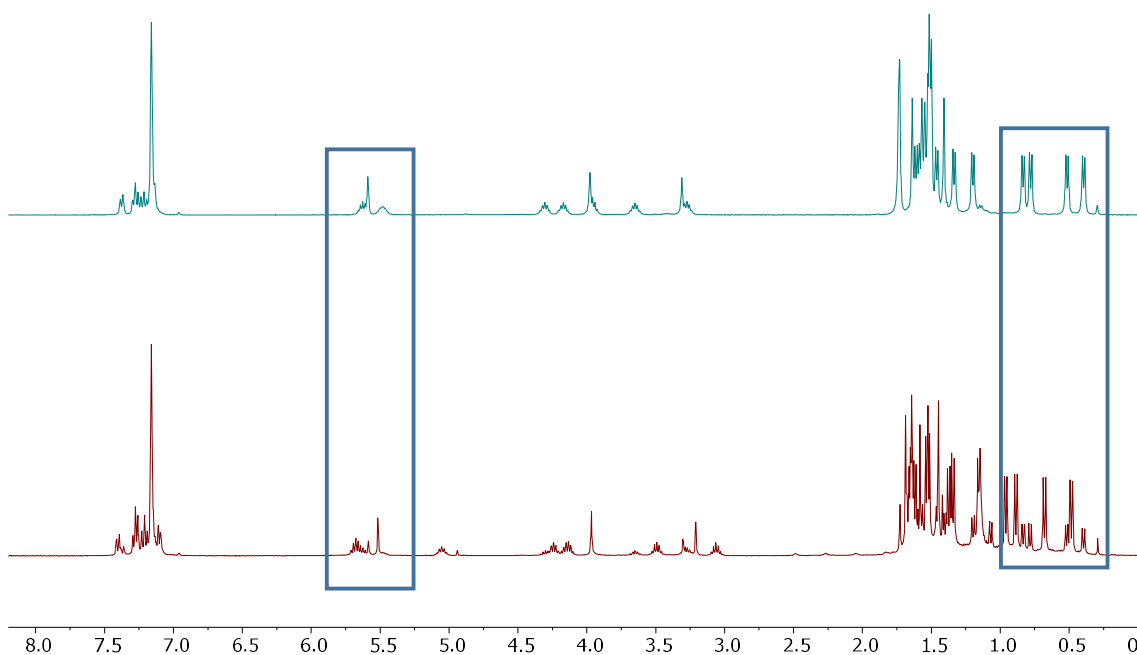
Figure 4. 10. Stacked ^{1}H-NMR (400 MHz, 293 K) from the reaction crudes of **20** (turquoise spectrum) and **96** (red spectrum) with two equivalents of NHC^{iPrMe}.

Based on the blank reactions, we confirmed that the nucleophilic addition requires two equivalents of NHC^{iPrMe} to proceed. The minor product observed on the reaction crude is assigned to **94** and the formation of the carbene-borane adduct **92** is only observed in the reaction of *NacNac*Al(BH$_4$)$_2$ with two equivalents of NHC^{iPrMe}. All in all, we suggest the reaction mechanism plotted in Scheme 4.13, which explains the formation of **91, 92** and **94**. On the one hand, the NHC^{iPrMe} could be inserted to the aluminium forming a pentavalent aluminium complex. Then, a second molecule of NHC^{iPrMe} could deprotonate this intermediate yielding **91**. Alternatively, a BH$_4$ could be displaced through the nucleophilic insertion of NHC^{iPrMe} which might further dehydrogenate the methyl on the backbone forming the carbene borane adduct. The latter pathway seems improbable because the signal of H$_2$ (δ=4.47 ppm)[247] was not identified in the reaction crude (Figure 4.5). The formation of the carbene-borane adduct might also stem from an S$_N$2 reaction between NHC^{iPrMe} and **29** forming the compound **93** and carbene borane adduct. Subsequently, compound **93** might undergo nucleophilic substitution with 2 equivalents of NHC^{iPrMe} resulting in the formation of compound **94**.
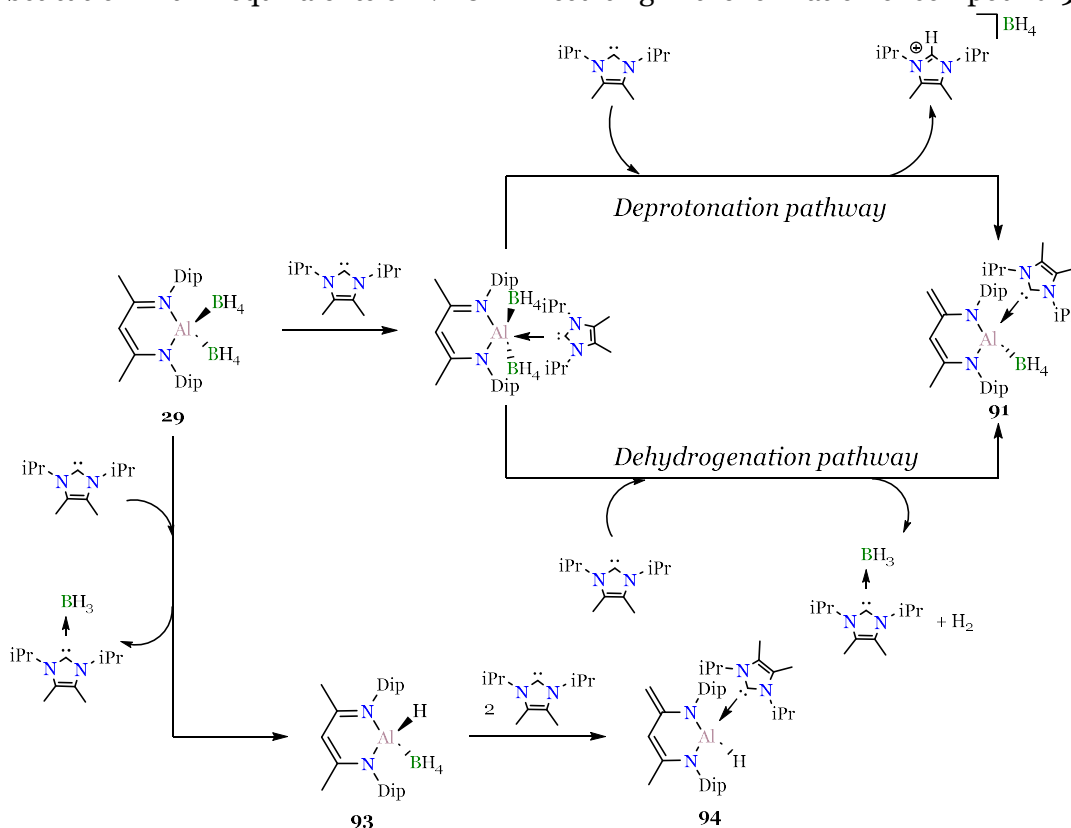
Scheme 4. 13. Plausible mechanisms on the formation of **91** and **94**.

The viability of the proposed mechanism was explored through quantum chemical calculations. The Gibbs energy profile is plotted on Scheme 4.14 at (CPCM:Et$_2$O)-DLPNO-CCSD(T)/cc-pVTZ//B3LYP-D3(BJ)/def2-SVP level of theory (see Appendix II, Table A-II.7). We considered the front side approximation of NHC^{iPrMe} towards **29** to form the Van der Waals complex **RC1** (Δ**G$_r$**=+11.5 kcal/mol). On the one hand, it can undergo nucleophilic attack on the aluminium (**TS1, ΔG‡**=18.4 kcal/mol) to obtain a pentacoordinated aluminium **INT1** (Δ**G**= +3.7 kcal/mol). The formation of **INT1** is only speculative since we could not detect by spectroscopic techniques. During the insertion of NHC^{iPrMe}, a rotation of apical [BH$_4$]$^-$ takes place, changing from κ^2 to κ^1-coordination, while the [BH$_4$]$^-$ in equatorial position remains in κ^2 coordination mode. On the other hand, **RC1** can proceed to BH$_3$ transfer (**TS3, ΔG‡**=+24.5 kcal/mol), leading to the carbene borane complex and **96** (Δ**G$_r$**= -26.5 kcal/mol). The insertion of

the NHC^{iPrMe} is kinetically more favoured than the BH$_3$ transfer. Therefore, the nucleophilic addition is predicted to be the most preferred path.

From the **INT1**, we have considered the deprotonation and dehydrogenation pathways according to Figure 4.13. In the dehydrogenation pathway, we initially take into account the detachment of [BH$_4$]$^-$ in apical position of aluminium, forming **INT2** in an endergonic process (ΔG =+9.9 kcal/mol). Then, the dehydrogenation occurs (**TS2, ΔG**= 29.9 kcal/mol) forming compound **94** and the release of H$_2$ and BH$_3$ (ΔG_r= -32.4 kcal/mol). The BH$_3$ is *trapped* by a second molecule of NHC^{iPrMe}. In the deprotonation pathway, a second molecule of NHC^{iPrMe} deprotonates the **INT1** through the **TS6** (ΔG=28.2 kcal/mol) forming **94** and the imidazolium salt [NHC^{iPrMe}]BH$_4$ (ΔG_r =-8.6 kcal/mol). The Gibbs activation energy for the dehydrogenation pathway (**TS2, $\Delta G^{\ddagger}$=26.6 kcal/mol**) is higher than the deprotonation pathway (**TS6, $\Delta G^{\ddagger}$=24.5 kcal/mol**), suggesting that the deprotonation reaction is more prominent than the dehydrogenation pathway. This agrees with the experimental observations where H$_2$ was not identified in the reaction crude.

The activation energy of the deprotonation pathway (**TS6, $\Delta G^{\ddagger}$=24.5 kcal/mol**) is the same as the BH$_3$ transfer reaction (**TS3**, **$\Delta G^{\ddagger}$=+24.5 kcal/mol**). Therefore, it suggests that both reactions are in competition, supporting the formation of the carbene borane adduct as a side product. The resulting compound **96** can also react with two equivalents of NHC^{iPrMe}, as shown in Scheme 4.12, in agreement with the identification of **91** in the reaction crude (Figure 4.5). As the nucleophilic insertion is more favoured over the BH$_3$ transfer, the formation of **94** is less prominent than the formation of **91**.

We also computed the deprotonation of the backbone with NHC^{iPrMe}. Firstly, the NHC^{iPrMe} approximates to **29** from the back side to form **RC2**. Then, the deprotonation occurs through **TS4** ($\Delta G^{\ddagger}$=+21.2 kcal/mol) forming the imidazole salt. We also considered the dehydrogenation of the imidazole, but it occurs with an unreachable **TS5** ($\Delta G^{\ddagger}$=+63.3 kcal/mol) at 40°C. Thus, this pathway is discarded.
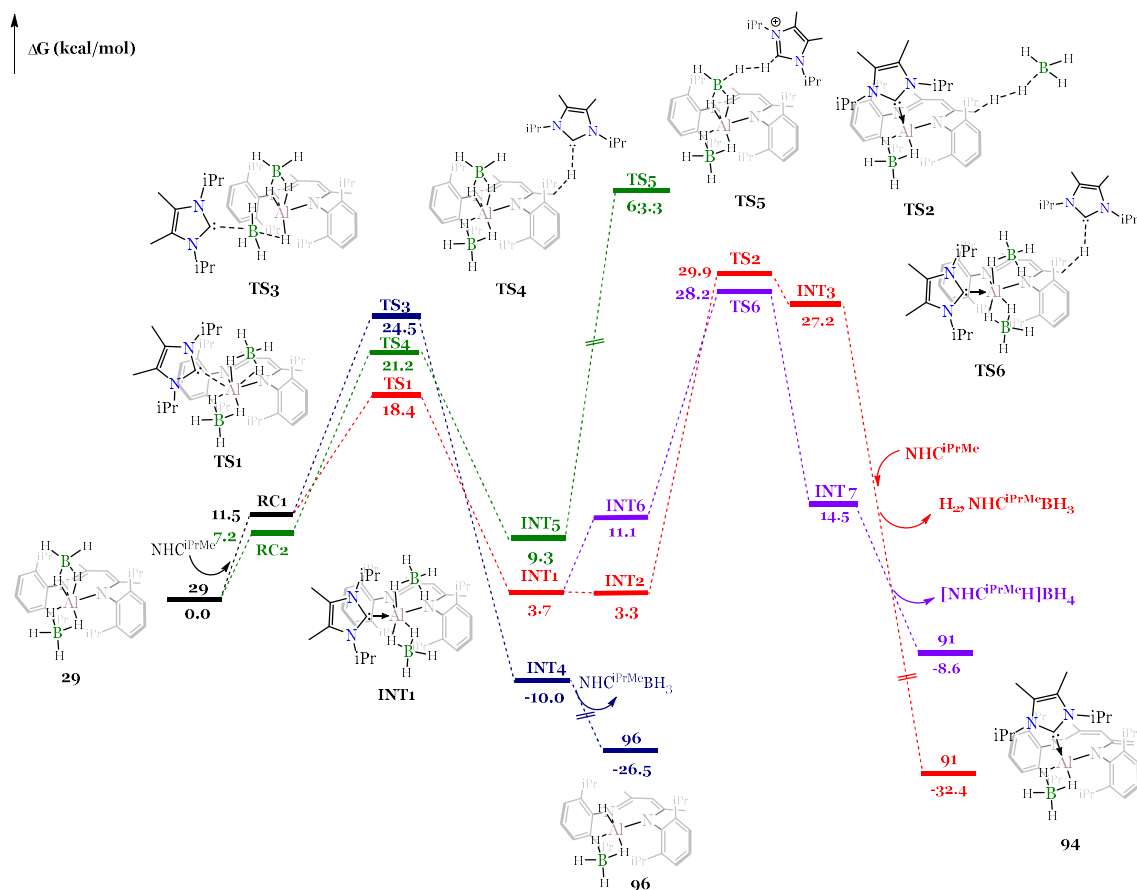
Scheme 4. 14. Gibbs energy profile at (CPCM:diethylether)-DLPNO-CCSD(T)/cc-pVTZ//B3LYP-D3(BJ)/def2-SVP level of energy. Relative energies are in kcal/mol. (iPr=iso-propyl).

4.4 Chemical bonding analysis of mono-substituted boralumanes.

We observed that the substituent on aluminium influences the spectroscopic and structural features of the $[BH_4]^-$ (Figure 4.12). For instance, the ^11B-NMR chemicals shifts (δ=-44.37 ppm (**88**) < δ=-37.71 ppm (**93**) < δ=-37.12 ppm (**87**) < δ=-36.28 ppm (**91**)) appear more high-fielded when the Al···B distance is shorter (2.064 Å (**88**) < 2.201 Å (**93**) < 2.158 Å (**87**) < 2.244 Å (**91**)). Compound **88** attracted our interest because, on the one hand, the $[BH_4]^-$ displays a κ^3 coordination. To the best of our knowledge, this coordination mode remained elusive in aluminium chemistry. However, Pozodeey and Boldyrev predicted a κ^3 coordination of BH_4 in $AlBH_4$ model by means of DFT and *ab initio* methods.[248] On the other hand, the Al-B distance in **88** is remarkably short, in the range of the B=Al distance (*vide supra*). Typically, the short distances are found in multiple bonds. In the field of transition metal complexes, the multiple bonds have attracted the attention for unusual bonding situations and their application for small molecule activation or catalysis.[249] The close proximity between two atoms is not always an indication of multiple bond. Several systems bearing short distances between beryllium atoms have been theoretically addressed.[250, 251] They are particularly interesting because there is no formal Be-Be bond albeit the considerable proximity of the beryllium atoms. In the case of beryllium hydrides, the bridging hydrogens *push* the beryllium nuclei together, yielding a short atomic distance. Recently, Handlington reported an anionic beryllium hydride dimer featuring remarkably short beryllium

distances (Be···Be=1.836(4)Å),[252] which is shorter than the reported Be-Be bond (2.0545(18) Å). [253]
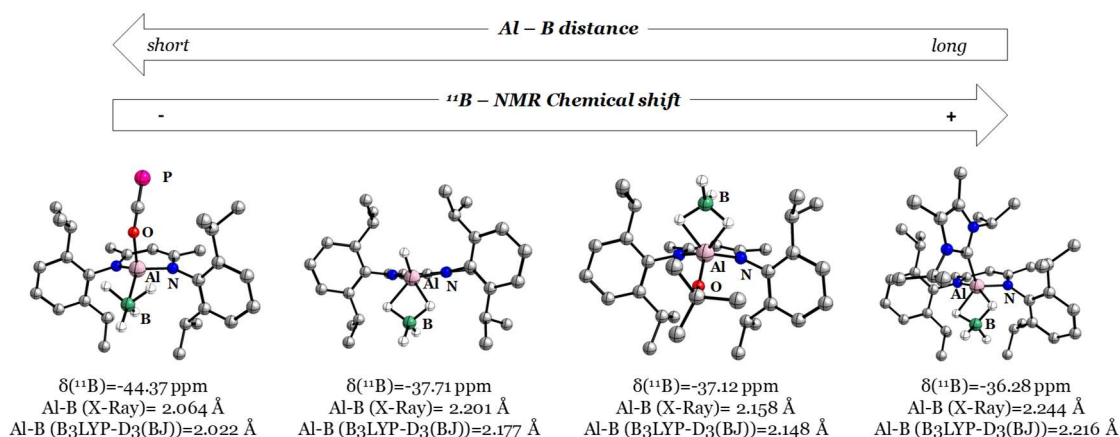
Figure 4. 11. ^{11}B-NMR resonances, X-Ray and computed Al···B distances of mono-substituted *NacNac* boralumanes. The chemical shifts are in ppm and the distances are in Å.

We firstly benchmark the geometries obtained from different levels of the theory, namely BP86-D3(BJ), B3LYP-D3(BJ), M06-2X and ωB97XD, in combination with def2-SVP basis set. (See selected bond and angles in Appendix II, Tables A-II.2-5). Most of the functionals converge to similar geometries but in compound **87** only the B3LYP-D3(BJ) yields the proper coordination (κ^2) of the $[BH_4]^-$ according to the SC-XRD data. The BP86-D3(BJ), M062X and ωB97XD underestimate the Al-B distance, which induces a κ^3 coordination of the $[BH_4]^-$. Thus, we selected the B3LYP-D3(BJ) functional for further analysis. We applied different chemical bonding tools, namely partial charges, bond orders/delocalization index, 3c-electron-sharing index (3c-ESI), topological analysis, and EDA-NOCV.

The partial charge of $[BH_4]^-$ fragment is similar for all the considered compounds and consistent with different AIM definitions (NAOs, QTAIM and TFVC). (see Appendix II, Tables A-II.7-14). The bond orders and delocalization indexes suggest a low-covalent character between Al and $[BH_4]^-$. Several authors have addressed the description of TM-H-B bonds bearing a $[BH_4]^-$ ligand with three-centre bond models.[248, 254] In this context, in Scheme 4.15 we show the three plausible bonding situations for the description of the Al-H-B bond. The half-arrow notation was coined by Green *et al.* to distinguish between the donation of a bond pair (half-arrow) to a lone pair (full-arrow).[254] The first plausible bonding scenario is the 3c-2e bond, which consists of two bonding electrons shared among the three atoms. The diborane (B_2H_6) is the archetypical molecule described with this type of interaction. The second feasible bonding situation is the agostic or anagostic interaction. The agostic bond was introduced by Brookhart and co-workers to explain the coordination of a C-H bond to transition metals.[255] This type of interaction is experimentally characterized by a reduction of the $^1J_{C-H}$ in the coordination complex ($^1J_{C-H}$=70-100 Hz) respect with the *free* C-H ($^1J_{C-H}\approx125$ Hz). If the $^1J_{C-H}$ does not substantially change, the interaction is considered anagostic. In the latter case, the interaction is dominated by electrostatic interactions with a low covalent character. The last plausible situation is the hydrogen bond which is unlikely to happen with the considered aluminium borohydrides since the aluminium is in the oxidation state of +3.

Covalent   Agostic/Anagostic interaction   Hydrogen bond
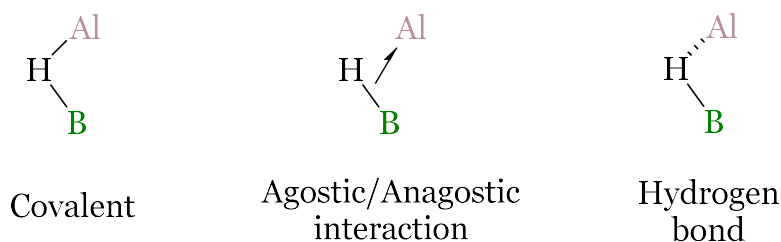
Scheme 4. 15. Schematic representation of the plausible bonding situations in Al-H-B bond.

The chemical bonding tools to characterize three-center bonds are quite diverse, *i.e.* Natural Bond Orbitals (NBO), Adaptative Natural Density Partitioning (AdNDP), Electron Localization Function (ELF), among others. Recently, García-Rodeja *et al.* categorize the interactions of C-H bond with different transition metal complexes applying the three-centre electron index (3c-ESI).[256] For single determinant wavefunction, the 3c-ESI is computed as

$$3c - ESI = 4 \sum_{i,j,k} n_i n_j n_k S_{ij}(A_1) S_{jk}(A_2) S_{ki}(A_3), \qquad (82)$$

where n_i is the occupation of the *i*-th spin-orbital and $S_{ij}(A_1)$ is the overlap between *i* and *j* spin-orbitals in the A_1.domain. The resulting values allow to distinguish between agostic (3c-ESI>0.040), anagostic (0.040<3c-ESI<0.005) and hydrogen bond (3c-ESI<0.005) interactions.

The 3c-ESI values of Al-H-B from compounds **87**, **88**, **91** and **93** are gathered in Table 4.2. We can clearly differentiate the bridging Al-H-B interaction, ranging from 0.025 to 0.029, from the non-bonding interaction, featuring values from 0.003 to 0.006. In the case of **88**, we identify three bridging interactions, which agrees with the κ³-coordination experimentally characterized, while **87**, **91** and **93** we identify two bridging interactions. According to the thresholds proposed by García-Rodeja *et al.*, the 3c-ESI suggests that the interaction between aluminium and borohydride is anagostic, independently to the coordination mode and the Al-B distance. As abovementioned, this type of interaction is characterized with a discrete variation of the coupling constants between the free and coordinated form. This is in agreement with the analysed systems since $^1J_{B-H}$ ($^1J_{B-H}$ =86.09 Hz (**87**), $^1J_{B-H}$ =86.06 Hz (**88**); $^1J_{B-H}$=83.80 Hz (**96**)) do not significantly change respect to the *free* [BH$_4$]$^-$ ([Na(15-crown-5)] [BH$_4$], $^1J_{B-H}$ =77Hz).[228] It is noteworthy that the thresholds proposed by García-Rodeja *et al.* are based on the interaction between a C-H bond and a TM. Thus, the anagostic assignation is a bit speculative because the Al-H-B interaction might have different thresholds. As a comparison, we computed the 3c-ESI of B_2H_6. The 3c-ESI values of the B-H-B bond are 0.066, almost three times higher than the Al-H-B. Therefore, the 3c-ESI suggests that the interaction between aluminium and the borohydride is far from the covalent situation.

Table 4. 2. 3c-ESI of Al-H-B of compounds **87**, **88**, **91** and **96** using QTAIM atomic definition at the B3LYP-D3(BJ)/def2-TZVPP//B3LYP-D3(BJ)/def2-SVP level of theory.

	87	**88**	**91**	**93**
Al-H$_b$-B	0.027	0.029	0.029	0.029
Al-H$_b$-B	0.028	0.029	0.025	0.029
Al-H$_t$-B[a]	0.006	0.024	0.003	0.004

[a]In the case of **91**, it should be considered as Al-H$_b$-B.

We decided to inspect the bonding situation from an energetic perspective by making use of EDA-NOCV. The energy components are gathered in Table 4.3 considering

the [NacNacAlR]$^+$ (R=OtBu, OCP, H, NHC^{iPrMe}) and [BH$_4$]$^-$ as reference states. The dissociation energy (-D_e) of **88** is approximately 20 kcal/mol higher than the rest of the compounds. Even though **88** suffers a higher preparation energy (ΔE_{prep}) penalty, it is compensated with a stronger interaction energy (ΔE_{int}). The electrostatic energy (ΔE_{elect}) is the main stabilizing contribution (*c.a.* 60%), expected for an anagostic interaction.[257] Interestingly, the magnitude of the ΔE_{elect} is almost constant within the considered systems. We observed noticeable differences in the Pauli repulsion (ΔE_{Pauli}) and the orbital relaxation (ΔE_{orb}) energies. As a general trend, we observed that the short Al-B distances are due to a low ΔE_{Pauli} and a more stabilizing ΔE_{orb} while the long Al-B distances bear higher ΔE_{Pauli} and weaker ΔE_{orb}.

Table 4. 3. EDA-NOCV of compounds **87**, **88**, **91** and **93** at B3LYP-D3(BJ)/TZ2P//B3LYP-D3(BJ)/def2-SVP level of theory. All energies are given in kcal/mol.

	87	**88**	**91**	**93**
ΔE_{int}	-159.0	-194.1	-157.1	-157.7
ΔE_{Pauli}	119.5	109.4	126.9	116.4
$\Delta E_{elect}{}^a$	-173.2 (62.2%)	-177.6 (58.5%)	-173.1 (60.9%)	-170.6 (62.2%)
$\Delta E_{disp}{}^a$	-11.4 (4.1%)	-10.1 (3.3%)	-12.9 (4.6%)	-9.4 (3.4%)
ΔE_{orb}	-93.8	-115.8	-97.9	-94.1
$\Delta E_{HF-corr}$	-0.1	0.0	-0.1	0.0
$\Delta E_{orb-corr}{}^a$	-93.9 (33.7%)	-115.8 (38.2%)	-98.0 (35.5%)	-94.1 (34.3%)
$\Delta E_{orb-\Delta\rho(1)}{}^b$	-44.7 (47.7%)	-54.6 (47.2%)	-48.2 (49.2%)	-47.7 (50.7%)
$\Delta E_{orb-\Delta\rho(2)}{}^b$	-17.4 (18.6%)	-19.0 (16.4%)	-17.2 (17.6%)	-18.1 (19.3%)
$\Delta E_{orb-\Delta\rho(3)}{}^b$	-8.0 (8.5%)	-16.2 (14.0%)	-7.4 (7.6%)	-7.6 (8.1%)
$\Delta E_{orb-rest}{}^b$	-23.7 (25.3%)	-26.0 (22.5%)	-25.1 (25.7%)	-20.6 (21.9%)
ΔE_{prep}	28.7	42.1	32.1	20.3
-D_e	-130.3	-152.0	-125.1	-137.4

The orbital relaxation is the second most stabilizing contribution, encompassing 40% of the stabilizing energy. The splitting of ΔE_{orb} into NOCV bonding channels contributions reveals three main orbital interactions: $\Delta E_{orb-\Delta\rho(1)}, \Delta E_{orb-\Delta\rho(2)}$ and $\Delta E_{orb-\Delta\rho(3)}$. Together, these interactions account for 75% of the orbital interaction (Table 4.4). Analysing the shape of the deformation densities of each bonding channel, we can categorize the interaction according to their symmetry (see Appendix II, Figures A-II.49-52). We identify two σ- interactions, arising from the interaction of [BH$_4$]$^-$ with the *p*-orbital from aluminium ($\Delta E_{orb-\Delta\rho(1)}$) and the σ*(Al-R) orbital ($\Delta E_{orb-\Delta\rho(3)}$), and a π-interaction originated from the out-of-phase combination of the σ*(Al-N) orbitals ($\Delta E_{orb-\Delta\rho(2)}$) (See Figure 4.8). The σ-interaction between the *p*-orbital of aluminium with [BH$_4$]$^-$ is the most stabilizing bonding channel, accounting for approximately 50 % of the ΔE_{orb}.
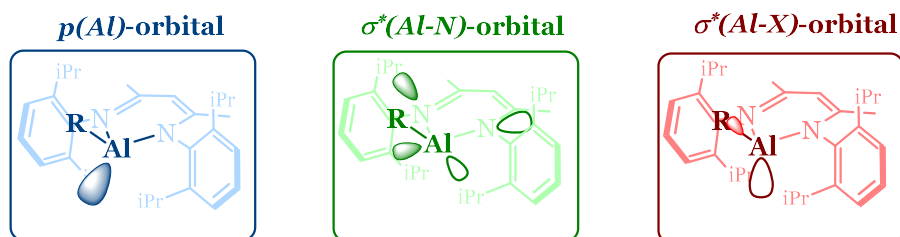
Figure 4. 12. Main fragment orbitals involved in the interaction with [BH$_4$]$^-$.

We analysed the fragment orbital energies to rationalize the differences in the obtained bonding channels (Figure 4.16). The interacting orbitals from the [BH$_4$]$^-$ fragment do not substantially change among the tested complexes (Figure 16,B). The *free* [BH$_4$]$^-$ has a T_d symmetry, in which the three t_2 orbitals are degenerated. However, the degeneracy is lost because the [BH$_4$]$^-$ is distorted upon coordination to aluminium. We found that the orbitals of the [*NacNac*AlR]$^+$ fragment are more informative in understanding the ΔE_{orb} of the different bonding channels (Figure 14, A). The energy of the empty *p*-orbital of aluminium, ranging from -8.00 eV to -6.27 eV, is lower than the σ*(Al-R) and σ*(Al-N), ranging from -4.11 eV to -2.26 eV. We observed that the σ*(Al-R) and σ*(Al-N) orbital energies do not follow a clear trend with the Al-B distance while the energy of the empty *p*-orbital of aluminium follows a trend with the Al-B distance. For shorter Al-B distances, the empty *p*-orbital of aluminium is more stabilised, whereas longer Al-B distance leads to higher energies of this orbital.
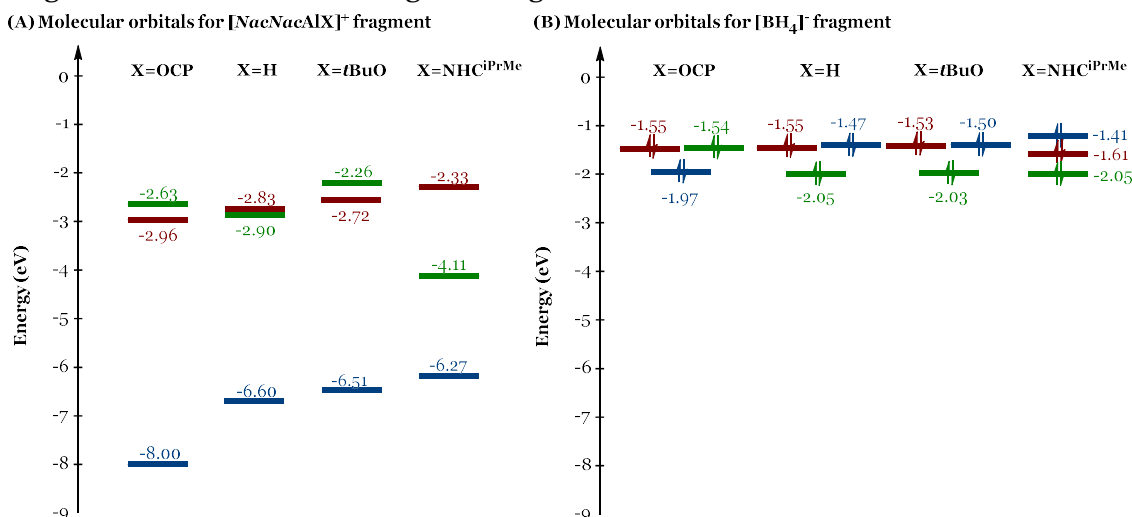
Figure 4. 13. (A) Main fragment orbitals diagram of the [NacNacAlX]$^+$ fragment; (B) Main fragment orbitals diagram of [BH$_4$]$^-$ fragment.

4.4 Synthesis and characterization di-substituted alumanes

We also explored functionalization of mono-substituted *NacNac* boralumanes. Since these molecules bear a [BH$_4$]$^-$ moiety, they can be potentially functionalized with nucleophiles. We attempted to functionalize **90** with an excess of NaPCO.
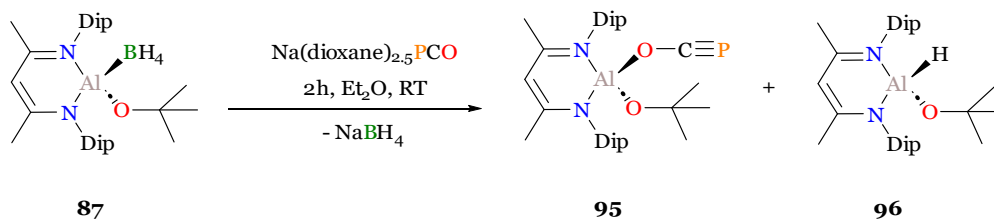
Scheme 4. 16. Nucleophilic substitution of **87** with NaPCO. (Dip=2,6-di-iso-propylphenyl)

The incorporation of the PCO anion was supported by NMR spectroscopy. On the one hand, ^{31}P-NMR reveals a singlet at $\delta=-321.72$ ppm which is slightly high-field shifted with respect to **91** ($\delta=-319.36$ ppm). The chemical shift indicates that the PCO is bound through the oxygen atom. On the other hand, ^{11}B-NMR is silent suggesting that the salt metathesis has occurred. The FT-IR reveals an absorption band at 1715 cm^{-1} (Appenix II, Figure A-II.40) assigned to the CO stretching from PCO. Moreover, we could determine an impurity of approximately 20% accordingly to NMR data which we could not replace (Appenix II, Figure A-II.36).

We attempted to crystalize the major product via slow evaporation in diethylether. Compound **95** was identified in the in the crystal lattice together with **96**. This data confirms the nucleophilic substitution of NaOCP. As predicted in the ^{31}P-NMR, the OCP is bounded through the oxygen on the axial place of aluminium. The Al-O distances (Al1-O2=1.732(6) Å and Al1-O1=1.677(4) Å) are slightly shorter than the boralumanes analogues **87** (Al-O=1.696(2) Å) and **88** (1.781(6) Å). The OCP is placed in an slightly bent coordination (Al-O-C=162.4(1)°) which clearly differs from **88**, where the coordination is more angular (Al-O-C= 143.3(6)°). In gas phase DFT calculations revealed that Al-O-C angle is around 140° which slightly differs depending on the functional used (see Appendix II, Table A-II.6). The obtuse Al-O-C angle might be attributed to the intermolecular interactions in the crystal lattice. The OCP moiety is almost perfectly lineal (O-C-P=178.8(2)°). The O2-C20 distance (1.210(0) Å) is shorter than C-O in **88** (1.256(6) Å), meanwhile C20-P1 (1.560(8) Å) is elongated respect to the C-P in **88** (1.549(1) Å). The linear coordination of PCO is not common in *p*-block elements since they tend to bound in a bent fashion.
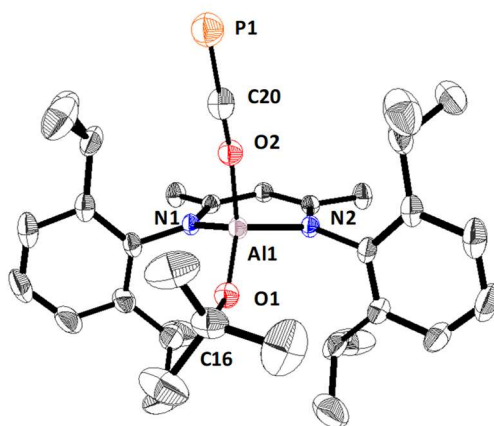
Figure 4. 14. Solid state structure of **95**. Thermal ellipsoids set to 50% probability. Selected experimental bond lengths [Å] and angles [°]: Al1-O1=1.677(4), Al1-O2=1.732(6), Al-N1=1.874(4), Al-N2=1.874(4), C20-O2=1.210(0), C20-P1=1.560(8), O1-C16=1.413(6), Al1-O2-C20=162.4(1), O2-C20-P1=178.6(9), Al1-O1-C16=140.8(9).

CHAPTER 5 – Tailoring phosphanylalumanes towards the synthesis of phosphaalumene

The synthesis of H, halide-functionalized phosphanylalumanes compounds is of high interest because the phosphorus and aluminium atoms bear a substituent that enables subsequent functionalization. For our propose, they serve as building blocks for synthetizing the Al=P bond via β-elimination reaction. The synthesis of H, halide phosphanylalumanes supported by a *NacNac* ligand has not been reported to the date. However, these types of compounds have been reported with different ligand systems. For instance, Tokitoh and co-workers prepared H, halide-functionalized phosphanylalumanes via salt metathesis of the corresponding phosphine and aluminium halide (see Section 1.3). In this context, we hypothesized that the salt metathesis of the *NacNac*AlX$_2$ (X=Cl, Br and I) and the lithiated boraphosphines (RPHLiBH$_3$) would yield the desired phosphanylalumane (Scheme 5.1). The *NacNac*AlX$_2$ have been functionalized by many types of anionic nucleophiles including phosphines (See sections 1. 2 and 1. 3), and the lithiated boraphosphines are easily accessible.[258] In this Chapter, we focus on the synthesis of *NacNac*AlXPHR (X=halogen, pseudo-halide) compounds, which is the required synthon to prepare the targeted phosphaalumene through β-elimination. Afterward, we explore the β-elimination reaction for the different types of phosphanylalumanes.
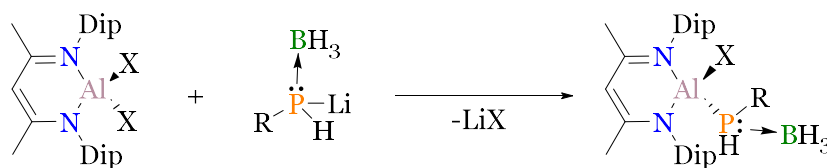
Scheme 5. 1. Proposed synthetic pathway to prepare H,halide-phosphanylalumanes (R=aryl, alkyl, amine; X=Cl, Br or I). (Dip=2,6-di-iso-propylphenyl).

We tested the salt metathesis between aluminium halides (X=I,Br,Cl) and lithiated boraphosphines in different conditions, but none of them lead to the desired product. We were obtaining unidentified products or the RPH$_2$BH$_3$ starting material. We also considered the dilithated phosphides but did not achieve the targeted molecule. Instead, we isolated solvent activation products or the primary phosphine. For example, we attempted the salt metathesis of *NacNac*AlI$_2$ with (*i*Pr)$_2$NPLi$_2$BH$_3$, which is generated *in-situ* -75ºC in THF (Scheme 5.2). We observed the formation of a precipitate from the reaction crude, presumably due to the salt elimination. In the ^{1}H-NMR, the broadness of the signals did not allow us to identify the nature of the products, but, in ^{31}P-NMR a broad singlet signal at 64.13 ppm. The chemical shift was too low-field shifted with respect to other reported phosphanylalumanes, such as *NacNac*Al(H)(PPh$_2$)$_2$ (δ(^{31}P)=-67.9 ppm)[35] or *NacNac*Al(PPh$_2$)$_2$ (δ(^{31}P)=-36.8 and -50.0 ppm),[259] suggesting that the reaction product does not bear the Al-P motif. The SC-XRD analysis displayed the 24-membered ring as a product of the THF activation (**98**). Such reactivity has already been reported in intramolecular Al/P Frustrated Lewis Pairs (FLP).[260] The refinement of **98** could not be completed due to the bad quality of the crystals. Thus, we could not make a proper analysis of the structure. However, it was sufficient to prove that LiI elimination occurs, suggesting the Al-P is eventually formed but it further reacts with THF through a ring-opening reaction.
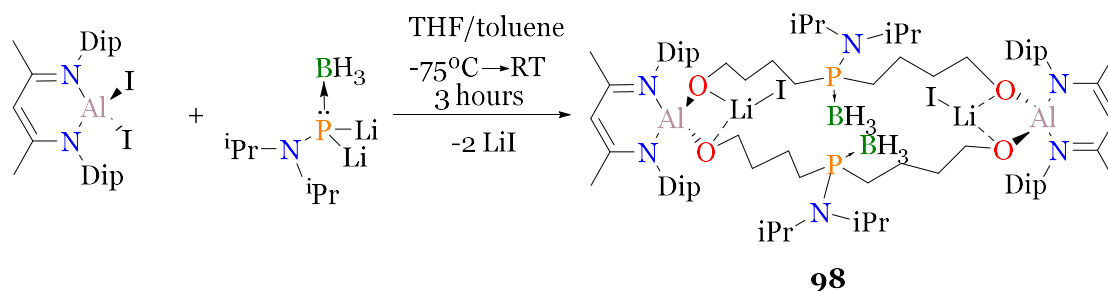
Scheme 5. 2. THF activation during salt metathesis reaction (Dip=2,6-di-iso-propylphenyl).
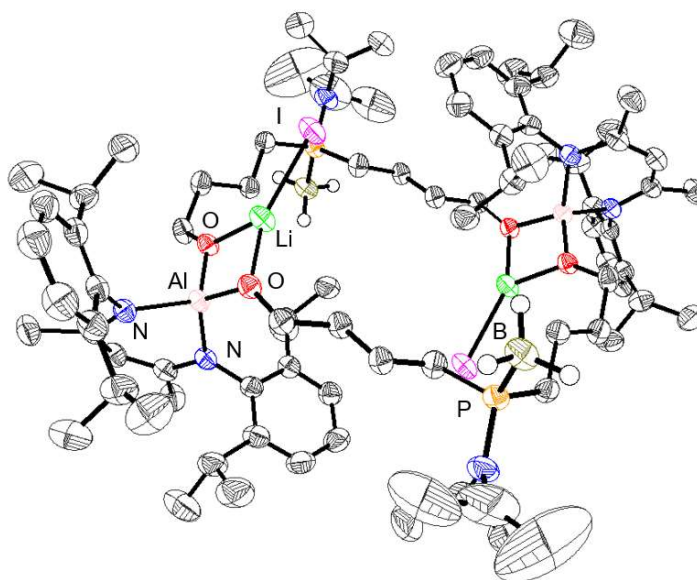
Figure 5. 1. X-ray structure of compound **98**.

Considering these outcomes from the salt metathesis reaction, we explored dehydrogenation pathway as a suitable strategy to synthesize mono-substituted phosphanylalumane. In section 1.1.2, we have exposed the ability *NacNac*AlH$_2$ to undergo dehydrogenation reaction towards different types of protic substrates. Moreover, in section 1.3, we have showcased the dehydrogenation reaction between aluminium hydrides and primary phosphines is a plausible synthetic pathway for the synthesis of phosphanylalumanes. Therefore, the dehydrogenation reaction is *a priori* a good candidate to prepare the desired mono-substituted phosphanylalumanes. As a drawback, it generally requires elevated temperatures or high pressures to promote the hydrogen release. For instance, Scheer and co-workers synthesised the NMe$_3$AlH$_2$PH$_2$WCO$_5$ by refluxing in *n*-hexane (~70°C) an equimolar mixture of NMe$_3$AlH$_3$ with [W(CO)$_5$PH$_3$].[94]

Our exploration of the dehydrogenation strategy started by reacting *NacNac*AlH$_2$ with the PhPH$_2$BH$_3$ in toluene (Figure 5.3, top). Remarkably, we observed the immediate conversion of the starting materials at room temperature. The PhPH$_2$BH$_3$ (δ=-58.1 ppm) is progressively consumed forming PhPH$_2$ (δ=-126.3 ppm) with no indications of dehydrogenation products (Figure 5.4, bottom-left). Additionally, in ^{11}B-NMR we identified the formation of **93** (δ=-37.71 ppm). These data suggests that PhPH$_2$BH$_3$ transfers the BH$_3$ to the *NacNac*AlH$_2$. The deprotection of boraphosphines is well-known but it is typically conducted nucleophiles such as secondary or tertiary amines.[261] The nucleophilic character of the Al-H bond is well-known in the literature (See Sections 1.1.1 and 1.1.2). For instance, Harder and Spielmann reported the double "BH$_3$" transfer of a sterically hindered primary boramine (DipNH$_2$BH$_3$) to *NacNac*AlH$_2$ yielding *NacNac*Al(BH$_4$)$_2$. More recently, a work led by Aldridge and Goicoechea showed the

reversible formation of borohydride using {H(9-BBN)}$_2$ (9-BBN=9-bora bicyclo (3.3.1)nonane) with series of *NacNac* aluminium hydrides. (See section 1.1.3 for further details).
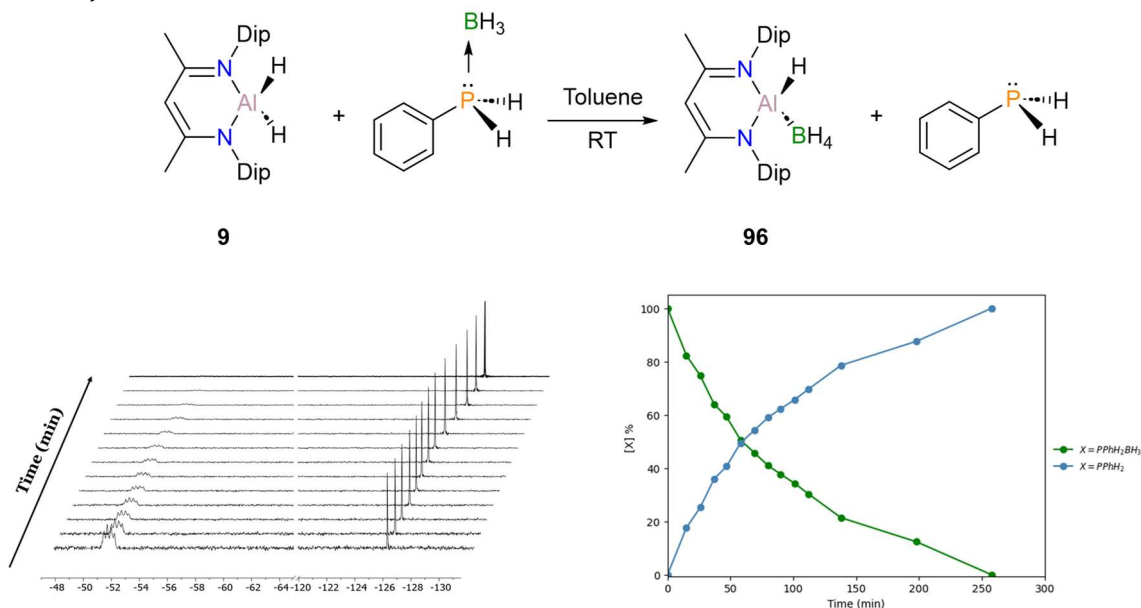
Figure 5. 2. BH$_3$ transfer reaction of PhPH$_2$BH$_3$ to *NacNac*AlH$_2$. On the bottom left, ^{31}P{^{1}H}-NMR in different reaction times. On the bottom right, temporal conversion of the PhPH$_2$BH$_3$ based on ^{31}P{^{1}H}-NMR (Dip=2,6-di-iso-propylphenyl).

5.1 Synthesis and characterization of (hydrido)phosphanylalumanes

In Chapter 4, we have demonstrated that borohydrides are good leaving groups for salt metathesis reactions. In this context, we envisioned that we could take advantage of the BH$_3$ transfer to prepare phosphanylalumanes. The *NacNac*AlH(BH$_4$) could undergo salt metathesis with an *in-situ* generated phosphide [RPH]$^-$ yielding the phosphanylalumanes. We equimolarly reacted *NacNac*AlH$_2$ with different alkyl and aryl boraphosphines in diethylether at room temperature. The reaction mixture was stirred for 2 hours to ensure the complete BH$_3$ transfer. Then, the reaction mixture is treated with one equivalent of NaHMDS leading to imminent colour change of the reaction crude from colourless to yellow and the formation of a white precipitate. After filtration and crystallization in diethylether, we isolated the (hydrido)phosphanylalumanes **99-102** in good to acceptable yields (Figure 5.5).

99 (R=Ph, 78%)
100 (R=Mes, 28%)
101 (R=Tip, 63%)
102 (R=^{t}Bu, 40%)
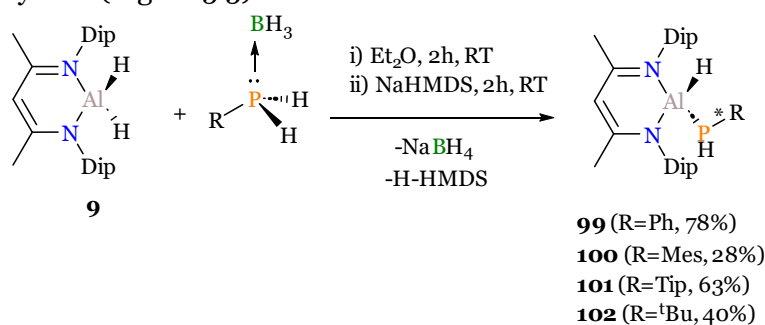
Figure 5. 3. Synthesis of phosphanylalumanes **99-102** (Dip=2,6-di-iso-propylphenyl, Ph=phenyl, Mes=mesityl, Tip=2,4,6-tris-iso-propylphenyl, tBu=tert-butyl).

The spectroscopic data is consistent with the formation of **99-102**. The ^{31}P-NMR displays a high fielded doublet signal at -155.32 ppm (**99**), -191.11 ppm (**100**) -192 ppm (**101**), and -115 ppm (**102**). The chemical shifts are similar to other phosphanylalumanes bearing an α-proton on the phosphine, such as Mes*(Cl)Al-PHMes* (δ(^{31}P)=-133 ppm) or NHC^{Me4}(Bbp)(Br)Al-P(H)Mes (**58**) (δ(^{31}P)=-157 ppm), but more shielded than the *NacNac*AlH(PPh$_2$) analogue reported by Nikonov and co-workers (δ(^{31}P)=-67.85 ppm).[262] The $^1J_{P-H}$ coupling constants range from $^1J_{P-H}$ =182.7 Hz (**102**) to $^1J_{P-H}$ =206.5 Hz (**101**), aligning well with other related compounds ($^1J_{P-H}$ =220 Hz (Mes*(Cl)Al-PHMes*); $^1J_{P-H}$ =206 Hz (NHC^{Me4}(Bbp)(Br)Al-P(H)Mes)). The ^{1}H-NMR of compounds **99-102** revealed two septets corresponding to the methine proton of the *iso*-propyls substituents from the *Dip* group. It is consistent with the inequivalent substituents on the equatorial and axial positions of the aluminium. The hydride on aluminium could not be unambiguously identified in the ^{1}H-NMR spectra due to the coupling with ^{27}Al nucleus. This phenomenon has already been observed with similar compounds.[263] The presence of the hydrides is confirmed by FT-IR where the typical Al-H stretching is assigned (**99**: 1802.4 cm^{-1}; **100**:1785.1 cm^{-1}; **101**: 1822.3 cm^{-1}, **102**: 1793.3 cm^{-1}).[262, 263]

The ^{1}H-NMR of **99** shows broad signals presumably due to the flexibility of the *NacNac* ligand. The dynamic behavior of *NacNac* ligand has already been studied by different authors. For instance, Hayes *et al.* studied the dynamic process of different *NacNac* dialkyl scandium in toluene solution.[264] They proposed that two out-of-plane conformers interconvert in solution through a planar transition state (See Scheme 5.3).
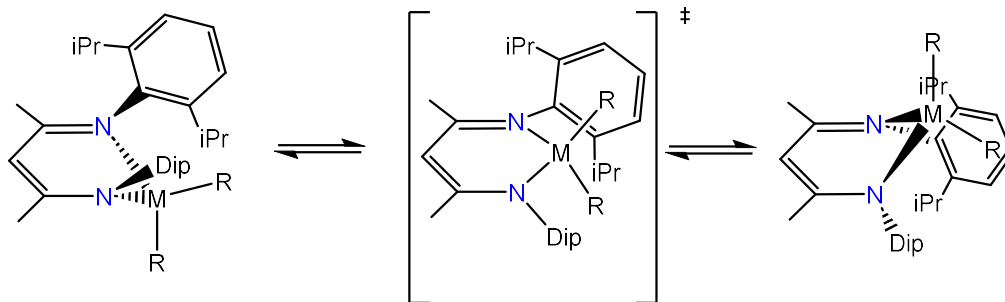
Scheme 5. 3. Schematic representation of the dynamic process of *NacNac* ligand (Dip=2,6-di-iso-propylphenyl).

To explore the dynamic process of **99** in solution, we employed variable temperature (VT) ^{1}H-NMR. This experiment allows us to understand the dynamic behavior of a molecule or to simplify the spectra if different conformers are present. Moreover, the activation energy ($\Delta G^{\ddagger}$) to interconvert conformers can be approximated with the VT- ^{1}H-NMR. The exchange rate (k_{exc}) is approximated using the equation $k_{exc} = \frac{\pi \Delta \nu}{\sqrt{2}}$, where $\Delta \nu$ is the maximum split of the chemical shifts. By solving the Eyring equation, one can obtain the $\Delta G^{\ddagger}$ of the process (see Appendix III for further details). Using this methodology, Hayes *et al.* reported the energy barriers of the different *NacNac* dialkylscandium, ranging from $\Delta G^{\ddagger}$=8.2 kcal/mol to $\Delta G^{\ddagger}$=13.7 kcal/mol at the coalescence temperatures between -60°C to 30°C. Nikonov and co-workers observed similar dynamism for *NacNac*Al(PPh$_2$)$_2$ in toluene solution. They obtained an energy barrier of $\Delta G^{\ddagger}$=17.0 kcal/mol at the coalescence temperature of 70°C.[259]

Figure 5.5 displays the ^{1}H-NMR spectra within the 4.0 ppm to 2.5 ppm range across different temperatures spanning from 223K to 333K. (see Appendix III for the full spectrum). Within this region, we identify the septet signals assigned to the methine proton of the *iso*-propyl substituents from the *Dip* group. At slow exchange regime (low temperature), we can identify two septets at 3.56 ppm and 3.11 ppm, and a multiplet arising from two overlapped septets. Upon heating, the three septet signals collapse into two, consistent with the interchange of two conformers of **99**. The energy barrier was

approximated to $\Delta G^{\ddagger}$=12.2 kcal/mol at a coalescence temperature of 253K. It is nearly 5 kcal/mol lower than the reported barrier of *NacNac*Al(PPh$_2$)$_2$ ($\Delta G^{\ddagger}$=17.0 kcal/mol), presumably due to the lower steric hindrance imposed by the substituents of the phosphine.
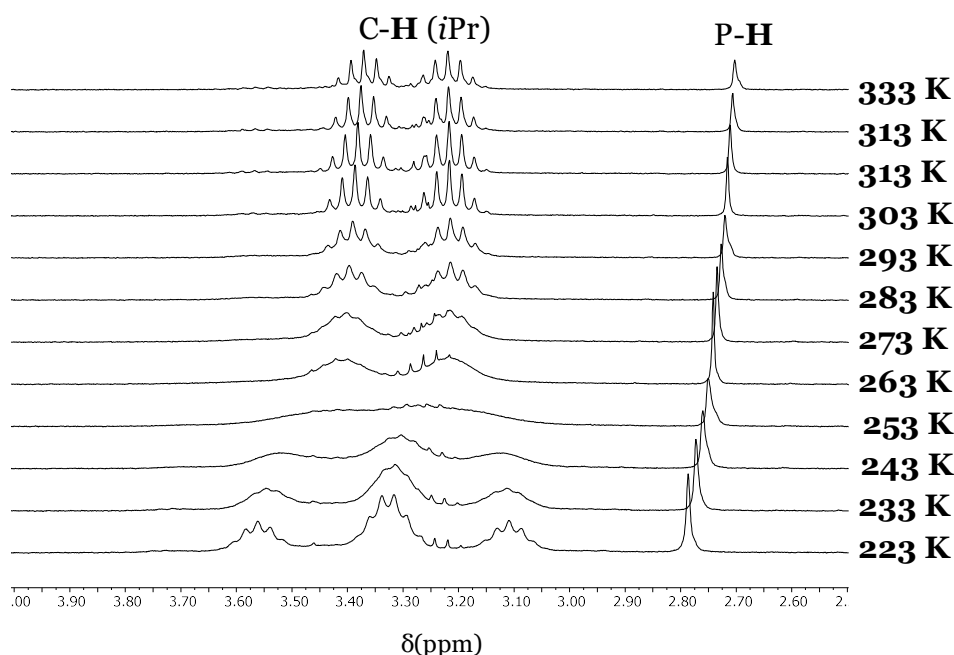
Figure 5. 4. ^{1}H-NMR spectra (300 MHz) in the region of 4.0 ppm to 2.5 ppm in toluene-d$_8$.

To confirm the isomeric exchange of **99**, we explored the mechanism using quantum chemical calculations. We considered two isomers: one with the phosphine situated in the equatorial position (**99**) and the other in the axial position (**99'**). The energy difference between **99** and **99´** is ΔG_r=+10.9 kcal/mol, indicating that the isomer **99** is the ground state in agreement with the SC-XRD data (*vide infra*). To model the kinetics of the reaction, we initially attempted to locate a planar transition state, as postulated for other *NacNac* complexes. However, we could not find a converged transition state geometry. Obviously, we discarded the *barrierless* process because the experimental data evidences a barrier of 12.2 kcal/mol. We inspected for alternative pathways to convert both isomers. We realized that, besides the relative positions of the phosphine, the main difference between **99** and **99´** is the orientation of the phenyl group form the phosphine. In the case of **99**, the phenyl is coplanar with the *Dip* group while in **99'** it points towards the *NacNac* ligand (see Figure 5.5). Therefore, a rotation of the Al-P bond must take place during the isomerization. We examined the Potential Energy Surface (PES) along the rotation of the Al-P bond. We could locate a transition state (**TS1**) bearing an activation energy barrier of $\Delta G^{\ddagger}$=12.5 kcal/mol, in perfect agreement with the experimental energy barrier. The aluminium in the **TS1** is not planar to the *NacNac* ligand (see Figure 5.5, right). The rotation of the Al-P bond occurs together with the shortening of the Al1-N1 distance, from 1.924 Å (**99**) to 1.914 Å (**TS1**), and an elongation of the Al-N2 bond, from 1.924 Å (**99**) to 1.961 Å (**TS1**). This enables the rotation of the phenyl group under the *Dip* substituent.

95
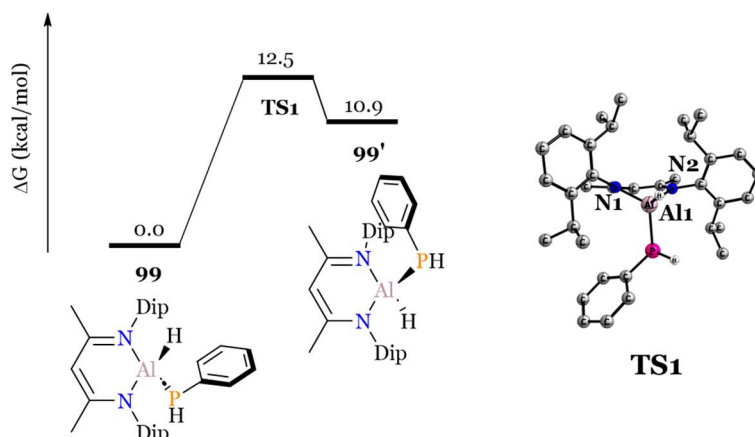
Figure 5. 5. Gibbs energy profile of the Al-P rotation at the B3LYP-D3(BJ)/def2-TZVPP//B3LYP-D3(BJ)/def2-SVP level of theory.

The SC-XRD confirmed the molecular structure of **99-102** (Figure 5.6). In all cases, the phosphine is located on the equatorial position of aluminium as other related compounds such as *NacNac*Al(H)(PPh$_2$).[35] The Al-P bond distances range from 2.358(5) Å (**99**) to 2.389(2) Å (**102**), which are slightly shorter than similar neutral and anionic (hydrido)phosphanylalumanes (Al-P=2.3971(6) Å (*NacNac*Al(H)(PPh$_2$)) and Al-P=2.409(8) Å ((NON^{Dip})Al(H)(PHMes))).[262, 263] The phosphanylalumanes bearing a triganol planar aluminium exhibit slightly shorter Al-P bonds than **99-102**, presumably due to the enhanced interaction between the lone pair of phosphorus with the empty *p*-orbital of aluminium.[90, 96] The Al-P-C$_{ipso}$ angle is more obtuse with more sterically hindered phosphines (98.05˚(**99**) <100.28˚(**100**) <105.76˚(**101**) <106.09˚(**102**)). The good quality of the crystals allowed us to allocate the hydrogens on the aluminium and phosphorus atoms, in good agreement with the abovementioned spectroscopic data.
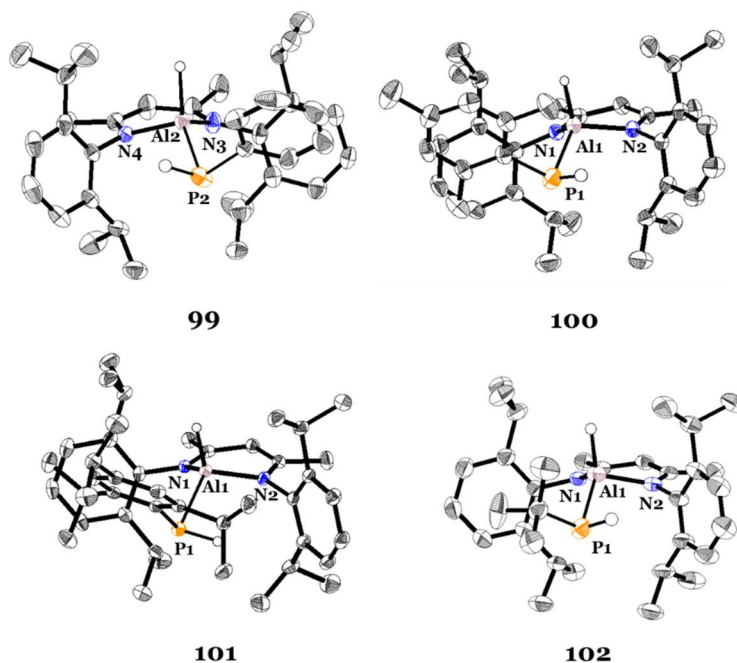
Figure 5. 6. Solid state structure of phosphanylalumanes **99-102** in the solid state. Displacement ellipsoids at 50% of probability level. Hydrogens attached to carbon are omitted for clarity. Selected experimental bond lenghts in Å and angles in degrees: **99**: Al2-P1=2.358(2)), Al-N4=1.893(2), Al-N3=1.891(2), Al-H=1.833(2); **100**: Al1-P1= 2.369(4), Al-N1=1.903(6), Al1-N2=1.910(1), Al1-H=1.509(2); **101**: Al1-P1=2.372(8), Al1-N1=1.910(6), Al1-N2=1.905(7), Al1-H=1.546(3), **102:** Al1-P1=2.389(3), Al1-N1=1.897(6), Al1-N2=1.897(7), Al1-H=1.5671(3).

The synthesis of the (hydrido)phosphanylalumanes **99-102** involves three reagents capable of reacting in a different manner. We decided to get insights into the reaction mechanism to elucidate the respective role of each reagent. We arbitrarily selected the synthesis of **99**. Scheme 5.3 outlines the potential reaction mechanisms. On the one hand, the NaHMDS reacts as a nucleophile towards **96**, leading to the *NacNac* hexamethyl silyl amino intermediate (**103**) and the $NaBH_4$ elimination. Compound **103** has previously been proposed as a reaction intermediate. Harder and co-workers computationally explored the reaction mechanism of the *NacNac* aluminium carbenoid with KHMDS to form the *NacNac* aluminyl derivative.[240] They proposed the initial formation of [*NacNac*AlN(SiMe₃)₂]K which further deprotonates the *NacNac* backbone. Therefore, the **103** could activate the P-H bond of the phosphine, yielding **99** and H-HMDS. On the other hand, the NaHMDS might function as a base. Firstly, it deprotonates the phosphine forming the sodium phosphide **104**. Then, the salt metathesis reaction between *NacNac*AlH(BH₄) and **104** forms **99** and $NaBH_4$.
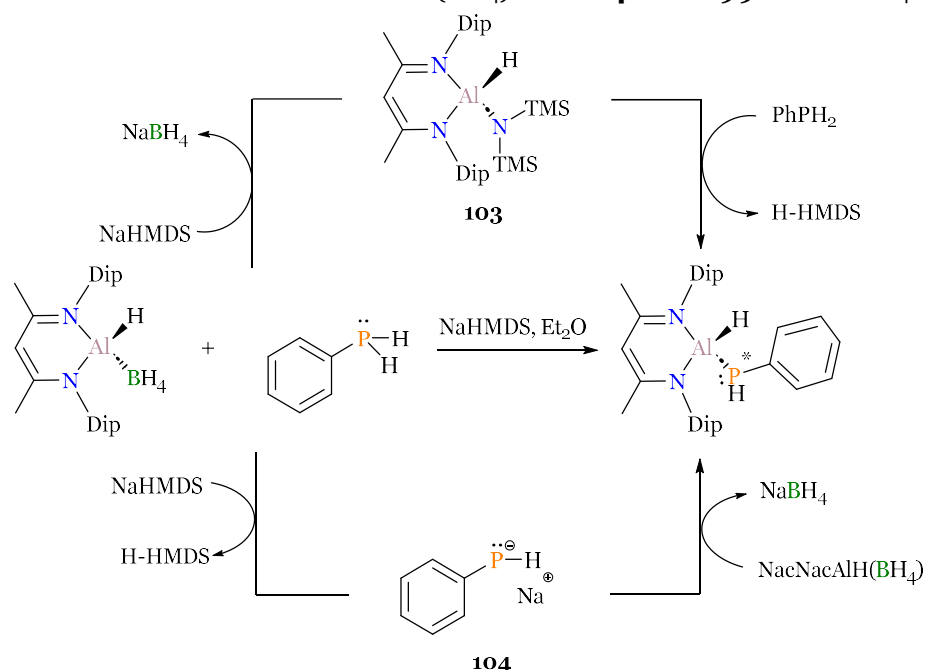
Scheme 5. 4. Plausible reaction mechanisms on the formation of phosphanylalumanes (Dip=2,6-di-iso-propylphenyl, TMS=tri-methylsilyl).

To elucidate the reaction mechanism, we selected LiHMDS as a base in order to decelerate the kinetics of the reaction (Scheme 5.4). After the addition of LiHMDS, the reaction mixture turns yellow, and it is stirred for 2 hours.
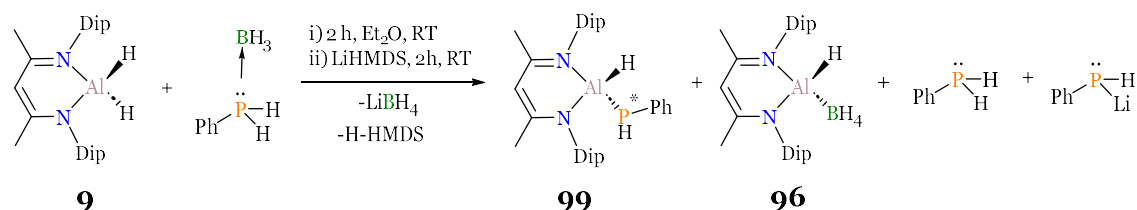
Scheme 5. 5. Synthesis of phosphanylalumane **99** employing LiHMDS as a base (Ph=phenyl, Dip=2,6-di-iso-propylphenyl).

The crude was analysed by multinuclear NMR in benzene-d_6, where different species could be identified (Figure 5.8). Firstly, we inspected the reaction crude by $^{31}P\{^1H\}$-NMR. We identified three distinct species: the PhPH₂ (δ= -125 ppm), [PhPH]Li (δ= -135 ppm) and *NacNac*AlHPHPh (δ= -155 ppm). Accordingly, the ^{31}P-NMR reveals

a doublet signal at -135 ppm and -155 ppm and a triplet at -125 ppm. The detection of [PhPH]⁻Li⁺ strongly supports the Brønsted base reactivity of LiHMDS. Thus, we ruled out the formation of *NacNac* aluminium hexamethylsilyl intermediate. Finally, we examined the ¹¹B{¹H}-NMR. We identified a main broad singlet at δ=-39.87 ppm assigned to LiBH₄ (see Appendix III, Figure A-III.63 for ¹¹B{¹H}-NMR).

— **³¹P{¹H}-NMR** — ——— **³¹P-NMR** ——— — **¹¹B{¹H}-NMR** —
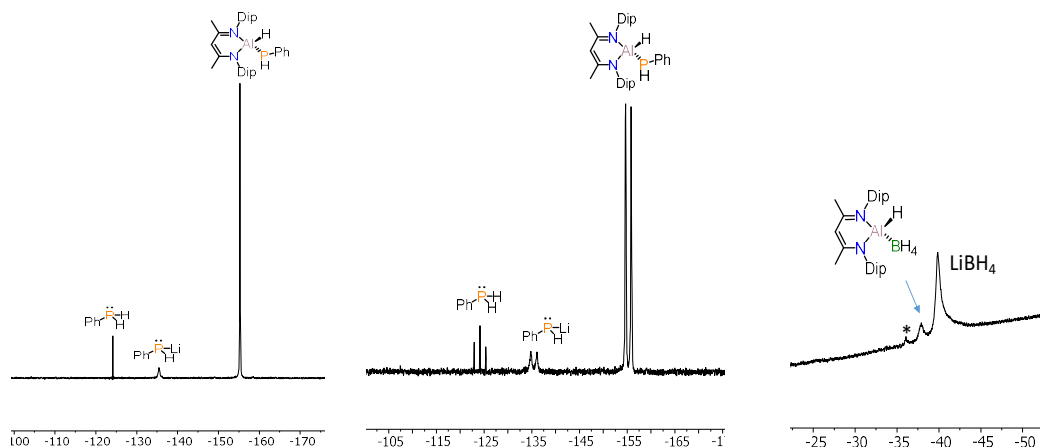
Figure 5. 7. ³¹P{¹H}-NMR, ³¹P-NMR and ¹¹B-NMR of the reaction crude (Dip=2,6-di-iso-propylphenyl)

. *Unidentified product.

5.1 Towards the synthesis of phosphaalumene

We have proposed the *β*-elimination as a plausible strategy to prepare the Al=P bond. This reaction is ubiquitous in organic chemistry to increase the bond multiplicity. It consists of cleaving two σ-bonds to form a new π-bond (Figure 5.8, top). For instance, the alkyl halides in the presence of a base can undergo *β*-elimination forming the corresponding alkene, with the exception for methane derivatives as they lack a proton in *β*-position.

The *β*-elimination has reached a broader scope beyond organic chemistry. Some main group multiple bonds, such as phosphasilenes, have been prepared with this synthetic approach. For instance, Driess and co-workers prepared a phosphasilene supported by a *NacNac* ligand via *β*-elimination of the corresponding *NacNac*-phosphasilane (Figure 5.8, bottom).[265] The reaction consists of reacting *NacNac*SiClPH₂ with LDA yielding the formation of a Si=P motif. Inspired by this methodology, we aimed to prepare the Al=P bond through a *β*-elimination of an H,halide-functionalized phosphalumane.
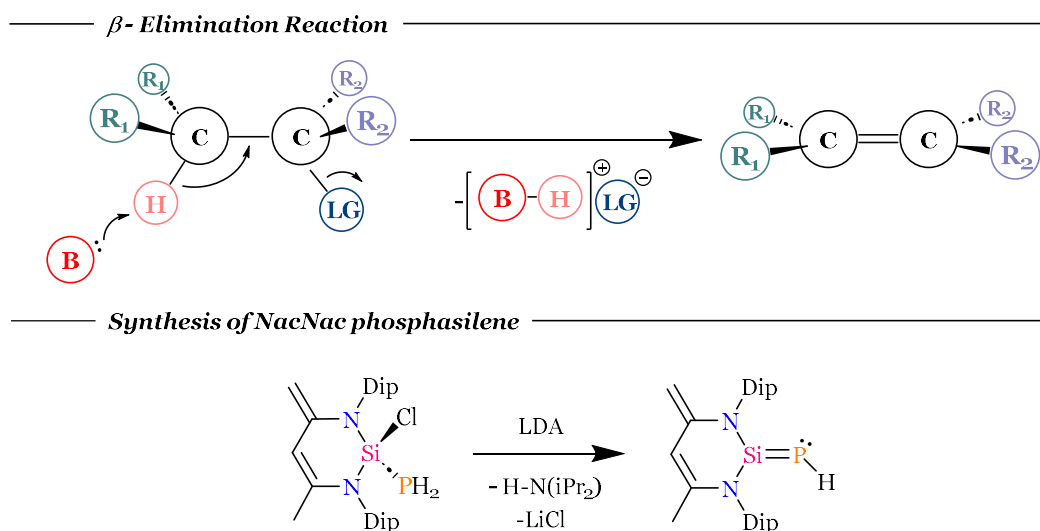
Figure 5. 8. On the top, a schematic representation of *β*-elimination; on the bottom, synthesis of *NacNac*-supported phosphasilene (Dip=2,6-di-iso-propylphenyl).

The compounds **99-102** bear an adjacent hydride and acidic proton suitable for the thermally induced H_2 elimination to obtain the Al=P motif. In this vein, von Hänisch and co-workers achieved alkane elimination of NHC-stabilised phosphanylalumanes.[92] However, the high temperatures required for this reaction (165°C) induced the separation of NHC from aluminium forming an heterocubane structure.[266] We attempted the dehydrogenation at 120°C in toluene but no indication of the phosphaalumene formation was detected. We also attempted the equimolar reaction of **99** with KHMDS, seeking for the *β*-elimination. Upon addition of the KHMDS to a solution of **99,** we observed the formation of a solid (Scheme 5.5). Despite our attempts to dissolve in common organic solvents, none of them were effective, suggesting the ionic nature of the compound. To enhance the solubility, we decided to react the solid with 18-crown-6 obtaining compound **107**. While **107** has a very poor solubility in aromatic solvents, it is soluble in THF, albeit accompanied by decomposition. Nevertheless, it was sufficient for multinuclear NMR characterization. The ^{1}H-NMR displays two doublet signals at δ=2.98 ($^1J_{H-H}$=2.20Hz) and δ=2.29 ppm ($^1J_{H-H}$=2.42 Hz) assigned to the methylene group. The assignment is supported by ^{13}C{^{1}H}-NMR and ^{13}C-DEPT135, showcasing a singlet at δ=75.23 ppm that features a negative peak in ^{13}C-DEPT135. The signal is in the same range as the methylene group of **91** (δ=83.64 ppm), albeit slightly deshielded compared to **107**. In ^{31}P-NMR we identify a doublet at δ=-139.19 ppm with a $^1J_{P-H}$ = 185.1 Hz. The NMR data strongly suggests that the deprotonation occurs on the methyl group of the *NacNac* backbone, yielding the anionic phosphanylalumane **107**.
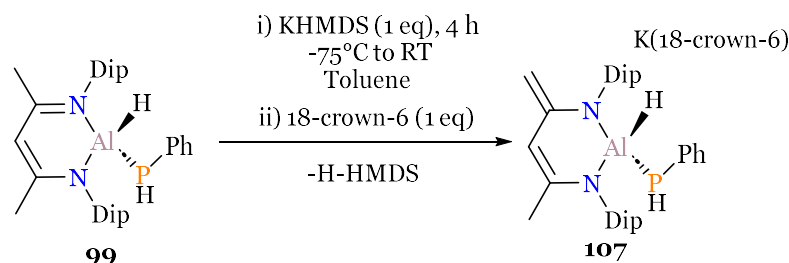
Scheme 5. 6. Synthesis of compound **107** (Dip=2,6-di-iso-propylphenyl).

Single crystals suitable for X-ray diffraction were isolated from the reaction crude in toluene at room temperature. The SC-XRD confirmed the backbone deprotonation in full agreement with the spectroscopic data (Figure 5.9, A). The inequivalent distances

between C1-C5 (1.421(1) Å) and C3-C4 (1.447(2) Å) point to a C=C and C-C bonds, respectively. The Al1-N1 (1.857(02) Å) and Al1-N2 (1.850(9) Å) are almost equivalent but shorter than neutral analogues **99-102**. The Al-P distance (2.409(1) Å) is considerably elongated with respect to the Al-P of **99.** However, it is in the range of the Al-P distance (2.4039(8) Å) of the anionic phosphanylalumane K[(NON^{Dip})Al(H)(PHMes)] reported by Coles and co-workers.[267] Interestingly, the different units of **107** are entangled in the crystal lattice. The interaction of potassium with the lone pair of the phosphorus (P···K=3.401(6) Å) and the methyl from *iso*-propyl groups (C···K=3.225(5)) arrange a 1D coordination polymer (Figure 5.9, B).
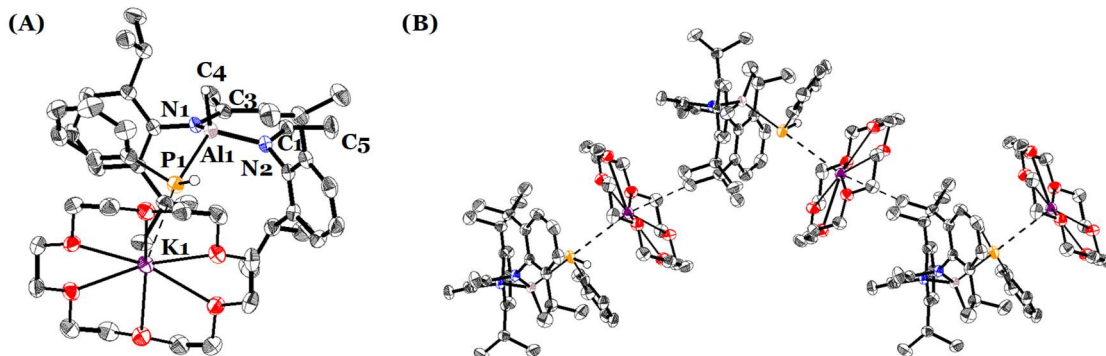
Figure 5. 9. (A) Molecular structure of **107** in the solid state. Displacement ellipsoids at 50% probability level. Hydrogens attached to carbon are omitted for clarity. Selected experimental bond lengths in Å and angles in degrees: Al1-P1=2.409(1), Al1-N2=1.851(1), Al1-N1=1.856(7), C1-C5=1.447(2), C1-C2=1.395(8), 1.427(1), C3-C4= 1.421(1), C3-N1=1.389(4), P1-K1=3.401(6), H1-Al1-P1=105.2(9); (B) Packaging of **107** in the crystal lattice.

We applied quantum chemical calculations to understand the underlying physical factors contributing to the Al-P bond distance differences between **99** and **107**. We studied the series of neutral phosphanylalumanes **99-102** and the ionic **107**. In the analysis of the frontier Kohn-Sham Molecular Orbitals of **90-102**, the HOMO has a high contribution from the σ Al-P bond. In contrast, the HOMO of **107** is located on the π-system of the *NacNac* ligand. The molecular orbital assigned to the Al-P σ-bond is located on the HOMO -2, which is slightly higher in energy (0.09 eV) than **99**.
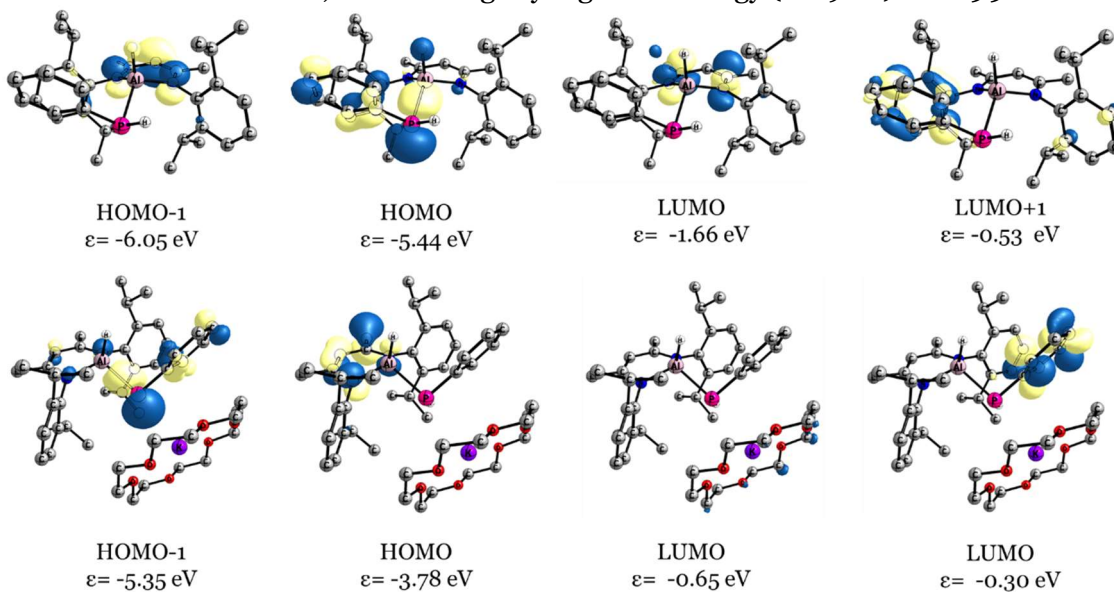
Figure 5. 10. Frontier Kohn-Sham molecular orbitals of **99** (top) and **107** (bottom) at the B3LYP-D3(BJ)/def2-TZVPP//B3LYP-D3(BJ)/def2-SVP level of theory. Isovalue = 0.05 a.u.

The natural population analysis revealed similar charge distribution along the Al-P bond, being highly positive aluminium (*c.a.* Q(Al) = 1.50 e and Q(P) = -0.20 e) (See Table A-III.3 in the Appendix III). The Al-P bond order of **107** (BO(Al-P)=0.59) is substantially lower than **99-102,** ranging from 0.72 to 0.71. We applied EDA-NOCV to get a deeper insight into the nature of the Al-P bond. Initially, we assessed whether the homolytic or heterolytic fragmentation of the Al-P bond better represents the bonding situation. We evaluated the *iFEF* index, using Hirshfeld and Löwdin AIM definition (see Chapter 3 for further details), and ΔE_{orb} for both fragmentations. The fragmentation which yields the lowest *iFEF* or $|\Delta E_{orb}|$ will correspond to the best fragment representation. In Table 5.1 are collected the numerical values for compounds **99** to **102** and **107**. The *iFEF* index is minimized for the heterolytic fragmentation independently to the AIM definition. In the same direction, the $|\Delta E_{orb\text{-}corr}|$ is minimized for the heterolytic fragmentation. Thus, we selected the heterolytic fragmentation of the Al-P bond to analyze the nature of the Al-P bond.

Table 5. 1. *iFEF* in Löwdin (Löw) and Hirshfeld (Hirsh) AIM definition and ΔE_{orb} values of compounds **99**, **100**, **101, 102** and **107** at the B3LYP-D3(BJ)/TZ2P//B3LYP-D3(BJ)/def2-SVP level of theory.

	iFEF (Löw)		*iFEF* (Hirsh)		$\Delta E_{orb\text{-}corr}$	
	Homolytic	Heterolytic	Homolytic	Heterolytic	Homolytic	Heterolytic
99	1.24	**0.85**	0.70	**0.40**	-127.9	**-106.7**
100	1.27	**0.93**	0.70	**0.41**	-128.4	**-111.0**
101	1.28	**0.94**	0.71	**0.41**	-129.8	**-110.4**
102	1.24	**0.95**	0.66	**0.38**	-120.6	**-111.7**
107	1.28	**0.74**	0.71	**0.34**	-156.9	**-72.9**

The EDA-NOCV results are gathered in Table 5.2. The interaction energies (ΔE_{int}) of neutral phosphanylalumanes range from ΔE_{int} = -176.1 kcal/mol (**99**) to ΔE_{int} = -188.4 kcal/mol (**102**), which is notably lower (more stabilizing) than **107** (ΔE_{int} = -85.1 kcal/mol). The electrostatic interaction (ΔE_{Elect}) in neutral phosphanylalumanes is more stabilizing than **107**, expectable for charged fragments. The orbital interaction (ΔE_{orb}) in neutral phosphanylalumanes ranges from -111.8 kcal/mol (**102**) -106.7 (**99**), which are higher than **107** (-72.9 kcal/mol).

Table 5. 2. EDA-NOCV of **99**, **100**, **101**, **102** and **107** at B3LYP-D3(BJ)/TZ2P//B3LYP-D3(BJ)/def2-SVP level of theory. Energies are given in kcal/mol.

	99	**100**	**101**	**102**	**107**
ΔE_{int}	-176.1	-178.5	-177.9	-188.4	-85.1
ΔE_{Pauli}	118.4	121.8	131.6	140.6	115.2
ΔE_{Elstat}[a]	-167.3 (56.8%)	-166.2 (55.4%)	-169.3 (54.7%)	-198.4 (60.3%)	-91.9 (45.9%)
ΔE_{Disp}[a]	-20.5 (7.0%)	-23.02 (7.7%)	-29.9 (9.6%)	-18.9 (5.7%)	-35.6 (17.8%)
ΔE_{orb}	-106.7	-111.1	-110.5	-111.8	-73.0
$\Delta E_{HF\text{-}Corr}$	0.0	0.1	0.1	0.0	0.1
$\Delta E_{orb\text{-}corr}$[a]	-106.7 (36.2%)	-111.0 (37.0%)	-110.4 (35.7%)	-111.7 (34.0%)	-72.9 (36.4%)
$\Delta E_{orb(\Delta\rho1)}$[b]	-76.2 (71.4%)	-79.0 (71.2%)	-77.6 (70.3%)	-78.4 (70.2%)	-50.3 (69.0%)
$\Delta E_{orb(rest)}$[b]	-30.5 (28.6%)	32.0 (28.8%)	-32.8 (29.7%)	-33.3 (29.8%)	-22.6 (31.0%)

[a]The value in parenthesis gives the percentage contribution to the total attractive interactions ΔE_{elstat} + $\Delta E_{orb\text{-}corr}$+ ΔE_{Disp}.
[b] The value in parenthesis gives the percentage contribution to the $\Delta E_{orb\text{-}corr}$.

The breakdown of the ΔE_{orb} term into bonding channels contributions reveals that the σ bonding channel ($\Delta E_{Orb,(\Delta\rho1)}$) is the most stabilizing contribution, accounting for approximately 70% of the ΔE_{orb}. We evaluated the *iFEF*$^{\sigma}$ which is the charge transfer in the Al-P σ bonding channel (See Chapter 3 for further details). In neutral phosphanylalumanes, the *iFEF*$^{\sigma}$ is above 0.30 *e* but in **107** the *iFEF*$^{\sigma}$ is below 0.30 e indicating a lower charge transfer. Therefore, the Al-P bond in **107** is more polarized towards phosphorus than **99-102**. The energy associated to the Al-P σ-bonding channel is about 30 kcal/mol more stabilizing in neutral phosphanylalumanes (ranging from -78.4 kcal/mol (**102**) to -76.2 kcal/mol (**99**)) than **107** (-50.3 kcal/mol). Molecular Orbital Theory can explain those differences. The Al-P σ-bond of **99** and **107** arises from the interaction between the occupied *p*-orbital of the phosphine and the empty *p*-orbital of the *NacNac*AlH fragment. The energy difference between those orbitals is higher in **99** (6.61 eV) than in **107** (0.14 eV), yielding a stronger σ-interaction in the neutral phosphanyalumane **99**.

(A) **σ-bonding channel**   **[PHPh]$^-$**   **[NacNacAlH]$^+$**

$\Delta E_{orb-\sigma}$=-76.2 ; $|\upsilon_{\alpha\beta}|$=0.84

iFEF$^{\sigma}$=0.34

HOMO (ε= +0.44 eV)

LUMO (ε=-7.05 eV)

(B) **σ-bonding channel**   **PHPh-K(18-Crown-6)**   **[NacNacAlH]**

$\Delta E_{orb-\sigma}$=-50.3 ; $|\upsilon_{\alpha\beta}|$=0.68

iFEF$^{\sigma}$=0.27

HOMO (ε= -2.91 eV)

LUMO (ε= -3.05 eV)
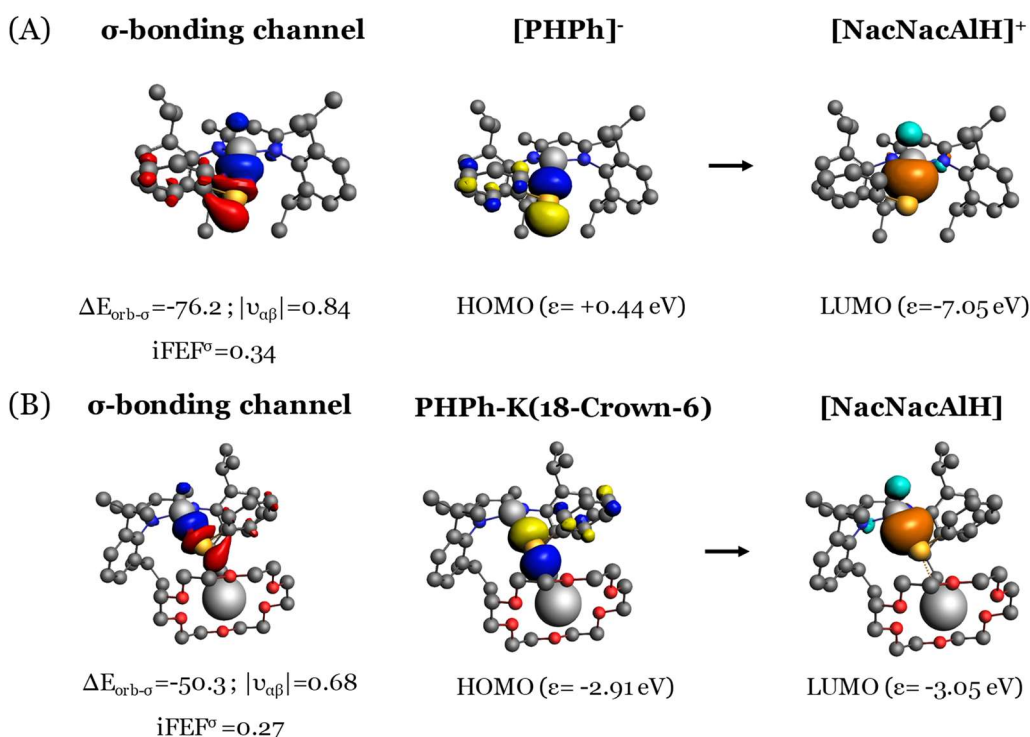
Figure 5. 11. Deformation densities associated with the σ-bonding channel of compound **99** (A) and **107** (B) (isovalue 0.003 a.u.) at B3LYP-D3(BJ)/TZ2P//B3LYP-D3(BJ)/def2-SVP level of theory. The associated energies $\Delta E_{orb-\sigma}$ are in kcal/mol and ν in a.u. The iFEF$^{\sigma}$ values are extracted using the Hirshfeld Atom in Molecules definition. The red color shows the charge outflow while blue shows charge density accumulation. The shape of the most important interacting occupied and vacant orbitals of the fragments are depicted (isovalue 0.05 a.u.). Hydrogens are omitted for clarity.

The synthetised (hydrido)phosphanylalumanes are not convenient synthons to prepare phosphaalumenes through *β*-elimination reaction because of the deprotonation on the *NacNac* backbone. We speculated two hypotheses to reason for the unsuccessful synthesis of phosphaalumene from (hydrido)phosphalumanes. On the one hand, the KHMDS tends to deprotonate the backbone because of the strength of the P-H bond. In this vein, Tokitoh and co-workers have already reported the difficulties to deprotonate the P-H bond in different type of H,X-functionalized phosphanlyalumanes (Scheme 5.7). For example, they attempted the *β*-elimination of Mes*(Cl)Al-PHMes* or NHC^{Me4}(Br)Al-P(H)Mes with strong bases such lithiated alkanes or aryls. No reaction was observed for NHC^{Me4}(Br)Al-P(H)Mes while Mes*(Cl)Al-PHMes* yields the formation of

Mes*Al(PHMes)₂. The deprotonation attempts using neutral bases such as DBU or NHC^{Me4} also were unsuccessful.
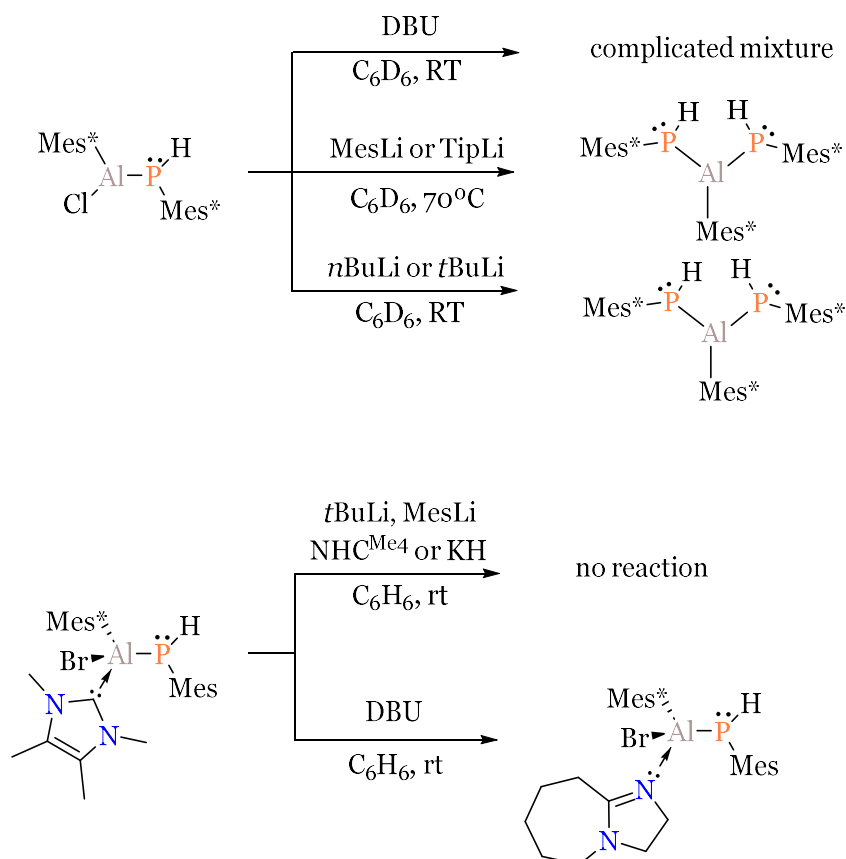
Scheme 5. 7. Selected examples of attempted *β*-elimination in H,halide-functionalized phosphanylalumanes.

On the other hand, the *β*-elimination in (hydrido)phosphanylalumanes might be disfavoured because the hydride is not a sufficiently good leaving group. We hypothesized that the *β*-elimination might be promoted by enhancing the leaving group quality. In Chapter 4, we proved that the [BH₄]⁻ is a good leaving group in aluminium chemistry. It allows the functionalization of aluminium with a variety of anionic nucleophiles via salt metathesis, including the preparation of Al-P motifs. Additionally, the mono-substituted *NacNac* boralumanes can be further functionalized with other nucleophiles (See Chapter 4, Figure 4.16), supporting the feasibility of *β*-elimination reaction. Based on these evidences, we prompted to explore the *β*-elimination of a boraphosphanylalumane to isolate the targeted *NacNac* supported phosphaalumene (Scheme 5.7). Unfortunately, the synthesis of boraphosphanylalumanes remain elusive requiring to develop a synthetic strategy to prepare them. In Chapter 4, we described that *NacNac*Al(BH₄)₂ allows a good control to the mono-substituted product in salt metathesis reactions. In this context, we presumed that phosphanylboralumanes could be obtained from a salt metathesis between **29** and an *in-situ* prepared phosphide [RPH]⁻.
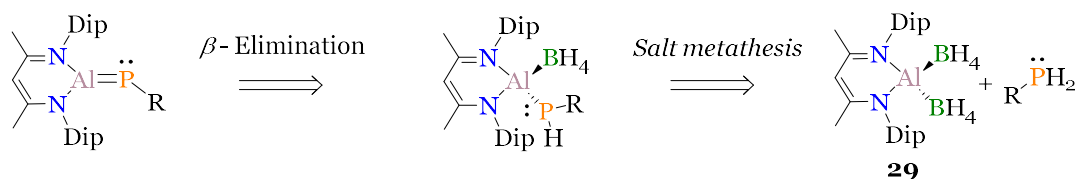
Scheme 5. 8. New retrosynthetic analysis for phosphaalumene.

The boraphosphanylalumanes were prepared by treating an equimolar mixture of *NacNac*Al(BH$_4$)$_2$ and RPH$_2$ (R=Ph or Mes) in diethylether at 0°C with NaHMDS (Scheme 5.9). Upon crystallization, compounds **108** and **109** are isolated in moderate to low yields. The ^{1}H-NMR of these compounds bear two septets and four doublets in agreement with the inequivalent substituents on aluminium. The ^{31}P-NMR displays a doublet at -149.3 ppm (**108**) and -191.1 ppm (**109**) which indicates the Al-P bond formation and the presence of an *α*-proton on the phosphorus atom. The ^{31}P-NMR chemical shifts of **108** and **109** are very similar to the hydride analogues (δ=-155 ppm (**99**) and δ=-191 ppm (**100**)). The ^{1}J$_{P-H}$ coupling constants are 197.14 Hz (**108**) and 201.88 Hz (**109**), which are larger than the hydride analogues (^{1}J$_{P-H}$ =189.77 Hz (**99**) and ^{1}J$_{P-H}$ =196.5 Hz (**100**)) In ^{11}B-NMR we identify a quintuplet at -35.9 ppm (**108**) and -35.2 ppm (**109**) supporting the coordination of a [BH$_4$]$^-$ on the aluminium atom.

29

R$_1$= Ph (**108**), 42%

R$_1$=Mes (**109**), 28 %
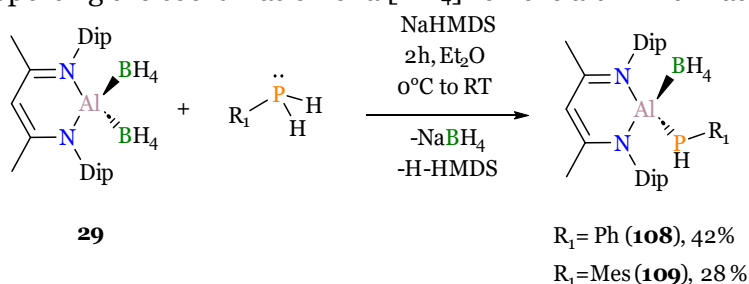
Scheme 5. 9. Synthesis of boraphosphanylalumanes **108** and **109**. (Ph=Phenyl, Mes=Mesityl)

The molecular structures of compounds **108** and **109** were confirmed by X-ray diffraction (Figure 5.13). They display similar structural features to (hydrido)phosphanylalumanes **99-102**. The aluminium presents a distorted tetrahedral geometry (N-Al-N =96.5(2)° (**108**) and N-Al-N=96.2(9)°; B-Al-P =114.5(7)° (**108**) and 113.3(2)° (**109**)). The Al-N distances in **108** and **109** (in **108**, Al1-N1=1.896(6)Å and Al1-N2=1.901(8) Å; in **109**, Al1-N1=Al1-N2=1.902(5) Å), similar to the neutral (hydrido)phosphanylalumanes (*vide supra*). The phosphine is bind in the equatorial position of aluminium. The Al-P bond distance is 2.352(2) Å in **108** and 2.350(6) Å in **109**, within the same range of the Al-P bond in (hydrido)phosphanylalumanes **99-102**. The borohydrides are coordinated on the axial position of aluminium, bearing an Al-B distance of 2.164(7) Å (**108**) and 2.155(2) Å (**109**). The good quality of the crystals allowed to locate the hydrides of [BH$_4$]$^-$, revealing a κ^2 -coordination mode.

108   **109**
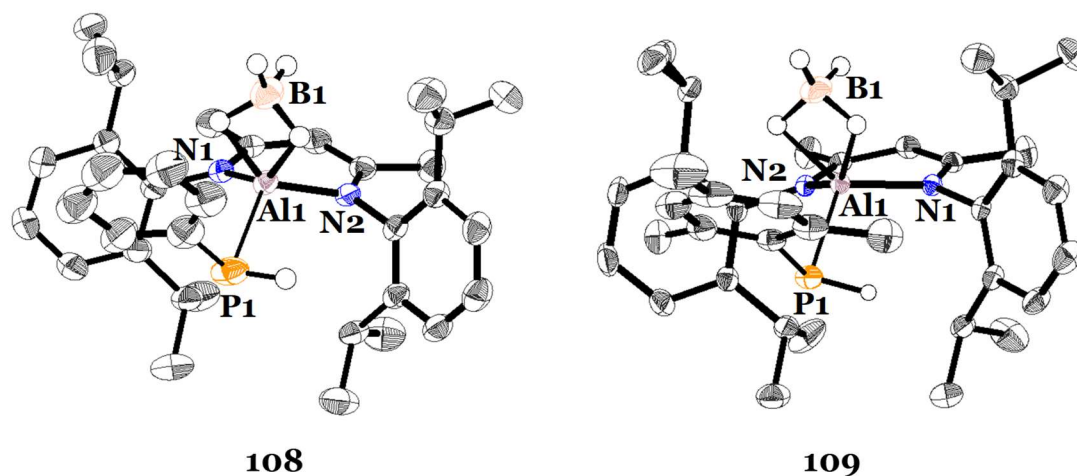
Figure 5. 12. Molecular structure of **108** and **109** in solid state. Displacement ellipsoids at 50% probability level. Hydrogens attached to carbon are omitted for clarity. Selected experimental bond lengths in Å and angles in degrees: **108**: Al1-P1=2.352(2), Al1-N1=1.896(6), Al1-N2=1.901(8), Al1-B1=2.164(7), B1-Al1-

P1=114.5(7); **109**: Al1-P1=2.350(6), Al1-N1=1.902(5), Al1-N2=1.902(5), Al1-B1=2.155(2), B1-Al1-P1= 113.3(2).

Compounds **108** and **109** are a versatile building blocks which allow to increase the molecular complexity to phopsphanylalumanes. The aluminium bears a $[BH_4]^-$ substituent, which is a good leaving group that can be functionalized with different nucleophiles, and the phosphine bears a P-H functionality which might allow further functionalization on the α-position of the phosphine. This type of compound opens the door to increase the library of functionalized phosphanylalumanes. For our purpose, they represent promising starting materials to prepare *NacNac* supported phosphaalumene. We explored the β-elimination reaction treating compound **109** with KHMDS in benzene at room temperature (Scheme 5.10). Upon the addition of KHMDS, the reaction mixture turns to dark-red and forms a precipitate. The ^{31}P-NMR reveals the formation of several compounds in which a broad singlet at -115 ppm is identified. The ^{11}B-NMR is silent, suggesting that the β-elimination has proceeded.
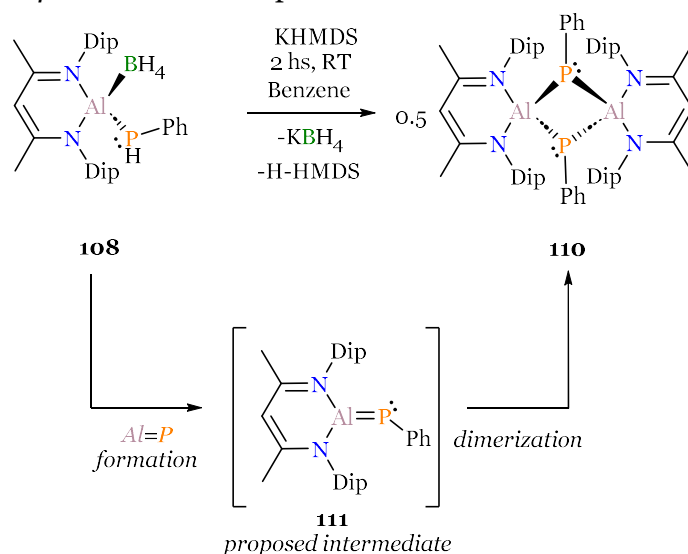
Scheme 5. 10. Synthesis of the cyclodiphosphalane **110**.

We isolated in poor yields (24%) the compound **110** as an orange solid, corresponding to the singlet at -115 ppm in ^{31}P-NMR. The ^{1}H-NMR spectrum at room temperature shows broad signals, presumably due to the dynamic behavior of **110**. We performed VT ^{1}H-NMR in toluene to get a better resolution of the ^{1}H-NMR of **110**. In Figure 5.13 we depict the ^{1}H-NMR of **110** at different temperatures ranging from -30°C to 90°C. At -30°C we identify the typical resonance of the *NacNac* ligand. Two septets at δ=3.00 ppm and δ=3.76 ppm assigned to the methine protons of the isopropyl groups and four doublets from the methyl substituents from the *Dip* group at δ=1.47 ppm, δ=1.11 ppm, δ=1.00 ppm and δ=0.25 ppm. When the temperature is raised, these resonances collapse into one septet. A similar pattern have been reported in *NacNac*Al(PPh$_2$)$_2$ by Nikonov and co-workers.[259] The dynamic process is assigned to the interconversion of the two out-of-plane conformers (*vide supra*). This process occurs with an energy barrier of ΔG=17.0 kcal/mol at the coalescent temperatures of 70°C.[259] In the case of **110**, the exchange has an energy barrier of ΔG = 14.5 kcal/mol at the coalescence temperature of 30°C (see Appendix III section AIII.10.2).
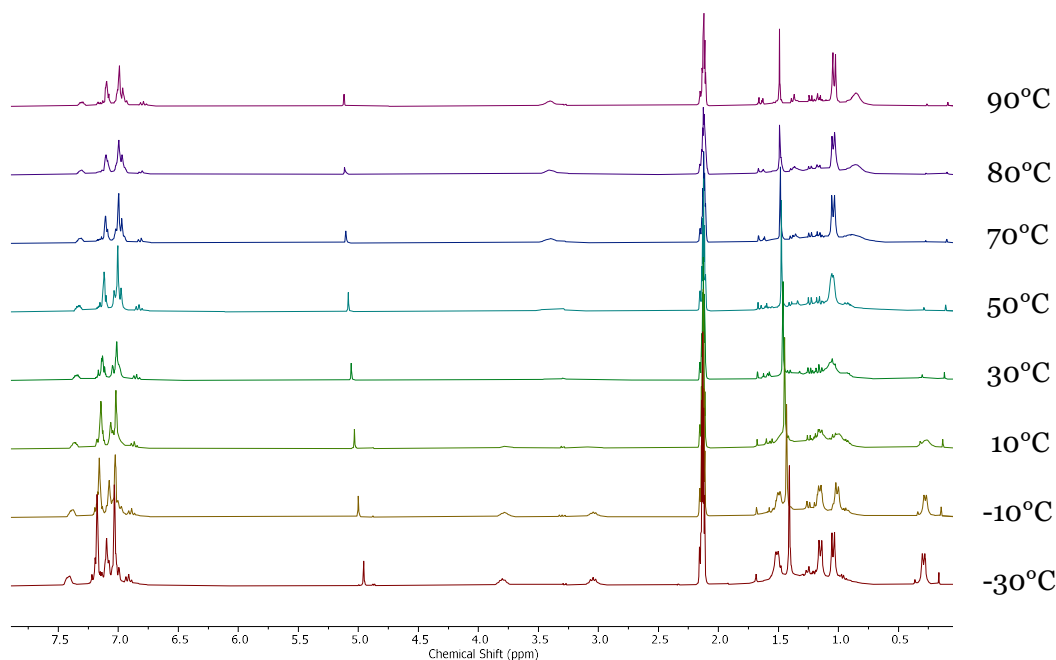
Figure 5. 13 ^{1}H-NMR spectra (300 MHz) of **110** at different temperatures of compound in toluene-d_8.

Single crystals suitable for X-Ray diffraction were obtained in benzene at room temperature (Figure 5.13). The Al-P bond distances are different depending on the relative position of aluminium. At the equatorial position, the Al-P is 2.334(2) Å while in the axial position is 2.324(7) Å. The Al-N bonds are asymmetric (Al1-N1= 1.941(3) Å and Al1-N2= 1.927(2) Å) but longer than the precursor **109**. The Al_2P_2 scaffold is planar where phenyl rings are disposed in *trans*-conformation. The structural features are similar to the cyclodiphospalane $[Cp^{3t}Al(\mu\text{-PPh})]_2$ reported by Hering-Junghans and Braunschweig groups (See section 1.4.2), bearing slightly shorter Al-P distances (c.a. 0.01 Å).

We propose that **110** is formed from a [2+2] cycloaddition of two transient phosphaalumene **111**. Similarly, Douglas and co-workers isolated [*NacNac*Fe(PPh)]$_2$ bearing a Fe_2P_2 four-membered ring, which is proposed to form via cycloaddition of two Fe=P transient species.[268] Hering-Junghans and co-workers have also postulated the Al=P transient species but, in their case, it undergoes to C-H of the Tip* substituent from the phosphine ligand.
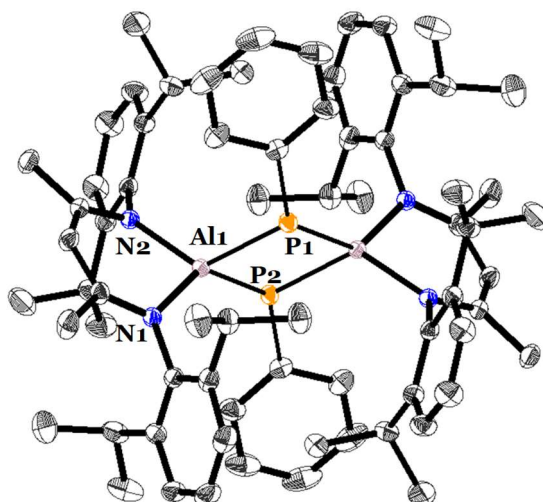
Figure 5. 14. Molecular structure of **110** in the solid state. Displacement ellipsoids at 50% probability level. Hydrogens attached to carbon are omitted for clarity. Selected experimental bond lengths in Å and angles in degrees: Al1-N2= 1.9272(3), Al1-N1=1.941(3), Al1-P1= 2.324(7), Al1-P2=2.334(2), P1-Al1-P2=85.6(3).

We recorded the UV-Vis spectra of **110** in toluene (Figure 5.14). It shows a maximum absorbance at 348 nm (3593±83 M·cm^{-1}) and two shoulders at 310 nm and 369 nm. We performed TD-DFT in order to assign the transitions. The computed spectrum is in good agreement with the experimental one (Figure 5.15, right). The maximal absorbance at 348 nm is assigned to the n →π* transition corresponding to the transition of HOMO-2 to LUMO+7 (see Figure A-III.57).
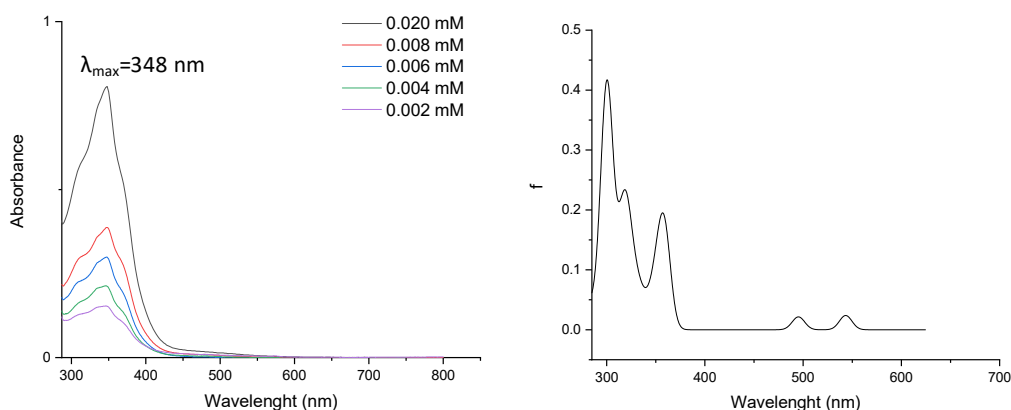
Figure 5. 15. On the left, UV-Vis spectrum of **110** in toluene with different concentrations. On the right, computed spectrum at the TD(PCM:toluene)/B3LYP-D3(BJ)/def2-TZVPP//B3LYP-D3(BJ)/def2-SVP level of theory.

The electronic structure of **110** was analysed by DFT calculations. The geometry at B3LYP-D3(BJ)/def2-SVP level of theory agrees with the solid-state structure. In Figure 5.16 are depicted the frontier Kohn-Sham molecular orbitals. The HOMO-1 and HOMO correspond to the in-phase and out-of-phase combination of the lone pairs on the phosphorus, respectively. The LUMO and LUMO+1 are located in the π-system on the *NacNac* ligand. The Intrinsic Atomic Orbitals (IBO)[269] locates four σ-bonding orbitals between Al-P highly polarized towards P and two π-orbitals associated to the lone pair on the phosphorus (see Appendix III, Figure A-III.70) .

HOMO-1	HOMO	LUMO	LUMO+1
ε= -4.64 eV	ε= -4.46 eV	ε= -1.48 eV	ε= -1.47 eV
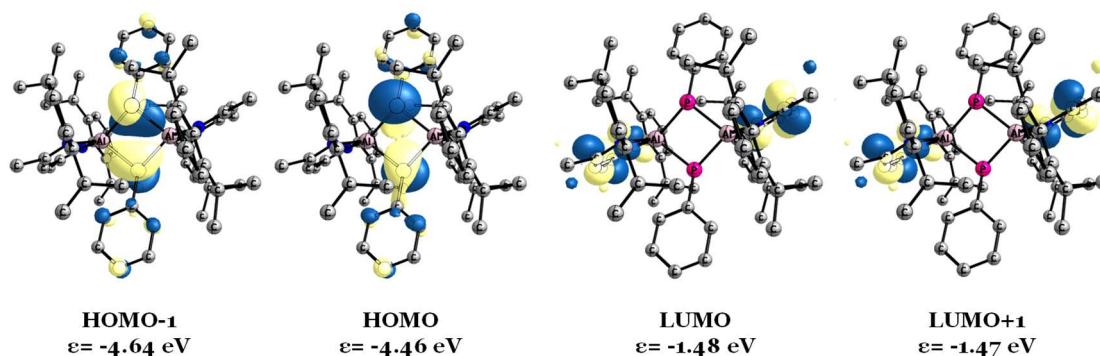
Figure 5. 16. Frontier Kohn-Sham Molecular Orbitals at B3LYP-D3(BJ)/def2-TZVPP//B3LYP-D3(BJ)/def2-SVP level of theory.

In order to rationalize the reactivity differences of **99** and **108** towards KHMDS, we modelled the corresponding *NacNac* deprotonation (purple line) and the *β*-elimination (turquoise line) pathways (Figure 5.17). In the case of **99** (Figure 5.17, top), the backbone deprotonation (**TS1**, ΔG=+13.6 kcal/mol) is more favored than the *β*-elimination (**TS2**, ΔG=+15.1 kcal/mol). However, in the case of **108** (Figure 5.17, bottom), this is reversed. The *β*-elimination (**TS3**, ΔG=+9.9 kcal/mol) is more favored than the backbone deprotonation (**TS4**, ΔG=+13.2). We realized that the backbone deprotonation pathway exhibits similar reaction barriers for **99** and **108** (ΔG‡=16.3 kcal/mol (**99**) and ΔG‡=+13.8 kcal/mol (**108**)) while the *β*-elimination is notably reduced for **108** (ΔG‡= 16.9 (**99**) and ΔG‡= 10.9 kcal/mol (**108**)). Thus, the *β*-elimination is substantially dependent on the leaving group quality while the deprotonation pathway is practically not affected.

Deprotonation of **99**
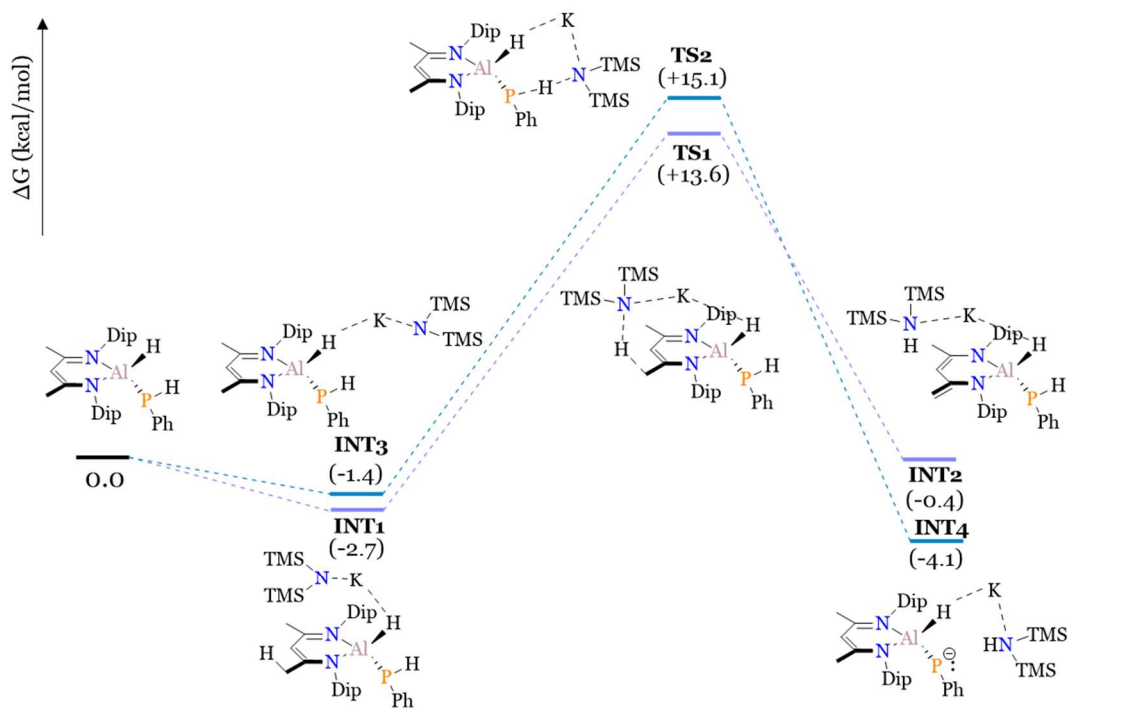
Deprotonation of **108**
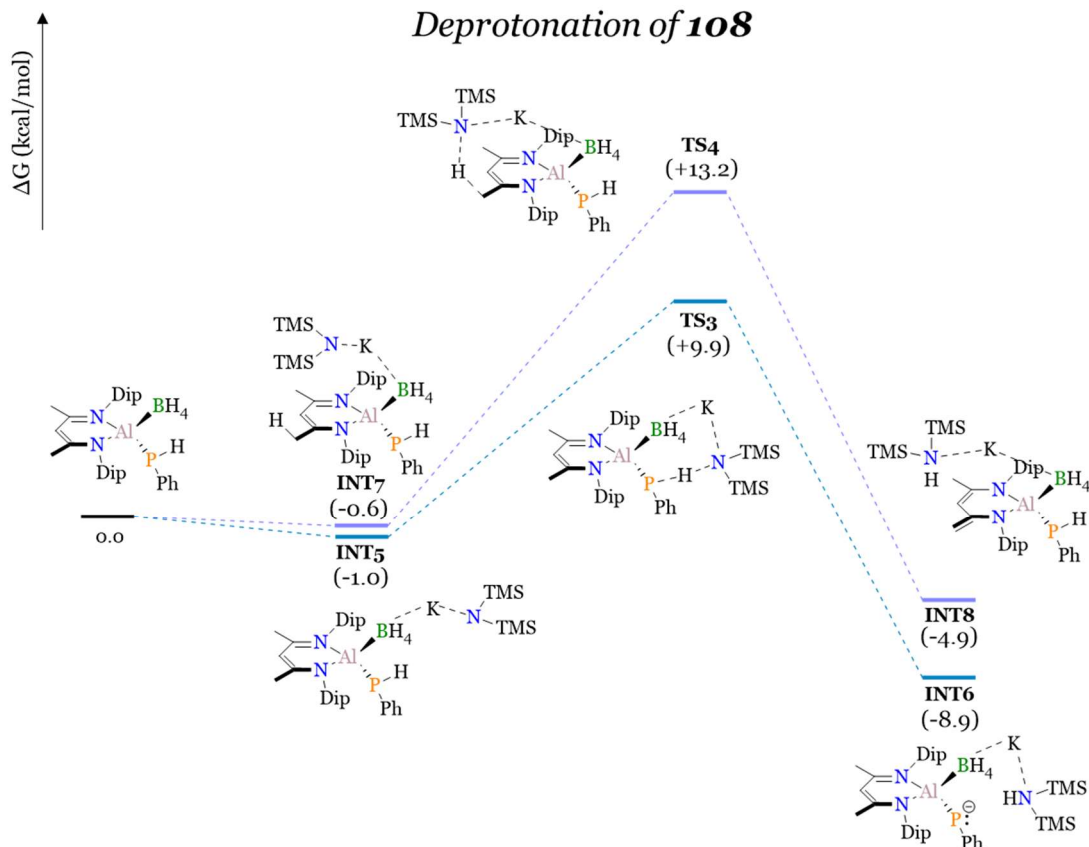
Figure 5. 17.Gibbs energy profile of the *NacNac* deprotonation and *β*-elimination of compounds **99** (top) and **110** (bottom) at PBE0-D3B(BJ)/def2-TZVPP//PBE0-D3(BJ)/def2-SVP level of theory.

The relative energies of *β*-elimination transition states **TS2** and **TS3** are substantially different (ΔG=+15.1 kcal/mol (**TS2**) and ΔG=+9.9 kcal/mol (**TS3**)). One

plausible explanation lies on the interaction between potassium and hydride (Figure 5.17). In **TS2** the distance between the potassium and the hydride (2.696 Å) is substantially longer than **TS3** (2.688 Å). This suggests that the interaction between potassium and the leaving group is stronger for the **TS3**, which stabilizes the transition state.
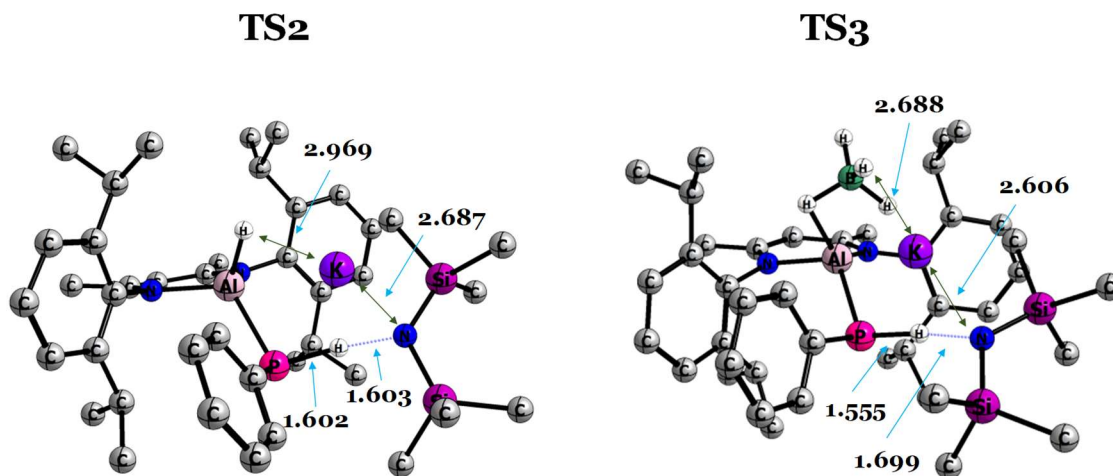
Figure 5. 18. Molecular structures of **TS2** (left) and **TS3** (right) at PBE0-D3(BJ)/def2-SVP level of theory. Distances are given in angstroms (Å).

CHAPTER 6 – Synthesis and reactivity of phospha-Grignard reagent

The Grignard reagents are a type of organomagnesium compounds with a general formula of RMgX, where R is an organic group and X is a halide. These compounds are textbook reagents to prepare secondary and tertiary alcohols from ketones and aldehydes. Besides their strong nucleophilic character, these reagents are very basic. In the case of substrates bearing acidic protons in β-position, the nucleophilic addition and the β-deprotonation reactions might compete. In these cases, the selectivity is improved towards the nucleophilic insertion with the addition of inorganic additives, such as ZnCl or LaCl$_3$•2LiCl.[270, 271] The incorporation of organic ligands to organomagnesium compounds allows the isolation of well-defined magnesium species, which could help to control the reactivity and selectivity of the Grignard reaction. The chemistry organomagnesium compounds supported by the *NacNac* ligand has attracted the interest of the inorganic community. This ligand stabilizes the magnesium with diverse types of functionalities and unusual oxidation states, *i.e.* Mg(I) or Mg(0).[272, 273] Moreover, it has found applications in catalysis. For instance, the *NacNac*Mg(THF)Me has shown to be a precatalyst for the intramolecular cyclization of aminoalkenes.[274] The *NacNac* magnesium compounds bearing a Mg-heteroatom have been proposed as nucleophilic reagents to prepare C-heteroatom bonds. However, they have shown unexpected or undesired reactivity patterns. For instance, Hill and co-workers explored the nucleophilic addition of the magnesium silanide *NacNac*MgSiMe$_2$Ph towards a variety of ketones with different electronic properties.[275] The reactions are substrate-dependent but none of the isolated products corresponds to the nucleophilic addition into the carbonyl carbon of the ketone. For instance, the treatment of two equivalents of 4-fluorobenzophenone to *NacNac*MgSiMe$_2$Ph undergoes nucleophilic addition of the SiMe$_2$Ph group on the *ortho*-position of the aryl group (**112**). In the reaction with acetophenone, the *NacNac*MgSiMe$_2$Ph deprotonates the methyl in α-position yielding the dimer **113** and SiHMe$_2$Ph.
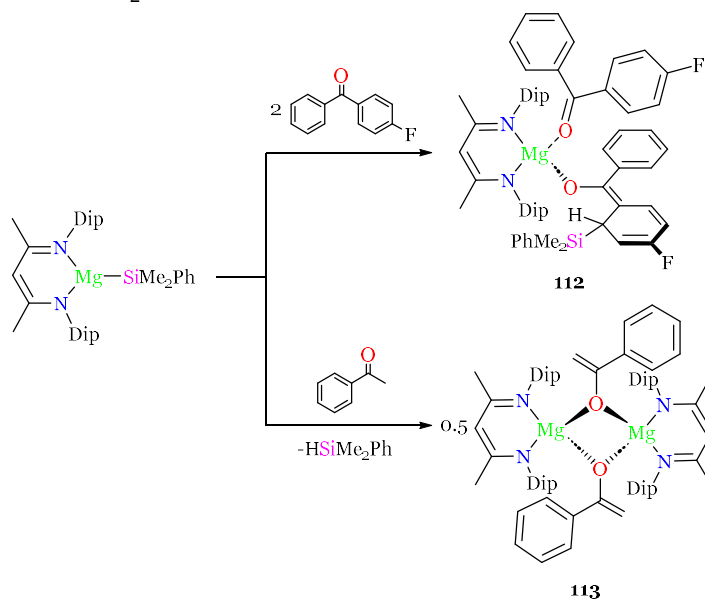
Figure 6.1. Selected reactions of magnesium silanide with ketones.

The magnesium amines (R$_2$N-MgX), also known as Hauser bases, are also very useful reagents in organic chemistry.[276] One of the drawbacks of these compounds is their

poor solubility even in THF solutions. The incorporation of LiCl improves their activity and solubility (Turbo Hauser bases).[277] The *NacNac* ligand supporting magnesium amines helps to increase the solubility and also to control the reactivity. For instance, Hevia and co-workers explored the reactivity of *NacNac*Mg(TMP) (TMP=2,2,6,6-tetramethylpiperidine) towards different organic substrates. It can deprotonate the benzoxazole, yielding the magnesium *α*-isocyanophenolate, or benzothiazole.[278] The *NacNac*Mg(TMP) regioselectively deprotonates the *para*-position of pyridine derivatives which subsequently undergoes a 1,2-addition yielding a diverse type of bipyridines.[279] Besides the Brønsed-base reactivity, Mulvey and co-workers have shown that *NacNac*Mg(TMP) can also react as a nucleophile, activating *tert*-BuNCO and *tert*-BuNCS.[280]

The magnesium phosphides, sometimes named phospha-Grignards, are the heavier analogues of magnesium amines. These compounds have been known for many decades and they have been characterized in different aggregation states such as monomer, dimer, oligomer, cluster or polymer (Figure 6.2).[281-284] The reactivity of phospha-Grignards has been explored in field of phosphido group transfer towards transition metal complexes. Hey *et al.* reacted (TMEDA)Mg(PHPh)$_2$ with NiCl$_2$(PCy$_2$CH$_2$)$_2$ which unexpectedly yield the diphosphane complex Ni(η-Ph-P=P-Ph)(PCy$_2$CH$_2$)$_2$.[281] Coles and co-workers studied the phosphide transfer of [Mg(μ-P(SiMe$_3$)$_2$Br(THF)]$_2$ towards Cp$_2$MCl$_2$ (M=Ti, Zr) complexes.[285] In the case of Cp$_2$TiCl$_2$ they observed the formation of (SiMe$_3$)$_2$P-P(SiMe$_3$)$_2$ and the cluster Cp$_2$TiMgX$_5$(thf)$_3$ (X=halogen), while Cp$_2$ZrCl$_2$ undergoes to the mono and di-substitution. The synthetic routes to prepare phospha-Grignards stabilised by *NacNac* ligand are very limited. To the best of our knowledge, only Coles and co-workers reported the synthesis of *NacNac*Mg(Et$_2$O)PR$_2$ (R=Ph, Cy) through the methane release reaction of *NacNac*MgMe with PHPh$_2$ and PHCy$_2$.[286]
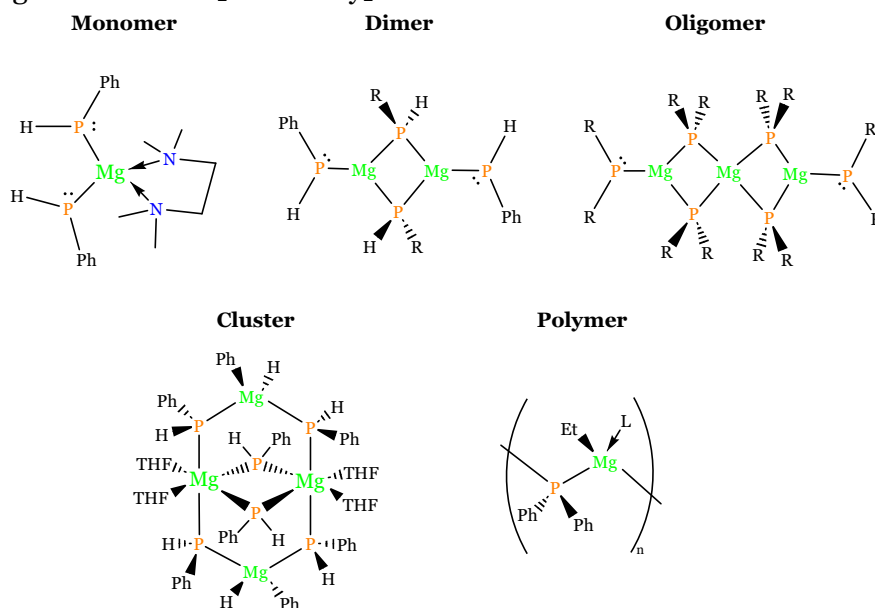
Figure 6. 2. Selected phospha-Grignard compounds in different aggregation states.

In Chapter 5, we have shown that the use of aluminium borohydrides as starting materials to prepare of Al-P motifs through salt metathesis reaction. The *s*-block elements typically display ionic bonds (with few exceptions) similar to aluminiumborohydrides. In this context, we envisioned that magnesium borohydrides could serve as synthons for salt metathesis reactions. In this chapter, we aim to explore the synthesis phospha-Grignards supported by *NacNac* ligand by making use of

magnesium borohydrides as synthons and study the reactivity of the isolated compounds.

6.1 Synthesis of phospha-Grignard

We designed the synthesis of *NacNac* phospha-Grignards inspired by the synthesis of boraphosphalumanes **108** and **109** (see Chapter 5 for further details). We mixed *NacNac*Mg(Et$_2$O)(BH$_4$) with phenylphospine in equimolar amounts in diethyl ether. The reaction mixture was cooled down to -78°C and treated with one equivalent of NaHMDS. The reaction mixture is stirred for 2 hours allowing it to reach room temperature. Upon filtration, the solution is concentrated and kept at -50°C, precipitating compound **115** as a colorless solid in acceptable yields. The ^{31}P-NMR reveals a doublet of triplets signal at -151.7 ppm ($^1J_{P-H}$=175.03 Hz, $^3J_{P-H}$=5.89 Hz) and the ^{11}B-NMR is silent, suggesting that the salt metathesis reaction has proceed. The ^{1}H-NMR of compound **115** reveals one septet ($^3J_{H-H}$=6.57 Hz) assigned to the methine proton of the *iso*-propyl substituents. It is consistent with the equivalent substituents in the axial and equatorial sides of magnesium. Compound **115** is soluble in ethereal solvents, partially soluble in aromatic organic solvents, and poorly soluble in hexane of pentane. Moreover, we observed that long exposure to vacuum leads to decomposition, yielding PhPH$_2$ and unidentified compounds. Additionally, we tested the synthesis of **115** with *NacNac*Mg(Et$_2$O)I starting material resulting in similar yields (57%).
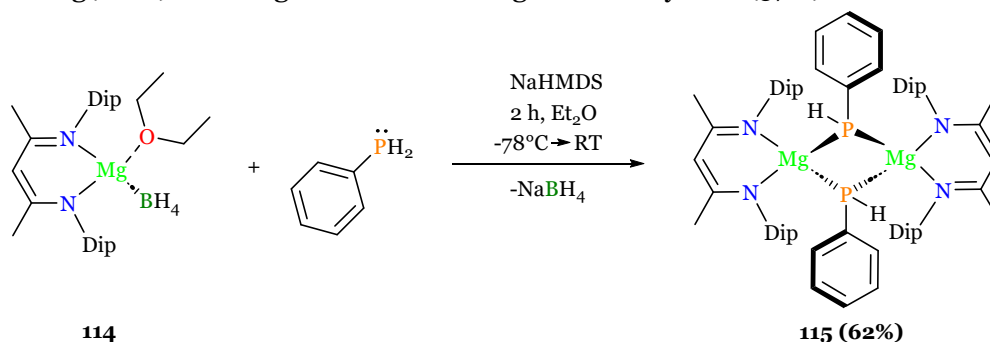
Scheme 6. 1. Synthesis of phospha-Grignard **115**.

The crystal structure of **115** is depicted in Figure 6.3. The molecular structure is dimeric bearing a Mg$_2$P$_2$ ring. The magnesium presents a distorted tetrahedral environment, bearing N1-Mg1-N2=93.7(4)° and P1-Mg1-P2= 75.2(4)°. The Mg-P bonds are slightly inequivalent (Mg1-P2=2.622(8) Å and Mg1-P2=2.615(2) Å) and longer than other cyclic unsupported phospha-Grignards.[285] The proton of the phosphine could be assigned in the electron density map, in agreement with the ^{31}P-NMR.
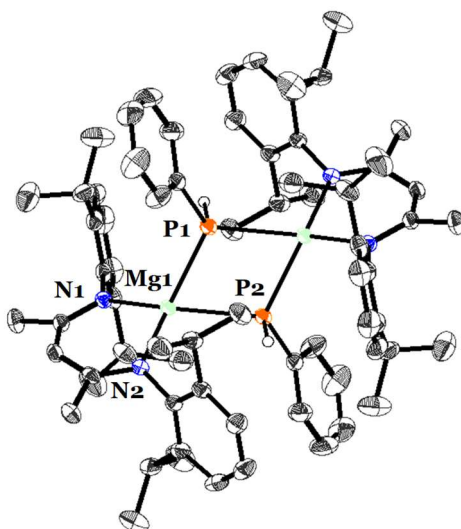
Figure 6. 3. Molecular structure of **115** in the solid state. Displacement ellipsoids at 50% of probability. Selected experimental bond lengths in Å and angles in degrees: Mg1-P1=2.622(8), Mg1-P2=2.615(2), Mg1-N1=2.508(6), Mg1-N2=2.049(4).

6.2 Nucleophilic addition of phospha-Grignard

The reactivity of phospha-Grignards has been mainly explored as phosphide transfer reagent (*vide supra*). Inspired by the aforementioned work from Hill and co-workers, we decided to explore the nucleophilic addition of **115** to benzophenone. In fact, some transition metal-phosphorus bonds have already activated benzophenone (Figure 6.4). For instance, Breen and Stephan studied the insertion of benzophenone towards $Cp_2ZrMe(PHMes^*)$, yielding the compound **116**.[287] Similarly, Walensky and co-workers explored the double insertion of benzophenone towards the Th-P bond, isolating the thorium-diphosphalcoholate **117**.[288]

116

Stephan, 2018

117

Walensky, 2018
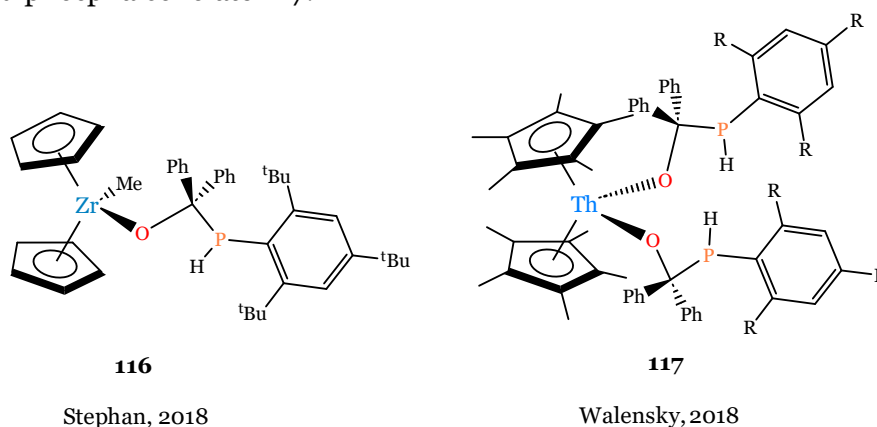
Figure 6. 4. Reported metal-phosphalcoholates (R=iPr or Mes).

Triel-phosphorus bonds can also activate the benzophenone. For instance, phosphaborenes can easily undergo [2+2] cycloaddition to benzophenone (Figure 6.5). Lerner and co-workers described the addition of a phosphaboradibenzofluvene to benzophenone yielding compound **118**.[289] The authors suggested that the addition undergoes thourgh a cyclic phosphaboraoxetane four-membered ring intermediate. Similar reactivity was observed for phosphinoborinium cation but the phosphaboraoxetane four-membered ring could be isolated. This chemistry has recently

flourished to the bora-phospha Witting reaction, a novel route to prepare phosphaalkenes from ketones, aldehydes, esters or amides.[290] In aluminium chemistry, Tokitoh and co-workers have tested the activation of benzophenone with phosphanylalumane **119**. However, they observe the formation of diphosphane Mes_2P-$PMes_2$ and the ketyl radical **120**. They propose that the diphosphane was formed via homo-coupling of $Mes_2P^{\bullet}$ radical.

Figure 6. 5. Selected examples of benzophenone activation with triel-phosphorus bonds.

The activation of benzophenone has also been explored with *s*-block phosphides. Breen and Stephan attempted nucleophilic addition of LiPHMes* towards benzophenone, but no addition product was observed.[287] Barozzino *et al.* studied the phosphination of carbonyl derivatives with lithiated borodiphenylphosphine ($Ph_2P(BH_3)Li$).[291] They find out that $Ph_2P(BH_3)Li$ has a ditopic character. The reactivity changes depending on the coordination side of lithium cation. At low temperatures (-78°C), the lithium is vicinal to the hydride yielding the phosphination reaction. At high temperatures (60°C), the lithium cation is neighbouring to the phosphorus resulting in the reduction reaction. The phosphination is postulated to undergo through lithium phosphalcoholate intermediate.

We reacted 4 equivalents of benzophenone with **115** in toluene at room temperature in the absence of light (Scheme 6.2). After the addition of benzophenone, the solution turns red and is stirred for 30 min to ensure complete conversion. The solution is dried under vacuum obtaining a red oil. It is re-dissolved in pentane and kept overnight at -35°C isolating **121** as an orange crystalline solid in acceptable yields (44%). The ^{31}P-NMR reveals a doublet signal at 10.35 ppm ($^1J_{P-H}$=220.70 Hz), clearly shifting towards low-field with respect to **115** ($\delta(^{31}P)$=-151.7 ppm, $^1J_{P-H}$=175.03 Hz). The chemical shift is more deshielded respect to the transition metal analogues with similar P-H coupling constants ($\delta(^{31}P)$=-8.6ppm ($^1J_{P-H}$=244.1 Hz) (**115**), $\delta(^{31}P)$=-15.76 ppm ($^1J_{P-H}$=222 Hz) (**116**, R=Me), $\delta(^{31}P)$=-27.38 ppm ($^1J_{P-H}$=224 Hz)) Compound **121** is stable in the solid state but in solution decomposes, especially in the presence of light (*vide infra*). Moreover, the overnight exposure to vacuum decomposes compound **121** to an identified white solid.

121

Scheme 6. 2. Synthesis of **121** through benzophenone activation with phospha-Grignard **115**.

Single crystals of **121** suitable for XRD were grown in pentane in the absence of light. The solid-state structure reveals a monomeric magnesium complex bound to a phosphalcoholate group. Additionally, a second molecule of benzophenone is coordinated to the axial position of magnesium. The Mg-O distances are different. The Mg1-O1 (1.995(4) Å) of the coordinated benzophenone (Mg1-O1 = 1.995(4) Å) is shorter than the Mg1-O2 bond (1.840(2) Å) of from the phosphalcoholate ligand. The C43-O2 distance (1.381(2) Å) is longer than the free benzophenone (1.23 Å),[292] expected for C=O activation. The C43-P1 (1.927(1) Å) is remarkably long for a C-P single bond according to the covalent radii (C-P=1.86 Å).[293] This feature is common in metal phosphalcoholates such as **116** and **117**, displaying similar bond distances (C-P=1.99 Å (**116**), C-P= 1.922 Å (**117**, R=Tip) and C-P=1.938 Å (**117**,R=Mes)).
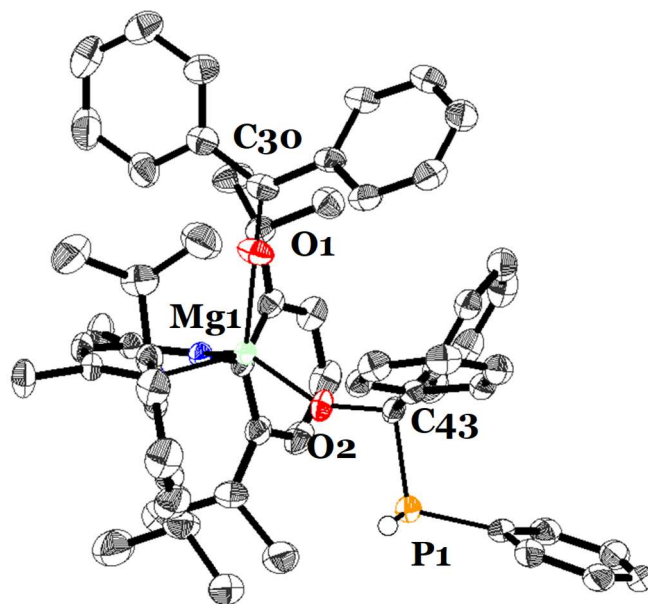
Figure 6. 6. Molecular structure of **121** in the solid state. Displacement ellipsoids at 50% of probability. Selected experimental bond lengths in Å and angles in degrees: Mg1-O1=1.995(4), Mg1-O2=1.840(2), C43-O2=1.381(2), C43-P1=1.927(1).

6.2.1 Mechanistic insights on the benzophenone activation

The isolation of compound **121** is an important outcome from the mechanistic point of view of the Grignard reaction. It is well-established that the nucleophilic addition of *traditional* Grignard reagents proceeds through the magnesium alcoholate intermediate **122** (Scheme 6.3). However, no structural characterization has been determined to the

date. Compound **121** bears the nucleophile bounded to the electrophilic carbon of the benzophenone, being iso-structural to the postulated magnesium alcoholate **122**.
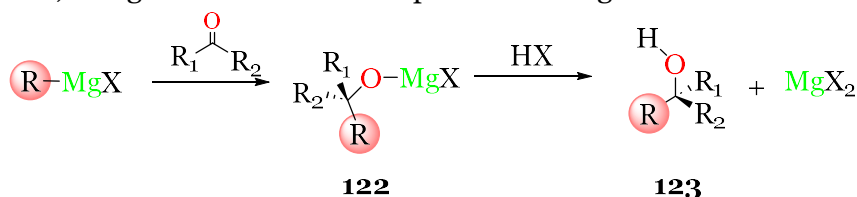
Scheme 6. 3. Mechanism of the Grignard reaction (R_1=aryl, alkyl or H; R_1=aryl, alkyl or H; X=halide).

The mechanism elucidation on the formation **122** is especially complex because of the presence of multiple Grignard species (Schlenk equilibrium), the involvement of coordinating solvent and the substrate/reagent dependence. The interest on revealing the reaction mechanism of this reaction is rooted to understand their selectivity. The formation of compound **122** might occur in two plausible pathways, namely the pairwise (polar) or radical mechanism (Figure 6.7). On the one hand, the polar or pairwise mechanism considers that the heterolytic cleavage of the Mg-R yields the formation of R-C bond. On the other hand, the radical mechanism, which proposes the homolytic cleavage of the Mg-R bond forming the magnesium ketyl radical and R$^{\bullet}$ which rebound to form the R-C bond.
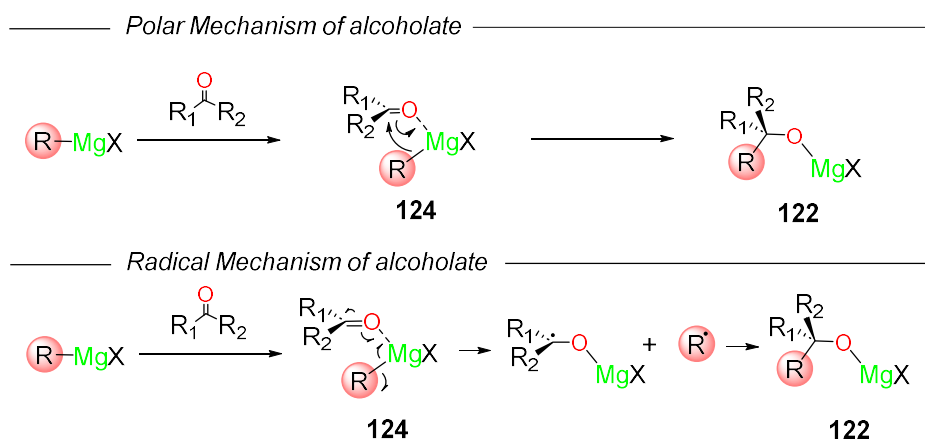
Figure 6. 7. Schematic representation of the reaction steps on Grignard reaction and plausible reaction mechanism of magnesium alcoholate (R_1=aryl, alkyl or H; R_1=aryl, alkyl or H; X=halide).

The radical mechanism was initially postulated by Blomberg and Mosher who explored the reaction of neopentyl Grignard to benzophenone.[294] They observed that the neopentyl is not inserted to the benzophenone reagent. Instead, they detected the formation of the benzopinacole presumably from the homocoupling of two ketyl radicals. The formation of radical intermediates was further supported by F. Bickelhaupt and co-workers who reported the formation of radicals in the reaction of phenylmagnesium bromide with phenanthrenequinone.[295] Along the years, different experiments have been designed in order to prove the formation of radical intermediates. For example, Ashby *et al.* explored the Grignard reaction mechanism of different reagents.[296] They analysed the products formed in the reactions of different Grignard reagents to benzophenone to get insights of the reaction mechanism. These experiments revealed the dependency of the Grignard reaction mechanism with the nature of the nucleophile and the ketone. The substrates with low reduction potential facilitate the Single Electron Transfer (SET), resulting in the radical mechanism.[296] In 2020, Peltzer *et al.* explored in-depth the reaction mechanism of Grignard reaction by quantum-chemical calculations and *ab-initio* dyamics.[297] They find out that the substrates with a low-lying π* C-O orbital

undergo through radical mechanism, while the others proceed through polar mechanism.

The nature of the Mg-P bond is different than Mg-C bond. For example, the electronegativity difference between magnesium and carbon ($\chi(C)$=2.544 and $\chi(Mg)$=1.293) is higher than magnesium and phosphours ($\chi(P)$= 2.253), yielding a less polarized bond. Thus, the reaction mechanism to form **121** might occur in a different mechanism than *traditional* Grignards. We followed the reaction by $^{31}P\{^1H\}$-NMR during 30 min where we only observed the formation of **121** (δ=10.35 ppm) (Scheme 6.4). After 30 min, no more conversion is observed indicating that the reaction has finished. Bickelhaupt and co-workers detected ketyl radicals in the reaction crude, which supported the radical mechanism pathway. We monitored the reaction with EPR spectroscopy to detect the formation of radicals on the course of the reaction. We observed the formation of a one radical specie with a g-factor of 2.0029. The hyperfine coupling could not be determined due to the broadness of the signal (see Scheme 6.4). The detection of radical species in the reaction crude might suggest the radical mechanism.
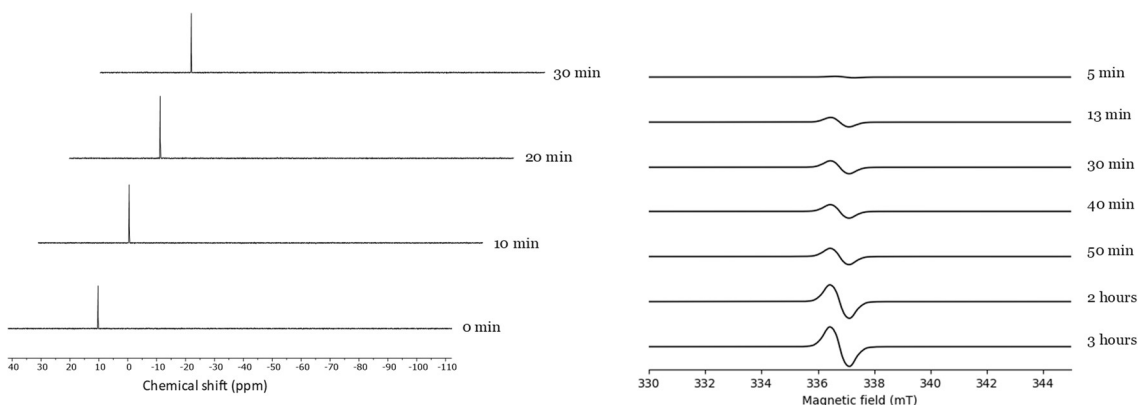
Scheme 6. 4. On the left, $^{31}P\{^1H\}$-NMR (121.4 MHz, 293 K) of the reaction crude after different reaction times. On the right, EPR of the crude at different reaction times.

In this context, we decided to examine the reaction mechanism on the formation of **121** with quantum chemical calculations (Figure 6.8). In the first step of the reaction, we considered that two equivalents of benzophenone monomerize compound **115** into two **INT1** molecules (ΔG=-11.3 kcal/mol). From **INT1**, we examined two pathways to activate benzophenone, namely polar mechanism and radical addition though homolytic splitting of the Mg-P bond. The polar mechanism firstly undergoes through a rotation of the phenylphosphine group (**INT2**, ΔG=-8.3 kcal/mol) to accommodate the lone pair of phosphorus pointing to the benzophenone. Then, the nucleophilic attack undergoes through a four-membered ring transition state (**TS1**, ΔG=+2.3 kcal/mol) with a Gibbs activation energy barrier of $\Delta G^{\ddagger}$=+13.6 kcal/mol. Then, a second molecule benzophenone coordinates to **INT3** yielding compound **121** (ΔG=-14.3 kcal/mol). The homolytic cleavage of the Mg-P bond requires a ΔG= +29.4 kcal/mol, which is about 16 kcal/mol higher than the activation energy for polar mechanism.
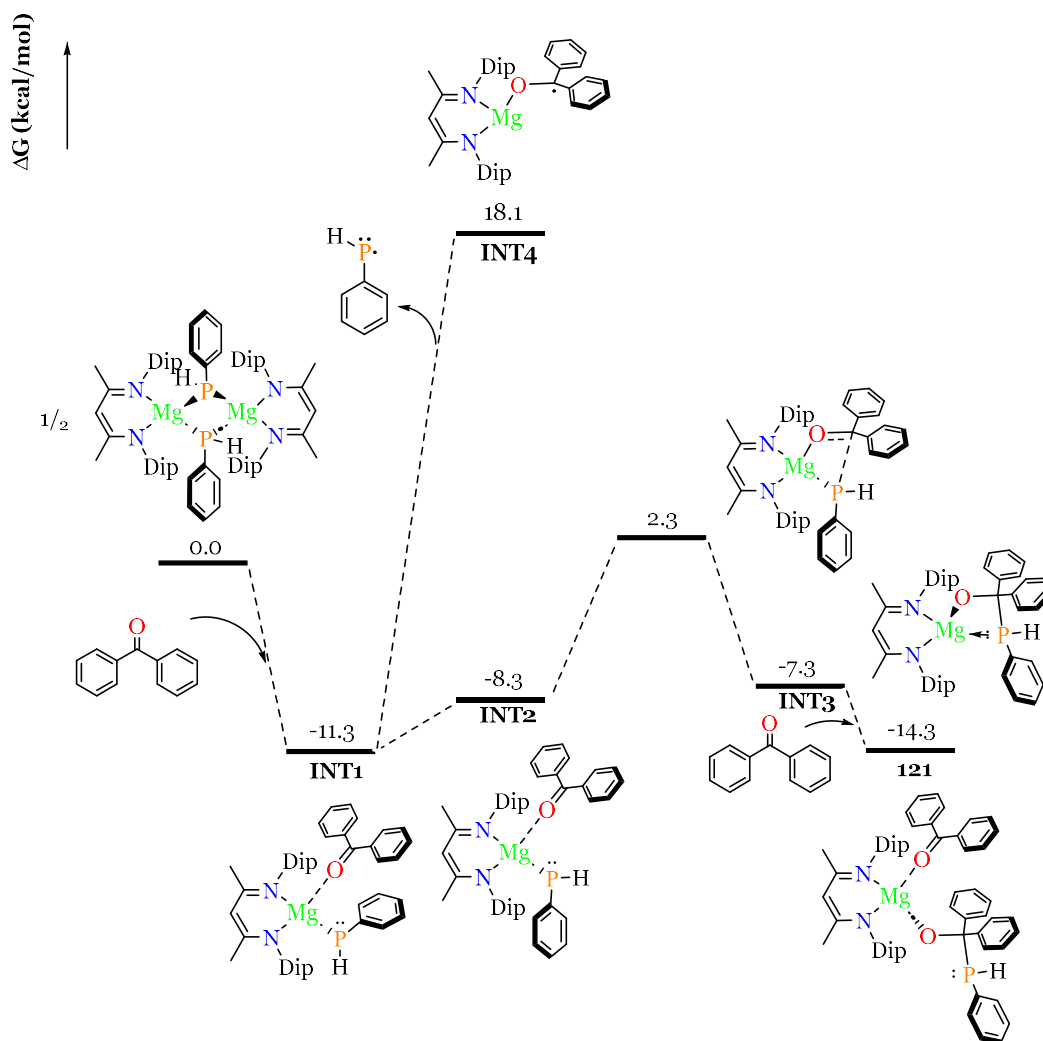
Figure 6. 8. Gibbs Energy profile on the formation of **121** at (PCM:toluene)-B3LYP-D3(BJ)/def2-TZVPP//B3LYP-D3(BJ)/def2-SVP.

The DFT calculations point towards the polar mechanism pathway. However, it does not explain the formation of radicals in the reaction crude. We realized that the formation of radical species persists even after the reaction is complected (see Scheme 6.4). We hypothesized that the radical compound could be formed from the decomposition product of **117**. In the absence of light, ^{31}P-NMR did not evidence any decomposition (Figure 6.9). However, the EPR showed the formation of the radical which with a broad signal with a g-factor of 2.0029, similar observed in the reaction crude. In Figure 6.9, there is the temporal evolution of the double integral of the EPR signal which increases along time. We only detect the radical in a μM concentration, which indicates that the radical evolution is very slow.
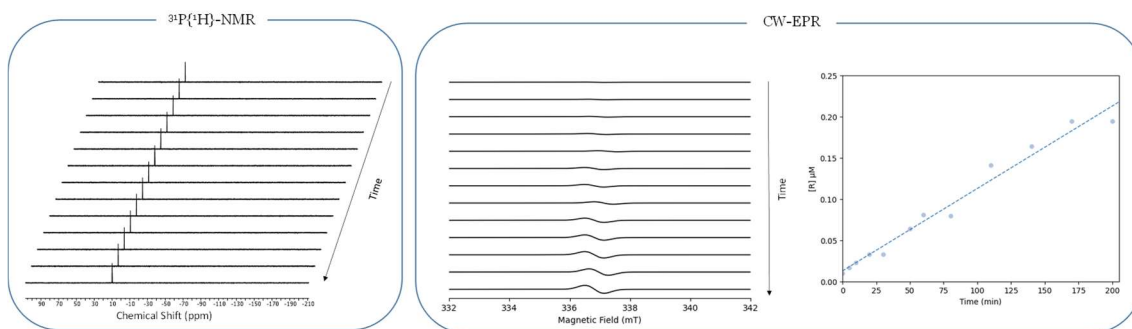
Figure 6. 9. Decomposition of **121** in the absence of light. On the left side, $^{31}P\{^1H\}$-NMR (121.5 MHz, 293 K) of **117** in toluene (1.09 mM) at different interval times. On the right side, CW-EPR spectra of **121** (1.09 mM) in toluene at different interval times.

The feasibility of the C-P homolytic splitting was explored with quantum chemical calculations. We examined the dissociation mechanism of **121** within the DFT framework. In the left side of Figure 6.10 is depicted the PES corresponding to the dissociation of C34-P1 in the singlet (green) and triplet (blue) electronic states. In the singlet curve, from 1.966 Å to 2.716 Å the CSS was found the ground state. However, from 2.866 Å to 3.116 Å the broken-symmetry solution (OSS) is slightly lower in energy than CSS wavefunction, which is consistent with homolytic cleavage of the C-P bond. The dissociation process rises to 27.7 kcal/mol, in agreement with the slow kinetics observed by EPR. The PES of the triplet state is dissociative from 2.116 Å, however it does not cross with the singlet curve in the computed C-P range. To deeply understand the dissociation process, we inspected the charge rearrangement along the C-P dissociation by analysing the fragment partial charges. In the right side of Figure 6.10 is depicted the partial charges of the different fragments, namely PHPh, *reduced* benzophenone (benzophenone 1), coordinative benzophenone (benzophenone 2) and *NacNac*Mg, along the C-P dissociation. In the ground state, the activated benzophenone (red curve) is significantly more charged than the coordinating benzophenone (cyan curve). Upon C-P bond elongation, a charge transfers from the activated benzophenone to [PHPh], while the rest of the fragments remain *innocent* along the scan. At 2.866 Å, the trend is reverted yielding a small charge transfer from [PHPh] to the benzophenone. It coincides with the change of the electronic structure, which switches from CCS to a broken symmetry solution. The spin populations in the PHPh and activated benzophenone fragments are +0.39 *e* and -0.38 *e*, respectively, indicating the radical character on these fragments. The spin polarization along the C-P bond increases for longer distances, reaching a spin population of +0.70 e on [PHPh] and -0.69 e to benzophenone. These results indicate that, along the C-P bond dissociation process, compound **107** *prefers* to decouple the σ-bonding electrons of the C-P bond rather than transferring them to the [PHPh] fragment.
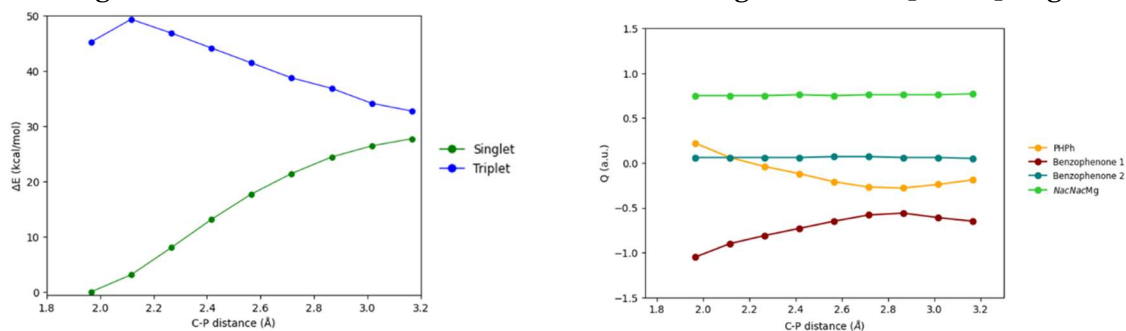
Figure 6. 10. On the left, singlet and triplet potential energy surface (PES) along the C-P bond cleavage at (CPCM:toluene)-uωb97XD/def2-TZVPP//uωB97XD/def2-SVP level of theory. On the right, fragment partial charges in singlet state along the C-P bond cleavage at (CPCM:toluene)-uωb97XD/def2-TZVPP//uωB97XD/def2-SVP level of theory.

6.2.2 Photodissociation of 121

We observed that **121** is light sensitive. Over 30 minutes, we observed how the solution turns from orange to deep blue (Figure 6.11).

0 min   10 min   20 min   30 min
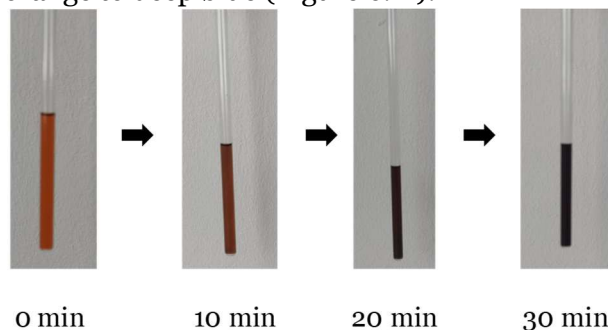
Figure 6. 11. Colour evolution of a solution of **121** under the ambient light at room temperature.

The UV-vis spectrum of compound **121** displays a maximum absorbance in the UV region at λ_{max}(Toluene)=321 nm with a medium extinction coefficient (ε_{max}=1996±42 L•mol^{-1}•cm^{-1}) (See Appenix IV, Figure A-IV.10). Exposing **121** in toluene under UV irradiation (λ=365 nm), the solution rapidly turns from orange to deep blue (See Figure 6.12). The blue colour of the solution suggests the formation of a ketyl radical **125**.[298] The UV-vis spectrum of the irradiated sample shows a new absorbance at λ=608 nm. It is blue-shifted respect to transition metal ketyls, such as K[Fe(Ph$_2$CO)N(SiMe$_3$)$_2$] (λ(Et$_2$O)=581 nm) or K[Co(Ph$_2$CO)N(SiMe$_3$)$_2$] (λ(Et$_2$O)=563 nm), but red-shifted respect to (K[COPh$_2$])$_4$ (λ(THF)=656 nm).[299, 300] We computed UV-Vis spectra of ketyl radical **125** showing an absorption maxima at 562 nm corresponding to a $\pi \rightarrow \pi^*$ transition. The computed spectrum is in good agreement with the experimental one, supporting the formation of **125** upon irradiation of **121**.
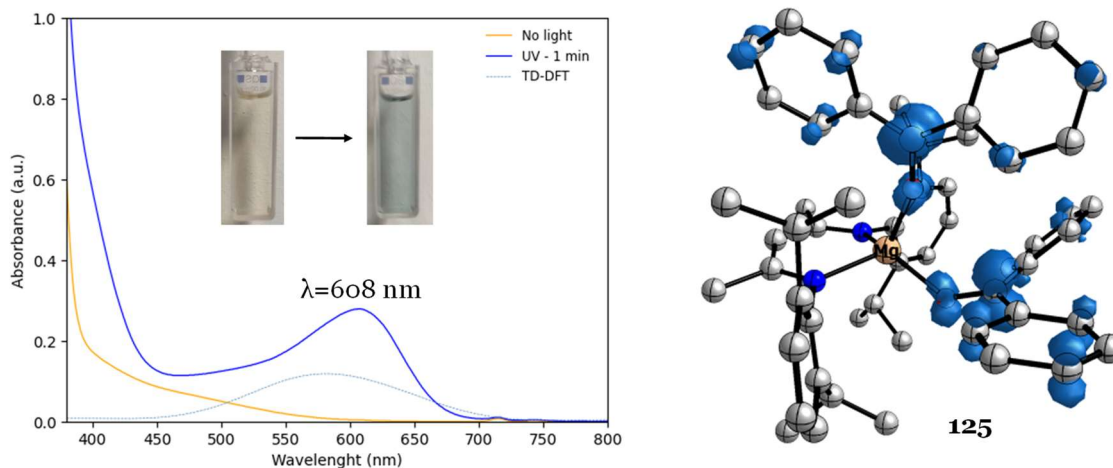
Figure 6. 12 On the left, UV-vis spectra of **121** before (orange line) and after (blue line) UV-irradiation (1 min) and simulated spectra at the PCM:toluene-TD-B3LYP-D3(BJ)/def2-TZVPP//B3LYP-D3(BJ)/def2-SVP. On the right, spin density of **125** at the B3LYP-D3(BJ)/def2-TZVPP//B3LYP-D3(BJ)/def2-SVP.

We qualitatively examined the photolysis of **121** by EPR spectroscopy along 80 min (Figure 6.13, right). The spectra reveal one absorption following a similar profile to the thermal decomposition (Figure 6.13). From 0 min to 50 min, we observed a rapid increase of the radical concentration. Then, from 50 min to 80 min, the radical concentration remains constant. Notably, the radical concentration increases faster than the decomposition in the absence of light (Figure 6.13, right). We examined the ^{31}P-NMR of the crude after 80 min of irradiation (Figure 6.13, left). We observed the resonance of

121 at δ=10.34 ppm and two new resonances assigned to the *meso-* and *rac-* $P_2H_2Ph_2$ diphosphane (δ=-66.38 ppm and -69.69 ppm, respectively).[301] We speculated that they could be formed from the homo-coupling of two phosphanyl radicals (PhPH·).
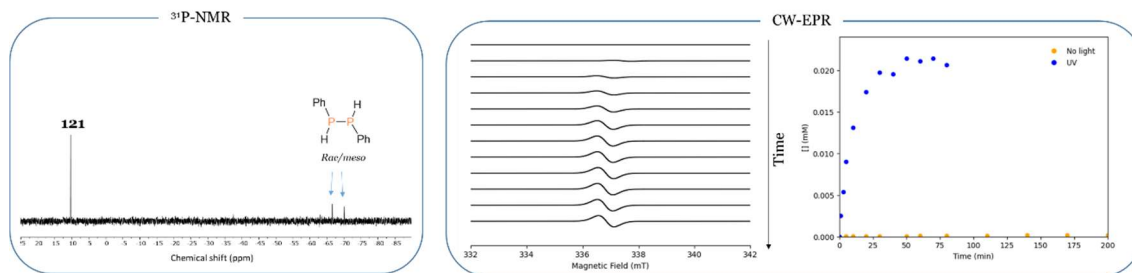
Figure 6. 13 Decomposition of **121** in toluene (1.09 mM) under UV irradiation at room temperature. On the left side, $^{31}P\{^1H\}$-NMR (121.4 MHz, 293 K) after 80 min of UV irradiation. On the right side, CW-EPR spectra of **121** in toluene at different interval times.

The photodissociation reaction of **121** was analysed by TD-DFT. We computed the excitation energies to several excited states along the dissociation path from a model system of **121**, where we replaced the *Dip* substituents of *NacNac* ligand by methyl groups. In Figure 6.14 we show the PES along the C-P bond of the model system (black line) and **121** (dashed grey line). Both curves are almost identical, indicating a good representability of the model system (Figure 6.14). We started analysing the singlet and triplet excited states in the ground state geometry. The transitions are characterized with the oscillator strength (*f*), which measures the probability of the transition, and the contributions of each single excitation (c_a^r), which is the contribution of a pair of orbitals contributes to a given transition. The *a* index refers to the occupied orbital while *r* refers to the empty orbital in their ground state. We examined 25 singlet excited states and 25 triplet excited states. We identified a singlet excited state S_{10} dominated by the transition of HOMO-1 to the LUMO+5 (c_{HOMO-}^{LUMO+} =0.58) with an oscillator strength of *f*=0.2350. The involved orbitals are shown in Figure 6.14. The HOMO-1 is mainly located on the σ bond with some π-contribution of the aryls, while LUMO+5 is located on π system of the aryl substituents and bears antibonding character to the C-P bond. The triplet exited state T_5 possess similar single excitation contributions to S_{10}. It is also dominated by the transition of HOMO-1 to the LUMO+5 (c_{HOMO-}^{LUMO+5}=0.38) but it is a spin-prohibited transition (*f* =0). Since the T_5 is lower in energy than S_1, an intersystem crossing (ISC) might occur from S_{10} →T_5. In fact, the benzophenone is known to undergo S_1 to T_1 ISC very efficently,[302] which it would not be surprising to occur in **121**. The excited state T_5 exhibits a clear dissociative pathway, consistent with the homolytic splitting of the C-P bond.
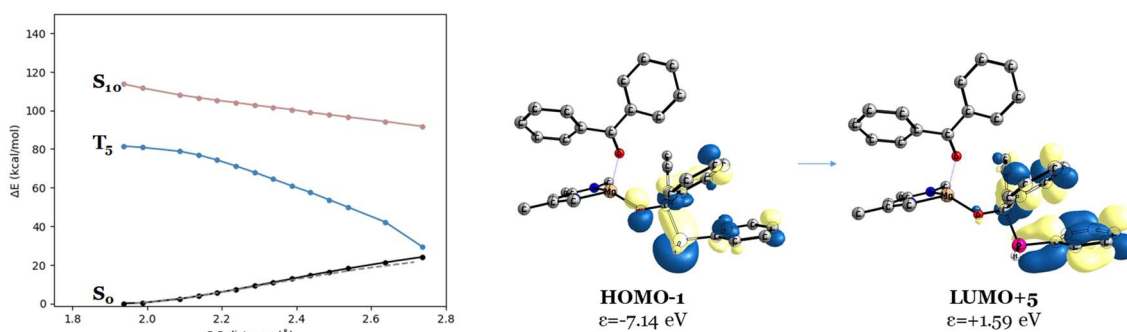
Figure 6. 14 On the left, PES of the (CPCM:toluene)-uωb97XD/def2-TZVPP//uωB97XD/def2-SVP level of theory. On the right, main orbital contributions to the inspected excited states.

All in all, we propose that **121** reaches a triplet state *α*-cleavage homolytically cleaving the C-P bond, yielding ketyl and phosphanyl radicals (Figure 6.15). The

photolysis of **121** has analogies with the photoinitiators (PI). These molecules feature efficient absorption of light generating reactive species such as radicals. The archetypical examples are the acyldiphenylphosphine oxides (ADPO). The irradiation of these molecules undergo triplet state *α*-cleavage to produce the benzoyl and phosphinoyl radicals.[303] Acylgermanes have shown analogous reactivity to ADPO yielding benzoyl and germanium-centred radical.[304]
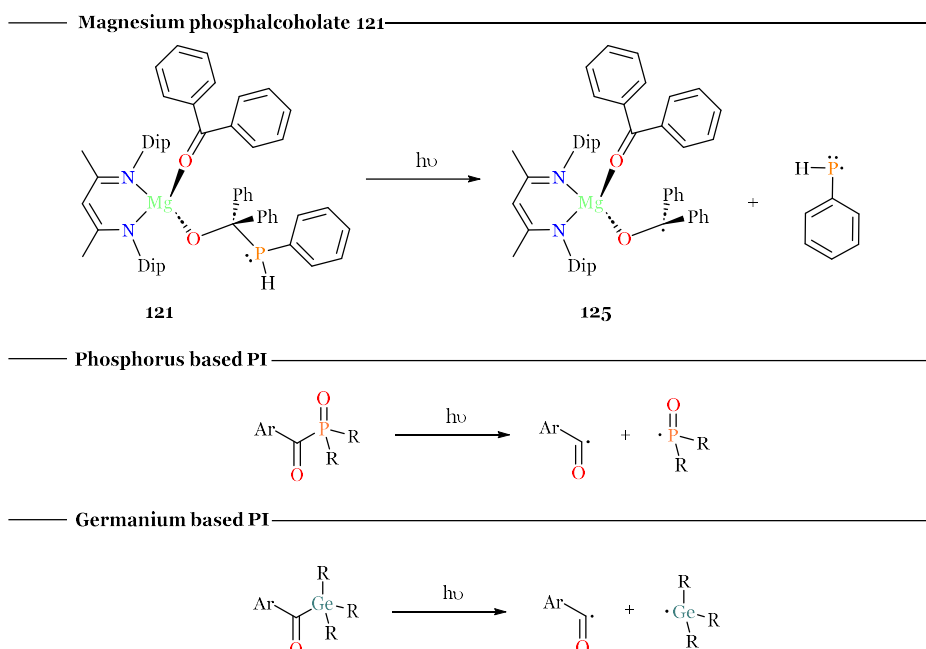
Figure 6. 15 Selected examples of α-cleavage of phosphorus and germanium based PI and **121**.

CHAPTER 7 – Conclusions

The following conclusions stem from this thesis:

In Chapter 3 we provide compelling evidence that the lowest ΔE_{orb} criterion in the context of EDA calculations should not be used in general to establish the best fragmentation and infer from formal oxidation states from it. We show that this criterion cannot properly distinguish proton and hydride character of the simplest 2nd and 3rd row AH_n compounds. It also fails to categorize the oxygen atoms in CO_2 as formally oxo (2-). We show that the energetic criterion is strongly biased towards low oxidation states, because of the high energy of the reference fragments in ionized states.

We introduce a new indicator, namely the inter-Fragment Electron Flow (*iFEF*), making use of the EDA-NOCV orbitals and occupations. We propose the minimization of the *iFEF* index as a much more appropriate and robust criterion to establish the best fragmentation pattern, and hence formal oxidation states. The *iFEF* index can be decomposed by contributions from the different bonding channels in the EDA-NOCV calculation, and it is shown to better account for the electron flow between the fragments than the NOCV eigenvalue itself. The new criterion shows an excellent behaviour in the systems tested, in line with the OS assignations obtained with other state-of-the-art density-based approaches.

In Chapter 4 we introduce the aluminium borohydrides as new building blocks in aluminium chemistry. The *NacNac*Al(BH$_4$)$_2$ resulted to be good synthon for salt metathesis reactions or nucleophilic additions. We show that we can control the mono-substitution for most of the tested nucleophiles, which has barely been reported with *NacNac* haloalumanes. We also explored the nucleophilic addition with an NHC, which displaces the [BH$_4$]$^-$ and deprotonates the *NacNac* backbone. The reaction mechanism was elucidated by blank reactions and quantum chemical calculations. State-of-the-art chemical bonding tools were employed to examine the interaction between aluminium and the BH$_4$ group. The *p*-orbital energy of aluminum is modulated by the nature of the substituent. This modulation results in varied coordination modes of BH$_4$ and influences the strength of the interaction between aluminum and BH$_4$.

Given the proved lability of the BH$_4$ group, we also developed a route to prepare (hydrido)phosphanylalumanes. The reaction of *NacNac*AlH$_2$ with boraphosphines yields the formation of the borohydride group though BH$_3$ transfer. Then, the *in-situ* formation of the phosphide with a base promotes the salt metathesis reaction, leading to the formation of the desired Al-P motif. This route was tested for aryl and alkyl primary phosphines with good to acceptable yields. Unfortunately, the synthetized (hydrido)phosphanylalumanes were not suitable synthons for β-elimination reaction with KHMDS. Instead of activating the P-H bond, we observed the *NacNac* deprotonation, probably because of the poor leaving group quality of the hydride.

We prepared boraphophanylalumanes, where the hydride is replaced by a much better leaving group like BH$_4$. We demonstrate that the *NacNac*Al(BH$_4$)PHPh undergoes the desired *β*-elimination reaction with KHMDS. We were able to isolate a diphosphadialane, which we propose that is formed from a [2+2] cycloaddition of two transient phosphaalumenes.

On the other hand, in this Thesis we uncover that the magnesium borohydrides are also good synthons for salt metathesis reactions, leading to the formation of Mg-P bonds. We achieved the synthesis of a *NacNac* phospha-Grignard reagent using the *NacNac*Mg(Et$_2$O)BH$_4$ as starting material. Alternatively, we also prepared the phospha-Grignard from the *NacNac*Mg(Et$_2$O)I starting material.

The reactivity of the isolated phospha-Grignard was explored towards benzophenone. We observed the nucleophilic addition towards the electrophilic carbon of the ketone, yielding the corresponding magnesium phosphaalcoholate. The reaction was monitored by spectroscopic techniques and the reaction mechanism was elucidated by computational techniques. The analysis of the reaction crude by EPR indicated the formation of an organic radical, but the DFT calculations strongly supported a pairwise pathway over a radical mechanism.

Experimental evidences indicate that the phosphaalcoholate is unstable in solution and it is light sensitive. Monitoring the decomposition in the dark indicate a slow formation of a magnesium ketyl radical, arising from the homolytic splitting of the C-P bond. The photodissociation of the phosphaalcoholate in the presence of UV-light was much faster than in the dark. DFT calculations indicate that the aforementioned homolytic cleavage of the C-P bond can proceed via excitation to a dissociative triplet state.

CHAPTER 8 – Experimental and computational details

All manipulations were carried out under argon atmosphere (Argon 5.0) using Schlenk line techniques or glovebox. The *NacNac*AlH$_2$, Na(dioxane)$_{2.5}$PCO, PhPH$_2$BH$_3$, MesPH$_2$BH$_3$, TipPH$_2$BH$_3$, *t*BuPH$_2$BH$_3$, MesPH$_2$, *NacNac*Mg(Et$_2$O)I, *NacNac*Mg(Et$_2$O)BH$_4$ were synthetized following the established procedures.[33, 258, 305, 306] NMR-spectra were recorded on a Bruker Avance III 400 and 300 spectrometer. ^{1}H and ^{13}C NMR were referenced using benzene, toluene or THF solvent peaks. ^{27}Al, ^{31}P and ^{11}B spectra were referenced with external standards (δ ^{27}Al(AlCl$_3$ in D$_2$O) = 0 ppm, δ ^{31}P (85% H$_3$PO$_4$ in D$_2$O)=0 ppm, δ ^{11}B(Et$_2$O·BF$_3$)= 0 ppm). C$_6$D$_6$ and toluene-d$_8$ were dried over K and vaccum-destilled before storage in the glovebox. The THF-d$_8$ was dried over CaH$_2$ and vaccum-destilled before storage in the glovebox. Fourier transformed infrared spectra (FT-IR) were recorded with a Bruker Vertex 70 spectrometer. Elemental analysis was performed on an Elementar vario Micro cube ®. Single crystal X-ray diffraction was carried out on Bruker AXS X8 Apex CCD and Bruker AXS D8 Venture diffractometers.

The geometry optimizations were performed using the Gaussian16.C01 software.[307] The stationary points were located with the Berny algorithm[308] using redundant internal coordinates. Analytical Hessians were computed to determine the nature of stationary points (one and zero imaginary frequencies for transition states and minima, respectively). Unscaled zero-point energies (ZPEs) and thermal corrections and entropy effects were computed using standard statistical-mechanics relationships for ideal gas. The atomic/fragment charges and bond orders were obtained using Topological Fuzzy Voronoi Cells (TFVC) 3D-space atomic definition, using 40 X 146 atomic grid for numerical integration with APOST-3D program,[309] and Natural Atomic Orbitals (NAO) with NBO.6 software[310] and QTAIM with AIMALL program.[311] The EDA-NOCV analysis was carried out using ADF 2019.103,[312] incorporating the scalar relativistic effects using Zeroth-Order Regular Approximation (ZORA). The Hirshfeld analysis of the NOCVs densities is called through the command "print NOCVHirshfeld".
The atomic/fragment charges and bond orders were obtained using Topological Fuzzy Voronoi Cells (TFVC) 3D-space atomic definition, using 40 x 146 atomic grid for numerical integration with APOST-3D program,[309] and Natural Atomic Orbitals (NAO) with NBO.6 software. [310] The topological analysis of the electron density and the delocalization indexes were done with AIMALL program.[311] The EOS analysis is performed with APOST-3D program. The simulation of UV-Vis spectra was carried out with ORCA software.

In Chapter III, all the optimizations were carried out at the BP86-D3(BJ)/def2-TZVPP level of theory. The chemical bond analysis was performed at the BP86-D3(BJ)/def2-TZVPP and BP86-D3(BJ)/def2-TZ2P level of theory. In the EDA-NOCV calculations, no frozen core approximation is applied. In the NOCV analysis the thresholds are set to RHOKMIN=0.0, EKMIN=0.0 and ENOCV=0.0.

In Chapter IV, all optimizations were computed with BP86,[313, 314]. B3LYP,[315, 316] M06-2X,[317] ωB97X-D3[318] functionals with the def2-SVP basis set.[319]. For BP86 and B3LYP functionals, Grimme dispersion correction D3[320] in combination with the Becke-Jonson damping function[321] were applied. The chemical bond analysis was performed at the B3LYP-D3(BJ)/def2-TZVPP and B3LYP-D3(BJ)/def2-TZ2P level of theory using the

geometries obtained from B3LYP-D3(BJ)/def2-SVP. The energies of the reaction mechanism were corrected CPCM:diethylether-DLPNO-CCSD(T)/cc-pVTZ using "NormalPNO" settings and RI approximation with def2/J and cc-pVTZ/C auxiliary basis set.[322-325] The solvation Gibbs energies were computed at B3LYP-D3BJ/def2-TZVPP using Conductor-like Continuum Polarization Model (CPCM) solvent model.[326]

In Chapter V, all the optimizations were carried out at the B3LYP-D3(BJ)/def2-SVP level of theory. The chemical bond analysis was performed at the B3LYP-D3(BJ)/def2-TZVPP and B3LYP-D3(BJ)/TZ2P level of theory using the geometries at the B3LYP-D3(BJ)/def2-SVP level of theory. The reaction mechanism was computed at the PBE0-D3(BJ)/def2-TZVPP//PBE0-D3(BJ)/def2-SVP using Conductor-like Continuum Polarization Model (CPCM) solvent model.

In Chapter VI, all the optimizations were carried out at the B3LYP-D3(BJ)/def2-SVP level of theory and ωB97X-D3/def2-SVP level of theory. The time-dependent DFT calculations were performed at the ωB97X-D3/def2-TZVPP//ωB97X-D3/def2-SVP level of theory.

CHAPTER 9 – References

1.   Yu, P., *Fundamentals of semiconductors*. Springer: 2005.

2.   Wells, R. L.; Gladfelter, W. L., Pathways to Nanocrystalline III-V (13–15) Compound Semiconductors. *J. Clust. Sci.* **1997,** *8* (2), 217-238.

3.   Schulz, S., Group 13/15 Organometallic Compounds—Synthesis, Structure, Reactivity and Potential Applications. In *Adv. Organomet. Chem.*, Academic Press: 2003; Vol. 49, pp 225-317.

4.   Malik, M. A.; Afzaal, M.; O'Brien, P., Precursor Chemistry for Main Group Elements in Semiconducting Materials. *Chem. Rev.* **2010,** *110* (7), 4417-4446.

5.   Wang, Z.; Wang, G.; Liu, X.; Wang, S.; Wang, T.; Zhang, S.; Yu, J.; Zhao, G.; Zhang, L., Two-dimensional wide band-gap nitride semiconductor GaN and AlN materials: properties, fabrication and applications. *J. Mater. Chem. C* **2021,** *9* (48), 17201-17232.

6.   Dankert, F.; Hering-Junghans, C., Heavier group 13/15 multiple bond systems: synthesis, structure and chemical bond activation. *Chem. Comm.* **2022,** *58* (9), 1242-1262.

7.   Roy, M. M. D.; Omaña, A. A.; Wilson, A. S. S.; Hill, M. S.; Aldridge, S.; Rivard, E., Molecular Main Group Metal Hydrides. *Chem. Rev.* **2021,** *121* (20), 12784-12965.

8.   Power, P. P., Main-group elements as transition metals. *Nature* **2010,** *463* (7278), 171-177.

9.   Aldridge, S.; Downs, A. J., Hydrides of the Main-Group Metals: New Variations on an Old Theme. *Chem. Rev.* **2001,** *101* (11), 3305-3366.

10.   Lai, Q.; Sun, Y.; Wang, T.; Modi, P.; Cazorla, C.; Demirci, U. B.; Ares Fernandez, J. R.; Leardini, F.; Aguey-Zinsou, K.-F., How to Design Hydrogen Storage Materials? Fundamentals, Synthesis, and Storage Tanks. *Adv. Sustain. Syst.* **2019,** *3* (9), 1900043.

11.   Yang, Z.; Zhong, M. D.; Ma, X. L.; Nijesh, K.; De, S.; Parameswaran, P.; Roesky, H. W., An Aluminum Dihydride Working as a Catalyst in Hydroboration and Dehydrocoupling. *J. Am. Chem. Soc.* **2016,** *138* (8), 2548-2551.

12.   Yang, Z.; Zhong, M.; Ma, X.; De, S.; Anusha, C.; Parameswaran, P.; Roesky, H. W., An Aluminum Hydride That Functions like a Transition-Metal Catalyst. *Angew. Chem. Int. Ed,* **2015,** *54* (35), 10225-10229.

13.   Stecher, O.; Wiberg, E., Über einen nichtflüchtigen, polymeren Aluminiumwasserstoff $(AlH_3)_x$ und einige flüchtige Verbindungen des monomeren AlH_3. *Ber. Dtsch. Chem.* **1942,** *75* (12), 2003-2012.

14.   Brower, F. M.; Matzek, N. E.; Reigler, P. F.; Rinn, H. W.; Roberts, C. B.; Schmidt, D. L.; Snover, J. A.; Terada, K., Preparation and properties of aluminum hydride. *J. Am. Chem. Soc.* **1976,** *98* (9), 2450-2453.

15.   Kurth, F. A.; Eberlein, R. A.; Schnöckel, H.; Downs, A. J.; Pulham, C. R., Molecular aluminium trihydride, AlH_3: generation in a solid noble gas matrix and characterisation by its infrared spectrum and Ab initio calculations. *Chem Comm* **1993,** (16), 1302-1304.

16.   Pullumbi, P.; Bouteiller, Y.; Manceron, L.; Mijoule, C., Aluminium, gallium and indium trihydrides. an IR matrix isolation and ab initio study. *Chem. Phys.* **1994,** *185* (1), 25-37.

17.   Wang, X.; Andrews, L.; Tam, S.; DeRose, M. E.; Fajardo, M. E., Infrared Spectra of Aluminum Hydrides in Solid Hydrogen: Al_2H_4 and Al_2H_6. *J. Am. Chem. Soc.* **2003,** *125* (30), 9218-9228.

18.   Schneider, H.; Hock, A.; Bertermann, R.; Radius, U., Reactivity of NHC Alane Adducts towards N-Heterocyclic Carbenes and Cyclic (Alkyl)(amino)carbenes: Ring Expansion, Ring Opening, and Al–H Bond Activation. *Chem. Eur. J* **2017,** *23* (50), 12387-12398.

19.   Cao, L. L.; Daley, E.; Johnstone, T. C.; Stephan, D. W., Cationic aluminum hydride complexes: reactions of carbene–alane adducts with trityl-borate. *Chem Comm* **2016,** *52* (30), 5305-5307.

20.   Bonyhady, S. J.; Collis, D.; Frenking, G.; Holzmann, N.; Jones, C.; Stasch, A., Synthesis of a stable adduct of dialane(4) (Al_2H_4) via hydrogenation of a magnesium(I) dimer. *Nat. Chem.* **2010,** *2* (10), 865-869.

21.   Mellerup, S. K.; Cui, Y.; Fantuzzi, F.; Schmid, P.; Goettel, J. T.; Bélanger-Chabot, G.; Arrowsmith, M.; Krummenacher, I.; Ye, Q.; Engel, V.; Engels, B.; Braunschweig, H., Lewis-Base Stabilization of the Parent Al(I) Hydride under Ambient Conditions. *J. Am. Chem. Soc.* **2019,** *141* (42), 16954-16960.

22.   Nagata, K.; Murosaki, T.; Agou, T.; Sasamori, T.; Matsuo, T.; Tokitoh, N., Activation of Dihydrogen by Masked Doubly Bonded Aluminum Species. *Angew. Chem. Int. Ed.* **2016,** *55* (41), 12877-12880.

23.   Wehmschulte, R. J.; Power, P. P., Synthesis and Characterization of [Mes*AlH₂]₂ (Mes* = 2,4,6-(tert-Bu)$_3$C$_6$H$_2$): A Base-Free Arylalane. *Inorg. Chem.* **1994,** *33* (25), 5611-5612.

24.   Fettinger, J. C.; Gray, P. A.; Melton, C. E.; Power, P. P., Hydroalumination of Alkenes and Alkynes by Primary Aluminum Hydrides under Mild Conditions. *Organometallics* **2014,** *33* (21), 6232-6240.

25.   Contreras, L.; Cowley, A. H.; Gabbaï, F. P.; Jones, R. A.; Carrano, C. J.; Bond, M. R., An intramolecularly base-stabilized monomeric organoaluminum dihydride. *J. Organomet. Chem.* **1995,** *489* (1), C1-C3.

26.   Cowley, A. H.; Gabbaï, F. P.; Isom, H. S.; Decken, A., New developments in the chemistry of organoaluminum and organogallium hydrides. *J. Organomet. Chem.* **1995,** *500* (1), 81-88.

27.   Dias, H. V. R.; Jin, W.; Ratcliff, R. E., Aluminum Derivatives of N-Isopropyl-2-(isopropylamino)troponimine. *Inorg Chem* **1995,** *34* (24), 6100-6105.

28.   Parks, J. E.; Holm, R. H., Synthesis, solution stereochemistry, and electron delocalization properties of bis(β-iminoamino)nickel(II) complexes. *Inorg. Chem.* **1968,** *7* (7), 1408-1416.

29.   Bourget-Merle, L.; Lappert, M. F.; Severn, J. R., The Chemistry of β-Diketiminatometal Complexes. *Chem. Rev.* **2002,** *102* (9), 3031-3066.

30.   Chamberlain, B. M.; Cheng, M.; Moore, D. R.; Ovitt, T. M.; Lobkovsky, E. B.; Coates, G. W., Polymerization of Lactide with Zinc and Magnesium β-Diiminate Complexes: Stereocontrol and Mechanism. *J. Am. Chem. Soc.* **2001,** *123* (14), 3229-3238.

31.   Basuli, F.; Aneetha, H.; Huffman, J. C.; Mindiola, D. J., A Fluorobenzene Adduct of Ti(IV), and Catalytic Carboamination to Prepare α,β-Unsaturated Imines and Triaryl-Substituted Quinolines. *J. Am. Chem. Soc.* **2005,** *127* (51), 17992-17993.

32.   Cui, C.; Roesky, H. W.; Hao, H.; Schmidt, H.-G.; Noltemeyer, M., The First Structurally Characterized Metal–SeH Compounds: [LAl(SeH)$_2$] and [L(HSe)AlSeAl(SeH)L]. *Angew. Chem. Int. Ed.* **2000,** *39* (10), 1815-1817.

33.   Yang, Z.; Zhong, M. D.; Ma, X. L.; Nijesh, K.; De, S.; Parameswaran, P.; Roesky, H. W., An Aluminum Dihydride Working as a Catalyst in Hydroboration and Dehydrocoupling. *J. Am. Chem. Soc.* **2016,** *138* (8), 2548-2551.

34.   Cui, C.; Roesky, H. W.; Schmidt, H.-G.; Noltemeyer, M.; Hao, H.; Cimpoesu, F., Synthesis and Structure of a Monomeric Aluminum(I) Compound [{HC(CMeNAr)2}Al] (Ar=2,6–iPr2C6H3): A Stable Aluminum Analogue of a Carbene. *Angew. Chem. Int. Ed.* **2000,** *39* (23), 4274-4276.

35.   Chu, T.; Korobkov, I.; Nikonov, G. I., Oxidative Addition of σ Bonds to an Al(I) Center. *J. Am. Chem. Soc.* **2014,** *136* (25), 9195-9202.

36.   González-Gallardo, S.; Jancik, V.; Cea-Olivares, R.; Toscano, R. A.; Moya-Cabrera, M., Preparation of Molecular Alumoxane Hydrides, Hydroxides, and Hydrogensulfides. *Angew Chem Int Ed* **2007,** *46* (16), 2895-2898.

37. Yang, Z.; Hao, P.; Liu, Z.; Ma, X.; Roesky, H. W.; Sun, K.; Li, J., Reactivity Studies of LAlH$_2$ (L =HC(CMeNAr)$_2$, Ar = 2,6-iPr$_2$C$_6$H$_3$) with 2-Aminobenzenethiol, 2-Aminophenol, and 1,4-Dithiane-2,5-diol. *Organometallics* **2012,** *31* (17), 6500-6503.

38. Liu, Y.; Ma, X.; Ding, Y.; Yang, Z.; Roesky, H. W., N-Tosyl Hydrazone Precursor for Diazo Compounds as Intermediates in the Synthesis of Aluminum Complexes. *Organometallics* **2018,** *37* (21), 3839-3845.

39. Jancik, V.; Peng, Y.; Roesky, H. W.; Li, J.; Neculai, D.; Neculai, A. M.; Herbst-Irmer, R., The First Structurally Characterized Aluminum Compound with Two SH Groups: [LAl(SH)$_2$] (L = N(Ar)C(Me)CHC(Me)N(Ar), Ar = 2,6-i-Pr2C$_6$H$_3$) and the Catalytic Properties of the Sulfur P(NMe$_2$)$_3$ System. *J. Am. Chem. Soc.* **2003,** *125* (6), 1452-1453.

40. Yang, Z.; Zhong, M.; Ma, X.; De, S.; Anusha, C.; Parameswaran, P.; Roesky, H. W., An Aluminum Hydride That Functions like a Transition-Metal Catalyst. *Angew. Chem. Int. Ed.* **2015,** *127* (35), 10363-10367.

41. Jakobsson, K.; Chu, T.; Nikonov, G. I., Hydrosilylation of Olefins Catalyzed by Well-Defined Cationic Aluminum Complexes: Lewis Acid versus Insertion Mechanisms. *ACS Catal.* **2016,** *6* (11), 7350-7356.

42. Ganesamoorthy, C.; Loerke, S.; Gemel, C.; Jerabek, P.; Winter, M.; Frenking, G.; Fischer, R. A., Reductive elimination: a pathway to low-valent aluminium species. *Chem Comm* **2013,** *49* (28), 2858-2860.

43. Brand, S.; Elsen, H.; Langer, J.; Grams, S.; Harder, S., Calcium-Catalyzed Arene C−H Bond Activation by Low-Valent Al(I). *Angew Chem Int Ed* **2019,** *58* (43), 15496-15503.

44. Butler, M. J.; Crimmin, M. R., Magnesium, zinc, aluminium and gallium hydride complexes of the transition metals. *Chem Comm* **2017,** *53* (8), 1348-1365.

45. Riddlestone, I. M.; Edmonds, S.; Kaufman, P. A.; Urbano, J.; Bates, J. I.; Kelly, M. J.; Thompson, A. L.; Taylor, R.; Aldridge, S., σ-Alane Complexes of Chromium, Tungsten, and Manganese. *J. Am. Chem. Soc.* **2012,** *134* (5), 2551-2554.

46. Abdalla, J. A. B.; Riddlestone, I. M.; Turner, J.; Kaufman, P. A.; Tirfoin, R.; Phillips, N.; Aldridge, S., Coordination and Activation of Al-H and Ga-H Bonds. *Chem. Eur. J* **2014,** *20* (52), 17624-17634.

47. Batuecas, M.; Gorgas, N.; Crimmin, M. R., Catalytic C−H to C−M (M = Al, Mg) bond transformations with heterometallic complexes. *Chem. Sci.* **2021,** *12* (6), 1993-2000.

48. Chen, W.; Hooper, T. N.; Ng, J.; White, A. J. P.; Crimmin, M. R., Palladium-Catalyzed Carbon−Fluorine and Carbon−Hydrogen Bond Alumination of Fluoroarenes and Heteroarenes. *Angew Chem Int Ed* **2017,** *56* (41), 12687-12691.

49.   Hooper, T. N.; Garçon, M.; White, A. J. P.; Crimmin, M. R., Room temperature catalytic carbon–hydrogen bond alumination of unactivated arenes: mechanism and selectivity. *Chem. Sci.* **2018,** *9* (24), 5435-5440.

50.   Ekkert, O.; White, A. J. P.; Toms, H.; Crimmin, M. R., Addition of aluminium, zinc and magnesium hydrides to rhodium(iii). *Chem Sci* **2015,** *6* (10), 5617-5622.

51.   Hooper, T. N.; Lau, S.; Chen, W.; Brown, R. K.; Garçon, M.; Luong, K.; Barrow, N. S.; Tatton, A. S.; Sackman, G. A.; Richardson, C.; White, A. J. P.; Cooper, R. I.; Edwards, A. J.; Casely, I. J.; Crimmin, M. R., The partial dehydrogenation of aluminium dihydrides. *Chem. Sci.* **2019,** *10* (35), 8083-8093.

52.   Gorgas, N.; White, A. J. P.; Crimmin, M. R., Cooperative C–H Bond Activation by a Low-Spin d^6 Iron–Aluminum Complex. *J. Am. Chem. Soc.* **2022,** *144* (19), 8770-8777.

53.   Stadler, B.; Gorgas, N.; White, A. J.; Crimmin, M. R., Double Deprotonation of CH$_3$CN by an Iron-Aluminium Complex. *Angew. Chem. Int. Ed.* **2023,** *135* (16), e202219212.

54.   Marks, T. J.; Kolb, J. R., Covalent Transition-Metal, Lanthanide, and Actinide Tetrahydroborate Complexes. *Chem. Rev.* **1977,** *77* (2), 263-293.

55.   Visseaux, M.; Bonnet, F., Borohydride complexes of rare earths, and their applications in various organic transformations. *Coord. Chem. Rev.* **2011,** *255* (3-4), 374-420.

56.   Besora, M.; Lledós, A., Coordination modes and hydride exchange dynamics in transition metal tetrahydroborate complexes. In *Contemporary Metal Boron Chemistry I*, 2007; pp 149-202.

57.   Guo, R.; Chen, X.; Elpelt, C.; Song, D.; Morris, R. H., Applications of ruthenium hydride borohydride complexes containing phosphinite and diamine ligands to asymmetric catalytic reactions. *Org. Lett.* **2005,** *7* (9), 1757-9.

58.   Langer, R.; Iron, M. A.; Konstantinovski, L.; Diskin-Posner, Y.; Leitus, G.; Ben-David, Y.; Milstein, D., Iron borohydride pincer complexes for the efficient hydrogenation of ketones under mild, base-free conditions: synthesis and mechanistic insight. *Chem. Eur. J* **2012,** *18* (23), 7196-209.

59.   Hu, X.; Soleilhavoup, M.; Melaimi, M.; Chu, J.; Bertrand, G., Air-Stable (CAAC)CuCl and (CAAC)CuBH$_4$ Complexes as Catalysts for the Hydrolytic Dehydrogenation of BH$_3$NH$_3$. *Angew. Chem. Int. Ed.* **2015,** *127* (20), 6106-6109.

60.   Hall, C.; Perutz, R. N., Transition Metal Alkane Complexes. *Chem. Rev.* **1996,** *96* (8), 3125-3146.

61.   Cendrowski-Guillaume, S. M.; Le Gland, G.; Nierlich, M.; Ephritikhine, M., Lanthanide borohydrides as precursors to organometallic compounds.

Mono(cyclooctatetraenyl) neodymium complexes. *Organometallics* **2000,** *19* (26), 5654-5660.

62. Schlesinger, H. I.; Sanderson, R. T.; Burg, A. B., A volatile compound of aluminum, boron and hydrogen. *J. Am. Chem. Soc.* **1939,** *61* (2), 536-536.

63. Schlesinger, H. I.; Sanderson, R. T.; Burg, A. B., Metallo Borohydrides. I. Aluminum Borohydride. *J. Am. Chem. Soc.* **1940,** *62* (12), 3421-3425.

64. Aldridge, S.; J. Blake, A.; J. Downs, A.; O. Gould, R.; Parsons, S.; R. Pulham, C., Some tetrahydroborate derivatives of aluminium: crystal structures of dimethylaluminium tetrahydroborate and the α and β phases of aluminium tris(tetrahydroborate) at low temperature. *Dalton Trans* **1997,** (6), 1007-1012.

65. Kollonitsch, J.; Fuchs, O., Preparation of Aluminium Borohydride and Its Applications in Organic Reductions. *Nature* **1955,** *176* (4492), 1081-1081.

66. Dovgaliuk, I.; Le Duff, C. S.; Robeyns, K.; Devillers, M.; Filinchuk, Y., Mild Dehydrogenation of Ammonia Borane Complexed with Aluminum Borohydride. *Chem Mater* **2015,** *27* (3), 768-777.

67. Bird, P. H.; Wallbridge, M., A study of metal borohydrides. The reaction of aluminium borohydride with various ligand molecules. *J. Am. Chem. Soc.* **1965**, 3923-3928.

68. Bailey, N.; Bird, P.; Wallbridge, M., Crystal structure of aluminum tetrahydroborate-trimethylamine at 25 and-160. deg. *Inorg Chem* **1968,** *7* (8), 1575-1581.

69. Titov, L. V.; Krasnoperova, V. D.; Rosolovskii, V. Y., Tetrabutylammonium aluminum hydride and its reaction with diborane. *Bull. Acad. Sci. USSR, Div. Chem. Sci.* **1972,** *21* (4), 716-718.

70. Ehemann, M.; Nöth, H.; Schmidt-Sudhoff, G., Metallboranate und Boranatometallate. VII. [11]B-kernresonanzspektroskopische Untersuchungen der Systeme $LiBH_4/Al(BH_4)_3$/Äther und $LiBH_4/Al(BH_4)_3$/Tetra-hydrofuran: Zur Frage der Existenz des Tripelhydrids Lithium-tetraboranato-aluminat $LiAl(BH_4)_4$. *Z. Anorg. Allg. Chem.* **1972,** *394* (1-2), 33-52.

71. Dou, D.; Liu, J.; Bauer, J. A. K.; Jordan IV, G. T.; Shore, S. G., Synthesis and Structure of Triphenylmethylphosphonium Tetrakis (tetrahydroborato) Aluminate, $[Ph_3MeP][Al(BH_4)_4]$, an Example of Eight-Coordinate Aluminum (III). *Inorg. Chem.* **1994,** *33* (24), 5443-5447.

72. Dovgaliuk, I.; Ban, V.; Sadikin, Y.; Cerny, R.; Aranda, L.; Casati, N.; Devillers, M.; Filinchuk, Y., The first halide-free bimetallic aluminum borohydride: synthesis, structure, stability, and decomposition pathway. *J. Phys. Chem. C* **2014,** *118* (1), 145-153.

73.   Schneider, S.; Hawkins, T.; Ahmed, Y.; Rosander, M.; Hudgens, L.; Mills, J., Green bipropellants: Hydrogen-rich ionic liquids that are hypergolic with hydrogen peroxide. *Angew. Chem. Int. Ed.* **2011,** *123* (26), 6008-6010.

74.   Bissinger, P.; Mikulcik, P.; Riede, J.; Schier, A.; Schmidbaur, H., Dimethylsiloxy-aluminiumdihalide dimers. Molecular structures of $[Me_2HSiOAlX_2]_2$ (X= Cl, I) and $[Me_3SiOAl (BH_4)_2]_2$. *J. Organomet. Chem.* **1993,** *446* (1-2), 37-43.

75.   Franz, D.; Irran, E.; Inoue, S., Synthesis, characterization and reactivity of an imidazolin-2-iminato aluminium dihydride. *Dalton Trans.* **2014,** *43* (11), 4451-61.

76.   Harder, S.; Spielmann, J., Unprecedented reactivity of an aluminium hydride complex with ArNH 2 BH 3: nucleophilic substitution versus deprotonation. *Chem. Comm.* **2011,** *47* (43), 11945-11947.

77.   Less, R. J.; Hanf, S.; García-Rodríguez, R.; Bond, A. D.; Wright, D. S., A $[HN(BH=NH_2)_2]^-$ dianion, Isoelectronic with a β-Diketiminate. *Organometallics* **2017,** *37* (5), 628-631.

78.   Caise, A.; Kolychev, E. L.; Hicks, J.; Fuentes, M. A.; Goicoechea, J. M.; Aldridge, S., Reversible borohydride formation from aluminium hydrides and {H(9-BBN)}₂: structural, thermodynamic and reactivity studies. *Dalton. Trans.* **2019,** *48* (29), 10845-10852.

79.   Stender, M.; Eichler, B. E.; Hardman, N. J.; Power, P. P.; Prust, J.; Noltemeyer, M.; Roesky, H. W., Synthesis and Characterization of $HC\{C(Me)N(C_6H_3-2,6-i-Pr_2)\}_2MX_2$ (M = Al, X = Cl, I; M = Ga, In, X = Me, Cl, I): Sterically Encumbered β-Diketiminate Group 13 Metal Derivatives. *Inorg Chem* **2001,** *40* (12), 2794-2799.

80.   Yang, Y.; Schulz, T.; John, M.; Ringe, A.; Roesky, H. W.; Stalke, D.; Magull, J.; Ye, H., Synthesis, characterization, and reaction of aluminum halide amides supported by a bulky beta-diketiminato ligand. *Inorg. Chem.* **2008,** *47* (7), 2585-92.

81.   Solis-Ibarra, D.; Gómora-Figueroa, A. P.; Zavala-Segovia, N.; Jancik, V., β-Diketiminate Gallium Amides: Useful Synthons in Gallium Chemistry. *Eur. J. Inorg. Chem.* **2009,** *2009* (29-30), 4564-4571.

82.   Liu, Z.; Lee, J. H. Q.; Ganguly, R.; Vidović, D., A Well-Defined Aluminum-Based Lewis Acid as an Effective Catalyst for Diels–Alder Transformations. *Chem. Eur. J.* **2015,** *21* (32), 11344-11348.

83.   Li, J.; Wu, P.; Jiang, W.; Li, B.; Wang, B.; Zhu, H.; Roesky, H. W., An Unusual and Facile Synthetic Route to Alumoles. *Angew. Chem. Int. Ed.* **2020,** *59* (25), 10027-10031.

84.   Abdalla, J. A. B.; Riddlestone, I. M.; Tirfoin, R.; Aldridge, S., Cooperative Bond Activation and Catalytic Reduction of Carbon Dioxide at a Group 13 Metal Center. *Angew. Chem. Int. Ed.* **2015,** *54* (17), 5098-5102.

85.   Timoshkin, A. Y., Group 13 imido metallanes and their heavier analogs [RMYR′]n (M=Al, Ga, In; Y=N, P, As, Sb). *Coord. Chem. Rev.* **2005,** *249* (19), 2094-2131.

86.   Davidson, N.; Brown, H. C., The Polymerization of Some Derivatives of Trimethylaluminum. *J. Am. Chem. Soc.* **1942,** *64* (2), 316-324.

87.   Fritz, G.; Trenczek, G., Die Bildung von $|(C_2H_5)_2PAlCl_2|_3$ aus $LiP(C_2H_5)_2$ und $AlCl_3$. *Z. Anorg. Allg. Chem.* **1961,** *313* (3-4), 236-240.

88.   Fritz, G.; Trenczek, G., $[H_2Al-P (C_2H_5)_2]_3$ und $Li[AlH_2\{P(C_2H_5)_2\}_2]$. *Angew. Chem.* **1963,** *75* (15), 723-723.

89.   Janik, J. F.; Duesler, E. N.; McNamara, W. F.; Westerhausen, M.; Paine, R. T., Synthesis and characterization of phosphinosilylalanes from $[(CH_3)_3Si]_3Al$. Crystal and molecular structure determinations of $\{[(CH_3)_3Si]_2AlP(C_6H_5)_2\}$ $_2, \{[(CH_3)_3Si]_2AlP(C_6H_5)[Si(CH_3)_3]\}$ $_2, \{[(CH_3)_3Si]_2AlP(H)(c-C_6H_{11})\}_3$, and $[\{[(CH_3)_3Si]_2N\}(C_6H_5)P]$ $_2$. *Organometallics* **1989,** *8* (2), 506-514.

90.   Wehmschulte, R. J.; Ruhlandt-Senge, K.; Power, P. P., Synthesis and Characterization of Unassociated Aluminum Monophosphides. *Inorg. Chem.* **1994,** *33* (15), 3205-3207.

91.   Driess, M.; Kuntz, S.; Merz, K.; Pritzkow, H., Novel Molecular Clusters Having Aluminum–Phosphorus, Aluminum–Arsenic, and Gallium–Arsenic Skeletons, and Synthesis of an Al4As6Li4 Rhombododecahedron. *Chem. Eur. J.* **1998,** *4* (9), 1628-1632.

92.   Kapitein, M.; Balmer, M.; Niemeier, L.; von Hänisch, C., Cyclic NHC-stabilized silylphosphinoalanes and -gallanes. *Dalton Trans* **2016,** *45* (14), 6275-6281.

93.   Tessier-Youngs, C.; Bueno, C.; Beachley, O. T., Jr.; Churchill, M. R., Transition-metal complexes of organoaluminum phosphides. Synthesis, characterization, and crystal and molecular structure of $Cr(CO)_5(PPh_2Al)(CH_2SiMe_3)_2NMe_3$. *Inorg Chem* **1983,** *22* (7), 1054-1059.

94.   Vogel, U.; Timoshkin, A. Y.; Scheer, M., Lewis Acid/Base Stabilized Phosphanylalane and -gallane. *Angew Chem Int Ed* **2001,** *40* (23), 4409-4412.

95.   Weinhart, M. A. K.; Lisovenko, A. S.; Timoshkin, A. Y.; Scheer, M., Phosphanylalanes and Phosphanylgallanes Stabilized only by a Lewis Base. *Angew Chem Int Ed* **2020,** *59* (14), 5541-5545.

96.   Haider, W.; Calvin-Brown, M. D.; Bischoff, I.-A.; Huch, V.; Morgenstern, B.; Müller, C.; Sergeieva, T.; Andrada, D. M.; Schäfer, A., Diarylpnictogenyldialkylalanes—Synthesis, Structures, Bonding Analysis, and CO_2 Capture. *Inorg Chem* **2022,** *61* (3), 1672-1684.

97.   Agou, T.; Ikeda, S.; Sasamori, T.; Tokitoh, N., Synthesis and Structure of Lewis Base-Coordinated Phosphanylalumanes Bearing P−H and Al−Br Moieties. *Eur. J. Inorg. Chem.* **2018,** *2018* (19), 1984-1987.

98.   Li, B.; Bauer, S.; Seidl, M.; Timoshkin, A. Y.; Scheer, M., Monomeric β-Diketiminato Group 13 Metal Dipnictogenide Complexes with Two Terminal EH2 Groups (E=P, As). *Chem. Eur. J* **2019,** *25* (60), 13714-13718.

99.   Mulliken, R. S., Overlap Integrals and Chemical Binding1. *J. Am. Chem. Soc.* **1950,** *72* (10), 4493-4503.

100.   Pitzer, K. S., Repulsive Forces in Relation to Bond Energies, Distances and Other Properties. *J. Am. Chem. Soc.* **1948,** *70* (6), 2140-2145.

101.   Jutzi, P., New Element-Carbon (p-p)π Bonds. *Angew. Chem. Int. Ed.* **1975,** *14* (4), 232-245.

102.   Goldberg, D. E.; Harris, D. H.; Lappert, M. F.; Thomas, K. M., A new synthesis of divalent group 4B alkyls M[CH(SiMe$_3$)$_2$]$_2$(M = Ge or Sn), and the crystal and molecular and molecular strcuture of the tin compound. *J. Chem. Soc., Chem. Comm.* **1976,** (7), 261-262.

103.   West, R.; Fink, M. J.; Michl, J., Tetramesityldisilene, a Stable Compound Containing a Silicon-Silicon Double Bond. *Science* **1981,** *214* (4527), 1343-1344.

104.   Yoshifuji, M.; Shima, I.; Inamoto, N.; Hirotsu, K.; Higuchi, T., Synthesis and structure of bis(2,4,6-tri-tert-butylphenyl)diphosphene: isolation of a true phosphobenzene. *J. Am. Chem. Soc.* **1981,** *103* (15), 4587-4589.

105.   Stender, M.; Phillips, A. D.; Wright, R. J.; Power, P. P., Synthesis and Characterization of a Digermanium Analogue of an Alkyne. *Angew Chem Int Ed* **2002,** *41* (10), 1785-1787.

106.   Pu, L.; Twamley, B.; Power, P. P., Synthesis and Characterization of 2,6-Trip$_2$H$_3$C$_6$PbPbC$_6$H$_3$-2,6-Trip$_2$ (Trip = C$_6$H2-2,4,6-i-Pr$_3$): A Stable Heavier Group 14 Element Analogue of an Alkyne. *J. Am. Chem. Soc.* **2000,** *122* (14), 3524-3525.

107.   Phillips, A. D.; Wright, R. J.; Olmstead, M. M.; Power, P. P., Synthesis and Characterization of 2,6-Dipp$_2$-H$_3$C$_6$SnSnC$_6$H$_3$-2,6-Dipp$_2$ (Dipp = C$_6$H$_3$-2,6-Pri$_2$): A Tin Analogue of an Alkyne. *J. Am. Chem. Soc.* **2002,** *124* (21), 5930-5931.

108.   Sekiguchi, A.; Kinjo, R.; Ichinohe, M., A Stable Compound Containing a Silicon-Silicon Triple Bond. *Science* **2004,** *305* (5691), 1755-1757.

109.   Power, P. P., π-Bonding and the Lone Pair Effect in Multiple Bonds between Heavier Main Group Elements. *Chem. Rev.* **1999,** *99* (12), 3463-3504.

110.   Knight, L. B., Jr.; Kerr, K.; Miller, P. K.; Arrington, C. A., ESR Investigation of the HBBH(X3Σ) Radical in Neon and Argon Matrixes at 4 K. Comparison with ab Initio SCF and CI Calculations. *J. Chem. Phys.* **1995,** *99* (46), 16842-16848.

111.   Wang, Y.; Quillian, B.; Wei, P.; Xie, Y.; Wannere, C. S.; King, R. B.; Schaefer, H. F.; Schleyer, P. v. R.; Robinson, G. H., Planar, Twisted, and Trans-Bent:

Conformational Flexibility of Neutral Diborenes. *J. Am. Chem. Soc.* **2008,** *130* (11), 3298-3299.

112.   Wang, Y.; Quillian, B.; Wei, P.; Wannere, C. S.; Xie, Y.; King, R. B.; Schaefer, H. F.; Schleyer, P. v. R.; Robinson, G. H., A Stable Neutral Diborene Containing a BB Double Bond. *J. Am. Chem. Soc.* **2007,** *129* (41), 12412-12413.

113.   Wang, Y.; Xie, Y.; Wei, P.; King, R. B.; Schaefer, H. F.; von R. Schleyer, P.; Robinson, G. H., A Stable Silicon(0) Compound with a Si=Si Double Bond. *Science* **2008,** *321* (5892), 1069-1071.

114.   Sidiropoulos, A.; Jones, C.; Stasch, A.; Klein, S.; Frenking, G., N-Heterocyclic Carbene Stabilized Digermanium (0). *Angew Chem Int Ed* **2009,** *48* (51), 9701-9704.

115.   Wang, Y.; Xie, Y.; Wei, P.; King, R. B.; Schaefer, H. F., III; Schleyer, P. v. R.; Robinson, G. H., Carbene-Stabilized Diphosphorus. *J. Am. Chem. Soc.* **2008,** *130* (45), 14970-14971.

116.   Abraham, M. Y.; Wang, Y.; Xie, Y.; Wei, P.; Schaefer III, H. F.; Schleyer, P. v. R.; Robinson, G. H., Carbene stabilization of diarsenic: from hypervalency to allotropy. *Chem. Eur. J* **2010,** *16* (2), 432-435.

117.   Wright, R. J.; Phillips, A. D.; Power, P. P., The [2 + 4] Diels–Alder Cycloadditon Product of a Probable Dialuminene, Ar'AlAlAr' (Ar' = C_6H_3- 2,6-Dipp$_2$; Dipp = C_6H_3-2,6-Pri$_2$), with Toluene. *J. Am. Chem. Soc.* **2003,** *125* (36), 10784-10785.

118.   Bag, P.; Porzelt, A.; Altmann, P. J.; Inoue, S., A Stable Neutral Compound with an Aluminum–Aluminum Double Bond. *J. Am. Chem. Soc.* **2017,** *139* (41), 14384-14387.

119.   Zhou, M.; Tsumori, N.; Li, Z.; Fan, K.; Andrews, L.; Xu, Q., OCBBCO: A Neutral Molecule with Some Boron–Boron Triple Bond Character. *J. Am. Chem. Soc.* **2002,** *124* (44), 12936-12937.

120.   Braunschweig, H.; Dewhurst, R. D.; Hammond, K.; Mies, J.; Radacki, K.; Vargas, A., Ambient-Temperature Isolation of a Compound with a Boron-Boron Triple Bond. *Science* **2012,** *336* (6087), 1420-1422.

121.   Frenking, G.; Holzmann, N., A Boron-Boron Triple Bond. *Science* **2012,** *336* (6087), 1394-1395.

122.   Cowley, A. H.; Lasch, J. G.; Norman, N. C.; Pakulski, M.; Whittlesey, B. R., Synthesis of a phospha-arsene and a phosphastibene; the first compounds with phosphorus–arsenic and phosphorus–antimony double bonds. *Chem Comm* **1983,** (16), 881-882.

123.   Fischer, R. C.; Power, P. P., π-Bonding and the Lone Pair Effect in Multiple Bonds Involving Heavier Main Group Elements: Developments in the New Millennium. *Chem. Rev.* **2010,** *110* (7), 3877-3923.

124.   Koner, A.; Sergeieva, T.; Morgenstern, B.; Andrada, D. M., A Cyclic Iminoborane-NHC Adduct: Synthesis, Reactivity, and Bonding Analysis. *Inorg. Chem.* **2021,** *60* (18), 14202-14211.

125.   Arif, A. M.; Boggs, J. E.; Cowley, A. H.; Lee, J. G.; Pakulski, M.; Power, J. M., Production of a boraphosphene (RB:PR') in the vapor phase by thermolysis of a sterically encumbered diphosphadiboretane. *J. Am. Chem. Soc.* **1986,** *108* (19), 6083-6084.

126.   Bartlett, R. A.; Feng, X.; Power, P. P., Synthesis and characterization of the phosphinidene borate complexes [Li(Et$_2$O)$_2$PRB(Mes)$_2$] and [Li(12-crown-4)$_2$][RPB(Mes)$_2$].THF [R = Ph, C$_6$H$_{11}$ or Mes (Mes = 2,4,6-Me$_3$C$_6$H$_2$)]: the first structurally characterized boron-phosphorus double bonds. *J. Am. Chem. Soc.* **1986,** *108* (21), 6817-6819.

127.   Petrie, M. A.; Shoner, S. C.; Dias, H. V. R.; Power, P. P., A Compound with a Boron–Arsenic Double Bond. *Angew. Chem. , Int. Ed.* **1990,** *29* (9), 1033-1035.

128.   Linti, G.; Nöth, H.; Polborn, K.; Paine, R. T., An Allene-analogous Boranylidenephosphane with B=P Double Bond: 1,1-Diethylpropyl(2,2,6,6-tetramethylpiperidino)-boranylidenephosphane-P-pentacarbonylchromium. *Angew Chem Int Ed* **1990,** *29* (6), 682-684.

129.   Rivard, E.; Merrill, W. A.; Fettinger, J. C.; Power, P. P., A donor-stabilization strategy for the preparation of compounds featuring P=B and As=B double bonds. *Chem. Comm.* **2006,** (36), 3800-3802.

130.   Rivard, E.; Merrill, W. A.; Fettinger, J. C.; Wolf, R.; Spikes, G. H.; Power, P. P., Boron–Pnictogen Multiple Bonds: Donor-Stabilized PB and AsB Bonds and a Hindered Iminoborane with a B–N Triple Bond. *Inorg Chem* **2007,** *46* (8), 2971-2978.

131.   Price, A. N.; Cowley, M. J., Base-Stabilized Phosphinidene Boranes by Silylium-Ion Abstraction. *Chem. Eur. J* **2016,** *22* (18), 6248-6252.

132.   Li, J.; Lu, Z.; Liu, L. L., A Free Phosphaborene Stable at Room Temperature. *J. Am. Chem. Soc.* **2022,** *144* (51), 23691-23697.

133.   von Hänisch, C.; Hampe, O., [{Li(thf)$_3$}$_2$Ga$_2${As(SiiPr$_3$)}$_4$]—A Compound with Gallium☐Arsenic Double Bonds. *Angew Chem Int Ed* **2002,** *41* (12), 2095-2097.

134.   Helling, C.; Wölper, C.; Schulz, S., Synthesis of a Gallaarsene {HC[C(Me)N-2,6-i-Pr$_2$-C$_6$H$_3$]$_2$}GaAsCp* Containing a Ga=As Double Bond. *J. Am. Chem. Soc.* **2018,** *140* (15), 5053-5056.

135.   Ganesamoorthy, C.; Helling, C.; Wölper, C.; Frank, W.; Bill, E.; Cutsail, G. E.; Schulz, S., From stable Sb- and Bi-centered radicals to a compound with a Ga=Sb double bond. *Nat. Comm.* **2018,** *9* (1), 87.

136.   Wilson, D. W. N.; Feld, J.; Goicoechea, J. M., A Phosphanyl-Phosphagallene that Functions as a Frustrated Lewis Pair. *Angew Chem Int Ed* **2020,** *59* (47), 20914-20918.

137.   Feld, J.; Wilson, D. W. N.; Goicoechea, J. M., Contrasting E–H Bond Activation Pathways of a Phosphanyl-Phosphagallene. *Angew. Chem. Int. Ed.* **2021,** *60* (40), 22057-22061.

138.   Taeufer, T.; Dankert, F.; Michalik, D.; Pospech, J.; Bresien, J.; Hering-Junghans, C., Photochemical formation and reversible base-induced cleavage of a phosphagallene. *Chem Sci* **2023,** *14* (11), 3018-3023.

139.   Fischer, M.; Nees, S.; Kupfer, T.; Goettel, J. T.; Braunschweig, H.; Hering-Junghans, C., Isolable Phospha- and Arsaalumenes. *J. Am. Chem. Soc.* **2021,** *143* (11), 4106-4111.

140.   Nees, S.; Wellnitz, T.; Dankert, F.; Härterich, M.; Dotzauer, S.; Feldt, M.; Braunschweig, H.; Hering-Junghans, C., On the Reactivity of Phosphaalumenes towards C–C Multiple Bonds. *Angew. Chem. Int. Ed.* **2023,** *62* (10), e202215838.

141.   Nees, S.; Fantuzzi, F.; Wellnitz, T.; Fischer, M.; Siewert, J.-E.; Goettel, J. T.; Hofmann, A.; Härterich, M.; Braunschweig, H.; Hering-Junghans, C., Cyclo-Dipnictadialanes. *Angew Chem Int Ed* **2021,** *60* (45), 24318-24325.

142.   Nees, S.; Beer, H.; Just, P.; Teichmeier, L. M.; Christoffer, L. E.; Guljam, A.; Kushik; Braunschweig, H.; Hering-Junghans, C., On the Reactivity of Mes*P(PMe3) towards Aluminum(I) Compounds – Evidence for the Intermediate Formation of Phosphaalumenes. *ChemPlusChem* **2023,** *n/a* (n/a), e202300078.

143.   Löwdin, P., Advances in Chemical Physics. *New York, London: Interscience* **1959,** *271*.

144.   Kurth, S.; Perdew, J. P., Role of the exchange–correlation energy: Nature's glue. *Int. J. Quantum Chem.* **2000,** *77* (5), 814-818.

145.   Hohenberg, P.; Kohn, W., Inhomogeneous Electron Gas. *Phys. Rev.* **1964,** *136* (3B), B864-B871.

146.   Kohn, W.; Sham, L. J., Self-Consistent Equations Including Exchange and Correlation Effects. *Phys. Rev.* **1965,** *140* (4A), A1133-A1138.

147.   Grimme, S.; Antony, J.; Ehrlich, S.; Krieg, H., A consistent and accurate ab initio parametrization of density functional dispersion correction (DFT-D) for the 94 elements H-Pu. *J. Chem. Phys.* **2010,** *132* (15).

148.   Grimme, S.; Ehrlich, S.; Goerigk, L., Effect of the Damping Function in Dispersion Corrected Density Functional Theory. *J. Comp. Chem.* **2011,** *32* (7), 1456-1465.

149.   Mulliken, R. S., Electronic Population Analysis on LCAO–MO Molecular Wave Functions. I. *J. Chem. Phys.* **2004,** *23* (10), 1833-1840.

150.   Martin, F.; Zipse, H., Charge distribution in the water molecule—A comparison of methods. *J. Comp. Chem.* **2005,** *26* (1), 97-105.

151.   Fonseca Guerra, C.; Handgraaf, J.-W.; Baerends, E. J.; Bickelhaupt, F. M., Voronoi deformation density (VDD) charges: Assessment of the Mulliken, Bader, Hirshfeld, Weinhold, and VDD methods for charge analysis. *J. Comp. Chem.* **2004,** *25* (2), 189-210.

152.   Löwdin, P. O., On the Non-Orthogonality Problem Connected with the Use of Atomic Wave Functions in the Theory of Molecules and Crystals. *J. Chem. Phys.* **1950,** *18* (3), 365-375.

153.   Reed, A. E.; Weinstock, R. B.; Weinhold, F., Natural population analysis. *J. Chem. Phys.* **1985,** *83* (2), 735-746.

154.   Poater, J.; Solà, M.; Bickelhaupt, F. M., Hydrogen–Hydrogen Bonding in Planar Biphenyl, Predicted by Atoms-In-Molecules Theory, Does Not Exist. *Chem. Eur. J.* **2006,** *12* (10), 2889-2895.

155.   Poater, J.; Solà, M.; Bickelhaupt, F. M., A Model of the Chemical Bond Must Be Rooted in Quantum Mechanics, Provide Insight, and Possess Predictive Power. *Chem. Eur. J.* **2006,** *12* (10), 2902-2905.

156.   Pendás, A. M.; Francisco, E.; Blanco, M. A.; Gatti, C., Bond Paths as Privileged Exchange Channels. *Chem. Eur. J.* **2007,** *13* (33), 9362-9371.

157.   Pauling, L.; Brockway, L. O.; Beach, J. Y., The Dependence of Interatomic Distance on Single Bond-Double Bond Resonance1. *J. Am. Chem. Soc.* **1935,** *57* (12), 2705-2709.

158.   Pauling, L., Atomic Radii and Interatomic Distances in Metals. *J. Am. Chem. Soc.* **1947,** *69* (3), 542-553.

159.   Coulson, C. A.; Jacobs, J., Conjugation across a single bond. *J. Chem. Soc.* **1949**, 2805-2812.

160.   Mayer, I., Charge, bond order and valence in the AB initio SCF theory. *Chem. Phys. Lett.* **1983,** *97* (3), 270-274.

161.   Mayer, I., Bond orders and valences in the SCF theory: a comment. *Theor. Chim. Acta* **1985,** *67* (4), 315-322.

162.   Bader, R. F. W.; Stephens, M. E., Spatial localization of the electronic pair and number distributions in molecules. *J. Am. Chem. Soc.* **1975,** *97* (26), 7391-7399.

163.   Mayer, I.; Salvador, P., Overlap populations, bond orders and valences for 'fuzzy' atoms. *Chem. Phys. Lett.* **2004,** *383* (3), 368-375.

164.   Salvador, P.; Duran, M.; Mayer, I., One- and two-center energy components in the atoms in molecules theory. *J. Phys. Chem.* **2001,** *115* (3), 1153-1157.

165.   Phipps, M. J. S.; Fox, T.; Tautermann, C. S.; Skylaris, C.-K., Energy decomposition analysis approaches and their evaluation on prototypical protein–drug interaction patterns. *Chem. Soc. Rev.* **2015,** *44* (10), 3177-3211.

166.   Kitaura, K.; Morokuma, K., A new energy decomposition scheme for molecular interactions within the Hartree-Fock approximation. *Int. J. Quantum Chem.* **1976,** *10* (2), 325-340.

167.   Ziegler, T.; Rauk, A., On the calculation of bonding energies by the Hartree Fock Slater method. *Theor. Chim. Acta* **1977,** *46* (1), 1-10.

168.   Raupach, M.; Tonner, R., A periodic energy decomposition analysis method for the investigation of chemical bonding in extended systems. *J. Chem. Phys.* **2015,** *142* (19), 194105.

169.   Hamlin, T. A.; Bickelhaupt, F. M.; Fernández, I., The Pauli Repulsion-Lowering Concept in Catalysis. *Accounts of Chemical Research* **2021,** *54* (8), 1972-1981.

170.   Bickelhaupt, F. M.; Nibbering, N. M. M.; Van Wezenbeek, E. M.; Baerends, E. J., Central bond in the three CN.cntdot.dimers NC-CN, CN-CN and CN-NC: electron pair bonding and Pauli repulsion effects. *J. Phys. Chem.* **2002,** *96* (12), 4864-4873.

171.   Khaliullin, R. Z.; Cobar, E. A.; Lochan, R. C.; Bell, A. T.; Head-Gordon, M., Unravelling the Origin of Intermolecular Interactions Using Absolutely Localized Molecular Orbitals. *J. Chem. Phys. A* **2007,** *111* (36), 8753-8765.

172.   Mao, Y.; Horn, P. R.; Head-Gordon, M., Energy decomposition analysis in an adiabatic picture. *Phys. Chem. Chem. Phys.* **2017,** *19* (8), 5944-5958.

173.   Andrada, D. M.; Foroutan-Nejad, C., Energy components in energy decomposition analysis (EDA) are path functions; why does it matter? *Phys. Chem. Chem. Phys.* **2020,** *22* (39), 22459-22464.

174.   Poater, J.; Andrada, D. M.; Solà, M.; Foroutan-Nejad, C., Path-dependency of energy decomposition analysis & the elusive nature of bonding. *Phys. Chem. Chem. Phys.* **2022,** *24* (4), 2344-2348.

175.   Solà, M.; Duran, M.; Poater, J., The energy components of the extended transition state energy decomposition analysis are path functions: the case of water tetramer. *Theoretical Chemistry Accounts* **2021,** *140* (3), 33.

176.   Zhao, L. L.; von Hopffgarten, M.; Andrada, D. M.; Frenking, G., Energy decomposition analysis. *Wiley Interdiscip. Rev. Comp. Mol. Sci.* **2018,** *8* (3), e13450.

177.   Khaliullin, R. Z.; Bell, A. T.; Head-Gordon, M., Analysis of charge transfer effects in molecular complexes based on absolutely localized molecular orbitals. *J. Chem. Phys.* **2008,** *128* (18), 184112.

178.   Mitoraj, M. P.; Michalak, A.; Ziegler, T., A Combined Charge and Energy Decomposition Scheme for Bond Analysis. *J. Chem. Theory Comput.* **2009,** *5* (4), 962-975.

179.   Karen, P.; McArdle, P.; Takats, J., Toward a comprehensive definition of oxidation state (IUPAC Technical Report). *Pure Appl Chem* **2014,** *86* (6), 1017-1081.

180.   Gimferrer, M.; Comas-Vilà, G.; Salvador, P., Can We Safely Obtain Formal Oxidation States from Centroids of Localized Orbitals? *Molecules* **2020,** *25* (1), 234.

181.   Thom, A. J. W.; Sundstrom, E. J.; Head-Gordon, M., LOBA: a localized orbital bonding analysis to calculate oxidation states, with application to a model water oxidation catalyst. *Phys. Chem. Chem. Phys.* **2009,** *11* (47), 11297-11304.

182.   Gimferrer, M.; Aldossary, A.; Salvador, P.; Head-Gordon, M., Oxidation State Localized Orbitals: A Method for Assigning Oxidation States Using Optimally Fragment-Localized Orbitals and a Fragment Orbital Localization Index. *J. Comp. Theor. Chem.* **2022,** *18* (1), 309-322.

183.   Ramos-Cordoba, E.;   Postils, V.; Salvador, P., Oxidation states from wave function analysis. *Journal of chemical theory* **2015,** *11* (4), 1501-1508.

184.   Postils, V.; Delgado-Alonso, C.; Luis, J. M.; Salvador, P., An objective alternative to IUPAC's approach to assign oxidation states. *Angew. Chem. Int. Ed.* **2018,** *130* (33), 10685-10689.

185.   Mayer, I., Non-orthogonal localized orbitals and orthogonal atomic hybrids derived from Mulliken's population analysis. *Chem. Phys. Lett.* **1995,** *242* (4), 499-506.

186.   Mayer, I., Atomic Orbitals from Molecular Wave Functions: The Effective Minimal Basis. *J. Phys. Chem.* **1996,** *100* (15), 6249-6257.

187.   Tonner, R.; Frenking, G., Divalent Carbon(0) Chemistry, Part 1: Parent Compounds. *Chem. Eur. J.* **2008,** *14* (11), 3260-3272.

188.   Tonner, R.; Frenking, G., Divalent Carbon(0) Chemistry, Part 2: Protonation and Complexes with Main Group and Transition Metal Lewis Acids. *Chem. - Eur. J.* **2008,** *14* (11), 3273-3289.

189.   Himmel, D.; Krossing, I.; Schnepf, A., Dative Bonds in Main-Group Compounds: A Case for Fewer Arrows! *Angew. Chem. Int. Ed.* **2014,** *53* (2), 370-374.

190.   Frenking, G., Dative Bonds in Main-Group Compounds: A Case for More Arrows! *Angewandte Chemie International Edition* **2014,** *53* (24), 6040-6046.

191.   Phipps, M. J. S.;   Fox, T.;   Tautermann, C. S.; Skylaris, C.-K., Energy decomposition analysis approaches and their evaluation on prototypical protein–drug interaction patterns. *Chem. Soc. Rev.* **2015,** *44* (10), 3177-3211.

192.   Zhao, L.; Pan, S.; Holzmann, N.; Schwerdtfeger, P.; Frenking, G., Chemical Bonding and Bonding Models of Main-Group Compounds. *Chem. Rev.* **2019,** *119* (14), 8781-8845.

193.   Hamlin, T. A.; Bickelhaupt, F. M.; Fernández, I., The Pauli Repulsion-Lowering Concept in Catalysis. *Acc. Chem. Res.* **2021,** *54* (8), 1972-1981.

194.   van der Lubbe, S. C. C.; Fonseca Guerra, C., The Nature of Hydrogen Bonds: A Delineation of the Role of Different Energy Components on Hydrogen Bond Strengths and Lengths. *Chem. Asian J.* **2019,** *14* (16), 2760-2769.

195.   Krapp, A.; Pandey, K. K.; Frenking, G., Transition Metal–Carbon Complexes. A Theoretical Study. *J. Am. Chem. Soc.* **2007,** *129* (24), 7596-7610.

196.   Fernández, I.; Frenking, G., Aromaticity in Metallabenzenes. *Chem. Eur. J.* **2007,** *13* (20), 5873-5884.

197.   Jerabek, P.; Schwerdtfeger, P.; Frenking, G., Dative and electron-sharing bonding in transition metal compounds. *J. Comput. Chem.* **2019,** *40* (1), 247-264.

198.   Frenking, G.; Hermann, M.; Andrada, D. M.; Holzmann, N., Donor–acceptor bonding in novel low-coordinated compounds of boron and group-14 atoms C–Sn. *Chem. Soc. Rev.* **2016,** *45* (4), 1129-1144.

199.   Landis, C. R.; Hughes, R. P.; Weinhold, F., Bonding Analysis of TM(cAAC)$_2$ (TM = Cu, Ag, and Au) and the Importance of Reference State. *Organometallics* **2015,** *34* (13), 3442-3449.

200.   Rösch, B.; Harder, S., New horizons in low oxidation state group 2 metal chemistry. *Chem. Comm.* **2021,** *57* (74), 9354-9365.

201.   Freeman, L. A.; Walley, J. E.; Gilliard, R. J., Synthesis and reactivity of low-oxidation-state alkaline earth metal complexes. *Nat. Synth.* **2022,** *1* (6), 439-448.

202.   Arrowsmith, M.; Braunschweig, H.; Celik, M. A.; Dellermann, T.; Dewhurst, R. D.; Ewing, W. C.; Hammond, K.; Kramer, T.; Krummenacher, I.; Mies, J.; Radacki, K.; Schuster, J. K., Neutral zero-valent s-block complexes with strong multiple bonding. *Nat. Chem.* **2016,** *8* (9), 890-894.

203.   Gimferrer, M.; Danés, S.; Vos, E.; Yildiz, C. B.; Corral, I.; Jana, A.; Salvador, P.; Andrada, D. M., The oxidation state in low-valent beryllium and magnesium compounds. *Chem. Sci.* **2022,** *13* (22), 6583-6591.

204.   Singh, A. P.; Samuel, P. P.; Roesky, H. W.; Schwarzer, M. C.; Frenking, G.; Sidhu, N. S.; Dittrich, B., A Singlet Biradicaloid Zinc Compound and Its Nonradical Counterpart. *J. Am. Chem. Soc.* **2013,** *135* (19), 7324-7329.

205.   Ramos-Cordoba, E.; Matito, E.; Mayer, I.; Salvador, P., Toward a Unique Definition of the Local Spin. *J. Chem. Theory Comput.* **2012,** *8* (4), 1270-1279.

206.   Belpassi, L.; Infante, I.; Tarantelli, F.; Visscher, L., The Chemical Bond between Au(I) and the Noble Gases. Comparative Study of NgAuF and NgAu$^+$ (Ng = Ar, Kr, Xe) by Density Functional and Coupled Cluster Methods. *J. Am. Chem. Soc.* **2008,** *130* (3), 1048-1060.

207.   Karen, P.; McArdle, P.; Takats, J., Comprehensive definition of oxidation state (IUPAC Recommendations 2016). **2016,** *88* (8), 831-839.

208. Martín Pendás, Á.; Francisco, E., The role of references and the elusive nature of the chemical bond. *Nat. Comm.* **2022,** *13* (1), 3327.

209. Zhou, Y.; Pan, S.; Dong, X.; Wang, L.; Zhou, M.; Frenking, G., Generation and Characterization of the Charge-Transferred Diradical Complex CaCO2 with an Open-Shell Singlet Ground State. *J. Am. Chem. Soc.* **2022,** *144* (18), 8355-8361.

210. Gimferrer, M.; Danés, S.; Vos, E.; Yildiz, C. B.; Corral, I.; Jana, A.; Salvador, P.; Andrada, D. M., Reply to the 'Comment on "The oxidation state in low-valent beryllium and magnesium compounds"' by S. Pan and G. Frenking, Chem. Sci., 2022, 13, DOI: 10.1039/D2SC04231B. *Chem. Sci.* **2023,** *14* (2), 384-392.

211. Salvador, P.; Vos, E.; Corral, I.; Andrada, D. M., Beyond the Classical Electron-Sharing and Dative Bond Picture: The Case of Spin-Polarized Bond. *Angew Chem Int Ed n/a* (n/a).

212. Ayers, P. W., Atoms in molecules, an axiomatic approach. I. Maximum transferability. *The Journal of Chemical Physics* **2000,** *113* (24), 10886-10898.

213. Schwarz, W. H. E.; Ruedenberg, K.; Mensching, L., Chemical deformation densities. 1. Principles and formulation of quantitative determination. *Journal of the American Chemical Society* **1989,** *111* (18), 6926-6933.

214. Mizuhata, Y.; Sasamori, T.; Tokitoh, N., Stable Heavier Carbene Analogues. *Chem. Rev.* **2009,** *109* (8), 3479-3511.

215. Liu, G.; Fedik, N.; Martinez-Martinez, C.; Ciborowski, S. M.; Zhang, X.; Boldyrev, A. I.; Bowen, K. H., Realization of Lewis Basic Sodium Anion in the NaBH$_3$– Cluster. *Angew Chem Int Ed* **2019,** *58* (39), 13789-13793.

216. Pan, S.; Frenking, G., Comment on "Realization of Lewis Basic Sodium Anion in the NaBH$_3^-$ Cluster". *Angew Chem Int Ed* **2020,** *132* (23), 8836-8839.

217. Liu, G.; Fedik, N.; Martinez-Martinez, C.; Ciborowski, S. M.; Zhang, X.; Boldyrev, A. I.; Bowen, K. H., Reply to the Comment on "Realization of Lewis Basic Sodium Anion in the NaBH3– Cluster". *Angew Chem Int Ed* **2020,** *59* (23), 8760-8764.

218. Foroutan-Nejad, C., The Na···B Bond in NaBH$_3^-$: A Different Type of Bond. *Angew Chem Int Ed* **2020,** *59* (47), 20900-20903.

219. Salvador, P.; Vos, E.; Corral, I.; Andrada, D. M., Beyond the Classical Electron-Sharing and Dative Bond Picture: The Case of Spin-Polarized Bond. *Angew. Chem. Int. Ed. n/a* (n/a).

220. Radenković, S.; Shaik, S. S.; Braïda, B., Na··· B Bond in NaBH$_3^-$: Solving the Conundrum. *Angew Chem Int Ed* **2021,** *133* (23), 12833-12836.

221. Pino-Rios, R.; Inostroza, D.; Tiznado, W., Neither too Classic nor too Exotic: One-Electron Na···B Bond in NaBH$_3^-$ Cluster. *Angew Chem Int Ed* **2021,** *133* (23), 12857-12863.

222. Sowlati-Hashjin, S.; Šadek, V.; Sadjadi, S.; Karttunen, M.; Martín-Pendás, A.; Foroutan-Nejad, C., Collective interactions among organometallics are exotic bonds hidden on lab shelves. *Nat. Chem.* **2022,** *13* (1), 2069.

223. Agou, T.; Ikeda, S.; Sasamori, T.; Tokitoh, N., Synthesis and Structure of Lewis-Base-Free Phosphinoalumane Derivatives. **2016,** *2016* (5), 623-627.

224. Jaiswal, A. K.; Prasad, P. K.; Young, R. D., Nucleophilic Substitution of Aliphatic Fluorides via Pseudohalide Intermediates. *Chem. Eur. J.* **2019,** *25* (25), 6290-6294.

225. Ayers, P. W.; Anderson, J. S. M.; Rodriguez, J. I.; Jawed, Z., Indices for predicting the quality of leaving groups. *Phys. Chem. Chem. Phys.* **2005,** *7* (9), 1918-1925.

226. Mei, Y. B.; Borger, J. E.; Wu, D. J.; Grützmacher, H., Salen supported Al-O-C≡P and Ga-P=C=O complexes. *Dalton Trans.* **2019,** *48* (13), 4370-4374.

227. Goicoechea, J. M.; Grützmacher, H., The Chemistry of the 2-Phosphaethynolate Anion. *Angew. Chem. Int. Ed.* **2018,** *57* (52), 16968-16994.

228. Sirsch, P.; Clark, N. L.; Onut, L.; Burchell, R. P.; Decken, A.; McGrady, G. S.; Daoud-Aladine, A.; Gutmann, M. J., Insights into Metal Borohydride and Aluminohydride Bonding: X-Ray and Neutron Diffraction Structures and a DFT and Charge Density Study of [Na (15-crown-5)][EH4](E= B, Al). *Inorg. Chem.* **2010,** *49* (24), 11395-11402.

229. Caise, A.; Jones, D.; Kolychev, E. L.; Hicks, J.; Goicoechea, J. M.; Aldridge, S., On the Viability of Catalytic Turnover via Al-O/B-H Metathesis: The Reactivity of beta-Diketiminate Aluminium Hydrides towards CO_2 and Boranes. *Chem. Eur. J.* **2018,** *24* (51), 13624-13635.

230. Yang, Y.; Schulz, T.; John, M.; Yang, Z.; Jiménez-Pérez, V. M.; Roesky, H. W.; Gurubasavaraj, P. M.; Stalke, D.; Ye, H., Organoaluminum Hydroxides Supported by β-Diketiminato Ligands: Synthesis, Structural Characterization, and Reactions. *Organometallics* **2008,** *27* (4), 769-777.

231. Pyykkö, P.; Atsumi, M., Molecular Single-Bond Covalent Radii for Elements 1–118. *Chem. Eur. J* **2009,** *15* (1), 186-197.

232. Pyykkö, P.; Atsumi, M., Molecular Double-Bond Covalent Radii for Elements Li–E112. *Chem. Eur. J.* **2009,** *15* (46), 12770-12779.

233. Hofmann, A.; Légaré, M. A.; Wüst, L.; Braunschweig, H., Heterodiatomic Multiple Bonding in Group 13: A Complex with a Boron−Aluminum π Bond Reduces CO_2. *Angew. Chem. Int. Ed.* **2019,** *58* (29), 9776-9781.

234. Edelstein, N., Bonding in metal borohydride complexes. *Inorg. Chem.* **1981,** *20* (1), 297-299.

235.   Cushion, M. G.; Mountford, P., Cationic and charge-neutral calcium tetrahydroborate complexes and their use in the controlled ring-opening polymerisation of rac-lactide. *Chem. Comm.* **2011,** *47* (8), 2276-2278.

236.   Soloveichik, G. L.; Andrus, M.; Lobkovsky, E. B., Magnesium borohydride complexed by tetramethylethylenediamine. *Inorg. Chem.* **2007,** *46* (10), 3790-1.

237.   Saar, D.; Petrucci, S., Infrared and ultrasonic spectra of sodium thiocyanate and lithium thiocyanate in tetrahydrofuran. *J. Phys. Chem.* **1986,** *90* (15), 3326-3330.

238.   Sinhababu, S.; Kundu, S.; Paesch, A. N.; Herbst-Irmer, R.; Stalke, D.; Roesky, H. W., A Route to Aluminumdiisocyanate and -diisothiocyanate from an Al(I) Precursor. *Eur J Inorg Chem* **2018,** (20-21), 2237-2240.

239.   Kuhn, N.; Henkel, G.; Kratz, T.; Kreutzberg, J.; Boese, R.; Maulitz, A. H., Derivate des Imidazols, VI. Stabile Carben-Borane. *Chem. Ber.* **1993,** *126* (9), 2041-2045.

240.   Grams, S.; Eyselein, J.; Langer, J.; Farber, C.; Harder, S., Boosting Low-Valent Aluminum(I) Reactivity with a Potassium Reagent. *Angew. Chem. Int. Ed.* **2020,** *59* (37), 15982-15986.

241.   Zhu, H.; Chai, J.; Stasch, A.; Roesky, H. W.; Blunck, T.; Vidovic, D.; Magull, J.; Schmidt, H. G.; Noltemeyer, M., Reactions of the Aluminum (I) Monomer LAl [L=HC{(CMe)(NAr)} 2; Ar= 2, 6-iPr$_2$C$_6$H$_3$] with Imidazol-2-ylidene and Diphenyldiazomethane. A Hydrogen Transfer from the L Ligand to the Central Aluminum Atom and Formation of the Diiminylaluminum Compound LAl (N= CPh$_2$)$_2$ *Eur. J. Inorg. Chem.* **2004,** *2004* (20), 4046-4051.

242.   Kuhn, N.; Kratz, T., Synthesis of Imidazol-2-Ylidenes by Reduction of Imidazole-2(3h)-Thiones. *Synthesis-Stuttgart* **1993,** (6), 561-562.

243.   Arduengo III, A. J.; Dias, H. R.; Calabrese, J. C.; Davidson, F., A stable carbene-alane adduct. *J. Am. Chem. Soc.* **1992,** *114* (24), 9724-9725.

244.   Krüger, J.; Wölper, C.; Auer, A. A.; Schulz, S., Formation and Cleavage of a Sb–Sb Double Bond: From Carbene-Coordinated Distibenes to Stibinidenes. *Eur J Inorg Chem* **2022,** *2022* (3), e202100960.

245.   Anker, M. D.; Colebatch, A. L.; Iversen, K. J.; Wilson, D. J. D.; Dutton, J. L.; Garcia, L.; Hill, M. S.; Liptrot, D. J.; Mahon, M. F., Alane-Centered Ring Expansion of N-Heterocyclic Carbenes. *Organometallics* **2017,** *36* (6), 1173-1178.

246.   Yow, S.; Gates, S. J.; White, A. J. P.; Crimmin, M. R., Zirconocene Dichloride Catalyzed Hydrodefluorination of C-F bonds. *Angew. Chem. Int. Ed.* **2012,** *51* (50), 12559-12563.

247.   Fulmer, G. R.; Miller, A. J. M.; Sherden, N. H.; Gottlieb, H. E.; Nudelman, A.; Stoltz, B. M.; Bercaw, J. E.; Goldberg, K. I., NMR Chemical Shifts of Trace Impurities:

Common Laboratory Solvents, Organics, and Gases in Deuterated Solvents Relevant to the Organometallic Chemist. *Organometallics* **2010,** *29* (9), 2176-2179.

248.   Pozdeev, A. S.; Boldyrev, A. I., Exploring the Structure and Bonding of Group 13 Homogeneous and Heterogeneous Hydrides with the X2H4 Stoichiometry: A Theoretical Investigation. *Inorg. Chem.* **2023,** *62* (20), 8019-8026.

249.   Wagner, F. R.; Noor, A.; Kempe, R., Ultrashort metal–metal distances and extreme bond orders. *Nat. Chem.* **2009,** *1* (7), 529-536.

250.   Yuan, C.; Zhao, X.-F.; Wu, Y.-B.; Wang, X., Ultrashort Beryllium–Beryllium Distances Rivalling Those of Metal–Metal Quintuple Bonds Between Transition Metals. *Angew. Chem. Int. Ed.* **2016,** *55* (50), 15651-15655.

251.   Cui, Z.-h.; Yang, W.-s.; Zhao, L.; Ding, Y.-h.; Frenking, G., Unusually Short Be–Be Distances with and without a Bond in Be_2F_2 and in the Molecular Discuses Be_2B_8 and $Be_2B_7^-$. *Angew. Chem. Int. Ed.* **2016,** *55* (27), 7841-7846.

252.   Hadlington, T. J., An anionic beryllium hydride dimer with an exceedingly short Be⋯Be distance. *Dalton Trans* **2024,** *53* (3), 882-886.

253.   Boronski, J. T.; Crumpton, A. E.; Wales, L. L.; Aldridge, S., Diberyllocene, a stable compound of Be(I) with a Be–Be bond. *Science* **2023,** *380* (6650), 1147-1149.

254.   Green, J. C.; Green, M. L. H.; Parkin, G., The occurrence and representation of three-centre two-electron bonds in covalent inorganic compounds. *Chem. Comm.* **2012,** *48* (94), 11481-11503.

255.   Brookhart, M.; Green, M. L. H., Carbon-hydrogen-transition metal bonds. *J. Organomet. Chem.* **1983,** *250* (1), 395-408.

256.   García-Rodeja, Y.; Feixas, F.; Matito, E.; Solà, M., Three-centre electron sharing indices (3c-ESIs) as a tool to differentiate among (an)agostic interactions and hydrogen bonds in transition metal complexes. *Phys. Chem. Chem. Phys.* **2022,** *24* (48), 29333-29337.

257.   Mitoraj, M. P.; Babashkina, M. G.; Robeyns, K.; Sagan, F.; Szczepanik, D. W.; Seredina, Y. V.; Garcia, Y.; Safin, D. A., Chameleon-like Nature of Anagostic Interactions and Its Impact on Metalloaromaticity in Square-Planar Nickel Complexes. *Organometallics* **2019,** *38* (9), 1973-1981.

258.   de Jong, G. B.; Ortega, N.; Lutz, M.; Lammertsma, K.; Slootweg, J. C., Easy Access to Phosphine-Borane Building Blocks. *Chem. Eur. J.* **2020,** *26* (68), 15944-15952.

259.   Chu, T.; Boyko, Y.; Korobkov, I.; Kuzmina, L. G.; Howard, J. A.; Nikonov, G. I., Oxidative Addition of Disulfides, Alkyl Sulfides, and Diphosphides to an Aluminum (I) Center. *Inorg. Chem.* **2016,** *55* (17), 9099-9104.

260.   Federmann, P.; Herwig, C.; Beckmann, F.; Cula, B.; Limberg, C., Ring-Opening of THF via an Intramolecular P/Al-Based Frustrated Lewis Pair: Assistance by C_6F_5 Groups beyond Electronegativity? *Organometallics* **2021,** *40* (24), 4143-4149.

261.   Lloyd-Jones, G. C.; Taylor, N. P., Mechanism of Phosphine Borane Deprotection with Amines: The Effects of Phosphine, Solvent and Amine on Rate and Efficiency. *Chem. Eur. J* **2015,** *21* (14), 5423-5428.

262.   Chu, T.; Korobkov, I.; Nikonov, G. I., Oxidative addition of sigma bonds to an Al(I) center. *J. Am. Chem. Soc.* **2014,** *136* (25), 9195-202.

263.   Evans, M. J.; Anker, M. D.; Coles, M. P., Oxidative Addition of Hydridic, Protic, and Nonpolar E–H Bonds (E = Si, P, N, or O) to an Aluminyl Anion. *Inorg. Chem.* **2021,** *60* (7), 4772-4778.

264.   Hayes, P. G.; Piers, W. E.; Lee, L. W. M.; Knight, L. K.; Parvez, M.; Elsegood, M. R. J.; Clegg, W., Dialkylscandium Complexes Supported by β-Diketiminato Ligands: Synthesis, Characterization, and Thermal Stability of a New Family of Organoscandium Complexes. *Organometallics* **2001,** *20* (12), 2533-2544.

265.   Hansen, K.; Szilvási, T.; Blom, B.; Inoue, S.; Epping, J.; Driess, M., A Fragile Zwitterionic Phosphasilene as a Transfer Agent of the Elusive Parent Phosphinidene (:PH). *J. Am. Chem. Soc.* **2013,** *135* (32), 11795-11798.

266.   Kapitein, M.; von Hänisch, C., Synthesis, Structures and Thermal Decomposition of Monomeric Aluminium, Gallium and Indium Silylphosphanides. *Eur J Inorg Chem* **2015,** *2015* (5), 837-844.

267.   Evans, M. J.; Anker, M. D.; Coles, M. P., Oxidative Addition of Hydridic, Protic, and Nonpolar E–H Bonds (E = Si, P, N, or O) to an Aluminyl Anion. *Inorg Chem* **2021,** *60* (7), 4772-4778.

268.   Bai, G.; Wei, P.; Das, A. K.; Stephan, D. W., P–H and P–P bond activation by Ni(i) and Fe(i) β-diketiminato-complexes. *Dalton Trans.* **2006,** (9), 1141-1146.

269.   Knizia, G., Intrinsic Atomic Orbitals: An Unbiased Bridge between Quantum Theory and Chemical Concepts. *J. Chem. Theory Comput.* **2013,** *9* (11), 4834-4843.

270.   Krasovskiy, A.; Kopp, F.; Knochel, P., Soluble Lanthanide Salts (LnCl₃·2 LiCl) for the Improved Addition of Organomagnesium Reagents to Carbonyl Compounds. *Angew. Chem. Int. Ed.* **2006,** *45* (3), 497-500.

271.   Hatano, M.; Ito, O.; Suzuki, S.; Ishihara, K., Zinc(II)-Catalyzed Addition of Grignard Reagents to Ketones. *J. Org. Chem.* **2010,** *75* (15), 5008-5016.

272.   Green, S. P.; Jones, C.; Stasch, A., Stable Magnesium(I) Compounds with Mg-Mg Bonds. *Science* **2007,** *318* (5857), 1754-1757.

273.   Rösch, B.; Gentner, T. X.; Eyselein, J.; Langer, J.; Elsen, H.; Harder, S., Strongly reducing magnesium(0) complexes. *Nature* **2021,** *592* (7856), 717-721.

274.   Crimmin, M. R.; Arrowsmith, M.; Barrett, A. G. M.; Casely, I. J.; Hill, M. S.; Procopiou, P. A., Intramolecular Hydroamination of Aminoalkenes by Calcium and Magnesium Complexes: A Synthetic and Mechanistic Study. *J. Am. Chem. Soc.* **2009,** *131* (28), 9670-9685.

275.   Okokhere-Edeghoghon, B.; Hill, M. S.; Mahon, M. F.; McMullin, C. L., Diverse reactivity of a magnesium silanide toward ketones. *Chem. Comm.* **2022,** *58* (76), 10711-10714.

276.   Hauser, C. R.; Walker, H. G., Jr., Condensation of Certain Esters by Means of Diethylaminomagnesium Bromide. *J. Am. Chem. Soc.* **1947,** *69* (2), 295-297.

277.   Krasovskiy, A.; Krasovskaya, V.; Knochel, P., Mixed Mg/Li Amides of the Type $R_2NMgCl·LiCl$ as Highly Efficient Bases for the Regioselective Generation of Functionalized Aryl and Heteroaryl Magnesium Compounds. *Angew. Chem. Int. Ed.* **2006,** *45* (18), 2958-2961.

278.   Baillie, S. E.; Blair, V. L.; Bradley, T. D.; Clegg, W.; Cowan, J.; Harrington, R. W.; Hernán-Gómez, A.; Kennedy, A. R.; Livingstone, Z.; Hevia, E., Isomeric and chemical consequences of the direct magnesiation of 1,3-benzoazoles using β-diketiminate-stabilized magnesium bases. *Chem. Sci.* **2013,** *4* (4), 1895-1905.

279.   Davin, L.; Clegg, W.; Kennedy, A. R.; Probert, M. R.; McLellan, R.; Hevia, E., Structural and Synthetic Insights into Pyridine Homocouplings Mediated by a β-Diketiminato Magnesium Amide Complex. *Chem. Eur. J.* **2018,** *24* (55), 14830-14835.

280.   Gauld, R. M.; Lynch, J. R.; Kennedy, A. R.; Barker, J.; Reid, J.; Mulvey, R. E., Expected and Unexpected Reactivities of Homoleptic LiNacNac and Heteroleptic NacNacMg(TMP) β-Diketiminates toward Various Small Unsaturated Organic Molecules. *Inorg. Chem.* **2021,** *60* (8), 6057-6064.

281.   Hey, E.; Engelhardt, L. M.; Raston, C. L.; White, A. H., Magnesium Phosphides– Synthesis and Structure of $[Mg(PHPh)_2(tmeda)]$. *Angew. Chem. Int. Ed.* **1987,** *26* (1), 81-82.

282.   Westerhausen, M.; Digeser, M. H.; Wieneke, B.; Nöth, H.; Knizek, J., Oligomeric Solvent-Free Magnesium Bis(phosphanides) – Molecular Structure of Trimeric Magnesium Bis[bis(trimethylsilyl)phosphanide]. *Eur J Inorg Chem* **1998,** *1998* (4), 517-521.

283.   Gärtner, M.; Görls, H.; Westerhausen, M., Arylphosphanide Complexes of the Alkaline-Earth Metals Magnesium, Calcium, Strontium, and Barium of the Formula $(THF)_nM[P(H)Ph]_2$ and Formation of Potassium Diphenylphosphinomagnesiates. *Inorg. Chem.* **2008,** *47* (4), 1397-1405.

284.   Issleib, K.; Deylig, H.-J., Alkali-Phosphorverbindungen und ihr reaktives Verhalten, XXVI. P-Substituierte Magnesiumphosphide. *Chem. Ber.* **1964,** *97* (4), 946-951.

285.   Day, B. M.; Coles, M. P., Synthesis and Reactivity of the Phospha-Grignard Reagent Mg(P{SiMe$_3$}$_2$)Br(thf). *Eur J Inorg Chem* **2010,** *2010* (34), 5471-5477.

286.   Taylor, M. J.; Coles, M. P.; Fulton, J. R., Reactivity of β-Diketiminato Magnesium Alkyl Complexes: Heterocumulenes and Phosphanes. *Aust. J. Chem.* **2015,** *68* (4), 635-640.

287.   Breen, T. L.; Stephan, D. W., Reactivity Studies of Methylzirconocene Phosphide Complexes. *Organometallics* **1996,** *15* (21), 4509-4514.

288.   Vilanova, S. P.; Tarlton, M. L.; Barnes, C. L.; Walensky, J. R., Double insertion of benzophenone into thorium-phosphorus bonds. *J. Organomet. Chem.* **2018,** *857*, 159-163.

289.   Breunig, J. M.; Hübner, A.; Bolte, M.; Wagner, M.; Lerner, H.-W., Reactivity of Phosphaboradibenzofulvene toward Hydrogen, Acetonitrile, Benzophenone, and 2,3-Dimethylbutadiene. *Organometallics* **2013,** *32* (22), 6792-6799.

290.   Borys, A. M.; Rice, E. F.; Nichol, G. S.; Cowley, M. J., The Phospha-Bora-Wittig Reaction. *J. Am. Chem. Soc.* **2021,** *143* (35), 14065-14070.

291.   Barozzino Consiglio, G.; Queval, P.; Harrison-Marchand, A.; Mordini, A.; Lohier, J.-F.; Delacroix, O.; Gaumont, A.-C.; Gérard, H.; Maddaluno, J.; Oulyadi, H., Ph$_2$P(BH$_3$)Li: From Ditopicity to Dual Reactivity. *J. Am. Chem. Soc.* **2011,** *133* (16), 6472-6480.

292.   Fleischer, E. B.; Sung, N.; Hawkinson, S., Crystal structure of benzophenone. *J. Phys. Chem.* **1968,** *72* (12), 4311-4312.

293.   Pyykkö, P.; Atsumi, M., Molecular single-bond covalent radii for elements 1-118. *Chem. Eur. J.* **2009,** *15* (1), 186-197.

294.   Blomberg, C.; Mosher, H. S., A radical process in a reaction of a grignard compound. *J. Organomet. Chem.* **1968,** *13* (2), 519-522.

295.   Blomberg, C.; Grootveld, H. H.; Gerner, T. H.; Bickelhaupt, F., Radical formation during reactions of Grignard reagents with quinones. *J. Organomet. Chem.* **1970,** *24* (3), 549-553.

296.   Ashby, E. C.; Bowers, J. R., Jr., Organometallic reaction mechanisms. 17. Nature of alkyl transfer in reactions of Grignard reagents with ketones. Evidence for radical intermediates in the formation of 1,2-addition product involving tertiary and primary Grignard reagents. *J. Am. Chem. Soc.* **1981,** *103* (9), 2242-2250.

297.   Peltzer, R. M.; Gauss, J.; Eisenstein, O.; Cascella, M., The Grignard Reaction – Unraveling a Chemical Puzzle. *J. Am. Chem. Soc.* **2020,** *142* (6), 2984-2994.

298.   Jones, C.; McDyre, L.; Murphy, D. M.; Stasch, A., Magnesium(I) reduction of benzophenone and anthracene: first structural characterisation of a magnesium ketyl. *Chem. Comm.* **2010,** *46* (9), 1511-1513.

299.   Sieg, G.; Pessemesse, Q.; Reith, S.; Yelin, S.; Limberg, C.; Munz, D.; Werncke, C. G., Cobalt and Iron Stabilized Ketyl, Ketiminyl and Aldiminyl Radical Anions. *Chem. Eur. J.* **2021,** *27* (67), 16760-16767.

300.   Scott, T. A.; Ooro, B. A.; Collins, D. J.; Shatruk, M.; Yakovenko, A.; Dunbar, K. R.; Zhou, H.-C., After 118 years, the isolation of two common radical anion reductants as simple, stable solids. *Chem. Comm.* **2009,** (1), 65-67.

301.   Böhm, V. P. W.; Brookhart, M., Dehydrocoupling of Phosphanes Catalyzed by a Rhodium(I) Complex. *Angew. Chem. Int. Ed.* **2001,** *40* (24), 4694-4696.

302.   McGarry, P. F.; Doubleday, C. E.; Wu, C.-H.; Staab, H. A.; Turro, N. J., UV—vis absorption studies of singlet to triplet intersystem crossing rates of aromatic ketones: effects of molecular geometry. *J. Photochem. Photobiol., A* **1994,** *77* (2), 109-117.

303.   Jockusch, S.; Turro, N. J., Phosphinoyl Radicals: Structure and Reactivity. A Laser Flash Photolysis and Time-Resolved ESR Investigation. *J. Am. Chem. Soc.* **1998,** *120* (45), 11773-11777.

304.   Haas, M.; Radebner, J.; Eibel, A.; Gescheidt, G.; Stueger, H., Recent Advances in Germanium-Based Photoinitiator Chemistry. *Chem. Eur. J.* **2018,** *24* (33), 8258-8267.

305.   Jupp, A. R.; Goicoechea, J. M., The 2-Phosphaethynolate Anion: A Convenient Synthesis and [2+2] Cycloaddition Chemistry. *Angewandte Chemie International Edition* **2013,** *52* (38), 10064-10067.

306.   Prust, J.; Most, K.; Müller, I.; Alexopoulos, E.; Stasch, A.; Usón, I.; Roesky, H. W., Synthesis and Structures of β-Diketoiminate Complexes of Magnesium. *Z. Anorg. Allg. Chem.* **2001,** *627* (8), 2032-2037.

307.   M. J. Frisch; G. W. Trucks; H. B. Schlegel; G. E. Scuseria; M. A. Robb; J. R. Cheeseman; G. Scalmani; V. Barone; B. Mennucci; G. A. Petersson; H. Nakatsuji; M. Caricato; X. Li; H. P. Hratchian; A. F. Izmaylov; J. Bloino; G. Zheng; J. L. Sonnenberg; M. Hada; M. Ehara; K. Toyota; R. Fukuda; J. Hasegawa; M. Ishida; T. Nakajima; Y. Honda; O. Kitao; H. Nakai; T. Vreven; J. A. Montgomery, J.; J. E. Peralta; F. Ogliaro; M. Bearpark; J. J. Heyd; E. Brothers; K. N. Kudin; V. N. Staroverov; R. Kobayashi; J. Normand; K. Raghavachari; A. Rendell; J. C. Burant; S. S. Iyengar; J. Tomasi; M. Cossi; N. Rega; J. M. Millam; M. Klene; J. E. Knox; J. B. Cross; V. Bakken; C. Adamo; J. Jaramillo; R. Gomperts; R. E. Stratmann; O. Yazyev; A. J. Austin; R. Cammi; C. Pomelli; J. W. Ochterski; R. L. Martin; K. Morokuma; V. G. Zakrzewski; G. A. Voth; P. Salvador; J. J. Dannenberg; S. Dapprich; A. D. Daniels; O. Farkas; J. B. Foresman;

J. V. Ortiz; J. Cioslowski; D. J. Fox Gaussian 16, Revision A.03. Gaussian, Inc.: Wallingford CT, 2016.

308.   Peng, C.; Ayala, P. Y.; Schlegel, H. B.; Frisch, M. J., Using redundant internal coordinates to optimize equilibrium geometries and transition states. *J. Comput. Chem.* **1996,** *17* (1), 49-56.

309.   Salvador, P.; Ramos-Cordoba, E.; Gimferrer, M.; Montilla, M., APOST-3D Program. *Universitat de Girona: Girona, Spain* **2020**.

310.   Glendening, E. D.; Badenhoop, J. K.; Reed, A. E.; Carpenter, J. E.; Bohmann, J. A.; Morales, C. M.; Landis, C. R.; Weinhold, F. *GENNBO 6.0*, GENNBO 6.0; Theoretical Chemistry Institute, University of Wisconsin: Madison, WI, 2013.

311.   Keith, T. A., AIMAll (Version 19.10.12). *TK Gristmill Software, Overland Park KS* **2019**.

312.   te Velde, G.; Bickelhaupt, F. M.; Baerends, E. J.; Fonseca Guerra, C.; van Gisbergen, S. J. A.; Snijders, J. G.; Ziegler, T., Chemistry with ADF. *Journal of Computational Chemistry* **2001,** *22* (9), 931-967.

313.   Becke, A. D., Density-functional exchange-energy approximation with correct asymptotic behavior. *Phys. Rev. A* **1988,** *38* (6), 3098-3100.

314.   Perdew, J. P., Density-functional approximation for the correlation energy of the inhomogeneous electron gas. *Phys. Rev. B* **1986,** *33* (12), 8822-8824.

315.   Becke, A. D., Density-functional thermochemistry. III. The role of exact exchange. *The Journal of Chemical Physics* **1993,** *98* (7), 5648-5652.

316.   Lee, C.; Yang, W.; Parr, R. G., Development of the Colle-Salvetti correlation-energy formula into a functional of the electron density. *Physical Review B* **1988,** *37* (2), 785-789.

317.   Zhao, Y.; Truhlar, D. G., The M06 suite of density functionals for main group thermochemistry, thermochemical kinetics, noncovalent interactions, excited states, and transition elements: two new functionals and systematic testing of four M06-class functionals and 12 other functionals. *Theor. Chem. Acc.* **2008,** *120* (1), 215-241.

318.   Chai, J.-D.; Head-Gordon, M., Long-range corrected hybrid density functionals with damped atom–atom dispersion corrections. *Phys. Chem. Chem. Phys.* **2008,** *10* (44), 6615-6620.

319.   Weigend, F.; Ahlrichs, R., Balanced basis sets of split valence, triple zeta valence and quadruple zeta valence quality for H to Rn: Design and assessment of accuracy. *Physical Chemistry Chemical Physics* **2005,** *7* (18), 3297-3305.

320.   Grimme, S.; Antony, J.; Ehrlich, S.; Krieg, H., A consistent and accurate ab initio parametrization of density functional dispersion correction (DFT-D) for the 94 elements H-Pu. *Journal of Chemical Physics* **2010,** *132* (15).

321.   Grimme, S.;   Ehrlich, S.; Goerigk, L., Effect of the Damping Function in Dispersion Corrected Density Functional Theory. *Journal of Computational Chemistry* **2011,** *32* (7), 1456-1465.

322.   Riplinger, C.; Neese, F., An efficient and near linear scaling pair natural orbital based local coupled cluster method. *The Journal of Chemical Physics* **2013,** *138* (3), 034106.

323.   Riplinger, C.; Sandhoefer, B.; Hansen, A.; Neese, F., Natural triple excitations in local coupled cluster calculations with pair natural orbitals. *The Journal of Chemical Physics* **2013,** *139* (13), 134101.

324.   Dunning, T. H., Jr., Gaussian basis sets for use in correlated molecular calculations. I. The atoms boron through neon and hydrogen. *The Journal of Chemical Physics* **1989,** *90* (2), 1007-1023.

325.   Weigend, F., Hartree–Fock exchange fitting basis sets for H to Rn †. *Journal of Computational Chemistry* **2008,** *29* (2), 167-175.

326.   Barone, V.; Cossi, M., Quantum Calculation of Molecular Energies and Energy Gradients in Solution by a Conductor Solvent Model. *The Journal of Physical Chemistry A* **1998,** *102* (11), 1995-2001.

APPENDIX I – Supporting information of Chapter III

AI.1 Amonia-borane (NH_3BH_3)

Table A-I. 1 EDA-NOCV of NH_3BH_3 at the BP86-D3(BJ)/TZ2P//BP86-D3(BJ)/def2-TZVPP level of theory. The lowest ΔE_{orb} and *iFEF* are highlighted in bold. Energy values are given in kcal/mol.

	NH_3 (singlet); BH_3 (singlet)	$[NH_3]^+$ (doublet); $[BH_3]^-$ (doublet)
ΔE_{int}	-46.5	-288.4
ΔE_{Pauli}	109.2	204.9
ΔE_{disp}[a]	-77.3 (49.7%)	-239.0 (48.5%)
ΔE_{elstat}[a]	-1.6 (1.1%)	-1.6 (0.3%)
ΔE_{orb}[a]	**-76.7** (49.3%)	-252.6 (51.2%)
$\Delta E_{orb\text{-}\sigma}$[b]	-66.5 (86.7%)	-238.2 (94.3%)
$\Delta E_{orb\text{-}rest}$[b]	-10.2 (13.3%)	-14.5 (5.7%)
$iFEF_{NH3}^{Frag}$ (*Löwdin*)	**0.57**	1.12
$iFEF_{BH3}^{Frag}$ (*Löwdin*)	**0.57**	1.12
$iFEF^{TOT}$ (*Löwdin*)	**0.57**	1.12
$iFEF_{NH3}^{Frag}$ (*Hirsh*)	**0.27**	0.71
$iFEF_{BH3}^{Frag}$ (*Hirsh*)	**0.27**	0.71
$iFEF^{TOT}$ (*Hirsh*)	**0.27**	0.71

[a] The value in parenthesis gives the percentage contribution to the total attractive interactions $\Delta E_{elstat} + \Delta E_{orb} + \Delta E_{disp}$. [b] The values in parenthesis gives the percentage contribution to the total orbital interaction ΔE_{orb}.

AII.2 AH$_n$ systems

Table A-I. 2 EDA-NOCV of AH$_n$ systems in the atomic heterolytic fragmentation (H(-1)) fragmentation the BP86-D3(BJ)/TZ2P//BP86-D3(BJ)/def2-TZVPP level of theory. Energy values are given in kcal/mol. *iFEF* values obtained using Löwdin AIM definition.

	ΔE_{orb}	*iFEF$_H$*	*iFEF$_X$*	*iFEF*
KH	-15.9	0.62	0.62	0.62
NaH	-16.1	0.60	0.60	0.60
LiH	-23.0	0.40	0.40	0.40
CaH$_2$	-73.7	0.57	1.14	1.14
MgH$_2$	-100.3	0.71	1.41	1.41
BeH$_2$	-684.3	0.69	1.38	1.38
BH$_3$	-770.9	0.84	2.42	2.43
H$_2$Se	-572.0	1.11	2.21	2.21
H$_2$S	-697.4	1.14	2.28	2.28
HBr	-339.8	1.28	1.28	1.28
HCl	-424.0	1.37	1.37	1.37
NH$_3$	-1835.5	1.14	3.43	3.43
H$_2$O	-1324.6	1.43	2.86	2.86
HF	-720.1	1.67	1.67	1.67

Table A-I. 3 EDA-NOCV of XH_n systems in the atomic heterolytic fragmentation (H(+1)) fragmentation the BP86-D3(BJ)/TZ2P//BP86-D3(BJ)/def2-TZVPP level of theory. Energy values are given in kcal/mol. *iFEF* values obtained using Löwdin AIM definition.

	ΔE_{orb}	*iFEF$_H$*	*iFEF$_X$*	*iFEF*
KH	-277.1	1.39	1.39	1.39
NaH	-266.1	1.42	1.42	1.42
LiH	-285.1	1.61	1.61	1.61
CaH_2	-506.1	1.44	2.89	2.89
MgH_2	-620.2	1.30	2.61	2.61
BeH_2	-206.2	1.31	2.63	2.63
BH_3	-962.6	1.19	3.58	3.58
H_2Se	-437.4	1.06	2.12	2.12
H_2S	-437.9	1.05	2.11	2.11
HBr	-186.8	0.96	0.96	0.96
HCl	-179.9	0.88	0.88	0.88
NH_3	-576.0	0.96	2.89	2.89
H_2O	-320.4	0.75	1.49	1.49
HF	-139.7	0.56	0.56	0.56

Table A-I. 4 EDA-NOCV of XH_n systems in the atomic homolytic fragmentation (H(0)) fragmentation the BP86-D3(BJ)/TZ2P//BP86-D3(BJ)/def2-TZVPP level of theory. Energy values are given in kcal/mol. *iFEF* values obtained using Löwdin AIM definition.

	ΔE_{orb}	*iFEF$_H$*	*iFEF$_X$*	*iFEF*
KH	-43.7	1.01	1.01	1.01
NaH	-42.9	1.01	1.01	1.01
LiH	-56.0	1.01	1.01	1.01
CaH$_2$	-154.2	1.01	2.02	2.02
MgH$_2$	-113.8	1.00	2.01	2.01
BeH$_2$	-143.9	1.00	2.00	2.00
BH$_3$	-341.8	1.02	3.00	3.01
H$_2$Se	-223.8	1.11	2.23	2.23
H$_2$S	-268.7	1.13	2.26	2.26
HBr	-133.3	1.13	1.13	1.13
HCl	-165.0	1.14	1.14	1.14
NH$_3$	-560.6	1.11	3.34	3.34
H$_2$O	-449.0	1.12	2.24	2.24
HF	-273.8	1.14	1.14	1.14

Table A-I. 5 EDA-NOCV of XH_n systems for the $X–H_n$ fragmentation at the BP86-D3(BJ)/TZ2P//BP86-D3(BJ)/def2-TZVPP level of theory. Energy values are given in kcal/mol. *iFEF* values obtained using Löwdin AIM definition.

	H(1-)		H(1+)		H(0)	
	ΔE_{orb}	iFEF	ΔE_{orb}	iFEF	ΔE_{orb}	iFEF
KH	**-15.9**	**0.62**	-277.1	1.39	-43.7	1.01
NaH	**-16.1**	**0.60**	-266.1	1.42	-42.9	1.01
LiH	**-23.0**	**0.40**	-285.1	1.61	-56.0	1.01
CaH$_2$	**-88.4**	**1.14**	-506.1	2.89	-127.1	2.02
MgH$_2$	-127.2	**1.41**	-620.2	2.61	**-113.8**	2.01
BeH$_2$	-266.3	**1.38**	-684.3	2.63	**-144.3**	2.00
BH$_3$	-1073.4	**2.42**	-816.0	3.58	**-273.5**	3.00
H$_2$Se	-638.5	2.21	-437.4	**2.12**	**-223.0**	2.22
H$_2$S	-782.4	2.27	-437.9	**2.11**	**-268.2**	2.25
HBr	-339.8	1.28	-186.8	**0.96**	**-133.3**	1.13
HCl	-424.0	1.37	-179.9	**0.88**	**-165.0**	1.14
NH$_3$	-2331.1	3.20	**-576.0**	**2.89**	-590.9	3.25
H$_2$O	-1503.5	2.78	**-320.4**	**1.49**	-461.7	2.14
HF	-720.1	1.67	**-139.7**	**0.56**	-273.8	1.14
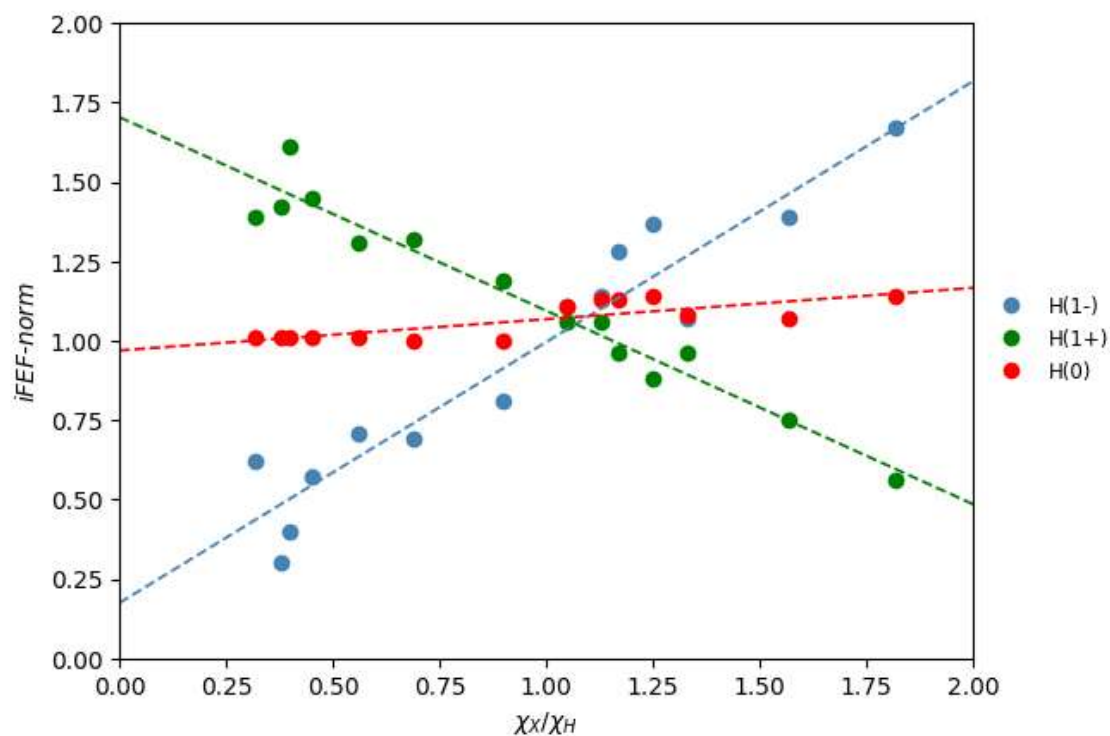
Figure A-I. 1 Correlation between iFEF and electronegativity ratio (χ_x/χ_H) in X–H_n fragmentation employing Löwdin AIM definition at the BP86-D3(BJ)/TZ2P//BP86-D3(BJ)/def2-SVP level of theory.
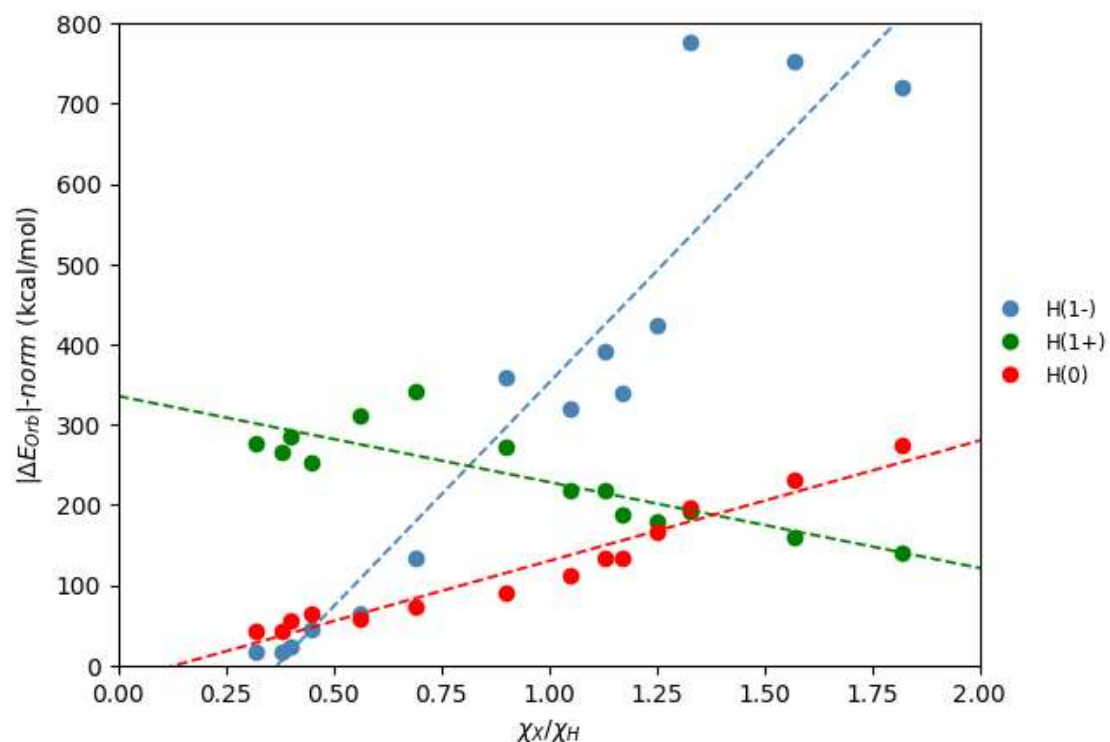
Figure A-I. 2 Correlation between normalized $|\Delta E_{orb}|$ and electronegativity ratio (χ_x/χ_H) in X–H_n fragmentation at the BP86-D3(BJ)/TZ2P//BP86-D3(BJ)/def2-SVP level of theory.

Table A-I. 6 EDA-NOCV of XH_n systems for the $H–AH_{n-1}$ fragmentation at the BP86-D3(BJ)/TZ2P//BP86-D3(BJ)/def2-TZVPP level of theory. Energy values are given in kcal/mol. *iFEF* values obtained using Löwdin AIM definition.

	H(1-)		H(1+)		H(0)	
	ΔE_{orb}	iFEF	ΔE_{orb}	iFEF	ΔE_{orb}	iFEF
KH	**-15.9**	**0.62**	-277.1	1.39	-43.7	1.01
NaH	**-16.1**	**0.60**	-266.1	1.42	-42.9	1.01
LiH	**-23.0**	**0.40**	-285.1	1.61	-56.0	1.01
CaH₂	**-38.2**	**0.59**	-287.7	1.44	-64.3	1.03
MgH₂	**-54.5**	**0.73**	-245.7	1.30	-61.2	1.02
BeH₂	-98.0	**0.69**	-237.2	1.31	**-74.7**	1.01
BH₃	-225.2	**0.84**	-214.0	1.24	**-104.4**	1.06
H₂Se	-269.8	1.17	-201.7	**1.06**	**-114.8**	1.13
H₂S	-329.2	1.23	-201.3	**1.05**	**-137.9**	1.15
HBr	-339.8	1.28	-186.8	**0.96**	**-133.3**	1.13
HCl	-424.0	1.37	-179.9	**0.88**	**-165.0**	1.14
NH₃	-473.6	1.69	**-183.2**	**1.00**	-218.6	1.35
H₂O	-571.1	1.64	**-163.5**	**0.77**	-236.6	1.27
HF	-720.1	1.67	**-139.7**	**0.56**	-273.8	1.14
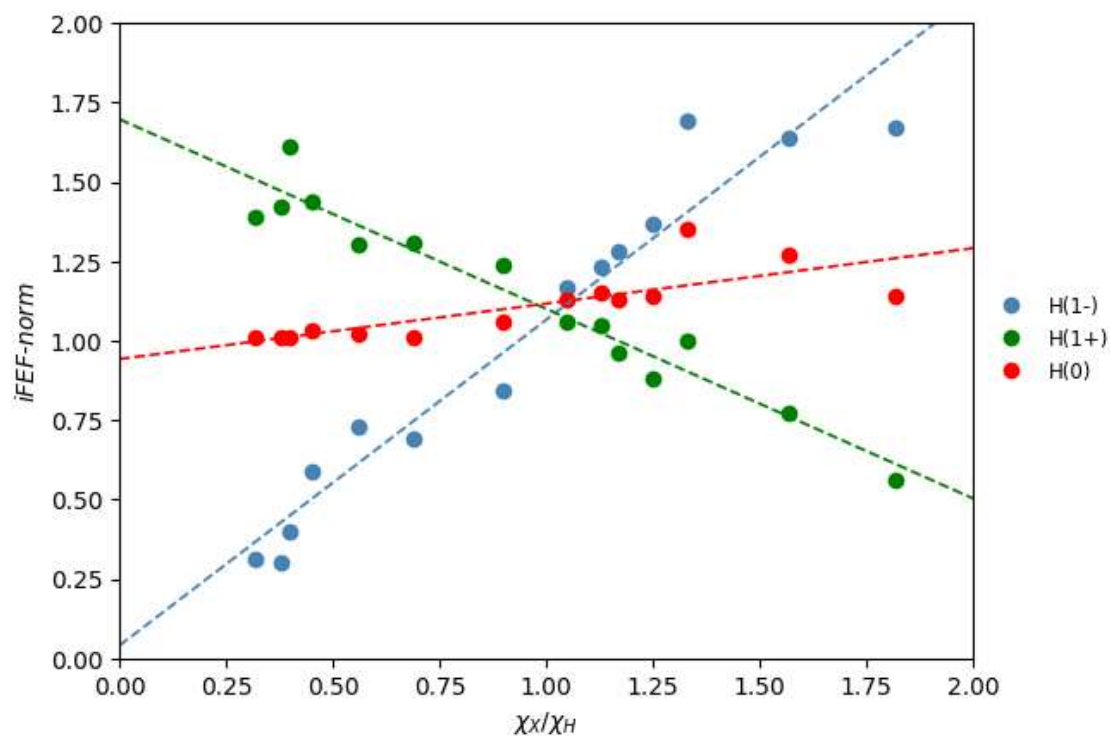
Figure A-I. 3 Correlation between iFEF and electronegativity ratio (χ_x/χ_H) in H–AH$_n$ fragmentation employing Löwdin AIM definition at the BP86-D3(BJ)/TZ2P//BP86-D3(BJ)/def2-SVP level of theory.
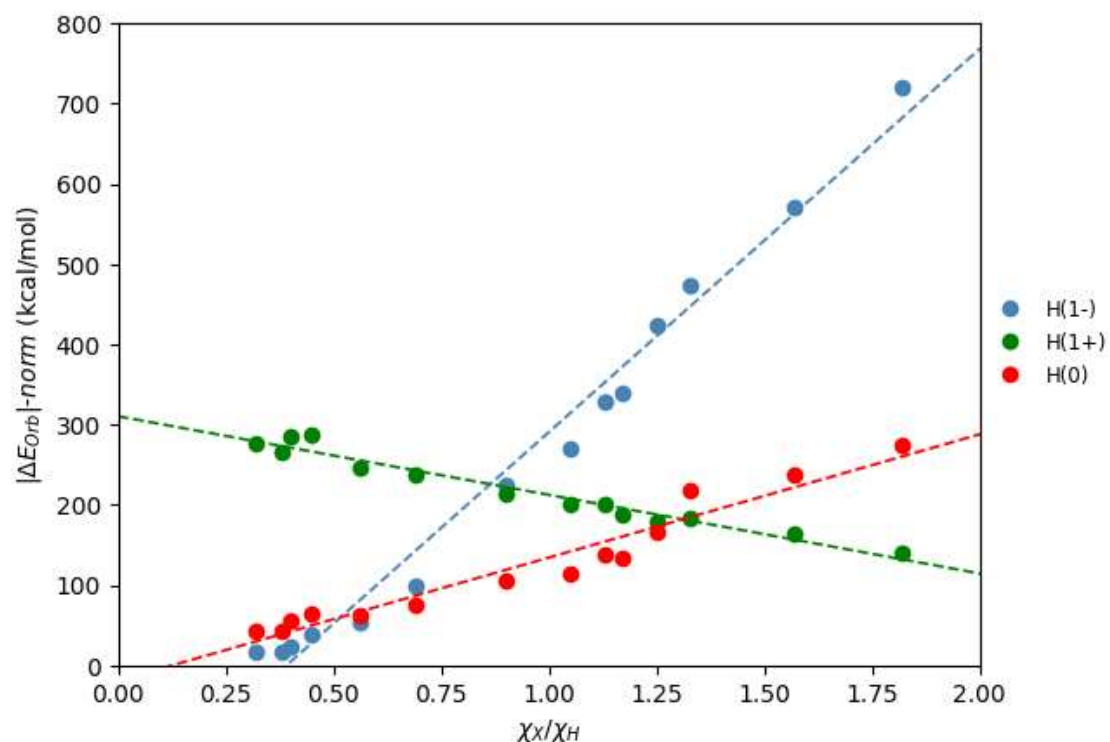
Figure A-I. 4 Correlation between $|\Delta E_{orb}|$ and electronegativity ratio (χ_x/χ_H) in H–AH$_n$ fragmentation employing Löwdin AIM definition at the BP86-D3(BJ)/TZ2P//BP86-D3(BJ)/def2-SVP level of theory.

Table A-I. 7 ΔE_{orb} and iFEF values for XH_n systems in all the fragmentation patterns at the BP86-D3(BJ)/TZ2P//BP86-D3(BJ)/def2-TZVPP level of theory. The lowest ΔE_{orb} and iFEF are highlighted in bold. Energy values are given in kcal/mol.

| | *Atomic Fragmentation* | | | | | | *H–XH_{n-1} Fragmentation* | | | | | | *X–H_n Fragmentation* | | | | | |
| | ΔE_{orb} | | | *iFEF* | | | ΔE_{orb} | | | *iFEF* | | | ΔE_{orb} | | | *iFEF* | | |
	H(1-)	H(1+)	H(o)	H(1-)	H(1+)	H(o)	H(1-)	H(1+)	H(o)	H(1-)	H(1+)	H(o)	H(1-)	H(1+)	H(o)	H(1-)	H(1+)	H(o)
KH	**-15.9**	-277.1	-43.7	**0.62**	1.39	1.01	**-15.9**	-277.1	-43.7	**0.62**	1.39	1.01	**-15.9**	-277.1	-43.7	**0.62**	1.39	1.01
NaH	**-16.1**	-266.1	-42.9	**0.60**	1.42	1.01	**-16.1**	-266.1	-42.9	**0.60**	1.42	1.01	**-16.1**	-266.1	-42.9	**0.60**	1.42	1.01
LiH	**-23.0**	-285.1	-56.0	**0.40**	1.61	1.01	**-23.0**	-285.1	-56.0	**0.40**	1.61	1.01	**-23.0**	-285.1	-56.0	**0.40**	1.61	1.01
CaH$_2$	**-73.7**	-506.1	-154.2	**1.14**	2.89	2.02	**-38.2**	-287.7	-64.3	**0.59**	1.44	1.03	**-88.4**	-506.1	-127.1	**1.14**	2.89	2.02
MgH$_2$	**-100.3**	-620.2	-113.8	**1.41**	2.61	2.01	**-54.5**	-245.7	-61.2	**0.73**	1.30	1.02	-127.2	-620.2	**-113.8**	**1.41**	2.61	2.01
BeH$_2$	-206.2	-684.3	**-143.9**	**1.38**	2.63	2.00	-98.0	-237.2	**-74.7**	**0.69**	1.31	1.01	-560.0	-684.3	**-144.3**	**1.38**	2.63	2.00
BH$_3$	-770.9	-962.6	**-341.8**	**2.43**	3.58	3.01	-225.2	-214.0	**-104.4**	**0.84**	1.24	1.06	-1073.4	-816.0	**-273.5**	**2.42**	3.58	3.00
H$_2$Se	-572.0	-437.4	**-223.8**	2.21	**2.12**	2.23	-269.8	-201.7	**-114.8**	1.17	**1.06**	1.13	-638.5	-437.4	**-223.0**	2.21	**2.12**	2.22
H$_2$S	-697.4	-437.9	**-268.7**	2.28	**2.11**	2.26	-329.2	-201.3	**-137.9**	1.23	**1.05**	1.15	-782.4	-437.9	**-268.2**	2.27	**2.11**	2.25
HBr	-339.8	-186.8	**-133.3**	1.28	**0.96**	1.13	-339.8	-186.8	**-133.3**	1.28	**0.96**	1.13	-339.8	-186.8	**-133.3**	1.28	**0.96**	1.13
HCl	-424.0	-179.9	**-165.0**	1.37	**0.88**	1.14	-424.0	-179.9	**-165.0**	1.37	**0.88**	1.14	-424.0	-179.9	**-165.0**	1.37	**0.88**	1.14
NH$_3$	-1835.5	-576.0	**-560.6**	3.43	**2.89**	3.34	-473.6	**-183.2**	-218.6	1.69	**1.00**	1.35	-2331.1	-576.0	-590.9	3.20	**2.89**	3.25
H$_2$O	-1324.6	**-320.4**	-449.0	2.86	**1.49**	2.24	-571.1	**-163.5**	-236.6	1.64	**0.77**	1.27	-1503.5	-320.4	-461.7	2.78	**1.49**	2.14
HF	-720.1	**-139.7**	-273.8	1.67	**0.56**	1.14	-720.1	**-139.7**	-273.8	1.67	**0.56**	1.14	-720.1	-139.7	-273.8	1.67	**0.56**	1.14

AI.3 Halomethanes (X-CH₃)

Table A-I. 8 EDA-NOCV of CH_3X (X=F, Cl, Br, I) at the BP86-D3(BJ)/TZ2P//BP86-D3(BJ)/def2-TZVPP level of theory. The lowest $|\Delta E_{orb}|$ and *i*FEF are highlighted in bold. Energy values are given in kcal/mol.

	F			Cl			Br			I		
	F(1-)	F(0)	F(1+)	Cl(1-)	Cl(0)	Cl(1+)	Br(1-)	Br(0)	Br(1+)	I(1-)	I(0)	I(1+)
ΔE_{int}	-303.0	-127.8	-615.0	-264.5	-97.0	-440.7	-253.8	-85.9	-398.3	-245.2	-74.4	-350.9
ΔE_{Pauli}	195.6	275.2	473.2	156.8	175.9	331.9	141.3	150.5	301.3	124.0	125.6	266.1
ΔE_{elstat}	-292.8	-113.6	-384.6	-211.7	-99.6	-387.9	-189.2	-95.1	-392.8	-166.5	-85.6	-380.9
ΔE_{disp}	-0.4	-0.4	-0.4	-1.4	-1.4	-1.4	-1.7	-1.7	-1.7	-2.2	-2.2	-2.2
ΔE_{orb}	**-205.4**	-289.0	-703.3	-208.3	**-171.9**	-383.4	-204.2	**-139.5**	-305.1	-200.5	**-112.2**	-233.9
iFEF(*Löwdin*)	**0.60**	1.11	1.57	**0.82**	1.05	1.27	**0.85**	1.08	1.40	**0.94**	1.03	1.23
iFEF(*Hirshfeld*)	**0.43**	0.82	1.22	**0.57**	0.76	0.94	**0.62**	0.76	0.86	**0.70**	0.76	0.78

Table A-I. 9 *ΔE_{orb}* and *iFEF* values of σ-bonding channel of CH$_3$X (X=F, Cl, Br, I) in the X(1-) fragmentation at the BP86-D3(BJ)/TZ2P//BP86-D3(BJ)/def2-TZVPP level of theory. Energy values are given in kcal/mol.

				Löwdin			Hirshfeld		
	$\Delta E_{orb\text{-}\sigma}$	*$\Delta E_{orb\text{-}\sigma(\alpha)}$*	*$\Delta E_{orb\text{-}\sigma(\beta)}$*	$\delta_{CH_3}^{\alpha,\sigma}$	$\delta_{CH_3}^{\beta,\sigma}$	*$iFEF^{\sigma}$*	$\delta_{CH_3}^{\alpha,\sigma}$	$\delta_{CH_3}^{\beta,\sigma}$	*$iFEF^{\sigma}$*
F	-162.5	-81.3	-81.3	0.26	0.26	0.51	0.19	0.19	0.37
Cl	-181.2	-90.6	-90.6	0.38	0.38	0.76	0.26	0.26	0.52
Br	-181.7	-90.8	-90.8	0.39	0.39	0.78	0.29	0.29	0.58
I	-183.6	-91.8	-91.8	0.44	0.44	0.88	0.32	0.32	0.64

Table A-I. 10 ΔE_{orb} and *iFEF* values of σ-bonding channel CH_3X (X=F, Cl, Br, I) in the X (0) fragmentation at the BP86-D3(BJ)/TZ2P//BP86-D3(BJ)/def2-TZVPP level of theory. Energy values are given in kcal/mol.

	$\Delta E_{orb\text{-}\sigma}$	$\Delta E_{orb\text{-}\sigma(\alpha)}$	$\Delta E_{orb\text{-}\sigma(\beta)}$	Löwdin			Hirshfeld		
				$\delta_{CH_3}^{\alpha,\sigma}$	$\delta_{CH_3}^{\beta,\sigma}$	$iFEF^\sigma$	$\delta_{CH_3}^{\alpha,\sigma}$	$\delta_{CH_3}^{\beta,\sigma}$	$iFEF^\sigma$
F	-266.1	-219.4	-46.8	-0.74	0.27	1.00	-0.50	0.22	0.72
Cl	-156.6	-106.6	-49.9	-0.60	0.39	0.99	-0.43	0.29	0.72
Br	-127.4	-80.3	-47.1	-0.60	0.40	1.00	-0.41	0.32	0.73
I	-103.0	-57.2	-45.8	-0.54	0.45	0.99	-0.39	0.35	0.74

Table A-I. 11 ΔE_{orb} and *iFEF* values of σ-bonding channel CH_3X (X=F, Cl, Br, I) in the X (1+) fragmentation at the BP86-D3(BJ)/TZ2P//BP86-D3(BJ)/def2-TZVPP level of theory. Energy values are given in kcal/mol.

				Löwdin			Hirshfeld		
	$\Delta E_{orb\text{-}\sigma}$	$\Delta E_{orb\text{-}\sigma(\alpha)}$	$\Delta E_{orb\text{-}\sigma(\beta)}$	$\delta_{CH_3}^{\alpha,\sigma}$	$\delta_{CH_3}^{\beta,\sigma}$	$iFEF^{\sigma}$	$\delta_{CH_3}^{\alpha,\sigma}$	$\delta_{CH_3}^{\beta,\sigma}$	$iFEF^{\sigma}$
F	-665.0	-332.5	-332.5	0.72	0.72	1.44	0.49	0.49	0.98
Cl	-352.5	-176.3	-176.3	0.59	0.59	1.18	0.40	0.40	0.80
Br	279.0	-139.5	-139.5	0.58	0.58	1.16	0.38	0.38	0.76
I	-211.3	-105.7	-105.7	0.53	0.53	1.06	0.36	0.36	0.72

AI.4 Carbon dioxide (CO_2)

Table A-I. 12 EDA-NOCV of CO_2 at the BP86-D3(BJ)/TZ2P//BP86-D3(BJ)/def2-TZVPP level of theory employing 3 atomic fragments. The lowest ΔE_{orb} and iFEF are highlighted in bold. Energy values are given in kcal/mol.

	C(0) (^{5}F)	C(2+) (^{3}P)	C(4+) (^{1}S)
ΔE_{int}	-514.9	-1323.7	-4189.3
ΔE_{Pauli}	986.0	793.6	506.6
ΔE_{elstat}	-415.0	-1066.9	-3232.3
ΔE_{disp}	-0.9	-0.9	-0.9
ΔE_{orb}	-1084.9	**-1049.5**	-1462.7
iFEF (Löwdin)	4.50	3.70	**3.11**
iFEF (Hirshfeld)	2.78	1.71	**0.30**

Table A-I. 13 *iFEF*[k] of the four main bonding channels of CO_2 at the BP86-D3(BJ)/TZ2P//BP86-D3(BJ)/def2-TZVPP level of theory employing 3 atomic fragments. Energy values are given in kcal/mol.

Fragmentation	C(0) (^{5}F)		C(2+) (^{3}P)		C(4+) (^{1}S)	
Spin	α	β	α	β	α	β
$\Delta E_{orb-\pi 1}$	-134.8	-42.5	-104.2	-91.4	-155.5	-155.5
iFEF $^{\pi 1}$*(Löw)*	0.79	0.37	0.37	0.37	0.37	0.37
iFEF $^{\pi 1}$*(Hirs)*	0.61	0.26	0.19	0.19	0.04	0.04
$\Delta E_{orb-\pi 2}$	-134.8	-42.5	-104.2	-91.4	-155.5	-155.5
iFEF $^{\pi 2}$*(Löw)*	0.79	0.37	0.37	0.37	0.37	0.37
iFEF $^{\pi 2}$*(Hirs)*	0.61	0.26	0.19	0.19	0.04	0.04
$\Delta E_{orb-\sigma(+,-)}$	-392.9	-87.6	-267.7	-119.9	-195.3	-195.3
iFEF $^{\sigma(+,-)}$ *(Löw)*	0.62	0.35	0.64	0.34	0.33	0.33
iFEF $^{\sigma(+,-)}$ *(Hirs)*	0.29	0.16	0.32	0.16	0.05	0.05
$\Delta E_{orb-\sigma(+,+)}$	-154.0	-87.6	-116.7	-76.1	-130.5	-130.5
iFEF $^{\sigma(+,+)}$ *(Löw)*	0.64	0.35	0.65	0.38	0.38	0.38
iFEF $^{\sigma(+,+)}$ *(Hirs)*	0.30	0.20	0.25	0.15	0.03	0.03
$\Delta E_{orb-rest}$	-8.3		-77.8		-189.2	

Table A-I. 14 EDA-NOCV of CO_2 at the BP86-D3(BJ)/TZ2P//BP86-D3(BJ)/def2-TZVPP level of theory employing 2 fragments (C and O_2). The lowest ΔE_{orb} and iFEF are highlighted in bold. Energy values are given in kcal/mol.

	C(0) (^{5}F)	C(2+) (^{3}P)	C(4+) (^{1}S)
ΔE_{int}	-519.8	-1451.8	-4710.3
ΔE_{Pauli}	1082.6	701.4	267.7
ΔE_{elstat}	-406.9	-1067.5	-3232.6
ΔE_{disp}	-0.6	-0.6	-0.6
ΔE_{orb}	-1194.9	**-1085.1**	-1744.8
iFEF (Löwdin)	4.08	3.69	**3.11**
iFEF (Hirshfeld)	2.25	1.52	**0.37**

Table A-I. 15 EDA-NOCV of CO_2 at the BP86-D3(BJ)/TZ2P//BP86-D3(BJ)/def2-TZVPP level of theory employing 2 fragments (C and O_2). The lowest ΔE_{orb} and iFEF are highlighted in bold. Energy values are given in kcal/mol.

Fragmentation	C(0) (^{5}F)		C(2+) (^{3}P)		C(4+) (^{1}S)	
Spin	α	β	α	β	α	β
$\Delta E_{orb\text{-}\pi 1}$	-194.0	-41.4	-109.0	-95.9	-175.1	-175.1
iFEF $\pi 1$(Löw)	0.56	0.47	0.37	0.37	0.37	0.37
iFEF $\pi 1$(Hirs)	0.36	0.26	0.20	0.20	0.05	0.05
$\Delta E_{orb\text{-}\pi 2}$	-194.0	-41.4	-109.0	-95.9	-175.1	-175.1
iFEF $\pi 2$(Löw)	0.56	0.37	0.37	0.37	0.37	0.37
iFEF $\pi 2$(Hirs)	0.36	0.26	0.20	0.20	0.05	0.05
$\Delta E_{orb\text{-}\sigma(+,-)}$	-382.1	-89.9	-250.3	-132.4	-239.7	-239.7
iFEF $\sigma(+,-)$ (Löw)	0.62	0.35	0.64	0.34	0.32	0.32
iFEF $\sigma(+,-)$ (Hirs)	0.29	0.16	0.32	0.16	0.05	0.05
$\Delta E_{orb\text{-}\sigma(+,+)}$	-156.8	-44.1	-114.9	-82.6	-154.4	-154.4
iFEF $\sigma(+,+)$ (Löw)	0.64	0.38	0.65	0.38	0.38	0.38
iFEF $\sigma(+,+)$ (Hirs)	0.30	0.20	0.26	0.16	0.04	0.04
$\Delta E_{orb\text{-}rest}$	-51.1		-95.1		-256.4	

APPENDIX II- Supporting information of Chapter IV

AII.1 Synthesis of 29:
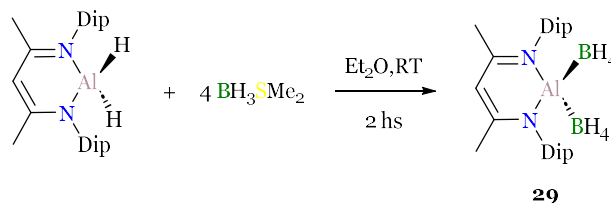
Procedure: An overnight dried 100 mL Schlenk flask was charged 1.140 g (0.255 mmol,1 eq) and dissolved in 50 mL of Et$_2$O. At room temperature, 0.97 mL of DMS.BH$_3$ (1.021 mmol, 4 eq) are added dropwise to the stirring solution. The reaction mixture is stirred for 3 hours. The solvent is removed under vacuum to obtain compound **29** as a white solid (1.128g, 93%).

^{1}H-NMR (300.13 MHz, 298 K, benzene-d_6): δ(ppm) = 1.06 (d, $^3J_{H-H}$= 6.76 Hz, 12H,C$_{ipr}$-Me$_2$), 1.40 (d, $^3J_{H-H}$= 6.69 Hz, 12H,C$_{ipr}$-Me$_2$), 1.51 (s, 6H, Me(NacNac)), 3.28 (sept, $^3J_{H-H}$= 6,74 Hz, 4H, C$_{ipr}$-H), 4.92(s, 1H,C$_γ$-H), 7.09(m,6H,Ar-H). The BH$_4$ could not be determined due to the broadness of the signal. **^{11}B-NMR (96.29 MHz, 298 K, benzene-d_6):** δ(ppm)= -36.57 (quint, $^1J_{B-H}$ =86.67 Hz).

Figure A-II. 1 ^{1}H-NMR (300.13 MHz, 298 K, benzene-d$_6$) of compound **29**.
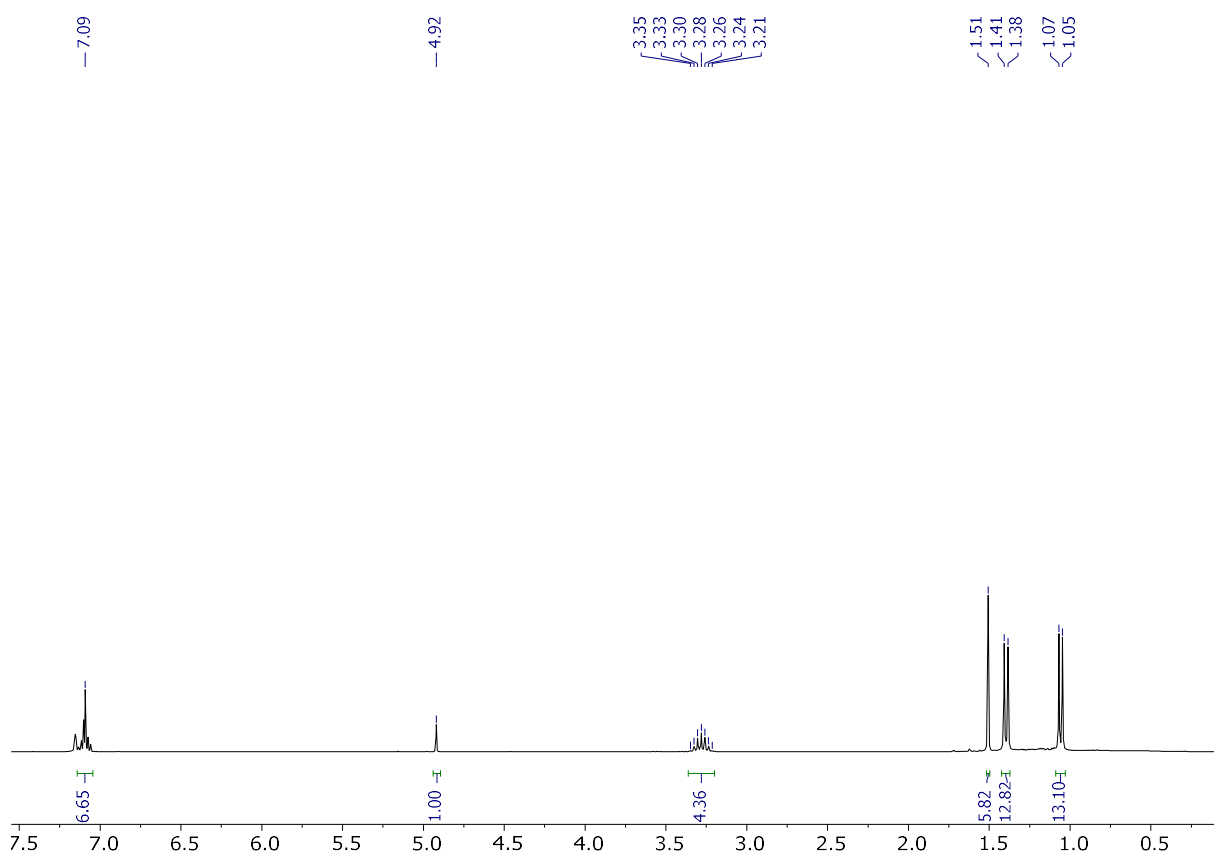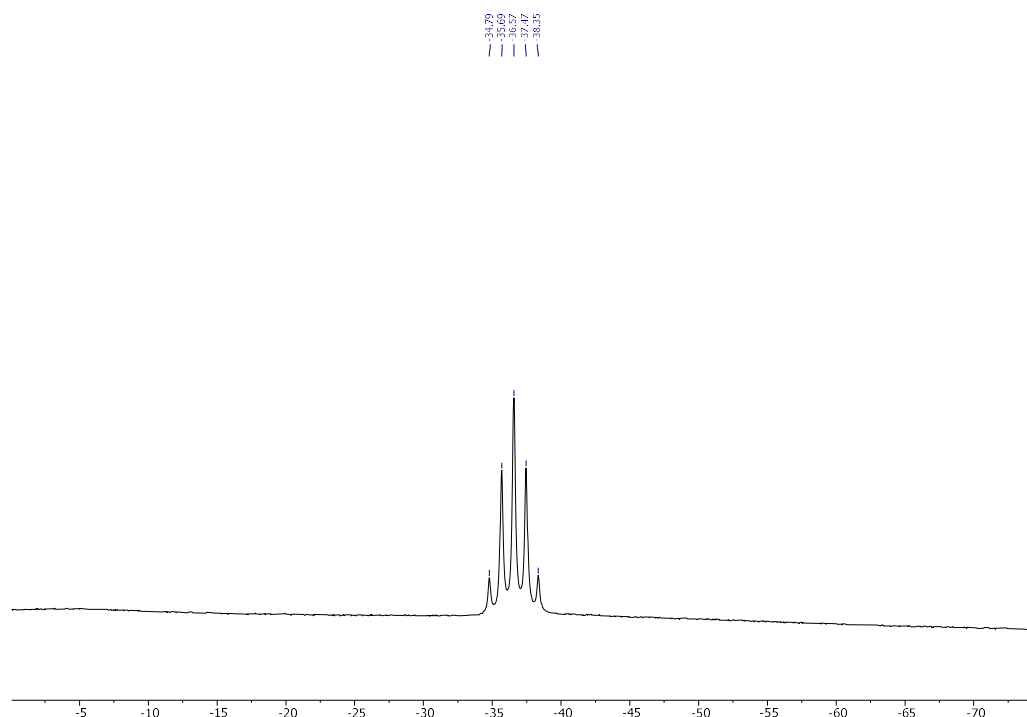
Figure A-II. 2 ^{11}B-NMR (96.29 MHz, 298 K, benzene-d_6) of compound **29**.

AII.2 Synthesis of NacNacAl(t-BuO)(BH$_4$) (87)
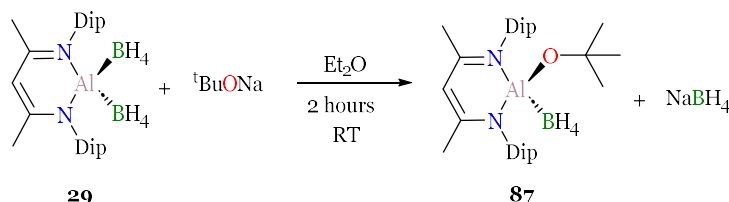
Procedure: An overnight oven dried 25mL Schlenk tube was charged with 100 mg of **29** (1 eq, 0.211 mmol) and 24 mg (1 eq, 0.211mmol) of *t*BuONa. Then, 5 mL of Et2O are added to form a white slurry solution. It is stirred for 2 hours at room temperature. The slurry solution is filtered off and the filtrated is dried under vaccum to obtain a pale yellow oil. It is triturated with hexane to obtain a pale-yellow solid. The solid is redissolved in Et$_2$O and kept at -35°C freezer overnight to yield colorless crystals. (69 mg, 62%).

^{1}H-NMR (400.13 MHz, 298 K, benzene-d_6): δ(ppm)= 0.89 (s, 9H, C$_{t-Bu}$-$\underline{Me}_3$), 1.03 (d, $^3J_{H-H}$= 6.93 Hz, 6H,C$_{ipr}$-$\underline{Me}_2$), 1.15 (d,$^3J_{H-H}$= 6.93 Hz, 6H, C$_{ipr}$-$\underline{Me}_2$), 1.48 (dd,$^3J_{H-H}$= 6.93 Hz, 12H C$_{ipr}$-$\underline{Me}_2$), 1.59 (s, 6H, $\underline{Me}$(NacNac)), 3.50 (sept,$^3J_{H-H}$= 6.27 Hz, 2H, C$_{ipr}$-$\underline{H}$), 3.73 (sept,$^3J_{H-H}$= 6.81 Hz, 2H, C$_{ipr}$-$\underline{H}$), 4.90 (s, 1H,C$_\gamma$-$\underline{H}$). (Aromatic protons are overlapped with the solvent peak). The B$\underline{H}_4$ could not be determined due to the broadness of the signal. **^{13}C{^{1}H} (100.61 MHz, 298 K, benzene-d_6):** δ(ppm)=23.77(backbone-$\underline{C}$H$_3$), 23.86(C$_{ipr}$-$\underline{C}$H$_3$), 24.82(C$_{ipr}$-$\underline{C}$H$_3$),25.13(C$_{ipr}$-$\underline{C}$H$_3$), 26.75 (C$_{ipr}$-$\underline{C}$H$_3$), 28.81($\underline{C}_{ipr}$-CH$_3$), 29.01($\underline{C}_{ipr}$-CH$_3$), 32.52 (C$_{t-Bu}$-$\underline{C}$H$_3$), 69.00 ($\underline{C}_{t-Bu}$-Me$_3$), 97.30 ($\underline{C}_\gamma$-backbone), 123.95 ($\underline{C}$-Ar), 125.23($\underline{C}$-Ar), 139.90($\underline{C}$-Ar),144.80($\underline{C}$-Ar), 145.74($\underline{C}$-Ar), 170.84(C$_\beta$-backbone). **^{11}B-NMR (128.3MHz, 298 K, benzene-d_6):** δ(ppm)= -37.12 (quint, J$_{B-H}$ =86.09 Hz). **^{27}Al-NMR (104.26 MHz, 272 K, benzene-d_6):** δ(ppm)= silent in the range of 190 to -190 ppm. **IR**: υ(cm^{-1}) =2485.7 (br, B-H), 2404.3 (br, B-H), 2281.8 (br, B-H), 2195.7 (br, B-H).

Elemental analyisis (%): calc for **87:** C: 74.42, H: 10.22, N:5.26; found: C: 73.80, H: 9.41, N:4.85. **Melting point:** 198°C
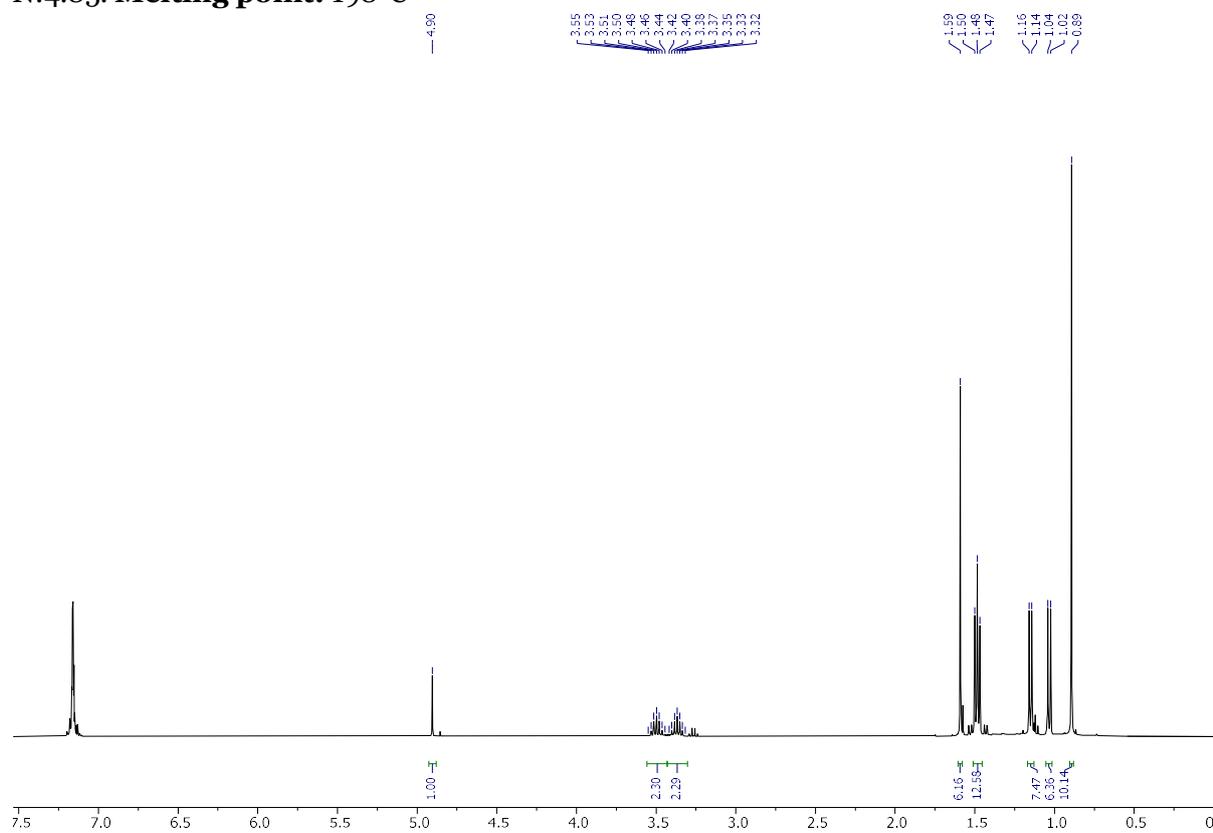
Figure A-II. 3 ^{1}H-NMR (400.13 MHz, 298 K, benzene-d_6) of compound **87**.
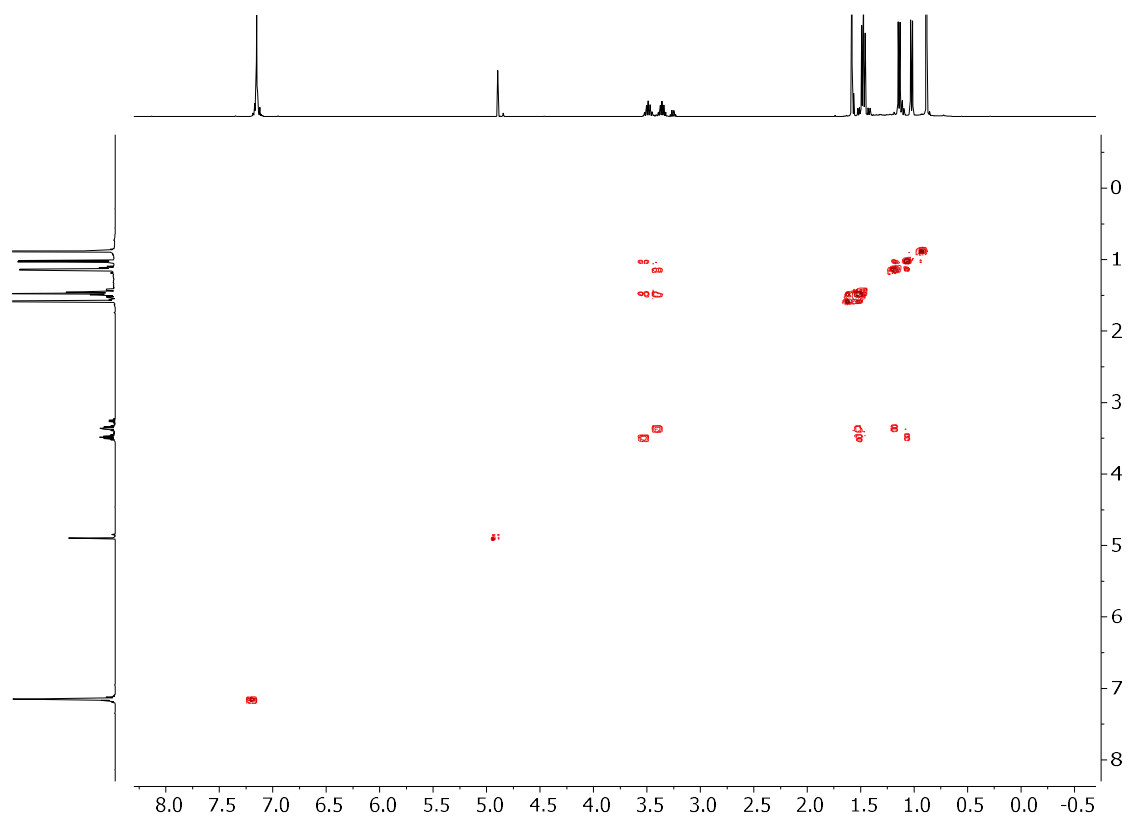
Figure A-II. 4 ¹H-¹H COSY NMR (400.13 MHz, 298 K, benzene-d₆) of compound **87**.
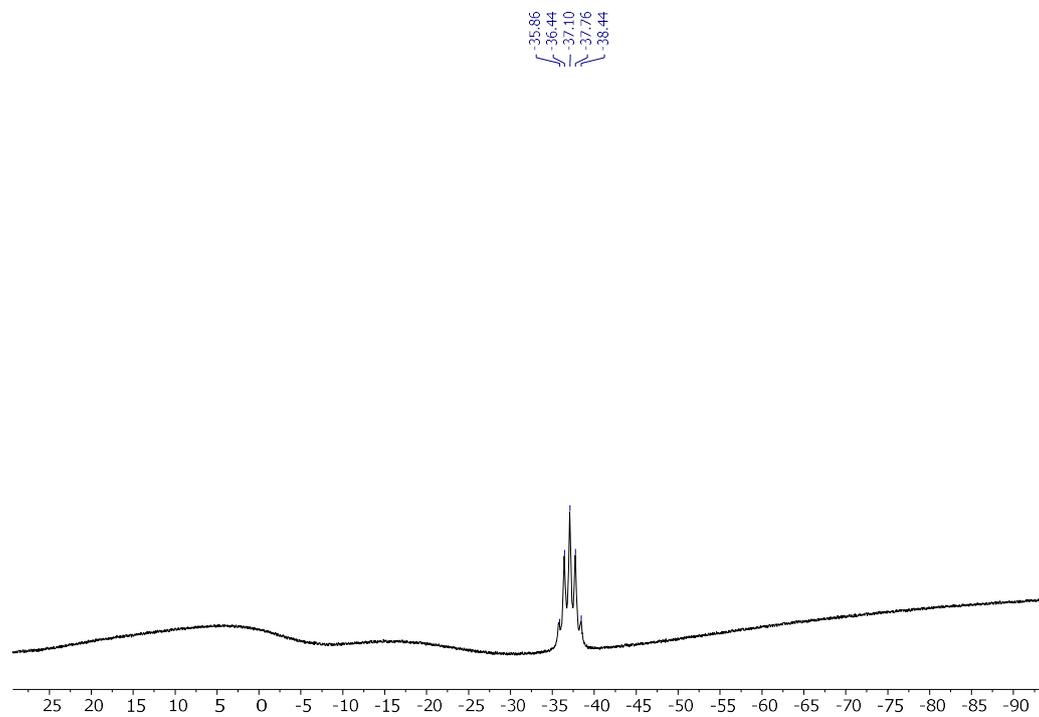
Figure A-II. 5 ¹¹B-NMR (128.4 MHz, 298 K, benzene-d₆) of compound **87**.
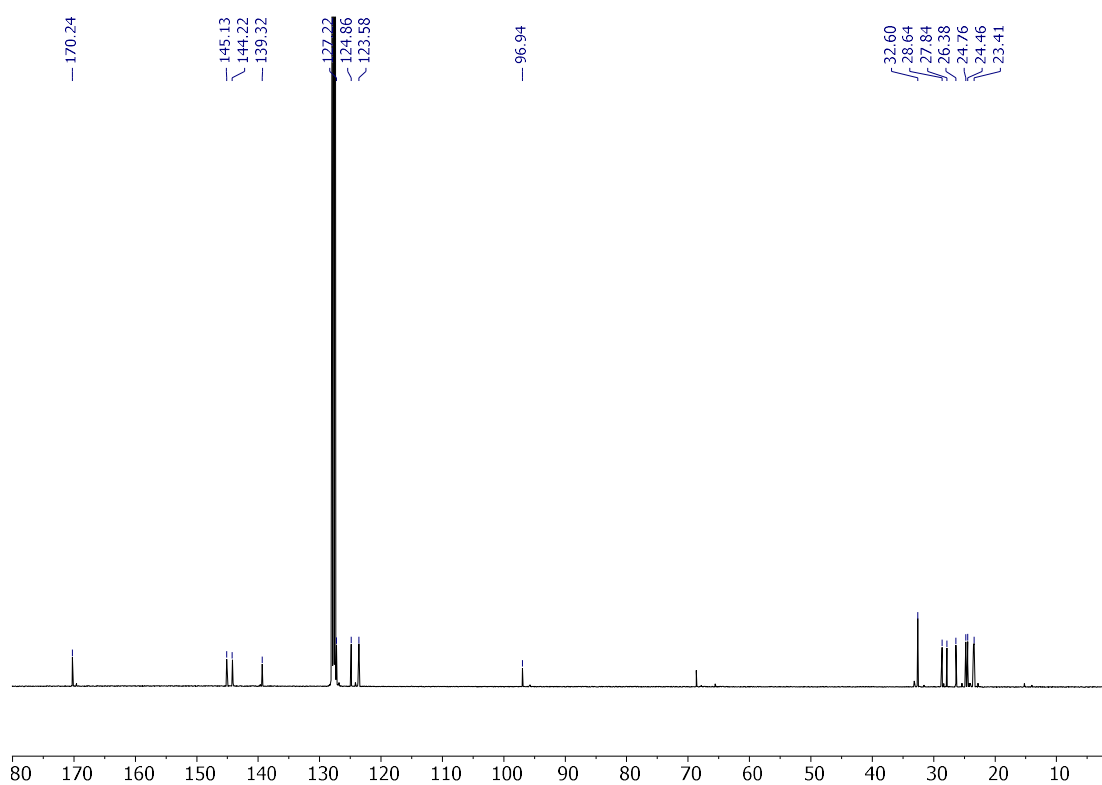
Figure A-II. 6 ^{13}C{^{1}H} (100.61 MHz, 298 K, benzene-d$_6$) of compound **87**.
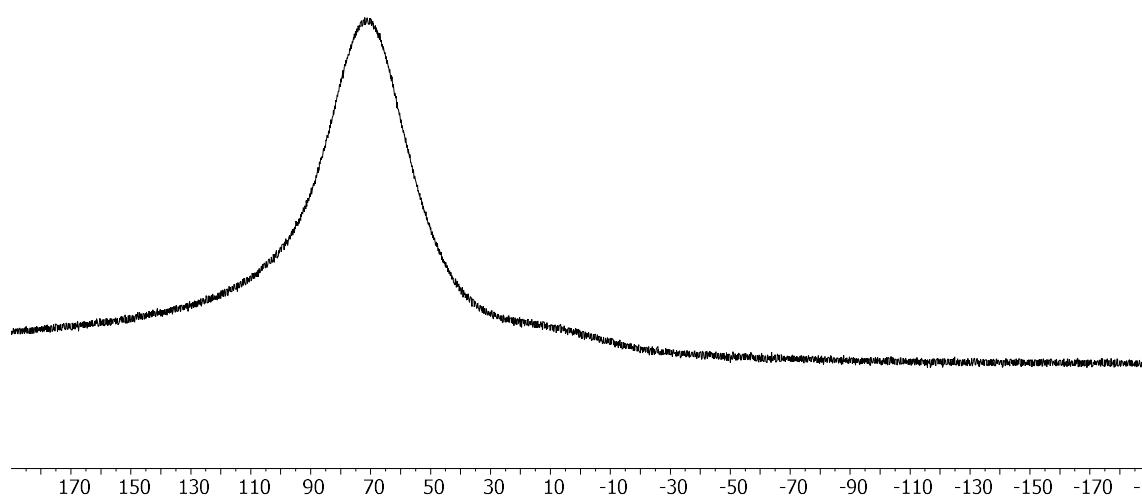
Figure A-II. 7 ^{27}Al-NMR (104.26 MHz, 272 K, benzene-d$_6$) of compound **87**.
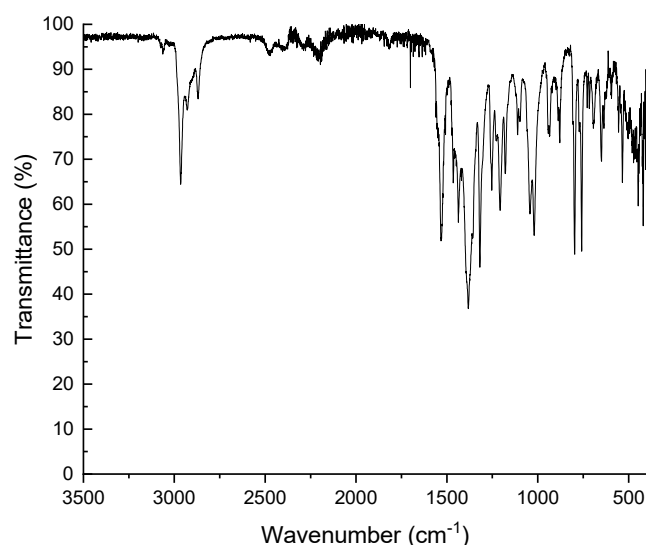
Figure A-II. 8 FT-IR spectrum of compound **87**.

AII.3 Synthesis of NacNacAl(OCP)(BH₄) (88):
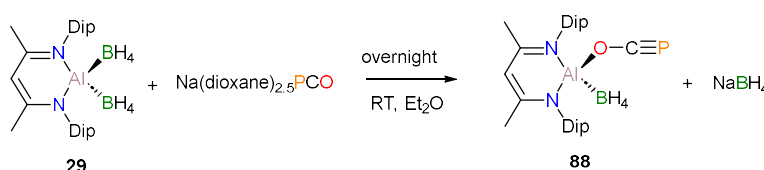
Procedure: In the glovebox, 200 mg (1 eq, 0.422 mmol) of NacNacAl(BH₄)₂ and 127 mg (1eq, 0.422 mmol) of NaPCO(dioxane)$_{2.5}$ are placed in a 25 ml Schlenk tube. Then, 4 mL of Et₂O are added and the reaction mixture is stirred overnight at room temperature. The solution is filtered off to obtain an orange solution. Then, the solution is concentrated until incipient precipitation. Then, compound **88** is crystallized at -35°C overnight. 113 mg (51.6%) of **88** are collected. Single crystals suitable for X-Ray diffraction were obtained from Et₂O at -30 °C overnight.

¹H-NMR (400.13 MHz, 298 K, benzene-*d₆*): δ(ppm)= 0.99 (d, 6H, ³J$_{H-H}$= 6.83 Hz, C$_{ipr}$-$\underline{Me}_2$), 1.28 (d, 6H, ³J$_{H-H}$ = 6.80 Hz, C$_{ipr}$-$\underline{Me}_2$), 1.32 (d, 6H, ³J$_{H-H}$ = 6.80 Hz, C$_{ipr}$-$\underline{Me}_2$), 1.51 (s, 6H, $\underline{Me}$(NacNac)), 1.53 (d, 6H, ³J$_{H-H}$ =6.64Hz, C$_{ipr}$-$\underline{Me}_2$), 3.03 (sept, 2H, ³J$_{H-H}$=6.83 Hz, C$_{ipr}$-$\underline{H}$), 3.72 (sept, 2H, ³J$_{H-H}$=6.85 Hz, C$_{ipr}$-$\underline{H}$), 4.98 (s, 1H, C$_\gamma$-$\underline{H}$), 7.01 (m, 2H,$\underline{Ar-H}$), 7.10 (d, 4H, ²J$_{H-H}$=4.62 Hz, Ar-$\underline{H}$). The B$\underline{H}_4$ could not be determined due to the broadness of the signal. **¹³C{¹H} (100.61 MHz, 298 K, benzene-*d₆*)** δ= 23.50 (backbone-$\underline{CH}_3$), 24.03(C$_{ipr}$-$\underline{CH}_3$), 24.32(C$_{ipr}$-$\underline{CH}_3$), 24.42(C$_{ipr}$-$\underline{CH}_3$), 25.03(C$_{ipr}$-$\underline{CH}_3$), 27.86($\underline{C}_{ipr}$-H), 28.79($\underline{C}_{ipr}$-H), 100.58 ($\underline{C}_\gamma$-H), 124.19 ($\underline{C}$-Ar), 125.13 ($\underline{C}$-Ar), 138.10 ($\underline{C}$-Ar), 143.23($\underline{C}$-Ar), 145.88($\underline{C}$-Ar), 149.23 (d, ¹J$_{P-C}$ = 3.16 Hz, P$\underline{C}$O), 173.29($\underline{C}_\beta$-H). **³¹P{¹H}-NMR (161.98 MHz, 298 K, benzene-*d₆*):** δ(ppm)= -319.36 (s). **(161.98 MHz, 298 K, benzene-*d₆*):** δ(ppm)= -319.36 (s). **¹¹B-NMR (128.38 MHz, 298 K, benzene-*d₆*):** δ(ppm)= -44.37 (quint, J$_{B-H}$ =86.06 Hz). **²⁷Al-NMR (104.28MHz, 298 K, benzene-*d₆*):** δ(ppm)=68.04 (bs). **IR**: υ(cm⁻¹)= 2493.0 (br,B-H), 2296.8 (br,B-H), 2157 (br,B-H),1693.0(C-O,s). **Melting point:** 198°C (decomposition to complex mixture of compounds).

Elemental analysis: calc for **88:** C: 69.50 % H: 8.75 % N: 5.40%; found: C:69.30%, H: 8.00%, N:5.03%.
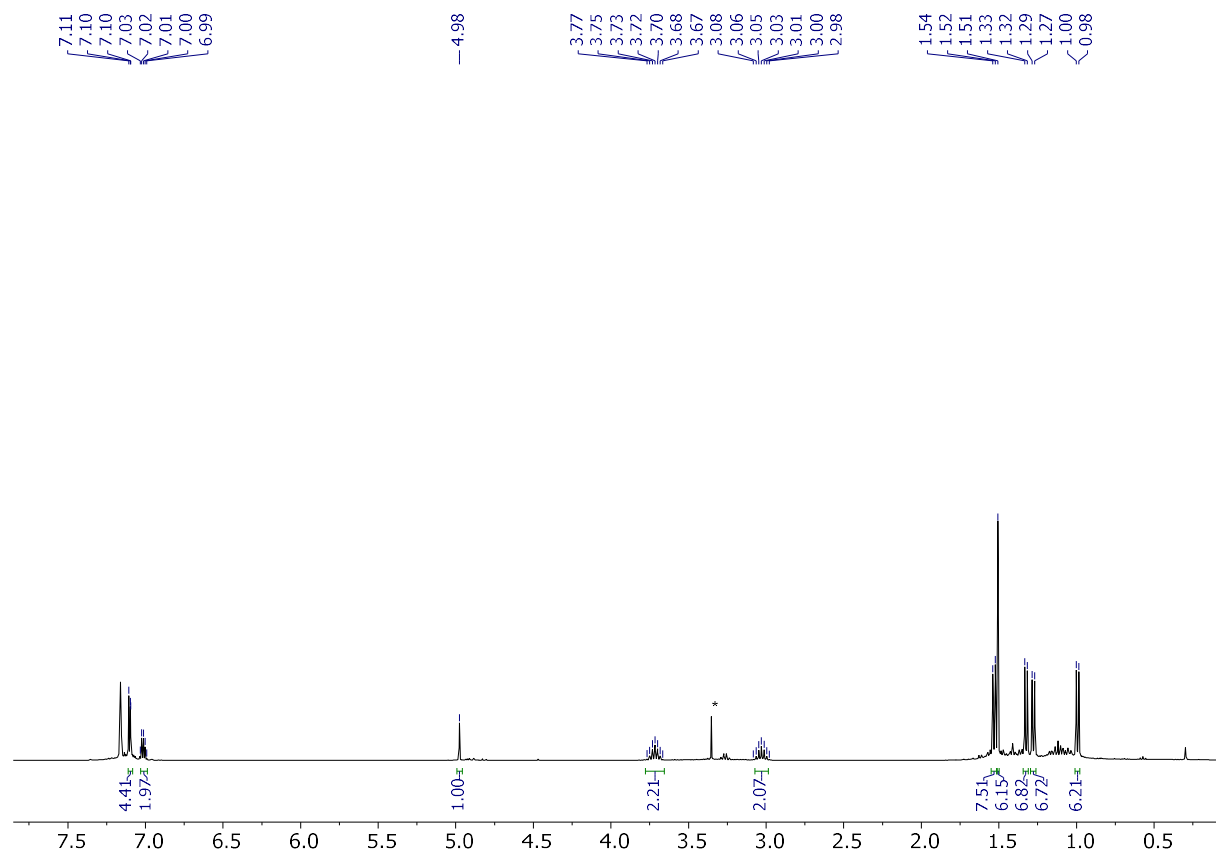
Figure A-II. 9 ^{1}H-NMR (400.13 MHz, 298 K, benzene-d$_6$) of compound **88**. *1,4-dioxane

Figure A-II. 10 ¹H-¹H COSY NMR (400.13 MHz, 298 K, benzene-d₆) of compound **88.**

Figure A-II. 11 ¹³C{¹H} (100.61 MHz, 298 K, benzene-d₆) of compound **88**.
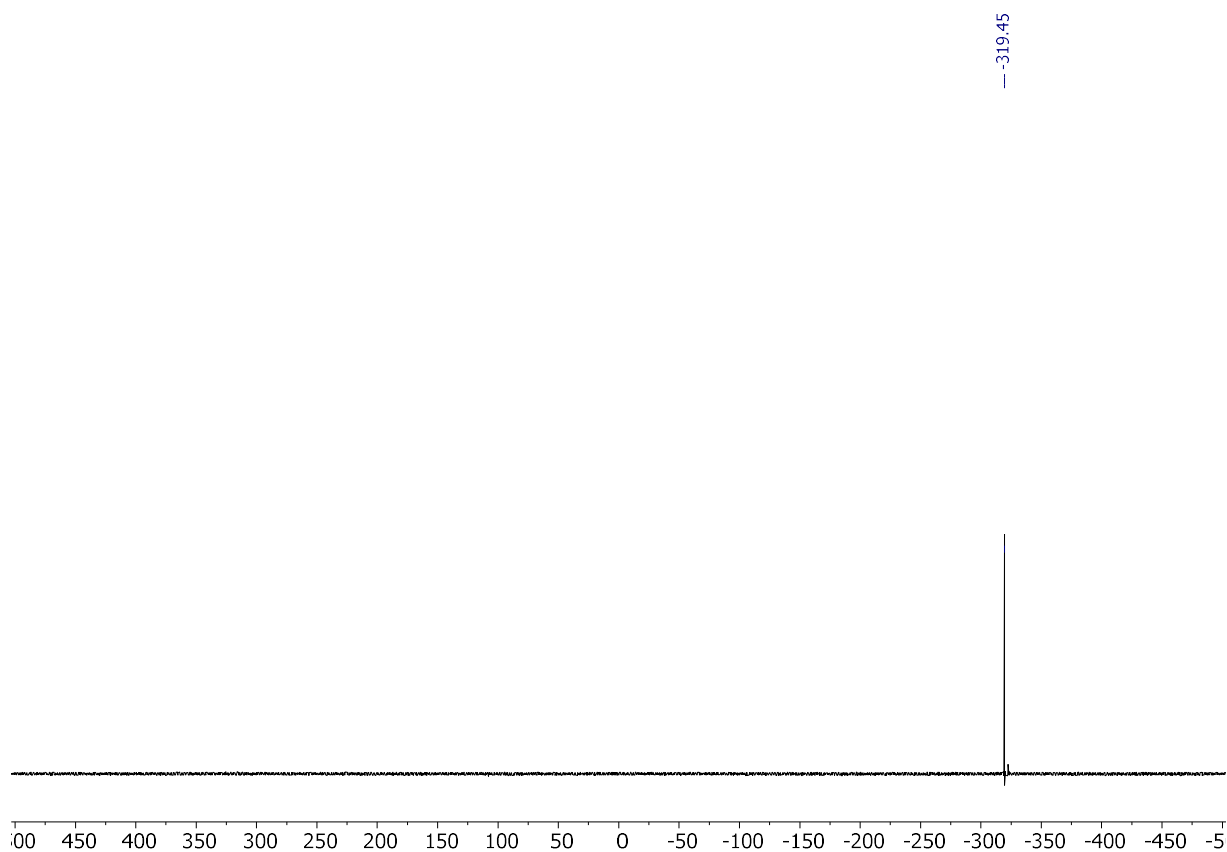
Figure A-II. 12 ^{31}P{^{1}H}-NMR (161.98 MHz, 298 K, benzene-d$_6$) of compound **88**.
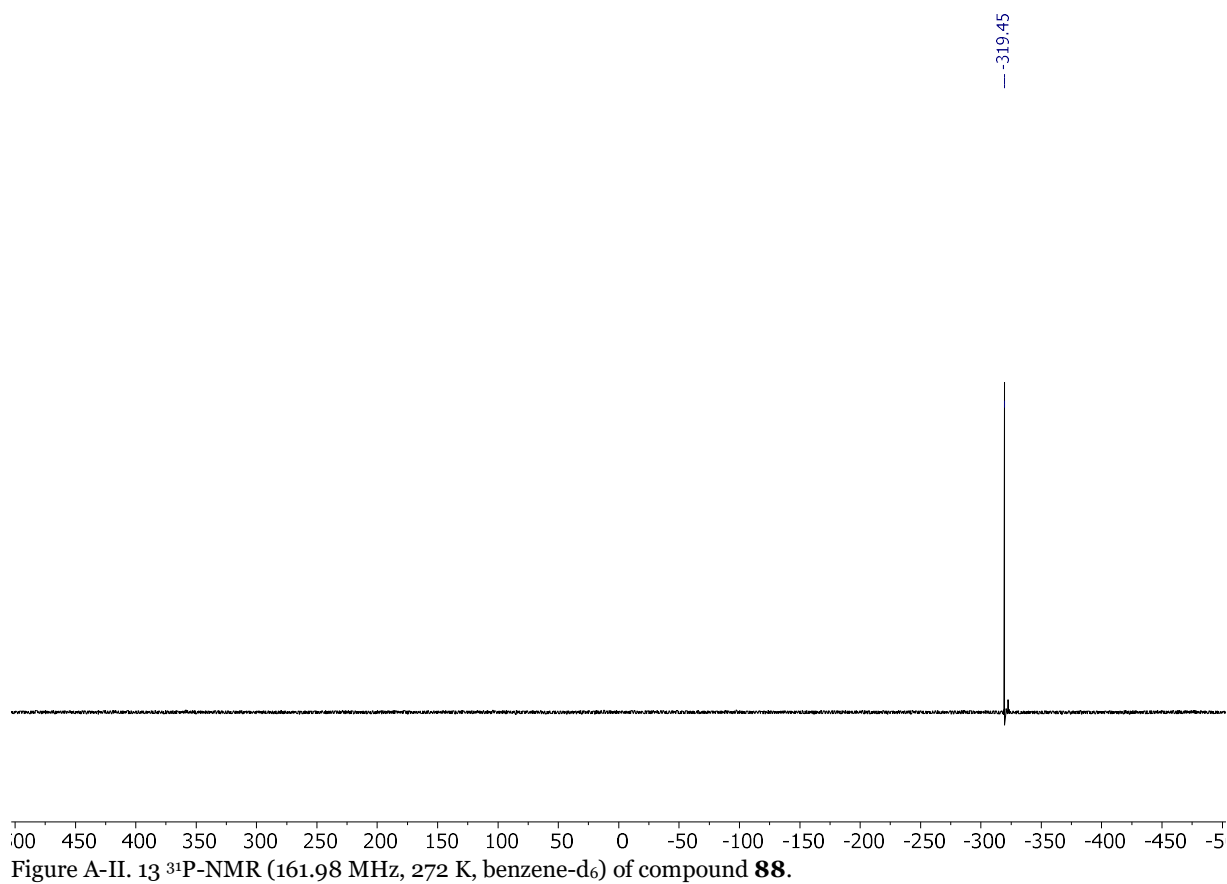
Figure A-II. 13 ^{31}P-NMR (161.98 MHz, 272 K, benzene-d$_6$) of compound **88**.
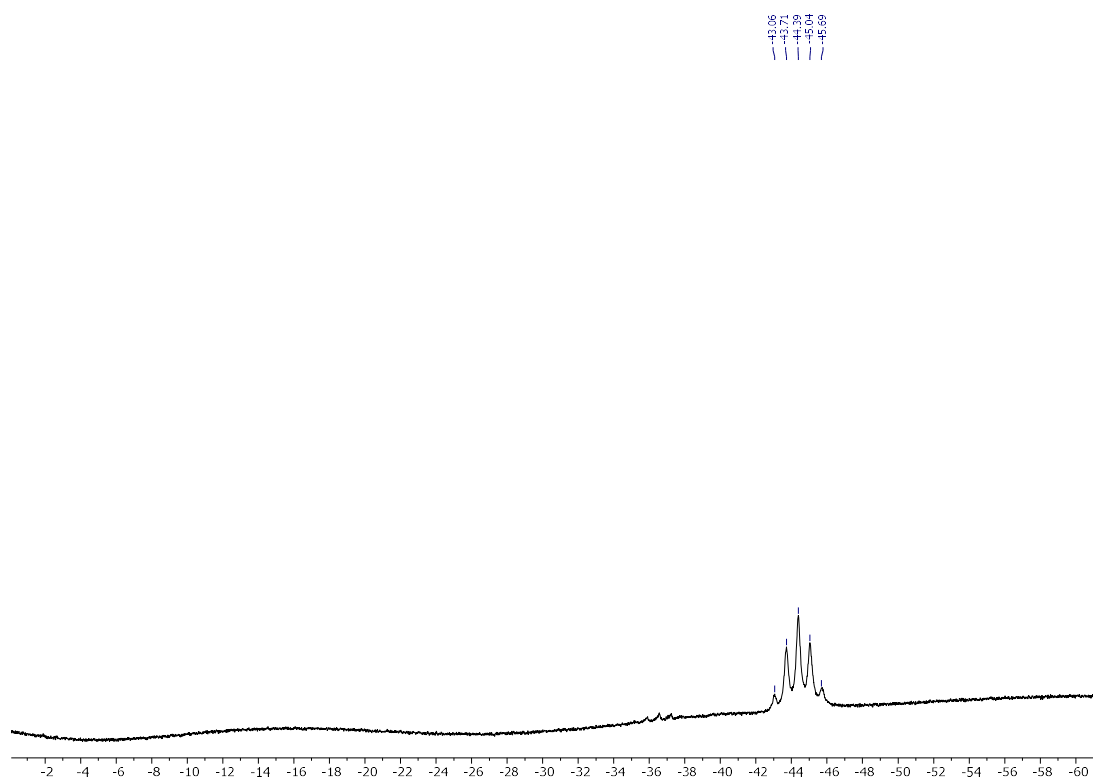
Figure A-II. 14 ^{11}B-NMR (128.4 MHz, 298 K, benzene-d$_6$) of compound **88**.
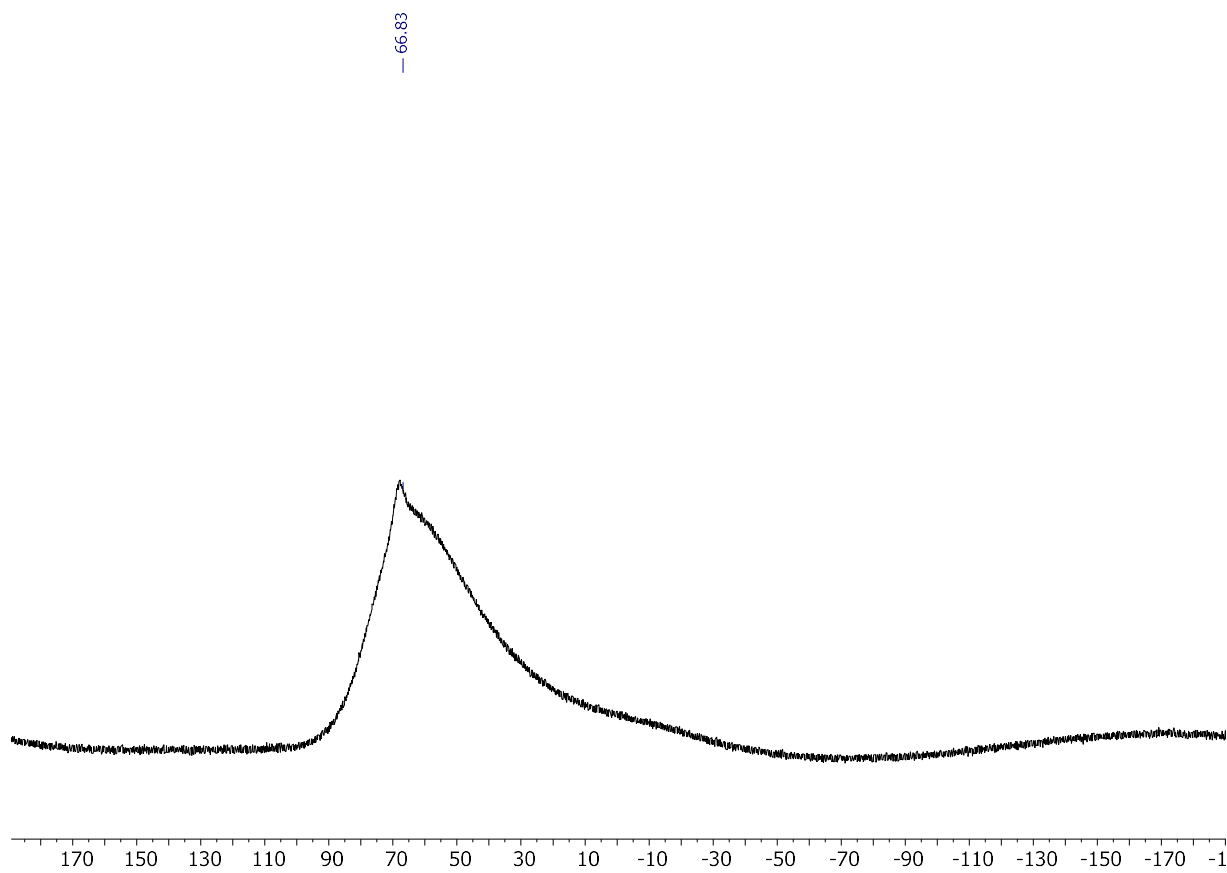
Figure A-II. 15 ^{27}Al-NMR (104.26 MHz, 293 K, benzene-d$_6$) of compound **88**.
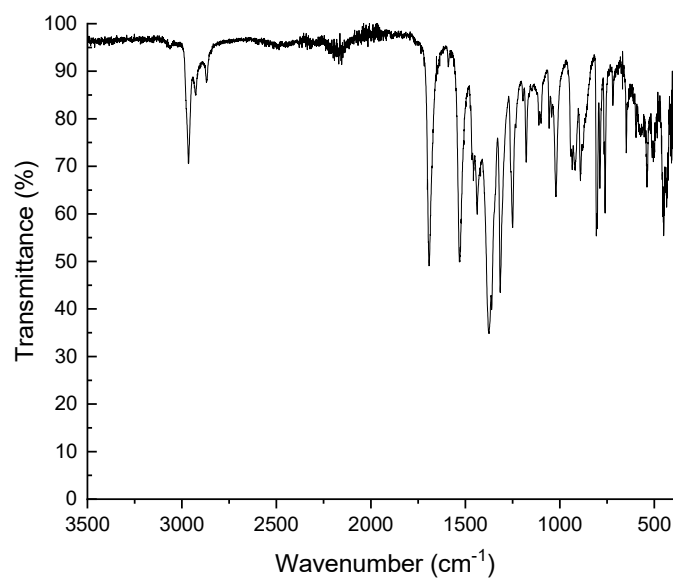
Figure A-II. 16 FT-IR spectrum of compound **88**.

AII.4 Attempted Synthesis of NacNacAl(NCS)(BH₄) (89):

29   **89**   **90**
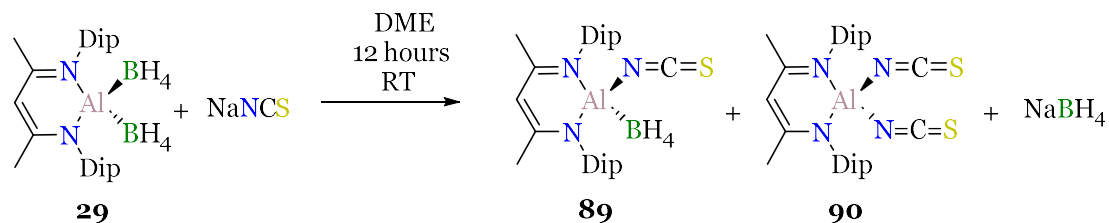
Procedure: 100 mg of NacNacAl(BH₄)₂ and 18 mg of NaNCS are charged in an overnight dried 25 mL Schlenk tube in 10 mL of DME. The reaction mixture is stirred for 12 hours at room temperature. The solvent is removed under vacuum to obtain a white solid. 3 mL of Et₂O are added to form a white slurry solution. The mixture is stirred for 30 min and then it is filtered off. The solid is washed several times with Et₂O.
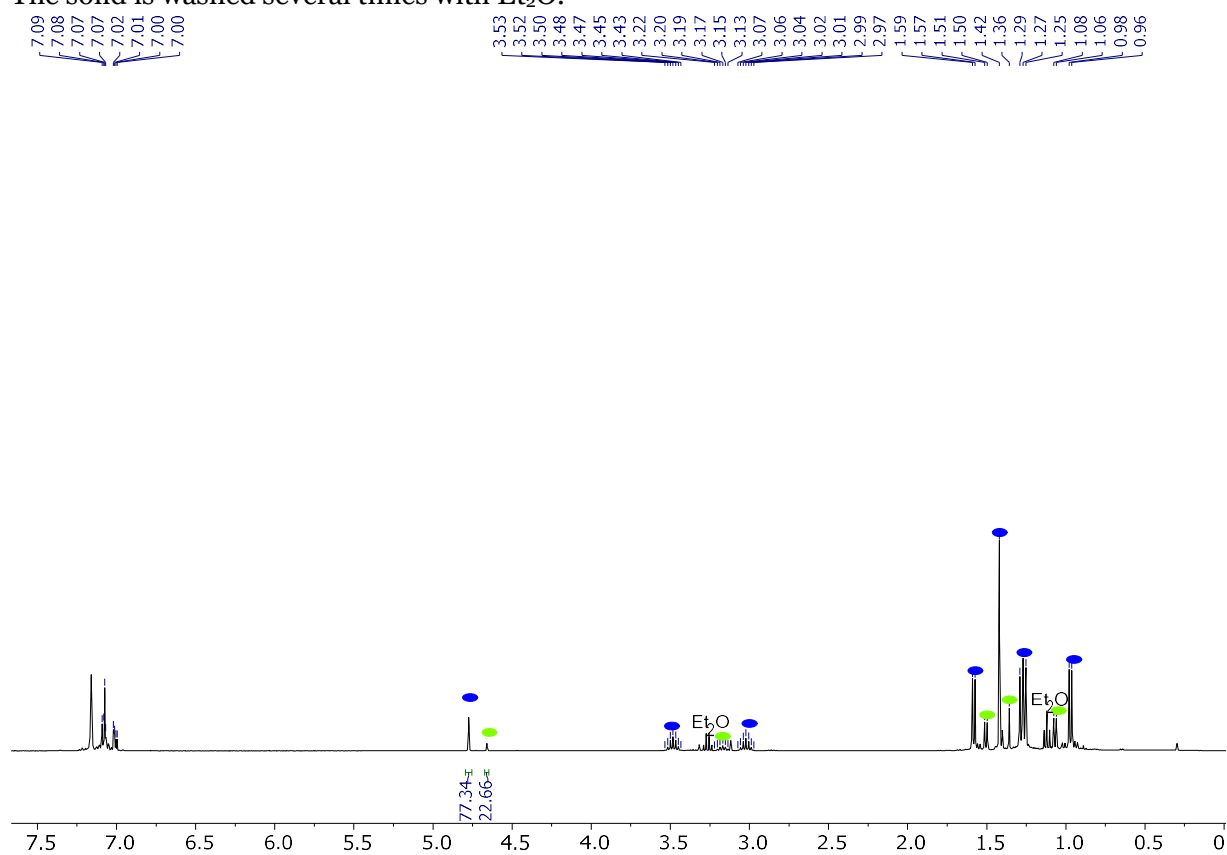
Figure A-II. 17 ¹H-NMR (400.13 MHz, 298 K, benzene-d₆) of compounds **89** (blue) and **90** (green).

187
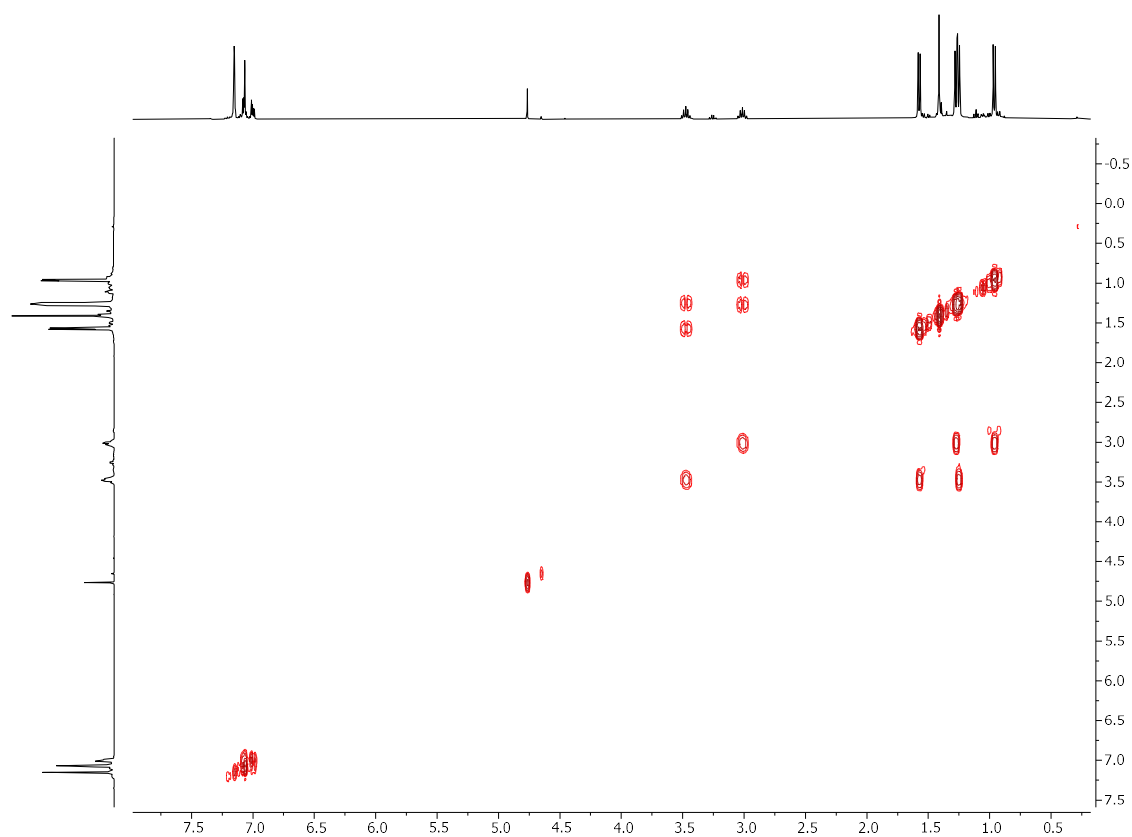
Figure A-II. 18 ¹H-¹H COSY NMR (400.13 MHz, 272 K, benzene-d₆) of compounds **89** and **90**.
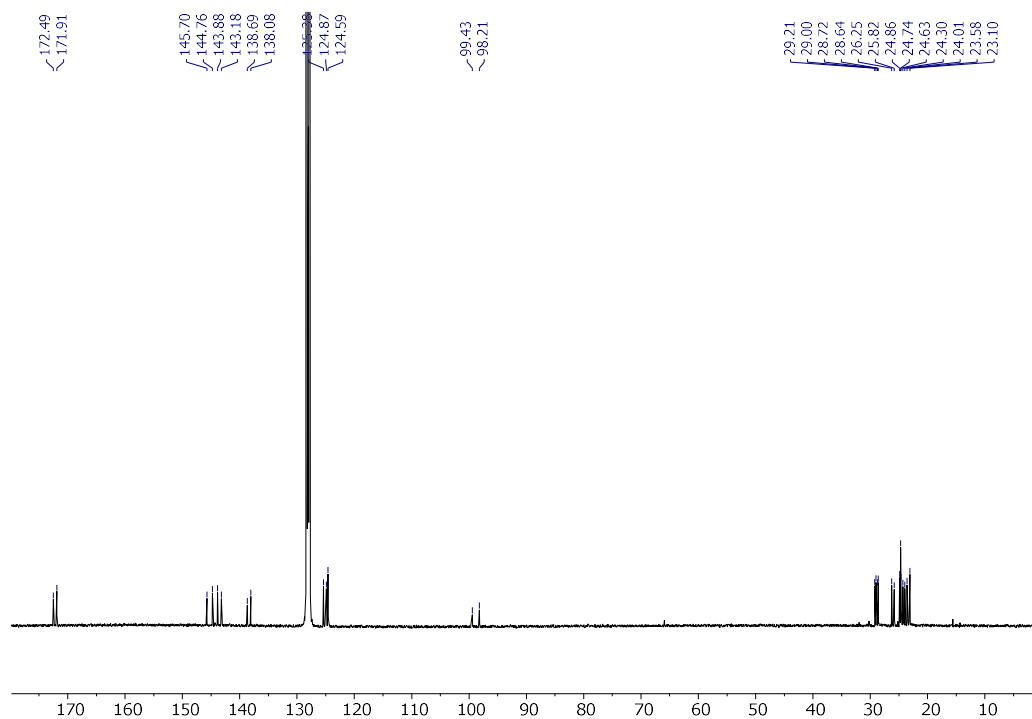
Figure A-II. 19 ¹³C{¹H} (100.61 MHz, 298 K, benzene-d₆) of compound **89** and **90**.
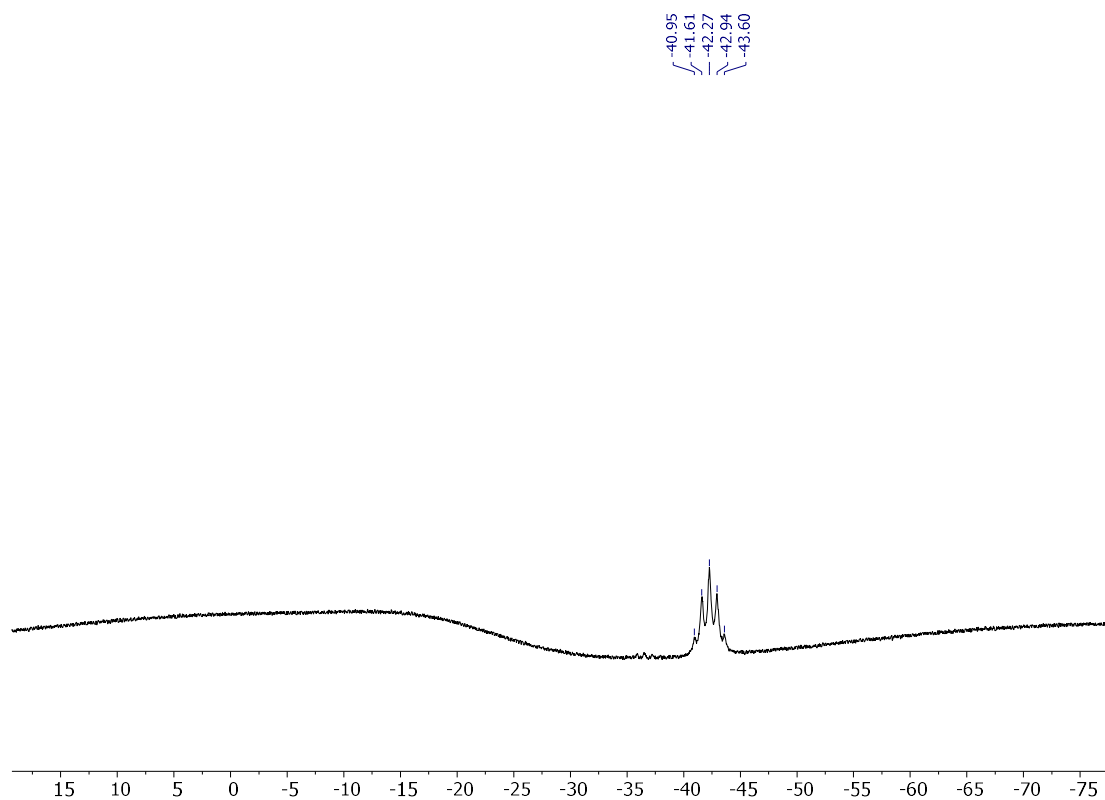
Figure A-II. 20 ^{11}B-NMR (128.4 MHz, 298 K, benzene-d$_6$) of compounds **89** and **90**.
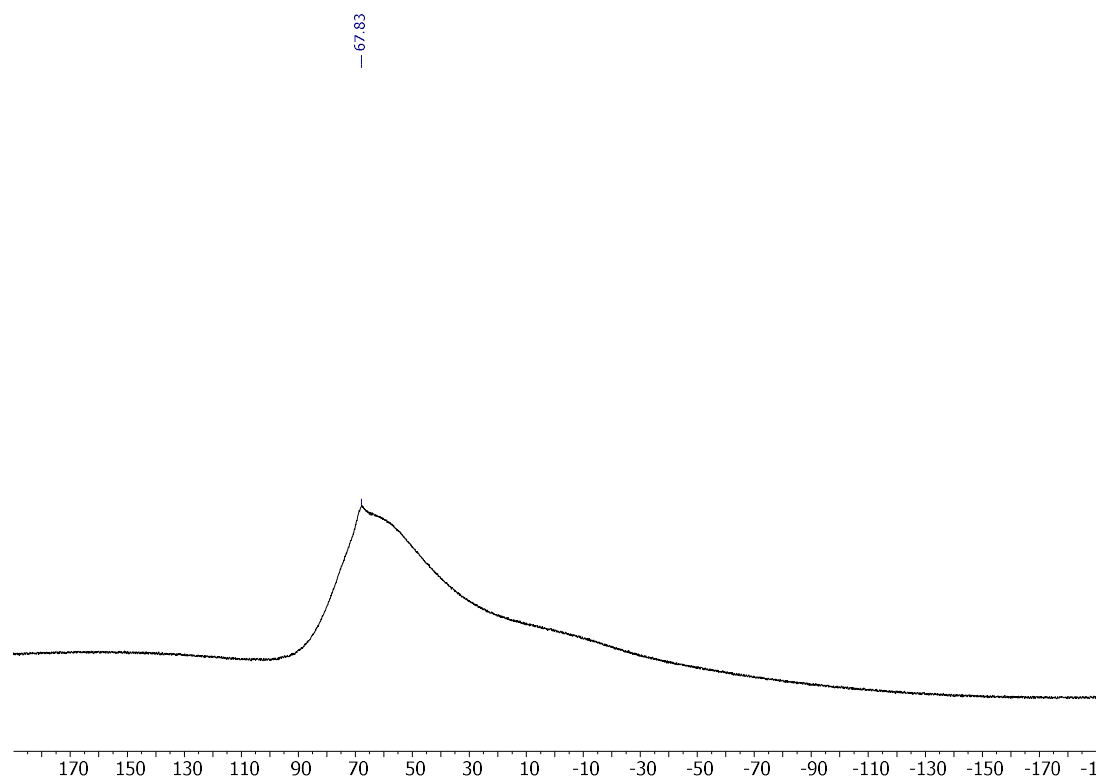
Figure A-II. 21 ^{27}Al-NMR (100.61 MHz, 272 K, benzene-d6) of compounds **89** and **90**.
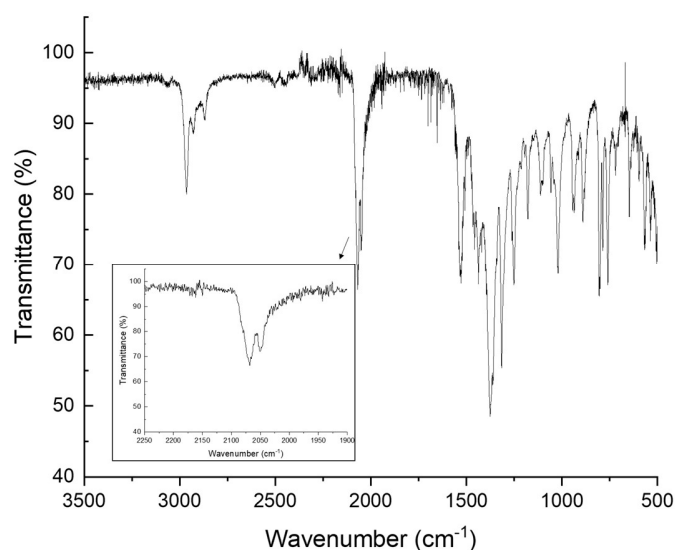
Figure A-II. 22 FT-IR spectrum of compound **89** and **90**.

AII.5 Synthesis of NacNacAl(NCS)₂ (90)
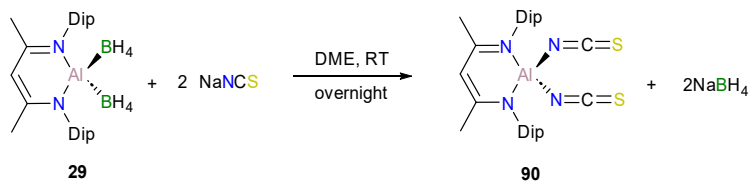
Procedure: 101 mg (0.213 mmol,1 eq) of NacNacAl(BH$_4$)$_2$ and 43 mg of NaNCS (2.5eq) are charged in an overnight dried 25 mL Schlenk tube. Then, 2 mL of DME are added and stirred overnight. The solvent is removed under vacuum to obtain a white solid. Around 8 mL of Et$_2$O are added to form a white slurry solution. The mixture is stirred for 30 min and then it is filtered off. The solid is washed several times with Et$_2$O. The filtrate is dried under vacuum to obtain a white solid (62 mg, 53%).

¹H-NMR (400.13 MHz, 272 K, benzene-d_6): 1.70 (d,$^2J_{H-H}$= 6.97 Hz, 12H, C$_{ipr}$-Me$_2$), 1.36 (s, 6H, Me-(NacNac)), 1.50 (d,$^2J_{H-H}$= 6.46 Hz, 12H, C$_{ipr}$-Me$_2$), 3.17 (sept, $^2J_{H-H}$= 6.46 Hz, 4H, C$_{ipr}$-H), 4.66 (s, C$_\gamma$ −H), 7.07(m, 6H, *m*-, *p*-, Ar-H). [a]The NMR matches with the one reported in the literature.[238]
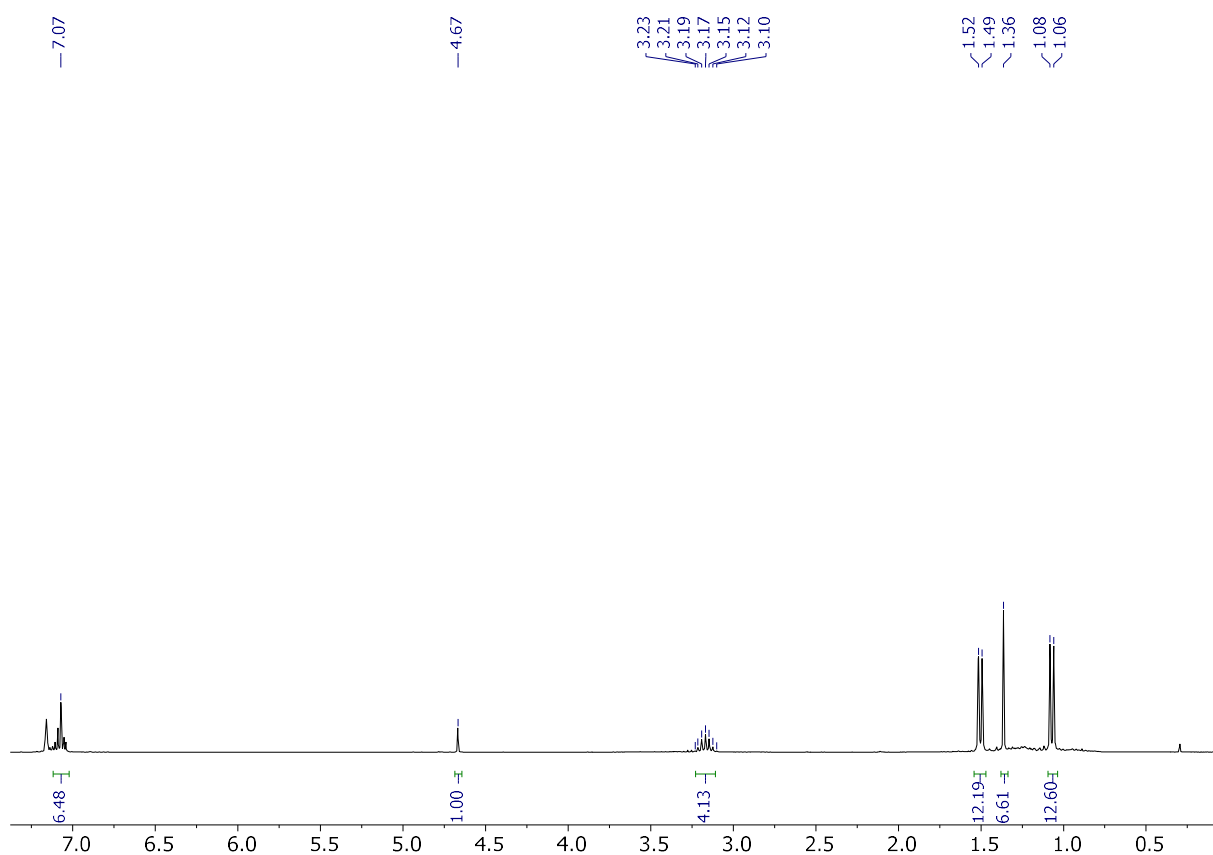
Figure A-II. 23 ^{1}H-NMR (400.13 MHz, 298 K, benzene-d_6) of compound **90**.^{a}

AII.6 Synthesis of NacNacAl(NHCiPrMe)(BH4) (91)
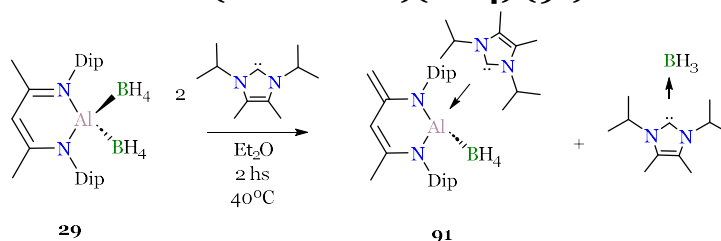
Procedure: An overnight dried Schlenk tube was charged with 50 mg (0.105 mmol, 1 eq) of **29** and dissolved 2 mL of Et$_2$O. A solution of 38 mg (0.216 mmol, 2.05 eq) of NHC^{Me2iPr} in 4 mL of Et$_2$O is added dropwise. Then, the solution is stirred for 2 hours in a sand bath at 40°C. Afterwards, a white turbulent solution is obtained. It is cooled down to room temperature. The white precipitate is filtered off and the solution is dried under vacuum. Then, the white solid is dissolved in the minimal amount of Et$_2$O and kept at -30°C overnight for crystallization to isolate compound **91** as colorless crystals. The mother liquors are concentrated and kept at -30°C to obtain different batches of crystals (Total: 39 mg, 55%).

^{1}H-NMR (400.13 MHz, 298 K, benzene-d_6): δ= 0.48 (d, $^3J_{H-H}$= 6.92 Hz, 3H, C$_{ipr}$-<u>Me</u>), 0.67 (d, $^3J_{H-H}$= 7.06 Hz, 3H, C$_{ipr}$-<u>Me</u>), 0.87 (d, $^3J_{H-H}$= 7.02 Hz, 3H, C$_{ipr}$-<u>Me</u>), 0.96 (d, $^3J_{H-H}$= 6.85 Hz, 3H, C$_{ipr}$-<u>Me</u>), 1.16 (d, $^3J_{H-H}$= 6.85 Hz, 3H, C$_{ipr}$-<u>Me</u>), 1.33 (d, $^3J_{H-H}$= 6.81 Hz, 3H, C$_{ipr}$-<u>Me</u>), 1.38 (d, $^3J_{H-H}$= 6.72 Hz, 3H, C$_{ipr}$-<u>Me</u>$_2$). 1.42 (s, 3H, NHC-<u>Me</u>), 1.51 (d, $^3J_{H-H}$= 6.81 Hz, 3H, C$_{ipr}$-<u>Me</u>), 1.54 (d, $^3J_{H-H}$= 6.72 Hz, 3H, C$_{ipr}$-<u>Me</u>), 1.61 (s, 3H, NHC-<u>Me</u>), 1.63 (d, $^3J_{H-H}$= 6.72 Hz, 3H, C$_{ipr}$-<u>Me</u>), 1.66 (d, $^3J_{H-H}$= 6.72 Hz, 3H, C$_{ipr}$-<u>Me</u>), 1.68 (d, $^3J_{H-H}$= could not be determined due to overlapping, 3H),

191

1.69 (s, 3H, Me(NacNac)), 3.07 (sept, $^3J_{H-H}$= 6.82 Hz, 1H, C_{ipr}-H), 3.23 (d, $^3J_{H-H}$= 1.03 Hz, 1H, $C_{methylene}$-H(NacNac)), 3.50 (sept, $^3J_{H-H}$=6.90 Hz, 1H, C_{ipr}-H), 3.99 ($^3J_{H-H}$= 1.02 Hz, $C_{methylene}$-H(NacNac)), 4.15 (sept, $^3J_{H-H}$= 6.74 Hz, 1H, C_{ipr}-H), 4.25 (sept, $^3J_{H-H}$= 6.78 Hz, 1H, C_{ipr}-H), 5.05 (sept, $^3J_{H-H}$= 7.00 Hz, 1H, C_{ipr}-H), 5.53 (s, 1H, C_γ-H), 5.68 (sept, $^3J_{H-H}$= 6.87 Hz, 1H, C_{ipr}-H), 7.11 (dd, $^3J_{H-H}$= 7.50 Hz, $^4J_{H-H}$= 1.80 Hz, 1H, *m*-Ar-H), 7.17 (overlapping with benzene signal), 7.22 (t, $^3J_{H-H}$= 7.58 Hz, 1H, *p*- Ar-H), 7.28 (m, overlap of a t and a dd, 2H, *m*-, *p*-, Ar-H), 7.41 (dd, $^3J_{H-H}$= 7.65 Hz, $^4J_{H-H}$= 1.67 Hz, 1H, *m*- Ar-H). The BH$_4$ could not be determined due to the broadness of the signal. **^{13}C{^{1}H} (100.61 MHz, 298 K, benzene-d_6)** δ= 10.14 (CH$_3$-NHC^{iPrMe}), 21.02 (C_{ipr}-CH$_3$), 21.64(C_{ipr}-CH$_3$), 22.13 (C_{ipr}-CH$_3$), 23.45 (C_{ipr}-CH$_3$), 23.55 (C_{ipr}-CH$_3$), 24.70 (C_{ipr}-CH$_3$), 24.74 (C_{ipr}-CH$_3$), 24.94 (C_{ipr}-CH$_3$), 25.31 (C_{ipr}-CH$_3$), 25.73 (C_{ipr}-CH$_3$), 25.89 (C_{ipr}-CH$_3$), 27.20 (C_{ipr}-CH$_3$), 27.26 (C_{ipr}-CH$_3$), 27.53 (C_{ipr}-CH$_3$), 27.66 (C_{ipr}-CH$_3$), 28.91 (C_{ipr}-CH$_3$), 28.98 (C_{ipr}-CH$_3$), 50.86 (C_{ipr}-H), 53.28 (C_{ipr}-H), 83.64 (CH$_2$-backbone), 106.52 (C_γ-H), 123.22 (C-Ar), 123.67 (C-Ar), 124.77 (C-Ar), 125.33 (C-Ar), 125.43 (C-Ar), 125.86 (C-Ar), 127.17 (C_α-NHC), 127.48 (C_α-NHC), 143.03 (C-Ar), 144.44 (C-Ar), 145.33(C$_\beta$-backbone), 146.17(C-Ar), 147.04(C-Ar), 149.16 (C-Ar), 149.23 (C-Ar), 154.48(C$_\beta$-backbone), 165.15(C$_{carb}$-NHC). **^{11}B-NMR (128.38 MHz, 298 K, benzene-d_6)** δ= -36.28 (bs). **^{27}Al-NMR (104.26 MHz, 272 K, benzene-d_6)** δ= silent in the range of 190 to -190 ppm. **Elemental analysis:** Do not match after several attempts. **Melting point:** 180 °C
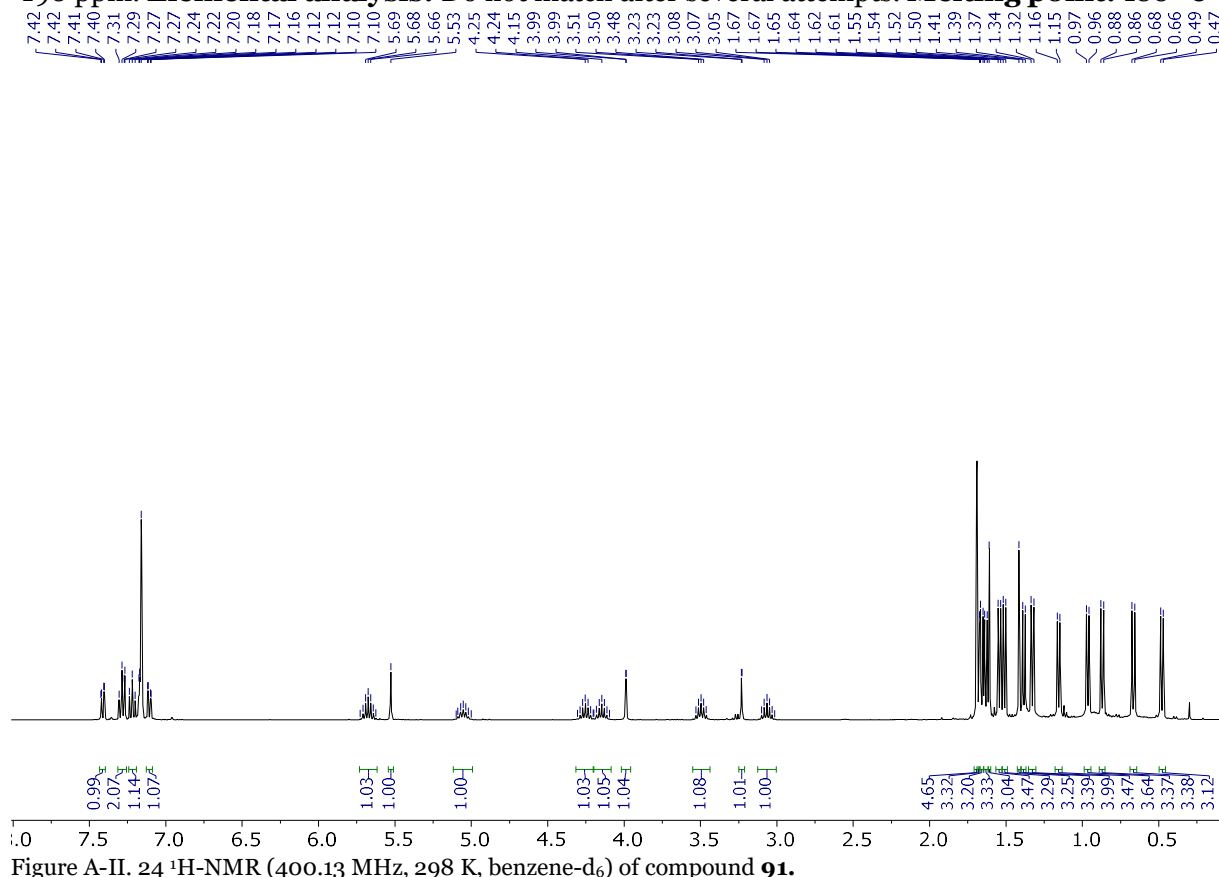
Figure A-II. 24 ^{1}H-NMR (400.13 MHz, 298 K, benzene-d_6) of compound **91.**
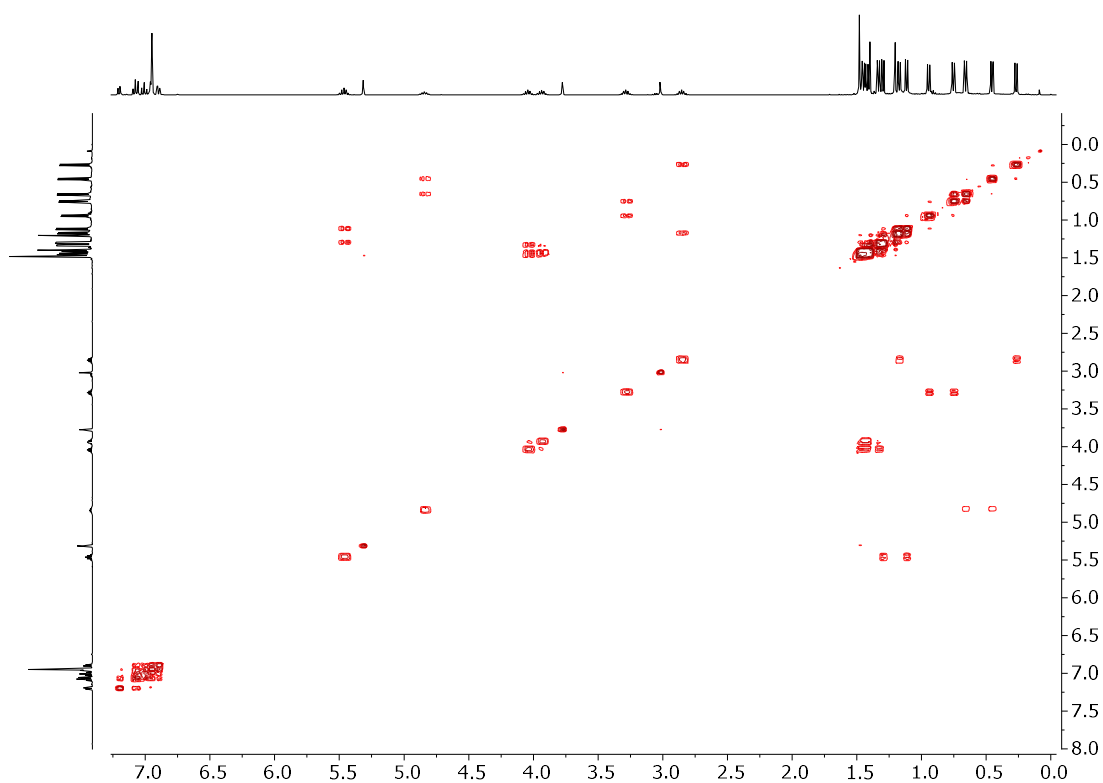
Figure A-II. 25 ¹H-¹H COSY NMR (400.13 MHz, 298 K, benzene-d₆) of compound **91**.
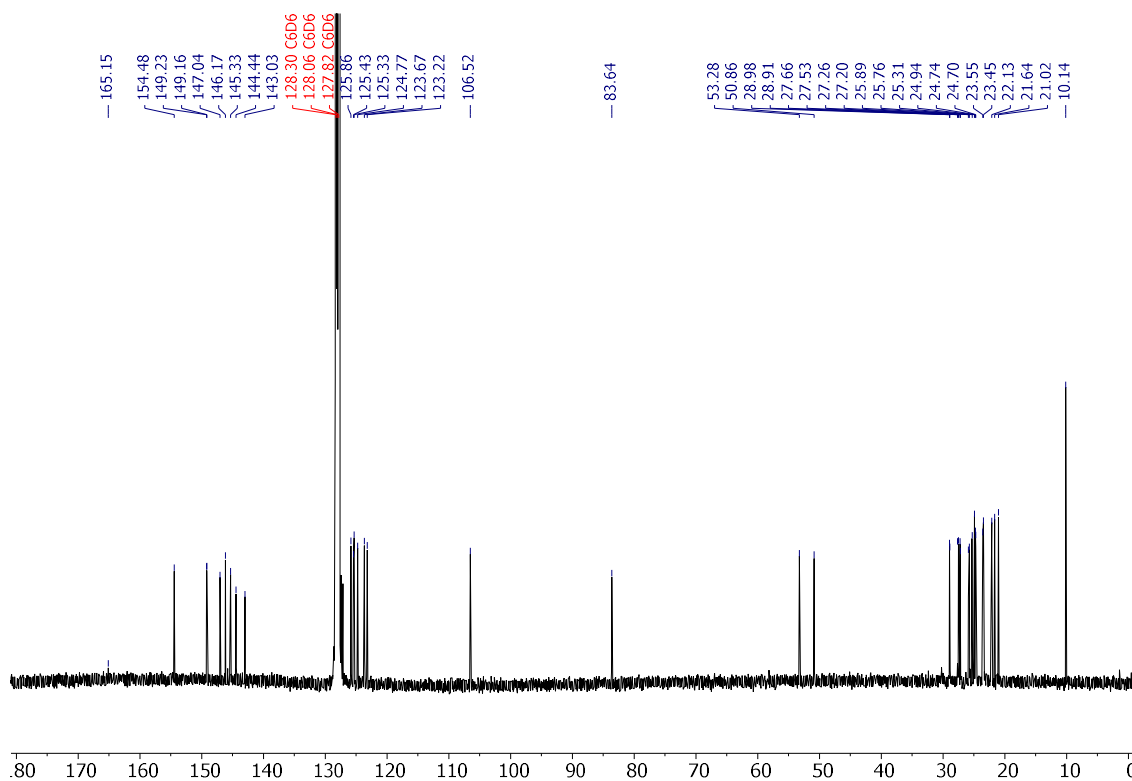
Figure A-II. 26 ¹³C{¹H} (100.61 MHz, 272 K, benzene-d₆) of compound **91**.
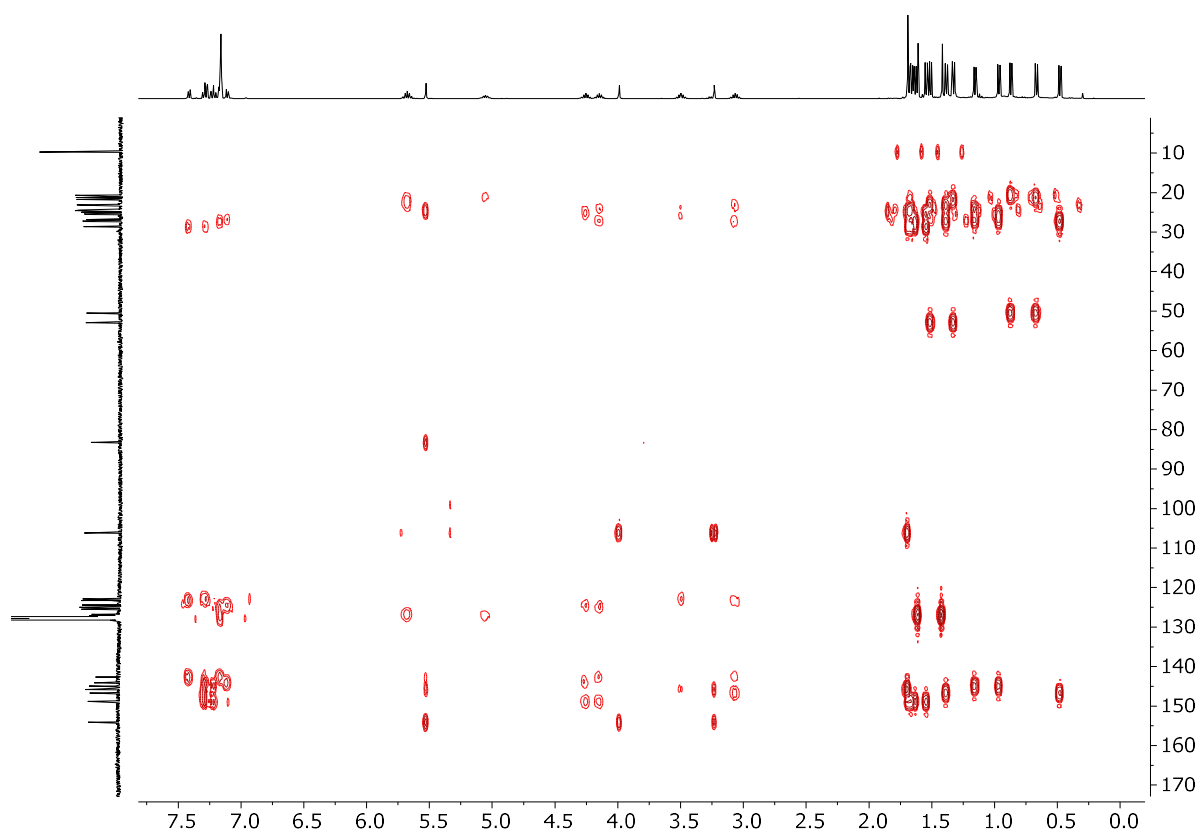
Figure A-II. 27 ^{13}C-^{1}H-HMBC of compound **91** in benzene-d$_6$.

Figure A-II. 28 ^{13}C-DEPT135 of compound **91** in benzene d$_6$.

Figure A-II. 29 ^{11}B-NMR (128.38 MHz, 272 K, benzene-d$_6$) of compound **91**.
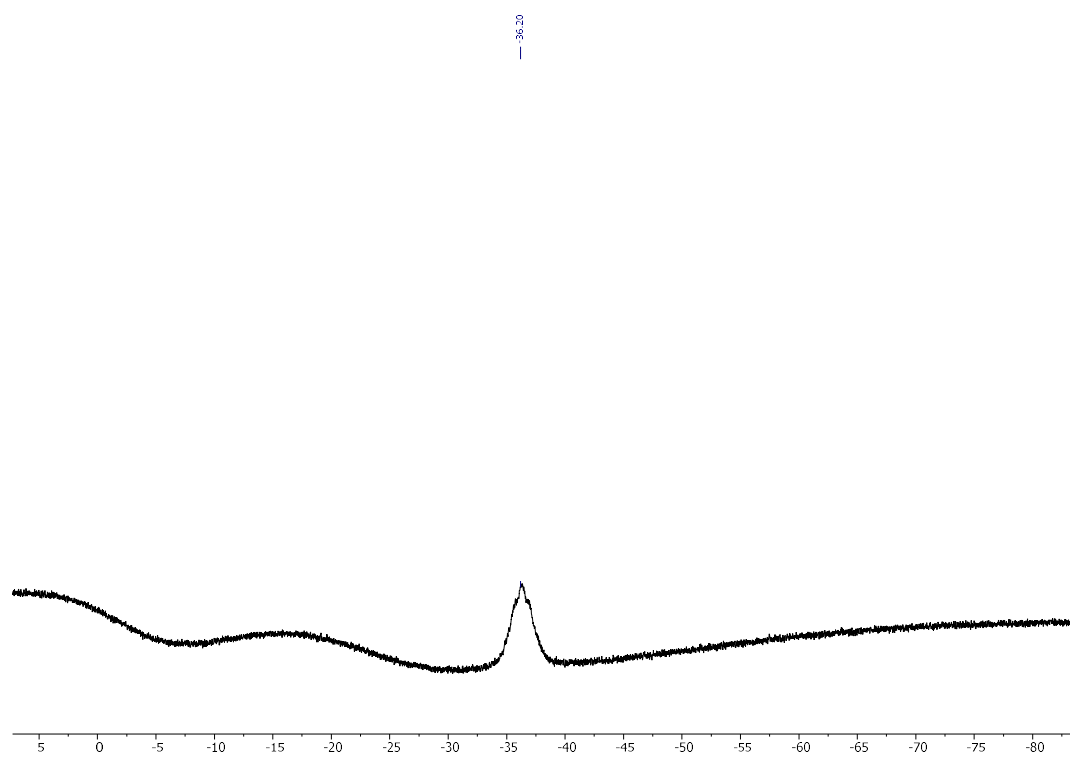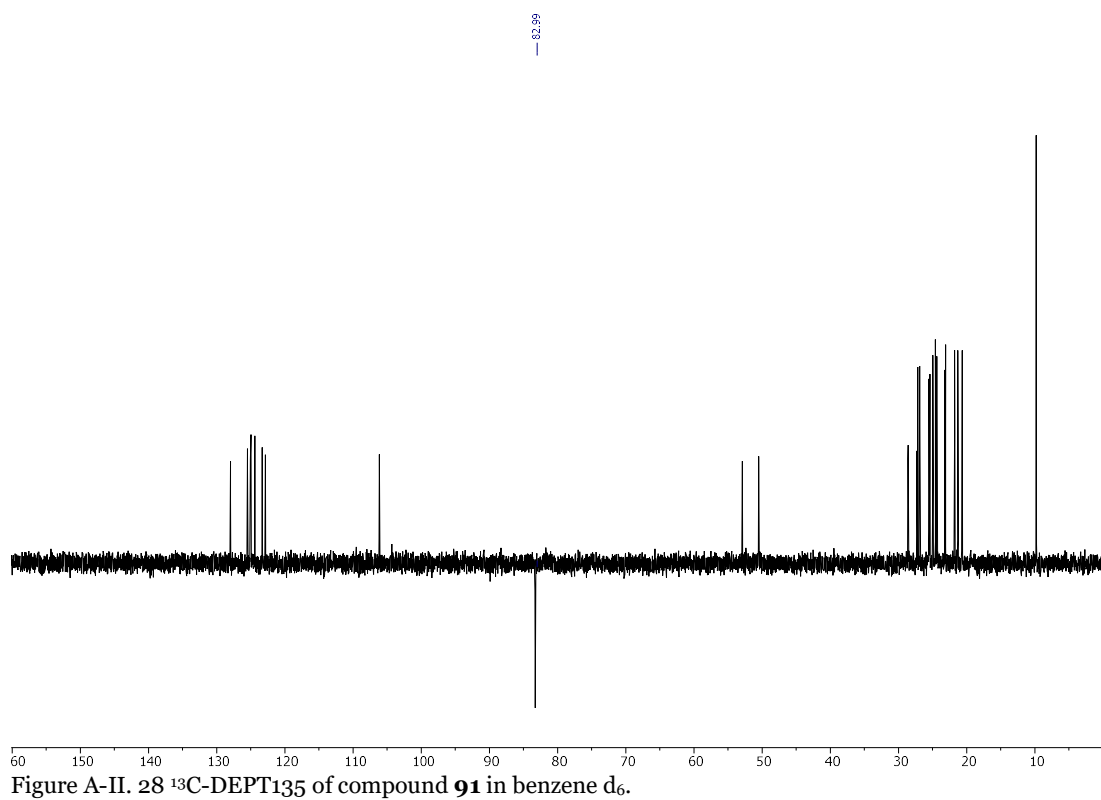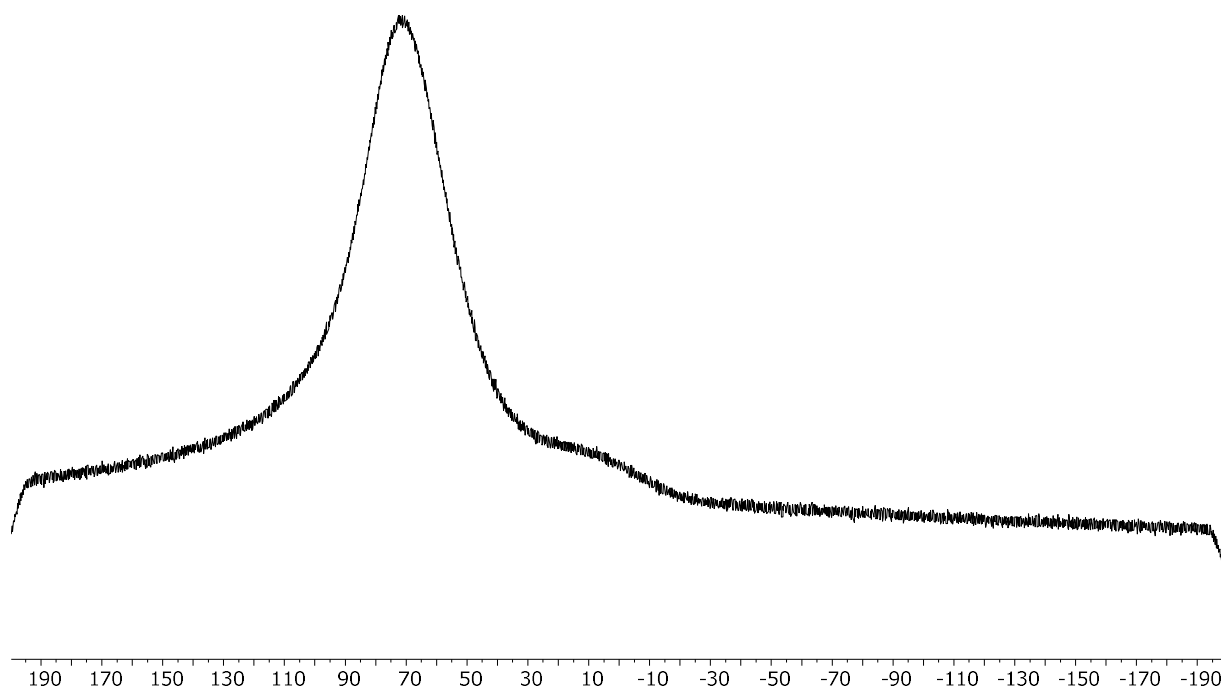
Figure A-II. 30 ^{27}Al-NMR (104.26 MHz, 298 K, benzene-d$_6$) of compound **91**.
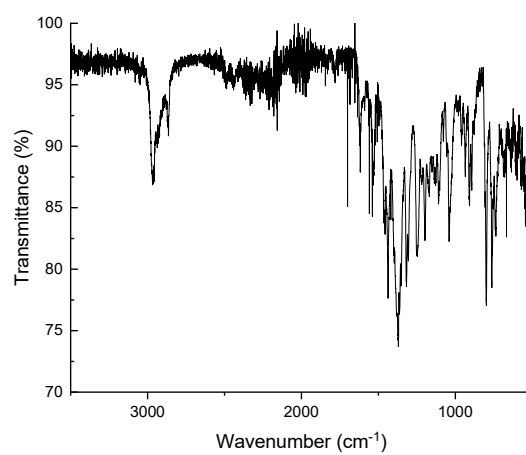
Figure A-II. 31 FT-IR spectrum of compound **91.**

AII.7 Synthesis of NacNacAlH(BH$_4$) (93):

Procedure: 100 mg (0.244 mmol, 1eq) of *NacNac*Al(BH$_4$)$_2$ and 106.74 mg (0.244 mmol, 1eq) of NacNacAlH$_2$ are placed in an Schlenk flask. Then, 2 ml of benzene are added, and the mixture is stirred on a preheated oil-bath at 70°C for 3 hours. The reaction crude is dried under vacuum to obtain a white-yellowish solid. Then, minimal amount of Et$_2$O is added and left to crystallize overnight at room temperature. The solution is decanted and after repeating the process twice 89.7 mg (87%) of compound **93** are obtained as yellowish crystals.

^{1}H-NMR (400.13 MHz, 298 K, benzene-d_6): δ(ppm)=1.10 (d,$^2J_{H-H}$= 6.85 Hz, 6H, C$_{ipr}$-$\underline{Me}_2$), 1.13 (d,$^2J_{H-H}$= 6.85 Hz, 6H, C$_{ipr}$-$\underline{Me}_2$), 1.36 (d,$^2J_{H-H}$= 6.72 Hz, 3H, C$_{ipr}$-$\underline{Me}_2$), 1.42 (d,$^2J_{H-H}$= 6.81 Hz, 6H, C$_{ipr}$-$\underline{Me}_2$), 1.52 (s,6H, $\underline{Me}$-(NacNac)), 3.30 (two overlapped septets, 4H, C$_{ipr}$-$\underline{Me}_2$), 4.88 (s,1H), 7.10 (m, 6H, *m*-, *p*-, Ar-$\underline{H}$). **^{13}C{^{1}H} (100.61 MHz, 298 K, benzene-d_6):** δ(ppm)=23.80 ($\underline{C}H_3$-backbone), 24.63 (C$_{ipr}$-$\underline{C}H_3$), 24.75(C$_{ipr}$-$\underline{C}H_3$), 24.89 (C$_{ipr}$-$\underline{C}H_3$), 25.60 (C$_{ipr}$-$\underline{C}H_3$), 28.59 ($\underline{C}_{ipr}$-CH$_3$), 28.85($\underline{C}_{ipr}$-CH$_3$), 97.52($\underline{C}$γ-H), 124.83 ($\underline{C}$-Ar), 124.97($\underline{C}$-Ar), 139.43($\underline{C}$-Ar),144.11($\underline{C}$-Ar),144.88($\underline{C}$-Ar), 171.26($\underline{C}_\beta$-backbone). **^{11}B-NMR (128.38 MHz, 298 K, benzene-d_6):** δ(ppm)= -37.63 (quint, $^1J_{B-H}$ =83.80 Hz) **^{27}Al-NMR (104.26 MHz, 298 K, benzene-d_6):** δ(ppm)= 105 (bs). **Elemental analysis:** calc for **93:** C: 75.64 % H: 10.17 % N: 6.08%; found: C:74.85%, H: 9.71%, N:6.11%. **Melting point:** 191°C.

Figure A-II. 32 ^{1}H-NMR (400.13 MHz, 298 K, benzene-d_6) of compound **93**.

Figure A-II. 33 ¹H-¹H COSY NMR (400.13 MHz, 298 K, benzene-d₆) of compound **93**.

Figure A-II. 34 ¹³C{¹H} (100.61 MHz, 298 K, benzene-d₆) of compound **93**.

Figure A-II. 35 ^{11}B-NMR (128.4 MHz, 298 K, benzene-d[6]) of compound **93**.

Figure A-II. 36 ^{27}Al-NMR (104.26 MHz, 298 K, benzene-d[6]) of compound **93**.

AII.8 Synthesis of NacNacAl(OCP)tBuO (95) and NacNacAl(H)tBuO (96):
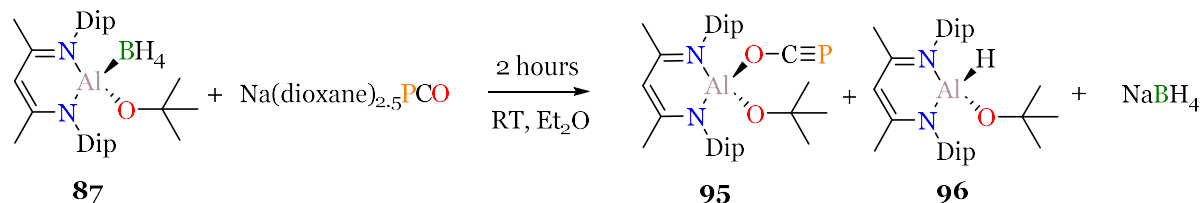
Procedure: In a 25 ml flask, 150 mg (1 eq, 0.281 mmol) of **87** are dissolved in 3 mL of Et$_2$O. The solution is stirred until the **87** is completely dissolved. Then, 89 mg of Na(dioxane)$_{2.5}$PCO (1.05 eq, 296 mmol) are added slowly in the stirring solution. The flask is taken out from the glovebox and connected to the Schlenk line. The solution is stirred for 2 hours at room temperature. The solvent is removed under vacuum. Then, 5 mL of diethylether are added to yield a slurry solution. It is filtered off and the solution obtained is dried under vacuum to obtain a pale-brown solid (105 mg).
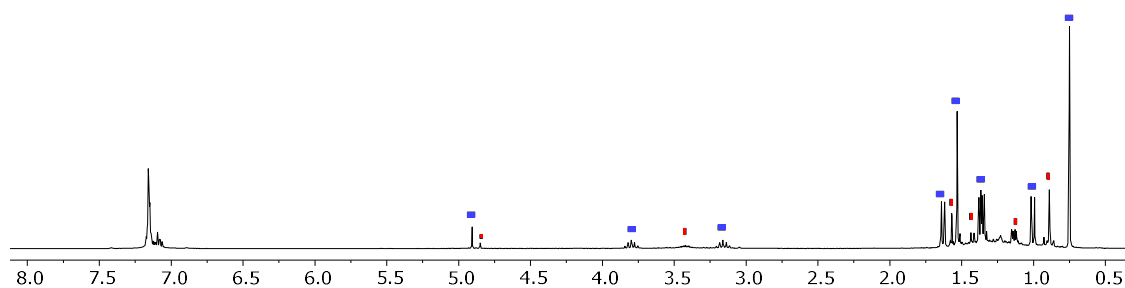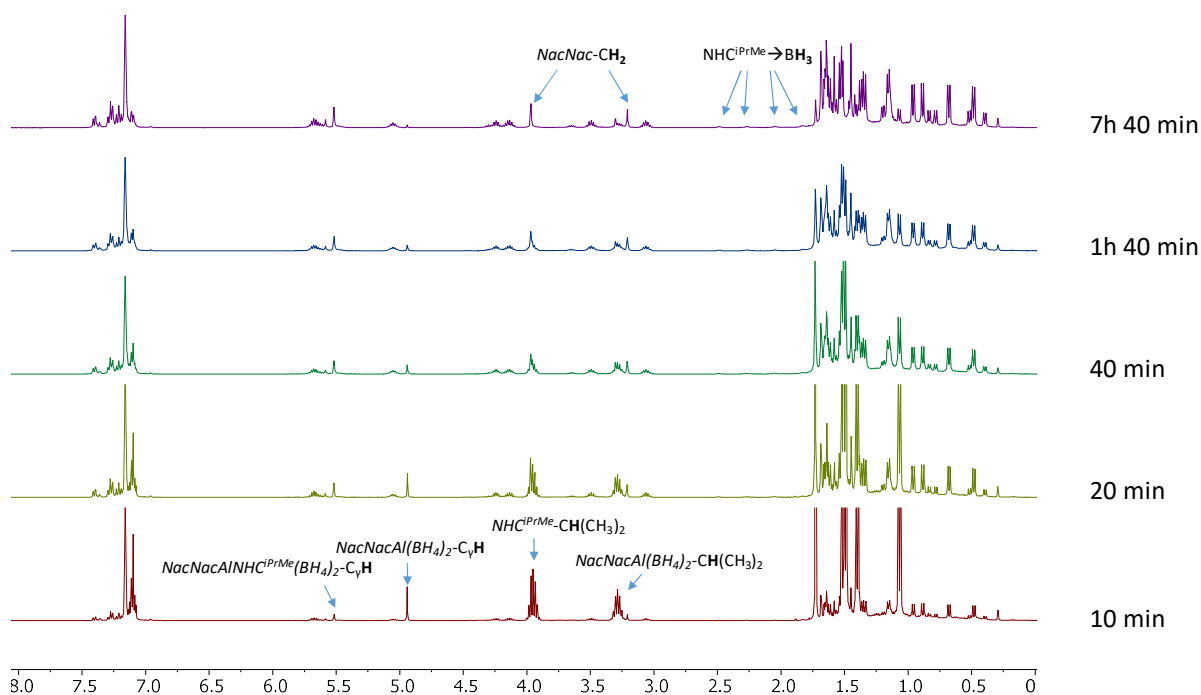

Figure A-II. 37 ^{1}H-NMR (400.13 MHz, 298 K, benzene-d_6) of compound **95** (blue) and **96** (red).
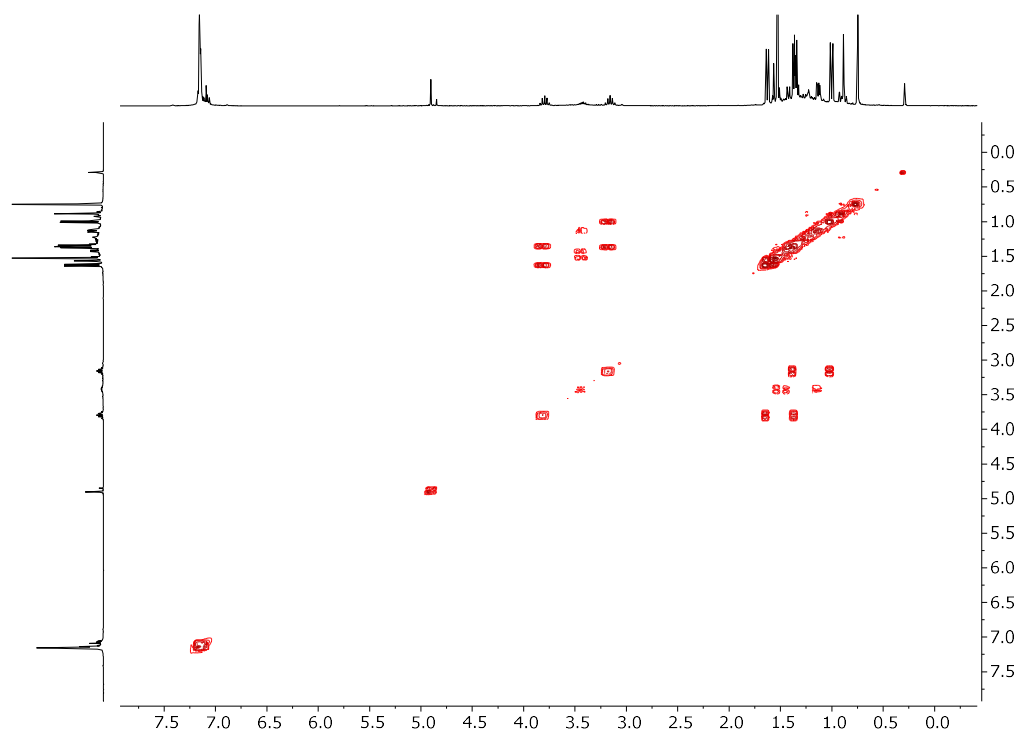
Figure A-II. 38 ¹H-¹H COSY NMR (400.13 MHz, 298 K, benzene-d₆) of compound **95** (blue) and **96** (red).
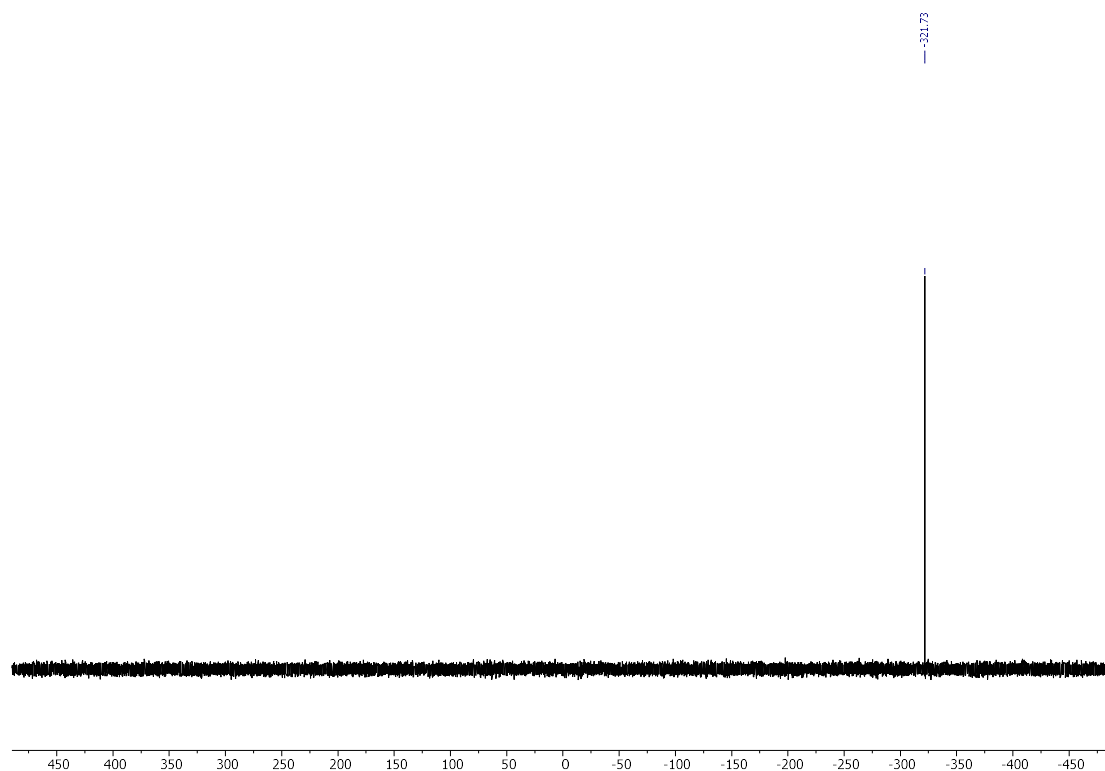
Figure A-II. 39 ³¹P-NMR (161.98 MHz, 298 K, benzene-d₆) of compound compound **95** (blue) and **96** (red).
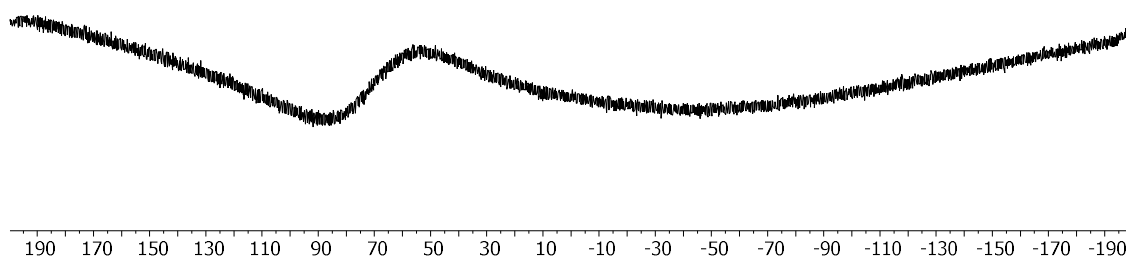
Figure A-II. 40 ^{27}Al-NMR (104.26 MHz, 298 K, benzene-d_6) of compound **95** (blue) and **96** (red).
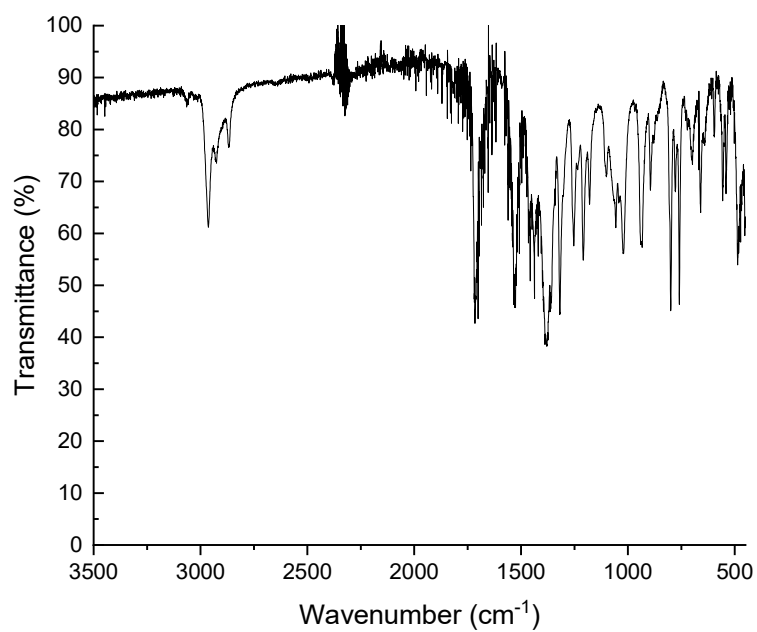
Figure A-II. 41 FT-IR spectrum of compound **95** (blue) and **96** (red).

AII.9 Crystallographic data

Refinement details for 87: All non H-atoms were located on the electron density maps and refined anisotropically. C- and B- bound H atoms were placed in positions of optimized geometry and treated as riding atoms. Their isotropic displacement parameters were coupled to the corresponding carrier atoms by a factor of 1.2 (CH, CH2, all BH) or 1.5 (CH3).
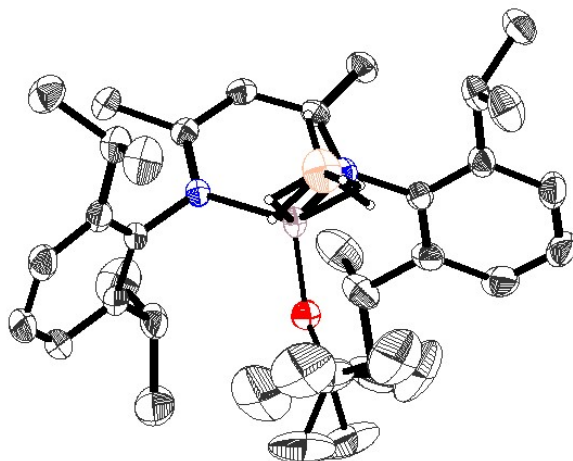
Refinement details for 88: All non H-atoms were located on the electron density maps and refined anisotropically. C- bound H atoms were placed in positions of optimized geometry and treated as riding atoms. Their isotropic displacement parameters were coupled to the corresponding carrier atoms by a factor of 1.2 (CH) or 1.5 (CH3). The B(1) bonded hydrogen atoms H1a, H1b, H1c and H1d were located on the electron density maps and their positional parameters were refined using isotropic displacement parameters which were set at 1.5 times the Ueq value of B(1).
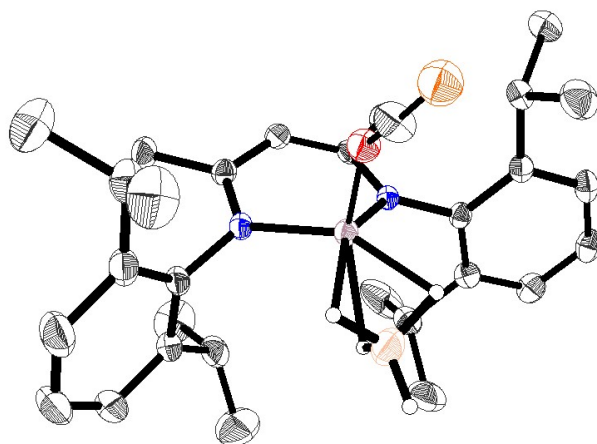
*Refinement details for **91**:* All non H-atoms were located on the electron density maps and refined anisotropically. The C2, C4, and C5 bonded H-Atoms as well as the Al1 and B1 bonded H-atoms were located on the electron maps. All other C-bound H atoms were placed in positions of optimized geometry and treated as riding atoms. The isotropic displacement parameters of all hydrogen atoms were coupled to the corresponding carrier atoms by a factor of 1.2 (CH, CH2, BH, AlH) or 1.5 (CH3).
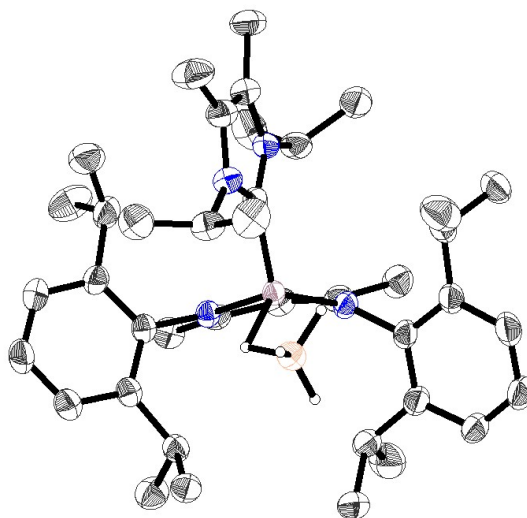
*Refinement details for **93**:*
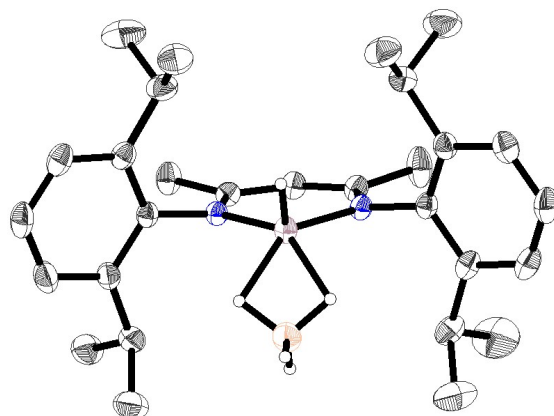
*Refinement details for **95** and **96**: All non H-atoms were located on the electron density maps and refined anisotropically. C-bound H atoms were placed in positions of optimized geometry and treated as riding atoms. Their isotropic displacement parameters were coupled to the corresponding carrier atoms by a factor of 1.2 (CH) or 1.5 (CH3). Disorder: There seem to be two complexes A (C34 H50 Al N2 O2 P) and B (C33 H51 Al N2 O) which are superimposed to 70 % of A and 30 % of B, respectively. Whereas in A Al1 is coordinated to a OCP ligand (occupancy 0.7), in B Al1 is coordinated to H1 (occupancy 0.3).*
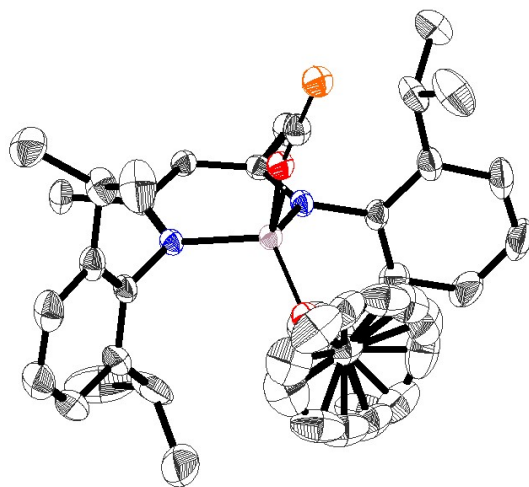
Table A-II. 1 Crystal data for compounds **87**, **88**, **93**, **95** and **96**.

Compound	**87**	**88**	**93**	**91**	**95 and 96**
CCDC code	2268228	2268229	2268231	2268243	2268230
Formula	$C_{33}H_{54}AlBN_2O$	$C_{30}H_{45}AlBN_2OP$	$C_{40}H_{64}AlBN_4$	$C_{29}H_{46}AlB\ N_2$	$C_{33.71}H_{50.30}AlN_2O_{1.70}P_{0.7}$
Crystal system	Monoclinic	Monoclinic	Monoclinic	Monoclinic	Orthorhombic
Space Group	P 2$_1$/m	P 2$_1$/c	P2$_1$/n	P2$_1$/c	P$_{nma}$
Volume (Å^3)	1648.14(13)	3117.67(11)	3956.8(2)	2903.17(13)	3362.27(17)
a	9.0777(4)	15.5308(3)	11.4737(4)	12.0580(3)	16.5923(5)
b	19.9593(9)	8.9216(2)	17.4734(5)	18.1134(4)	20.7328(5)
c	10.0318(4)	22.5631(4)	19.7414(6)	18.1134(4)	9.7739(3)
α	90	90	90°	90°	90
β	114.938(2)	94.266(1)	91.308(2)°.	105.4340(10)°.	90
γ	90	90	90	90°	90
Z	2	4	4	4	4
Formula weight (g/mol)	532.57	518.44	638.74	460.47	559.60
Density (g/mL)	1.073	1.105	1.072	1.053	1.105
Absorption coefficient (mm^{-1})	0.087	0.140	0.666	0.088	0.123
F(000)	584	1120	1400	1008	1215
Temperature (K)	133(2)	133(2)	133(2)	133(2)	133(2)
Total numb. Reflections	20259	54952	46357	63275	65468
Final R indices [I>2σ(l)]	R=0.0450 wR2 = 0.1169	R=0.0450 wR2=0.1149	R=0.0530 wR2 = 0.1362	R = 0.0510 wR2 = 0.1269	R=0.0445 wR2=0.1236
Largest diff. Peack and hole (e·A^{-3})	0.345 and-0.352	0.303 and -0.561	0.559 and -0.221	0.393 and -0.302	0.509 and -0.343
GoF	1.065	1.033	1.024	1.027	1.044

AII.10 Mechanism elucidation of compound 91
AII.10.1 Monitoring the synthesis of 91
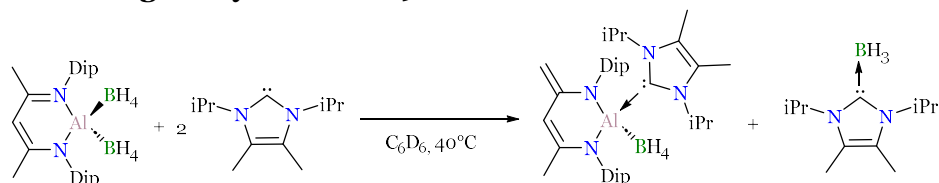
Procedure: In an NMR tube, 10 mg of *NacNac*DipAl(BH$_4$)$_2$ (0.022 mmol, 1 eq) are dissolved in 0.4 ml of C$_6$D$_6$. Then, 7 mg of NHC^{iPrMe} (0.044mmol, 2eq) are added. The reaction is heated at 40°C and followed by ^{1}H-NMR, ^{11}B-NMR and ^{11}B{^{1}H}-NMR.

Figure A-II. 42 ^{1}H-NMR (400.13 MHz, 298 K, benzene-d$_6$) of the crude.
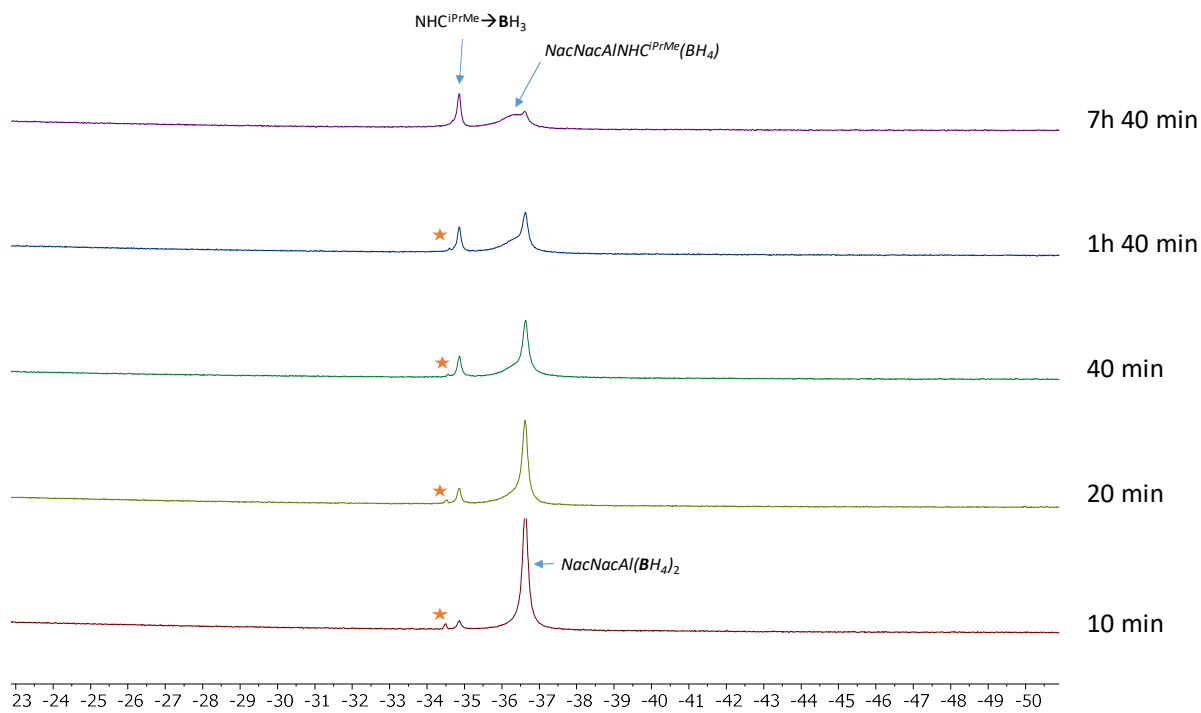
Figure A-II. 43 $^{11}B\{^1H\}$-NMR (128.4 MHz, 298 K, benzene-d_6) of the crude.
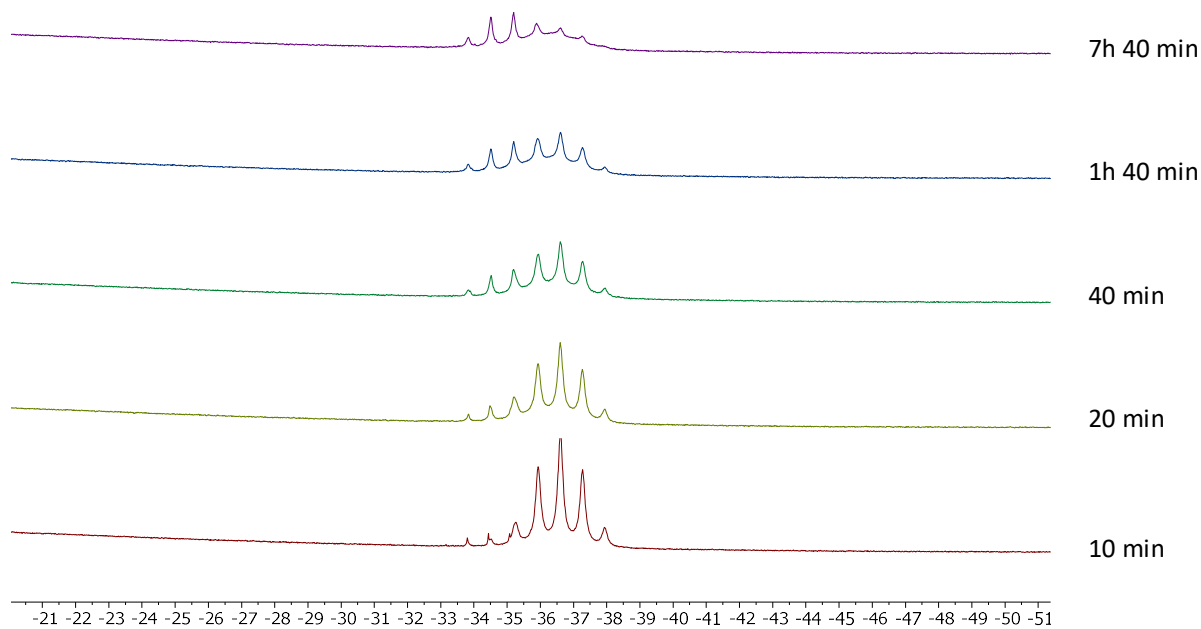
Figure A-II. 44 ^{11}B-NMR (128.4 MHz, 298 K, benzene-d_6) of the crude.

AII.10.2 Blank reaction I
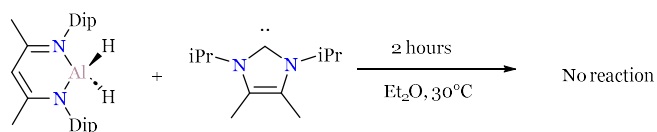
Procedure: In an NMR tube, 10 mg of *NacNac*DipAlH$_2$ (1 eq, 0.022mmol) and 4 mg of NHC^{iPrMe} (1 eq, 0.022mmol) are dissolved in 0.5 mL of Et$_2$O. The reaction mixture is heated at 30°C for 2 hours. The reaction crude is dried under vacuum and analysed by ^{1}H-NMR.
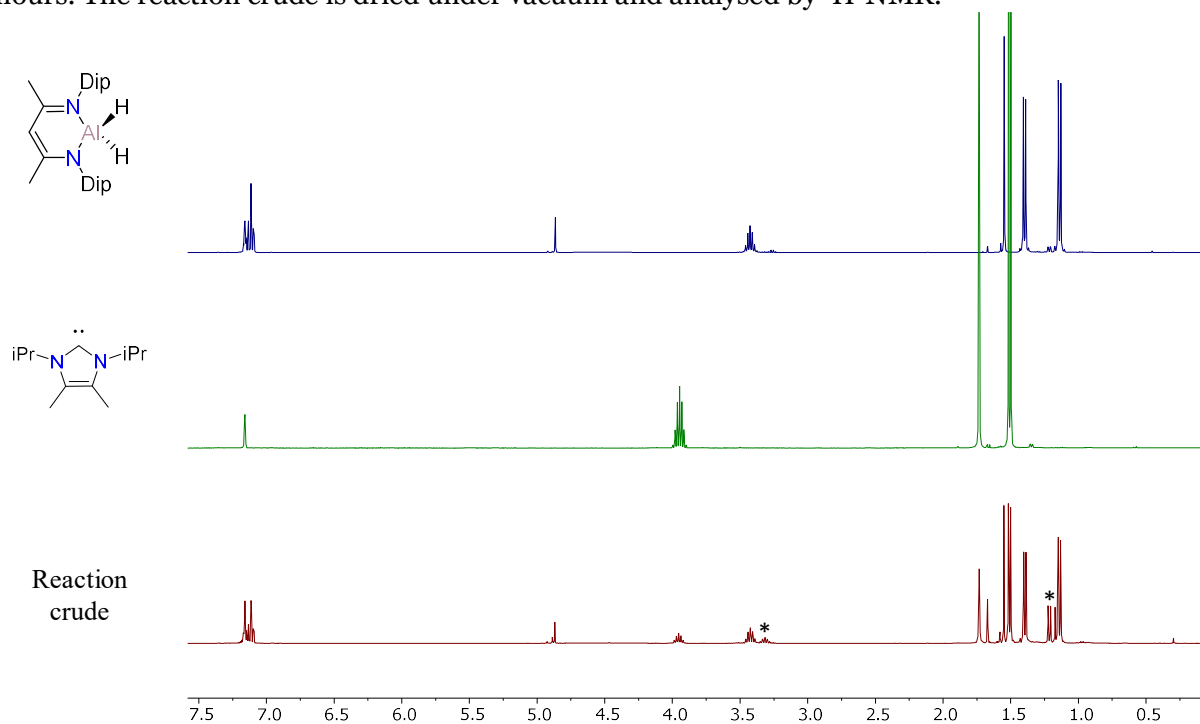
Figure A-II. 45 ^{1}H-NMR (400.13 MHz, 272 K, benzene-d$_6$) of the crude. *Signals from *NacNac*Dip-H.

AII.10.3 Blank reaction III
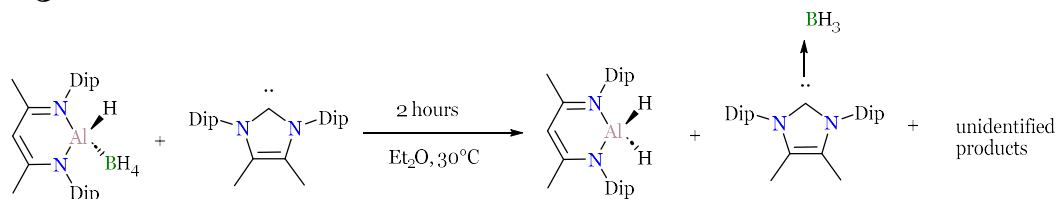
Procedure: In an NMR tube, 10 mg of *NacNac*DipAlHBH$_4$ (1 eq, 0.022mol) and 9 mg of NHC^{DipMe} (1 eq, 0.022mol) are dissolved in 0.5 mL of Et$_2$O. The reaction mixture is heated at 30°C for 2 hours. The reaction crude is dried under vaccum and analysed by ^{1}H-NMR.

Figure A-II. 46 ^{1}H-NMR (400.13 MHz, 298 K, benzene-d$_6$) of the crude.

-2 -4 -6 -8 -10 -12 -14 -16 -18 -20 -22 -24 -26 -28 -30 -32 -34 -36 -38 -40 -42 -44 -46 -48 -50 -52 -54 -56 -58 -60 -62

Figure A-II. 47 ^{11}B-NMR (128.4 MHz, 272 K, benzene-d_6) of the crude.

AII.11 Geometries benchmark with DFT

Table A-II. 2 Benchmark of functionals using def2-SVP basis set of compound **87**. All distances are given in Å and the angles in degrees.

	X-Ray	B3LYP-D3BJ	wB97XD	BP86-D3BJ	M062X
B-Al	2.158	2.149	2.117	2.125	2.126
Al-H	1.845	1.841	1.861	1.874	1.842
Al-H	1.845	1.858	1.882	1.886	1.874
Al-H	2.479	2.525	2.376	2.396	2.397
B-H(al)	1.256	1.247	1.250	1.256	1.250
B-H(al)	1.256	1.246	1.249	1.256	1.248
B-H	1.075	1.205	1.205	1.213	1.203
B-H	1.153	1.219	1.227	1.232	1.223
O-Al	1.696	1.716	1.716	1.732	1.715
Al-N	1.893	1.914	1.908	1.919	1.902
Al-N	1.893	1.915	1.910	1.922	1.903
O-Al-B	115.47	119.3	119.7	120.7	120.6
Coordination BH_4	κ^2	κ^2	κ^3	κ^3	κ^3

Table A-II. 3 Benchmark of functionals using def2-SVP basis set of compound **88**. All distances are given in Å and the angles in degrees.

	X-Ray	B3LYP-D3BJ	wB97XD	BP86-D3BJ	M062X
B-Al	2.064	2.023	2.023	2.027	2.025
Al-H	1.813	1.906	1.912	1.926	1.903
Al-H	1.850	1.906	1.912	1.926	1.903
Al-H	1.969	1.996	1.998	2.001	1.977
B-H(al)	1.166	1.247	1.251	1.257	1.247
B-H(al)	1.157	1.247	1.251	1.257	1.247
B-H	1.019	1.197	1.198	1.206	1.195
B-H	1.028	1.234	1.240	1.246	1.239
O-Al	1.782	1.812	1.811	1.835	1.804
Al-N	1.877	1.893	1.889	1.898	1.886
Al-N	1.871	1.893	1.889	1.898	1.886
O-Al-B	111.8	111.7	111.9	111.1	111.8
Coordination BH$_4$	κ^3	κ^3	κ^3	κ^3	κ^3

Table A-II. 4 Benchmark of geometries using def2-SVP basis set of compound **91** All distances are given in Å and the angles in degrees.

	X-Ray	B3LYP-D3BJ	wB97XD	BP86-D3BJ	M062X
B-Al	2.244	2.216	2.213	2.198	2.201
Al-H	1.723	1.822	1.829	1.852	1.825
Al-H	1.877	1.884	1.895	1.893	1.887
Al-H	2.754	2.783	2.770	2.717	2.704
B-H(al)	1.142	1.257	1.260	1.266	1.259
B-H(al)	1.115	1.244	1.249	1.256	1.248
B-H	1.095	1.206	1.210	1.216	1.209
B-H	1.104	1.211	1.213	1.220	1.209
Ccarb-Al	2.061	2.066	2.074	2.058	2.075
Al-N	1.844	1.865	1.861	1.873	1.859
Al-N	1.844	1.857	1.850	1.868	1.850
Ccarb-Al-B	108.83	109.5	109.4	110.7	110.2
Coordination BH$_4$	κ^2	κ^2	κ^2	κ^2	κ^2

Table A-II. 5 Benchmark of geometries using def2-SVP basis set of compound **93**. All distances are given in Å and the angles in degrees.

	X-Ray	B3LYP-D3BJ	wB97XD	BP86-D3BJ	M062X
B-Al	2.201	2.177	2.156	2.141	2.127
Al-H	1.760	1.843	1.855	1.883	1.879
Al-H	1.765	1.843	1.855	1.883	1.859
Al-H	2.687	2.663	1.584	1.594	1.579
B-H(al)	1.116	1.252	1.256	1.262	1.249
B-H(al)	1.120	1.252	1.256	1.262	1.252
B-H	0.995	1.217	1.222	1.230	1.224
B-H	1.118	1.208	1.208	1.214	1.202
Al-N	1.892	1.929	1.925	1.936	1.917
Al-N	1.890	1.929	1.925	1.936	1.916
Coordination BH_4	κ^2	κ^2	κ^2	κ^2	κ^2

Table A-II. 6 Benchmark of geometries using def2-SVP basis set of compound **95**. All distances are given in Å and the angles in degrees.

	X-Ray	B3LYP-D3BJ	wB97XD	BP86-D3BJ	M062X
O(tBu)-Al	1.678	1.704	1.701	1.717	1.699
O(OCP)-Al	1.732	1.790	1.790	1.806	1.772
Al-N	1.875	1.885	1.880	1.890	1.882
Al-N	1.875	1.892	1.890	1.897	1.878
O-C (OCP)	1.210	1.259	1.254	1.266	1.254
C-P (OCP)	1.561	1.570	1.563	1.586	1.562
O-Al-O	118.2	116.1	115.9	117.1	118.1
Al-O-C (OCP)	162.4	147.6	148.9	143.7	159.5

Table A-II. 7 Absolute energies at different levels of theory. All the energies are given in Hartrees.

| Method | B3LYP-D3(BJ)- Gas phase | | | | | B3LYP-D3(BJ)- PCM Def2-TZVPP E [Ha] | DLPNO-CCSD(T) cc-pVTZ E [Ha] | Gibbs energies | | | |
| Basis set | def2-SVP | | | | Def2-TZVPP E [Ha] | | | $G^{GP\text{-}B3LYP}$ | $G^{PCM\ B3LYP}$ | $\Delta G_{solv}^{\ B3LYP\ d}$ | $G^{CCSDT\ e}$ |
	TCE^a	TCH^b	TCG^c	E [Ha]							
NHC^{iPrMe}-BH$_3$	0.34464	0.34558	0.28403	-567.05092	-567.67649	-567.68613	-566.33894	-567.39245	-567.40210	-6.05049	-355211.16607
NHC^{iPrMe}	0.31004	0.31098	0.25288	-540.35925	-540.95668	-540.96352	-539.70893	-540.70380	-540.71064	-4.29371	-338518.36471
29	0.75918	0.76013	0.65096	-1535.55488	-1537.05025	-1537.05810	-1533.48517	-1536.39929	-1536.40714	-4.92853	-961873.72665
96	0.72267	0.72267	0.61496	-1508.90212	-1510.36701	-1510.37361	-1506.89098	-1509.75205	-1509.75865	-4.13845	-945207.40628
91	1.01865	1.01960	0.88435	-2048.11519	-2050.17149	-2050.18246	-2045.45428	-2049.28714	-2049.29811	-6.88299	-1282994.95659
H$_2$	0.01230	0.01324	-0.00159	-1.17393	-1.17994	-1.18007	-1.17230	-1.18153	-1.18167	-0.08347	-736.71366
BH$_3$	0.02887	0.02981	0.00840	-26.59129	-26.62560	-26.62621	-26.53734	-26.61720	-26.61781	-0.38006	-16647.55686
RC1	1.07384	1.07478	0.92998	-2075.92741	-2078.02129	-2078.02900	-2073.20894	-2077.09131	-2077.09903	-4.84207	-1300380.61404
TS1	1.07332	1.07426	0.93341	-2075.92200	-2078.01413	-2078.02251	-2073.20068	-2077.08071	-2077.08910	-5.26060	-1300373.69626
INT1	1.07328	1.07422	0.93435	-2075.94309	-2078.03309	-2078.04486	-2073.22166	-2077.09874	-2077.11051	-7.39030	-1300388.39753
INT2	1.07232	1.07327	0.93020	-2075.92866	-2078.02196	-2078.05021	-2073.20160	-2077.09176	-2077.12001	-17.72827	-1300388.75596
TS2	1.06708	1.06802	0.92510	-2075.90053	-2077.99250	-2078.00534	-2073.16963	-2077.06740	-2077.08024	-8.05648	-1300362.22617
INT3	1.06969	1.07064	0.92567	-2075.90107	-2077.99430	-2078.00614	-2073.17550	-2077.06863	-2077.08047	-7.42903	-1300364.91776
TS3	1.07086	1.07180	0.92697	-2075.90633	-2077.99987	-2078.00859	-2073.18420	-2077.07290	-2077.08162	-5.47070	-1300367.60338
INT4	1.07236	1.07330	0.92819	-2075.96031	-2078.05213	-2078.06420	-2073.23701	-2077.12394	-2077.13601	-7.57371	-1300402.07930
RC2	1.07327	1.07422	0.92772	-2075.90892	-2078.02506	-2078.03724	-2073.20899	-2077.09734	-2077.10952	-7.64480	-1300384.86034
TS4	1.06758	1.06852	0.92290	-2075.93007	-2078.00071	-2078.01484	-2073.17990	-2077.07780	-2077.09194	-8.87161	-1300370.85811
INT5	1.07253	1.07348	0.92865	-2075.91834	-2078.01254	-2078.03473	-2073.19656	-2077.08389	-2077.10608	-13.92421	-1300382.76003
TS5	1.06796	1.06891	0.92153	-2075.83754	-2077.93370	-2077.94285	-2073.11655	-2077.01217	-2077.02133	-5.74322	-1300328.84101
INT6	1.38637	1.38637	1.20630	-2616.32181	-2619.00575	-2619.01812	-2612.94419	-2617.79946	-2617.81182	-7.76009	-1638899.40783
TS6	1.38100	1.38195	1.20628	-2616.30255	-2618.98318	-2618.99726	-2612.91519	-2617.77690	-2617.79097	-8.83167	-1638882.29149
INT7	1.38632	1.38726	1.21201	-2616.31836	-2619.00141	-2619.02021	-2612.93800	-2617.78940	-2617.80819	-11.79389	-1638895.96943
[NHC^{iPrMe}H]BH$_4$	0.36353	0.36448	0.29947	-568.19266	-568.82534	-568.84674	-567.47880	-568.52587	-568.54728	-13.43010	-355924.13638

^{a}Thermal Correction to Energy ^{b} Thermal correction to Enthalpy ^{c}Thermal correction to Gibbs free energy ^{d} $\Delta G_{solv}^{\ B3LYP}$= $G^{PCM\ B3LYP}$ - $G^{GP\text{-}B3LYP}$ ^{e} G^{CCSDT}=E^{CCSDT}+TCG+ $\Delta G_{solv}^{\ B3LYP}$

AII.13 Partial charges, bond orders and topological analysis

Table A-II. 8 Charges of compound **87** at B3LYP-D3(BJ)/def2-TZVPP//B3LYP-D3(BJ)/def2-SVP.

	Q_{AIM}	Q_{TFVC}	Q_{NPA}
Al	2.48	2.29	2.08
B	1.66	1.96	-0.75
H1	-0.67	-0.77	-0.03
H2	-0.67	-0.77	-0.03
H3	-0.59	-0.68	0.03
H4	-0.56	-0.60	0.07
BH_4	-0.83	-0.86	-0.73

Table A-II. 9 Bond orders of compound **87** at B3LYP-D3(BJ)/def2-TZVPP//B3LYP-D3(BJ)/def2-SVP.

	$\delta_{DI}(A,B)$	BO_{TFVC}	BO_{NAO}
Al-B	0.04	0.04	0.24
Al-H1	0.11	0.13	0.11
Al-H2	0.10	0.14	0.11
Al-H3	0.02	0.03	0.03
B-H1	0.47	0.39	0.86
B-H2	0.47	0.39	0.86
B-H3	0.56	0.47	0.95
B-H4	0.58	0.47	0.97

Table A-II. 10 Charges of compound **88** at B3LYP-D3(BJ)/def2-TZVPP//B3LYP-D3(BJ)/def2-SVP.

	Q_{AIM}	Q_{TFVC}	Q_{NPA}
Al	2.48	2.33	1.99
B	1.59	1.93	-0.81
H1	-0.63	-0.76	0.02
H2	-0.63	-0.76	0.02
H3	-0.62	-0.76	0.02
H4	-0.53	-0.58	0.10
BH_4	-0.82	-0.93	-0.65

Table A-II. 11 Bond orders of compound **88** at B3LYP-D3(BJ)/def2-TZVPP//B3LYP-D3(BJ)/def2-SVP.

	$\delta_{DI}(A,B)$	BO_{TFVC}	BO_{NAO}
Al-B	0.06	0.05	0.32
Al-H1	0.09	0.12	0.11
Al-H2	0.09	0.12	0.11
Al-H3	0.03	0.10	0.09
B-H1	0.52	0.42	0.86
B-H2	0.52	0.42	0.86
B-H3	0.52	0.43	0.88
B-H4	0.61	0.50	0.96

Table A-II. 12 Charges of compound **91** at B3LYP-D3(BJ)/def2-TZVPP//B3LYP-D3(BJ)/def2-SVP.

	Q_{AIM}	Q_{TFVC}	Q_{NPA}
Al	2.43	2.20	1.92
B	1.69	1.97	-0.71
H1	-0.69	-0.76	-0.04
H2	-0.67	-0.78	-0.03
H3	-0.58	-0.65	0.04
H4	-0.57	-0.63	0.04
BH$_4$	-0.82	-0.84	-0.86

Table A-II. 13 Bond orders of compound **91** at B3LYP-D3(BJ)/def2-TZVPP//B3LYP-D3(BJ)/def2-SVP.

	$\delta_{DI}(A,B)$	BO_{TFVC}	BO_{NAO}
Al-B	0.04	0.04	0.23
Al-H1	0.12	0.17	0.13
Al-H2	0.10	0.14	0.11
Al-H3	0.01	0.02	0.01
B-H1	0.48	0.37	0.83
B-H2	0.46	0.39	0.85
B-H3	0.56	0.47	0.96
B-H4	0.58	0.46	0.97

Table A-II. 14 Charges of compound **93** at B3LYP-D3(BJ)/def2-TZVPP//B3LYP-D3(BJ)/def2-SVP.

	Q_{AIM}	Q_{TFVC}	Q_{NPA}
Al	2.39	2.21	1.63
B	1.68	1.97	-0.69
H1	-0.68	-0.77	-0.03
H2	-0.68	-0.77	-0.03
H3	-0.60	-0.68	0.01
H4	-0.56	-0.61	0.05
BH$_4$	-0.84	-0.86	-0.69

Table A-II. 15 Bond orders of compound **93** at B3LYP-D3(BJ)/def2-TZVPP//B3LYP-D3(BJ)/def2-SVP.

	$\delta_{DI}(A,B)$	BO_{TFVC}	BO_{NAO}
Al-B	0.04	0.04	0.27
Al-H1	0.12	0.15	0.14
Al-H2	0.12	0.15	0.14
Al-H3	0.01	0.02	0.01
B-H1	0.46	0.39	0.83
B-H2	0.46	0.39	0.83
B-H3	0.56	0.47	0.98
B-H4	0.58	0.47	0.98

Table A-II. 16 ESI-3c of B_2H_6 using QTAIM partition at B3LYP-D3(BJ)/def2-TZVPP//B3LYP-D3(BJ)/def2-SVP level of theory.

Centers	B_2H_6
B-H-B	0.066
B-H-B	0.066
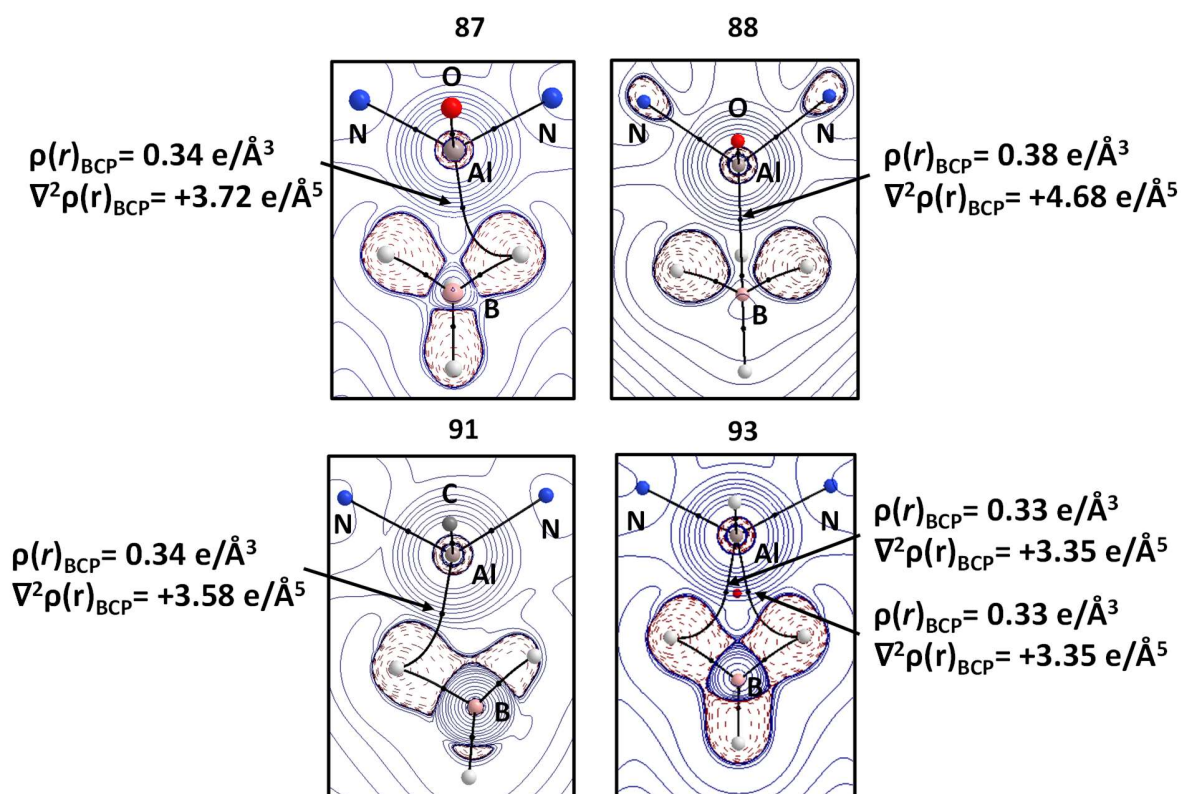
Figure A-II. 48 Plot of the Laplacian electron density of compounds **87**, **88**, **91**, **93** at the B3LYP-D3(BJ)/def2-TZVPP//B3LYP-D3(BJ)/def2-SVP level of theory. The blue lines indicate positive $\nabla^2\rho(\mathbf{r})$ region and red lines indicate the negative $\nabla^2\rho(\mathbf{r})$ region. The solid black lines indicate the bond paths, the black dots indicate Bond Critical Points (BCP) and the red dots indicate Ring Critical Points (RCP).

Table A-II. 17 Electron density and Lapacian values at the bond critical point at B3LYP-D3(BJ)/def2-TZVPP//B3LYP-D3(BJ)/def2-SVP level of theory. $\rho(\mathbf{r})_{BCP}$ values are given in e/Å^3 and $\nabla^2\rho(\mathbf{r})_{BCP}$ in e/Å^5.

Compound	$\rho(\mathbf{r})_{BCP}$	$\nabla^2\rho(\mathbf{r})_{BCP}$
87	0.34	3.72
88	0.38	4.68
91	0.34	3.58
93	0.33	3.35
	0.33	3.35

AII.13 Deformation densities

Deformation densites	[NacNacAlOtBu]$^+$	[BH$_4$]$^-$

$\Delta E_{\rho(1)}$= -44.7; $|\upsilon_{\alpha\beta}|$= 0.54

LUMO= -6.51 eV
$\upsilon_{\alpha\beta}$= 0.44

HOMO=-1.50 eV
$\upsilon_{\alpha\beta}$=-0.22

$\Delta E_{\rho(2)}$= -17.4 ; $|\upsilon_{\alpha\beta}|$= 0.29

LUMO+8= -2.26 eV
$\upsilon_{\alpha\beta}$=0.06

HOMO-1=-1.53 eV
$\upsilon_{\alpha\beta}$=-0.20

$\Delta E_{\rho(3)}$= -8.0 ; $|\upsilon_{\alpha\beta}|$=0.20

LUMO+6= -2.72 eV
$\upsilon_{\alpha\beta}$= 0.03

HOMO-2=-2.03 eV
$\upsilon_{\alpha\beta}$= -0.03
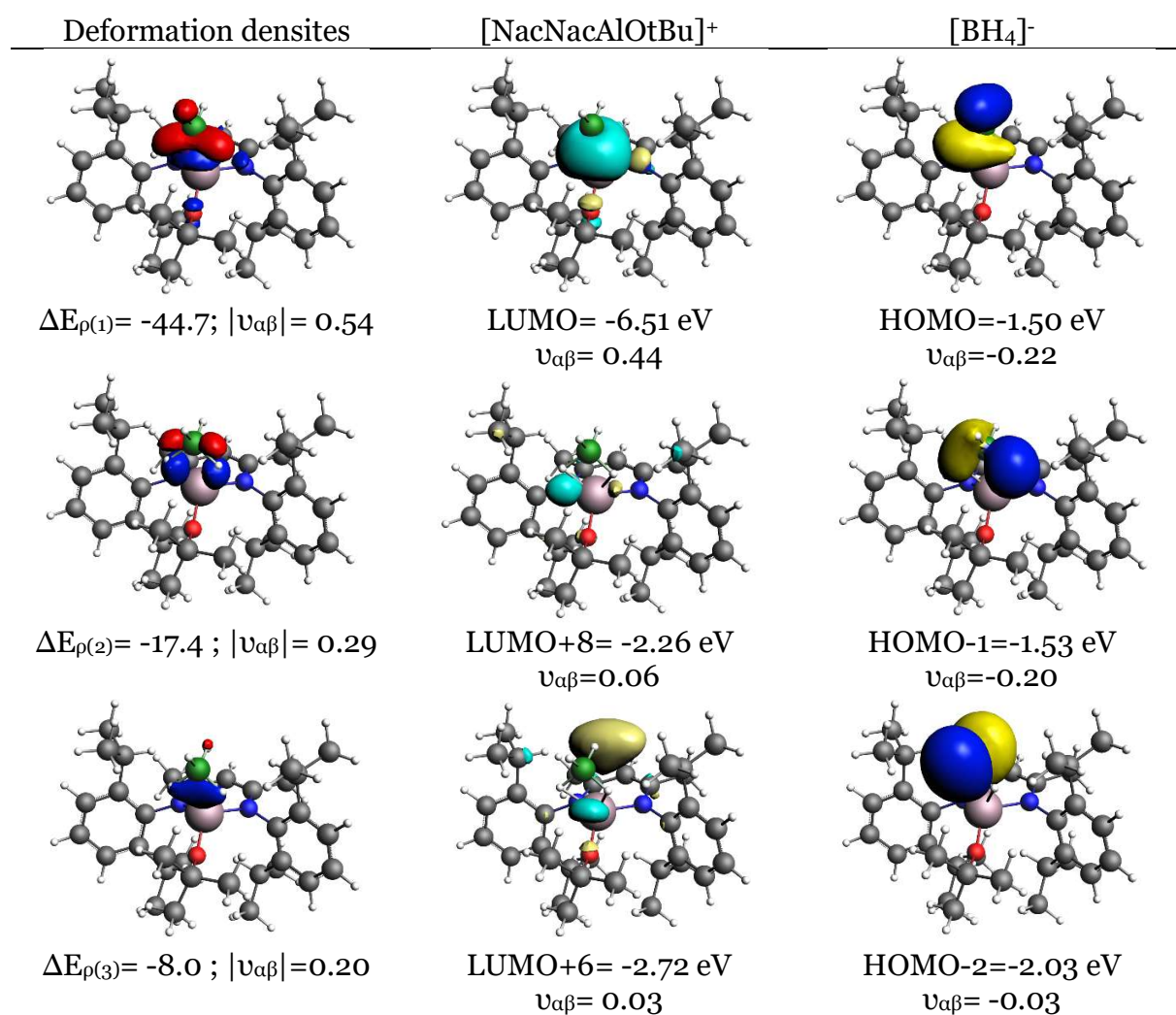
Figure A-II. 49 Deformation densities Δρ (isovalue 0.001 a.u.) of the pairwise orbital interactions between [NacNacAltBuO]$^+$ and [BH$_4$]$^-$ of compound **87**. Associated energies ΔE (in kcal/mol) and eigenvalues ν (in a.u.). The red color shows the charge density accumulation.

Deformation densites	[NacNacAlOCP]$^+$	[BH$_4$]$^-$

$\Delta E_{\rho(1)}$= -54.6; $|\upsilon_{\alpha\beta}|$= 0.59

LUMO=-8.00 eV
$\upsilon_{\alpha\beta}$=0.52

HOMO-2= -1.97 eV
$\upsilon_{\alpha\beta}$=-0.28

$\Delta E_{\rho(2)}$= -19.0; $|\upsilon_{\alpha\beta}|$= 0.30

LUMO+9=-2.63 eV
$\upsilon_{\alpha\beta}$=0.09

HOMO-1= -1.55eV
$\upsilon_{\alpha\beta}$=-0.16

$\Delta E_{\rho(3)}$= -16.2; $|\upsilon_{\alpha\beta}|$=0.28

LUMO+8= -2.96eV
$\upsilon_{\alpha\beta}$= 0.06

HOMO= -1.54 eV
$\upsilon_{\alpha\beta}$= -0.14
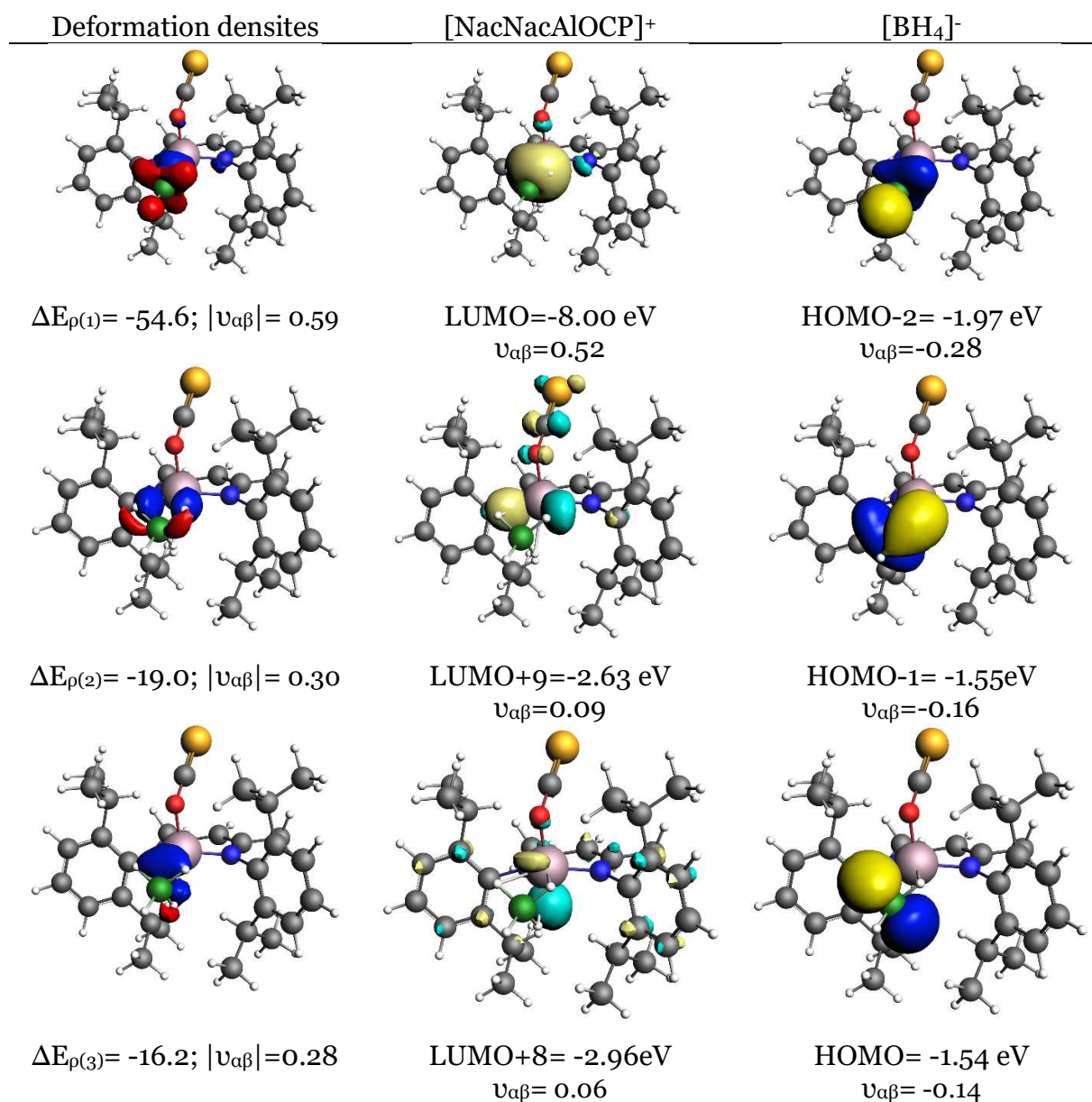
Figure A-II. 50 Deformation densities $\Delta\rho$ (isovalue 0.001 a.u.) of the pairwise orbital interactions between [NacNacAlOCP]$^+$ and [BH$_4$]$^-$ of compound **88**. Associated energies ΔE (in kcal/mol) and eigenvalues υ (in a.u.). The red color shows the charge density accumulation.

Deformation densites	[NacNacAlNHC]$^+$	[BH$_4$]$^-$

$\Delta E_{\rho(1)}$= -48.2; $|\upsilon_{\alpha\beta}|$= 0.57

LUMO= -6.27 eV
$\upsilon_{\alpha\beta}$=0.44

HOMO= -1.41 eV
$\upsilon_{\alpha\beta}$=-0.28

$\Delta E_{\rho(2)}$= -17.2 ; $|\upsilon_{\alpha\beta}|$= 0.30

LUMO+1=-4.11eV
$\upsilon_{\alpha\beta}$=0.04

HOMO-1= -1.61 eV
$\upsilon_{\alpha\beta}$=-0.21

$\Delta E_{\rho(3)}$= -7.4; $|\upsilon_{\alpha\beta}|$=0.20

LUMO+8= -2.33 eV
$\upsilon_{\alpha\beta}$= 0.02

HOMO -2= -2.05 eV
$\upsilon_{\alpha\beta}$= -0.03
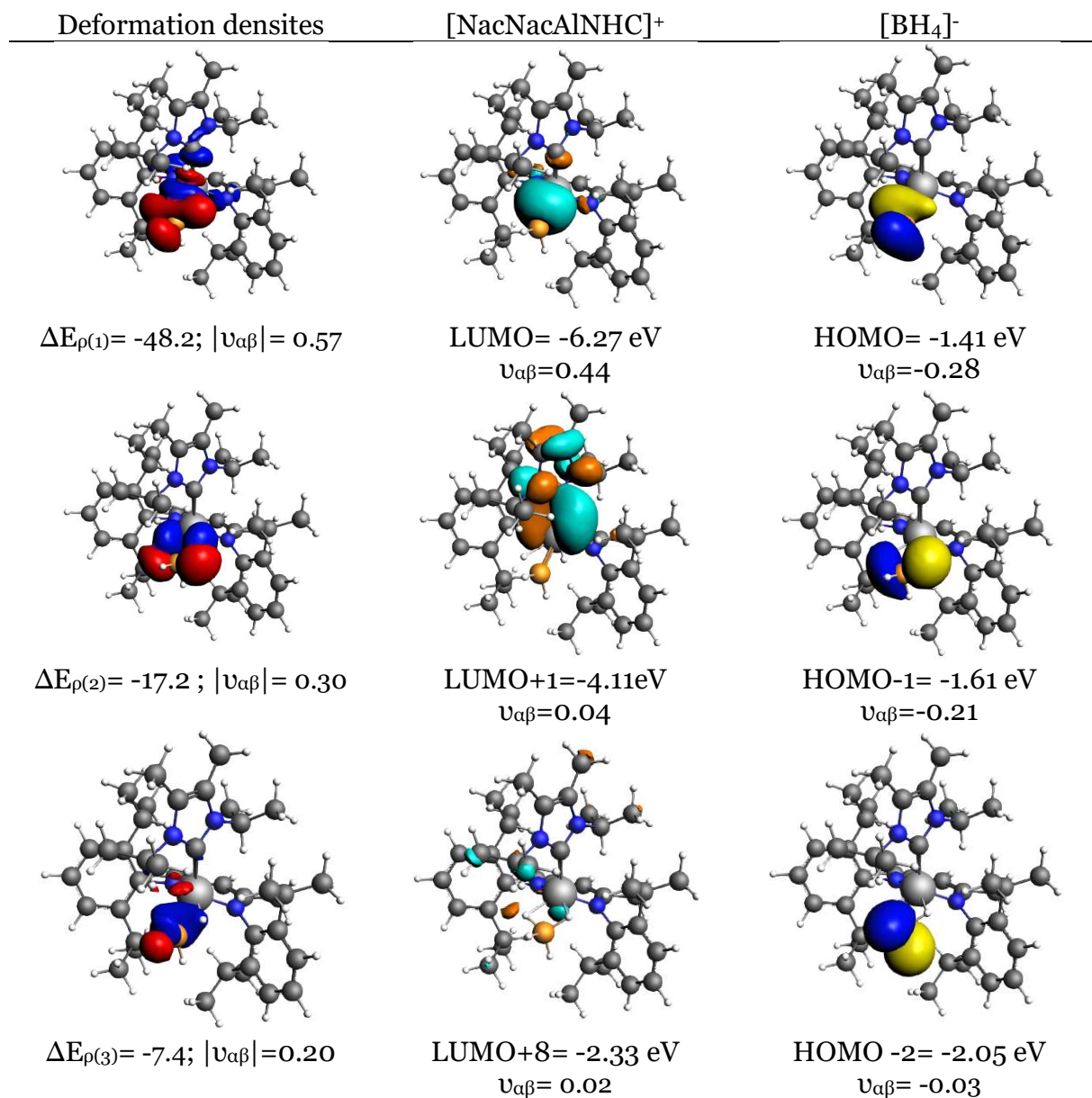
Figure A-II. 51 Deformation densities $\Delta\rho$ (isovalue 0.001 a.u.) of the pairwise orbital interactions between [*NacNac*AlNHC]$^+$ and [BH$_4$]$^-$ of compound **91**. Associated energies ΔE (in kcal/mol) and eigenvalues υ (in a.u.). The red color shows the charge density accumulation.

Deformation densites	[NacNacAlH]$^+$	[BH$_4$]$^-$

$\Delta E_{\rho(1)}$= -47.7; $|\upsilon_{\alpha\beta}|$= 0.57

LUMO= -6.60 eV
$\upsilon_{\alpha\beta}$=0.46

HOMO= -1.47 eV
$\upsilon_{\alpha\beta}$=-0.28

$\Delta E_{\rho(2)}$= -18.1 ; $|\upsilon_{\alpha\beta}|$= 0.30

LUMO+6=-2.90 eV
$\upsilon_{\alpha\beta}$= 0.08

HOMO-1= -1.55 eV
$\upsilon_{\alpha\beta}$=-0.23

$\Delta E_{\rho(3)}$= -7.6; $|\upsilon_{\alpha\beta}|$= 0.20

LUMO+7= -2.83 eV
$\upsilon_{\alpha\beta}$= 0.01

HOMO-2= -2.05 eV
$\upsilon_{\alpha\beta}$= -0.01
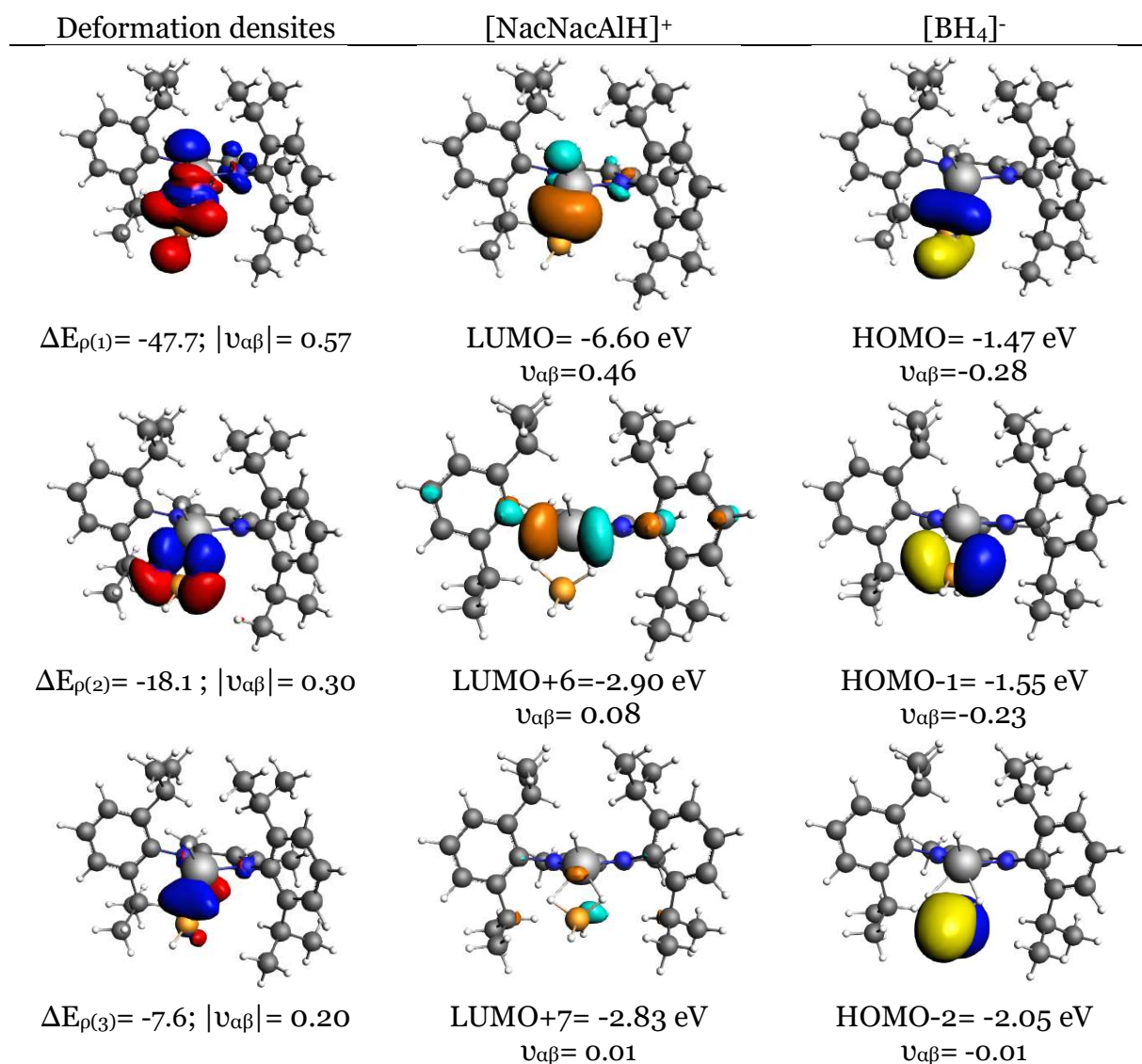
Figure A-II. 52 Deformation densities $\Delta\rho$ (isovalue 0.001 a.u.) of the pairwise orbital interactions between [*NacNac*AlH]$^+$ and [BH$_4$]$^-$ of compound **93**. Associated energies ΔE (in kcal/mol) and eigenvalues υ (in a.u.). The red color shows the charge density accumulation.

APPENDIX III- Supporting information of Chapter V

AIII.1 Synthesis of compound 99:
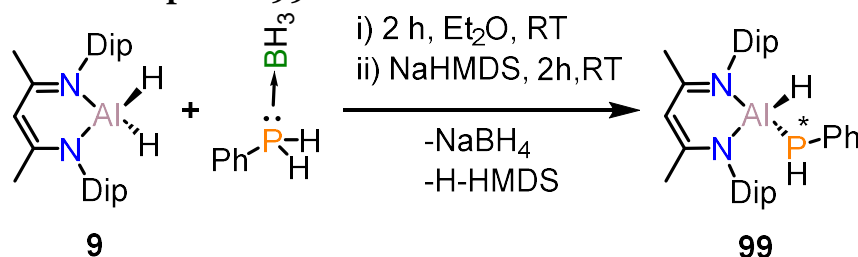
Procedure: In an Schlenk flask, 0.191 g (1 eq, 0.473 mmol) of *NacNac*AlH$_2$ and 0.058 g of PH$_2$PhBH$_3$ (1.1 eq, 0.520 mmol) are dissolved in 10 mL of diethylether. The reaction mixture is stirred for 2 hours at room temperature. Then, a solution of NaHMDS (0.086 g (1.1 eq, 0.520 mmol) in 5mL) is added to the reaction crude dropwise yielding a slurry pale yellow solution. The reaction mixture is stirred for 2h at room temperature. Then, the reaction mixture is filtered with cannula and the resulting solution is concentrated until incipient precipitation kept in the freezer (-24°C) overnight yielding a pale yellow crystals. The mother liquors are concentrated and kept for crystallization obtaining a total 0.185 mg (78%).

^{1}H-NMR (400.13 MHz, 298 K, toluene-d_8): δ(ppm)= 1.01 (bs, 6H, C$_{iPr}$-$\underline{Me}$), 1.12 (d, $^2J_{H-H}$= 6.79 Hz, 6H,C$_{ipr}$-$\underline{Me_2}$), 1.54 (doublet and singlet overlapped, 12H, $\underline{Me}$ (*NacNac*) and C$_{ipr}$-$\underline{Me_2}$), 2.41 (d,$^1J_{P-H}$= 189.77 Hz, 1H , P-$\underline{H}$), 1.52 (s, 6H, $\underline{Me}$(*NacNac*)), 3.27 (sept, 2H, C$_{ipr}$-$\underline{H}$), 3.34 (sept, 2H, C$_{ipr}$-$\underline{H}$), 4.88 (s, 1H, C$_\gamma$-$\underline{H}$), 7.10 (m, 6H, *m*-, *p*-C$_{Ar}$-$\underline{H}$).**^{13}C{^{1}H} (100.61 MHz, 298 K, toluene-d_8)** δ(ppm)= 22.93 (C$_{ipr}$-$\underline{C}$H$_3$), 24.49 (C$_{ipr}$-$\underline{C}$H$_3$), 24.91(C$_{ipr}$-$\underline{C}$H$_3$), 25.68(C$_{ipr}$-$\underline{C}$H$_3$), 28.15($\underline{C}_{ipr}$-CH$_3$), 29.26 ($\underline{C}_{ipr}$-CH$_3$), 97.40($\underline{C}_\gamma$-H), 124.26($\underline{C}$-Ar). 124.46($\underline{C}$-Ar), 127.54($\underline{C}$-Ar), 133.29($\underline{C}$-Ar), 133.43($\underline{C}$-Ar), 136.88 (d,$^1J_{P-C}$=19.74 Hz, $\underline{C}_{ipso}$-Ar), 139.93($\underline{C}_{ipso}$-Ar), 143.37($\underline{C}_{meta}$-Ar), 145.23($\underline{C}_{meta}$-Ar), 170.58 ($\underline{C}_\beta$-backbone). **^{31}P{^{1}H}-NMR (161.98 MHz, 298 K, toluene-d_8):** δ(ppm)= -155.32 (s). **^{31}P-NMR (161.98 MHz, 298 K, toluene-d_8):** δ(ppm)= -155.32 (d, $^1J_{P-H}$ =189.77). **^{11}B-NMR (128.38 MHz, 298 K, toluene-d_8)**: δ(ppm)= silent in the range of +50 ppm to -50 ppm.**^{27}Al-NMR (104.26 MHz, 298 K, toluene-d_8)**: δ(ppm)= silent in the range of 190 to -190 ppm. **Elemental analyisis (%):** calc for **99:** C: 75.78, H: 8.72, N: 5.05; found: C: 76.38, H: 8.87, N: 4.78. **Melting point:** 185°C.
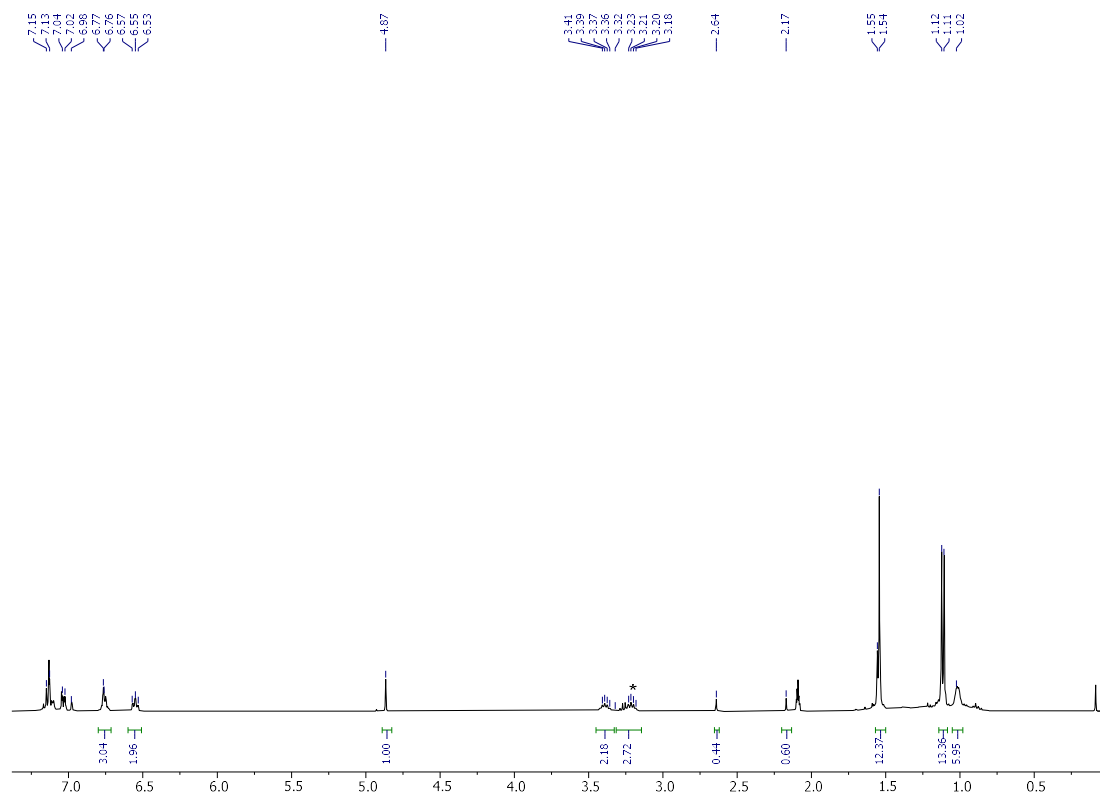
Figure A-III. 1. ¹H-NMR (400.13 MHz, 298 K, toluene-d₈) of compound **99**. *Et₂O
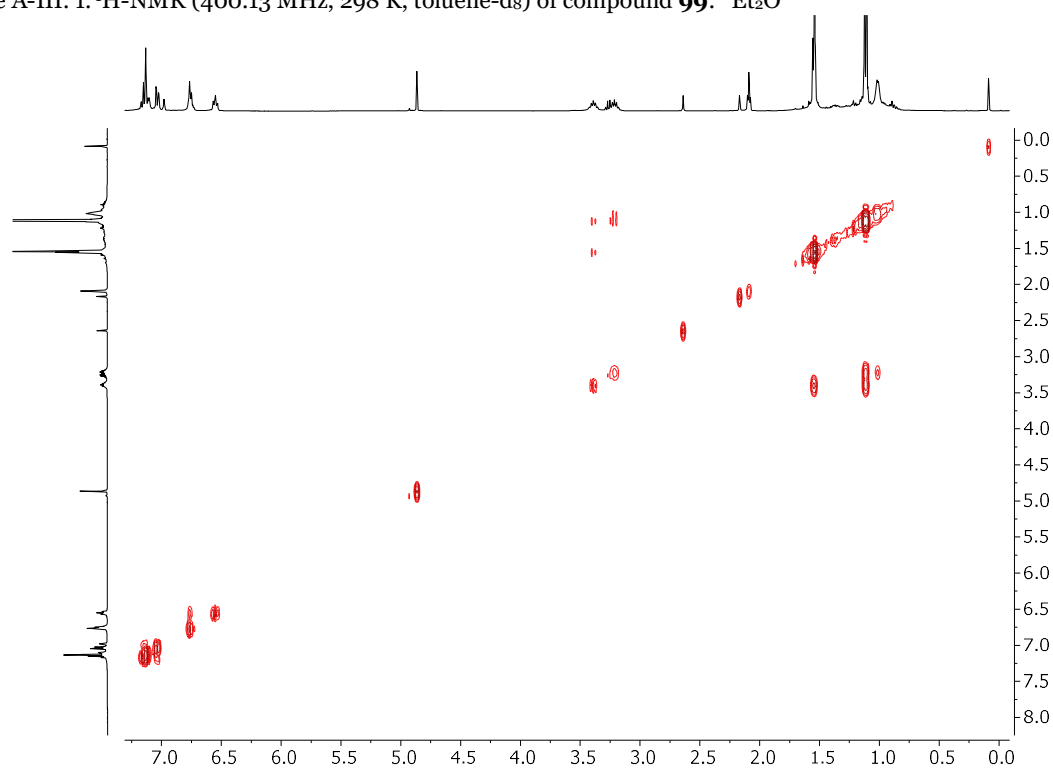
Figure A-III. 2. ¹H-¹H-COSY-NMR (400.13 MHz, 298 K, toluene-d₈) of compound **99** in toluene-*d₈*.
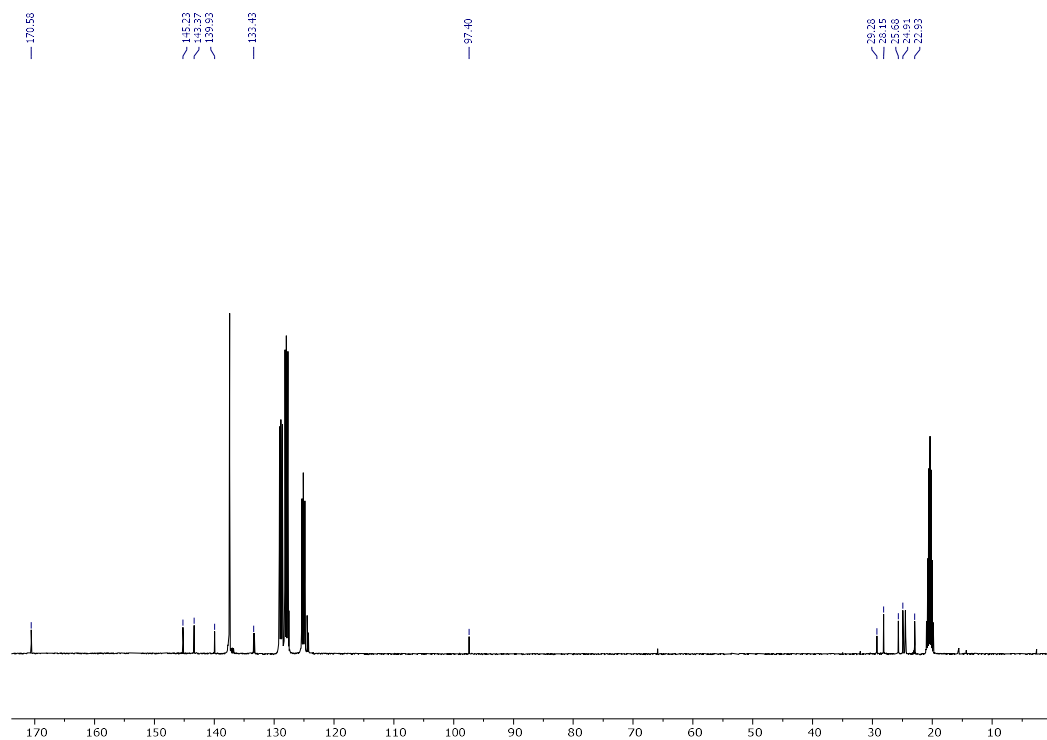
Figure A-III. 3. $^{13}C\{^1H\}$-NMR (100.61 MHz, 298 K, toluene-d_8) of compound **99** in toluene-d_8.
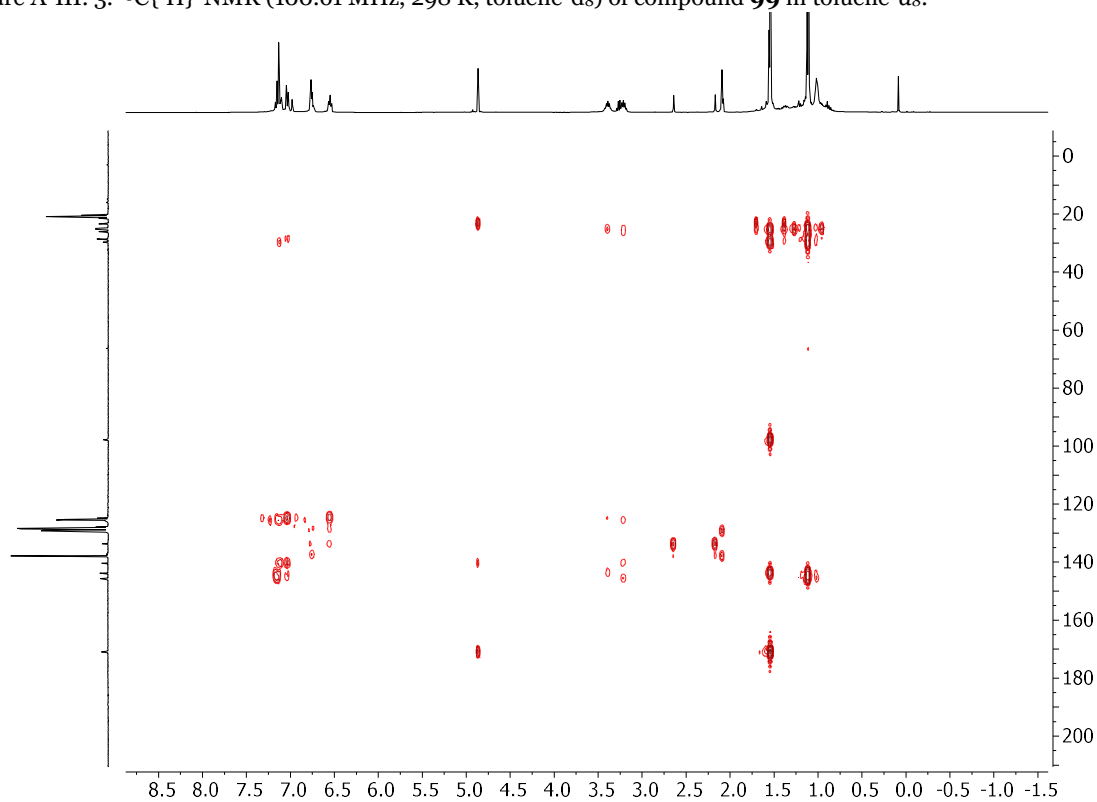
Figure A-III. 4. HMBC (298 K, toluene-d_8) of compound **99**.

-155.33
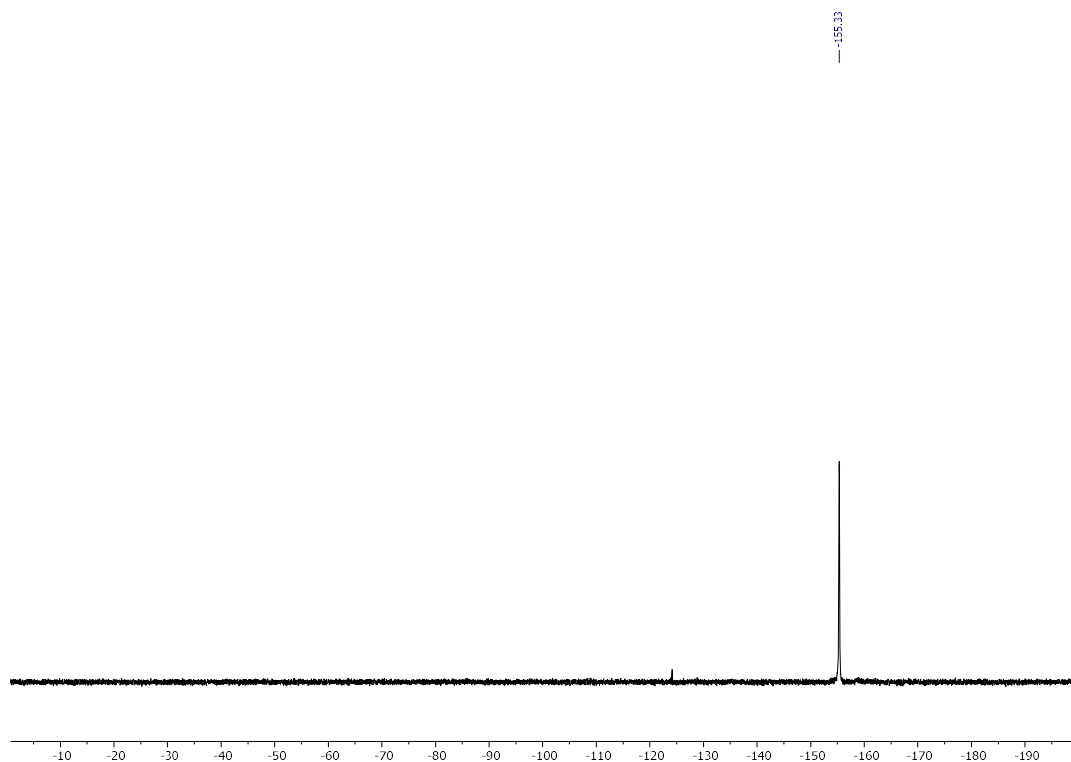
Figure A-III. 5. ^{31}P{^{1}H}-NMR (161.98 MHz, 298 K, toluene-d$_8$) of compound **99**.

-148 -150 -152 -154 -156 -158 -160 -162
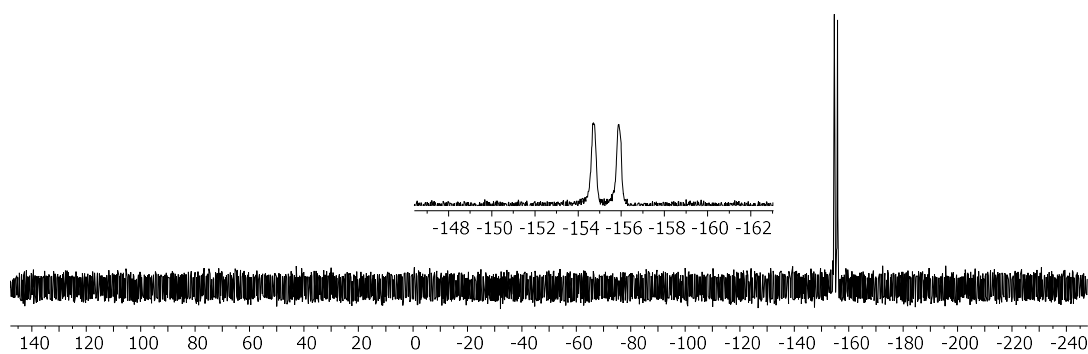
Figure A-III. 6. ^{31}P-NMR (161.98 MHz, 298 K, toluene-d$_8$) of compound **99**.
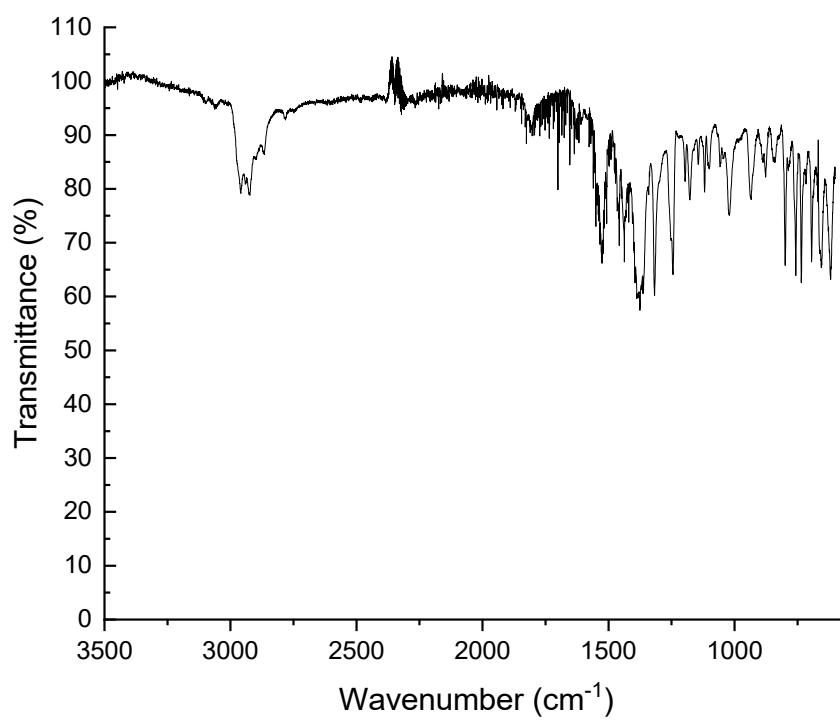
Figure A-III. 7. IR spectrum of compound **99**.

AIII.2 Synthesis of compound 100:
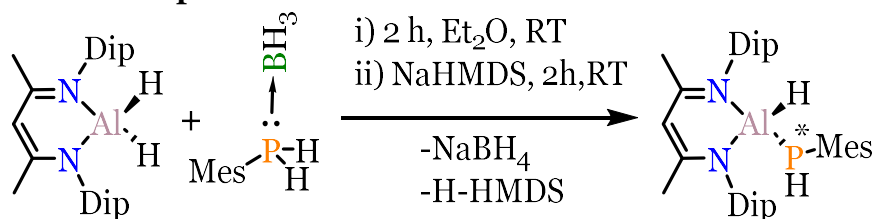
Procedure: In an Schlenk flask 0.053g (1 eq, 0.144 mmol) of *NacNac*AlH$_2$ and 0.019 g (1 eq, 0.114 mmol) MesPH$_2$BH$_3$ are disposed. Then, 2 mL of Et$_2$O are added and the reaction mixture is stirred for 2 hours at room temperature. Then, a solution 0.021 g (1 eq, 0.114 mmol) of NaHMDS in 2 mL of Et$_2$O is added dropwise to the solution. Upon addition, the solution becomes yellow and slurry. The solution is filtered off and concentrated in about 1 mL and kept at -35°C. The obtained colorless crystals are washed with hexane and dried under vaccum. The mother liquors are kept in the -35°C freezer for another batch of crystals. A total of 21 mg (28%) are collected.

^{1}H-NMR (400.13 MHz, 298 K, toluene-d_8): δ(ppm)= 1.07 (d, $^2J_{H-H}$= 6.73 Hz,6H, C$_{iPr}$-Me), 1.11 (two overlaped doublets, 12H,C$_{ipr}$-Me), 1.55 (s, 6H, Me(*NacNac*)), 1.58 (d, $^2J_{H-H}$= 6.96 Hz,6H, C$_{iPr}$-Me), 1.70(s, 6H, *o*-Me-Mes), 2.06 (s, 3H, *p*-Me-Mes) 2.52, (d,$^1J_{P-H}$= 196.5 Hz, 1H, P-H), 3.20 (sept,$^2J_{H-H}$= 6.74 Hz, 2H, C$_{ipr}$-H), 3.33 (sept,$^2J_{H-H}$= 6.88 Hz, 2H, C$_{ipr}$-H), 4.88 (s, 1H,C$_\gamma$-H), 6.61 (s, 2H, *m*-C$_{Mes}$-H), 6.98 (bt,1H, *m*-C$_{Dip}$-H), 7.02 (*m*-C$_{Dip}$-H). The resonances in the aromatic region could not be assigned due to overlap with toluene-d$_8$.**^{13}C{^{1}H} (100.61 MHz, 298 K, toluene-d_8)** δ(ppm)=23.38(CH$_3$, *NacNac*), 23.79 (d, CH$_3$-Mes, $^1J_{C-P}$=11.91 Hz), 24.02 (d, CH$_3$-Mes. $^1J_{C-P}$=11.91 Hz), 24.52(C$_{ipr}$-CH$_3$), 24.91(C$_{ipr}$-CH$_3$), 25.68 (C$_{ipr}$-CH$_3$), 28.18(C$_{ipr}$-CH$_3$), 29.62(C$_{ipr}$-CH$_3$), 29.66(s, C$_{ipr}$-CH$_3$), 97.50 (s, C$_\gamma$-H), 124.47(s, C-Ar), 125.04 (s, C-Ar), 128.51 (s, C-Ar), 131.53 (d, $^1J_{C-P}$=22.73 Hz, C-Ar), 133.16 (s, C-Ar), 140.45(d, $^1J_{C-P}$=7.69 Hz, C-Ar)), 140.61(s, C-Ar), 143.72(s, C-Ar), 145.26 (s, C-Ar), 170.65 (s, C$_\beta$-NacNac).**^{31}P-NMR (161.98 MHz, 298 K, toluene-d_{86}):** δ(ppm)= -191.11 (s).**^{31}P{^{1}H}-NMR (161.98 MHz, 298 K, toluene-d_8):** δ(ppm)= -191.11 (dd,$^1J_{P-H}$= 196.5 Hz, $^3J_{P-H}$= 19.35 Hz). **^{27}Al-NMR (104.26 MHz, 272 K, toluene-d_8):** δ(ppm)= silent in the range of 190 to -190 ppm. **Melting point:** 183°C

Figure A-III. 8. ¹H-NMR (400.13 MHz, 298 K, toluene-d$_8$) of compound **100**.

Figure A-III. 9. ¹H-¹H -COSY-NMR(298 K, toluene-d$_8$) of compound **100**.
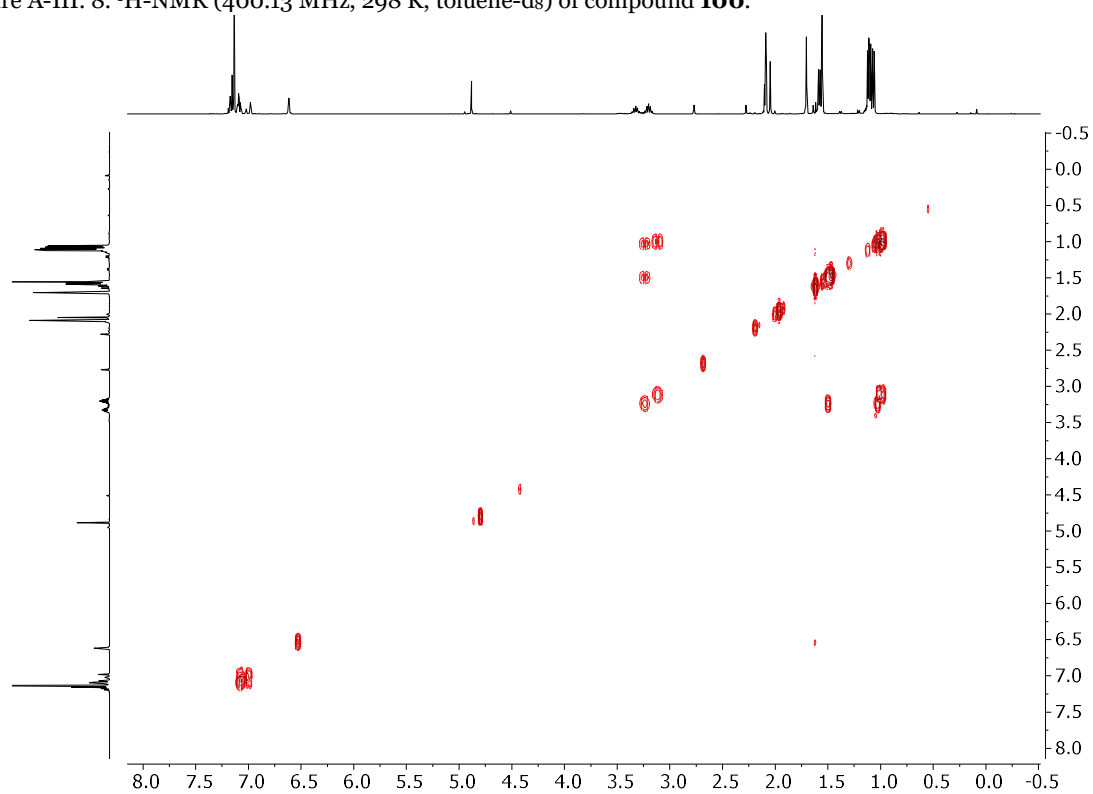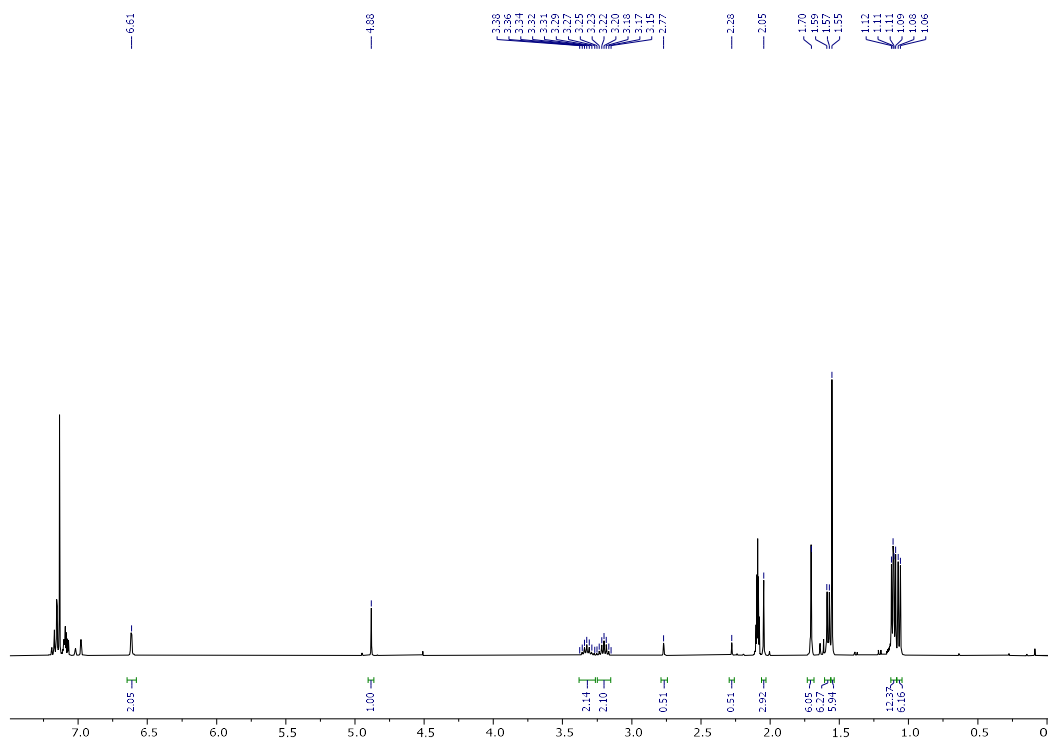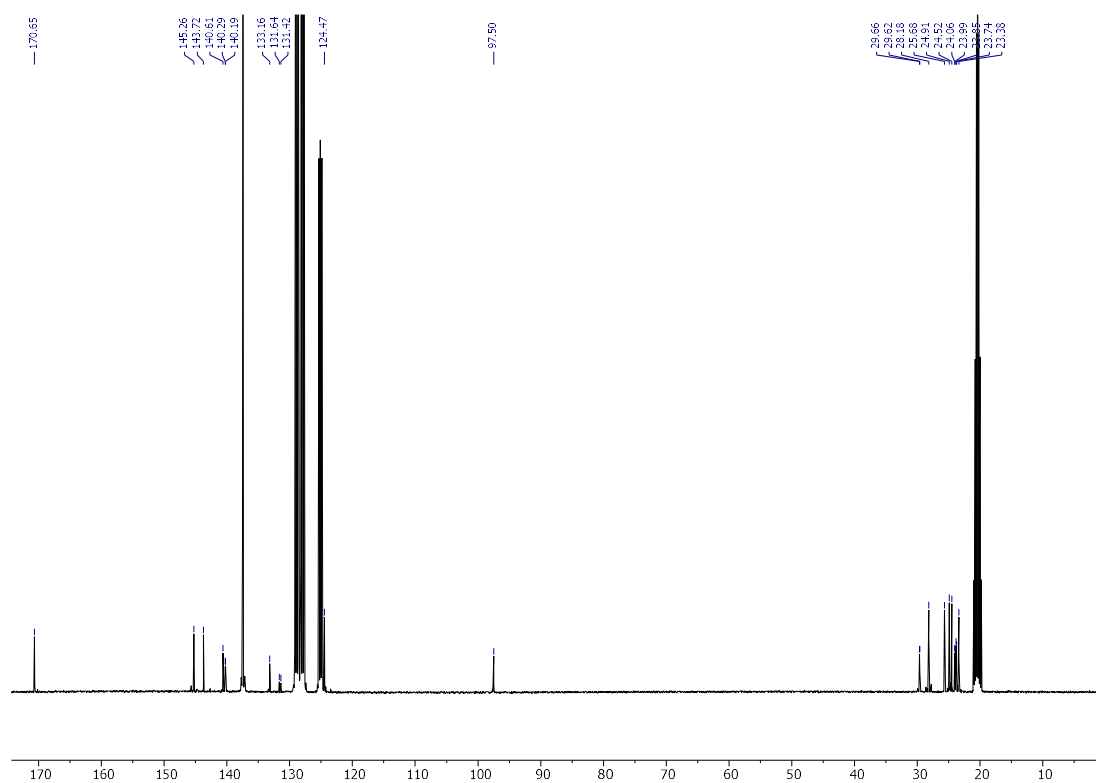
Figure A-III. 10. ¹³C{¹H}-NMR (100.61 MHz, 298 K, toluene-d$_8$) of compound **100.**
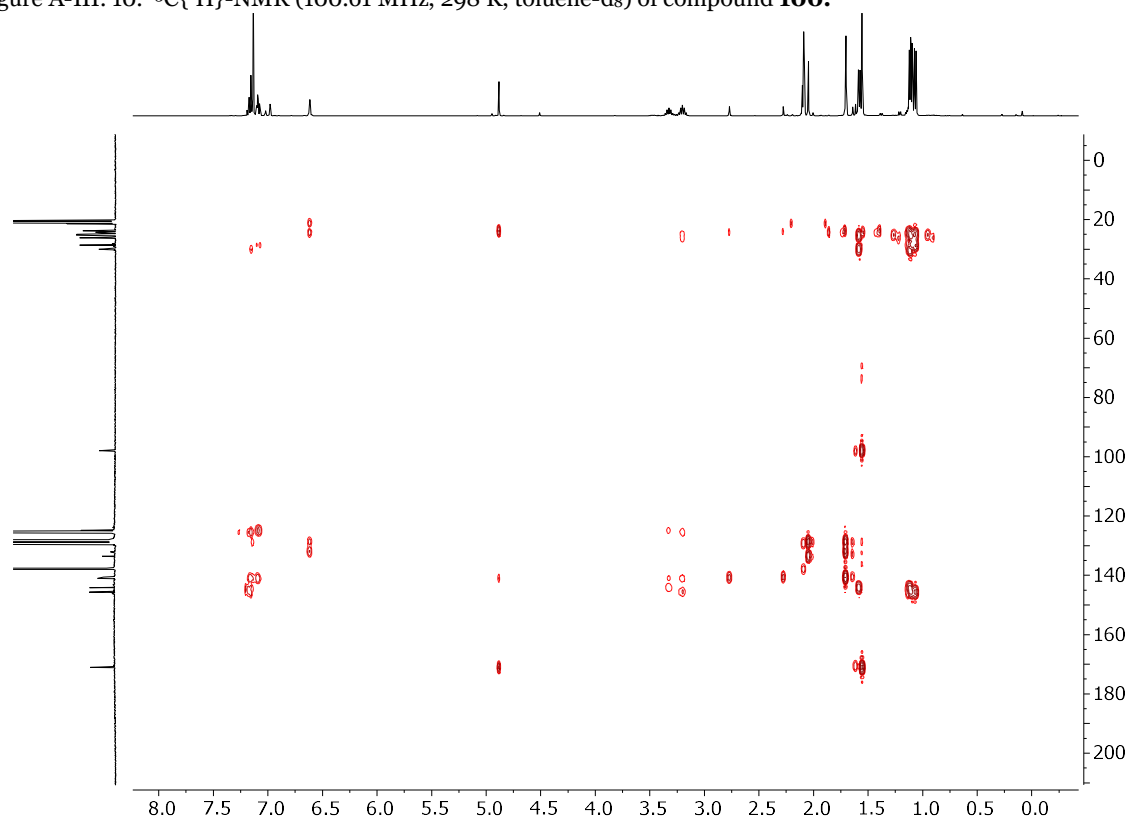
Figure A-III. 11. HMBC (298 K, toluene-d$_8$) of compound **100**.
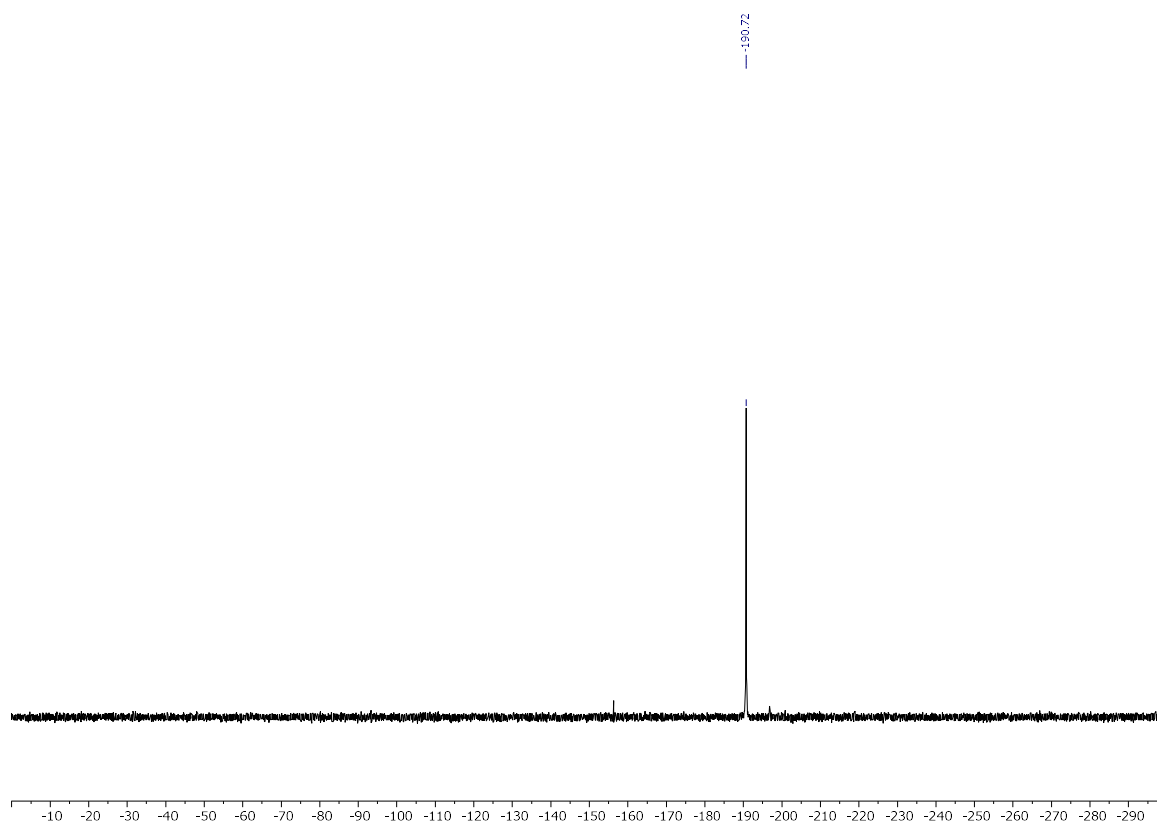
Figure A-III. 12. ^{31}P{^{1}H}-NMR(161.98 MHz, 298 K, toluene-d$_8$) of compound **100**.
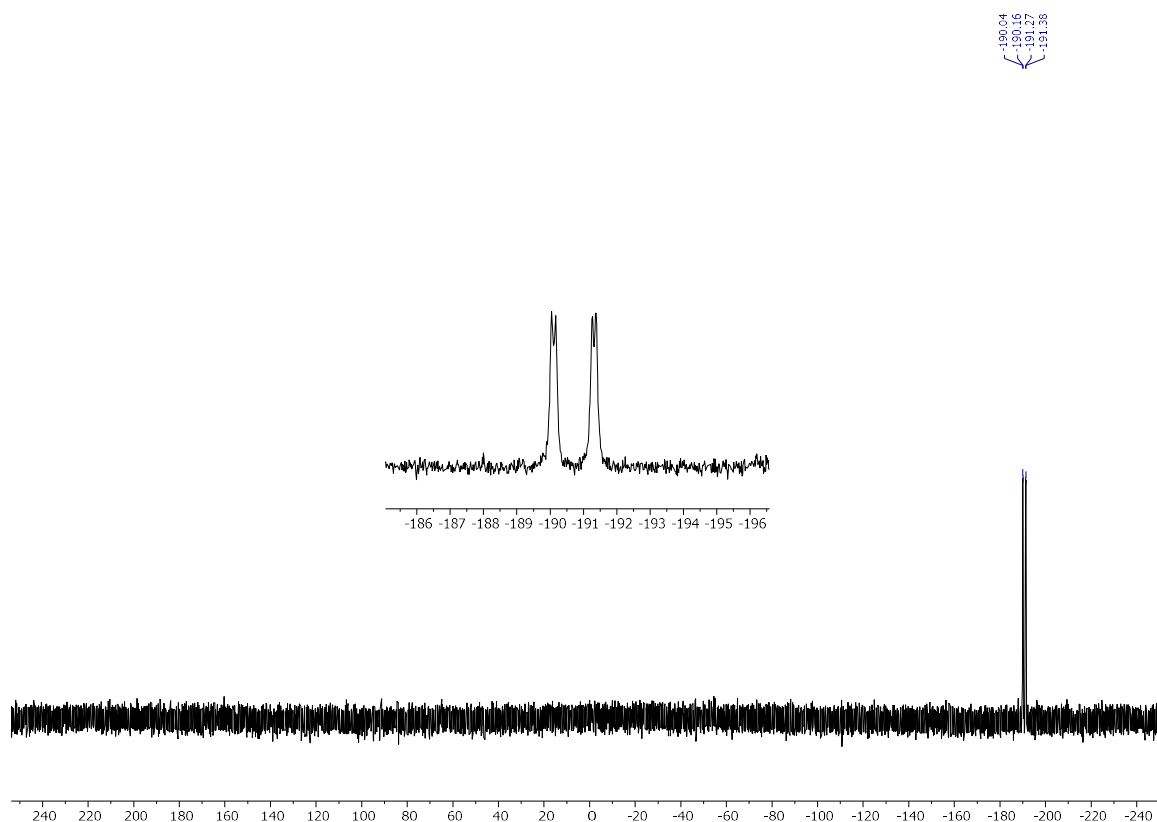
Figure A-III. 13. ^{31}P-NMR (161.98 MHz, 298 K, toluene-d$_8$) of compound **100**.
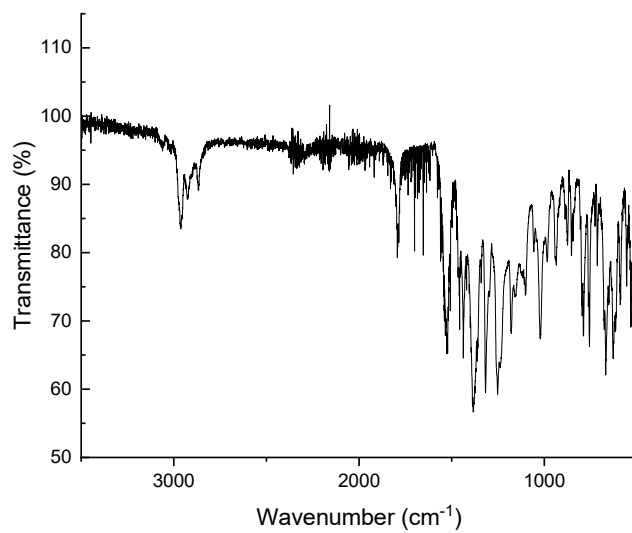
Figure A-III. 14. IR spectrum of compound **100**.

AIII.3 Synthesis of compound 101:
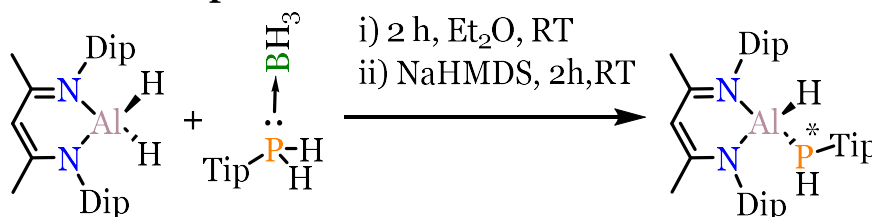
Procedure: In a 100 mL Schlenk flask, 200 mg of *NacNac*AlH$_2$ (1 eq, 0.448 mmol) are dissolved in 10 mL of diethylether. Then, a solution of 123 mg of TipPH$_2$BH$_3$(1.1 eq, 0.493 mmol) in 5 ml of diethylether are added. The reaction mixture is stirred for 2 hours at room temperature. Then, a solution of 90 mg NaHMDS (1.1 eq, 0.493 mmol) in 10 mL is added dropwise to the solution. The solution turns to slurry and yellow and is stirred for 2 hours. The white solid is filtered off and the resulting solution is concentrated until incipient precipitation. Then, it is kept at -30ºC for crystallization to isolate **101**. Upon three crystallizations we isolate 0.235 g of **101**. (77%)

^{1}H-NMR (400.13 MHz, 298 K benzene-d_6):[Mixture of conformers is found, only the major one is informed] δ(ppm)= 1.07 (d, $^2J_{H-H}$= 2.96 Hz, 6H, C$_{iPr}$–<u>Me</u>), 1.09 (d, $^2J_{H-H}$= 7.78 Hz, 12H,C$_{ipr}$-<u>Me</u>), 1.11 (d, $^2J_{H-H}$= 6.58 Hz, 12H, C$_{ipr}$-<u>Me</u>), 1.20 (d, $^2J_{H-H}$= 6.79 Hz, 12H,C$_{ipr}$-<u>Me</u>), 1.51 (s, 6H, C<u>H</u>$_3$-NacNac), 1.61 (d, $^2J_{H-H}$= 6.86 Hz, 12H,C$_{ipr}$-<u>Me</u>), 2.39 (sept,$^2J_{H-H}$= 6.66 Hz, 2H, C$_{ipr}$-<u>H</u>), 2.76 (d, $^1J_{P-H}$= 201.96 Hz, 1H, C$_{ipr}$-<u>Me</u>$_2$), 3.27 (sept,$^2J_{H-H}$= 6.60 Hz, 2H, C$_{ipr}$-<u>H</u>), 2.76 (sept, $^2J_{H-H}$= 6.97 Hz, 1H, C$_{ipr}$-<u>H</u>), 2.77 (d,1H, $^1J_{P-H}$=202.27 Hz, P-<u>H</u>), 3.22 (sept, $^2J_{H-H}$= could not be determined due to overlap with Et$_2$O,2H, C$_{ipr}$-<u>H</u>), 3.37 (sept, $^2J_{H-H}$= 6.75 Hz, 1H, C$_{ipr}$-<u>H</u>), 4.89 (s,1H, <u>C</u>$_\gamma$-*NacNac*), 6.99 (d, $^4J_{H-H}$=2.01Hz ,2H, C-<u>H</u>(Ar)), 7.05 (dd, 2H $^4J_{H-H}$ =6.12; $^4J_{H-H}$=2.97Hz, C-<u>H</u>(Ar)) 7.14 (m, 4H, C-<u>H</u>(Ar)).**^{13}C{^{1}H} (100.61 MHz, 298 K, benzene-d_6)** [Mixture of conformers is found, only the major one is informed] δ(ppm)=23.45 (s, <u>Me</u>(*NacNac*)), 23.67 (s, <u>Me</u>-iPr), 23.85 (d, J_{P-C}=7.21 Hz, <u>Me</u>-iPr), 24.27 (s, <u>Me</u>-iPr), 24.43 (s, <u>Me</u>-iPr), 25.01 (s, <u>Me</u>-iPr), 26.22 (s, <u>C</u>-H(iPr)), 28.20 (s, <u>C</u>-H(iPr)), 29.84 (d, J_{P-C}=5.13 Hz, <u>C</u>-H(iPr)), 33.05 (d, J_{P-C}=10.10Hz, <u>C</u>-H(iPr)), 34.66 (s, <u>C</u>-H(iPr)), 97.60 (s, <u>C</u>$_\gamma$-NacNac), 120.36 (s, <u>C</u>-H(Ar)), 124.48 (s, <u>C</u>-H(Ar)), 125.08 (s, <u>C</u>-H(Ar)), 127.66 (s, <u>C</u>-H(Ar)), 130.04 (d, J_{P-C}=26.21 Hz, <u>C</u>$_{ipso}$-Tip), 140.60 (s, <u>C</u>$_{ipso}$-Dip), 143.68 (s, <u>C</u>$_{meta}$-Dip), 145.10 (s, C$_{meta}$-Dip), 145.43 (d, J_{P-C}=6.68 Hz, C$_{meta}$-Tip), 150.95(d, J_{P-C}=7.97 Hz, C$_{meta}$-Tip), 170.84 (s, <u>C</u>$_\beta$-NacNac). **^{31}P-NMR (161.97 MHz, 298 K, benzene-d_6)**: δ(ppm)= -194.61 (s). **^{31}P{^{1}H}-NMR (161.97 MHz, 298 K, benzene-d_6)**: δ(ppm)= -194.61 (dd, $^1J_{P-H}$= 206.47 Hz; $^3J_{P-H}$=19.98 Hz). **^{27}Al-NMR (104.26 MHz, 298 K, benzene-d_6):** δ(ppm)= silent in the range of 190 to -190 ppm. **Elemental analyisis (%)**: calc. C:77.61%, H: 9.77%, N: 4.11%; found C:76.83%, H: 9.90%, N 4.11%. **Melting point**: 142ºC
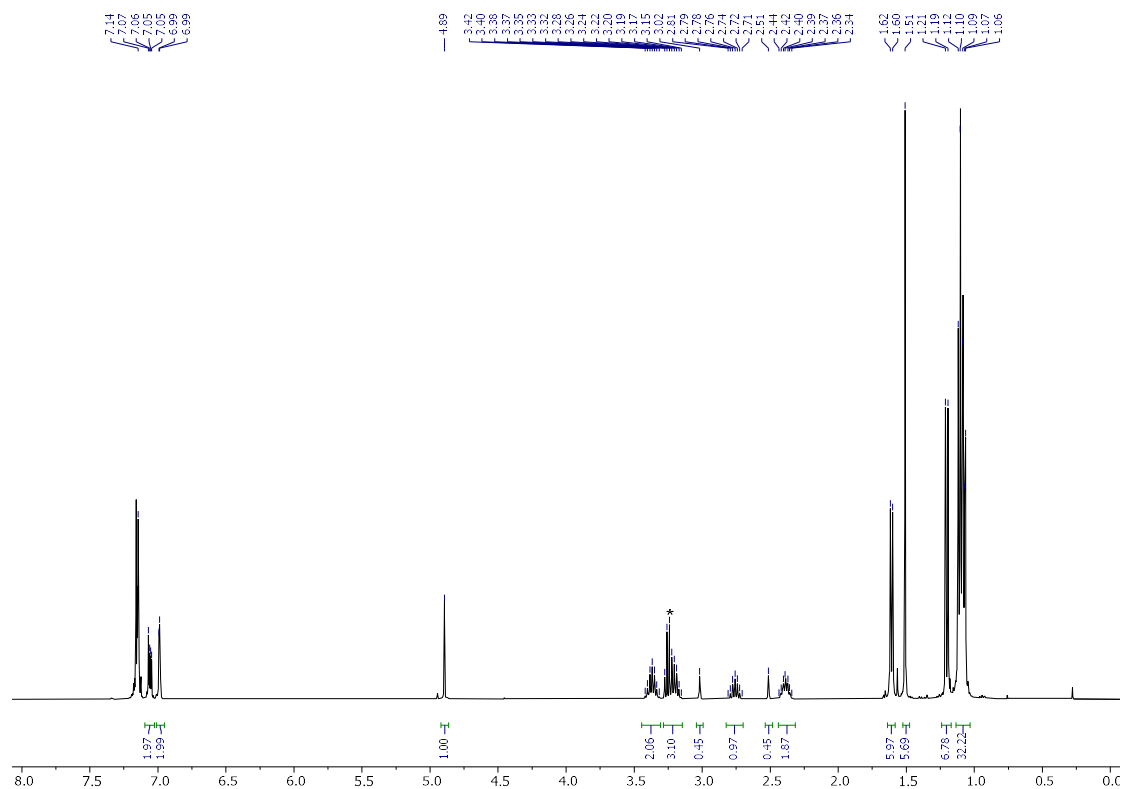
Figure A-III. 15. ¹H-NMR (400 MHz, 298 K, benzene-d₆) of compound **102** in benzene-*d₆*. (*Diethylether)
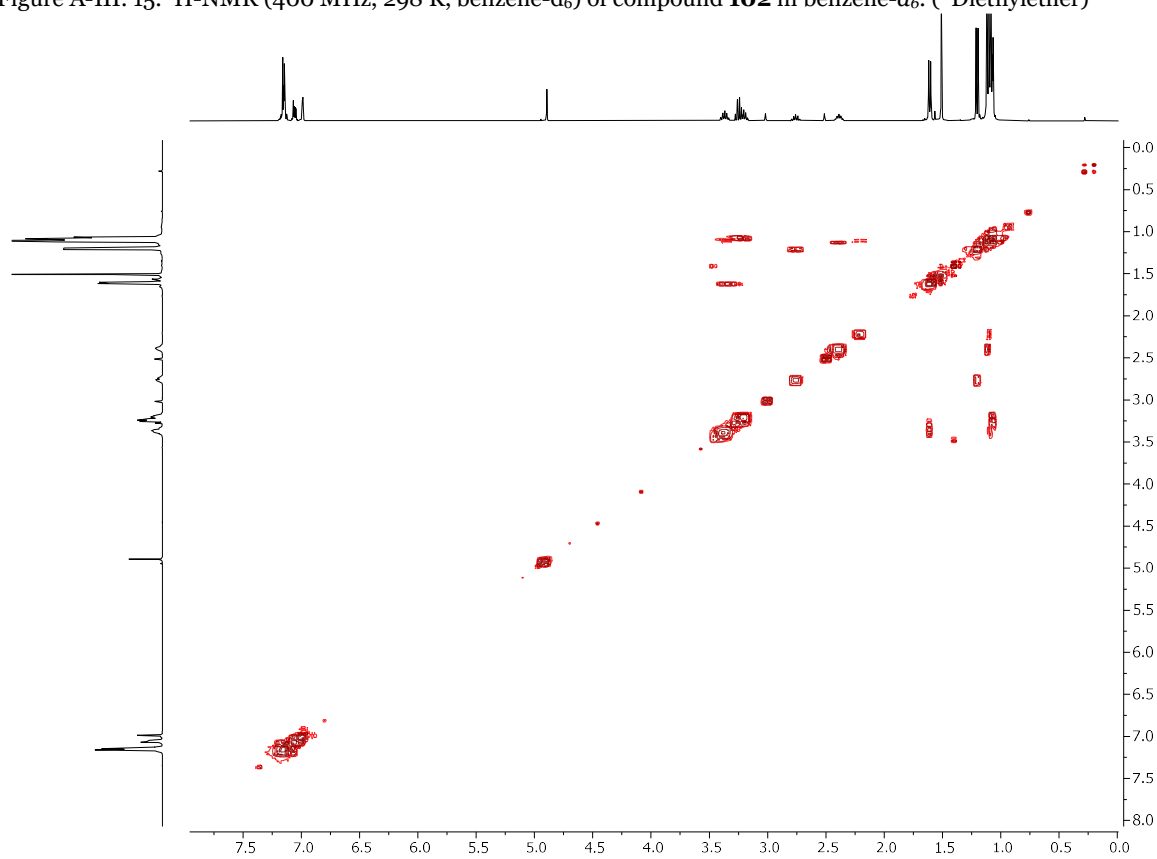
Figure A-III. 16. ¹H-¹H-COSY-NMR(298 K, benzene-d₆) of compound **102** in benzene-*d₆*.
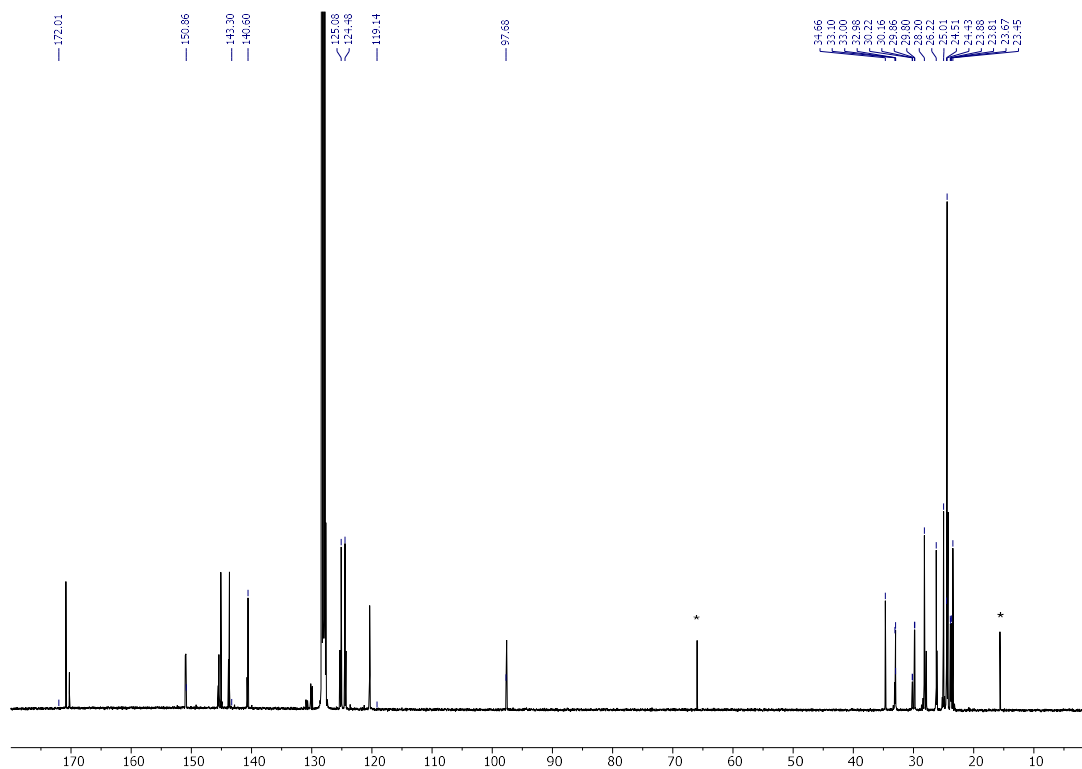
Figure A-III. 17. ^{13}C{^{1}H}-NMR (100.61 MHz, 298 K, benzene-d$_6$) of compound **102**.(*Diethylether)
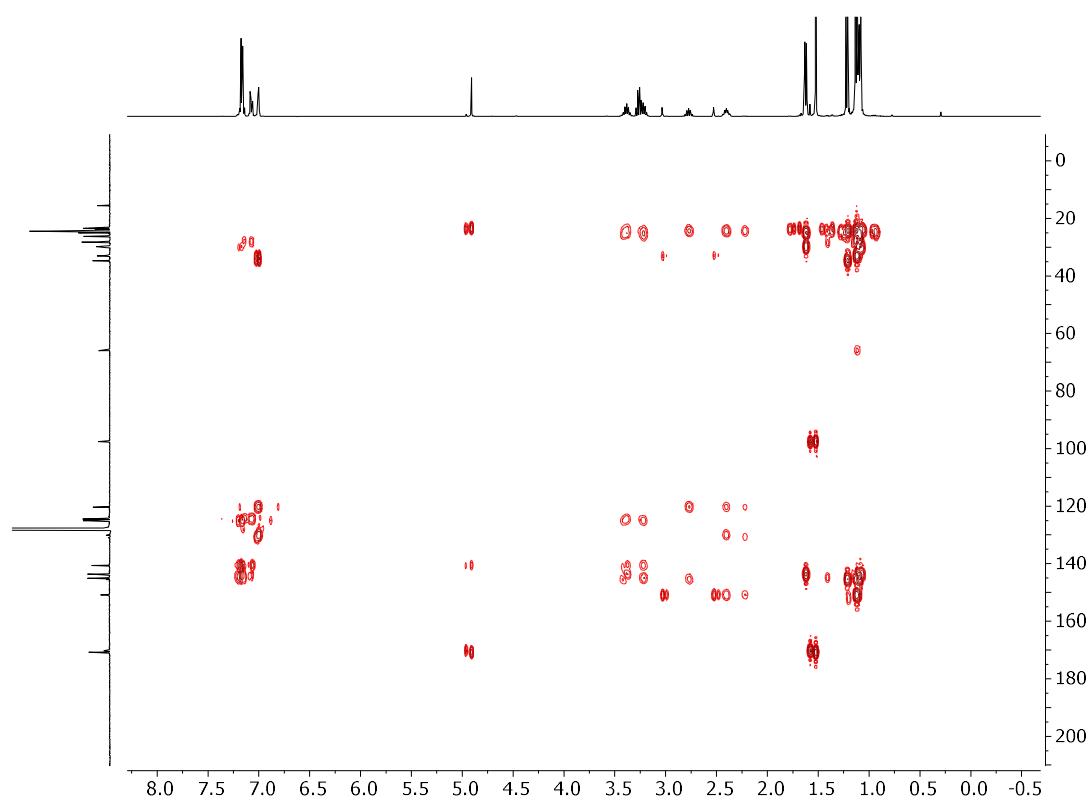
Figure A-III. 18. HMBC (298 K, benzene-d$_6$) of compound **102.**

194.62
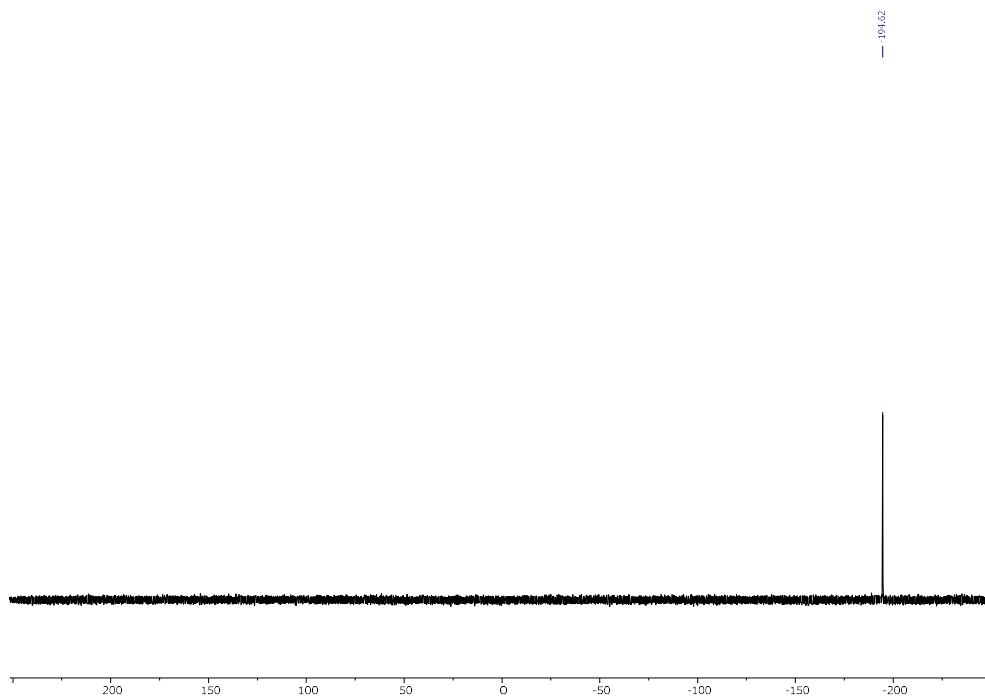
Figure A-III. 19. ^{31}P{^{1}H}-NMR(161.98 MHz, 298 K, benzene-d$_6$) of compound **102**.

-193.92
-195.23
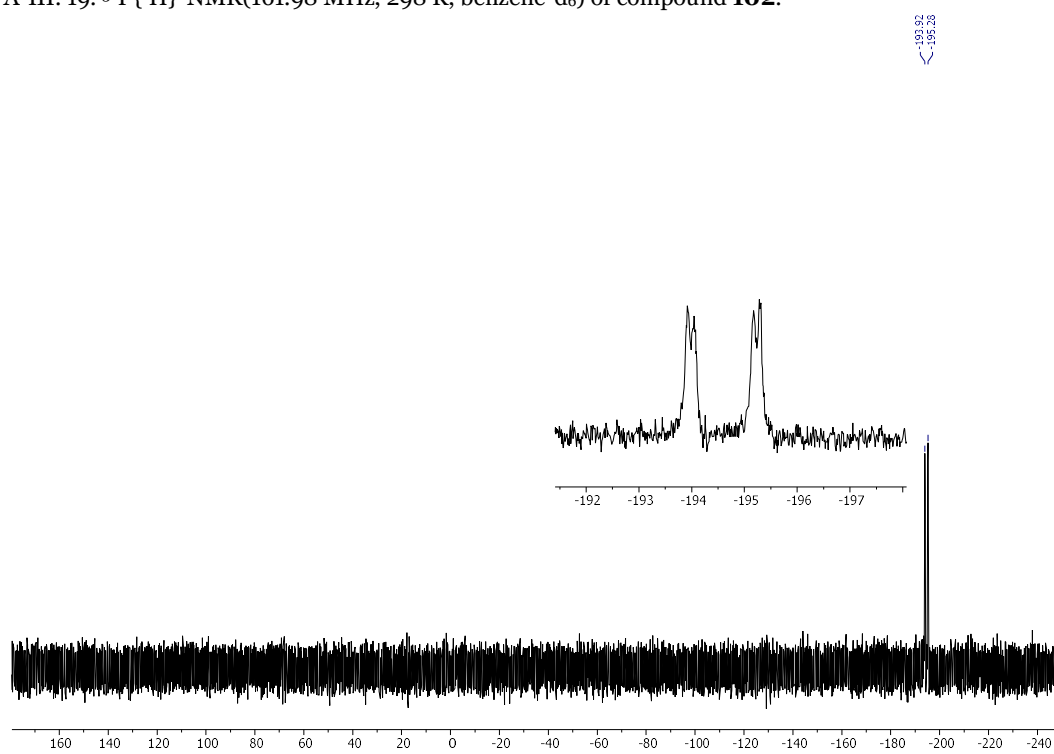
Figure A-III. 20. ^{31}P-NMR (161.98 MHz, 298 K, benzene-d$_6$) of compound **102.**
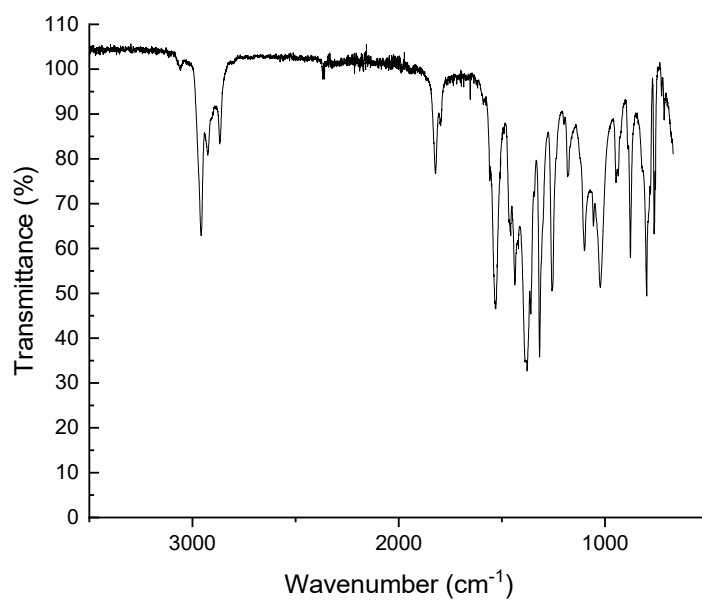
Figure A-III. 21. IR spectrum of compound **101**.

AIII.4 Synthesis of compound 102
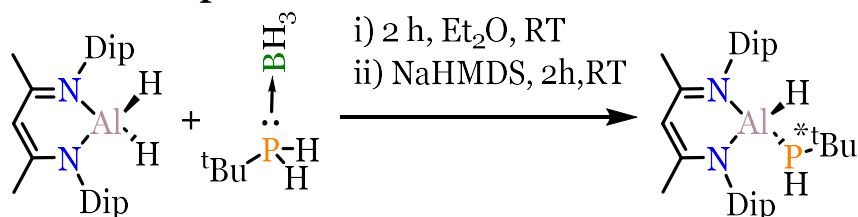
Procedure: In a 100 mL Schlenk flask, 200 mg of *NacNac*AlH$_2$ (1 eq, 0.448 mmol) are dissolved in 10 mL of diethylether. Then, a solution of 52 mg of *t*BuPH$_2$BH$_3$(1.1 eq, 0.493 mmol) in 5 ml of diethylether are added. The reaction mixture is stirred for 2 hours at room temperature. Then, a solution of 90 mg NaHMDS (1.1 eq, 0.493 mmol) in 10 mL is added dropwise to the solution. The solution turns to slurry and yellow and is stirred for 2 hours. The white solid is filtered off and the resulting solution is concentrated until incipient precipitation. Then, it is kept at -30°C for crystallization to isolate **102**. Upon three crystallizations we isolate 95 mg (40%) of **102**.

¹H-NMR (400.13 MHz, 298 K, benzene-*d₆*): [Two conformers are found in a ratio of 1:1] δ(ppm)= 1.03 (s, 6H, <u>Me</u>-*t*Bu), 1.06 (s, 6H, <u>Me</u>-*t*Bu), 1.11 (d,6H,$^3J_{H-H}$=6.76 Hz, C-<u>H</u>(iPr)), 1.14 (d, 12H, $^3J_{H-H}$=7.03 Hz, C-<u>H</u>(iPr)), 1.16 (d, 6H, $^3J_{H-H}$=7.30 Hz, C-<u>H</u>(iPr)), 1.40 (d, 6H, $^3J_{H-H}$=7.03 Hz, C-<u>H</u>(iPr)), 1.47 (d, 6H, $^3J_{H-H}$=7.03 Hz, C-<u>H</u>(iPr)), 1.55 (s, 6H, <u>Me</u>-*NacNac*), 1.58 (s, 6H, <u>Me</u>-*NacNac*), 3.43 (sept,8H, the coupling constants could not be determined due to signal overlap), 4.86 (s, 1H, C$_\gamma$-<u>H</u>), 4.81 (s, 1H, C$_\gamma$-<u>H</u>), 7.11(m,Ar-<u>H</u>, the coupling constants could not be determined due to signal overlap).**¹³C{¹H} (100.61 MHz, 298 K, benzene-*d₆*):** [Mixture of conformers is found] δ(ppm)=22.57(s, <u>Me</u>₃(*NacNac*)), 22.90 (s, <u>Me</u>₃(*NacNac*)), 24.24, 24.61, 25.16, 25.95, 27.95, 28.17, 34.87, 34.90, 95.90 (s, <u>C</u>$_\gamma$-*NacNac*), 96.86 (s, <u>C</u>$_\gamma$-*NacNac*), 124.23, 124.45, 124.52, 138.99, 140.10, 143.43, 144.25, 144.76, 169.89(s, <u>C</u>$_\beta$-*NacNac*), 170.21(s, <u>C</u>$_\beta$-*NacNac*). **³¹P-NMR (161.98 MHz, 298 K, benzene-*d₆*):** δ(ppm)= -116.58 (d, $^1J_{P-H}$=182.65 Hz).**³¹P{¹H}-NMR (161.98 MHz, 298 K, benzene-*d₆*)**: δ(ppm)= -116.48 (s).**²⁷Al-NMR (104.26 MHz, 272 K, benzene-*d₆*):** δ(ppm)= silent in the range of 190 to -190 ppm. **Elemental analysis (%):** calc for **102**: C:74.12, H:9.80, N:5.24; found: C: 75.46, H: 9.66, N: 5.68. Melting point: 146°C
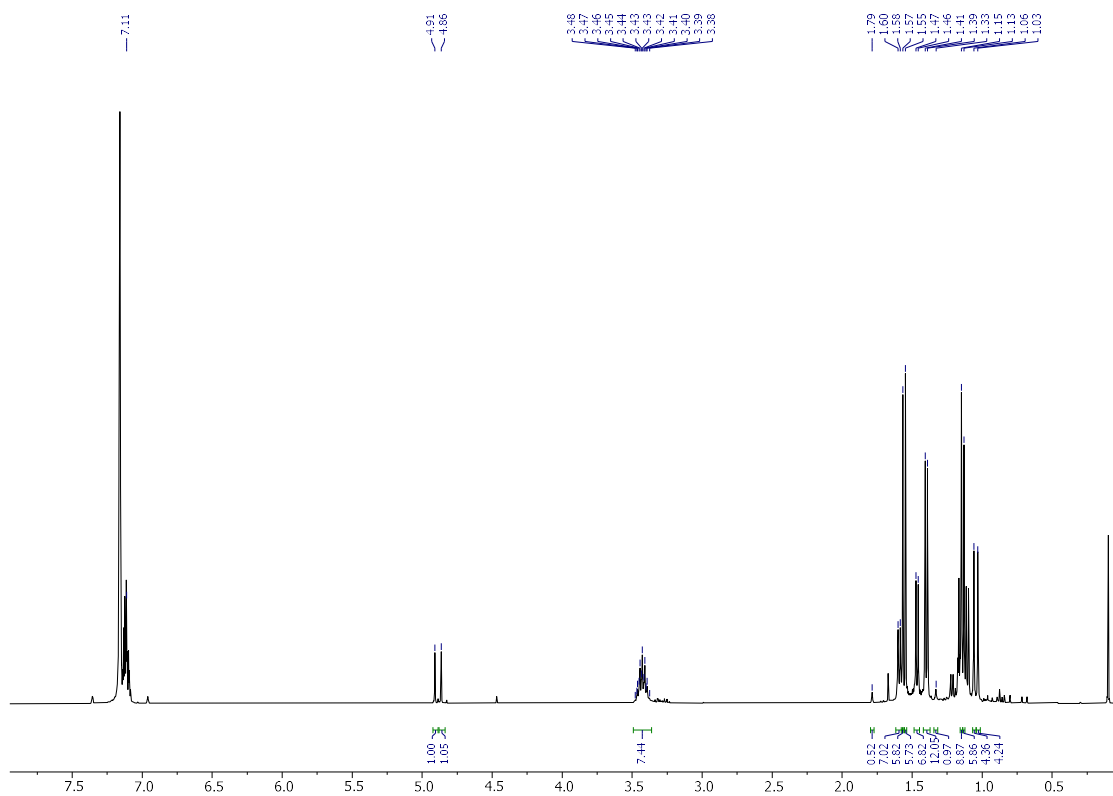
Figure A-III. 22. ¹H-NMR (400.1 MHz, 298K, benzene-d₆) of compound **102**.
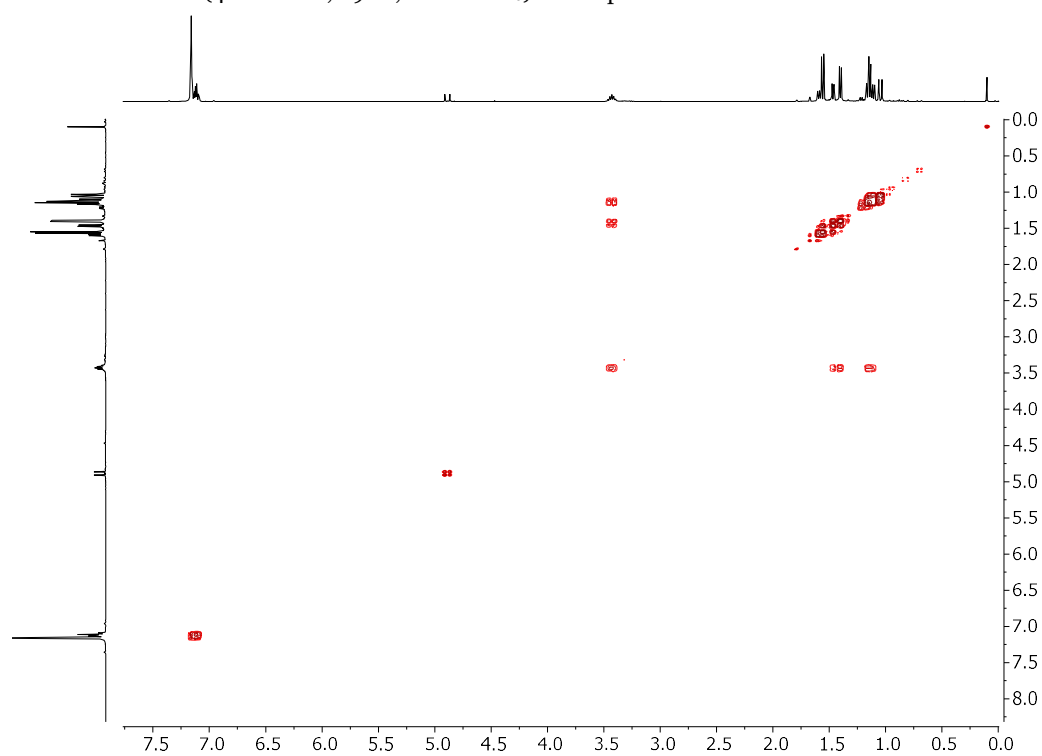
Figure A-III. 23. ¹H-¹H-COSY-NMR(298K, benzene-d₆) of compound **102**.
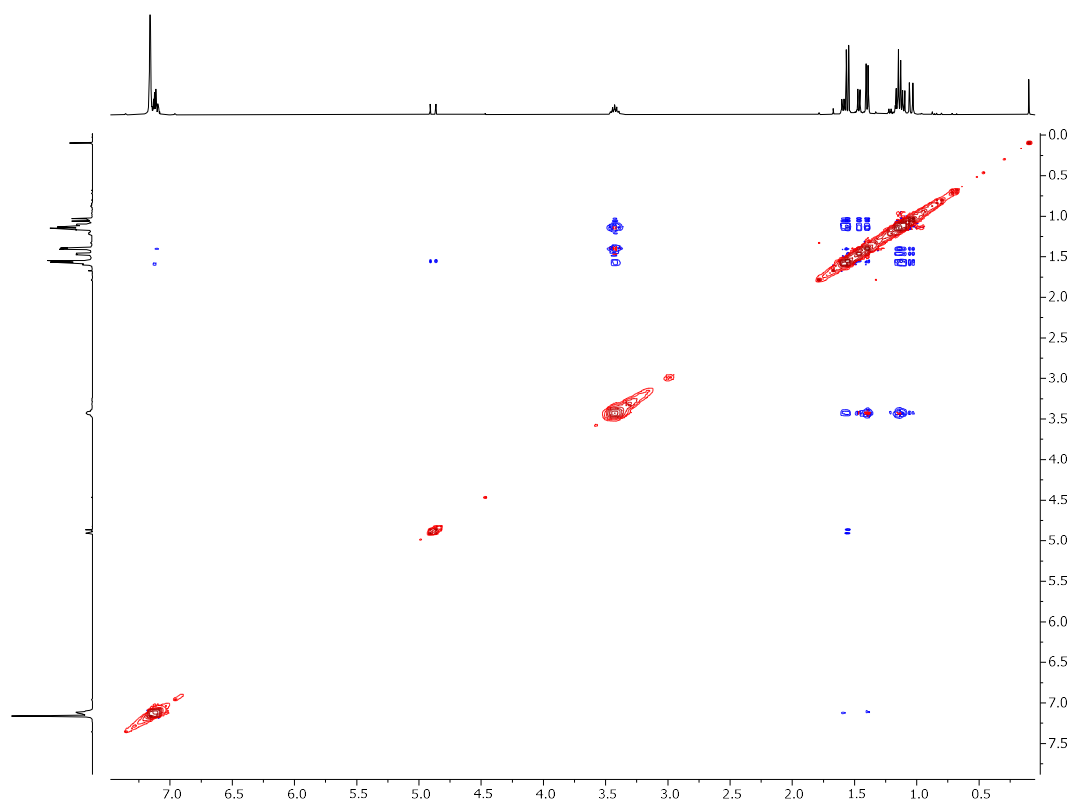
Figure A-III. 24. NOESY (298K, benzene-d₆) of compound **102**.
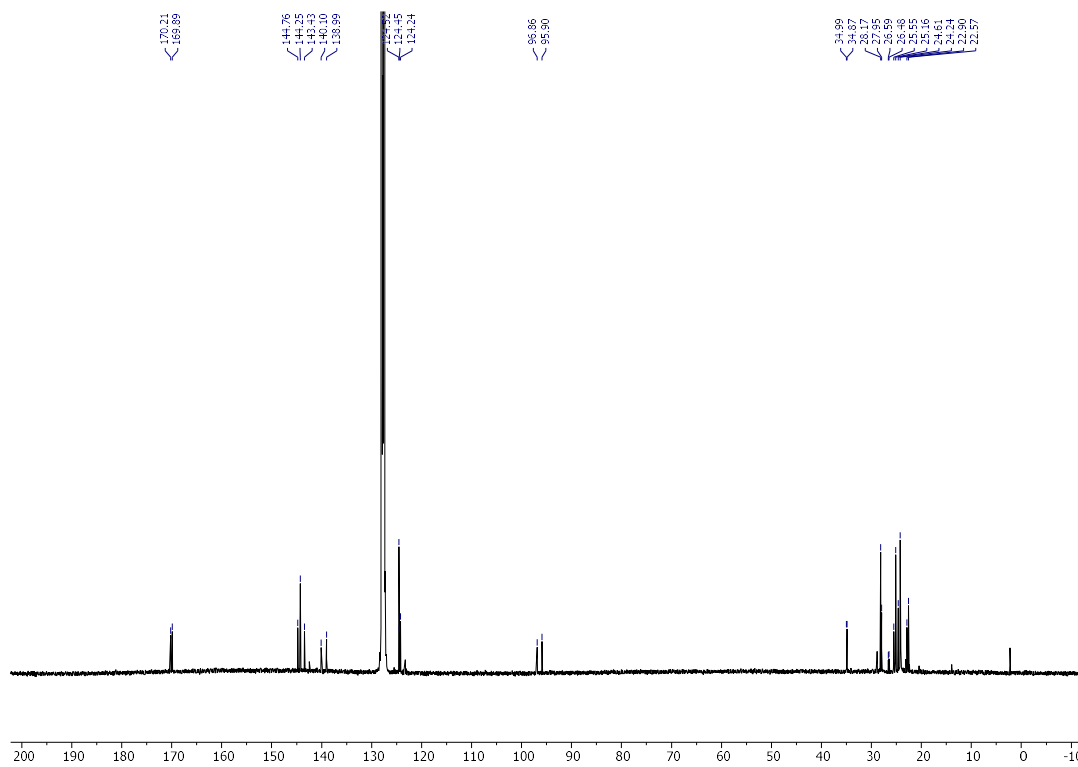
Figure A-III. 25. ¹³C{¹H}-NMR (100.61 MHz, 298K, benzene-d₆) of compound **102**.
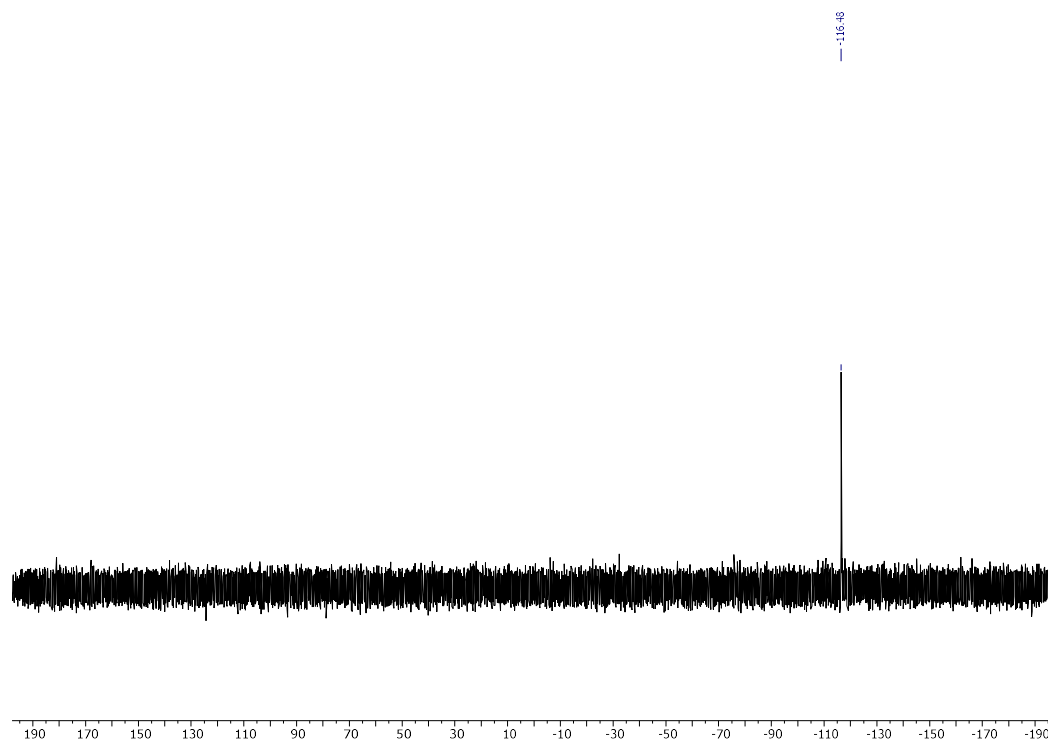
Figure A-III. 26. ^{31}P{^{1}H}-NMR (161.98 MHz, 298K, benzene-d$_6$) of compound **102** in benzene-*d$_6$*.
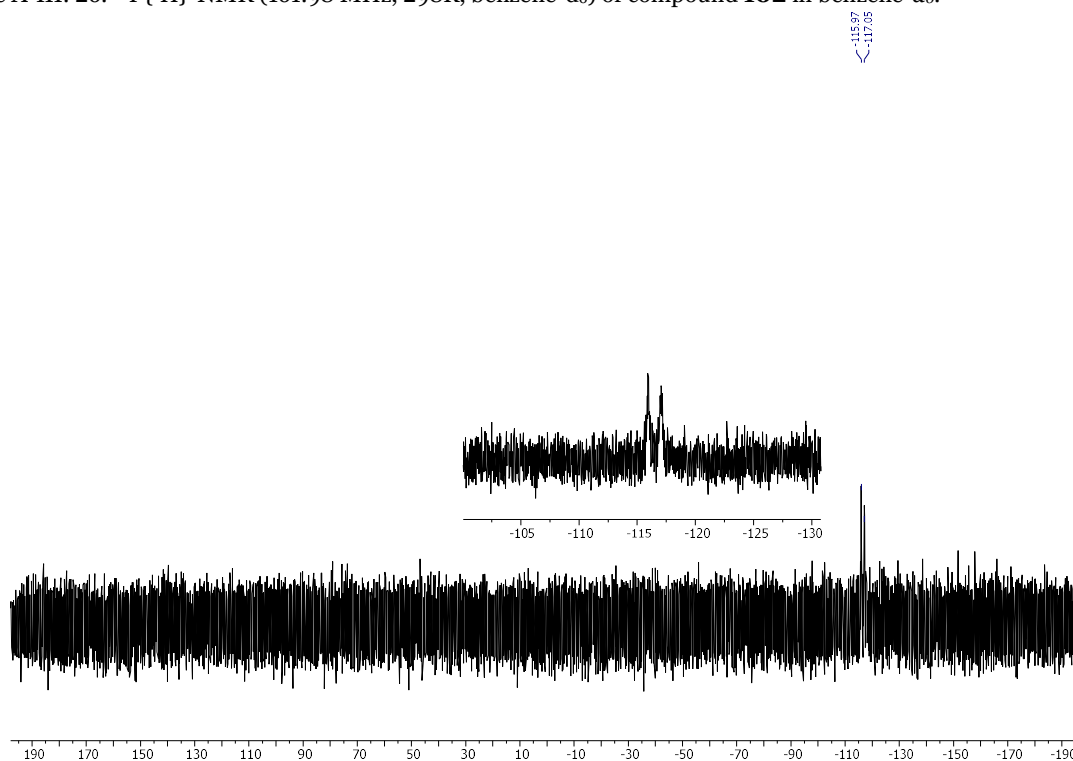
Figure A-III. 27. ^{31}P-NMR (161.98 MHz, 298K, benzene-d$_6$) of compound **102** in benzene-*d$_6$*.
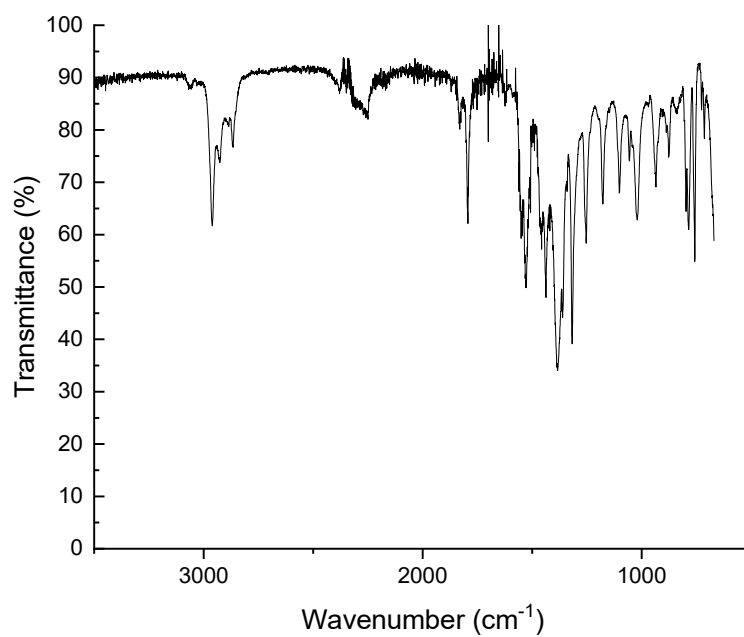
Figure A-III. 28. IR spectra of compound **102** .

AIII.6 Synthesis of 107
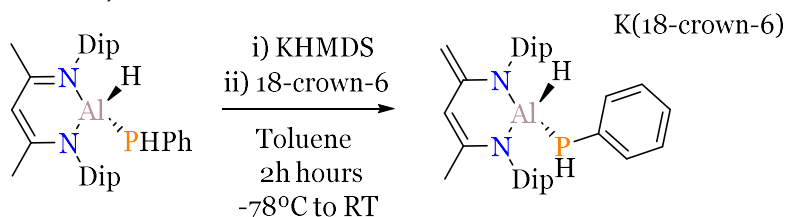
Procedure: A Schlenk tube was charged with 52 mg (1eq, 0.094 mmol) of NacNacAlHPHPh and dissolved in 2 mL of toluene and cold down to -78°C. A solution of KHMDS (19 mg, 1eq, 0.094 mmol) in 2 mL of toluene is added dropwise and stirred for 2 hours reaching room temperature. The reaction crude turns to a slurry orange solution. Then, a solution of 18-crown-6 (25 mg, 1eq, 0.094 mmol) in 2 mL of toluene is added dropwise at room temperature. During the addition, the solution turns to dark green and slowly becomes to yellow and slurry. The reaction crude is dried under vacuum and the obtained oil is washed several times with hexane and Et_2O to obtain a pale yellow solid (32 mg, 39%).

^{1}H-NMR (400.13 MHz, 298 K, benzene-d_6): δ(ppm)= 0.86(d, $^2J_{H-H}$= 6.83 Hz, 3H, C_{iPr}-Me), 0.95 (d, $^2J_{H-H}$= 6.83 Hz, 3H, C_{iPr}-Me), 1.13, 1.15, 1.17, 1.18, 1.19, 1.20, 1.21, 1.22, 1.25, 1.26, 1.33, 1.35, 1.37, 1.46 (s, 3H,CH_3-NacNac), 1.89 (d, $^1J_{P-H}$= 184.89Hz, 1H,P-H), 2.30 (d, $^1J_{H-H}$= 2.36 Hz, 1H, $CH(CH_2)$), 2.97 (d, $^1J_{H-H}$= 2.20 Hz, 1H, $CH(CH_2)$), 3.15 (sept, $^2J_{H-H}$= 6.83 Hz, 1H, C_{ipr}-H), 3.84 15 (sept, $^2J_{H-H}$= 6.83 Hz, 1H, C_{ipr}-H), 3.95 (two overlapped sept, the coupling constant could not be determined, 2H, C_{ipr}-H), 4.69 (s, 1H, C_γ-H), 6.27 (m, 2H, Ar-H), 6.50(m, 3H, Ar-H), 6.95. **^{13}C{^{1}H} (100.61 MHz, 272 K, benzene-d_6)** δ(ppm)=21.10, 23.66, 24.15, 16.44, 27.12, 28.03, 28.79, 29.23, 71.29, 75.23, 199.55, 122.11, 123.17, 133,62, 143,26, 144,88, 145.13, 155.53, 146.88, 148.34, 148.73, 149.19, 157.78. **^{31}P-NMR (161.96 MHz, 298 K, benzene-d_6)**: δ(ppm)= -139.18 ppm ($^1J_{P-H}$=180.18 Hz)**^{31}P{^{1}H}-NMR (161.96 MHz, 298 K, benzene-d_6):** δ(ppm)= -139.18 ppm**^{27}Al-NMR (104.26 MHz, 298 K, benzene-d_6):** δ(ppm)= silent in the range of 190 to -190 ppm. **Elemental analysis (%):** Did not match after several attempts. **Melting point:** 202°C
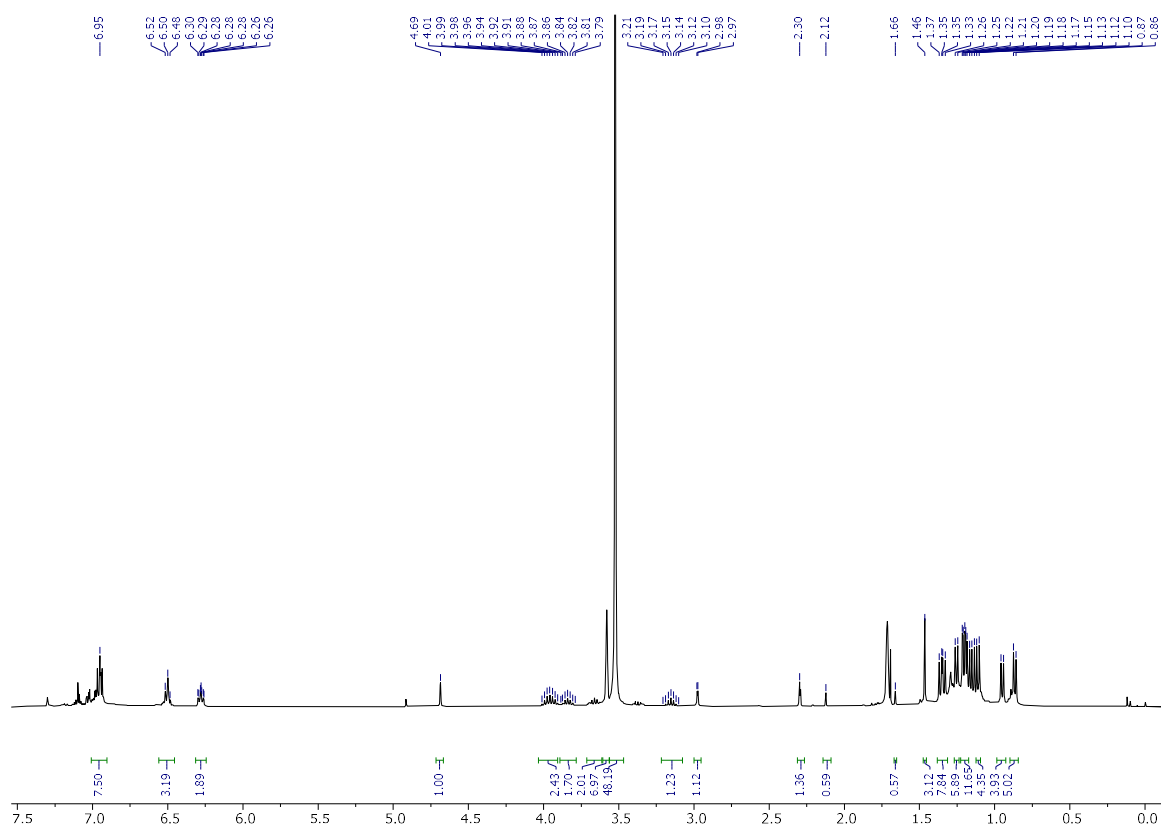
Figure A-III. 29 ¹H-NMR (400.13, 298K, THF-d₈) of compound **107**.
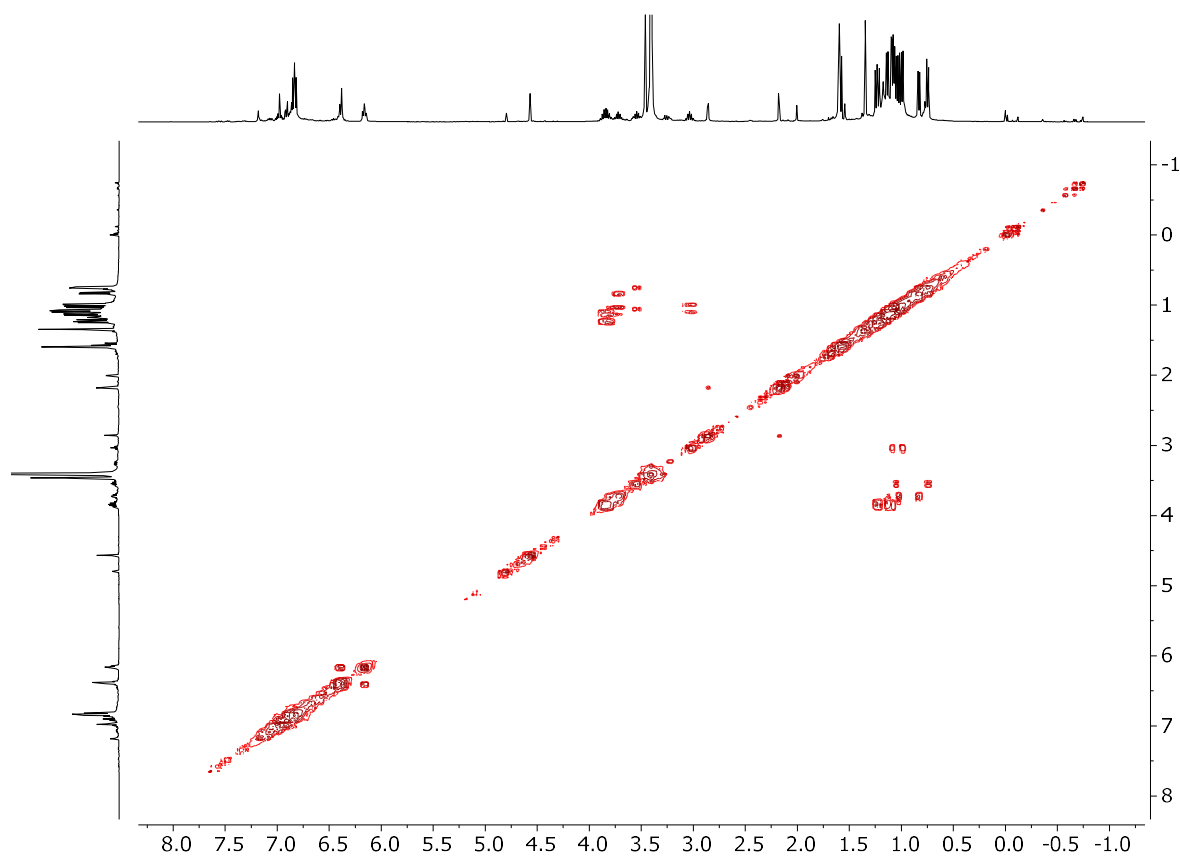
Figure A-III. 30 ¹H-¹H-COSY-NMR(298K, THF-d₈) of compound **107** in THF-*d₆*.
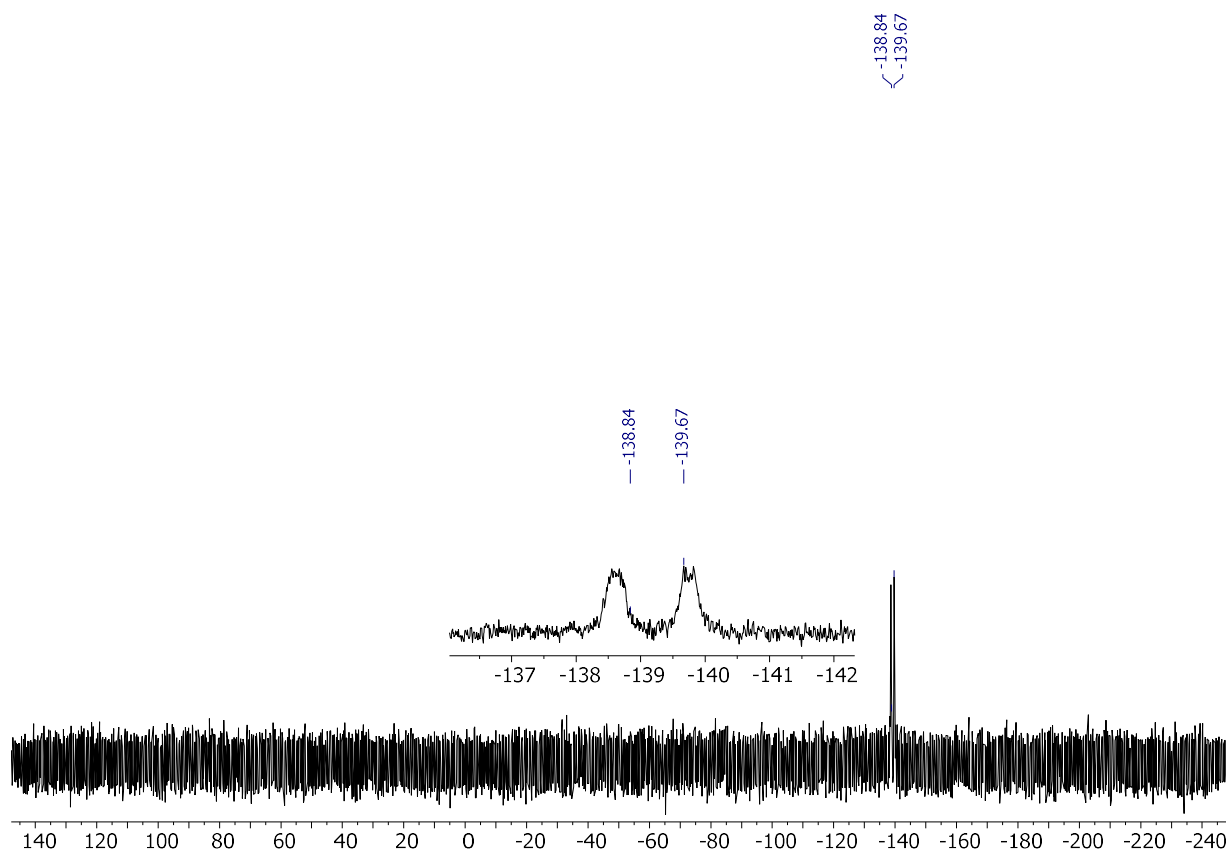
−139.18

140 120 100 80 60 40 20 0 -20 -40 -60 -80 -100 -120 -140 -160 -180 -200 -220 -240

Figure A-III. 31 ^{31}P{^{1}H}-NMR (161.98 MHz, 298 K, thf-d8) of compound **107.**

Figure A-III. 32 ^{31}P-NMR (161.98 MHz, 298 K, thf-d8) of compound **107.**
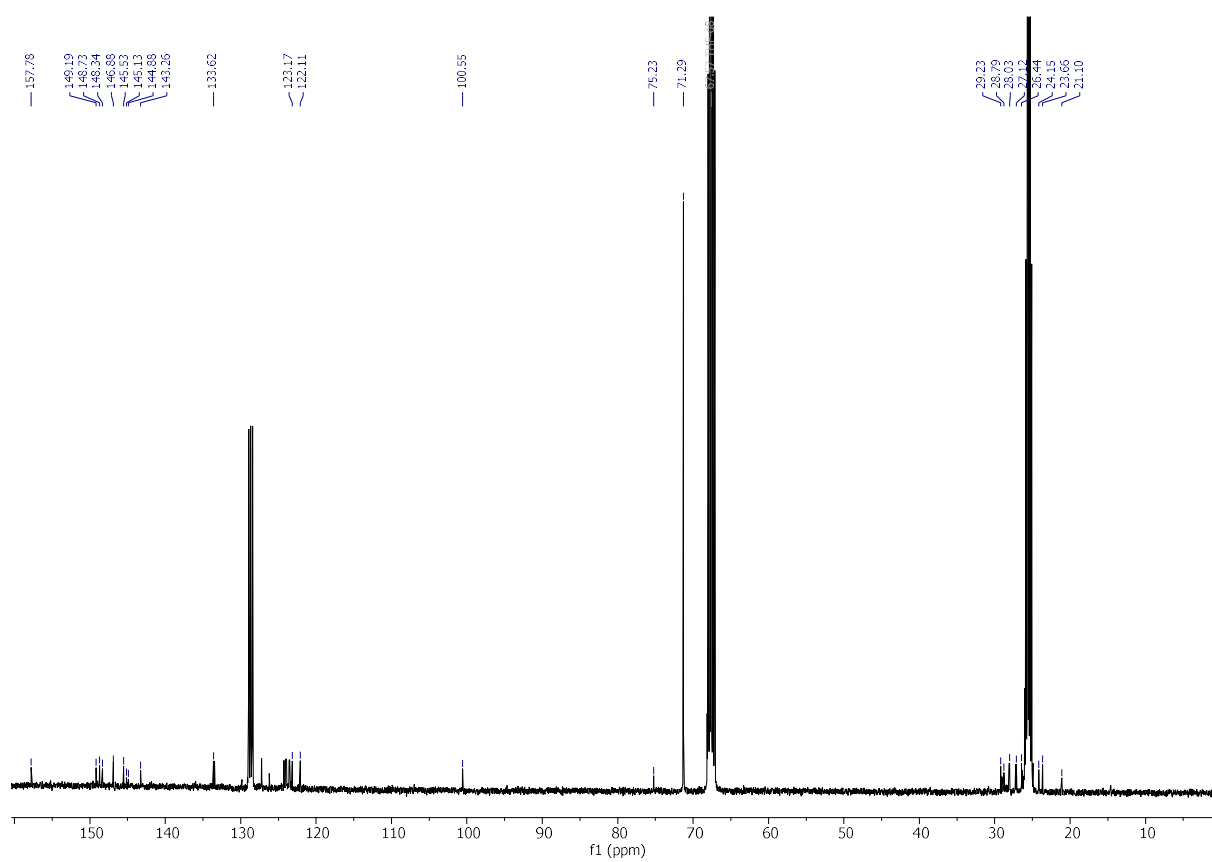
Figure A-III. 33 ^{13}C{^{1}H}-NMR (100.61 MHz, 298K, thf-d$_8$) of compound **107**.
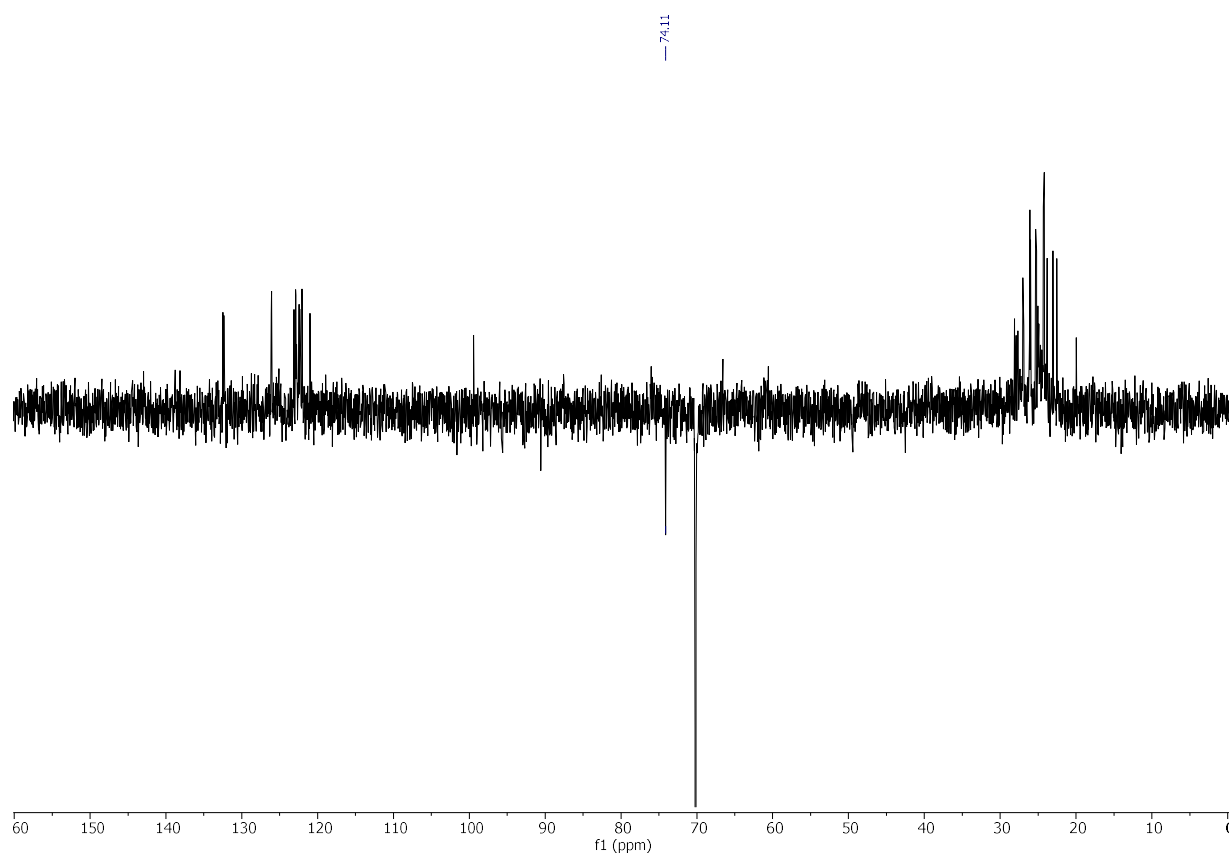
Figure A-III. 34. ^{13}C-DEPT135 (100.61 MHz, 298K, thf-d$_8$) of compound **107**.

AIII.7 Synthesis of compound 108:
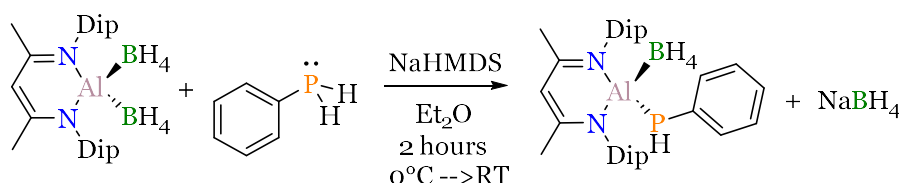
Procedure: In a 100 mL Schlenk flask, 1g of *NacNac*Al(BH$_4$)$_2$ (2.108 mmol,1eq) are dissolved in 40 mL of Et$_2$O. Then, 2.43 mL of a 10 % solution of PH$_2$Ph (2.108 mmol,1eq) in hexane is added. The solution is cooled down to 0°C. Then, a solution of NaHMDS (0.405 g in 20 mL, 2.213mmol, 1.05eq) are added dropwise. During the addition, the solution becomes orange and slurry due to the precipitation of NaBH$_4$. Then, the solution is filtered off and washed with 10 mL of Et$_2$O. The obtained orange solution is concentrated under vacuum until incipient precipitation is observed. Then, the solution is genteelly heated and it is kept at -20°C. After 2 hours, pale-yellow crystals are formed. The solution is decanted and the mother liquid is concentrated and kept in the -20°C freezer overnight for crystallization. This procedure is repeated 3 times (1st crop=0.256g; 2nd crop=0.216g; 3rd crop= 0.027g). Total weight 0.499 g (41.6%).

^{1}H-NMR (400.13 MHz, 298 K, benzene-d_6): δ(ppm)= 1.03 (d, 6H, ^{2}J$_{H-H}$= 6.87 Hz, C$_{ipr}$-<u>Me$_2$</u>), 1.09 (d, 6H, ^{2}J$_{H-H}$= 6.65 Hz, C$_{ipr}$-<u>Me$_2$</u>), 1.23 (d, 6H, ^{2}J$_{H-H}$= 6.26 Hz, C$_{ipr}$-<u>Me$_2$</u>), 1.56 (s, 6H, <u>Me$_3$</u>(NacNac)), 1.58 (d, 6H, ^{2}J$_{H-H}$= 6.90 Hz, C$_{ipr}$-<u>Me$_2$</u>), 2.63 (d,1H, ^{1}J$_{P-H}$= 194.04H, P-<u>H</u>), 3.21(sept, 2H, C$_{ipr}$-<u>H</u>), 3.42 (sept, 2H, ^{2}J$_{H-H}$= 5.70 Hz, C$_{ipr}$-<u>H</u>), 4.94 (s, 1H C$_γ$-<u>H</u>), 6.56 (m, 2H, Ar-<u>H</u>), 6.82 (m,3H, Ar-<u>H</u>), 7.14 (m, Ar-<u>H</u>).**^{13}C{^{1}H} (100.61 MHz, 298 K, benzene-d_6)**: δ(ppm)= 23.70(<u>Me</u>-(*NacNac*)), 24.03(<u>Me</u>-Dip), 24.10 (<u>Me</u>-Dip), 24.36 (<u>Me</u>-Dip), 25.08 (<u>Me</u>-Dip),25.17 (<u>Me</u>-Dip), 26.49 (<u>C</u>$_{iPr}$-Dip), 28.29(<u>C</u>$_{iPr}$-Dip), 29.87, 29.93, 98.29(<u>C</u>$_γ$-*NacNac*), 124.52 (<u>C</u>$_{Ar}$-Dip), 124.87(<u>C</u>-HPh), 125.76 (C$_{Ar}$-Dip), 133.62 (<u>C</u>-Ph,^{1}J$_{P-C}$=14.33 Hz), 136.36 (<u>C</u>-Ph, ^{1}J$_{P-C}$=18.64 Hz, 139.57(<u>C</u>-Dip), 144.01(<u>C</u>$_{Ar}$-Dip), 145.99 (<u>C</u>$_{Ar}$-Dip), 170.73 (<u>C</u>$_β$-*NacNac*).**^{31}P{^{1}H}-NMR (161.97 MHz, 298 K, benzene-d_6):** δ(ppm)= -149.29 (s). **^{31}P-NMR (161.97 MHz, 298 K, benzene-d_6):** δ(ppm)= -149.29 (d, ^{1}J$_{P-H}$ =197.14 Hz). **^{11}B-NMR (128.38 MHz, 298 K, benzene-d_6):** δ(ppm)= -35.97 (quint, ^{1}J$_{B-H}$ =85.13 Hz). **^{27}Al-NMR (104.26 MHz, 298 K, benzene-d_6):** δ(ppm)= silent in the range of 190 to -190 ppm. **APPI-MS (toluene):** calc. [M]$^+$=568.369 ; found. [M]$^+$=568.370. **Melting point:**130°C
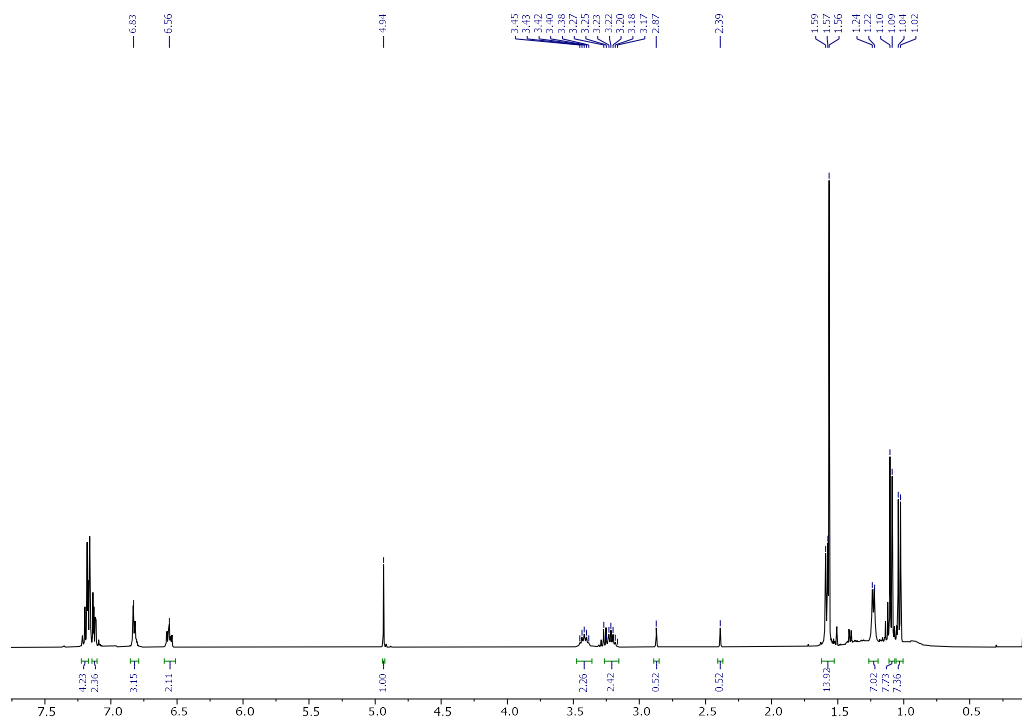
Figure A-III. 35 ¹H-NMR (400.13 MHz, 298 K, benzene-d_6) of compound **108**.
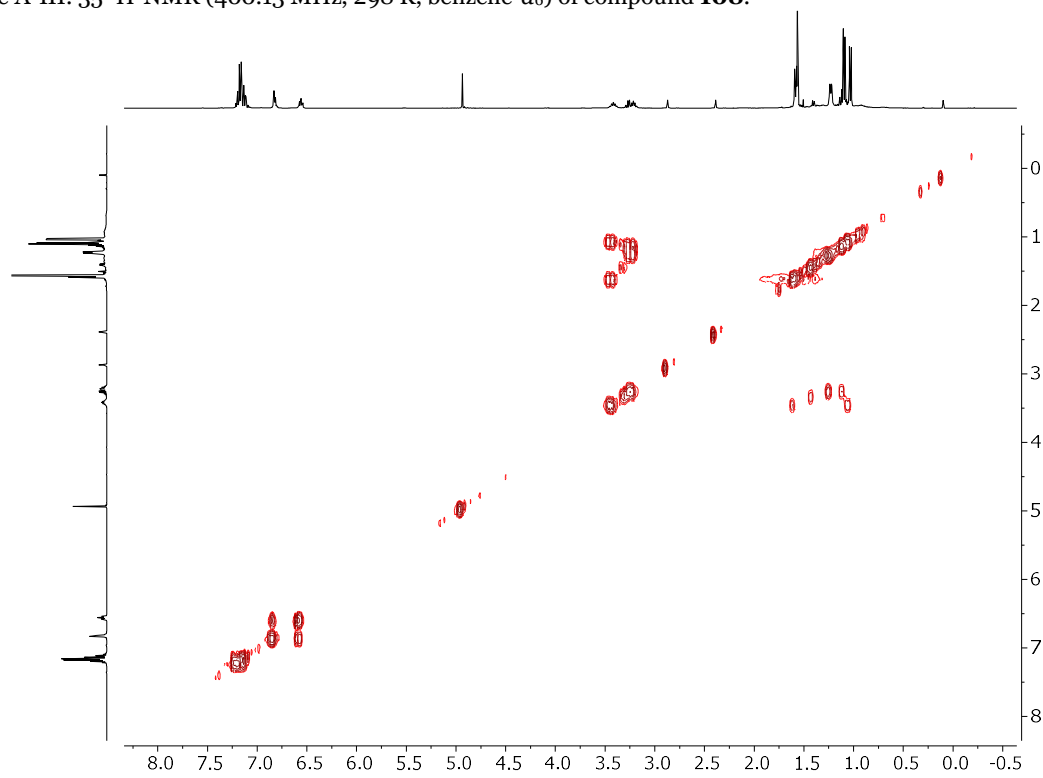
Figure A-III. 36. ¹H-¹H-COSY-NMR (298 K, benzene-d_6) of compound **108.**

-149.24

Figure A-III. 37. ^{31}P{^{1}H}-NMR (161.98 MHz, 298 K, benzene-d_6) of compound **108**.

-34.89
-35.31
-35.98
-36.63
-37.03

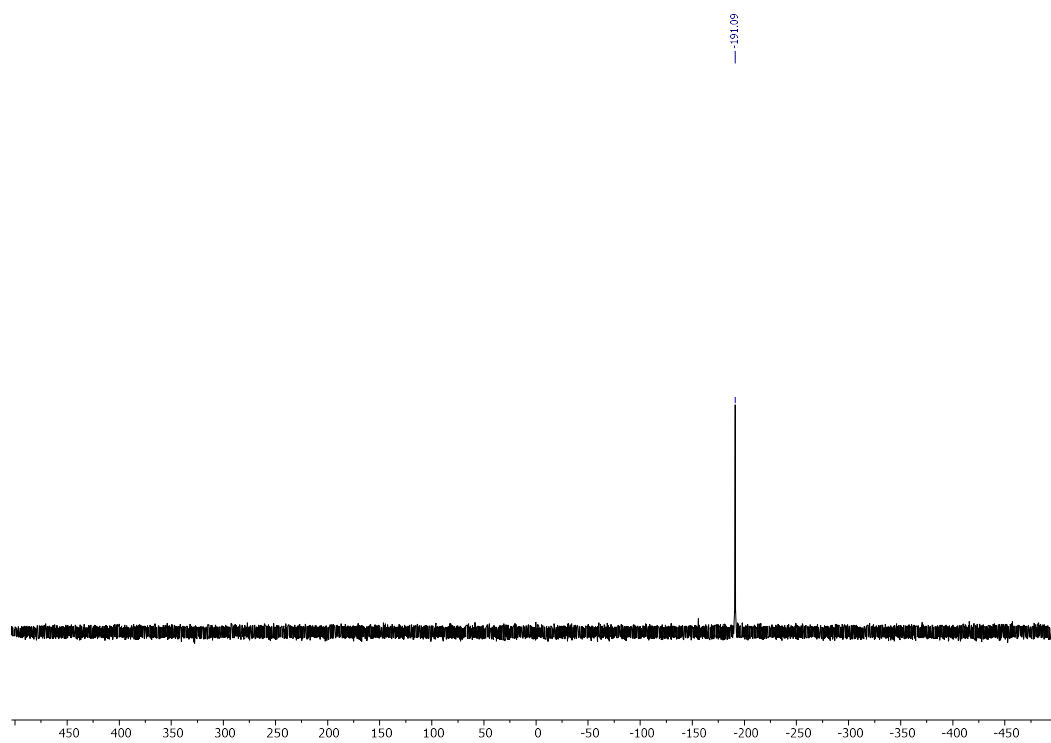Figure A-III. 38 ^{11}B-NMR (128.4 MHz, 272 K, benzene-d$_6$) of compound **108**.
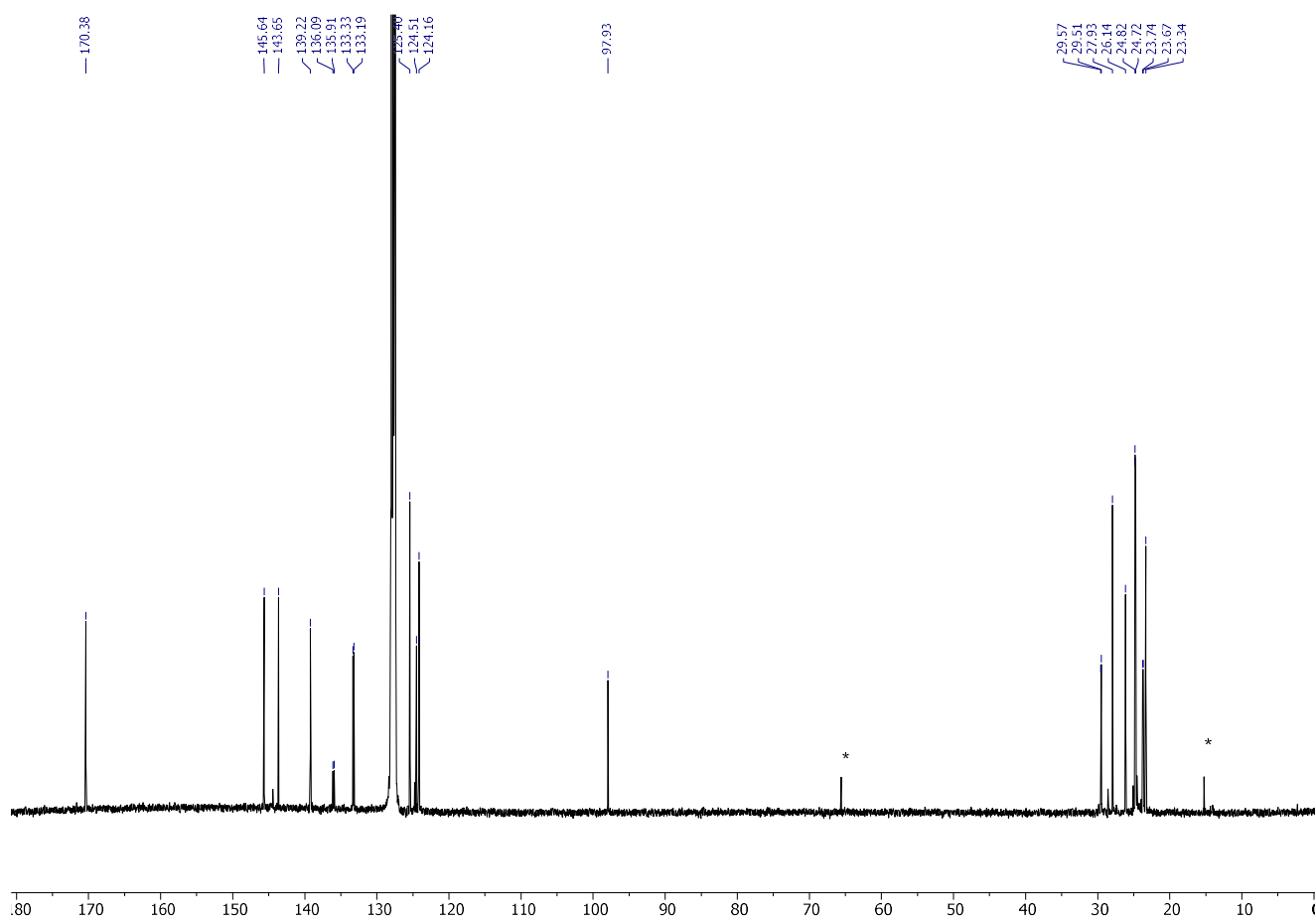
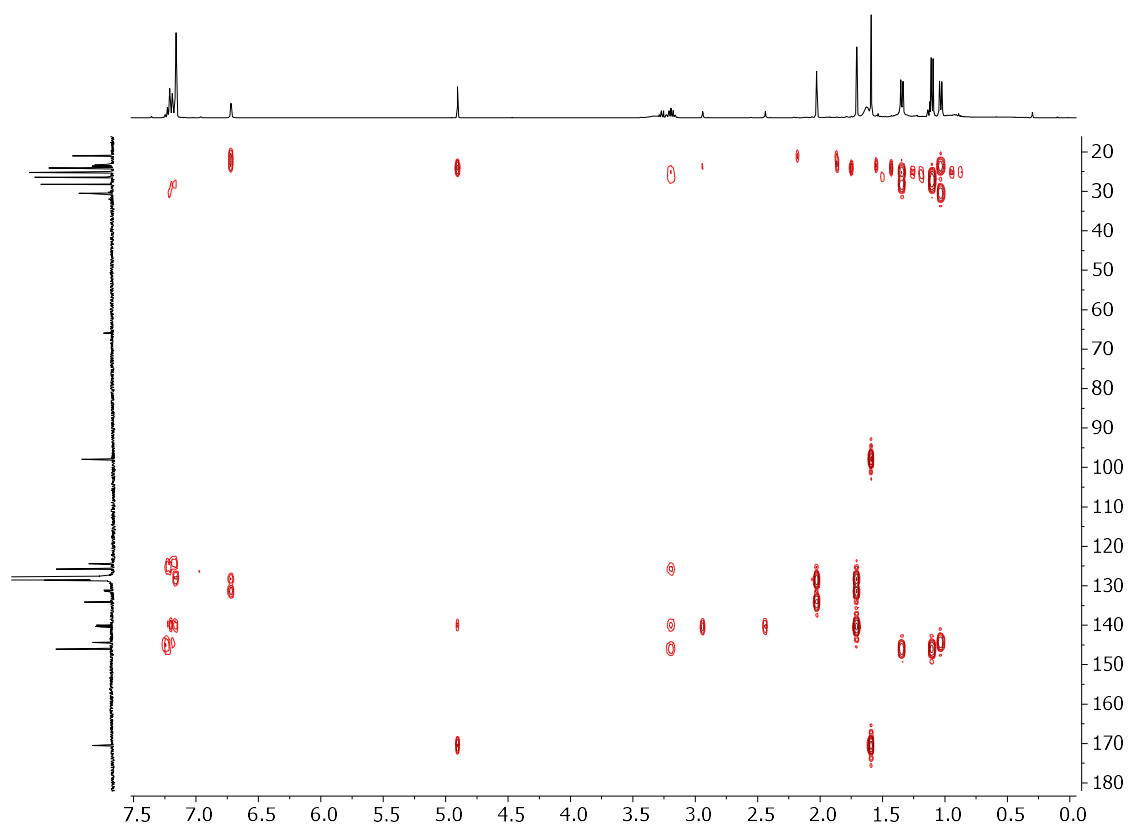Figure A-III. 39. $^{13}C\{^1H\}$-NMR (100.61 MHz, 298 K, benzene-d_6) of compound **108**. *diethylether
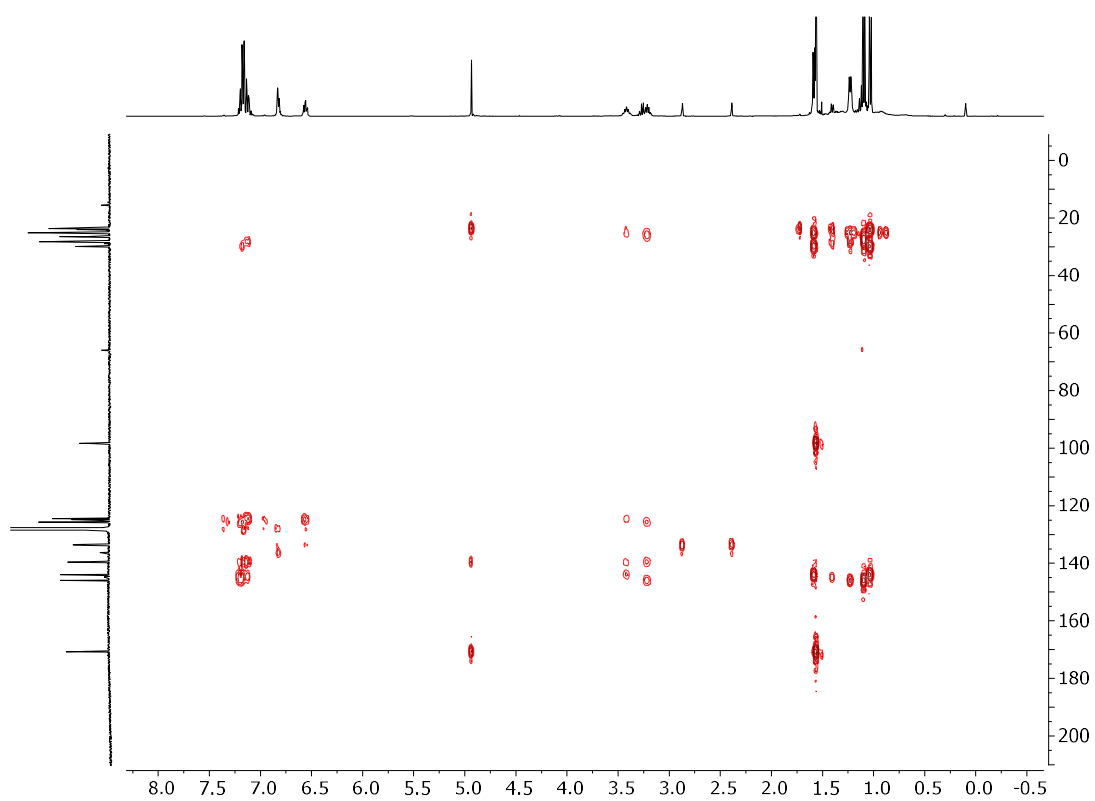
Figure A-III. 40. HMBC of compound **108** in benzene-*d₆*.
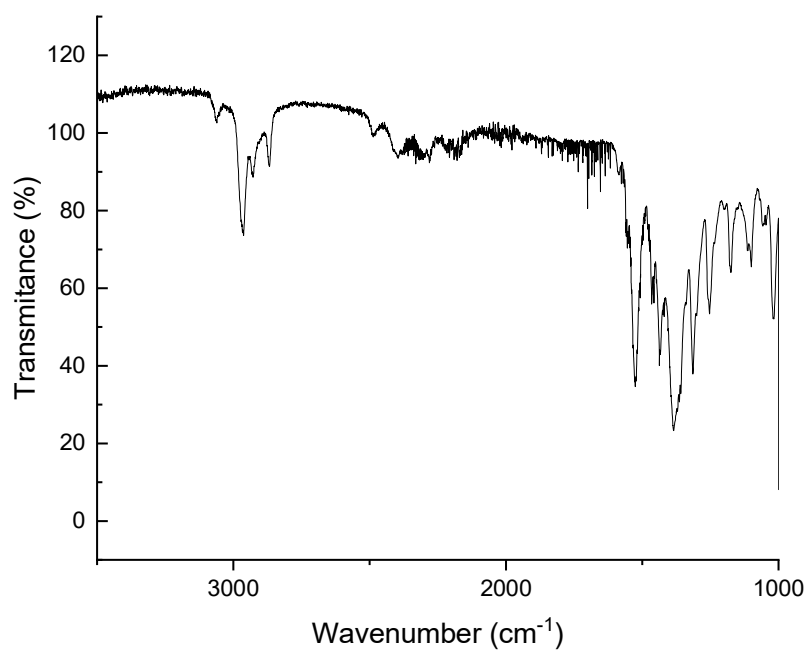
Figure A-III. 41. IR spectrum of compound **108**.

AIII.8 Synthesis of 109:
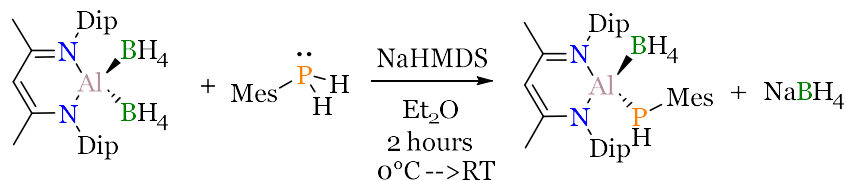
Procedure: In a 100 mL Schlenck flask, 0.308 g of NacNacAl(BH$_4$)$_2$ (0.649 mmol,1eq) are dissolved in 20mL of Et$_2$O. Then, 0.104g PH$_2$Mes (0.649 mmol,1eq) in 10 mL of diethylether are drop-wised added. The solution is cooled down to 0°C. Then, a solution of NaHMDS (0.125 g, 0.681 mmol,1.05eq) in 10 mL in diethylether are added dropwise. During the addition, the solution becomes yellow and slurry due to the precipitation of NaBH$_4$. Then, the solution is filtered off and washed with 10 mL of Et$_2$O. The obtained orange solution is concentrated under vacuum until incipient precipitation is observed. Then, the solution is genteelly heated, and it is kept at -20°C. After 2 hours, pale-yellow crystals are formed. The solution is decanted and the mother liquid is concentrated and kept in the -20°C freezer for crystallization. This procedure is repeated 2 times (1st crop=0.051g ; 2nd crop= 0.060g , total=0.111g (28%)).

^{1}H-NMR (400.13 MHz, 298 K, benzene-d_6): δ(ppm)= 1.03 (d, 6H, $^2J_{H-H}$=6.77Hz, Me-Dip), 1.10 (d, 6H, $^2J_{H-H}$=6.66Hz, Me-Dip), 1.34 (d, 6H, $^2J_{H-H}$=6.58Hz, Me-Dip), 1.59 (s, 6H, Me-NacNac), 1.63 (bs, 6H, Me-Dip), 1.70 (s, 6H, o-Me-Mes), 2.03 (s, 6H, p-Me-Mes), 2.69 (d, 1H, P-H, $^1J_{P-H}$=200.78 Hz), 3.19 (sept, 2H, C-H(iPr), $^3J_{H-H}$=6.63 Hz), 3.32 (bs, 2H, C-H(iPr)), 4.90 (s, 1H, C$_\gamma$-H), 6.72 (s, 2H, m-C-H(Mes)) 7.21 (m, 6H, m- and p-C-H(Dip)).**^{13}C{^{1}H} (100.61 MHz, 298 K, benzene-d_6):** δ(ppm)= 21.03 (s, Me-Mes), 23.32(d, Me-Mes,J_{C-P}=12.16 Hz), 23.65 (d, Me-Mes,J_{C-P}=7.91 Hz), 24.05(CH$_3$-NacNac), 25.16 (s, Me-iPr), 25.24 (s, Me-iPr), 26.40 (s, Me-iPr), 28.25(s, C$_{iPr}$-Dip), 30.48 (s, C$_{iPr}$-Dip), 30.54 (s, C$_{iPr}$-Dip), 97.93, 124.42, 125.77, 128.56 (d, C$_{Ar}$-Mes, $^3J_{C-P}$=3.07 Hz), 131.26 (d, C$_{Ar}$-Mes, $^3J_{C-P}$=21.53Hz) 134.12, 140.00 (s, C$_{Ar}$-Dip), 140.39 (d, C$_{Ar}$-Mes,$^1J_{C-P}$=10.32Hz), 144.36 (s, C$_{Ar}$-Dip), 146.06 (s, C$_{Ar}$-Dip), 170.49 (s, C$_\beta$-NacNac).**^{31}P{^{1}H}-NMR (161.97 MHz, 298 K, benzene-d_6):** δ(ppm)= -191.14 (s). **^{31}P-NMR (161.97 MHz, 298 K, benzene-d_6):** δ(ppm)= -191.14 (d, J_{P-H} =201.88 Hz). **^{11}B-NMR (128.38, 298 K, benzene-d_6):** δ(ppm)= -35.26 (quint, J_{B-H} = Hz). **^{27}Al-NMR (104.26, 298 K, benzene-d_6):** δ(ppm)= silent in the range of 190 to -190 ppm. **APPI-MS:** calc. [M+H]$^+$ = 611.424 ; found. [M+H]$^+$=611.423. **Melting point:** 170°C
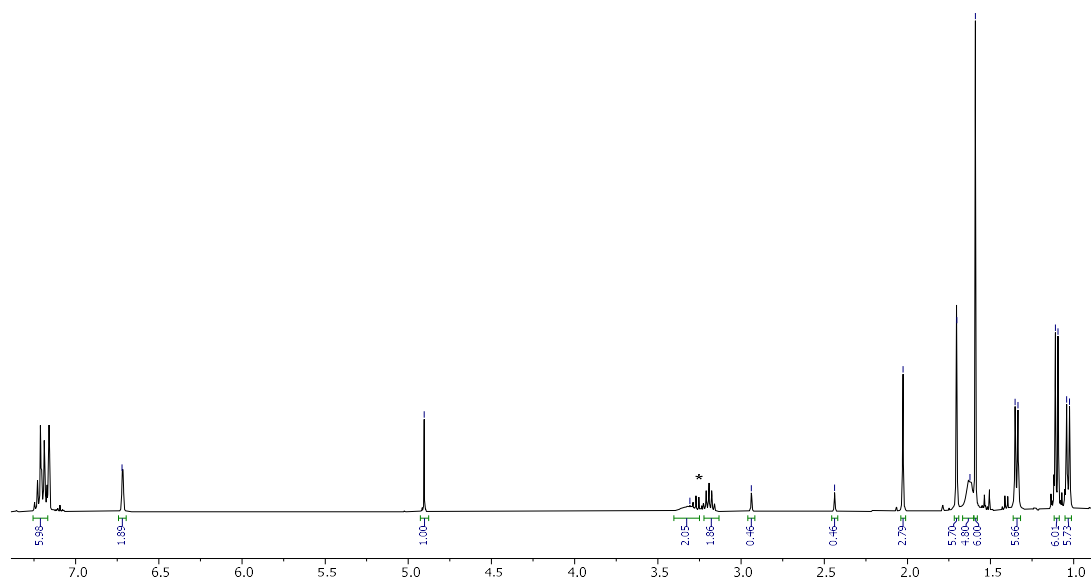
Figure A-III. 42. ¹H-NMR (400.13 MHz, 298 K, benzene-d_6) of compound **109**.
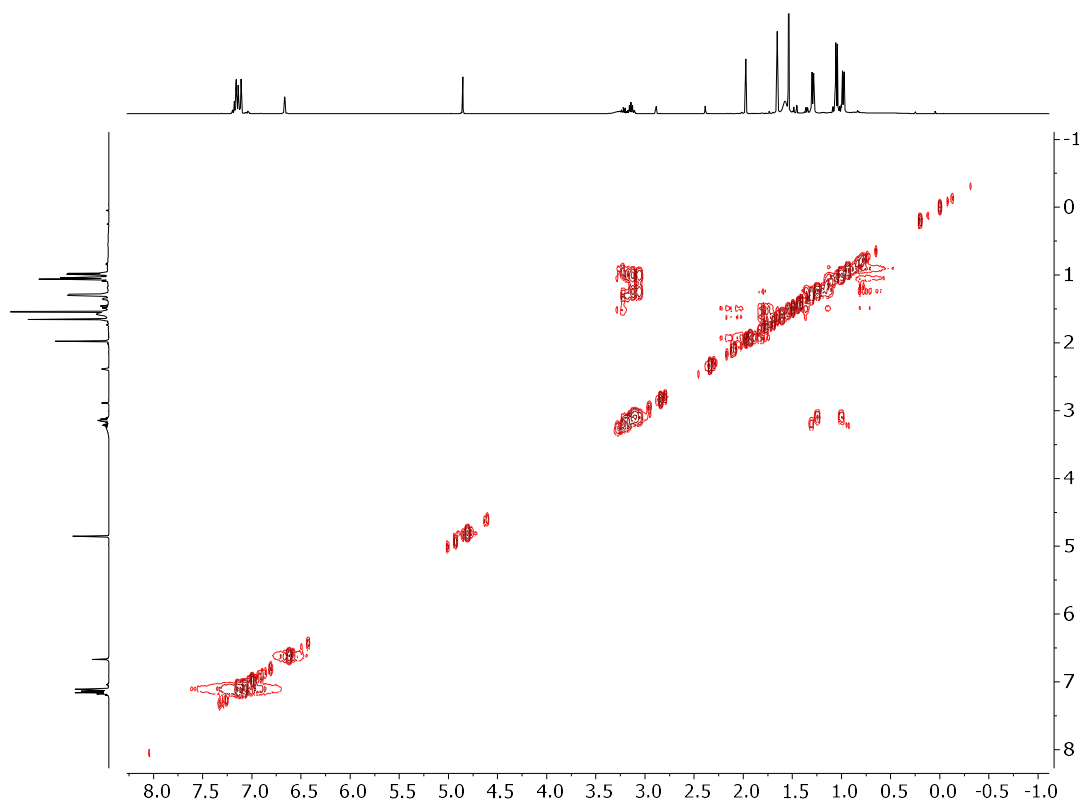
Figure A-III. 43. ¹H-¹H-COSY-NMR (400.13 MHz, 298 K, benzene-d_6) of compound **109.**

Figure A-III. 44. $^{31}P\{^{1}H\}$-NMR(161.96 MHz, 298 K, benzene-d_6) of compound **109**.
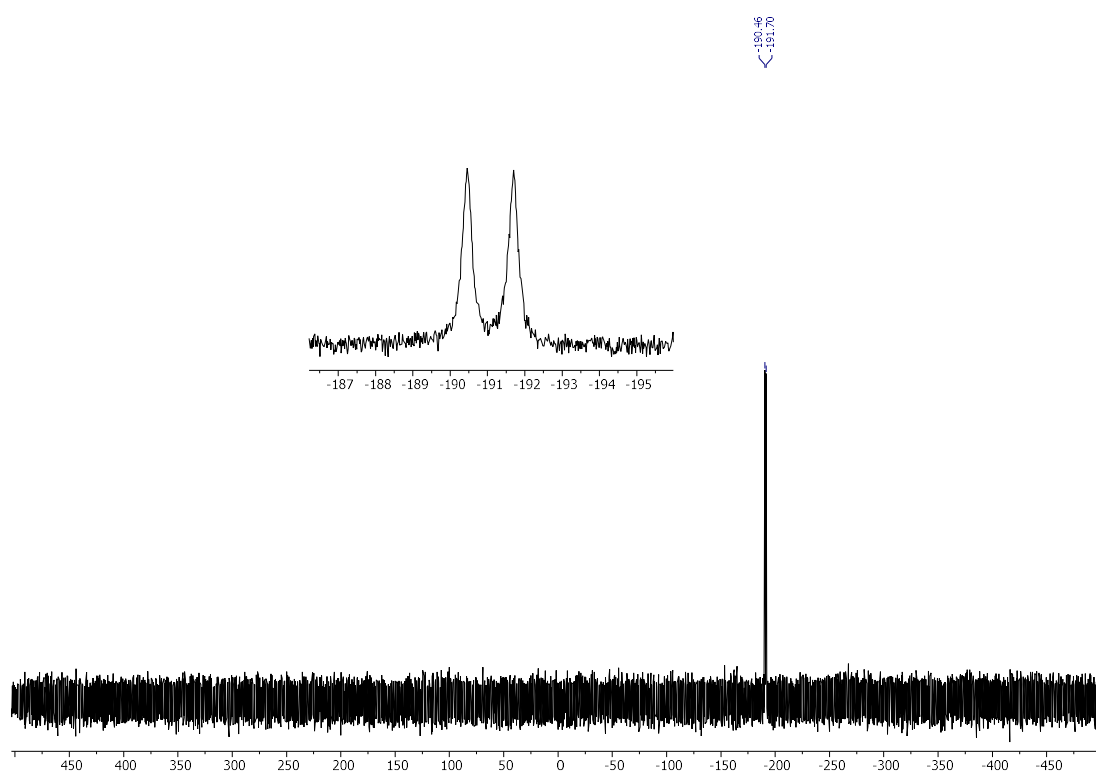
Figure A-III. 45. ^{31}P- NMR(161.96 MHz, 298 K, benzene-d_6) of compound **109**.

33.39
34.58
35.25
35.86
36.54
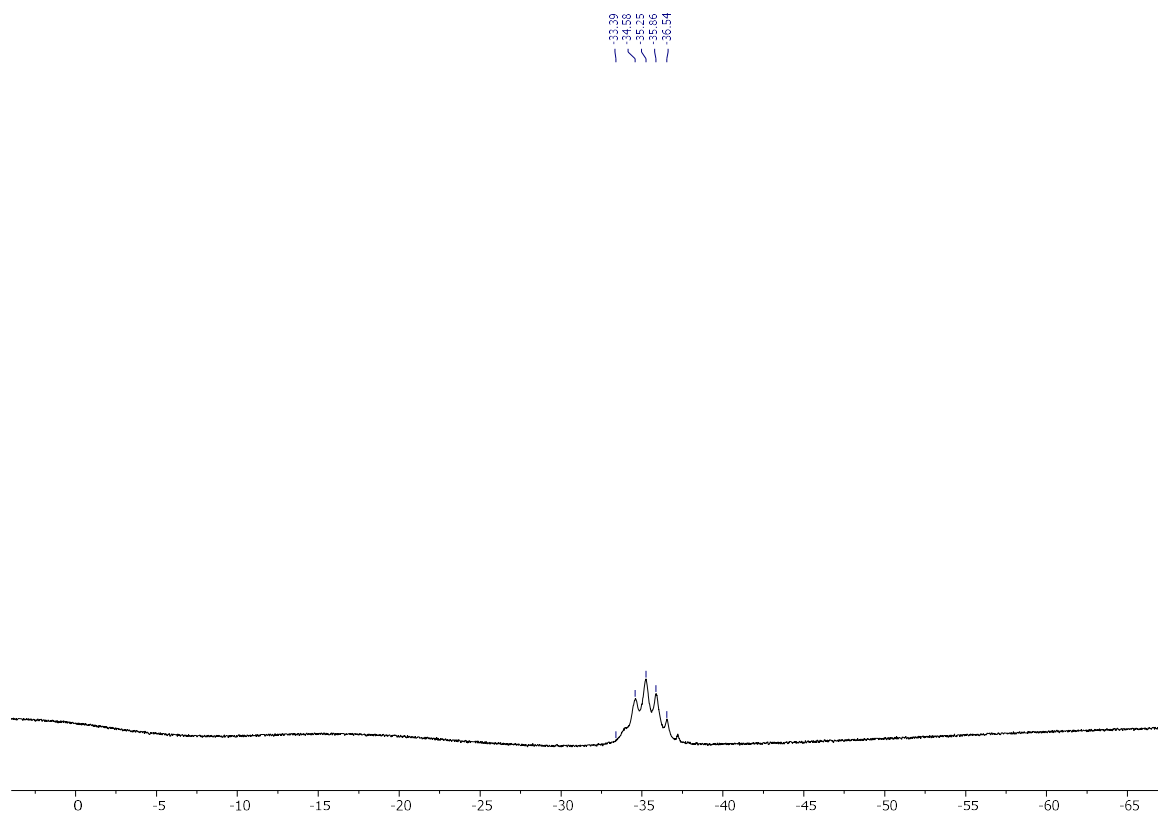
Figure A-III. 46. ^{11}B-NMR (128.4 MHz, 298 K, benzene-d_6) of compound **109**.

170.13
145.70
144.00
139.98
139.64
133.75
130.98
130.77
125.41
124.06
97.57
30.19
30.12
27.90
26.05
24.88
24.80
23.70
23.33
23.26
23.02
22.90
20.62
15.26
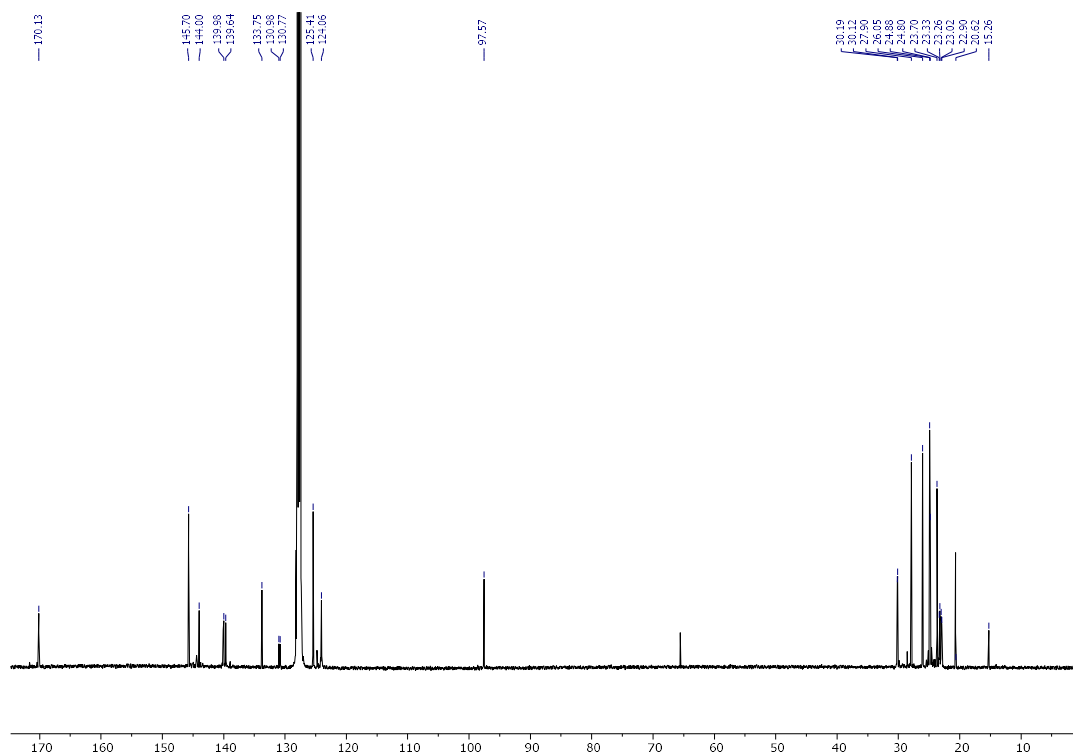
Figure A-III. 47. ^{13}C{^{1}H}-NMR(100.61 MHz, 298 K, benzene-d_6) of compound **109**.

Figure A-III. 48. HMBC of compound **109** in benzene-*d₆*.

Figure A-III. 49 Image of the crystals of compound **109**.
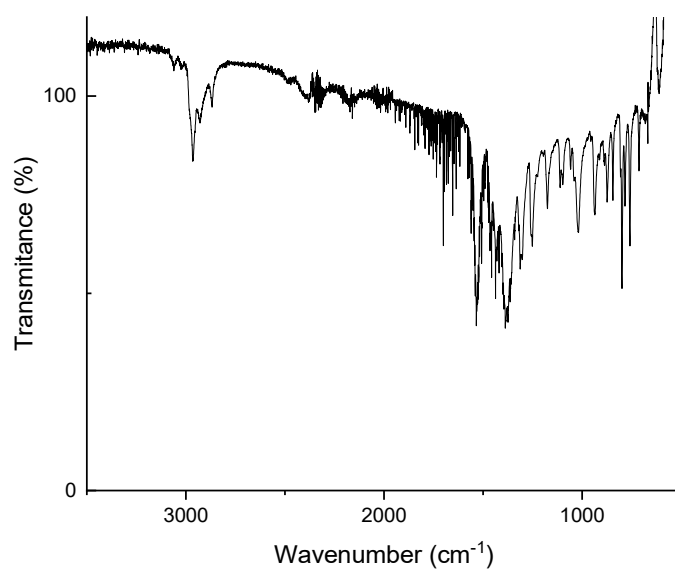
Figure A-III. 50. IR spectrum of compound **108**.

AIII.9 Synthesis of 110:
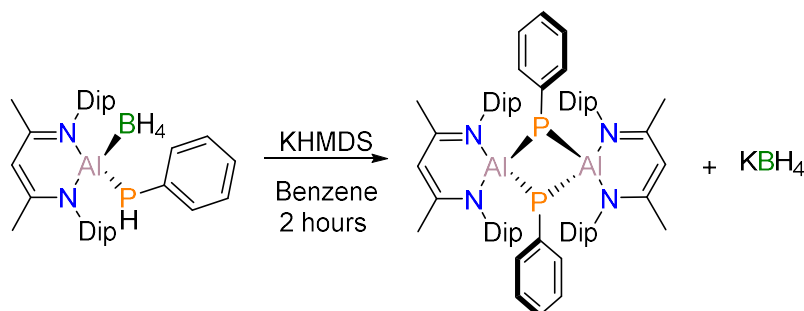
Procedure: In a 100 mL Schlenk flask, 0.251 g (1 eq, 0.441 mmol) of NacNacAlBH$_4$PHPh are dissolved in 5 mL of benzene which is dropwise added to a solution of 0.144 g KHMDS (1.3 eq, 0.574 mmol) in 5 mL of benzene. The reaction mixture is stirred for 2 hours. The crude is lyophilized for 2 hours and extracted several times with pentane. 59 mg (24%) are obtained as a red solid. Single crystals are obtained from benzene solution at room temperature.

^{1}H-NMR (400.13 MHz, 298 K, benzene-d_6): δ(ppm)= 0.30 (b, 12 H, Me-Dip), 1.40 (s, 12 H, Me-NacNac), 2.06 (bs, 4H, CHMe$_2$), 3.77 (bs, 4H, CHMe$_2$), 4.89 (s, 2H,C$_\gamma$-H), 6.88 (tt, 2H, ^{3}J$_{H-H}$=7.36 Hz, ^{4}J$_{H-H}$=1.07 Hz, C$_{Ar}$-H), 7.02 (m, 24H, C$_{Ar}$-H), 7.40 (m, 4H, C$_{Ar}$-H).**^{31}P{^{1}H}-NMR (161.97 MHz, 298 K, benzene-d_6):** δ(ppm)= -115.26 (bs)**^{31}P-NMR (161.97 MHz, 298 K, benzene-d_6):** δ(ppm)= -115.21 (bs)**^{11}B-NMR (128.37 MHz, 298 K, benzene-d_6):** δ(ppm)= silent in the range of +50 to -50 ppm.**^{27}Al-NMR (104.26 MHz, 298 K, benzene-d_6):** δ(ppm)= silent in the range of 190 to -190 ppm. **UV/Vis (Toluene):** λ$_{max}$=348 nm (3593±83 M·cm^{-1}). **Elemental analysis:** Did not match after several attempts. **Melting point:** 207°C.
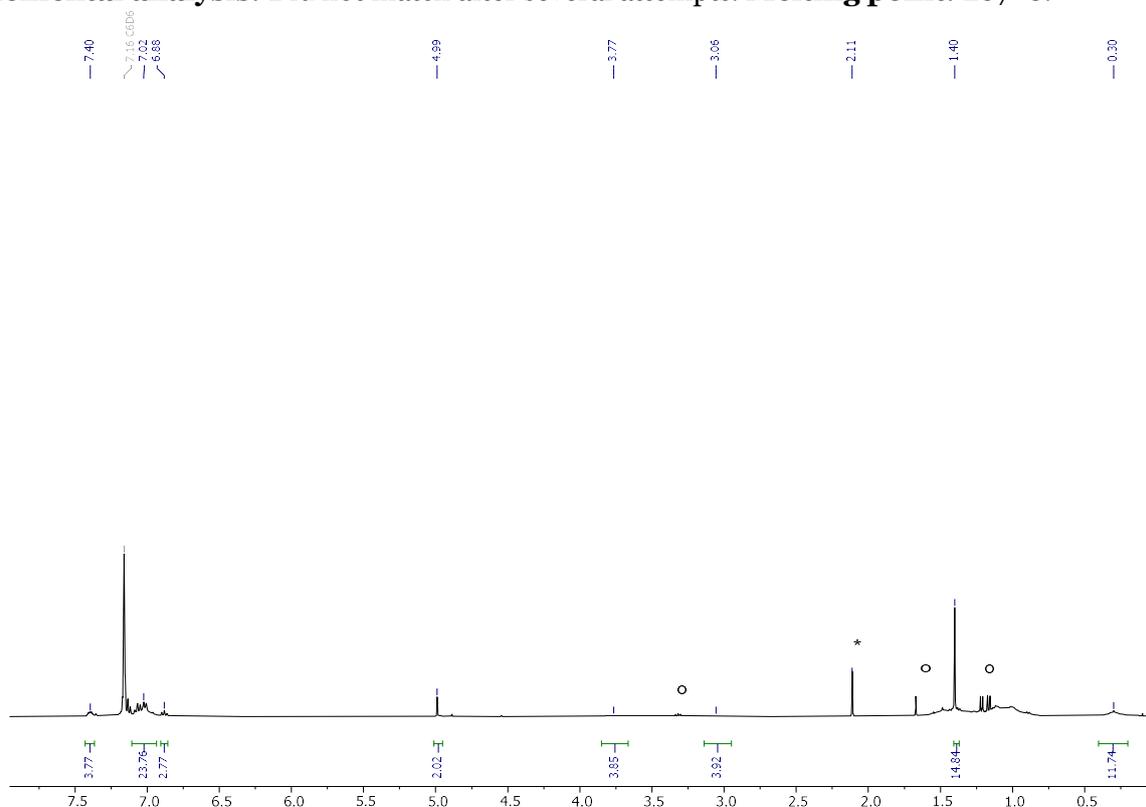
Figure A-III. 51. ^{1}H-NMR (400.13 MHz, 293 K, benzene-d_6) of compound **110**. *toluene ^{o}unknown impurity.
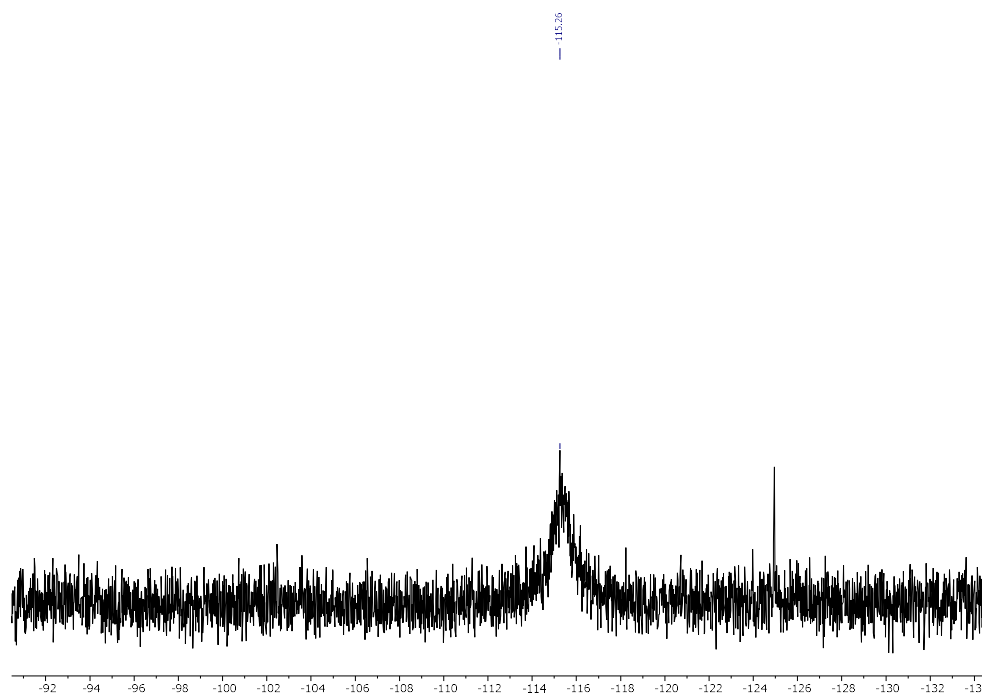
Figure A-III. 52. $^{31}P\{^{1}H\}$-NMR (161.98 MHz, 298 K, benzene-d$_6$) of compound **110.**
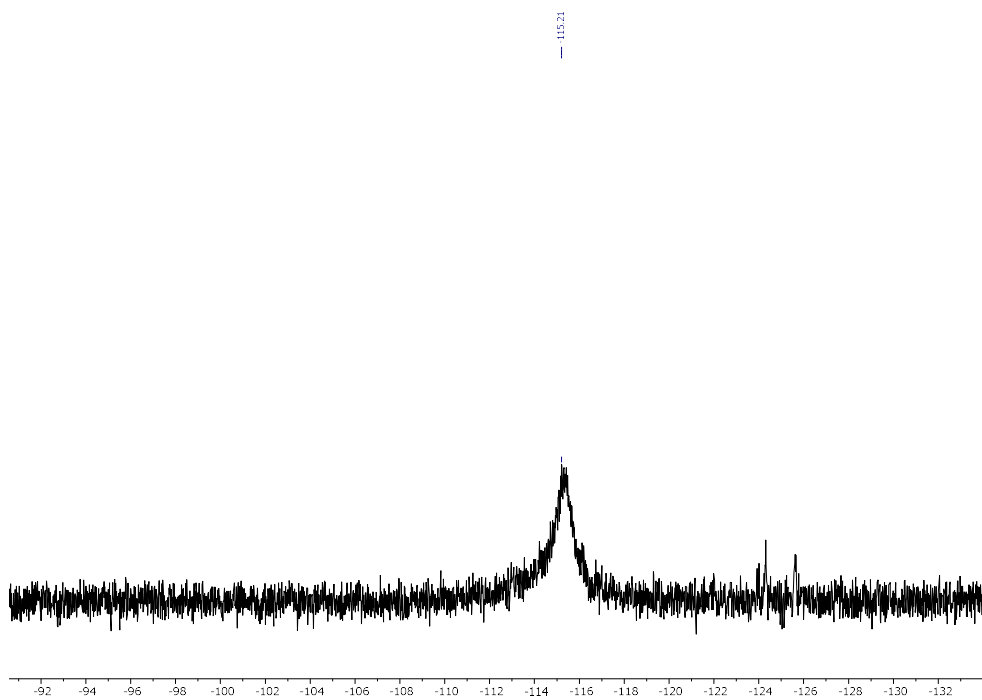
Figure A-III. 53. ^{31}P-NMR (161.98 MHz, 298 K, benzene-d$_6$) of compound **110.**.
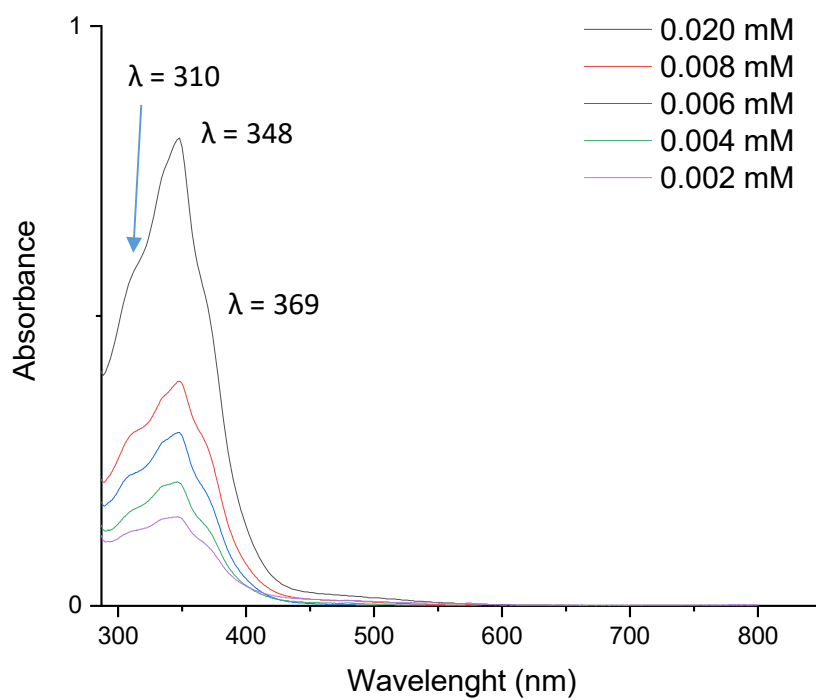
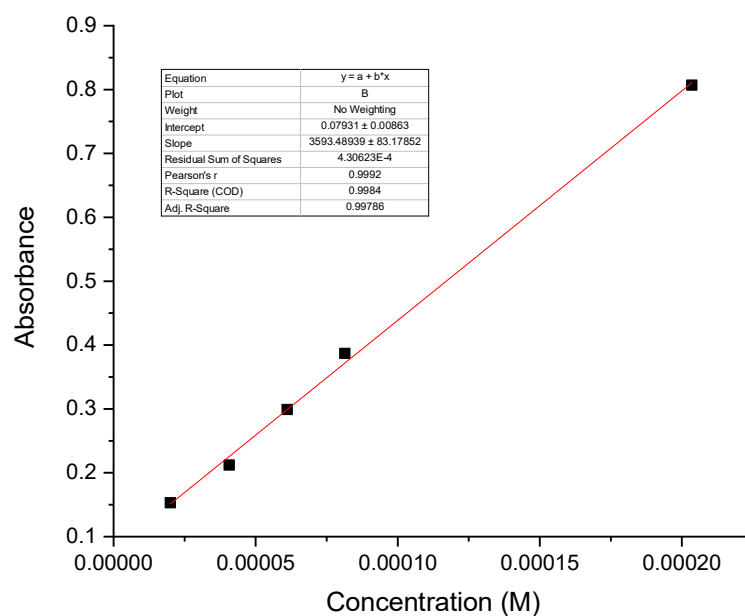Figure A-III. 54. UV-Vis spectra of compound **110** in toluene in different concentrations.

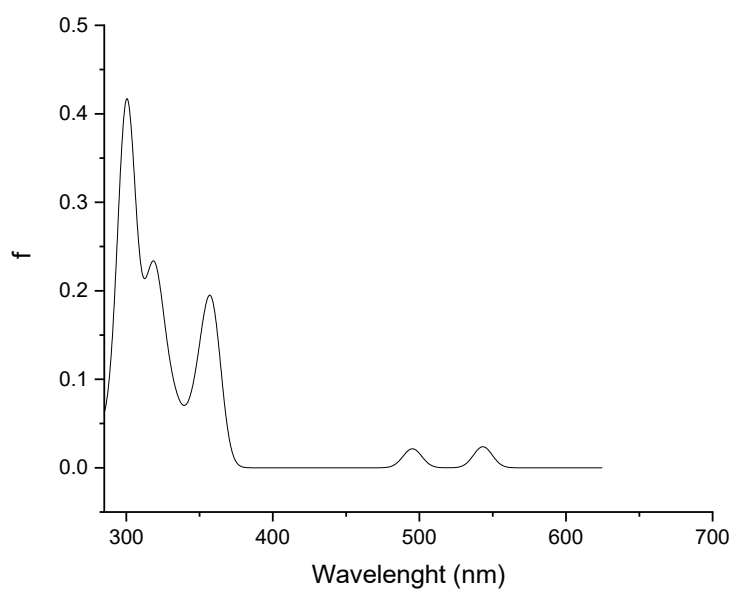Figure A-III. 55. Linear regression of compound **110** in toluene at λ=348 nm.

Figure A-III. 56. Simulated UV-Vis spectra of compound **110** at TD-PCM(toluene)/B3LYP-D3(BJ)/def2-TZVPP//B3LYP-D3(BJ)/def2-SVP level of theory. The middle bandwith was arbitrary selected to 15 nm.

Table A-III. 1. Main absorption bands of **110** at TD-PCM(toluene)/B3LYP-D3(BJ)/def2-TZVPP//B3LYP-D3(BJ)/def2-SVP level of theory.

	λ(nm)	f	Assignment[a,b]
1	359.1	0.144883849	H→L+2 0.944042 (c= -0.97161809)
2	317.4	0.168008052	H-2→L+7 0.192504 (c= -0.43875259)
			H-2 →L+9 0.658528 (c= -0.81149712)
3	301.3	0.159446172	H-3 →L 0.468093 (c= -0.68417347)
			H-1 →L+13 0.362640 (c= -0.60219596)
4	299.6	0.245454088	H-3 →L 0.343919 (c= -0.58644581)
			H-1 → L+13 0.524479 (c= 0.72420940)

[a]H means HOMO and L means LUMO. [b] corresponds to the coefficient of the excitation to the CI wavefunciton.

HOMO → LUMO+2

HOMO-2 → LUMO-7

HOMO-2 → LUMO+9

HOMO-3 → LUMO

HOMO-1 → LUMO+13
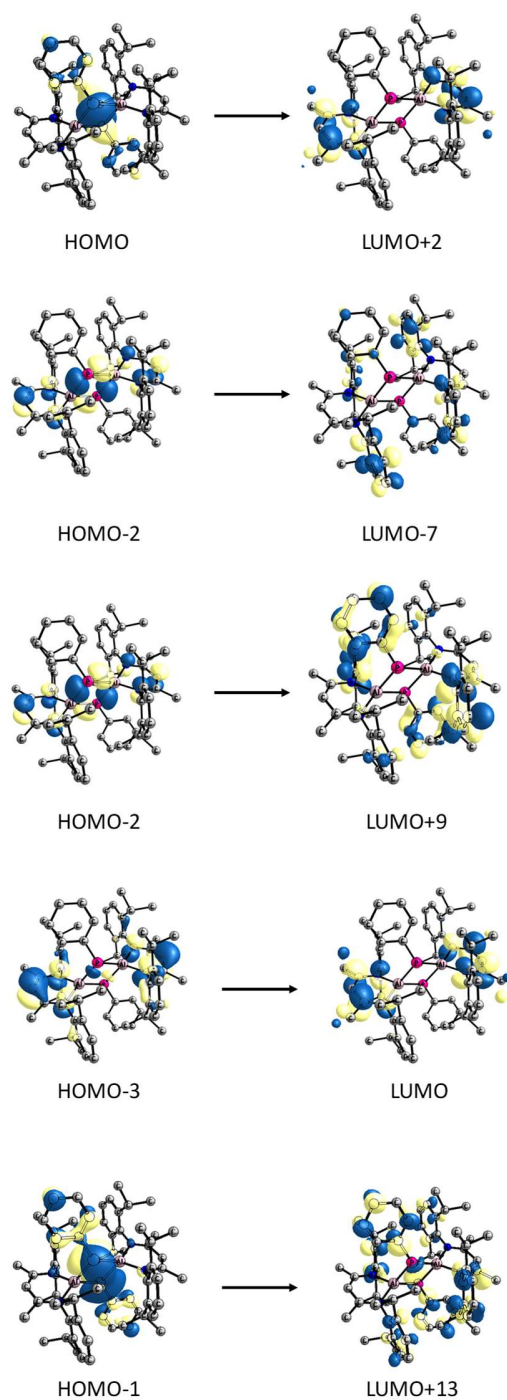
Figure A-III. 57. Selected MO transitions of TD-DFT of compound 108 at TD-PCM(toluene)/B3LYP-D3(BJ)/def2-TZVPP//B3LYP-D3(BJ)/def2-SVP.

AIII.10 Variable Temperature (VT) NMR experiments
AIII.10.1 VT of compound 99

A Variation Temperature (VT) NMR experiment was elaborated to understand the dynamic behavior of **5a** in solution. The experiment was performed following the ^{1}H-NMR spectra along the interval of 223 K to 333 K in toluene-*d$_8$*. The obtained spectra are summarized in Figure A-III.55.
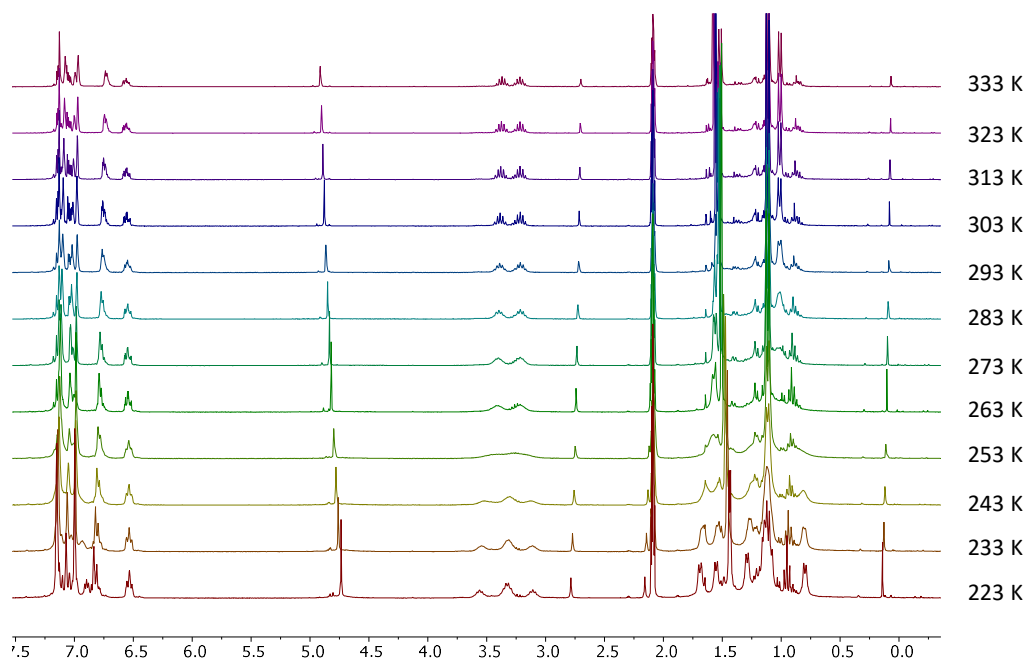
Figure A-III. 58. VT-^{1}H-NMR (300.13 MHz, toluene-d8) of compound **99.**
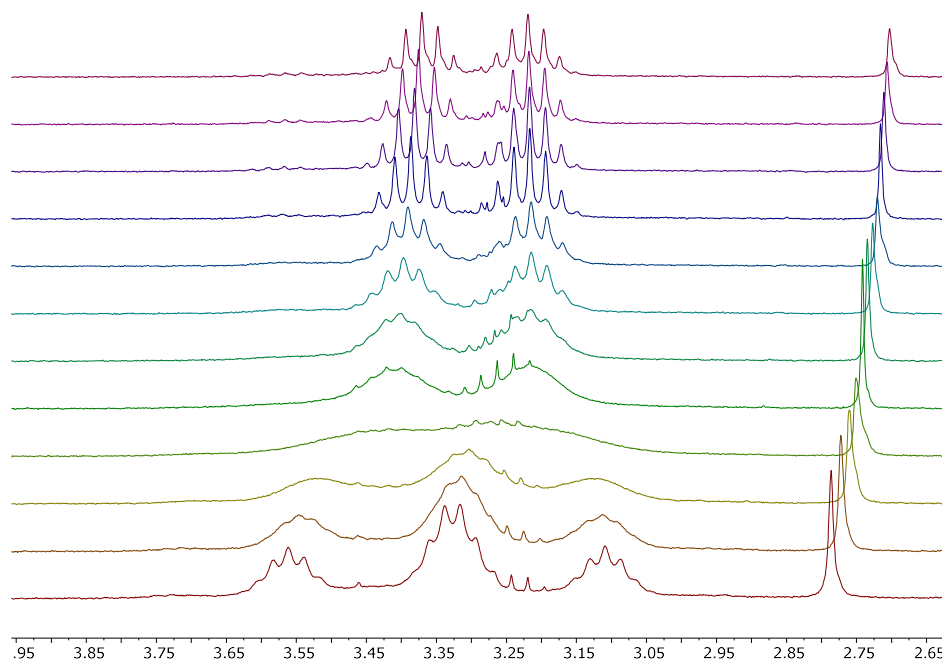
Figure A-III. 59. Zoom-in on the range of 4.00 ppm to 2.65 ppm of VT-^{1}H-NMR (300.13 MHz, toluene-d$_8$) of compound **99.**

Those differences are rooted on the exchange between the two diastereoiosomers which yield two sets of septets. The exchange is explained through an in-plane to out-of-plane bending.

We measure the exchange constant (k_{exch}) of this processes following the Eq. 83

$$k_{ex} = \frac{\pi\,(\Delta v)}{\sqrt{2}} \quad ; \quad \Delta v = v_2 - v_1 \tag{83}$$

Where Δv is the difference between the two resonances. In our case, we selected the chemical shifts of the septets being $v_2 = 3.56\,ppm$ and $v_2 = 3.34\,ppm$. Introducing these values in Eq 84 we obtain a $k_{ex} = 146.52$ Hz.

$$k_{exch} = \frac{\pi\,(3.56 - 3.34)(300\,)}{\sqrt{2}} = 146.52\,Hz$$

The activation energy $\Delta G^{\dagger}$ of this process is obtained with Eyring equation (Eq. 2):

$$k_{exch} = \frac{k_b T_c}{h}\,e^{\frac{-\Delta G^{\dagger}}{RT_c}} \tag{84}$$

The k_b is the Boltzmann constant ($k_b = 1.381 \cdot 10^{-2}\,J/K$), h is the Plank constant ($h = 6.626 \cdot 10^{-34}\,J/Hz$), R is the gas constant ($R = 8.314\,J \cdot mol^{-1} \cdot K^{-1}$) and T_c is the coalescence temperature ($T_c = 253\,K$). Isolating $\Delta G^{\dagger}$ from Eq 2, the $\Delta G^{\dagger}$ is obtained as:

$$\Delta G^{\dagger} = -RT_c \ln\left(\frac{k_{exc}\,h}{k_b T_c}\right) = -8.314 \cdot 253 \cdot \ln\left(\frac{146.52 \cdot 6.626 \cdot 10^{-34}}{1.381 \cdot 10^{-23} \cdot 253}\right) = 72106\,\frac{J}{mol}$$

$$= 12.2\,kcal/mol$$

AIII.10.2 VT of compound 110
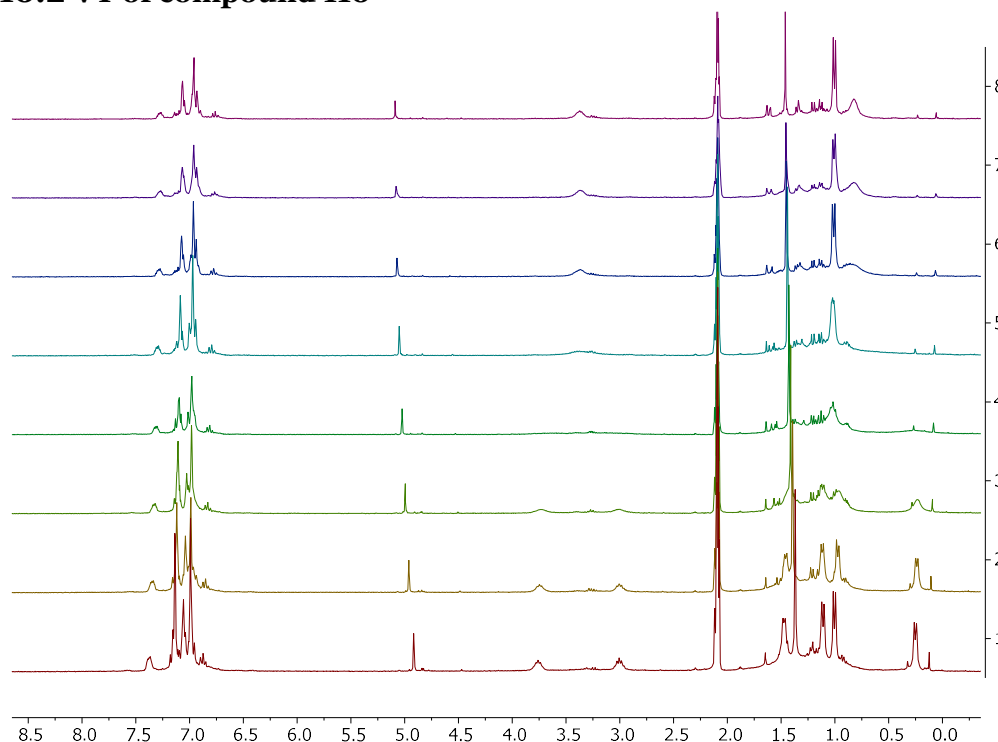
Figure A-III. 60. VT-¹H-NMR (300 MHz, toluene-d₈) of compound **110**.

We measure the exchange constant (k_{exch}) of this processes following the Eq. 83

$$k_{exch} = \frac{\pi\,(\Delta\nu)}{\sqrt{2}} \quad ; \quad \Delta\nu = \nu_2 - \nu_1 \tag{83}$$

Where $\Delta\nu$ is the difference between the two resonances. In our case, we selected the chemical shifts of the septets being $\nu_2 = 3.76\ ppm$ and $\nu_2 = 3.00\ ppm$. Introducing these values in Eq 83 we obtain a $k_{exch}=$ 226.57 Hz.

$$k_{exc} = \frac{\pi\,(3.76 - 3.01)(300\,)}{\sqrt{2}} = 226.57\ Hz$$

The activation energy $\Delta G^{\dagger}$ of this process is obtained with Eyring equation (Eq. 84):

$$k_{ex} = \frac{k_b T_c}{h} e^{\frac{-\Delta G^{\dagger}}{RT_c}} \tag{84}$$

The k_b is the Boltzmann constant ($k_b = 1.381 \cdot 10^{-23} J/K$), h is the Plank constant ($h = 6.626 \cdot 10^{-34}\ J/Hz$), R is the gas constant ($R = 8.314\ J \cdot mol^{-1} \cdot K^{-1}$) and T_c is the coalescence temperature ($T_c = 303\ K$). Isolating ΔG† from Eq 2, the ΔG† is obtained as:

$$\Delta G^{\dagger} = -RT_c \ln\left(\frac{k_{exch} h}{k_b T_c}\right) = -8.314\ \cdot 303 \cdot \ln\left(\frac{226.57 \cdot 6.626 \cdot 10^{-34}}{1.381 \cdot 10^{-23} \cdot 303}\right) = 14.5\ kcal/mol$$

AIII.11 Mechanism elucidation of the synthesis of phosphalumane 99
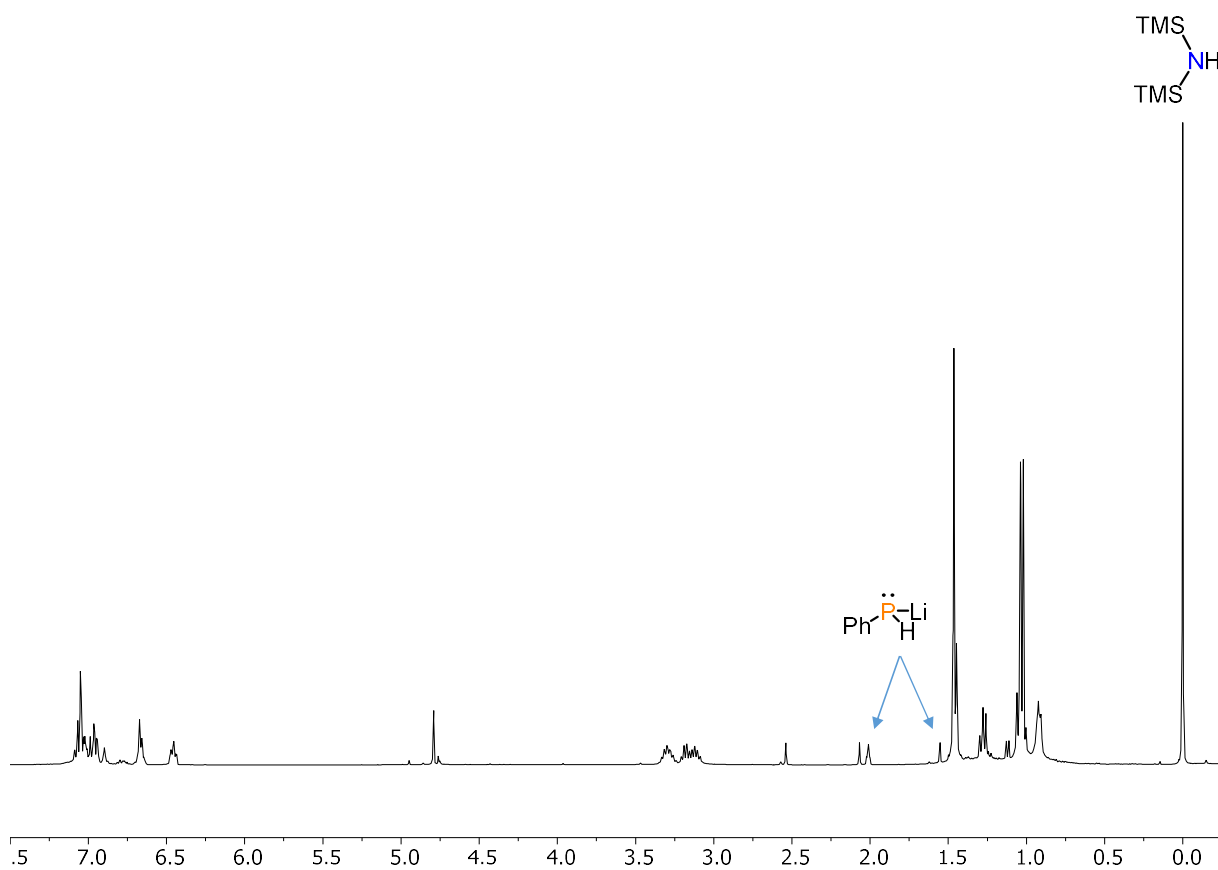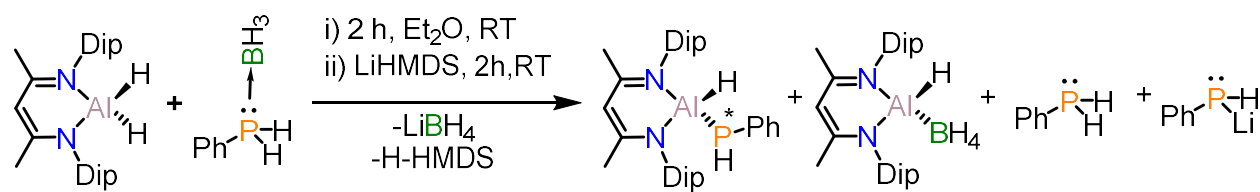
Figure A-III. 61. ^{1}H-NMR (400.13 Hz, 298 K, benzene-d_6) of the reaction crude.
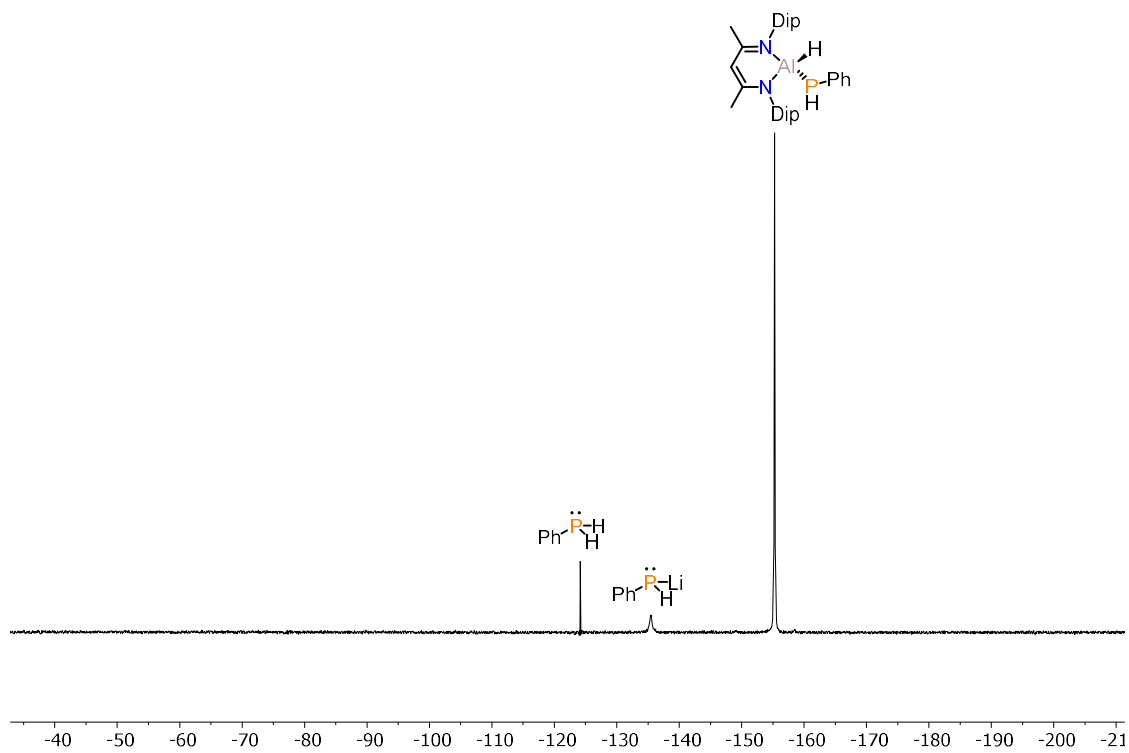
Figure A-III. 62. ^{31}P{^{1}H}-NMR (161.98 MHz, 298 K, benzene-d$_6$) of the reaction crude .
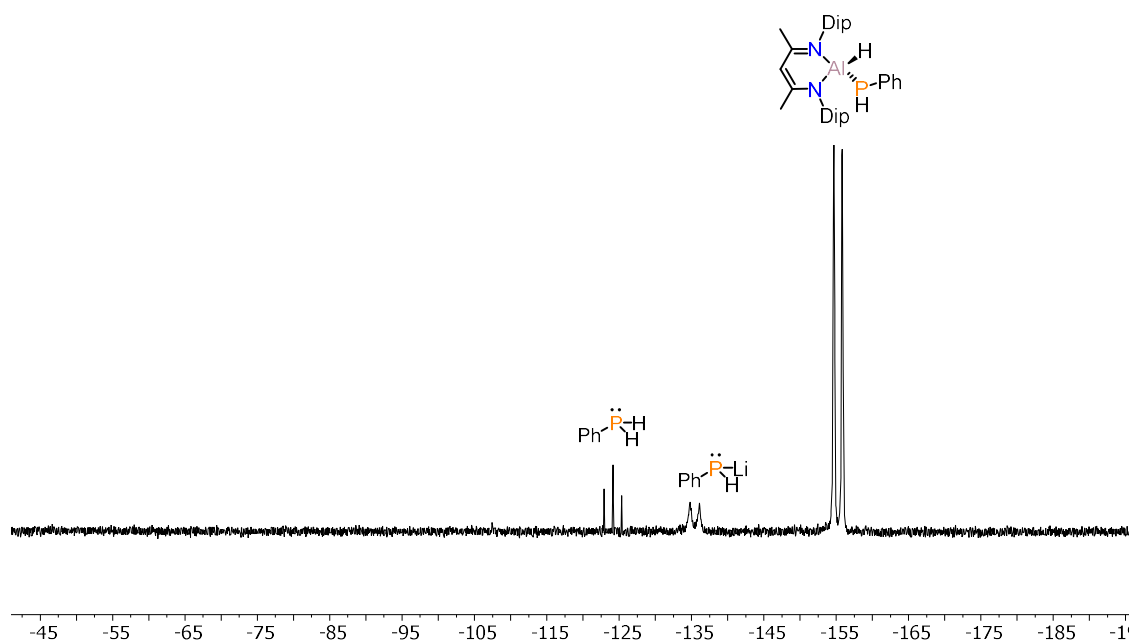
Figure A-III. 63. ^{31}P{^{1}H}-NMR (161.98 MHz, 298 K, benzene-d$_6$) of the reaction crude in benzene-*d$_6$*.

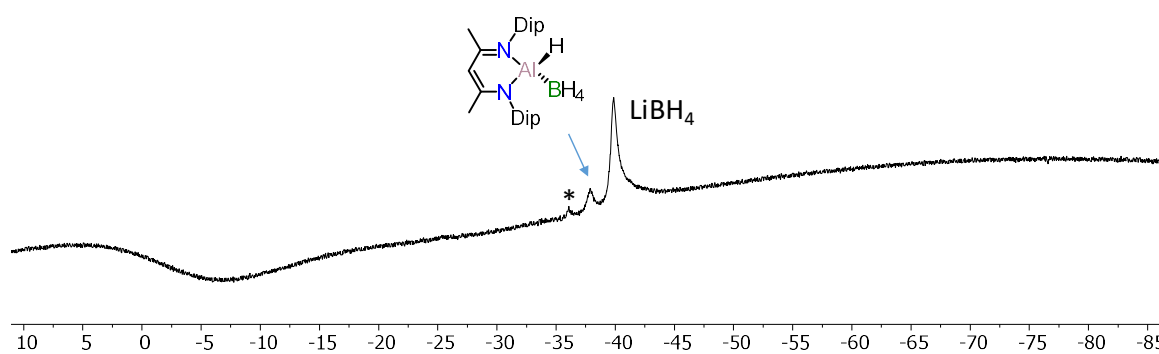Figure A-III. 64. $^{11}B\{^1H\}$-NMR (128.28 MHz, 293 K, benzene-d6) of the reaction crude in C_6D_6. *Unidentified compound.
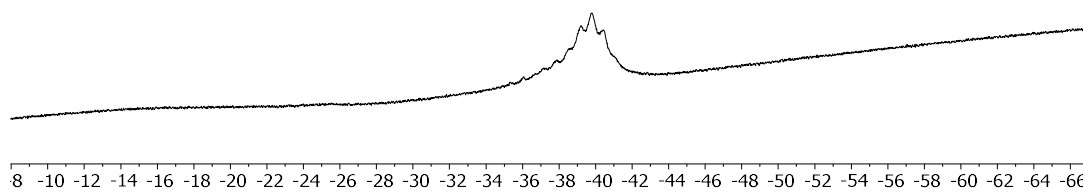
Figure A-III. 65. $^{11}B\{^1H\}$-NMR (128.28 MHz, 293 K, benzene-d$_6$) of the reaction crude in C_6D_6.

Figure A-III. 66. $^{11}B\{^1H\}$-NMR (75.5 MHz, 293 K, C_6D_6/Et$_2$O) of LiBH$_4$.

AIII.12 X-Ray data

Table A-III. 2. Crystal data of **99, 100, 101, 102, 107, 108, 109** and **110**.

Compound	**99**	**100**	**101**	**102**	**107**	**108**	**109**	**110**
Formula	$C_{35}H_{48}AlN_2P$	$C_{38}H_{54}AlN_2P$	$C_{48}H_{76}AlN_2O\ P$	$C_{33}H_{52}AlN_2\ P$	$C_{47}H_{71}AlKN_2O_6P$	$C_{35}H_{51}AlBN_2P$	$C_{38}H_{57}\ AlBN_2$	$C_{82}H_{104}Al_2N_4P_2$
Crystal system	Triclinic	Monoclinic	Orthorhombic	Monoclinic	Monoclinic	Triclinic	Orthorhombic	Monoclinic
Space Group	P-1	P21/n	P212121	P21/m	P21/n	P-1	Pmn2₁	C2/c
Volume (Å³)	3355.4(4)	3594.5(6)	4587.0(3)	1674.30(10)	4859.5(4)	1706.7(3)	1817.47(7)	7256.5(5)
A	12.3001(9)	13.8132(12)	12.5510(5)	8.9101(3)	11.1137(5)	10.3506(10)	20.3502(5)	19.3749(7)
B	18.1376(13)	14.5907(15)	14.6112(5)	19.7282(7)	19.8901(9)	12.2034(10)	8.7683(2)	17.6769(7)
C	18.2686(12)	17.8380(19)	25.0127(9)	10.3520(3)	22.1078(9)	14.3370(14)	10.1855(2)	21.4460(7)
A	118.462(2)	90	90	90	90	91.412(3)	90	90
B	93.192(2).	91.092(4).	90	113.0580(10)	96.077(2)	99.130(3)	90	98.9020(10)
Γ	106.135(2).	90	90	90	90°.	106.825(3)	90	90
Z	4	4	4	2	4	2	2	4
Formula weight (g/mol)	554.70	596.78	755.05	534.71	857.10	568.53	610.61	1261.59
Density (g/mL)	1.098	1.103	1.093	1.061	1.172	1.106	1.116	1.155
Absorption coefficient (mm⁻¹)	0.132	0.128	0.114	0.130	0.206	0.131	0.127	0.130
F(000)	1200	1296	1656	584	1848	616	664	2720
Temperature (K)	132(2)	153(2)	133(2)	133(2)	133(2)	153(2)	152(2)	153(2)
Total numb. Reflections	103068	86372	104106	25327	77605	63792	27568	83714
Final R indices [I>2σ(l)]	R1 = 0.0521, wR2 = 0.1198 R1 = 0.0999, wR2 = 0.1451	R1 = 0.0393, wR2 = 0.1046 R1 = 0.0490, wR2 = 0.1125	R1 = 0.0337, wR2 = 0.0787 R1 = 0.0413, wR2 = 0.0842	R1 = 0.0513, wR2 = 0.1410 R1 = 0.0639, wR2 = 0.1525	R1 = 0.0520, wR2 = 0.0944 R1 = 0.1023, wR2 = 0.1174	R1 = 0.0472, wR2 = 0.1152 R1 = 0.0622, wR2 = 0.1258	R1 = 0.0338, wR2 = 0.0744 R1 = 0.0420, wR2 = 0.0786	R1 = 0.0359, wR2 = 0.0882 R1 = 0.0426, wR2 = 0.0932
Largest diff. Peack and hole (e·A⁻³)	0.825 and -0.329	0.249 and -0.245	0.268 and -0.199	0.783 and -0.421	0.229 and -0.320	0.351 and -0.460	0.181 and -0.183	0.318 and -0.264
GoF	1.015	1.054	1.046	1.051	1.010	1.040	1.043	1.032

*Refinament details for **99***: All non H-atoms were located on the electron density maps and refined anisotropically. C- bound H atoms were placed in positions of optimized geometry and treated as riding atoms. Their isotropic displacement parameters were coupled to the corresponding carrier atoms by a factor of 1.2 (CH) or 1.5 (CH3). The hydrogen atoms bound on Al1, Al2, P1 and P2 were located on the electron density maps. Their isotropic displacement parameters were coupled by a factor of 1.2.

Disorder: The phenyl ring on P2 (C65C70), one isopropyl group (C44C46) and one methyl group (C33) was split over two positions. For the refinement of the disorder some restraints were applied in the refinement.
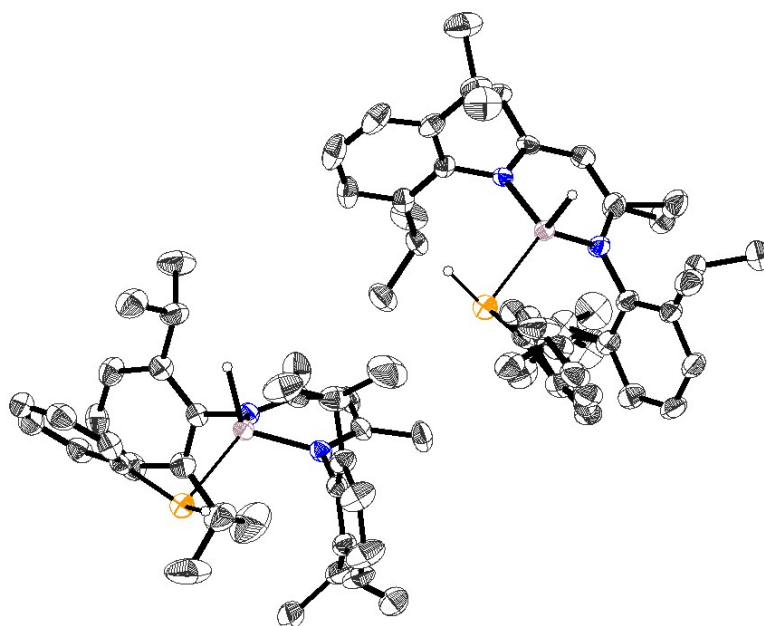
*Refinement details for **100***: All non H-atoms were located in the electron density maps and refined anisotropically. C-bound H atoms were placed in positions of optimized geometry and treated as riding atoms.Their isotropic displacement parameters were coupled to the corresponding carrier atoms by a factor of 1.2 (CH) or 1.5 (CH3). The Al and P bonded H-atoms were located in the electron density maps. Their positional parameters were refined using isotropic displacement parameters which were set at 1.2 times the Ueq value of the parent atoms. The P bonded H-atoms were split over two positions.
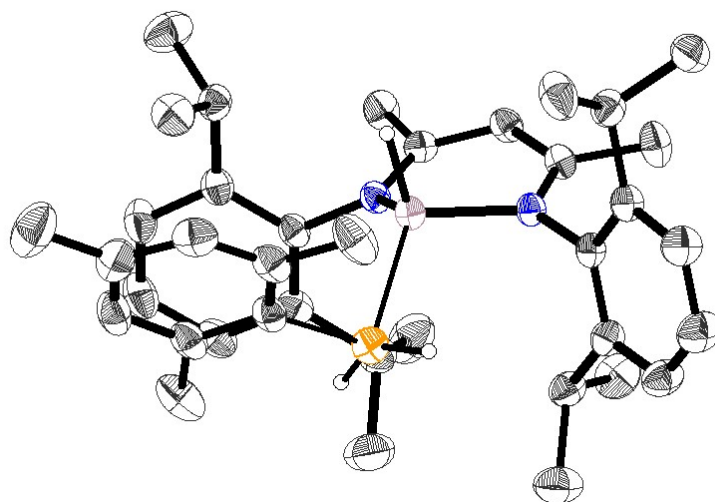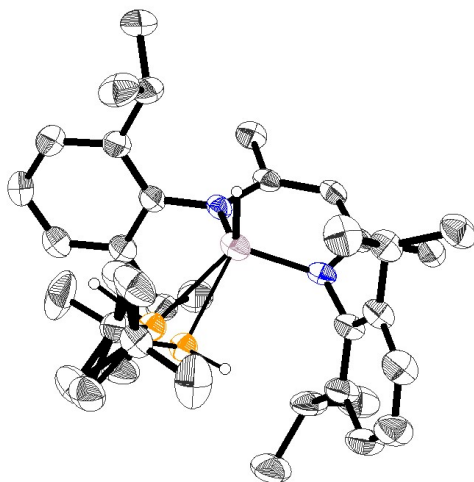
*Refinament details for **101***: All non H-atoms were located on the electron density maps and refined anisotropically. C-bound H atoms were placed in positions of optimized geometry and treated as riding atoms. Their isotropic displacement parameters were coupled to the corresponding carrier atoms by a factor of 1.2 (CH, CH2) or 1.5 (CH3). The Al1 and P1 bonded H atoms were located on the electron density maps and their positional parameters were refined using isotropic displacement parameters which were set at 1.5 times the Ueq value of the parent atoms.
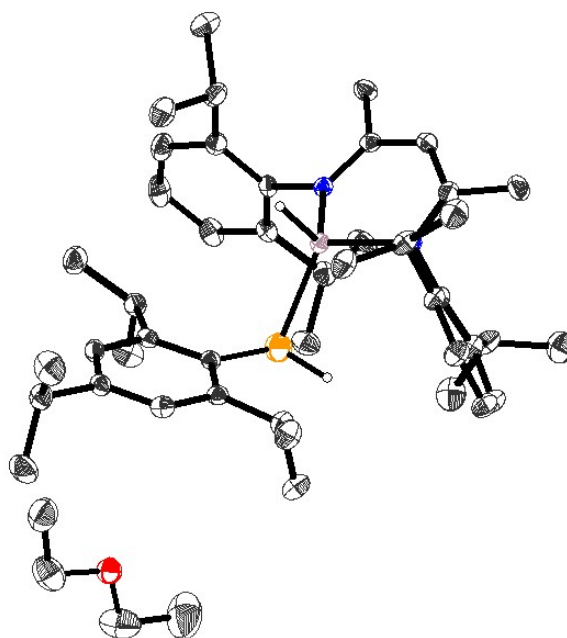
*Refinament details for **102***: All non H-atoms were located on the electron density maps and refined anisotropically. C-bound H atoms were placed in positions of optimized geometry and treated as riding atoms. Their isotropic displacement parameters were coupled to the corresponding carrier atoms by a factor of 1.2 (CH) or 1.5 (CH3). Disorder: The P1-

isopropylfragment is placed on a crystallographic mirror plane, and hence was refined each to a occupancy of 0.5 using the PART -1 instruction of SHELX. The electron density of the hydrogen atoms bound to Al1(H1a) or P1(H2a) was found on the electron density maps. Their positional parameters were refined using isotropic displacement parameters which were set at 1.2 times the Ueq value ofthe corresponding parent atoms.
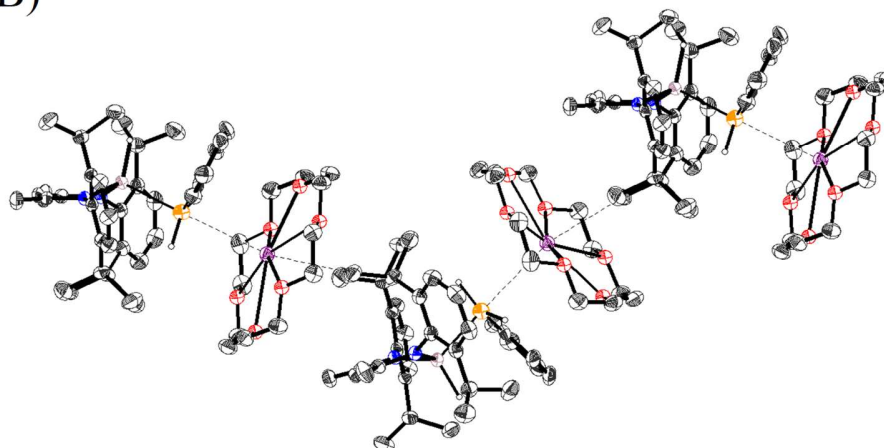

*Refinament details for **107***: All non H-atoms were located on the electron density maps and refined anisotropically. C-bound H atoms were placed in positions of optimized geometry and treated as riding atoms. Their isotropic displacement parameters were coupled to the corresponding carrier atoms by a factor of 1.2 (CH, CH2) or 1.5 (CH3).

Disorder: The backbone of coordinated ligand shows resonance and no distinct sequence of single and double bonds. So the methylene and methyl groups were refined as a disorder problem of 50 %. The aluminium bonded proton H1A and the phosphorus bonded protons H1P and H2P were located on the electron density map. However, in the close proximity of P1 two electron density peaks were found, which were set at a 50 % probability, each. Their isotropic displacement parameters were coupled to the corresponding carrier atoms by a factor of 1.2 times the Ueq value of the parent atom.
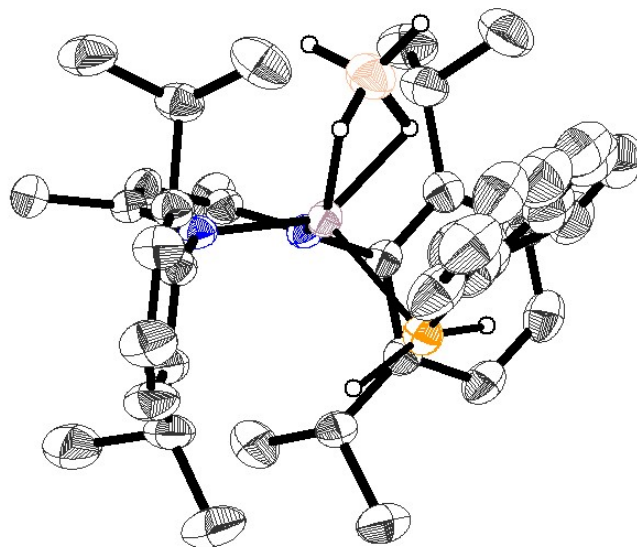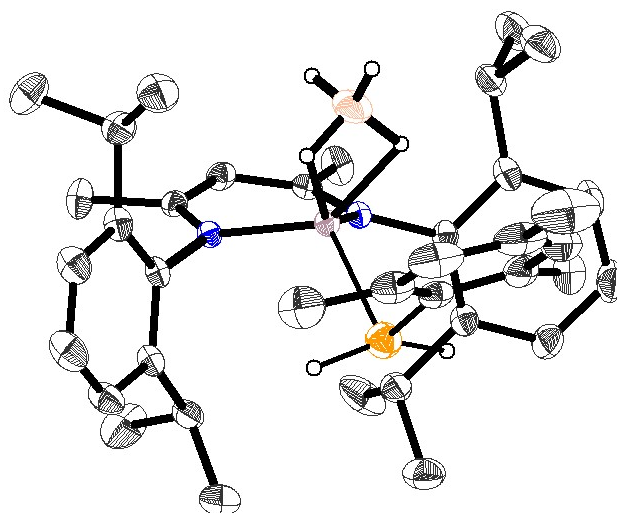
A)

B)
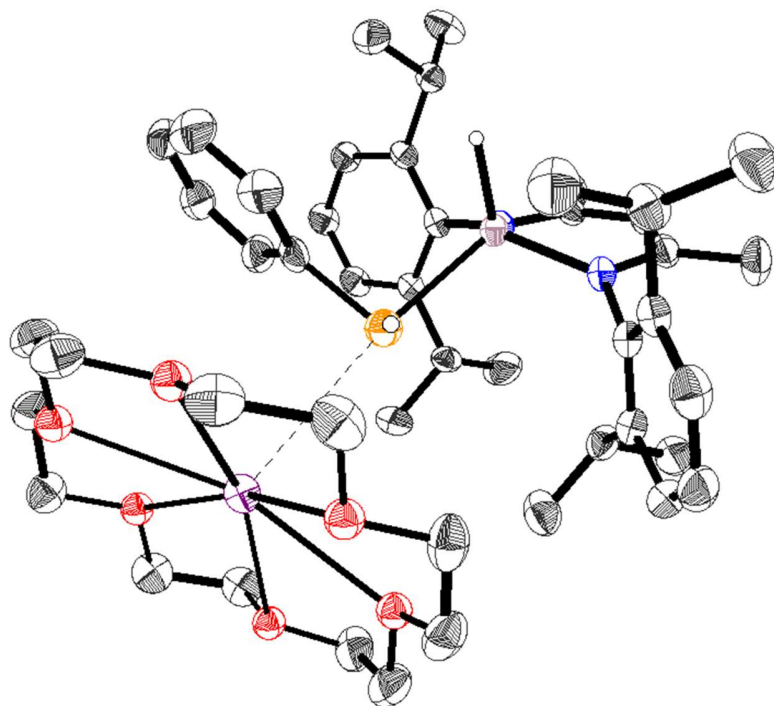
*Refinament details for **108**:* All non H-atoms were located in the electron density maps and refined anisotropically. C-bound H atoms were placed in positions of optimized geometry and treated as riding atoms.Their isotropic displacement parameters were coupled to the corresponding carrier atoms by afactor of 1.2 (CH) or 1.5 (CH3). The boron bonded H atoms H1a, H1b, H1c and H1d and theP bonded H atoms H2a and H2b were located in the electron density maps. Their positional parameters were refined using isotropic displacement parameters which were set at 1.2 times the Ueq value of the parent atoms. Disorder: The phenyl ring is split over two positions. The P bonded H-atoms H2a and H2b were included into the split refinement. Their occupancy factors refined to 0.75 for the major component.

*Refinament details for **109***: All non H-atoms were located in the electron density maps and refined anisotropically. C-bound H atoms were placed in positions of optimized geometry and treated as riding atoms. Their isotropic displacement parameters were coupled to the corresponding carrier atoms by a factor of 1.2 (CH) or 1.5 (CH3). The P1 and B1 bonded H atoms H1P and H1a, H1b, H1c and H1d respectively, were located on the electron density maps. Their positional parameters were refined using isotropic displacement parameters which were set at 1.2 times the Ueq value of the corresponding atoms.

*Refinament details for **110***: All non H-atoms were located in the electron density maps and refined anisotropically. C-bound H atoms were placed in positions of optimized geometry and treated as riding atoms. Their isotropic displacement parameters were coupled to the corresponding carrier atoms by a factor of 1.2 (CH) or 1.5 (CH3).
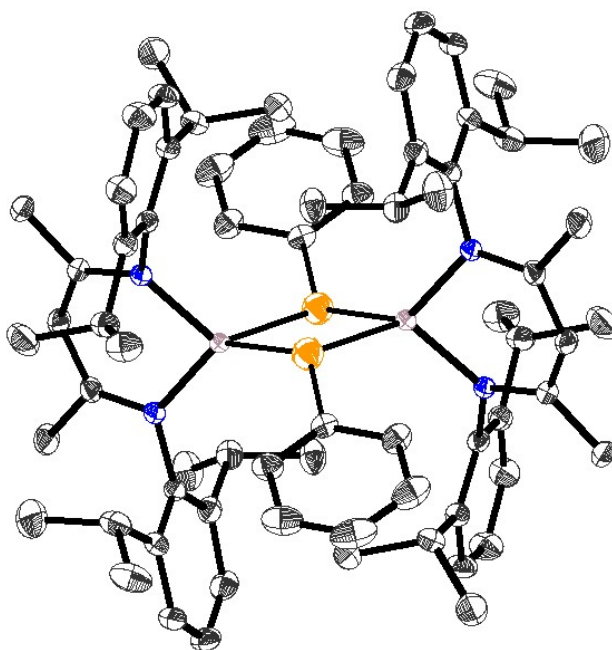
AIII.13 Electronic structure and Chemical Bonding

HOMO-1	HOMO	LUMO	LUMO+1
ε=-6.05 eV	ε= -5.44 eV	ε=-1.66 eV	ε=-0.53 eV
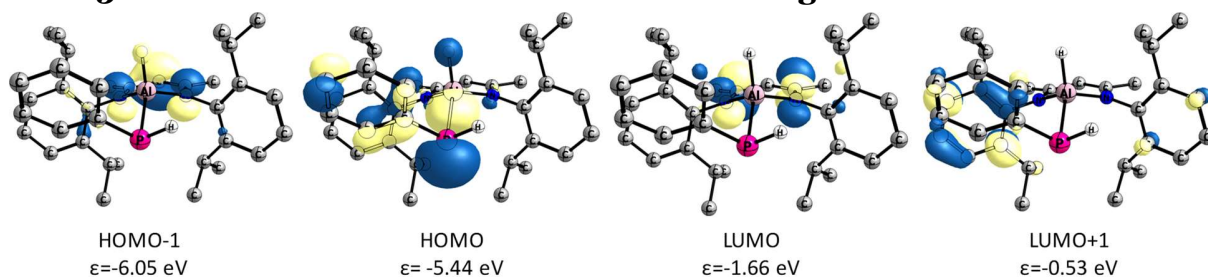
Figure A-III. 67 Frontier Kohn-Sham Molecular Orbitals of **99** at B3LYP-D3(BJ)/def2-TZVPP//B3LYP-D3(BJ)/def2-SVP level of theory. Isovalue=0.05 a.u.

HOMO-1	HOMO	HOMO-1	HOMO-1
ε=-5.99 eV	ε=-5.07 eV	ε=-1.58 eV	ε=-0.52 eV
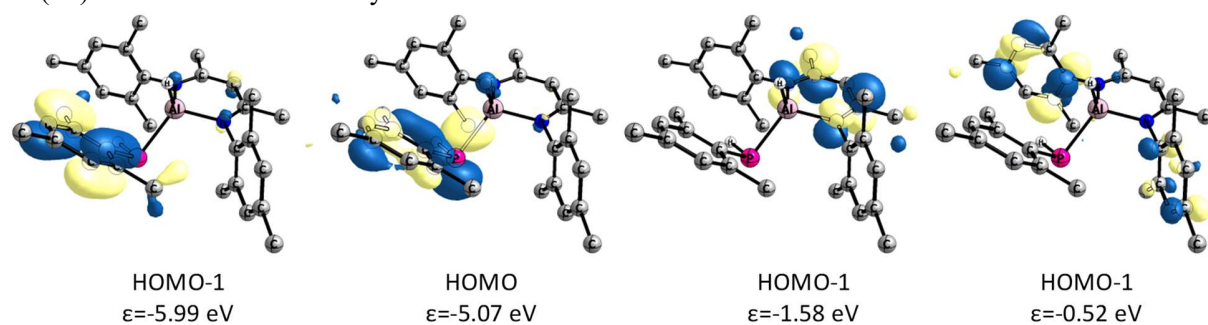
Figure A-III. 68. Frontier Kohn-Sham Molecular Orbitals of **100** at B3LYP-D3(BJ)/def2-TZVPP//B3LYP-D3(BJ)/def2-SVP level of theory. Isovalue=0.05 a.u.

HOMO-1	HOMO	LUMO	LUMO+1
ε= -5.99 eV	ε= -5.13 eV	ε= -1.65 eV	ε= -0.40 eV
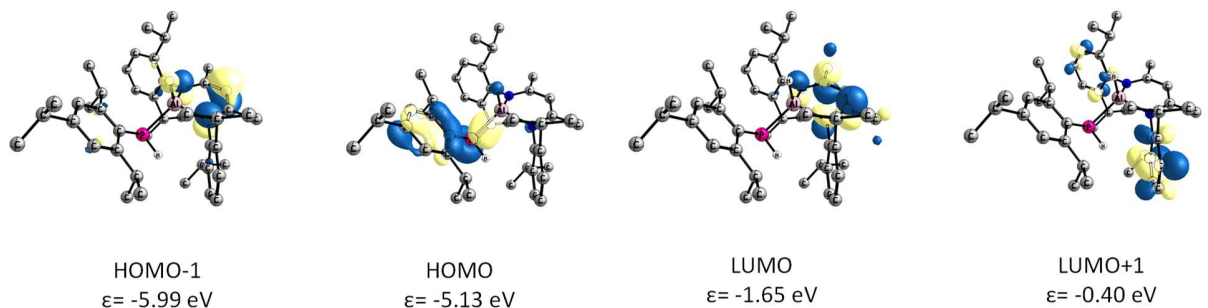
Figure A-III. 69. Frontier Kohn-Sham Molecular Orbitals of **101** at B3LYP-D3(BJ)/def2-TZVPP//B3LYP-D3(BJ)/def2-SVP level of theory. Isovalue=0.05 a.u.

| HOMO-1 | HOMO | LUMO | LUMO+1 |
| ε= -5.96 eV | ε= -5.44 eV | ε= -1.61 eV | ε= -0.48 eV |

Figure A-III. 70. Frontier Kohn-Sham Molecular Orbitals of **102** at B3LYP-D3(BJ)/def2-TZVPP//B3LYP-D3(BJ)/def2-SVP level of theory. Isovalue=0.05 a.u.

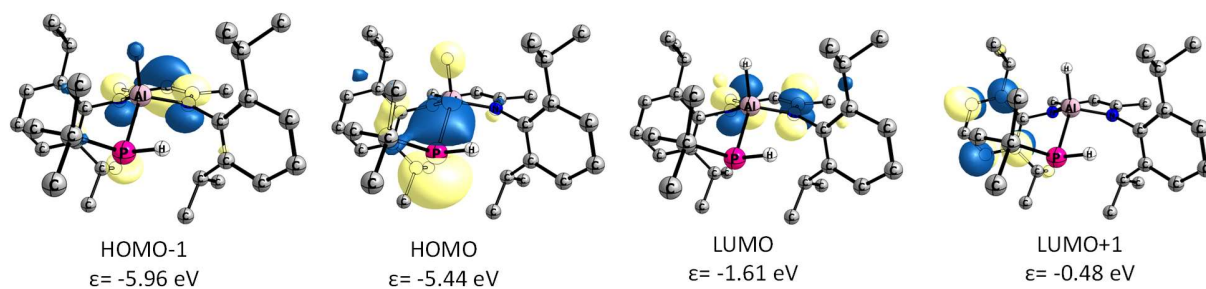| HOMO-2 | HOMO | LUMO | LUMO+1 |
| ε= -5.35 eV | ε= -3.78 eV | ε= -0.65 eV | ε= -0.30 eV |

Figure A-III. 71. Frontier Kohn-Sham Molecular Orbitals of **107** at B3LYP-D3(BJ)/def2-TZVPP//B3LYP-D3(BJ)/def2-SVP level of theory. Isovalue=0.05 a.u.

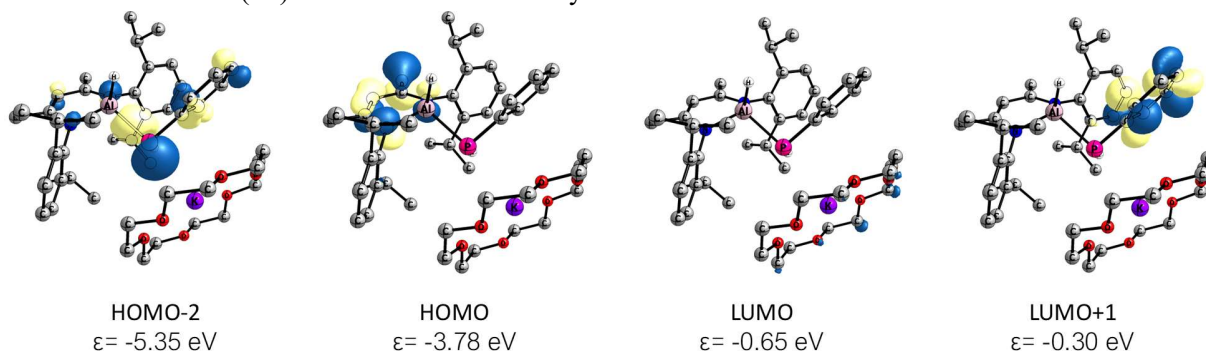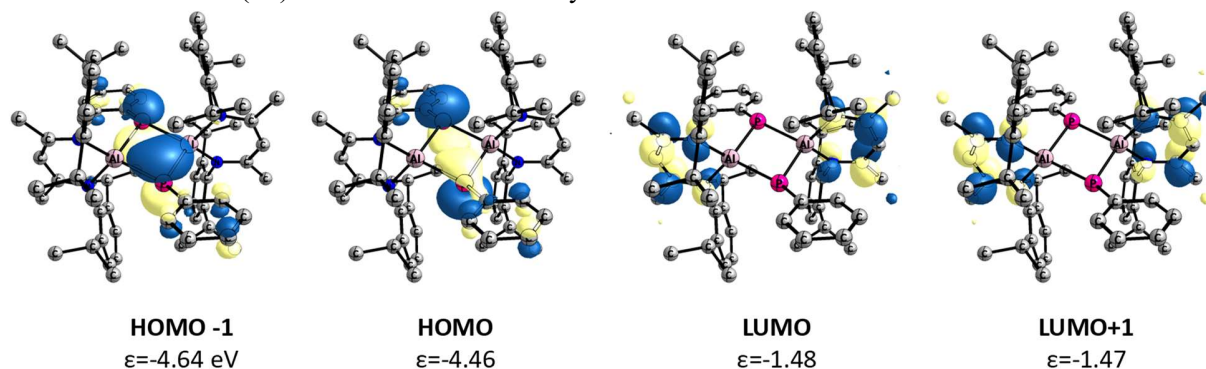| HOMO -1 | HOMO | LUMO | LUMO+1 |
| ε=-4.64 eV | ε=-4.46 | ε=-1.48 | ε=-1.47 |

Figure A-III. 72. Frontier Kohn-Sham Molecular Orbitals of **110** at B3LYP-D3(BJ)/def2-TZVPP//B3LYP-D3(BJ)/def2-SVP level of theory. Isovalue=0.04 a.u.

Table A-III. 3. NPA Charges and WBI of compunds **99, 100, 101, 102, 107** and **110** at B3LYP-D3(BJ)/def2-TZVPP//B3LYP-D3(BJ)/def2-SVP level of theory.

	99	100	101	102	107	110
Q (Al)	1.51	1.50	1.52	1.50	1.57	1.58
Q (P)	-0.15	-0.17	-0.18	-0.22	-0.21	-0.59
WBI (Al-P)	0.71	0.72	0.72	0.71	0.59	0.69/0.73

π- IBOs

Al: 0.05 ; P: 0.87   Al: 0.05 ; P: 0.87

σ- IBOs

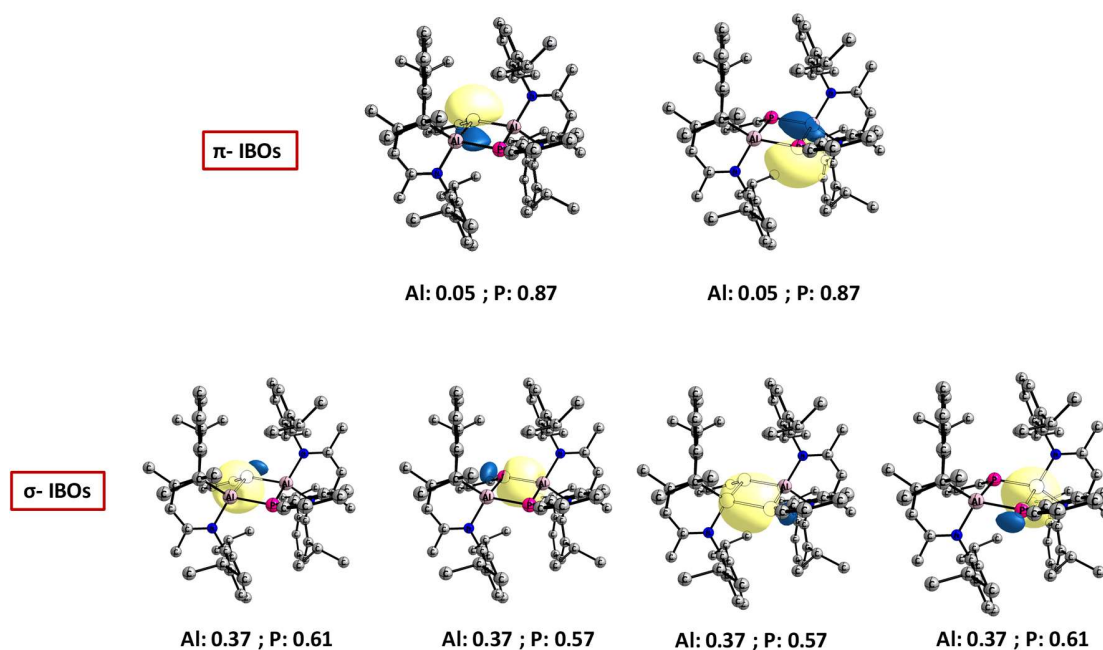Al: 0.37 ; P: 0.61   Al: 0.37 ; P: 0.57   Al: 0.37 ; P: 0.57   Al: 0.37 ; P: 0.61

Figure A-III. 73. Selected IBOs of **110** at B3LYP-D3(BJ)/def2-TZVPP//B3LYP-D3(BJ)/def2-SVP level of theory. Isovalue=0.04 a.u.

Deformation density	[PHPh]$^-$	[NacNacAlH]$^+$

$\Delta E_{orb-\Delta\rho(1)}$=-76.2 ; $|\upsilon_{\alpha\beta}|$=0.84
Δq(PHPh)= -0.34
Δq(NacNacAlH)= +0.34

HOMO (ε=+0.44 eV)
$\upsilon_{\alpha\beta}$=-0.63
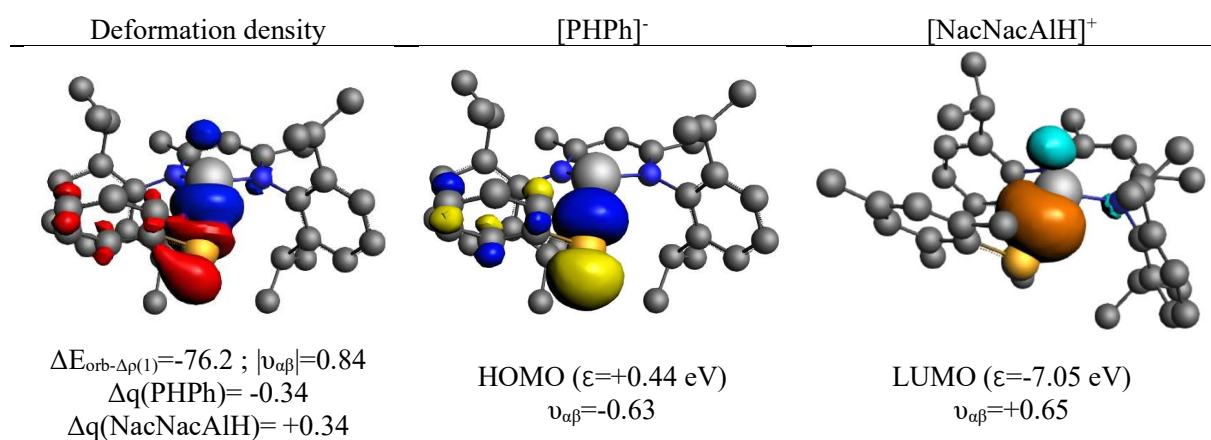
LUMO (ε=-7.05 eV)
$\upsilon_{\alpha\beta}$=+0.65

Figure A-III. 74. Deformation densities $\Delta\rho$ (isovalue 0.003 a.u.) of the pairwise orbital interactions between [NacNacAlH]$^+$ and [PHPh]$^-$ of compound **99**. Associated energies ΔE (in kcal/mol) and eigenvalues ν (in a.u.). The red color shows the charge density accumulation. Shape of the most important interacting occupied and vacant orbitals (isovlaue 0.05 a.u.) of fragments. Hydrogens are omitted for clarity.
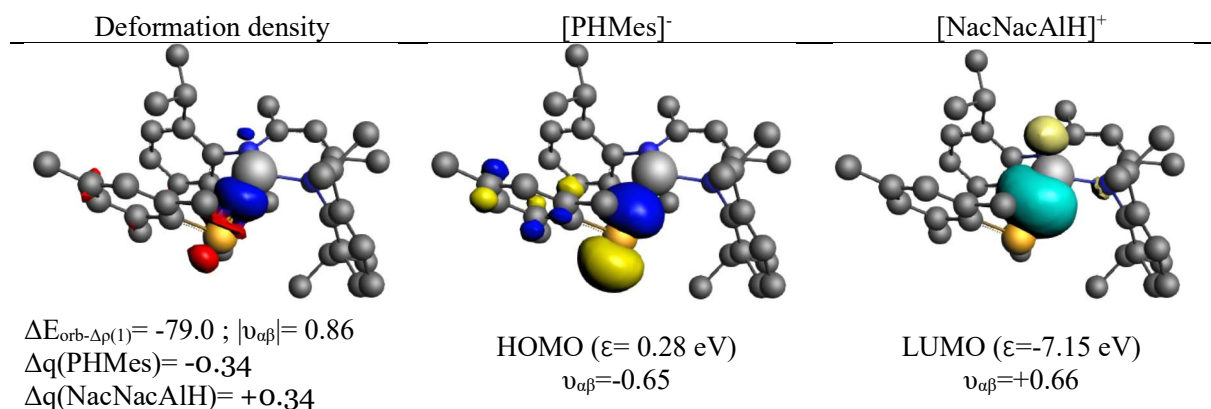
Deformation density	[PHMes]$^-$	[NacNacAlH]$^+$

$\Delta E_{orb-\Delta\rho(1)}$= -79.0 ; $|\upsilon_{\alpha\beta}|$= 0.86
Δq(PHMes)= -0.34
Δq(NacNacAlH)= +0.34

HOMO (ε= 0.28 eV)
$\upsilon_{\alpha\beta}$=-0.65

LUMO (ε=-7.15 eV)
$\upsilon_{\alpha\beta}$=+0.66

Figure A-III. 75. Deformation densities $\Delta\rho$ (isovalue 0.003 a.u.) of the pairwise orbital interactions between [NacNacAlH]$^+$ and [PHMes]$^-$ of compound **100**. Associated energies ΔE (in kcal/mol) and eigenvalues ν (in a.u.). The red color shows the charge density accumulation. Shape of the most important interacting occupied and vacant orbitals (isovlaue 0.05 a.u.) of fragments. Hydrogens are omitted for clarity.
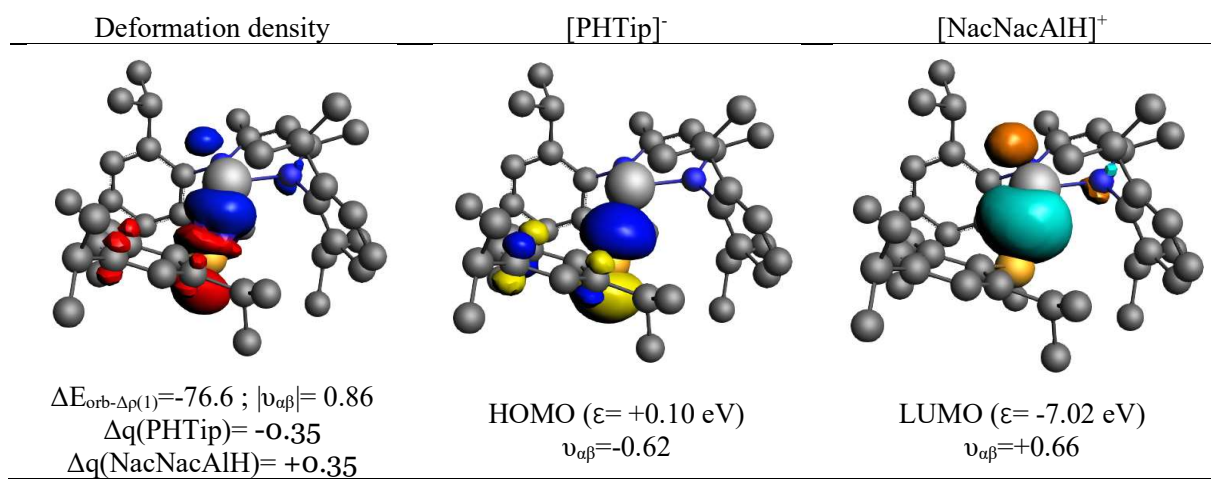
Deformation density	[PHTip]$^-$	[NacNacAlH]$^+$

$\Delta E_{orb-\Delta\rho(1)}$=-76.6 ; $|\upsilon_{\alpha\beta}|$= 0.86
Δq(PHTip)= -0.35
Δq(NacNacAlH)= +0.35

HOMO (ε= +0.10 eV)
$\upsilon_{\alpha\beta}$=-0.62

LUMO (ε= -7.02 eV)
$\upsilon_{\alpha\beta}$=+0.66

Figure A-III. 76. Deformation densities $\Delta\rho$ (isovalue 0.003 a.u.) of the pairwise orbital interactions between [NacNacAlH]$^+$ and [PHPh]$^-$ of compound **101**. Associated energies ΔE (in kcal/mol) and eigenvalues ν (in a.u.). The red color shows the charge density accumulation. Shape of the most important interacting occupied and vacant orbitals (isovlaue 0.05 a.u.) of fragments. Hydrogens are omitted for clarity.
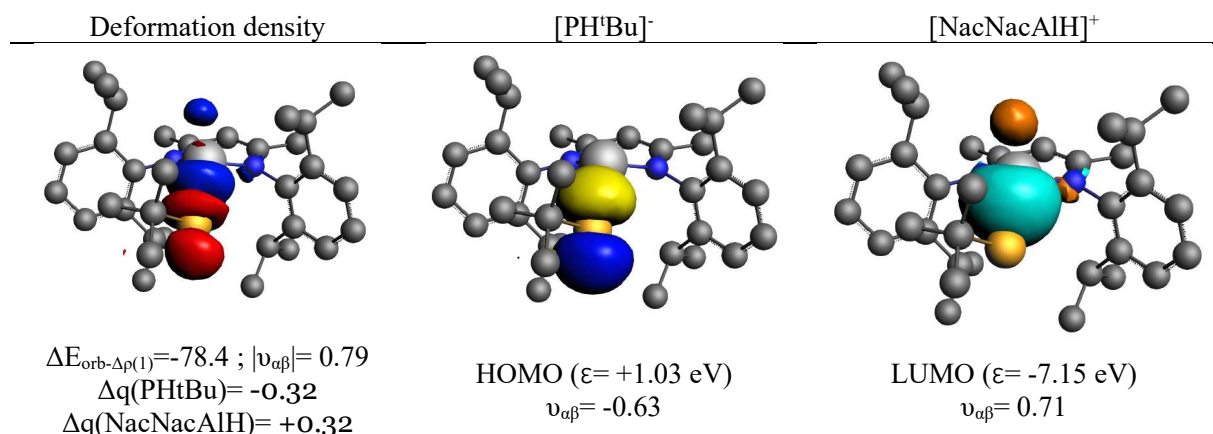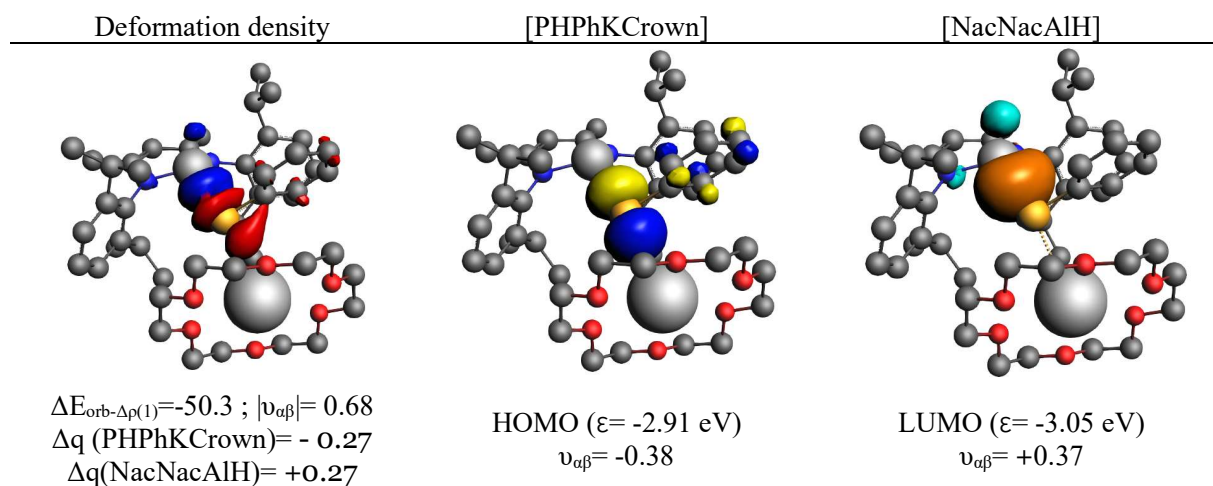
Deformation density	[PHᵗBu]⁻	[NacNacAlH]⁺

$\Delta E_{orb-\Delta\rho(1)}$=-78.4 ; $|\upsilon_{\alpha\beta}|$= 0.79
Δq(PHtBu)= -0.32
Δq(NacNacAlH)= +0.32

HOMO (ε= +1.03 eV)
$\upsilon_{\alpha\beta}$= -0.63

LUMO (ε= -7.15 eV)
$\upsilon_{\alpha\beta}$= 0.71

Figure A-III. 77. Deformation densities $\Delta\rho$ (isovalue 0.003 a.u.) of the pairwise orbital interactions between [NacNacAlH]⁺ and [PHPh]⁻ of compound **102**. Associated energies ΔE (in kcal/mol) and eigenvalues ν (in a.u.). The red color shows the charge density accumulation. Shape of the most important interacting occupied and vacant orbitals (isovlaue 0.05 a.u.) of fragments. Hydrogens are omitted for clarity.

Deformation density	[PHPhKCrown]	[NacNacAlH]

$\Delta E_{orb-\Delta\rho(1)}$=- 50.3 ; $|\upsilon_{\alpha\beta}|$= 0.68
Δq (PHPhKCrown)= - 0.27
Δq(NacNacAlH)= +0.27

HOMO (ε= -2.91 eV)
$\upsilon_{\alpha\beta}$= -0.38

LUMO (ε= -3.05 eV)
$\upsilon_{\alpha\beta}$= +0.37

Figure A-III. 78. Deformation densities $\Delta\rho$ (isovalue 0.003 a.u.) of the pairwise orbital interactions between [NacNacAlH] and [PHPhKCrown] of compound **107**. Associated energies ΔE (in kcal/mol) and eigenvalues ν (in a.u.). The red color shows the charge density accumulation. Shape of the most important interacting occupied and vacant orbitals (isovlaue 0.05 a.u.) of fragments. Hydrogens are omitted for clarity.

APPENDIX IV- Supporting information of Chapter VI

AIV.1 Synthesis of 115
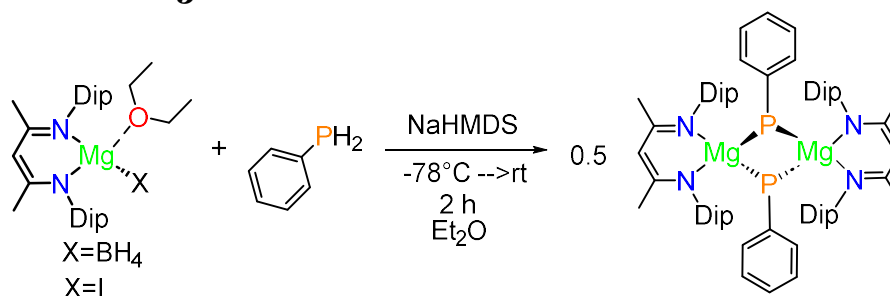
Procedure 1: 200 mg of *NacNac*Mg(Et$_2$O)BH$_4$ are placed in a Schlenk flask and dissolved in 20 mL of Et$_2$O. Then, 0.92 mL of PH$_2$Ph (10% in hexanes) is added dropwise at room temperature. The solution is cooled down to -78°C. Then, a solution of NaHMDS (0.073 g in 10 mL of Et$_2$O) is added dropwise. The solution is stirred for 10 min at -78°C and the Schlenk flask is taken out of the cold bath. The reaction mixture is stirred for 2 hours until it reaches room temperature. The solution is filtered off with a cannula to obtain a pale-yellow solution. The volume is reduced in vacuum until incipient precipitation. The solution is cooled down to -50 °C for two hours where colorless crystals are grown. The resulting solution is kept at -24°C overnight to get a new batch of product (129 mg, 62%). Single crystals were grown from a concentrated solution in Et$_2$O.

Procedure 2: 256 mg of *NacNac*Mg(Et$_2$O)I (0.422 mmol, 1eq) are placed in a Schlenk flask and dissolved in 10 mL of Et$_2$O forming a white slurry solution. Then 0.5 mL of PH2Ph (10% in hexanes) is added dropwise at room temperature. The solution is cooled down to -78°C. Then, a solution of NaHMDS (124 mg in 5mL of Et$_2$O) is added dropwise. The solution is stirred for 10 min at -78°C and the Schlenk flask is removed from the cold bath. The reaction mixture is stirred for 2 hours reaching room temperature. The solution is filtered off with a cannula to obtain a pale-yellow solution. The volume is reduced until incipient precipitation and kept at -50°C for two hours. Compound **115** precipitates as a white solid (126 mg, 57%).

^{1}H-NMR (400.13 MHz, 298 K, THF-d_8): δ(ppm)= 1.17 (t, 48H, C$_{iPr}$-Me), 1.69 (s, 12H, Me(NacNac)), 3.18 (sept, 8H, $^3J_{H-H}$ = 6.57 Hz, C$_{ipr}$-H), 4.91 (s, 2H, C$_\gamma$-H), 6.42(m, 10H, P(H)C$_6$H$_5$), 7.15 (m, 12H, Ar-H). **^{13}C{^{1}H} (100.61 MHz, 298 K, THF-d_8)** δ(ppm)= 23.29 (s, CH$_3$), 23.70 (s, CH$_3$), 27.91 (s, C$_{ipr}$), 94.23 (s, C$_\gamma$), 120.24 (s, C$_{Ar}$-H), 123.48 (s, C$_{Ar}$-H), 124.86 (s, C$_{Ar}$-H), 126.83(s, C$_{Ar}$-H), 126.80, 130.86 (d, C$_{Ar}$-H, J$_{C-P}$=14.71 Hz), 142.15 (s, C$_{ipso}$-Ar), 146.30 (d, J$_{C-P}$=30.21 Hz), 168.48 (s, C$_\beta$-*NacNac*). **^{31}P{^{1}H}-NMR (161.97 MHz, 298 K, THF-d_8):** δ(ppm)= -151.75 (s). **^{31}P-NMR (161.97 MHz, 298 K, THF-d_8):** -151.75 (dt, $^1J_{P-H}$=175.03 Hz, $^3J_{P-H}$=5.89 Hz). **Elemental analysis:** calc.: C: 76.29% H:8.60% N:5.08%, found; C: 76.19%, H: 9.14%, N:5.95%. **Melting point:** >200°C
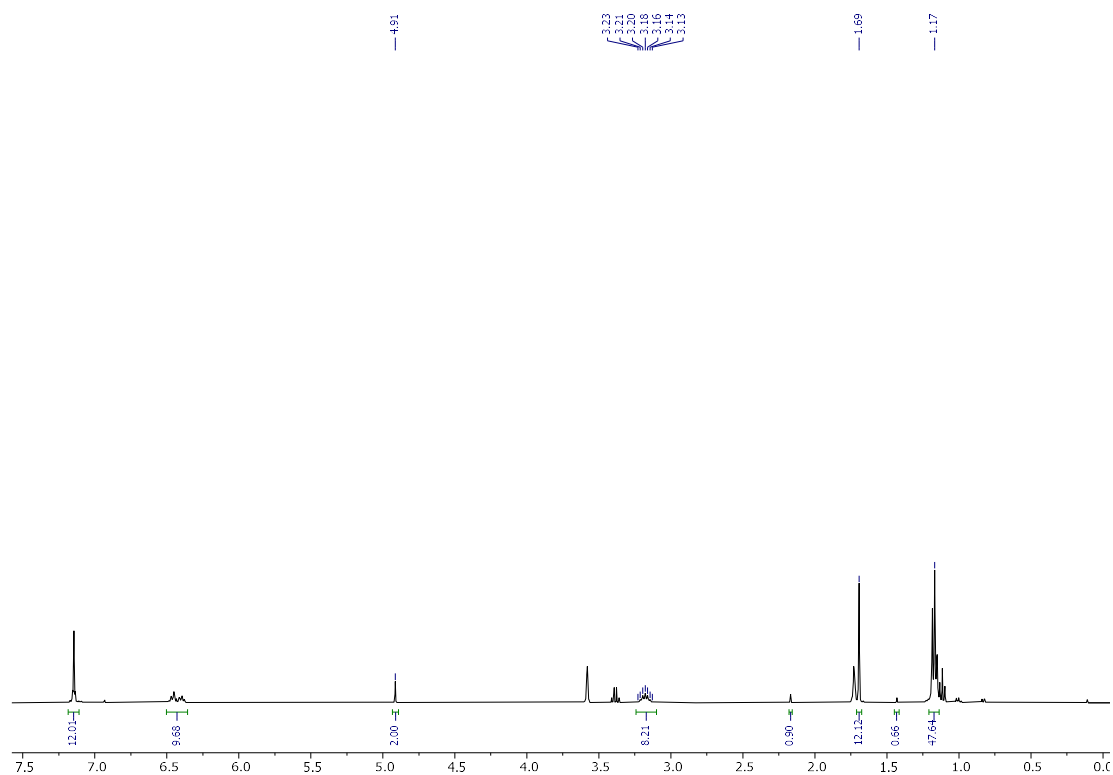
Figure A-IV. 1. ¹H-NMR (400.13 MHz, 298 K, thf-d_8) of compound **115**.
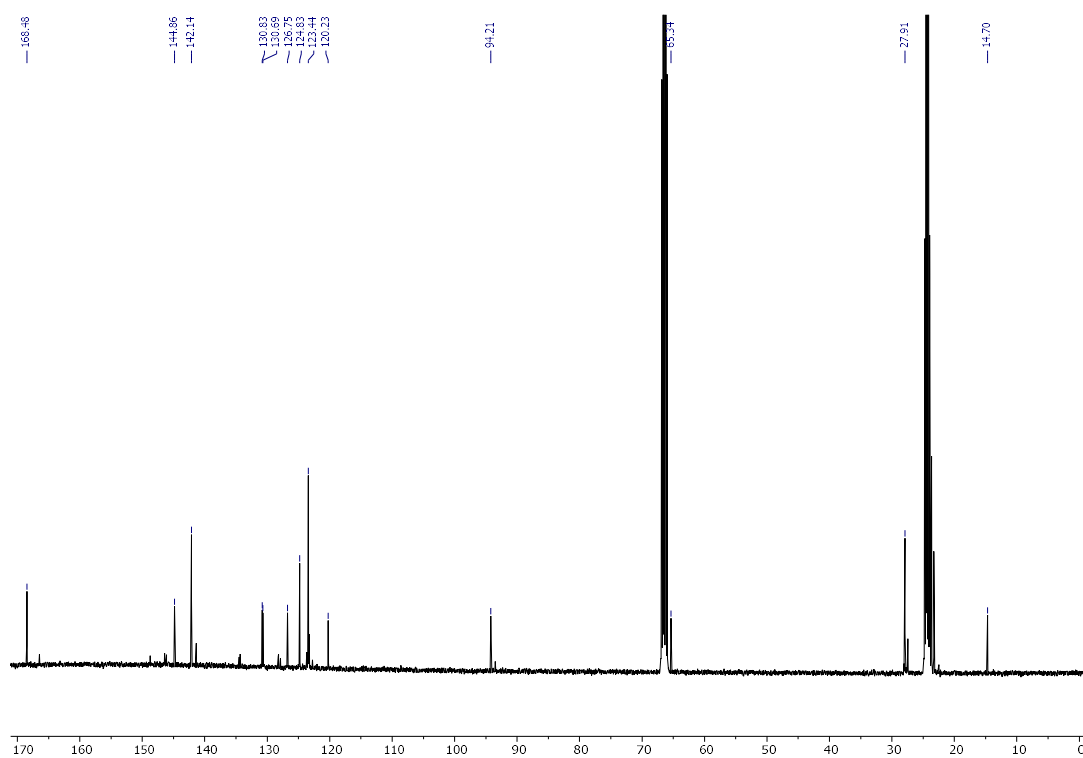
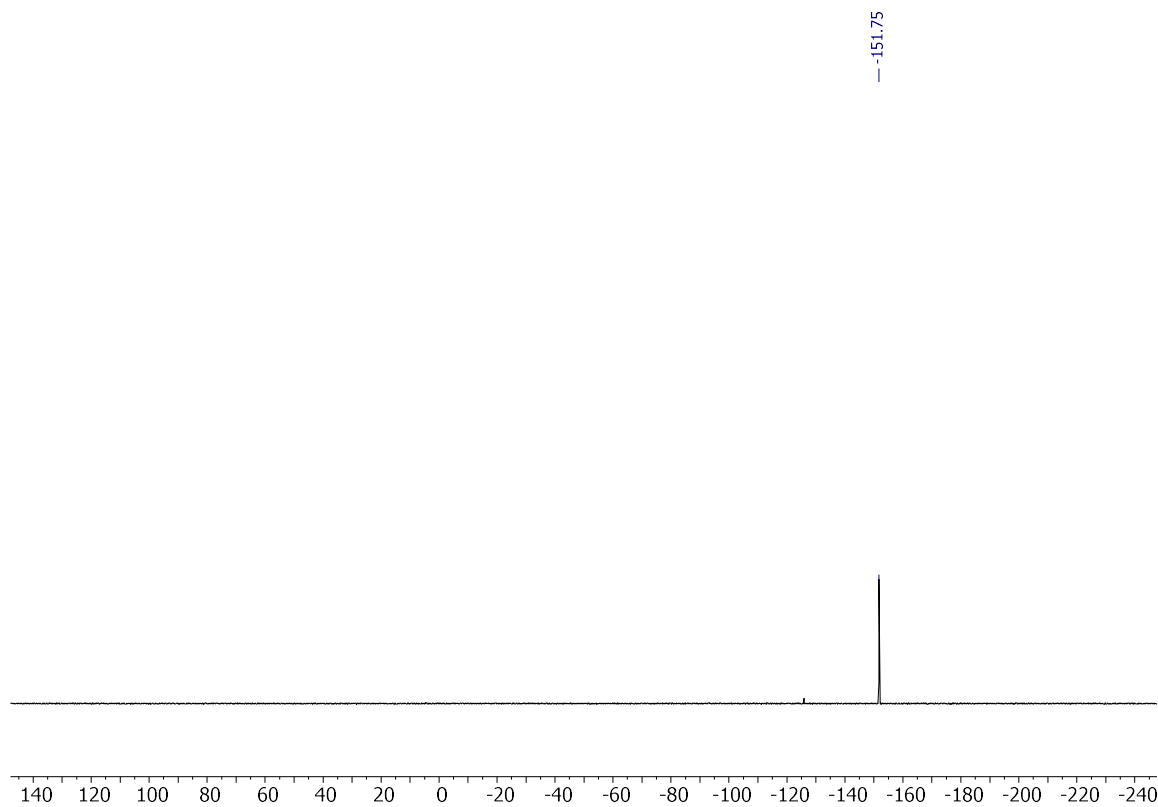Figure A-IV. 2. ¹³C{¹H}-NMR (100.61 MHz, 298 K, thf-d8) of compound **115**.

Figure A-IV. 3. ^{31}P{^{1}H}-NMR (161.97 MHz, 272 K, thf-d$_8$) of compound **115** in benzene-*d$_6$*.
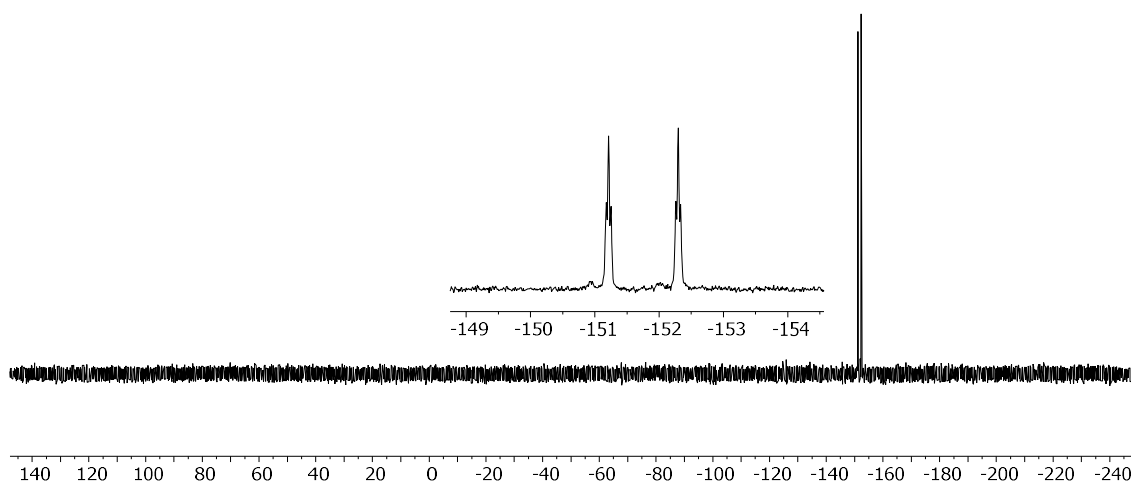

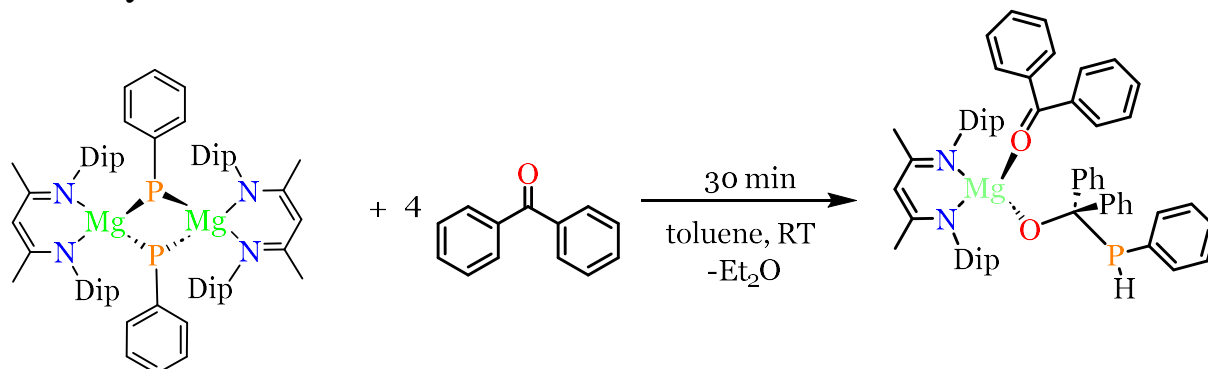Figure A-IV. 4. ^{31}P-NMR (161.97 MHz, 272 K, thf-d$_8$) of compound **115**.

AIV.2 Synthesis of 121

Procedure: In a vial, 40 mg of **110** (1 eq, 0.064 mmol) are dissolved in 2 mL of toluene to form a white slurry solution. Then, a solution of 23 mg (2 eq, 0.128 mmol) in 2 mL of toluene is added dropwise in the absence of light. The reaction crude immediately becomes orange and stirred for 30 min. The solvent is evaporated under vacuum to obtain an orange oil. It is triturated with pentane or hexane to obtain an orange solid. It is filtered off and dried under vacuum. The mother liquors are concentrated and kept in the freezer at -30°C to get another portion of **121**. (26 mg, 44%). Single crystals are obtained from a saturated solution in hexane or pentane at -30°C to obtain block shaped orange crystals.

¹H-NMR (400.13 MHz, 272 K, benzene-d_6): δ(ppm)= 0.70 (bs, 12H, C_{iPr}-<u>Me</u>), 1.33 (bs, 12H, C_{iPr}-<u>Me</u>), 1.74 (s, 6H, <u>Me</u>(NacNac)), 2.80 (bs, 2H, C_{ipr}-<u>H</u>), 3.72 (s, 1H, P-<u>H</u>), 3.78 (bs, 2H, C_{ipr}-<u>H</u>), 5.12 (s, 1H, C_γ-<u>H</u>), 6.93 (m, C_{Ar}-<u>H</u>), 7.16 (m, C_{Ar}-<u>H</u>), 7.45 (bs, 2H, C_{Ar}-<u>H</u>), 7.84 (bs, 4H, C_{Ar}-<u>H</u>). **¹³C{¹H} (100.61 MHz, 272 K, benzene-d_6)** δ(ppm)= 24.19 (s, <u>C</u>H$_3$), 94.39 (s, <u>C</u>$_\gamma$), 123.67 (<u>C</u>$_{Ar}$-H), 124.94 (<u>C</u>$_{Ar}$-H), 126.65 (<u>C</u>$_{Ar}$-H), 135.20 (d, <u>C</u>$_{Ar}$-H, J_{C-P}=13.88 Hz), 138.36 (d, <u>C</u>$_{Ar}$-H, J_{C-P}=29.07 Hz), 146.12 (s,<u>C</u>$_\beta$-*NacNac*). **³¹P{¹H}-NMR (161.97 MHz, 272 K, benzene-d_6):** 10.35 (s), **³¹P-NMR (161.97 MHz, 272 K, benzene-d_6):** 10.35 (d, ¹J_{P-H}=217.57 Hz). **Elemental analysis:** calc : C:80.30 H:7.38 N:3.06; found: C: 79.40 H:7.46 N:3.08. **Melting point:** 138°C (decomposes turning into blue solid).
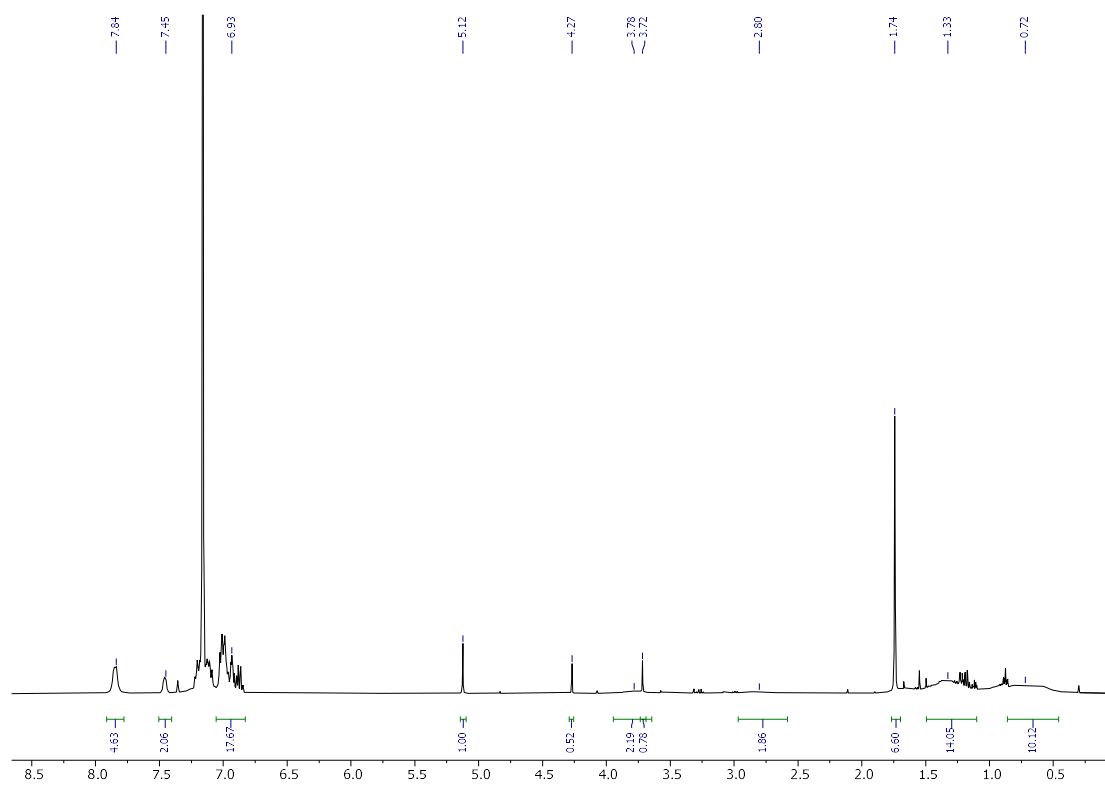
Figure A-IV. 5. ¹H-NMR (400.13 MHz, 293 K, benzene-d_6) of compound **121**.
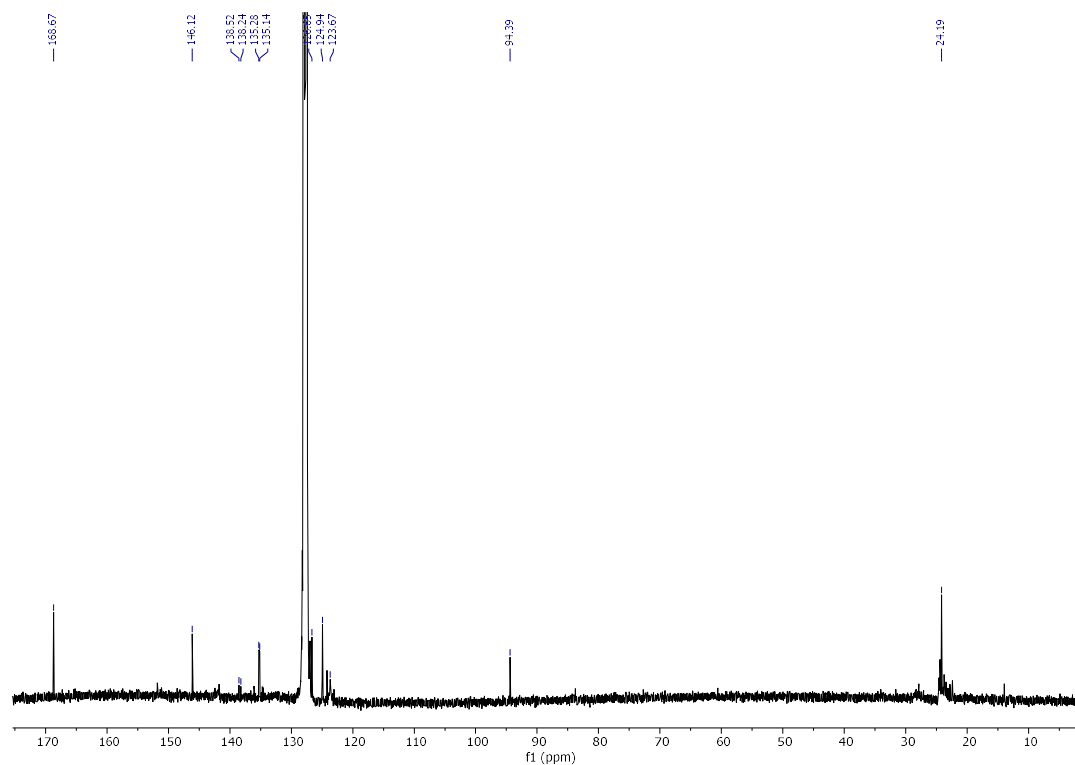
Figure A-IV. 6. ¹³C{¹H}-NMR (100.61, 298K, benzene-d₆) of compound **121**.
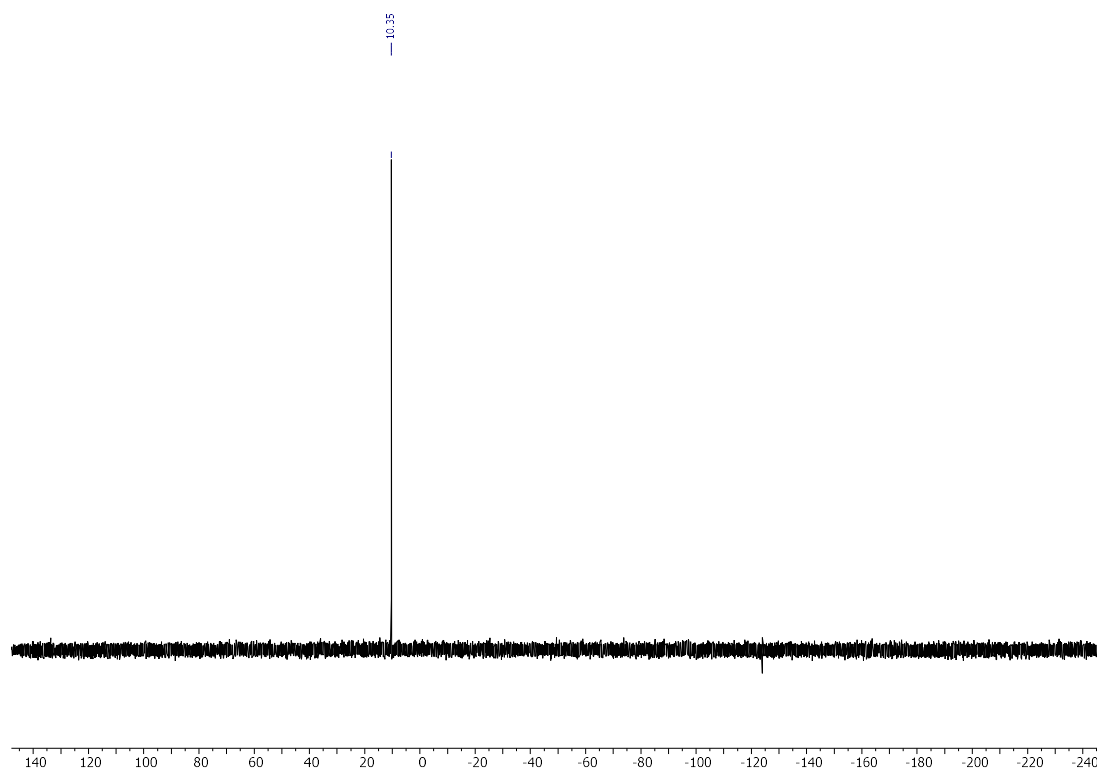
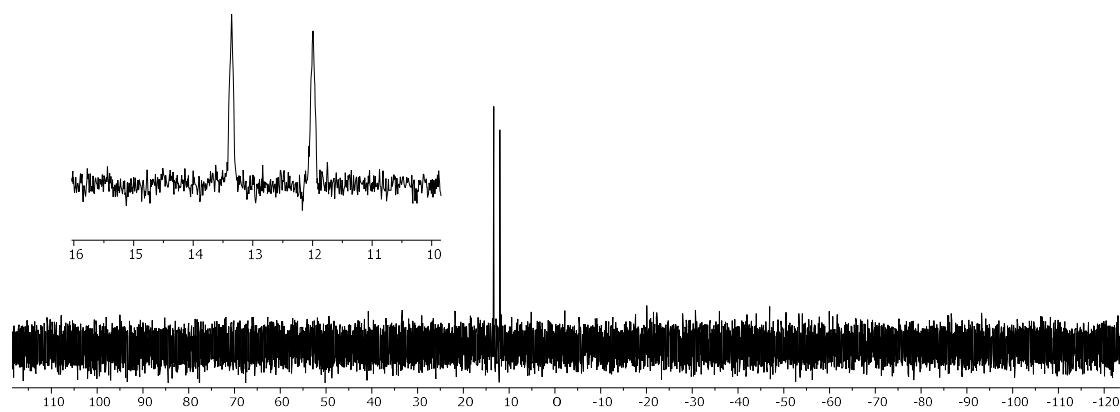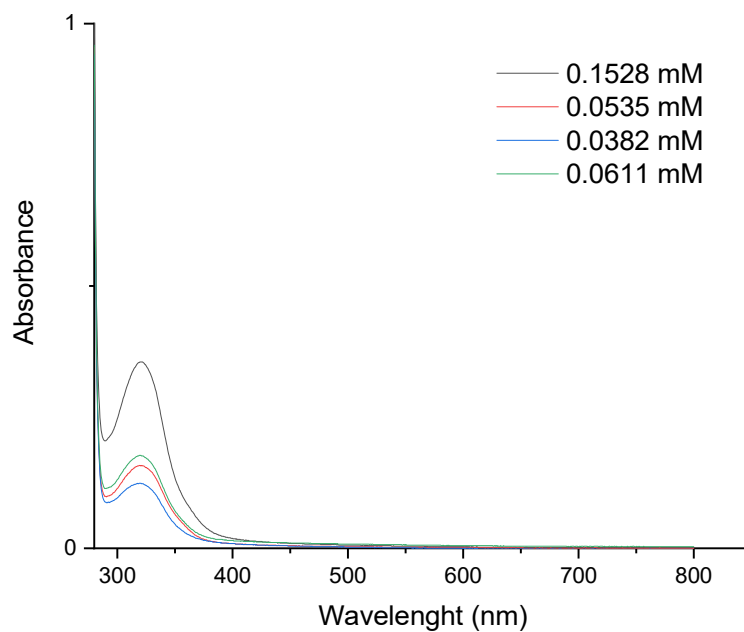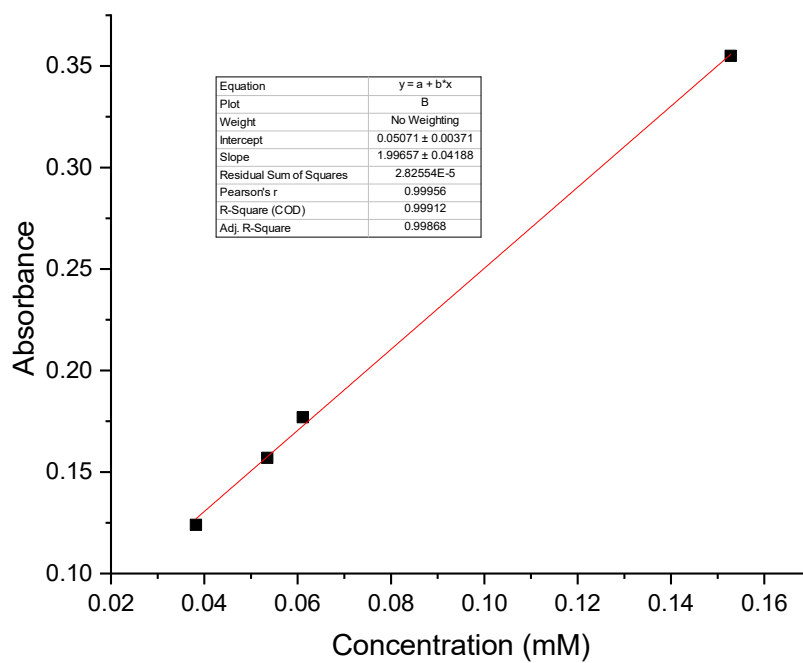Figure A-IV. 7. ^{31}P{^{1}H}-NMR (161.97 MHz, 293 K, benzene-d$_6$) of compound **121.**

Figure A-IV. 8. ^{31}P-NMR (161.97 MHz, 293 K, benzene-d$_6$) of compound **121.**

Figure A-IV. 9. UV-Vis spectra of compound **121** in toluene in different concentrations.

Figure A-IV. 10. Linear regression of compound **121** in toluene at λ= 321 nm.

AIV.3 Crystal data

Table A-IV. 1. Crystal data of compounds **115** and **121**.

Compound	**115**	**121**
Formula	$C_{77}H_{102}Mg_2N_4P_2$	$C_{67}H_{81}MgN_2O_2P$
Crystal system	Triclinic	Monoclinic
Space Group	P-1	$P2_1/c$
Volume (Å³)	1738.25(19)	5861.7(3)
a	11.3979(7)	21.4905(7)
b	13.4553(8)	16.6324(5)
c	13.8842(9)	17.2806(5)
α	100.912(2)	90
β	114.038(2)	108.3800(10)
γ	107.101(2)	90
Z	1	4
Formula weight (g/mol)	1194.18	1001.61
Density (g/mL)	1.141	1.135
Absorption coefficient (mm⁻¹)	0.125	0.102
F(000)	646	2160
Temperature (K)	154(2)	143(2)
Total numb. Reflections	24430	2160
Final R indices [I>2σ(l)]	R1 = 0.0442, wR2 = 0.0968 R1 = 0.0811, wR2 = 0.1126	R1 = 0.0505, wR2 = 0.1174 R1 = 0.0721, wR2 = 0.1318
Largest diff. Peak and hole (e·A⁻³)	0.274 and -0.297	0.485 and -0.449
GoF	1.015	1.048

*Refinament details for **110**:* All non H-atoms were located in the electron density maps and refined anisotropically. C-bound H atoms were placed in positions of optimized geometry and treated as riding atoms. Their isotropic displacement parameters were coupled to the corresponding carrier atoms by a factor of 1.2 (CH,) or 1.5 (CH3). The P bonded H-atom was located on the electron density maps and its positional parameters were refined using isotropic displacement parameters which were set at 1.2 times the Ueq value of the phosphorous atom.
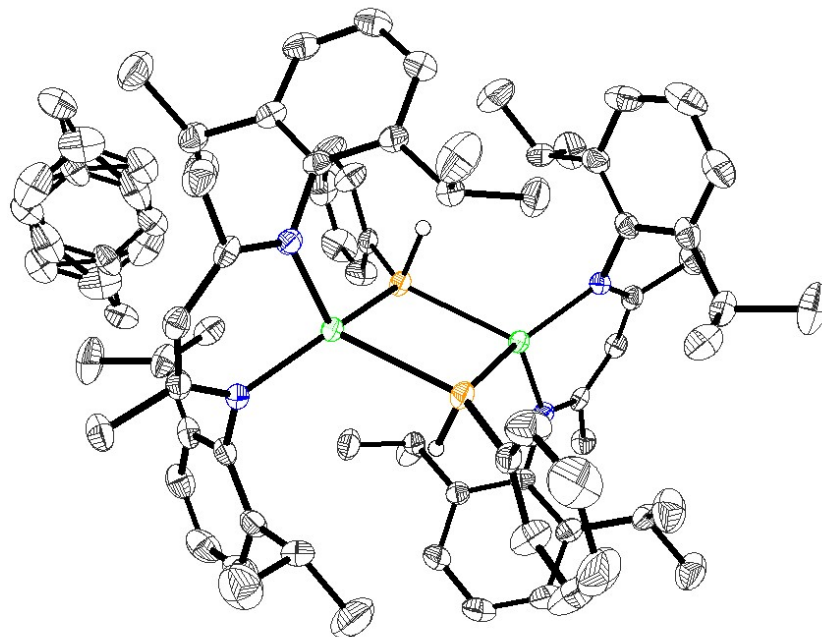
*Refinament details for **121**:* All non H-atoms were located in the electron density maps and refined anisotropically. C-bound H atoms were placed in positions of optimized geometry and treated as riding atoms. Their isotropic displacement parameters were coupled to the corresponding carrier atoms by a factor of 1.2 (CH, CH_2) or 1.5 (CH_3). The P bonded H-atom was located in the electron density maps. Its positional parameters were refined using isotropic displacement parameters which were set at 1.2 times the U_{eq} value of P1.
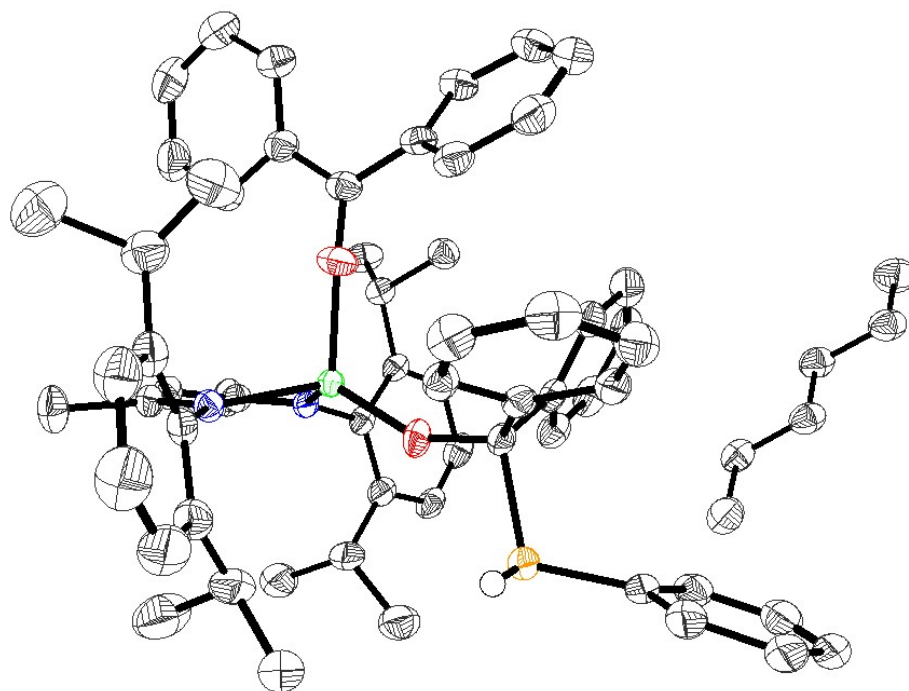
AIV.4 EPR studies

In an quartz tube, 4 mg of **121** are dissolved in 4 ml of toluene. Then, the decomposition is followed by ^{31}P-NMR and EPR in the absence of light and with UV-irradiation.

Table A-IV. 2 EPR data of the decomposition of **121** in the dark.

time (min)	g	Amplitude	Width	Double int	[R] (µM)
0	2.0032	380.93	0.6423	157.2	10.2
5	2.0032	609.42	0.6473	255.3	16.6
10	2.0029	881.84	0.6283	348.1	22.6
20	2.0028	1219.78	0.6425	503.5	32.7
30	2.0028	1191.06	0.6528	507.6	32.9
50	2.0029	2457.12	0.635	990.8	64.3
60	2.0028	3017.42	0.6438	1250.7	81.1
80	2.0029	3062.03	0.6335	1228.9	79.7
110	2.0029	5282.88	0.6421	2178.1	141.3
140	2.0029	6186.29	0.6393	2528.4	164.0
170	2.0029	7440.07	0.6348	2998.1	194.5
200	2.0029	7427.83	0.6358	3002.6	194.8
230	2.0029	9183.53	0.6328	3677.4	238.6

Table A-IV. 3. EPR data of the decomposition of **121** under UV light.

time (min)	g	Amplitude	Width	Double int	[R] (mM)
0	2.0033	124.45	0.6049	45.5	0.0
1	2.0032	98621.18	0.6255	38585.6	2.5
3	2.0029	212704.37	0.6250	83087.6	5.4
5	2.0029	373814.33	0.6085	138413.1	9.0
10	2.0029	577105.43	0.5920	202254.7	13.1
20	2.0029	810869.10	0.5745	267627.5	17.4
30	2.0029	939636.54	0.5690	304217.7	19.7
40	2.0029	997627.18	0.5490	300685.8	19.5
50	2.0029	1039045.25	0.5635	329930.4	21.4
60	2.0030	1069977.97	0.5515	325436.2	21.1
70	2.0029	1075424.05	0.5543	330422.4	21.4
80	2.0029	1044803.83	0.5515	317779.4	20.6

AIV.5 Computational studies

Table A-IV. 4 Relative energies of the of the C-P scan in the singlet and triplet electronic states at the uωB97XD/def2-TZVPP// uωB97XD/def2-SVP level of theory.

C-P Distance (Å)	$\Delta E^{singlet}$ (kcal/mol)	$\Delta E^{triplet}$ (kcal/mol)
1.966	0.0	45.2
2.116	3.1	49.3
2.266	8.0	46.8
2.416	13.1	44.1
2.566	17.7	41.4
2.716	21.4	38.7
2.866	24.4[a] (24.5)[b]	36.8
3.016	26.4[a] (26.9)[b]	34.1
3.166	27.7[a] (27.9)[b]	32.7

[a]Energy of the Open Shell Singlet solution [b]Energy of the Closed Shell Singlet solution.

Table A-IV. 5 Partial charges along the C-P scan in the singlet electronic state using TFVC atomic partition at the uωB97XD/def2-TZVPP// uωB97XD/def2-SVP level of theory.

C-P Distance (Å)	Q(PHPh)	Q(Benzophenone1)	Q(benzophenone2)	Q(NacNacMg)
1.966	0.22	-1.05	0.06	0.75
2.116	0.06	-0.90	0.06	0.75
2.266	-0.04	-0.81	0.06	0.75
2.416	-0.12	-0.73	0.06	0.76
2.566	-0.21	-0.65	0.07	0.75
2.716	-0.27	-0.58	0.07	0.76
2.866	-0.28[a] (-0.35)[b]	-0.56[a] (-0.50)[b]	0.06[a] (0.06)[b]	0.76[a] (0.76)[b]
3.016	-0.24[a] (-0.42)[b]	-0.61[a] (-0.43)[b]	0.06[a] (0.06)[b]	0.76[a] (0.76)[b]
3.166	-0.19[a] (-0.31)[b]	-0.65[a] (-0.54)[b]	0.06[a] (0.06)[b]	0.76[a] (0.76)[b]

[a]Energy of the Open Shell Singlet solution [b]Energy of the Closed Shell Singlet solution.

Table A-IV. 6. Relative and absolute energies of the of the C-P scan in the singlet and triplet electronic states at the uωB97XD/def2-TZVPP// uωB97XD/def2-SVP level of theory.

C-P Distance (Å)	Singlet		Triplet	
	E(Ha)	ΔE (kcal/mol)	E(Ha)	ΔE (kcal/mol)
1.938	-2309.156	0.00	-2309.09	40.17
1.988	-2309.155	0.31	-2309.09	40.58
2.088	-2309.152	2.35	-2309.09	40.58
2.138	-2309.149	3.83	-2309.09	43.17
2.188	-2309.147	5.48	-2309.08	44.70
2.238	-2309.144	7.23	-2309.07	53.14
2.288	-2309.141	9.05	-2309.07	52.35
2.338	-2309.138	10.90	-2309.07	51.55
2.388	-2309.135	12.74	-2309.07	50.70
2.438	-2309.132	14.64	-2309.08	49.80
2.488	-2309.129	16.39	-2309.08	47.87
2.538	-2309.127	18.07	-2309.08	46.88
2.638	-2309.122	21.22	-2309.08	49.80
2.738	-2309.117	24.06	-2309.08	47.87
2.838	-2309.113	26.63	-2309.08	46.88